The Dissertation Committee for Jeremy James Jagodzinski certifies that this is the approved version of the following dissertation:

A Diode Laser-Based Velocimeter Providing Point Measurements in Unseeded Flows Using Modulated Filtered Rayleigh Scattering (MFRS)

Committee:

Philip L. Varghese, Supervisor

David S. Dolling

Noel T. Clemens

Laxminarayan L. Raja

Matthew J. Hall

A Diode Laser-Based Velocimeter Providing Point Measurements in Unseeded Flows Using Modulated Filtered Rayleigh Scattering (MFRS)

by

Jeremy James Jagodzinski, B.S.

Dissertation

Presented to the Faculty of the Graduate School of

The University of Texas at Austin

in Partial Fulfillment

of the Requirements

for the Degree of

Doctor of Philosophy

The University of Texas at Austin

December, 2007

To Christi Greene

Acknowledgements

It has been a privilege and honor for me to have received my education at the University of Texas at Austin. I consider myself particularly fortunate to have worked with and learned from the exceptional faculty in the Department of Aerospace Engineering. My advisor in the department, Dr. Philip Varghese, provided interminable support of my bumpy progress these past nine years, offering patient guidance when solicited, experimental insight when needed, and riveting conversation whenever I wanted to talk. To paraphrase Sir Isaac Newton, if I have seen further it is surely by standing on the shoulders of Dr. Philip Varghese. I also gained invaluable insight into my research from Dr. Noel Clemens. His gracious manner brought me solace when I was stymied by some aspect of my experiment and his uncanny ability to see straight to the heart of the problem was absolutely indispensable. I have always appreciated the quick wit and academic integrity of Dr. David Dolling. He's a first-rate engineer, teacher, and human being and someone I have always looked up to. Though I had limited personal interaction with the other members of my committee, Dr. Laxminarayan Raja and Dr. Matthew Hall, I am honored by their participation in my Ph.D. defense and thankful for their time. I would also like to thank Dr. David Goldstein for his encouragement and for the enticing offer to study computational fluid dynamics, Dr. Hans Mark for inspiring me to pursue experimental research, Dr. Armand Chaput for his friendship and fellowship, and Drs. Karl Schulz, Manfred Fink, Dennis Deppe, and Paul Danehy for their help and insight.

The Department of Aerospace Engineering at the University of Texas has an extremely talented support staff. Frank Wise was my go-to-guy anytime I had a question concerning electronics. Scott Messec was my go-to-guy anytime I had a question concerning computers. By far the biggest benefit I received from both of these gentlemen, however, was their friendship; I will sorely miss taking lunch breaks with Scott and smoke breaks with Frank. As a nuts-and-bolts kind of guy it was hard for me to stay out of the Aerospace Machine Shop. As the person in charge of that facility, Rick Maldonado always made me feel right at home and always took time out of his busy schedule to offer a helping hand. Donna Soward ensured that the equipment I needed for my experiment was forthcoming and always offered up a tasty treat and some kind words when I was beating down her door. I would also like to thank Nita Pollard, Bonnie Northcutt, and Tina Woods for their administration and encouragement.

Besides offering unwavering financial support of my education, my Mom and Dad and Grandma and Grandpa have always demonstrated boundless patience, thoughtful encouragement, and unconditional love. These remarkable people are my touchstones, and each is in their own way a personal hero of mine. There is simply no doubt in my mind… I was blessed with the best Mom and Dad and Grandma and Grandpa ever. There is no way I could have written this dissertation without them. I am doubly blessed for the family I have in Texas and damn lucky for the life I found with Christi Greene. Christi is the love of my life and my best friend, a woman of genuine kindness, boundless creativity, and powerful intellect. She offered me endless encouragement when I needed it most – thank you for your patience – and continues to introduce me to the happiest moments imaginable – thank you for your love. The love and kindness of Kim, Stacey, and Barbara Greene helped to soften my edges and the experience. Oso and Abby offered constant companionship and happy distractions during the writing of this dissertation. I would also like to thank my sister Jessie for her love, my Great Uncle Jim for his example, Bob for loving my Mom, Margie for loving my Dad, and my Uncle Paul for his help machining the converging nozzle.

All work and no play… well, it's just plain boring. I have been and continue to be blessed by an incredible group of friends. I would like to thank Bert and Kate, Don and Heidi, Lanny and Bob, Kira and John, Doc and Judy, Karl and Judy, Carl, Steph, Dylan, James, Jim, Stew, Pruitt, Fred, Malachy, Jeff, Christiaan, Rob, and Paul for the encouragement and good-times offered by each. I would like to thank my cycling buds for getting me outside on so many beautiful days, and AJ for his friendship and funding.

Finally, I would like to thank the National Aeronautics and Space Administration (NASA grant NAG3-2240), the National Science Foundation (NSF grant CTS-9871249), and the School of Engineering (Thrust Fellowship) for the financial support offered by each.

A Diode Laser-Based Velocimeter Providing Point Measurements in Unseeded Flows Using Modulated Filtered Rayleigh Scattering (MFRS)

Publication No. ___________________

Jeremy James Jagodzinski, PhD.
The University of Texas at Austin, 2007

Supervisor: Philip L. Varghese

The development to date of a diode-laser based velocimeter providing point-velocity-measurements in unseeded flows using molecular Rayleigh scattering is discussed. The velocimeter is based on modulated filtered Rayleigh scattering (MFRS), a novel variation of filtered Rayleigh scattering (FRS), utilizing modulated absorption spectroscopy techniques to detect a strong absorption of a relatively weak Rayleigh scattered signal. A rubidium (Rb) vapor filter is used to provide the relatively strong absorption; alkali metal vapors have a high optical depth at modest vapor pressures, and their narrow linewidth is ideally suited for high-resolution velocimetry. Semiconductor diode lasers are used to generate the relatively weak Rayleigh scattered signal; due to their compact, rugged construction diode lasers are ideally suited for the environmental extremes encountered in many experiments.

The MFRS technique utilizes the frequency-tuning capability of diode lasers to implement a homodyne detection scheme using lock-in amplifiers. The optical frequency of the diode-based laser system used to interrogate the flow is rapidly modulated about a reference frequency in the D_2-line of Rb. The frequency modulation is imposed on the Rayleigh scattered light that is collected from the probe volume in the flow under investigation. The collected frequency modulating Rayleigh scattered light is transmitted through a Rb vapor filter before being detected. The detected modulated absorption signal is fed to two lock-in amplifers synchronized with the modulation frequency of the source laser. High levels of background rejection are attained since the lock-ins are both frequency and phase selective. The two lock-in amplifiers extract different

Fourier components of the detected modulated absorption signal, which are ratioed to provide an intensity normalized frequency dependent signal from a single detector.

A Doppler frequency shift in the collected Rayleigh scattered light due to a change in the velocity of the flow under investigation results in a change in the detected modulated absorption signal. This change in the detected signal provides a quantifiable measure of the Doppler frequency shift, and hence the velocity in the probe volume, provided that the laser source exhibits acceptable levels of frequency stability (determined by the magnitude of the velocities being measured). An extended cavity diode laser (ECDL) in the Littrow configuration provides frequency tunable, relatively narrow-linewidth lasing for the MFRS velocimeter. Frequency stabilization of the ECDL is provided by a proportional-integral-differential (PID) controller based on an error signal in the reference arm of the experiment. The optical power of the Littrow laser source is amplified by an antireflection coated (AR coated) broad stripe diode laser. The single-mode, frequency-modulatable, frequency-stable O(50 mW) of optical power provided by this extended cavity diode laser master oscillator power amplifier (ECDL-MOPA) system provided sufficient scattering signal from a condensing jet of CO_2 to implement the MFRS technique in the frequency-locked mode of operation.

Table of Contents

List of Tables……………………………………………………………………………xi

List of Figures…………………………………………………………………………....xii

Chapter 1: Introduction…………………………………………………………………1

Chapter 2: Laser Anemometry…………………………………………………………..4

2.1 Introduction……………………………………………………………………..4

2.2 Particle Tracking Anemometers…………………………………………………...7

2.3 Laser Doppler Anemometers……………………………………………………12

2.3.1 Laser Doppler Velocimetry (LDV)……………………………………….14

2.3.2 Interferometric Laser Doppler Anemometry (I-LDA)……………………………21

2.3.3 Planar Doppler Velocimetry (PDV)…………………………………………31

2.3.4 Competing Research……………………………………………………...34

Chapter 3: Modulated Filtered Rayleigh Scattering (MFRS)…………………………...37

3.1 Introduction……………………………………………………………………..37

3.2 Rayleigh Scattering……………………………………………………………..40

3.3 Absorption Spectroscopy………………………………………………………70

3.3.1 The Einstein Coefficients………………………………………………72

3.3.2 The Hyperfine Structure of Rubidium…………………………………………83

3.3.3 Theoretical Model of the D_2-Line of Rb in Natural Isotopic Abundance………...89

3.3.4 A Heuristic Model of the Doppler Broadened ***F***=3 Ground State Transition of ^{85}Rb in the D_2-Line of Rb in Natural Isotopic Abundance……...94

3.4 A Description of Modulated Absorption Spectroscopy from the Temporal Perspective………………………………………..102

3.5 Noise……………………………………………………………………………154

3.5.1 Shot Noise…………………………………………………………………...155

3.5.2 Johnson Noise………………………………………………………………160

3.5.3 RAM-Induced Noise………………………………………………………...160

3.5.4 Laser Excess Noise…………………………………………………………162

3.6 Theoretical Signal-to-Noise Ratio of Preliminary MFRS Measurements………………163

Chapter 4: Practical Implementation of the MFRS Velocimeter……………………………..173
4.1 Introduction…………………………………………………………………………..173
4.2 The Sweep Mode of Operation………………………………………………………174
4.3 The Frequency-Locked Mode of Operation…………………………………………185
4.3.1 The Ratioed Detection Scheme……………………………………………...188
4.3.2 Frequency Stabilization……………………………………………………..192
4.3.3 Optical Power Amplification………………………………………………..205
4.3.4 Frequency-Locked MFRS Velocity
Measurements in a Supersonic Expansion of CO_2……………………………210
Chapter 5: Conclusions…………………………………………………………………….220
Appendix A: A General Discussion of Lock-In Amplifiers……………………………………221
A.1 Introduction…………………………………………………………………………221
A.2 Simple Description of Homodyne Detection Utilizing a Lock-In Amplifier…………..222
A.3 Equivalent Noise Bandwidth (ENBW) of a Lock-In Amplifier………………………..223
Appendix B: Classical Theory of Atomic Absorption…………………………………………..230
Appendix C: Gain Characteristics of the R636-10 PMT………………………………………..239
Appendix D: Vapor Pressure…………………………………………………………………245
Appendix E: A Description of Modulated Absorption
Spectroscopy from the Spectral Perspective…………………………………...248
Appendix F: Laser Beam Propagation and Transformation……………………………………260
F.1 Mathematical Representation of a Propagating Laser Beam…………………………...260
F.2 Thin-Lens, Paraxial Theory of Gaussian Beam Transformation………………………271
Appendix G: Development of the Coupling Optics for the BAL MOPA System………………275
References…………………………………………………………………………………….292
Vita……………………………………………………………………………………………299

List of Tables

Table 3.1 Known or estimated experimental parameters for the simple Rayleigh scattering experiment illustrated in Figure 3.5 and discussed above………………59

Table 3.2 Magnetic dipole and electric quadrupole coupling constants of the $5^2S_{1/2}$ ground state and the $5^2P_{3/2}$ excited state of ^{85}Rb and ^{87}Rb…………85

Table 3.3 Transition probabilities for hyperfine transitions in the D_2-line of ^{85}Rb and ^{87}Rb…...88

Table 3.4 Fundamental physical constants……………………………………………………...93

Table 3.5 Physical and optical properties of Rb………………………………………………...93

Table 3.6 Summary of theoretical models used to predict the first- and second-harmonic lock-in signals detected from molecular Rayleigh scattering during preliminary MFRS experiments……………145

Table 3.7 Instrumental parameters describing preliminary frequency-locked MFRS measurements utilizing molecular Rayleigh scattering from air…………...146

Table A.1 ENBWs of one-, two-, three-, and four-pole low-pass RC-filters…………………...229

List of Figures

Figure 2.1 PIV system……………………………………………………………………..8

Figure 2.2 PIV image processing………………………………………………………..9

Figure 2.3 Illustrating the Doppler effect…………………………………………………13

Figure 2.4 Schematic of reference beam LDV……………………………………………15

Figure 2.5 Schematic of differential LDV…………………………………………………18

Figure 2.6 Interference pattern in probe volume of differential LDV…………………..20

Figure 2.7 Demonstrating inadequacies of the fringe model…………………………..20

Figure 2.8 The planar FPI……………………………………………………………………21

Figure 2.9 Airy pattern for planar FPI……………………………………………………..23

Figure 2.10 The confocal FPI……………………………………………………………...25

Figure 2.11 Interferometric LDA – Operational mode #1…………………………………26

Figure 2.12 Airy pattern for a confocal FPI as a function of aperture size……………...27

Figure 2.13 PDV experimental arrangement………………………………………………31

Figure 2.14 Iodine absorption profile in the range of a frequency-doubled Nd:YAG…………..32

Figure 2.15 Correlating the Doppler frequency shift to the change in detected intensity………33

Figure 2.16 Illustration of modulated absorption spectroscopy……………………………34

Figure 3.1 Generic FRS experimental setup……………………………………………….38

Figure 3.2 Linear electric dipole under the influence of an external electric field……………...41

Figure 3.3 Illustration of the scattering geometry for the MFRS velocimeter…………………..45

Figure 3.4 Illustrating the effects of aberrations on the detected Rayleigh scattered power……49

Figure 3.5 Simple Rayleigh scattering experiment………………………………………...55

Figure 3.6 Manufacture specifications of uniformity of PMT radiant sensitivity
along the X- and Y-axis of the PMT photocathode at V_{PMT}=90 V…………………56

Figure 3.7 Measured y-axis and z-axis spatial intensity profiles of probe laser beam…………56

Figure 3.8 A sample of voltages measured with the
probe laser beam vertically and horizontally polarized…………………………….58

Figure 3.9 A sample of voltages measured with a vertically polarized probe
laser beam blocked up beam of the probe volume versus unblocked……………...61

Figure 3.10 Spectral profiles of Rayleigh scattered light at various *Y*-parameters……………...68

Figure 3.11 The Doppler broadened D_2-line of Rb
in natural isotopic abundance at room temperature……………………………...71

Figure 3.12 Generic two-level atomic transition……………………………………………..72
Figure 3.13 Hyperfine energy splitting within D_2-line of ^{85}Rb…………………………………86
Figure 3.14 Hyperfine energy splitting within D_2-line of ^{87}Rb…………………………………87
Figure 3.15 Direct absorption measurement of D_2-line of isotopic Rb made through z=100 mm vapor cell at T=20.8 °C compared to simulated D_2-line of isotopic Rb……………………94
Figure 3.16 Pictorial description of maximum modulated absorption signal…………………...95
Figure 3.17 A measurement of the ***F***=3 ground state transition of ^{85}Rb through a $z \cong$ 100mm cell of Rb vapor in natural isotopic abundance at $T \cong$ 22.2°C compared to our heuristic model……………………...98
Figure 3.18 Twenty consecutive measurements of the ***F***=2 and ***F***=3 ground state transitions of ^{85}Rb through a $z \cong$ 100mm cell of Rb vapor in natural isotopic abundance at $T \cong$ 22.2°C…………………...99
Figure 3.19 A measurement of the ***F***=2 ground state transition of ^{85}Rb through a $z \cong$ 100mm cell of Rb vapor in natural isotopic abundance at $T \cong$ 22.2°C compared to our heuristic model……………………...101
Figure 3.20 Experimental schematic of MFRS scattering arm…………………………………104
Figure 3.21 Fourier coefficients at T=20.2° C and m=0.571 as a function of normalized relative angular frequency…………………………116
Figure 3.22 A portion of the D_2-line measured by detecting the probe laser power after passage through a z=100 mm cell of Rb in natural isotopic abundance at T=20.2° C………………117
Figure 3.23 Measured D_2-line normalized to one outside the bandwidth of an atomic transition…………………………………...118
Figure 3.24 Measured Doppler broadened ***F***=2 ground state transition in the D_2-line of ^{85}Rb compared to the heuristic model of this transition at T=20.2° C………………………………123
Figure 3.25 Measured **1*f***-profiles corresponding to the Doppler broadened ***F***=2 ground state transition in the D_2-line of ^{85}Rb compared to **1*f***-simulations at m=0.11 and m=0.476 (T=20.2°C)………………125

Figure 3.26 **1*f***-profiles covering the ***F***=2 and ***F***=3 ground
state transitions in the D_2-line of ^{85}Rb measured with
modulation frequencies ranging from ν_m=2.00 kHz-2.18 kHz…………………..126
Figure 3.27 Illustration of driven, damped mechanical harmonic oscillator……………………128
Figure 3.28 Peak amplitude in measured **1*f***-profile corresponding
to ***F***=2 ground state transition in D_2-line of ^{85}Rb
versus modulation frequency employed during measurement…………………...130
Figure 3.29 Normalized oscillation amplitude versus modulation (i.e. driving) frequency…….132
Figure 3.30 Phase of modulated absorption signal versus modulation (i.e. driving) frequency...132
Figure 3.31 **2*f***-profile corresponding to ***F***=2 Doppler broadened ground state
transition in D_2-line of ^{85}Rb measured during "validation" experiment
at ν_m=2.09 kHz and G_m=0.5 compared to several **2*f***-profile simulations………..136
Figure 3.32 **1*f***- and **2*f***-profiles measured during the "validation" experiment
with ν_m=2.09 kHz and G_m=0.5 and corresponding to ***F***=3
Doppler broadened ground state transition in D_2-line of ^{85}Rb versus
comparable **1*f***- and **2*f***-profiles simulated at *T*=20.2°C and *m*=0.476……………137
Figure 3.33 Measured ***F***=3 Doppler broadened ground state transition in D_2-line
of ^{85}Rb compared to heuristic model of this transition at *T*=20.2° C…………….138
Figure 3.34 Normalized Gaussian lineshape used to model
the spectral broadening of frequency modulated Rayleigh
scattered radiation collected during preliminary MFRS experiments
compared to a **1*f***-profile simulation neglecting spectral line broadening………..140
Figure 3.35 **1*f***-profile corresponding to the ***F***=3 ground state
transition in the D_2-line of ^{85}Rb and simulated assuming
monochromatic Rayleigh scattered radiation compared to
simulation incorporating thermal broadening of scattered radiation…………….149
Figure 3.36 **2*f***-profile corresponding to the ***F***=3 ground state
transition in the D_2-line of ^{85}Rb and simulated assuming
monochromatic Rayleigh scattered radiation compared to
simulation incorporating thermal broadening of scattered radiation…………….149

Figure 3.37 **1*f***-profiles corresponding to the Doppler broadened ***F***=2 and ***F***=3 ground state transitions in the D_2-line of ^{87}Rb and ^{85}Rb, respectively, detected utilizing frequency modulated molecular Rayleigh scattering collected from a probe volume of static air at lab temperature and standard pressure using vertically and horizontally polarized probe laser light…152

Figure 3.38 Experimentally acquired **1*f***-profiles corresponding to the Doppler broadened ***F***=3 ground state transition of ^{85}Rb versus comparable spectrally broadened **1*f***-profile simulation………………….153

Figure 3.39 RMS noise detected in the scattering arm during preliminary frequency-locked MFRS measurements utilizing molecular Rayleigh scattering from air…163

Figure 3.40 Theoretical 1st- and 2nd- harmonic lock-in signal-to-noise detected with a τ_L=1 s lock-in integration time during preliminary MFRS measurements in static air while sweeping the modulating probe laser frequency across half of the ***F***=3 ground state transition of ^{85}Rb…………166

Figure 3.41 Normalized 1st-harmonic lock-in signals calculated with m=1.4-2.4 and z=100 mm and corresponding to Doppler broadened ***F***=3 ground state transition of ^{85}Rb at T_{Rb}=293.35 K………………...168

Figure 3.42 Normalized 2nd-harmonic lock-in signals calculated with m=1.4-2.4 and z=100 mm and corresponding to Doppler broadened ***F***=3 ground state transition of ^{85}Rb at T_{Rb}=293.35 K………………...169

Figure 3.43 Theoretical 1st- and 2nd-harmonic lock-in S/N detected from static room air with the modulation index optimized for second harmonic detection versus the experimentally legitimate modulation index utilized during preliminary frequency-locked measurements...170

Figure 4.1 Experimental setup for the MFRS velocimeter in the sweep mode of operation……176

Figure 4.2 Doppler-shifted **2*f***-profile acquired in the scattering arm from a supersonic jet of N_2 compared to an unshifted **2*f***-profile acquired in the reference arm……177

Figure 4.3 Sample post-processing VI………………………………………………………..178

Figure 4.4 MFRS sweep mode velocity measurements in a supersonic expansion of N_2………180

Figure 4.5 Reference and scattering profiles corresponding to the first, nineteenth, and twenty-seventh velocity measurements illustrated in Figure 4.4……………181

Figure 4.6 Theoretical 2^{nd}-harmonic lock-in signal-to-noise corresponding to the Doppler broadened ***F***=3 ground state transition of ^{85}Rb and resulting from molecular Rayleigh scattering collected and detected during preliminary sweep mode measurements with the experimentally legitimate modulation index *m*=2.2 versus *m*=0.476………..185
Figure 4.7 The MFRS velocimeter in the frequency-locked mode of operation………………..189
Figure 4.8 Frequency dependent, scattering intensity independent ratio profiles………………192
Figure 4.9 Summing circuit…………………………………………………………………..193
Figure 4.10 PID circuit………………………………………………………………………194
Figure 4.11 The Littrow laser cavity…………………………………………………………196
Figure 4.12 Basic Littrow configuration……………………………………………………...198
Figure 4.13 Regulated high-voltage amplifier………………………………………………..201
Figure 4.14 Illustrating how the Littrow laser is stabilized to a zero-crossing in the ***1f***-profile...202
Figure 4.15 Comparing the first-harmonic lock-in signal detected in the reference arm with the Littrow laser cavity unstabilized versus stabilized with proportional feedback…204
Figure 4.16 First-harmonic lock-in signal detected in the reference arm with the Littrow laser stabilized by proportional (P) feedback versus proportional and differential (PD) feedback……………………204
Figure 4.17 The essential components of a BAL MOPA system……………………………….207
Figure 4.18 Comparing index-guided diodes (MO) to gain-guided diodes (BAL)……………..207
Figure 4.19 The fourth (and final) BAL MOPA system………………………………………...208
Figure 4.20 Scattering arm as configured during preliminary frequency-locked experiments…211
Figure 4.21 Raw ***1f*** reference profiles and ***1f*** and ***2f*** scattering profiles acquired during the calibration phase of the frequency-locked experiment……………….212
Figure 4.22 Accounting for the different data update rates of analog versus digital lock-ins…..213
Figure 4.23 A sample of the ***1f***-profile acquired in the reference arm and the ***1f***- and ***2f***-profiles simultaneously acquired in the scattering arm during a single negative-going calibration scan…………...214
Figure 4.24 ***1f***:***2f*** and ***2f***:***1f*** calibration profiles derived from the raw scattering profiles acquired during the calibration phase of the frequency-locked experiment……..216

Figure 4.25 Raw first harmonic-to-second harmonic and second harmonic-to-first-harmonic lock-in ratios detected in the scattering arm during the measurement phase of the experiment……………217
Figure 4.26 Some frequency-locked velocity measurements…………………………………...218
Figure A.1 Simple schematic of a digital lock-in amplifier……………………………………..221
Figure A.2 Simple illustration of modulated absorption spectroscopy…………………………223
Figure A.3 Pictorial description of equivalent “brick-wall” noise bandwidth for single-pole low-pass RC-filter……………………………..225
Figure A.4 Calculating ENBW of single-pole low-pass RC-filter……………………………...227
Figure B.1 The Lorentz atom……………………………………………………………………234
Figure C.1 Typical collection efficiency vs. photocathode-to-first dynode voltage for side-looking PMT…………………………………...240
Figure C.2 Schematic of R636-10 PMT utilizing E717-63 socket……………………………...241
Figure C.3 Manufacture specified gain vs. PMT supply voltage curve for R636-10 PMT……..243
Figure E.1 Pictorial description of variable definition in Eq. E.13……………………………...251
Figure F.1 Pictorial diagram of a spherical wave………………………………………………262
Figure F.2 Pictorial diagram of propagating wavefront…………………………………………263
Figure F.3 Spatial intensity profiles measured along the slow and fast optical axes of the collimated Littrow laser beam…………………………...268
Figure F.4 The lowest-, first-, and second-order Hermite-Gaussian functions…………………269
Figure F.5 Parameters defining the free space propagation of a BSMI Gaussian beam………...272
Figure F.6 Illustrating the thin-lens formula from geometric optics……………………………273
Figure F.7 Nomenclature used in thin-lens, paraxial calculations with Gaussian beams……….273
Figure G.1 An illustration of efficient coupling………………………………………………...275
Figure G.2 Optical system for preliminary BAL MOPA system………………………………276
Figure G.3 The preliminary BAL MOPA system………………………………………………277
Figure G.4 ***2f***-profiles acquired by direct modulated absorption of the input beam (i.e. Littrow output beam) and (un)amplified BAL output beam…………278
Figure G.5 Huygens’ diffraction fast axis (x-axis) encircled energy calculated using a Zemax simulation of the preliminary MOPA system………..281
Figure G.6 Fast axis (x-axis) encircled energy for redesigned BAL MOPA system……………282
Figure G.7 Spatial intensity profiles for the collimated beam entering lens L_2…………………285

Figure G.8 Spatial intensity profiles for the beam diverging from the final focus……………...286
Figure G.9 The third BAL MOPA system……………………………………………………287
Figure G.10 Trans-impedance amplifier…………………………………………………...289
Figure G.11 Two-lens imaging technique……………………………………………………290

Chapter 1: Introduction

The primary goal of my graduate research was to make a point-velocity-measurement in an unseeded flow using molecular Rayleigh scattering. I specifically focused my efforts on the development of a frequency-locked mode of operation for the so-called modulated filtered Rayleigh scattering (MFRS) velocimeter. MFRS velocimetry was the brain-child of my advisor in the department of Aerospace Engineering at the University of Texas, Dr. Philip Varghese, and as conceived offers an experimentally viable albeit theoretically challenging approach to a difficult problem.

The MFRS technique is essentially a novel variation of FRS utilizing modulated absorption spectroscopy techniques to improve detectability of the relatively weak Rayleigh scattered light. The MFRS velocimeter utilizes a relatively low-power, relatively inexpensive diode laser-based system to provide a weak Rayleigh scattered signal from a probe volume in the flow under investigation. To implement homodyne detection, the optical frequency of the diode-based laser beam interrogating the flow under investigation is modulated. The frequency modulation of the interrogating beam is imposed on the light scattered from the molecules present in the probe volume. This frequency-modulated scattered light is collected from the probe volume in the flow under investigation and transmitted through a rubidium (Rb) vapor filter before being detected. The detected modulated absorption signal is sent to a lock-in amplifier synchronized with the modulation frequency to provide high levels of background noise rejection. The resulting lock-in signal provides a measure of the Doppler frequency shift of the Rayleigh scattered light due to a bulk velocity in the probe volume.

My primary goals while writing this dissertation were to clearly discuss the theoretical details of MFRS and to describe the experimental success I had while implementing the MFRS technique. With a reliable theoretical model of MFRS and the benefit of experimental hindsight I hope to encourage the further development of MFRS velocimetry. If someone does continue where I left off, I am confident that the discussion contained in the following pages is thorough enough to help that person improve upon my results.

This dissertation begins with a brief review of laser anemometry in Chapter 2. The discussion in Chapter 2 focuses on two approaches to laser-based velocity measurements – particle tracking anemometry and laser Doppler anemometry – and provides a general introduction to what I consider to be prevailing laser-based velocimeters. Specifically, one prominent particle tracking anemometry technique will be discussed – particle imaging velocimetry (PIV) – and four prominent laser Doppler anemometry techniques will be discussed – laser Doppler velocimetry (LDV), interferometric laser Doppler anemometry (I-LDA), planar Doppler velocimetry (PDV), and filtered Rayleigh scattering (FRS). In addition, I discuss two techniques similar to MFRS: frequency-modulated filtered light scattering (FM FLS) and point Doppler velocimetry (pDV). Like the MFRS technique, FM FLS and pDV are premised on detecting a modulated absorption of collected Rayleigh scattering using lock-in amplifiers. The intention of the discussion in Chapter 2 is to set a baseline for evaluating not only the novelty of MFRS velocimetry, but also its potential merits.

The measurement capabilities of a particular experiment are generally surmised by calculating the expected signal-to-noise (S/N) ratio. My intention in writing Chapter 3 was to provide a realistic calculation of the expected signal-to-noise ratio during preliminary frequency-locked MFRS experiments. Chapter 3 begins with a discussion of the theoretical underpinnings of the MFRS technique: Rayleigh scattering, absorption spectroscopy, and modulated absorption spectroscopy. A thorough understanding of each of these topics is necessary to calculate the expected signal when utilizing the MFRS technique – i.e. the lock-in signal. After discussing the noise sources that corrupt MFRS measurements, I calculate the expected signal-to-noise ratio with the MFRS velocimeter configured as it was during preliminary frequency-locked experiments using molecular Rayleigh scattering from static room air.

The rigorous theoretical model developed in Chapter 3 and the accompanying analysis offer significant insight into MFRS velocimetry. For instance, a simple Rayleigh scattering experiment introduced to validate the developed scattering theory clearly indicates that the largest obstacle to meaningful MFRS measurements utilizing molecular Rayleigh scattering is dust. There is no simple way to avoid the collection and detection of dust scattering in an ambient lab environment. I also show that reliable calculations of the expected S/N ratio must account for the spectral broadening of molecular Rayleigh scattered radiation. Rayleigh scattered radiation exhibits significant spectral broadening that results in a dramatic decrease in the detected modulated absorption signal. Finally, I conclude Chapter 3 by using the developed theory to consider the impact that modulation depth and Rb cell temperature have on the expected S/N ratio. Analysis shows that the S/N ratio during preliminary frequency-locked MFRS experiments could have been substantially improved by increasing the modulation depth and heating the Rb vapor cell.

Chapter 4 discusses the results of two MFRS velocity measurements that I made: one in a sweep mode of operation and one in a frequency-locked mode of operation. Though both measurements were made in an unseeded flow, both relied on condensate scattering to provide an adequate S/N: the sweep mode velocity measurements relied on scattering from water vapor entrained into the supersonic expansion of N_2 interrogated and the frequency-locked velocity measurements relied on scattering from CO_2 condensate in the supersonic expansion of CO_2 interrogated. Due to its limited temporal resolution, I quickly abandoned development of the sweep mode of operation and focused my efforts on development of the frequency-locked mode of operation; the temporal resolution of the frequency-locked mode of operation is limited only by the required lock-in time constant, whereas the temporal resolution of the sweep mode of operation is limited by the need to sweep. The frequency-locked mode of operation is an attractive alternative to the sweep mode of operation, but is complicated by the need to account for scattering intensity fluctuations and by the need to frequency stabilize the probe laser. Chapter 4 will discuss the steps I took toward successful implementation of the frequency-locked mode of operation: A ratioed detection scheme was developed to normalize out scattering intensity fluctuations, a proportional-integral-differential (PID) controller was designed and built to provide feedback for optical frequency stabilization based on an error signal in the reference arm of the experiment, and an extended-cavity diode laser master oscillator power amplifier (ECDL-MOPA) system was constructed to provide relatively narrow linewidth, frequency tunable, frequency stable probe laser power.

I conclude this dissertation in Chapter 5 by considering the theoretical measurement capabilities of an optimized MFRS velocimeter using a commercially available, 1 W diode-based laser system. The calculations are promising.

Chapter 2: Laser Anemometry

2.1 Introduction

> *It is the fate of new truths to begin as heresies and end as superstitions.*
>
> -T. H. Huxley

The physics of flows is broadly defined by three concepts – conservation of mass, conservation of momentum, and conservation of energy – that are mathematically described by five scalar partial differential equations, which I will classify as the Navier-Stokes equations. As they stand, these five equations are not sufficient to describe a flow and additional models are required for closure. These models are tested by comparing the flow structure predicted by the theory to the flow structure observed in experiments. For certain simple flows we are able to solve the Navier-Stokes equations by making physically reasonable approximations. It is from experimental studies of these canonical flows that we first gained faith in the correctness with which the Navier-Stokes equations and the supplementary models describe flow processes. Computers have afforded us an opportunity to study more sophisticated flows for which no analytic solution is available, but the validity of the numerical models employed must still be tested by experimental observation.

Our understanding of the natural world is based on observation. As our minds search for patterns in abstruse phenomena, observation provides the needed clues, and it is the care and completeness with which our observations are carried out that lends credence to our conclusions. As our vision of the world expands so too does our understanding. Theories once considered conclusive may be called into question upon closer inspection, and new theories may evolve. The world has been closely scrutinized these past millennia, and we have reached a point where advancement of our scientific thinking requires advanced diagnostics. Such is the state of affairs for science in general, and the field of fluid mechanics is no exception. To capture the complexities of a flow within relatively simple, predictive models, we must understand the complexities. This can only be accomplished with the aid of new observations offered by novel diagnostics.

In 1889 Mach and Salcher introduced optical diagnostic techniques for flow visualization to the field of fluid mechanics [1]. Their shadowgraphs of supersonic jet flows provided qualitative insight into the overall global properties of the flow. Today, shadowgraph, schlieren, and interferometry are established optical diagnostic techniques providing high-quality images in unseeded flows. All three techniques give some measure of flow density. However, since the images obtained are integrated across the flow field along the line of sight, they cannot be used for quantitative flow measurements except in steady flows about extremely simple geometries.

Before the introduction of laser diagnostics for fluid mechanics, experimentalists relied on intrusive point-measurement probes – hot wire anemometers, pitot probes, and thermocouples – to make quantitative measurements in flows. The intrusive nature of these probes has three distinct disadvantages: intrusive transducers disturb the flow under investigation; the spatial resolution and physical location of the measurement are limited by the physical size of the transducer; and physical probes are unable to withstand the environmental extremes encountered in some contemporary flow investigations. The past four decades have seen the deliberate development of laser diagnostic techniques specifically to avoid these disadvantages.

Laser-based diagnostic techniques use a laser beam to make measurements in a flow under investigation. With the rare exception of thermal breakdown – i.e. the high intensity of a tightly focused, high power laser beam can result in dissociation of molecular constituents in the flow – the perturbations introduced into the flow by the interrogating laser beam are negligible. In other words, laser light is essentially non-intrusive. In addition, laser light can be manipulated to provide extremely high spatial resolution. For instance, using a diffraction-limited focusing objective, a collimated basic single mode ideal (BSMI) Gaussian laser beam (i.e. supporting only the TEM_{00} fundamental spatial mode) can be focused to a $1/e^2$ spot size of [2],

$$d_o{}' \propto \frac{4\lambda f}{\pi d_o} \cong 1.27 F_{\#}\lambda \, , \tag{2.1}$$

where d_o' is the $1/e^2$ spot size (i.e. the diameter that encapsulates ~87% of the laser power in the focused spot), d_o is the $1/e^2$ waist diameter of the collimated input beam to the focusing objective, f is the effective focal length of the focusing objective, and λ is the wavelength of the laser beam. Assuming that the laser beam is well collimated – i.e. that the waist diameter doesn't increase appreciably before it reaches the focusing objective – then the second expression is a reasonable approximation with $F_{\#} = f/d_o$. Using a beam expander to increase the diameter of the collimated laser beam (thereby also improving the collimation), focused spot sizes on the order of a few microns are attainable with fast, diffraction-limited focusing objectives. (For critical focusing applications, diffraction effects introduced by the edges of the lens aperture must be considered.

As a general rule of thumb, aperture truncation must be accounted for when focusing faster than $F_{\#}$=2.8 [3]). Finally, laser light can withstand the harshest environments. For instance, laser light can be used to measure plasma and combustion temperatures, temperatures that would destroy or limit the lifetime of intrusive probes.

One laser-based diagnostic instrument that has enjoyed considerable progress is the laser anemometer. Laser anemometers probe a flow under investigation with laser light. Elastically scattered and/or absorbed and re-emitted light is collected from a point, plane, or volume in the flow and is detected. The signal of the collected and detected light is then processed to provide a velocity measurement at a point, or in a plane or volume. This dissertation discusses a laser anemometer conceived of by Dr. Philip Varghese of the Department of Aerospace Engineering at the University of Texas and which is based on a technique that he termed modulated filtered Rayleigh scattering (MFRS). The MFRS velocimeter is a novel variation of filtered Rayleigh scattering (FRS), and as conceived has the potential to provide point-velocity-measurements in unseeded flows using commercially available diode-based laser systems.

Before proceeding to a discussion of the MFRS velocimeter, it is prudent to first examine the prevailing technologies in laser anemometry. The intent of this discussion is to set a baseline for evaluating not only the novelty of the MFRS technique, but also its potential merits. I have broadly classified the prevailing laser velocimeters into two categories for discussion:

(i) *Particle tracking anemometers*: Seed particles or tagged molecules in the flow elastically scatter and/or absorb and re-emit the light of an interrogating collimated laser sheet or beam. Time resolved two-dimensional images of the interrogated flow are recorded. (Three-dimensional imaging is possible using stereoscopic or holographic techniques). Scattering molecules clearly evident in each exposure are tracked from image to image and one- or two-components of the velocity in the plane of the laser sheet are inferred.

(ii) *Laser Doppler anemometers*: Seed particles or natural constituents in the flow elastically scatter and/or absorb and re-emit light of an interrogating collimated laser sheet or beam. The Doppler frequency shift of the scattered or re-emitted light resulting from the bulk motion of the scattering particles is measured. Knowing the geometry of the experiment, the velocity is calculable.

To preserve a modicum of clarity and coherence in this dissertation the discussion of each technique is necessarily brief. The details of particle tracking anemometers are not particularly relevant to our research; I would broadly categorize the MFRS velocimeter that we are developing as a laser Doppler anemometer (LDA). The LDA concepts that are relevant to our research will be expanded on in the next chapter on the MFRS technique.

2.2 Particle Tracking Anemometers

Two prominent techniques for particle tracking anemometry are planar imaging velocimetry (PIV), alternatively known as particle tracking velocimetry (PTV), and laser induced fluorescence (LIF). These techniques are conceptually similar, but differ in the details. The primary difference between PIV and LIF is the imaged scattering process; PIV images elastic scattering from seed particles introduced into the flow and LIF images the irradiative emission of light absorbed by tagged molecules or seed molecules in the flow. To illustrate the concept of particle tracking anemometry I have chosen to discuss PIV in this section.

Consider the PIV system illustrated in Figure 2.1. A pulsed laser sheet interrogates a plane in the flow under investigation, illuminating seed particles (e.g. porous silica) in the plane at the pulse period of the laser, Δt. Cameras synchronized with the pulse timing of the laser record images of the illuminated seed particles – i.e. of the Mie scattering from the seed particles – in the plane of the laser sheet. By comparing two such images separated in time by Δt, the projected two-dimensional particle displacements, Δx and Δy, in the plane interrogated by the laser sheet can be calculated,

$$\Delta x = \frac{1}{M}\Delta X ; \Delta y = \frac{1}{M}\Delta Y . \tag{2.2}$$

M is the magnification of the imaging system and ΔX and ΔY are the x- and y-particle displacements in the image area (IA). Knowing the laser pulse period we can calculate the x- and y-velocity in the measurement plane, u_x and u_y, respectively:

$$u_x = {\Delta x}/{\Delta t} ; u_y = {\Delta y}/{\Delta t} . \tag{2.3}$$

Aside from the difficulties associated with uniformly seeding the interrogated flow, the need to accurately and efficiently process the recorded data poses a significant challenge for the PIV practitioner. Assuming that the seed density is low enough that each processed IA contains only one particle, a simple peak finding algorithm could be employed to determine the displacement of the particle in a double exposure of the measurement volume. This particular technique is what is referred to as particle tracking velocimetry (PTV). Unfortunately, heavier seeding is required to obtain continuous velocity data [4]. With low density particle seeding, there is no guarantee that each IA sampled will contain a particle pair; statistically some image areas sampled will have multiple particle pairs and some image areas will have none. Though heavier seeding effectively guarantees continuous velocity information, it also implies that more than one particle pair will be recorded in each IA.

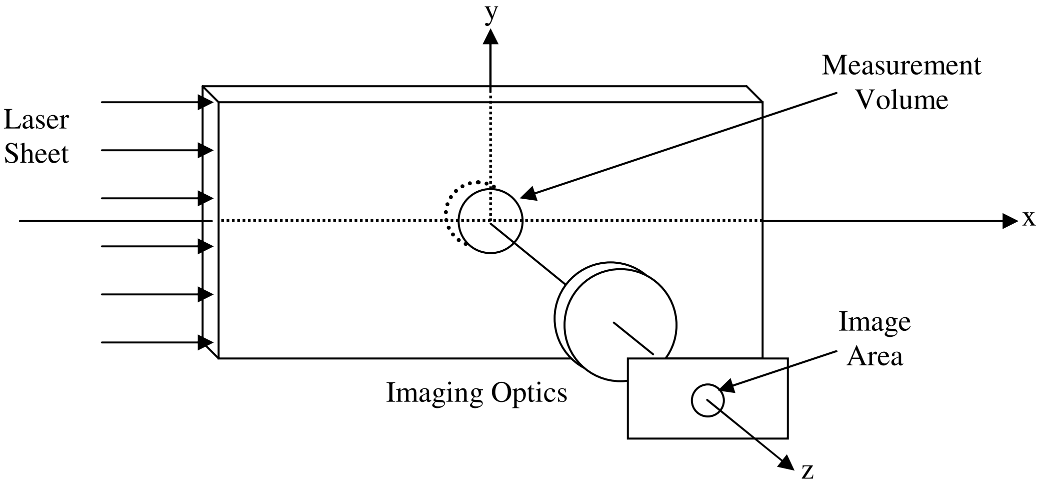

Figure 2.1 PIV system

To illustrate the ambiguities associated with sampling multiple particle pairs, consider a doubly exposed image of two particle pairs, as in Figure 2.2. It is not possible to uniquely determine the particle pairs in Figure 2.2a, and it is therefore impossible to uniquely determine the fluid motion, as shown in Figure 2.2b. Maybe particles A and B translated to a new position represented by particles C and D. Perhaps particles A and B rotated in a vortical deformation to a new position represented by particle D and C. Mathematically, the probable motion of the centroid of every possible particle pair can be represented by an autocorrelation function (ACF) derived from the doubly exposed image, as outlined in Figure 2.2.

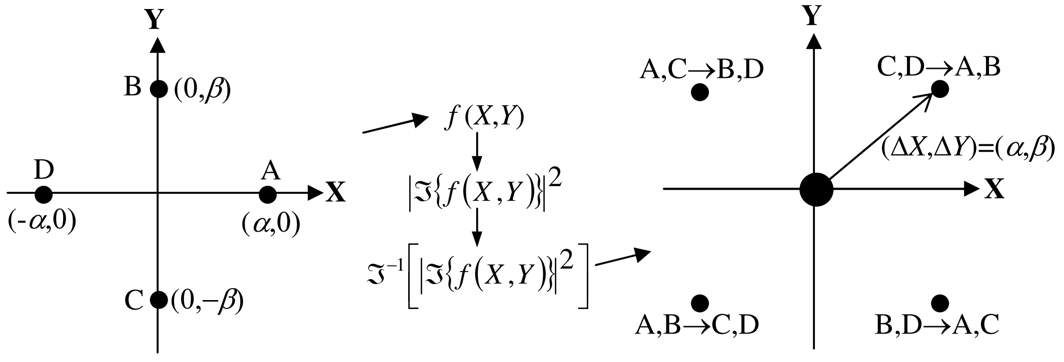

(a) $f(X,Y)$ (b) ACF

Figure 2.2 PIV image processing

To demonstrate, let us model the illuminated seed particles in the image of Figure 2.2a as delta functions,

$$f(X,Y)=\sum_{i=A,B,C,D}\delta\left(\vec{\zeta}-\vec{\zeta}_i\right),\ \vec{\zeta}=(X,Y). \tag{2.4}$$

We derive a so-called Young's fringe pattern by calculating the squared modulus of the Fourier transform of the doubly exposed image,

$$\Im\{f(X,Y)\}=F\left(k_x,k_y\right)=\int_{-\infty}^{\infty}\int_{-\infty}^{\infty}f(X,Y)e^{\hat{\imath}\left(k_xX+k_yY\right)}\mathrm{d}X\mathrm{d}Y\ , \tag{2.5}$$

where k_x and k_y define the x- and y-spatial-frequencies in the complex Fourier transform plane. Representing the doubly exposed image by Eq. 2.4 we find,

$$F\left(k_x,k_y\right)=2\cos k_x\Delta X+2\cos k_y\Delta Y \tag{2.6}$$

and

$$\left|F\left(k_x,k_y\right)\right|^2=4\cos^2 k_x\Delta X+4\cos^2 k_y\Delta Y+8\cos k_x\Delta X\cos k_y\Delta Y \tag{2.7}$$

The ACF is derived by taking the inverse Fourier transform of Young's fringe pattern. (The required transforms were at one time performed optically [4,5]. Modern PIV systems utilize computers to digitally cross-correlate the acquired images). Taking the inverse transform of Eq. 2.7 we find,

$$
\begin{aligned}
\Im^{-1}\left\{F\left(k_x,k_y\right)\right\} &= \frac{1}{(2\pi)^2}\int_{-\infty}^{\infty}\int_{-\infty}^{\infty}\left|F\left(k_x,k_y\right)\right|^2 \mathrm{e}^{-\hat{\imath}\left(k_xX+k_yY\right)}\mathrm{d}k_x\mathrm{d}k_y \\
&= \frac{1}{\pi^2}\int_{-\infty}^{\infty}\int_{-\infty}^{\infty}\cos^2\left(k_x\Delta X\right)\mathrm{e}^{-\hat{\imath}\left(k_xX+k_yY\right)}\mathrm{d}k_x\mathrm{d}k_y \leftarrow \mathbf{C}_1 \\
&\quad + \frac{1}{\pi^2}\int_{-\infty}^{\infty}\int_{-\infty}^{\infty}\cos^2\left(k_y\Delta Y\right)\mathrm{e}^{-\hat{\imath}\left(k_xX+k_yY\right)}\mathrm{d}k_x\mathrm{d}k_y \leftarrow \mathbf{C}_2 \\
&\quad + \frac{2}{\pi^2}\int_{-\infty}^{\infty}\int_{-\infty}^{\infty}\cos\left(k_x\Delta X\right)\cos\left(k_y\Delta Y\right)\mathrm{e}^{-\hat{\imath}\left(k_xX+k_yY\right)}\mathrm{d}k_x\mathrm{d}k_y \leftarrow \mathbf{C}_3 \qquad (2.8)
\end{aligned}
$$

where,

$$
\begin{aligned}
\mathbf{C}_1 &= \frac{4}{\pi^2}\int_{-\infty}^{\infty}\int_{-\infty}^{\infty}\left(2+\mathrm{e}^{\hat{\imath}2k_x\Delta X}+\mathrm{e}^{-\hat{\imath}2k_x\Delta X}\right)\mathrm{e}^{\hat{\imath}(k_xX+k_yY)}\mathrm{d}k_x\mathrm{d}k_y \\
&= \frac{4}{\pi^2}\int_{-\infty}^{\infty}\int_{-\infty}^{\infty}\left(2\mathrm{e}^{\hat{\imath}k_xX}+\mathrm{e}^{\hat{\imath}k_x(X+2\Delta X)}+\mathrm{e}^{\hat{\imath}k_x(X-2\Delta X)}\right)\mathrm{e}^{\hat{\imath}k_yY}\mathrm{d}k_x\mathrm{d}k_y
\end{aligned}
$$

$$
\mathbf{C}_1 = 32\delta\left(X,Y\right)+16\delta\left(X+2\Delta X,Y\right)+16\delta\left(X-2\Delta X,Y\right) \qquad (2.9\text{a})
$$

Similarly,

$$
\mathbf{C}_2 = 32\delta\left(X,Y\right)+16\delta\left(X,Y+2\Delta Y\right)+16\delta\left(X,Y-2\Delta Y\right) \qquad (2.9\text{b})
$$

and

$$
\begin{aligned}
\mathbf{C}_3 &= 32\left[\delta\left(X+\Delta X,Y+\Delta Y\right)+\delta\left(X+\Delta X,Y-\Delta Y\right)\right] \\
&\quad +32\left[\delta\left(X-\Delta X,Y+\Delta Y\right)+\delta\left(X-\Delta X,Y-\Delta Y\right)\right]
\end{aligned} \qquad (2.9\text{c})
$$

Putting it all together we find,

$$
\begin{aligned}
\Im^{-1}\left\{F\left(k_x,k_y\right)\right\} &= 64\delta\left(X,Y\right) \\
&\quad +32\left[\delta\left(X+\Delta X,Y+\Delta Y\right)+\delta\left(X+\Delta X,Y-\Delta Y\right)\right] \\
&\quad +32\left[\delta\left(X-\Delta X,Y+\Delta Y\right)+\delta\left(X-\Delta X,Y-\Delta Y\right)\right] \\
&\quad +16\left[\delta\left(X+2\Delta X,Y\right)+\delta\left(X-2\Delta X,Y\right)+\delta\left(X,Y+2\Delta Y\right)+\delta\left(X,Y-2\Delta Y\right)\right]
\end{aligned} \qquad (2.10)
$$

Eq. 2.10 represents a correlation of the image in Figure 2.2 with itself. The optimum correlation occurs when there is no displacement, as represented by the first term in Eq. 2.10. The images are also correlated when they are displaced with respect to each other by $\pm\Delta X$ and $\pm\Delta Y$, as represented by the next four terms. The final four terms in Eq. 2.10 represent a correlation at displacements of $\pm 2\Delta X$ and $\pm 2\Delta Y$. When interpreting the image as containing particle pairs, however, these four terms are not meaningful. Figure 2.2b represents graphically the derived ACF. The four points away from the origin represent the four correlated displacements of the two bi-directional particle pairs. Which one do we pick?

Efficient correlation techniques have been developed that account for the ambiguities associated with processed PIV images, and can provide spatial resolution on the order of 100 μm in a limited field of view [6]. Image shifting is a common technique employed to differentiate negative velocities from positive velocities. Essentially, the second exposure on a double pulse recording is displaced a known amount from the first exposure using a scanning mirror [7] or by an electro-optic displacement [8]. If the image shift is greater than the maximum particle displacement in the doubly exposed image, then negative velocities can be unambiguously determined.

Optimum correlation techniques also reduce PIV measurement biases [9]. For instance, fast moving particles have large displacements. There is a higher probability therefore that the exposure of a fast moving particle will fall outside of the image area. This so-called out-of-plane error biases the measurement towards lower velocities. In addition, if the PIV system is unable to distinguish the displacement of a low velocity particle due to insufficient spatial resolution in the correlation technique, then the measurement will be biased toward higher velocities.

The accuracy of PIV techniques is limited by these biases, as well as by the accuracy with which the time and image position can be measured. Typically, the time of each exposure can be measured with accuracy on the order of 10 ns, and since typical pulse periods are orders of magnitude longer, the uncertainty in the temporal measurement is generally negligible. Utilizing short pulse lasers (e.g. O(10 ns) pulse duration), the uncertainty in position is effectively the result of camera resolution and shot noise, and is on the order of a few microns.

Measurement biases introduce the largest uncertainties, and effectively limit the dynamic range for accurate velocity measurements. The accuracy of low velocity measurements is dictated by the ability of the correlation algorithm to detect small particle displacements, which in turn depends on the seed uniformity and size, as well as the magnification and aberrations of the imaging system. The accuracy of high velocity measurements is dictated by out-of-plane biases. Generally, the correlation biases limit the dynamic range for accurate PIV measurements to approximately 10dB.

The techniques developed for efficient, accurate PIV measurements have been incorporated into commercially available correlation cameras. Utilizing the computing power provided by today's personal computers, these correlation cameras form the basis of real-time PIV measurements conducted today. Real time three-component PIV measurements have been performed using stereoscopic and holographic techniques [10-12]. In addition, the short pulse periods possible with Q-switched lasers have made PIV a viable technique for turbulent, high-speed flow measurements. PIV has evolved into a powerful technique, limited primarily by the need to seed the flow. There are five disadvantages to flow seeding [13]:

(i) Velocity measurements are inferred from the movement of discrete seed particles. Great care must be taken when inferring bulk fluid velocity from this spatially discrete measurement data. How faithfully the discrete data represents the flow field depends on the seed uniformity, density, and size, as well as the data processing algorithm.

(ii) It is extremely difficult to seed particles uniformly into the flow field. The experimental difficulties associated with particle seeding are compounded by this fact. The non-uniformities in seed distribution can mask dominant structures in the flow field. As a consequence, only after the measurement data has been processed is it possible to determine whether the seed distribution and density is suitable.

(iii) The seed density is limited by secondary scattering effects, sampling ambiguities, and coherent scattering effects [14].

(iv) Velocity measurements inferred from the movement of discrete seed particles only represents the bulk fluid velocity provided that those seed particles follow the flow. Particle lag is a common problem in high speed, turbulent flows. It is generally difficult to determine whether laser velocimeters that rely on particle seeding capture rapid velocity fluctuations that may be present in the flow.

(v) Finally, seed particles can contaminate the flow facility.

Any one of these disadvantages can plague laser-based velocity measurements that rely on flow seeding – e.g. particle imaging velocimetry, laser Doppler velocimetry, and planar Doppler velocimetry. The primary advantage of the MFRS velocimeter as conceived is that it does not require flow seeding.

2.3 Laser Doppler Anemometers

The Doppler effect was first formulated by Ch. Doppler in 1842 [15]. It is demonstrated in our daily lives every time a train blows its horn: When the train is moving toward us the frequency of the horn sounds higher (i.e. it has a higher pitch) and when it's moving away from us the frequency sounds lower. In general, the Doppler effect is experienced whenever there is relative motion between a source of harmonic waves (e.g. acoustic waves or electromagnetic waves) and an observer. Imagine a source of harmonic waves traveling toward an observer at a velocity V, as in Figure 2.3. The observer perceives a shorter wavelength emanating from the source as a result of their relative motion. For instance, assume that the source generates a wave with a period of $T=1/\nu_o$, where ν_o is the wave frequency. During each period of oscillation the source travels a distance $VT=V/\nu_o$. The wavelength of the source traveling toward the observer is therefore shortened from the perspective of the observer by,

$$\Delta\lambda_o \propto -V/\nu_o \ . \tag{2.11}$$

The frequency of an electromagnetic wave is related to the wavelength, $\nu_o=c/\lambda_o$, where c is the speed of light and λ_o is the wavelength of the light. Therefore, in the context of electromagnetic radiation Eq. 2.11 can be recast:

$$\Delta\nu = \nu_D \propto V/\lambda_o = V\nu_o/c \ . \tag{2.12}$$

The Doppler effect is the cornerstone of laser Doppler anemometry. In this case, the traveling "sources" are the molecules or seed particles moving with the bulk velocity of the flow that scatter incident radiation. The "observer" is a detector. The Doppler frequency shift formula in Eq. 2.12 is only slightly modified to account for the geometry of the experiment, as will be discussed in the next sub-section, but the basic concept is unchanged. Each of the four techniques discussed below rely on measurements of the Doppler frequency shift to determine the flow velocity. It is the specific method employed to measure the Doppler frequency shift that distinguishes them.

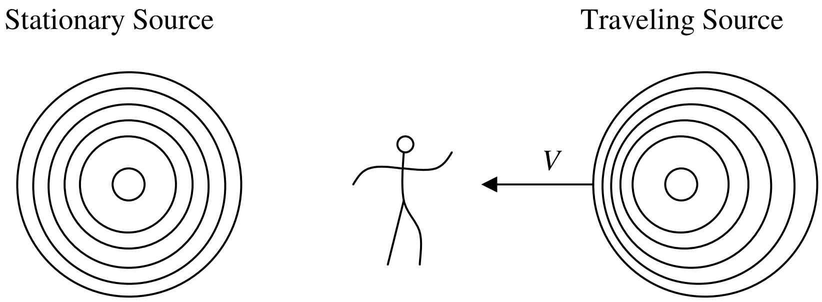

Figure 2.3 Illustrating the Doppler effect

The discussion begins with an introduction to the pioneering laser Doppler anemometry technique, laser Doppler velocimetry (LDV). LDV has traditionally measured the Doppler frequency shift by photomixing the collected Doppler shifted scattered light with a reference beam. An interferometric method for determining the Doppler frequency shift will be discussed next, followed by an introduction to a planar technique – planar Doppler velocimetry (PDV). (Another planar technique, planar laser induced fluorescence (PLIF), will not be discussed. It is primarily utilized for measurements of thermodynamic properties, not velocities. In addition, it is conceptually similar to PDV. The primary difference between PDV and PLIF is the detected radiation; PDV detects elastic scattering from seed particles introduced into the flow and PLIF detects spontaneous emissions from seed molecules that have been irradiated by resonant light). PDV utilizes a molecular vapor filter to quantify the Doppler frequency shift of seed particles moving in the plane of a laser sheet. It is a two-dimensional extension of a point technique that is generally called filtered Rayleigh scattering (FRS). FRS experiments employ a molecular or atomic vapor filter to determine the Doppler frequency shift of the collected Rayleigh scattered light, and require a high power laser source to provide a detectable signal from molecular scattering. This section will conclude with a discussion of two recently developed FRS-based techniques – frequency modulated filtered light scattering (FM-FLS) and point Doppler velocimetry (pDV) – that employ frequency modulation spectroscopy techniques to provide a detectable Rayleigh scattered signal with relatively low power lasers. In this regard, they are identical to our proposed MFRS velocimeter. It is in the details that they differ.

2.3.1 Laser Doppler Velocimetry (LDV)

The first laser Doppler velocimetry (LDV) measurement was conducted over forty years ago by Yea and Cummins [16]. They measured the velocity of a pipe flow by collecting light scattered from small particles suspended in the fluid. The scattered light from the flowing particles exhibited a Doppler frequency shift, which was determined by photomixing the scattered light and a reference beam on a single detector. Knowing the geometry of the experiment, Yea and Cummins calculated the bulk velocity of the pipe flow from the measured Doppler frequency shift.

Figure 2.4a is a schematic of a generic reference beam laser Doppler velocimeter, similar to that first employed by Yea and Cummins. A single laser is employed with a centerline frequency of ν_o. A small portion of the laser beam power is split off, transmitted through an acousto-optic modulator, and directed onto a photodetector. The modulator shifts the centerline frequency of this reference beam by ν_M. The majority of the laser power is directed into the flow under investigation. Laser light scattered from seed particles traveling with the flow is Doppler shifted in frequency by $\Delta\nu_D$ from the perspective of the collection optics. This Doppler frequency shifted scattered light is collected and relayed to the photodetector. Provided that the optical path difference between the reference beam and the "scattering" beam is less than the coherence length of the laser, then the reference and scattered light are coherently mixed on the detector, resulting in a sinusoidal signal at a frequency of $|\nu_M - \nu_D|$. If the sideband frequency shift is greater than the maximum possible Doppler frequency shift, $\Delta\nu_M > \Delta\nu_D|_{\max}$, then the sign of the flow velocity can be unambiguously determined.

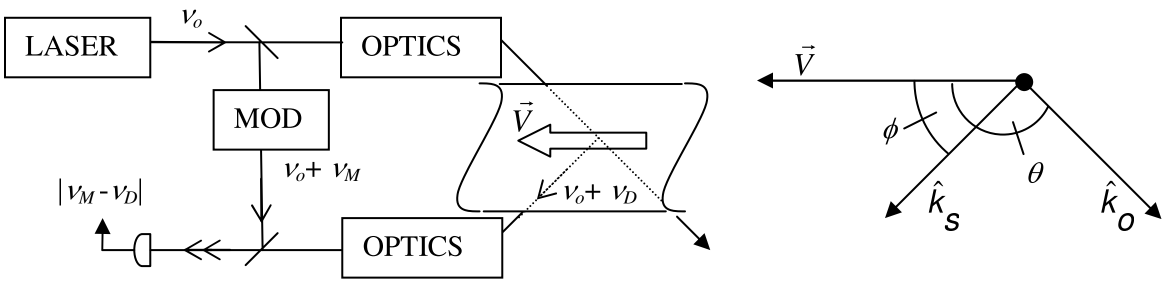

(a) (b)

Figure 2.4 Schematic of reference beam LDV

Figure 2.4b defines the geometry of the reference beam laser Doppler velocimeter. A seed particle moving in the flow perceives a laser frequency, ν', that is Doppler shifted from the *stationary source* of frequency ν_o,

$$\nu' = \nu_o\left(1 - \frac{V}{c}\cos\theta\right) = \nu_o + \Delta\nu_D\,, \tag{2.13}$$

where V is the speed of the seed particle, c is the speed of light, and θ is the angle formed by the interrogating laser beam and the direction of the particle motion. The light that is elastically scattered from the seed particle is collected at an angle ϕ from the direction of the particle motion. This elastically scattered light can be envisioned as originating from the particle itself, and since the particle is moving relative to a *stationary detector*, the detector perceives a Doppler shifted frequency,

$$\nu_S = \nu'\left(1+\frac{V}{c}\cos\phi\right). \tag{2.14}$$

Combining Eqs. 2.13 and 2.14 and recognizing that $V \ll c$ we find,

$$\begin{aligned}\nu_s &= \nu_o\left(1-\frac{V}{c}\cos\theta\right)\left(1+\frac{V}{c}\cos\phi\right) = \nu_o\left[1-\frac{V}{c}\cos\theta+\frac{V}{c}\cos\phi-\left(\frac{V}{c}\right)^2\cos\theta\cos\phi\right]\\ &\left.\begin{aligned}&\cong \nu_o\left[1-\frac{V}{c}\left(\cos\theta-\cos\phi\right)\right]\\ &= \nu_o+\Delta\nu_D\end{aligned}\right\}\Rightarrow \Delta\nu_D = V\frac{\nu_o}{c}\left(\cos\phi-\cos\theta\right)\end{aligned} \tag{2.15}$$

Introducing the wave vectors $\vec{k}_o = \frac{2\pi}{\lambda_o}\hat{k}_o$ and $\vec{k}_s = \frac{2\pi}{\lambda_s}\hat{k}_s$ ($\lambda_o \approx \lambda_s$), where $\hat{k}_o$ and $\hat{k}_s$ are the unit vectors illustrated in Figure 2.4b, we can recast the formula for the Doppler frequency shift in Eq. 2.15 in terms of angular frequency,

$$\boxed{\Delta\omega_D = \left(\vec{k}_s-\vec{k}_o\right)\cdot\vec{V} = \vec{K}_s\cdot\vec{V}} \tag{2.16}$$

where $\vec{K}_s$ is the so-called sensitivity vector.

Photomixing of electromagnetic radiation was first investigated by Forrester et al. in 1955 [17]. To demonstrate the effect let us consider two electromagnetic waves with different frequencies, $\omega_1 > \omega_2$ and $k_1 > k_2$, but equal amplitudes, $E_{o1} = E_{o2}$. To accommodate scalar analysis, let us assume that the two waves are traveling along the same path in the same direction. We will also assume that there is no initial phase mismatch between the two waves:

$$E_1 = E_{o1}\cos\left(k_1x-\omega_1t\right) \tag{2.17a}$$

$$E_2 = E_{o1}\cos\left(k_2x-\omega_2t\right) \tag{2.17b}$$

The superposition of these two waves is,

$$E = E_{o1}\left[\cos\left(k_1x-\omega_1t\right)+\cos\left(k_2x-\omega_2t\right)\right]. \tag{2.18}$$

Utilizing the trigonometric identity,

$$\cos x+\cos y = 2\cos\tfrac{1}{2}(x+y)\cos\tfrac{1}{2}(x-y), \tag{2.19}$$

we can recast Eq. 2.18,

$$E = 2E_{o1}\cos\left(k_mx-\omega_mt\right)\cos\left(\bar{k}x-\bar{\omega}t\right), \tag{2.20}$$

where,

$$\begin{aligned} k_m &= \tfrac{1}{2}(k_1 - k_2) \equiv \text{modulation wavenumber}\\ \bar{k} &= \tfrac{1}{2}(k_1 + k_2) \equiv \text{average wavenumber}\\ \omega_m &= \tfrac{1}{2}(\omega_1 - \omega_2) \equiv \text{modulation frequency}\\ \overline{\varpi} &= \tfrac{1}{2}(\omega_1 + \omega_2) \equiv \text{average frequency} \end{aligned} \tag{2.21}$$

The superposition in Eq. 2.20 may be regarded as a traveling wave of frequency $\overline{\varpi}$ with a modulated amplitude $E_o(x,t)$,

$$E = E_o(x,t)\cos(\bar{k}x - \overline{\varpi}t);\, E_o(x,t) = 2E_{o1}\cos(k_m x - \omega_m t) \tag{2.22}$$

In photomixing applications, the irradiance of the superposition defined in Eq. 2.22 is detected. At optical frequencies, $\overline{\varpi}$ is so large that it generally cannot be resolved by the detector. Consider using a detector with an averaging time T placed at x=0:

$$\left\langle E^2 \right\rangle_T \propto \tfrac{1}{2}\left\langle E_o^2(x,t)\right\rangle_T \left[1 + \operatorname{sinc}\overline{\varpi}T \cos 2\overline{\varpi}T\right] \xrightarrow{\lim T >> \frac{2\pi}{\overline{\varpi}}} \tfrac{1}{2}\left\langle E_o^2(x,t)\right\rangle_T \tag{2.23}$$

In general, $\omega_1 \approx \omega_2$ and the averaging time is short enough to resolve the modulated amplitude at an angular frequency of $\omega_m = 1/2(\omega_1 - \omega_2)$:

$$\begin{aligned} \left\langle E_o^2(x,t)\right\rangle_T &\cong E_o^2(x,t)\\ &= 4E_{o1}^2\cos^2(k_m x - \omega_m t)\\ \left\langle E_o^2(x,t)\right\rangle_T &= 2E_{o1}^2\left[1 + \cos(2k_m x - 2\omega_m t)\right] \end{aligned} \tag{2.24}$$

The point is that the detected signal modulates with a beat frequency of $\omega_m = ½(\omega_1 - \omega_2)$. It is this beat frequency that is detected to determine the Doppler frequency shift with laser Doppler anemometers utilizing photomixing, such as LDV. Beats are also produced if there is a phase or amplitude mismatch between the photomixed reference and scattered waves, but the signal exhibits less contrast due to incomplete cancellation between the two waves. The expected signal can be derived, however, by introducing a matching coefficient [18].

Most modern laser Doppler velocimeters employ a differential Doppler configuration, as shown in Figure 2.5a. In this case, two laser beams probe the flow under investigation. The radiation scattered by seed particles moving with a velocity $\vec{V}$ through the intersection of the two beams is collected and photomixed on a single detector. If ω_1, $\vec{k}_1$ and $\omega_2 = \omega_1 + \omega_M$, $\vec{k}_2$ are the angular frequencies and wave vectors of the first and second beams, respectively, then from Eq. 2.16 the Doppler frequency shifted scattered radiation from each beam is,

$$\omega_{s1} = \omega_1 + \left(\vec{k}_{s1} - \vec{k}_1\right)\cdot\vec{V} \tag{2.25a}$$

$$\omega_{s2} = \omega_2 + \left(\vec{k}_{s2} - \vec{k}_2\right)\cdot\vec{V} = \left(\omega_1 + \omega_M\right) + \left(\vec{k}_{s2} - \vec{k}_2\right)\cdot\vec{V} \tag{2.25b}$$

Since the scattered radiation is collected in a single direction, as in Figure 2.5b, and since $\left|\vec{k}_2\right| \cong \left|\vec{k}_1\right|$, we can assume $\vec{k}_{s1} = \vec{k}_{s2}$. The detected beat frequency is therefore,

$$\omega_B = \omega_{s2} - \omega_{s1} \cong \omega_M - \left(\vec{k}_2 - \vec{k}_1\right)\cdot\vec{V} = \omega_M - \vec{K}\cdot\vec{V} = \omega_M - \omega_D\,, \tag{2.26}$$

where,

$$\vec{K} = \left(\vec{k}_2 - \vec{k}_1\right); \left|\vec{K}\right| = \frac{4\pi}{\lambda_1}\sin\left(\alpha/2\right) \tag{2.27}$$

defines the direction of the measured velocity component.

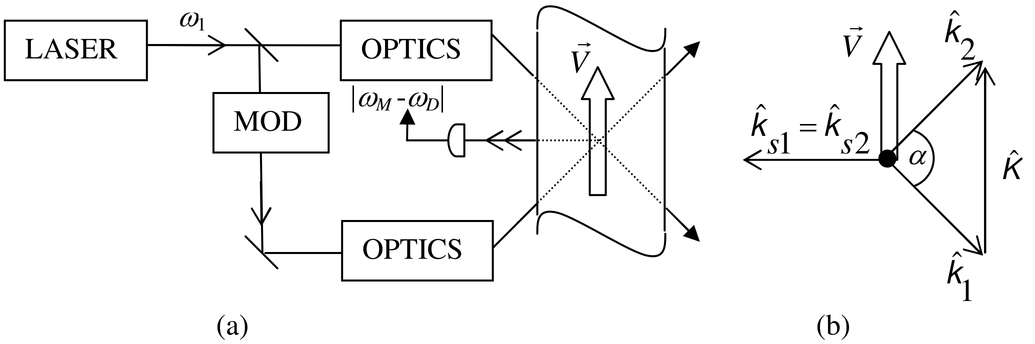

Figure 2.5 Schematic of differential LDV

One of the primary advantages of the differential LDV is that the detected beat frequency in Eq. 2.26 is independent of the detector position. The detector can therefore be positioned to accommodate the experiment or to maximize the collected Mie scattered signal. In addition, the probe volume can be visualized when utilizing the differential scheme; i.e. the intersection of the two laser beams defines the probe volume. Finally, the laser frequency stability requirement is greatly relaxed.

The signal generated by a seed particle traveling through the intersection of the two beams in a differential laser Doppler velocimeter is frequently described by a fringe model. Consider the superposition of two similarly polarized laser beams of equal amplitude, $E_{o1}=E_{o2}$, and with angular frequencies ω_1 and $\omega_2=\omega_1+\omega_M$,

$$E_1 = E_{o1}\cos\left(\vec{k}_1\cdot\vec{r}-\omega_1 t\right) \tag{2.28a}$$

$$E_2 = E_{o1}\cos\left(\vec{k}_2\cdot\vec{r}-\omega_2 t\right) \tag{2.28b}$$

As with the derivation of Eq. 2.24, it can be shown that the total field intensity of the two interfering beams is,

$$I(\vec{r},t) = 4I_o\cos^2\frac{\delta(\vec{r},t)}{2} = 2I_o\left[1+\cos\delta(\vec{r},t)\right], \tag{2.29}$$

where I_o is the intensity of both waves and $\delta(\vec{r},t)$ is the interference term,

$$\begin{aligned}\delta(\vec{r},t) &= (\omega_2-\omega_1)t-\left(\vec{k}_2-\vec{k}_1\right)\cdot\vec{r}\\ &= \omega_M t-\left(\vec{k}_2-\vec{k}_1\right)\cdot\vec{r}\end{aligned}$$

$$\delta(\vec{r},t) = \omega_M t-\vec{K}\cdot\vec{r} \tag{2.30}$$

Assume that the two laser beams intersect in the XZ-plane at angles ±α/2 from the z-axis, as in Figure 2.6. The interference term is then,

$$\delta(\vec{r},t) = \omega_M t-K_x x; K_x = \frac{4\pi}{\lambda_1}\sin\left(\alpha/2\right), \tag{2.31}$$

and a seed particle traveling through the probe volume with an x-component of velocity *u* will generate a modulated signal,

$$I_s(t)\propto\cos\left[(\omega_M-K_x u)t\right] \tag{2.32}$$

Comparing the modulation frequency in Eq. 2.30 with the beat frequency defined in Eqs. 2.26 and 2.27 we see that the signal predicted by the fringe model is equivalent to the Doppler effect-based prediction. (The conditions ensuring equivalence of the fringe and Doppler effect-based approaches are described by Rinkevichius [19,20]). To thoroughly understand the generated LDV signal, however, it is necessary to consider the Doppler-based signal generated by the scattered radiation. For instance, consider two laser beams polarized in the XZ-plane that intersect at α=90°, as in Figure 2.7. Since the beams are orthogonally polarized – i.e. $\hat{e}_1\perp\hat{e}_2$ – no interference pattern is generated at their intersection. Rayleigh scattered radiation from a molecule traveling through the intersection of the two beams will also be linearly polarized in the XZ-plane. However, since the scattered radiation is detected in the same direction, their polarizations coincide – i.e. $\hat{e}_{s1}=\hat{e}_{s2}$ – and a photomixed signal generates beats according to Eqs. 2.26 and 2.27. In addition, the fringe model does not account for the phase shifts and the polarization rotations of Mie scattered radiation [21].

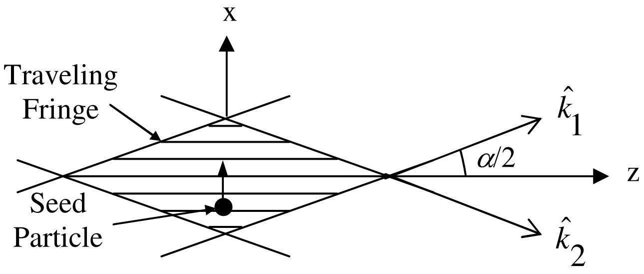

Figure 2.6 Interference pattern in probe volume of differential LDV

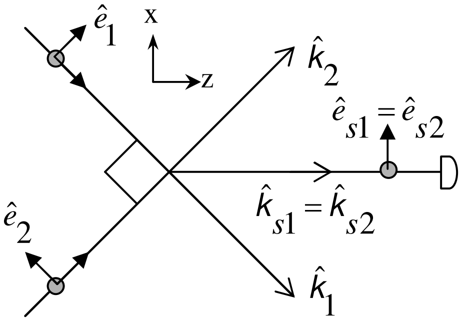

Figure 2.7 Demonstrating inadequacies of the fringe model

The primary difficulty associated with the differential LDV technique is ensuring that the flow is properly seeded; i.e. that the proper concentration of seed particles are introduced into the flow with a relatively uniform spatial distribution. If a relatively low concentration of seed particles is uniformly introduced into the flow, odds are that only one particle is in the probe volume at any given time. This also implies that most of the time there is no particle in the probe volume. The resulting detector signal in this case is a sequence of discrete wave packets, the width of which is a function of the particle residence time in the probe volume and the frequency of which is proportional to the velocity as defined in Eq. 2.26. Due to inevitable non-uniformities in the spatial distribution of the seed particles, the measurements are random in time and cannot resolve rapid velocity fluctuations. This leads to biasing errors in the measured velocity. (For a discussion of LDV biasing errors refer to the panel report edited by Edwards [22].)

The biasing errors in LDV measurements would disappear if the technique could resolve rapid velocity fluctuations. Unfortunately, this would require unattainable control over the seed concentration and distribution. Biasing errors always exist in LDV measurements. They can only be *minimized* by properly seeding the flow; i.e. quasi-continuous velocity measurements are only obtained when a proper concentration of seed particles are introduced relatively uniformly into the flow field. If the seed concentration is too low, the laser Doppler velocimeter is operating in the monoparticle regime as described above. If the particle concentration is too high, then several particles will be present in the probe volume at any given moment and cross-particle interference corrupts the signal. The interference is completely random due to the fact that the seed particles are randomly distributed in space. Matters are further complicated by the fact that the proper seed concentration depends on the flow velocities that will be encountered in the experiment. This also implies that biasing errors effectively limit the dynamic range of accurate velocity measurements.

Even with ideal seeding, measurements of the instantaneous frequency (and therefore the instantaneous velocity) would be precarious. The instantaneous frequency is defined as the time derivative of the instantaneous phase, $\omega=\mathrm{d}\varphi/\mathrm{d}t$. Even if the seed particles entering the probe volume are traveling at a constant velocity, the instantaneous frequency will still exhibit fluctuations due to phase variations introduced by each discrete Mie scattering particle. It is impossible to distinguish these fluctuations from those originating from a change in velocity. Nonetheless, turbulence measurements have been attempted using LDV. The results generally suffer from poor spatial and temporal resolution [23].

2.3.2 Interferometric Laser Doppler Anemometry (I-LDA)

Interferometric laser Doppler anemometry (I-LDA), like laser Doppler velocimetry, measures a single-component of velocity in a small probe volume by detecting the Doppler frequency shift of scattered radiation resulting from the bulk motion of the scattering particles. (Multi-component velocity measurements are possible with reference beam LDVs and I-LDAs by detecting the Doppler frequency-shifted scattered radiation along multiple – e.g. orthogonal – directions). Whereas LDV relies on the photomixing technique to determine the Doppler frequency shift, I-LDA utilizes a Fabry-Perot interferometer (FPI) to measure the Doppler frequency shift.

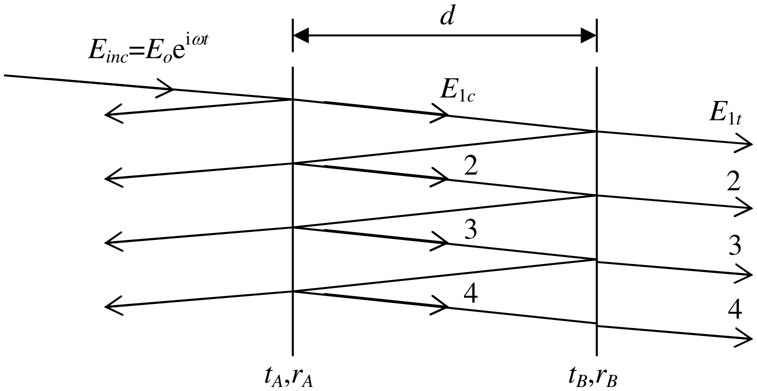

Figure 2.8 The planar FPI

Figure 2.8 illustrates the operational principle of a planar FPI, which is essentially two planar mirrors separated by some distance d. The front and rear mirrors of the FPI in Figure 2.8 are assumed to have transmissivities of t_A and t_B and reflectivities of r_A and r_B, respectively. (Absorption generally causes a negligible phase shift at the mirrors, and effectively decreases the cavity finesse. We will neglect this effect in our analysis). The circulating intensity in this FPI is the result of multiple beam interference, and can be derived from a simple scalar analysis. Consider a monochromatic laser beam of angular frequency ω ($K = \omega / c = 2\pi/\lambda \equiv$ wave number) and electric field amplitude E_o – i.e. $E_{inc} = E_o \mathrm{e}^{\hat{\imath}\omega t}$ – entering the planar FPI in Figure 2.8 at near normal incidence. The electric field amplitude within the FPI is simply the superposition of circulating waves, E_{nc},

$$\left.\begin{aligned} E_{1c} &= E_o t_A \mathrm{e}^{\hat{\imath}\omega t} \\ E_{2c} &= E_o t_A r_B r_A \mathrm{e}^{\hat{\imath}(\omega t - \delta)} \\ E_{3c} &= E_o t_A r_B^2 r_A^2 \mathrm{e}^{\hat{\imath}(\omega t - 2\delta)} \\ &\ldots \end{aligned}\right\} \Rightarrow \begin{aligned} E_c &= E_{1c} + E_{2c} + E_{3c} + \ldots \\ &= E_o t_A \mathrm{e}^{\hat{\imath}\omega t}\left[1 + r_A r_B \mathrm{e}^{-\hat{\imath}\delta} + \left(r_A r_B \mathrm{e}^{-\hat{\imath}\delta}\right)^2 + \ldots\right] \\ E_c &= E_o t_A \mathrm{e}^{\hat{\imath}\omega t}\left(1 - r_A r_B \mathrm{e}^{-\hat{\imath}\delta}\right)^{-1} \end{aligned} \tag{2.33}$$

where $\delta = 2Kd$ is the accrued phase shift of the laser beam after one roundtrip within the FPI. The circulating intensity follows:

$$\begin{aligned} I_c &\propto E_c E_c^* \\ &= E_o^2 \left[\frac{t_A}{1 - r_A r_B(\cos\delta - \hat{\imath}\sin\delta)}\right]\left[\frac{t_A}{1 - r_A r_B(\cos\delta + \hat{\imath}\sin\delta)}\right] \end{aligned}$$

$$I_c = I_{inc}\left[\frac{t_A^2}{\left(1 + r_A^2 r_B^2\right) - 2 r_A r_B \cos\delta}\right] \tag{2.34}$$

The transmitted beam intensity can be derived in like manner:

$$I_t = I_{inc}\left[\frac{(t_A t_B)^2}{\left(1 + r_A^2 r_B^2\right) - 2 r_A r_B \cos\delta}\right] \tag{2.35}$$

Noting that,

$$\sin^2\frac{\delta}{2} = \frac{1}{2}(1 - \cos\delta) \rightarrow 2\cos\delta = 2 - 4\sin^2\frac{\delta}{2} \tag{2.36}$$

and defining the reflectance $R \equiv r_A r_B$ and the transmittance $T = (1-R) \equiv t_A t_B$, Eq. 2.35 can be recast in a simplified form,

$$I_t = I_{inc}\left[\frac{(1-R)^2}{(1-R)^2 + 4R\sin^2 \delta/2}\right] = I_{inc}\left[\frac{1}{1 + F\sin^2 \delta/2}\right] \tag{2.37}$$

where F is the coefficient of finesse for the cavity,

$$F = \frac{4R}{(1-R)^2} \tag{2.38}$$

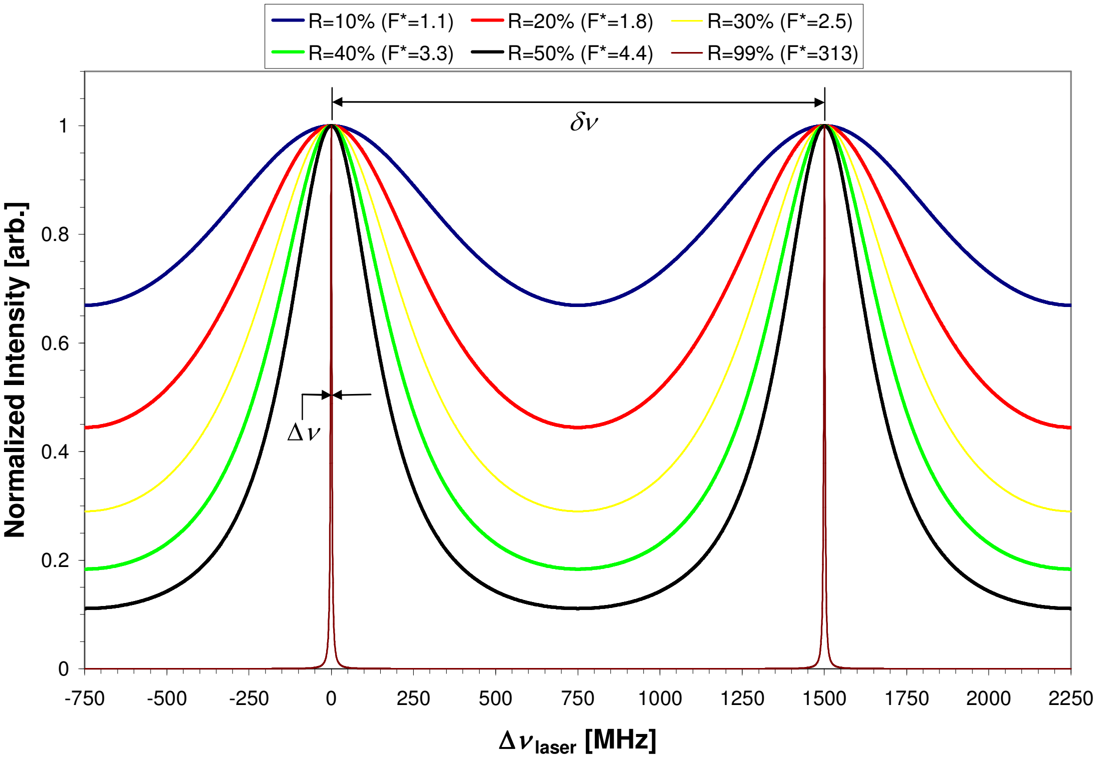

Figure 2.9 Airy pattern for planar FPI

Eq. 2.37 is the so-called Airy function defining the transmitted intensity through the FPI as a function of the frequency of the incident radiation and the mirror separation. Figure 2.9 shows the Airy function as a function of the frequency of incident radiation. The plot was generated by assuming that radiation with a centerline wavelength of λ=780 nm enters a planar FPI with a fixed mirror separation of d=10 cm at normal incidence. The frequency separation between the transmission maxima, referred to as the free spectral range (FSR), can be derived from Eq. 2.37 [14],

$$\delta\nu = {}^{cK}\!\big/_{\delta}, \tag{2.39}$$

as can the full-width at half-maximum (FWHM) of transmission feature itself,

$$\Delta\nu = \delta\nu \frac{(1-R)}{\pi\sqrt{R}}. \tag{2.40}$$

A FPI is most frequently defined in terms of its finesse, *F**, which is the ratio of the FSR to the FWHM,

$$F^{*} = {}^{\delta\nu}\!\big/_{\Delta\nu} = \frac{\pi\sqrt{R}}{(1-R)} = \frac{\pi}{2}\sqrt{F} \tag{2.41}$$

The finesse effectively represents the number of interfering waves in the FPI (i.e. the photon lifetime in the cavity). The intracavity beam will make many roundtrips in a cavity with highly reflective mirrors – i.e. with a large finesse. This results in a narrower transmission feature due to more complete cancellation of the interfering waves, as demonstrated in Figure 2.9.

Essentially all interferometric laser Doppler anemometers today utilize a confocal FPI, which has two identical planar-concave cavity mirrors separated by the mirror radius of curvature, *r*, as shown in Figure 2.10. The Airy function for a confocal FPI is still defined as in Eq. 2.37 with an accrued phase shift after one intracavity roundtrip of [24],

$$\delta = K\Delta s \tag{2.42}$$

where,

$$\Delta s = 4d + \frac{\rho_1^2 \rho_2^2 \cos 2\theta}{d^3} + \text{h.o.t.s} \tag{2.43}$$

The expression for the roundtrip optical path length, *Δs*, in Eq. 2.43 was derived by assuming that the incident laser beam enters the cavity near its optical axis at nearly normal incidence, as in Figure 2.10:

$$\left.\begin{array}{l} \rho_1 << d \\ \theta << 1 \end{array}\right\} \Rightarrow \rho_2 << d \tag{2.44}$$

As mentioned above, for a confocal FPI the mirrors are separated by the radius of curvature of the mirror surfaces, *r*:

$$d = r + \Delta\varepsilon \tag{2.45}$$

In Eq. 2.45, $\Delta\varepsilon$ accommodates any deviation of the mirror separation from the confocal condition.

The concentric rings in Figure 2.10 illustrate the radial interference fringes that are supported in a confocal FPI. These radial interference fringes will be discussed in greater detail below.

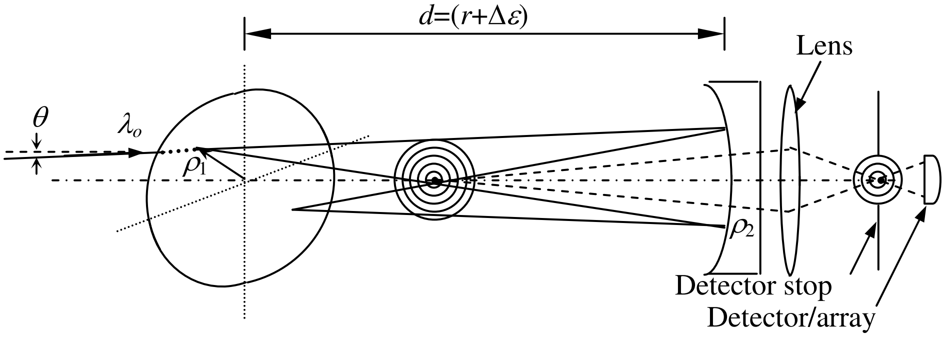

Figure 2.10 The confocal FPI

Three operational modes of I-LDA have been popularized by laser diagnosticians. Each of these operational modes utilize a confocal FPI to measure the Doppler frequency shift of Rayleigh scattered radiation from molecules in the flow. In one operational mode, the confocal FPI is effectively used as a high-resolution spectrometer. A portion of the interrogating laser beam is split off to serve as a reference beam. This reference beam and the Doppler frequency shifted scattered radiation collected from a probe volume in the flow are directed into the FPI, as shown in Figure 2.11a. The length of the FPI is linearly tuned over approximately one FSR. Knowing the FSR of the confocal Fabry-Perot cavity, the frequency shift of the collected Rayleigh scattered radiation relative to the reference beam can be determined, and a single velocity component in the probe volume can be calculated [25].

The accuracy of the measured velocity depends on the accuracy with which the free spectral range in known. From Eqs. 2.39 and 2.42, we see that the free spectral range is a function of the mirror separation:

$$\left.\begin{array}{l} \delta\nu = {}^{c}\!/\!{}_{\Delta s} \\ \Delta s \cong \left(r+\Delta\varepsilon\right)+\dfrac{\rho_1^2\rho_2^2\cos 2\theta}{\left(r+\Delta\varepsilon\right)^3} \xrightarrow{\theta=0\to\rho_1=\rho_2=\rho;\Delta\varepsilon<<r} \Delta s \cong \left(r+\Delta\varepsilon\right)+\dfrac{\rho^4}{r^3} \end{array}\right\} \Rightarrow$$

$$\Rightarrow \delta\nu \cong \frac{c}{r+\Delta\varepsilon+\dfrac{\rho^4}{r^3}} \tag{2.46}$$

For accurate velocity measurements, the FPI must be calibrated using a known frequency reference (e.g. an atomic absorption feature). In addition, the measurement assumes that the cavity length changes linearly with time as the cavity is tuned across one FSR. This must also be confirmed.

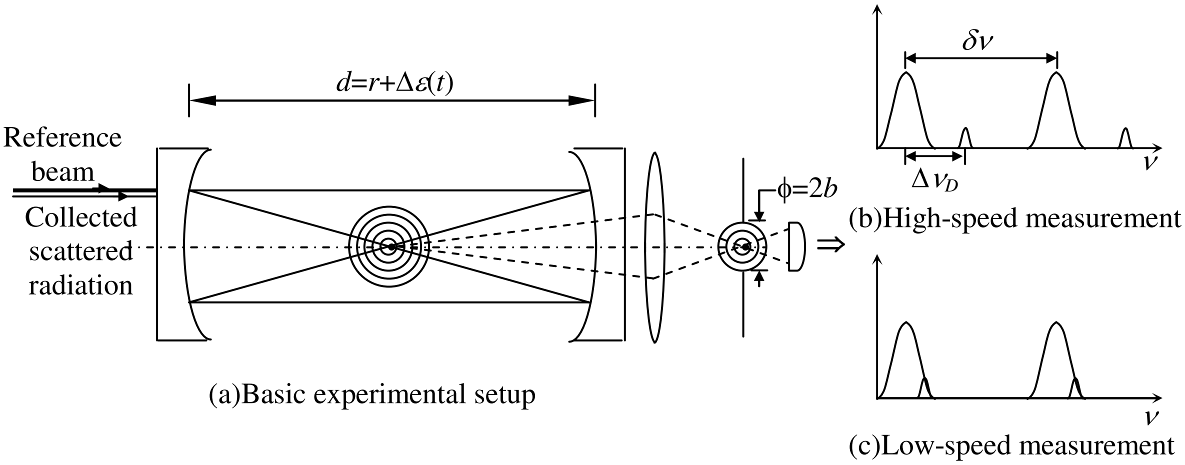

(a)Basic experimental setup

(b)High-speed measurement

(c)Low-speed measurement

Figure 2.11 Interferometric LDA – Operational mode #1

This first operational mode is best suited for measurements in high-speed flows for which the Doppler frequency shift is easily resolved, as in Figure 2.11b. Figure 2.11c illustrates the difficulty associated with low-speed flow measurements. To measure speeds approaching zero, the FPI finesse would need to approach infinity. For a confocal FPI, Eq. 2.41 implies that nearly perfect alignment (i.e. strict adherence to the confocal condition) of almost perfectly reflecting mirrors would be required. In fact, the practical low-speed limitation of this first operational mode is set by the relatively large detector aperture required to measure the relatively weak Rayleigh scattered radiation transmitted through the FPI. (This statement assumes that the laser linewidth and the broadened Rayleigh scattered radiation profile are sufficiently narrow, and can essentially be modeled as a Dirac delta functions in frequency. This is not necessarily a realistic assumption, but a detailed analysis would detract from the aim of this section, which is simply to introduce interferometric laser Doppler anemometry).

Referring to Figure 2.11, a detector with a finite circular aperture of radius *b* would measure a transmitted signal of,

$$P(\lambda,d,b)=\int_{\rho} I(\lambda,d,\rho)2\pi\rho\,\mathrm{d}\rho \tag{2.47}$$

where $I(\lambda,d,\rho)$ is the Airy pattern transmitted through the FPI. Combining Eqs. 2.37 and 2.42-2.44, and assuming that $\theta=0$, $\rho_1=\rho_2=\rho$, and $\Delta\varepsilon<<r$,

$$I(\lambda,d,\rho)=I(\lambda,\Delta\varepsilon,\rho)=I_{inc}\frac{1}{1+F\sin^2\left\{\left(\pi/\lambda\right)\left[4(r+\Delta\varepsilon)+\rho^4/r^3\right]\right\}} \tag{2.48}$$

Combining Eqs. 2.47 and 2.48,

$$P(\lambda,\Delta\varepsilon,b)=2\pi I_{inc}\int_0^b\frac{\rho}{1+F\sin^2\left\{\left(\pi/\lambda\right)\left[4(r+\Delta\varepsilon)+\rho^4/r^3\right]\right\}}\mathrm{d}\rho \tag{2.49}$$

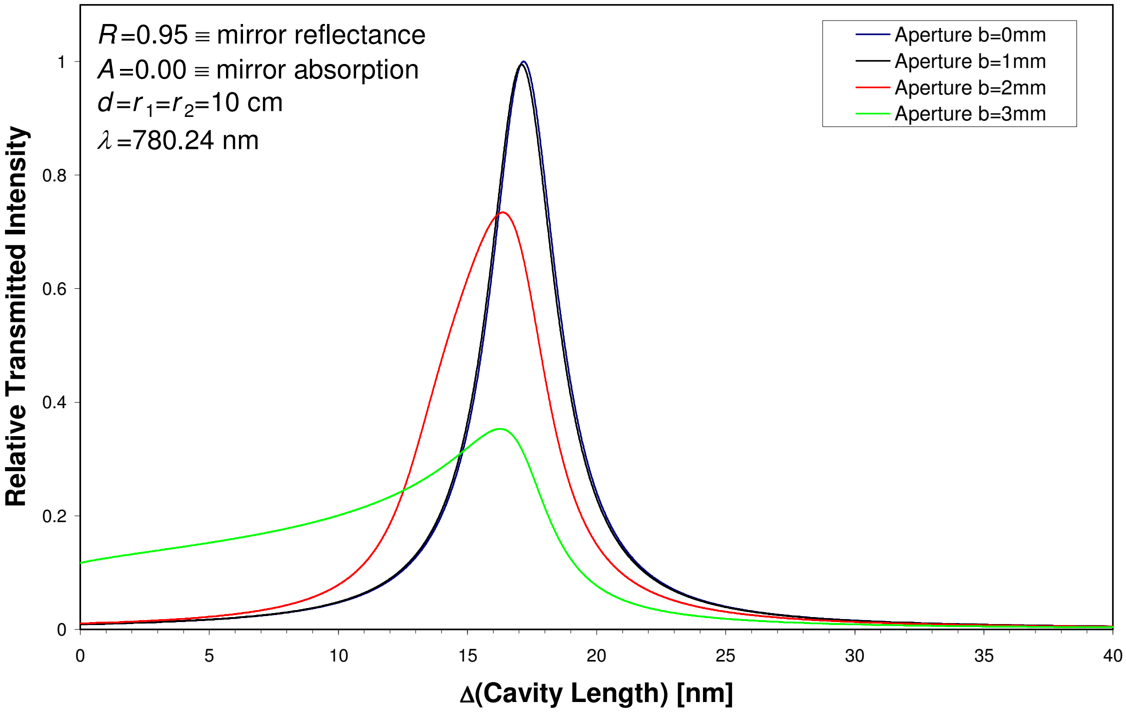

Figure 2.12 Airy pattern for a confocal FPI as a function of aperture size

Figure 2.12 is a plot of the detected signal in Eq. 2.49 as a function of $\Delta\varepsilon$ - i.e. the deviation of the mirror separation from the confocal condition – for various aperture radii, *b*. The plot assumes that a monochromatic beam of wavelength λ=780 nm is incident on a confocal FPI with a mirror reflectance of R=95% and a mirror radius of curvature of r=10 cm and that the Airy pattern is imaged onto a detector at unit conjugate ratio. From the figure we see that the larger the aperture, the more highly de-centered and asymmetric the detected transmission profile, and the lower the resolving power. It is this reduction in resolving power with increasing aperture size that sets the low velocity limit of the first operational mode discussed above; i.e. the low velocity limit is a compromise between the light gathering power required of the weak Rayleigh scattered signal and the resolving power of the FPI. (The resolving power of Fabry-Perot interferometers can be dramatically improved using modulation techniques [26]. When modulation techniques are employed, the first operational mode of I-LDA is conceptually similar to the MFRS velocimeter in the sweep mode of operation).

A second operational mode uses the same experimental setup illustrated in Figure 2.11a with two modifications: The mirror separation of the FPI is held constant (i.e. $\Delta\varepsilon \approx 0$=constant) and the detector is replaced with a CCD CMOS array or camera [27]. In this second mode of operation, the radial fringe pattern supported in the confocal FPI is imaged onto the camera. From Eq. 2.48 (which was derived by assuming that $\theta = 0$, $\rho_1 = \rho_2 << r$, and $\Delta\varepsilon << r$) we find that the maximum fringe intensities occur for,

$$\frac{\pi}{\lambda}\left[4(r+\Delta\varepsilon)+\frac{\rho^4}{r^3}\right]=m\pi \tag{2.50}$$

where m=0,1,2,… is the fringe order. In other words, the radius of the m^{th}-order interference ring is,

$$\rho_m \cong \left\{\left[m\lambda - 4(r+\Delta\varepsilon)\right]r^3\right\}^{1/4} \tag{2.51}$$

In the second operational mode, the radial separation between the lowest-order imaged fringe corresponding to the reference beam and the lowest-order imaged fringe corresponding to the Doppler shifted Rayleigh scattered radiation is used to provide a measure of the relative frequency shift, and hence the velocity. An auto-correlation technique is generally used to determine the spacing of the radial rings in the double ring fringe pattern generated by the reference beam and the scattered radiation [28]. The low velocity limit is still set by the resolving power of the FPI, which is compromised by the large detector aperture required to accommodate the weak Rayleigh scattered signal.

The primary advantage of the second interferometric operational mode over the first operational mode discussed is that the temporal resolution of the velocity measurements is not limited by the need to sweep the FPI; i.e. the velocity measurements can be made quasi-continuously. This advantage comes at a price, however. From Eq. 2.51 we see that the fringe radius is not merely a function of the transmitted wavelength, but is also a nonlinear function of the mirror separation. Assuming that the wavelength of the reference beam is known and stable, then the spacing of the reference fringes effectively provides a measure of the cavity separation. In the absence of a frequency-stable reference beam, accurate quantitative measurements in the second interferometric mode of operation require a relatively stable confocal FPI.

The final operational mode is particularly suited to the measurement of low velocities or rapid velocity fluctuations. Rather than use the FPI as a high-resolution spectrometer, the edge of the transmission profile is used as a frequency discriminator [25,29]. The cavity length of the FPI is tuned – or alternatively, the frequency of the interrogating laser beam is tuned – such that the interrogating laser beam frequency coincides with a particular set point of the FPI's transmission profile. Rayleigh scattered light is collected from a probe volume in the flow under investigation and is transmitted through the FPI. Provided that the width of the Rayleigh scattered radiation profile is narrower than the width of the FPI's transmission profile, than a Doppler frequency shift of the Rayleigh scattered light results in a measurable change in the detected signal transmitted through the FPI. After careful experimental calibration, this change in the detected signal can be directly correlated to the Doppler frequency shift, and hence the velocity.

There are several disadvantages to this particular operational mode. The accuracy of this technique depends on the cavity finesse, with high finesse FPIs providing the highest accuracy. Unfortunately, higher cavity finesse results in a narrower the transmission profile (and requires a narrower Rayleigh scattered spectrum to resolve the Doppler frequency shift). Therefore, the dynamic range of this technique is severely limited by the high resolution required for accurate velocity measurements at low velocities. The accuracy of the velocity measurements also depends on the stability of the frequency set point. A shift in the frequency of the interrogating laser beam would be misinterpreted as a Doppler frequency shift, and attributed to a velocity in the probe volume unless the FPI tracks the change. This technique therefore requires stabilization of the interrogating laser frequency *and* the FPI cavity length. Alternatively, the FPI cavity can be locked to the interrogating laser frequency. Also, since the detected power of the collected Rayleigh scattered radiation transmitted through the FPI is directly correlated to the Doppler frequency shift, it is necessary to account for fluctuations in the probe laser power, P_o, and in the number density of molecules in the probe volume, N_o – i.e. $P_{\text{detected}} \propto P_{\text{scattered}} I_t \propto N_o P_o I_t$. This is accomplished using a cumbersome two-detector scheme: One detector detects the Rayleigh scattered radiation directly, $P_{\text{detector,1}} \propto N_o P_o$, and the second detector detects the Rayleigh scattered radiation transmitted through the FPI, $P_{\text{detector,2}} \propto N_o P_o I_t$:

$$\frac{P_{\text{detector,2}}}{P_{\text{detector,1}}} \propto I_{\text{t}}(\lambda) \tag{2.52}$$

In many regards MFRS velocity measurements in the frequency-locked mode of operation are conceptually similar to I-LDA measurements in the third operational mode. In particular, even though each technique employs its own frequency discriminator – i.e. MFRS measurements rely on a Doppler broadened absorption feature in the D_2-line of Rb and I-LDA measurements rely on an Airy profile – both techniques suffer from the same experimental complexities. Whereas I-LDA measurements require two detectors, however, the frequency-locked MFRS velocimeter utilizes a ratio detection scheme to account for scattering power fluctuations with only one detector. Frequency-locked MFRS measurements still require a frequency stable probe laser and a temperature stable Rb vapor cell, but there is no *practical* limit to the dynamic range of high resolution velocity measurements theoretically possible with the frequency-locked MFRS velocimeter.

I believe that the most difficult experimental aspect of I-LDA measurements in the third operational mode or MFRS measurements in the frequency-locked mode is acquiring an accurate calibration profile. Accurate velocity measurements using either technique require a calibration profile that accounts for the thermodynamics of the flow under investigation. Since the frequency dependent signal measured using either technique is sensitive to the spectral lineshape of collected and detected scattering, a calibration profile acquired in static air could not, for instance, be used to make velocity measurements in a supersonic expansion of CO_2. Imagine trying to measure the velocity in the boundary layer of a hypersonic flow. Due to the large temperature gradients present, velocity measurements made near the edge of the boundary layer would require a different calibration profile than velocity measurements made near the surface. As will be discussed in the next chapter, I never managed to acquire a reliable, repeatable calibration profile in the scattering arm of the MFRS velocimeter utilizing molecular Rayleigh scattering. I imagine that it is equally difficult to acquire a calibration profile for I-LDA measurements in the third operational mode.

2.3.3 Planar Doppler Velocimetry (PDV)

Planar Doppler velocimetry (PDV), alternatively known as Doppler global velocimetry (DGV) or filtered planar scattering (FPS), is conceptually similar to the third I-LDA operational mode introduced at the end of the previous sub-section (and in many regards to the frequency-locked MFRS velocimeter). However, rather than use the edge of a FPI transmission profile as a frequency discriminator, PDV utilizes the edge of a molecular absorption feature as a frequency discriminator. Since the absorption properties of a molecular gas are independent of the propagation angle through the gas, scattering from a wide field of view (i.e. from a plane) can be collected and filtered by the molecular vapor filter.

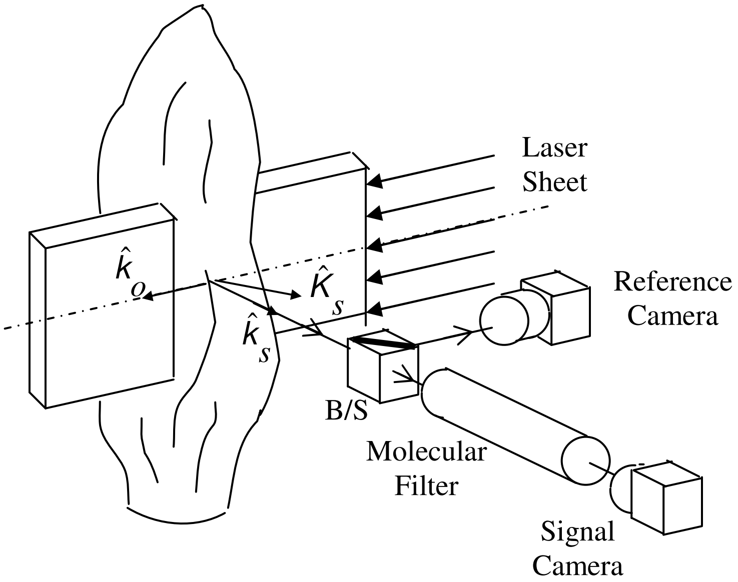

Figure 2.13 PDV experimental arrangement

Figure 2.13 shows a typical PDV optical arrangement for measurement of a single velocity component in a two-dimensional plane. (The PDV technique can be configured to measure two or three velocity components). The laser sheet is typically generated by a high power, pulsed, narrow linewidth, injection-seeded, frequency-doubled Nd:YAG laser, and frequency discrimination is provided by an iodine vapor filter [30,31,32]. Mie scattering from condensed seed molecules (e.g. acetone condensate, ethanol condensate, condensed ice crystals) or seed particles in the laser sheet is collected, transmitted through the iodine filter, and imaged by a signal camera. By using a short-pulse laser, a series of essentially instantaneous time resolved images of the Mie scattering in the laser sheet in generated; when continuous lasers are used and average measurements obtained, seed non-uniformities in rapidly fluctuating flows may generate biases in the measurements [32]. Velocity data in the plane is inferred from the intensity of the imaged scattering, which is a function of the interrogating laser frequency, the laser sheet intensity, the scattering cross-section of each seed molecule, the iodine filter profile, and the Doppler frequency shift of the Mie scattered radiation due to the bulk velocity of the scattering particles.

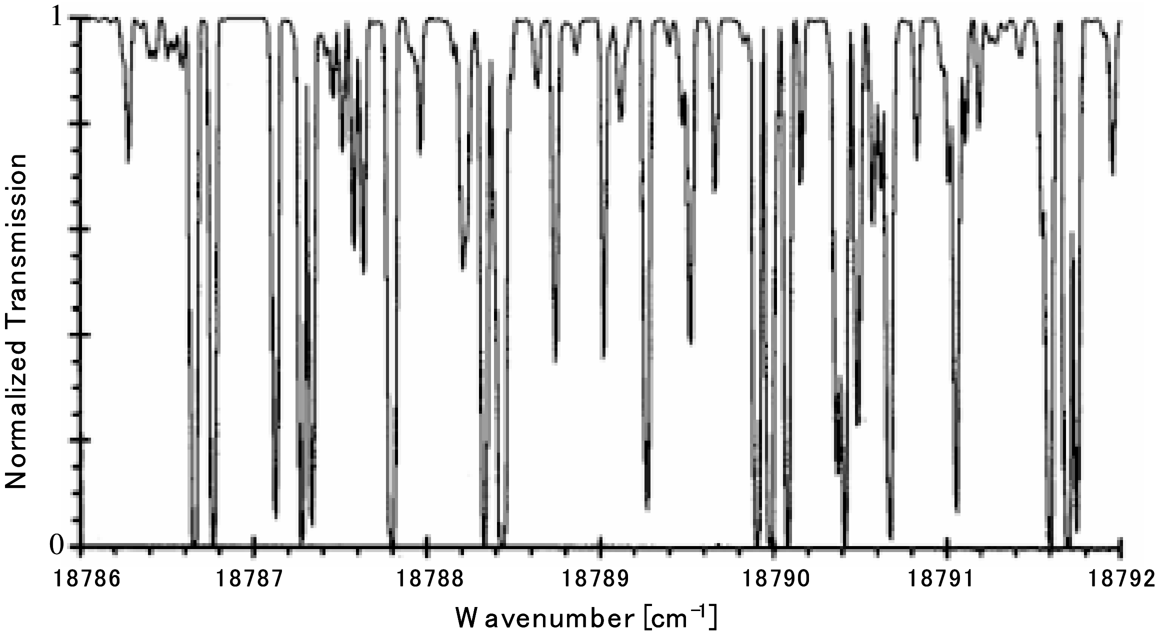

Figure 2.14 Iodine absorption profile in the range of a frequency-doubled Nd:YAG [31]

The laser frequency is typically stabilized to an absorption peak in the iodine filter profile. In this case, reflections from walls and windows that would degrade the signal-to-noise (S/N) of the detected Mie scattering image are strongly attenuated by the iodine filter. The dependence of the Mie scattering image on the laser sheet intensity and the Mie scattering cross-section can be normalized out by detecting an unfiltered reference image as in Figure 2.13. Figure 2.14 shows the iodine absorption spectrum in the range of a frequency-doubled Nd:YAG laser. A great deal of experimental work has been carried out to accurately characterize the iodine absorption profile, and careful measurements have been used to correct theoretical models [33].

Knowing the laser frequency and filter profile, and having normalized out the laser sheet intensity and scattering cross-section dependence of the Mie scattered signal, the image intensity can be directly correlated to the Doppler frequency shift of the Mie scattered radiation, and hence the velocity of the seed particles in the laser sheet. This is demonstrated in Figure 2.15 for a generic absorption feature. The length, temperature, and vapor pressure of the iodine vapor filter must be tailored to the particular experiment. Nitrogen is often added to the cell in order to pressure broaden the iodine absorption profile and spread the intensity contrast over the velocity range of interest.

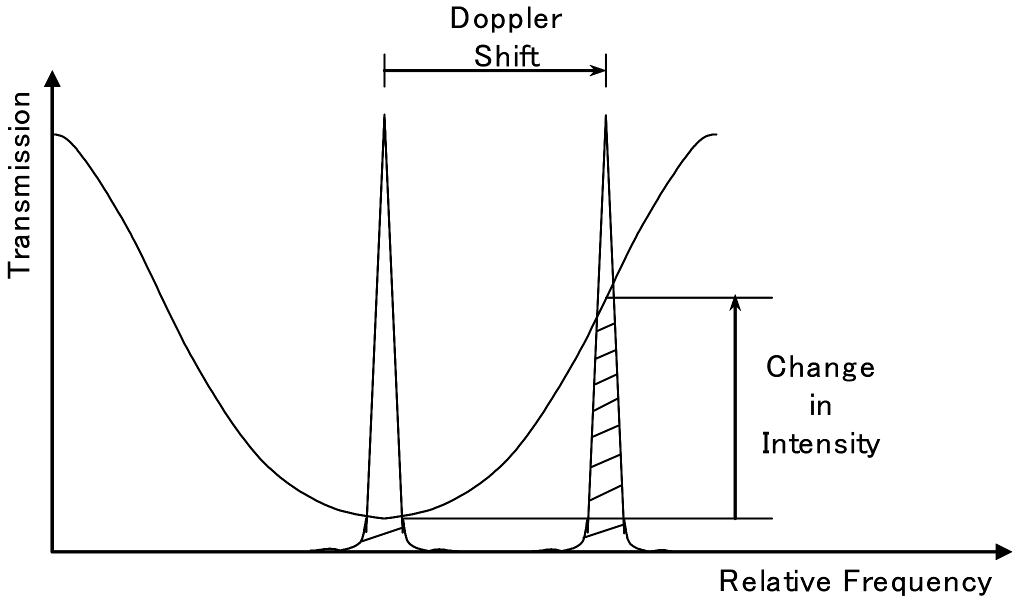

Figure 2.15 Correlating the Doppler frequency shift to the change in detected intensity

For accurate PDV measurements the frequency of the interrogating laser beam must be stable and the filter profile must be known and constant. The primary disadvantage of the technique, however, is its reliance on a high power laser and flow seeding to provide a sufficient S/N in the detected images. PDV is nonetheless a powerful optical diagnostic technique, and is useful where a planar perspective of the flow field is desired.

2.3.4 Competing Research

Planar Doppler velocimetry is a planar extension of a point technique that is referred to as filtered Rayleigh scattering (FRS), which uses an atomic or molecular vapor filter to quantify the Doppler frequency shift of Rayleigh scattered light collected from a probe volume in the flow under investigation. Even with the measurement confined to a point (i.e. with a relatively high intensity in the measurement probe volume when compared to the intensity in a measurement plane), FRS still requires a relatively high power laser source to provide a detectable signal from molecular Rayleigh scattering. The following section briefly introduces two concepts similar to MFRS, that use modulated absorption spectroscopy techniques to improve detectability of the weak Rayleigh scattered signal: Frequency-modulated filtered light scattering (FM-FLS) and point Doppler velocimetry (pDV).

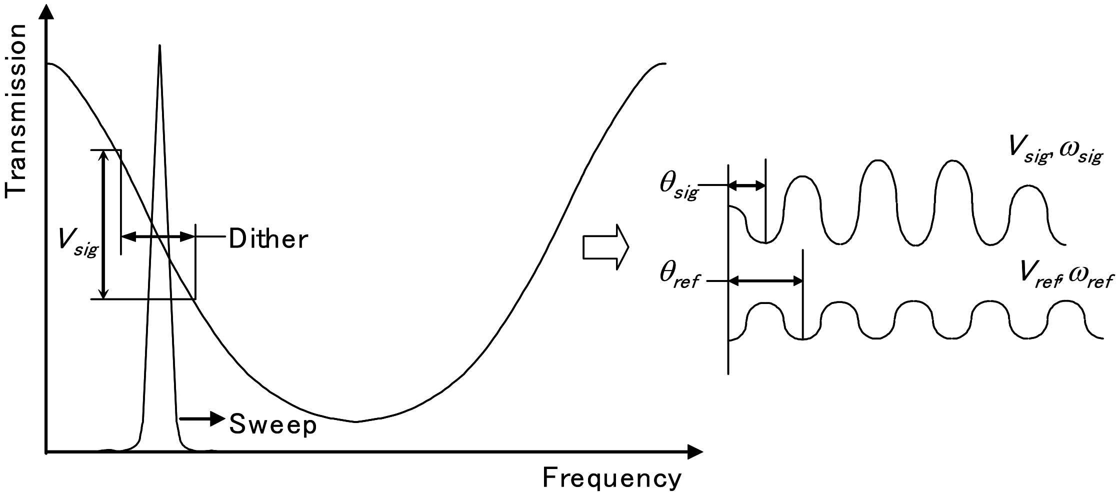

Figure 2.16 Illustration of modulated absorption spectroscopy

FM-FLS, pDV, and MFRS are all premised on detecting a modulated absorption of the collected Rayleigh scattered signal using lock-in amplifiers. Consider a laser beam that is slowly swept in frequency across an absorption feature, as in Figure 2.16. If the laser frequency is simultaneously dithered at a rapid rate, ω_{sig}, then a modulated absorption signal is generated at the dither frequency. Homodyne detection (i.e. single frequency detection) of the measured modulated absorption signal is accomplished with a lock-in amplifier that is synchronized with the dither frequency. The lock-in amplifier multiplies the modulated absorption signal, $V_{sig}\sin(\omega_{sig}t+\theta_{sig})$, by the synchronized internal reference signal, $V_{ref}\sin(\omega_{ref}\ t+\theta_{ref})$. With the internal reference synchronized to the dither frequency – i.e. with $\omega_{ref}=\omega_{sig}$ – the resulting signal has a DC-component and an AC-component. All AC-components (e.g. including noise at $\omega_{sig}\neq\omega_{ref}$) are extinguished by a low-pass RC-filter internal to the lock-in amplifier, and a phase sensitive signal proportional to the modulated absorption amplitude is output from the lock-in. (Homodyne detection utilizing lock-in amplifiers is further discussed in Appendix A).

FM-FLS was developed by Grinstead et al. at Princeton University [34]. They utilized a Ti:sapphire laser operated in a ring cavity configuration that provided approximately 600 mW of narrow linewidth lasing at 770 nm. Coarse frequency tuning was provided by a galvenometer-driven, intracavity tilt plate that changed the effective cavity length of the laser. A resonant electro-optic modulator was used to impose a 100 MHz frequency sideband on the Ti:sapphire output.

During operation of the FM-FLS velocimeter, Rayleigh scattered light collected from a probe volume interrogated by the modulated laser output is passed through a potassium vapor filter (^{39}K) and detected by a PMT. The frequency of the Ti:sapphire laser is continuously tuned to keep the frequency of the Doppler shifted Rayleigh scattered light centered on an absorption peak of the inhomogeneously broadened D$_1$-line of ^{39}K ($4^2P_{1/2}\leftarrow4^2S_{1/2}$) at 769.9 nm. This is accomplished by monitoring the first harmonic of the modulated absorption signal (i.e. the **1*f***-signal) provided by the 100 MHz electro-optic modulator; the 100 MHz modulated absorption signal is first mixed down to 100 kHz for homodyne detection by a digital lock-in.

The first harmonic of the modulated absorption signal output by a lock-in amplifier approximates the first derivative of the Doppler broadened absorption profile, with a zero-crossing at the absorption peak. Therefore, any drift on the Doppler shifted Rayleigh scattered light frequency from the absorption peak results in a **1*f***-signal. This error signal is sent to an analog proportional-integral (PI) controller used for closed-loop feedback control of the Ti:sapphire frequency. With the Rayleigh scattered light stabilized to an absorption peak in the D$_1$-line of potassium – the frequency of which is well known – the Doppler frequency shift of scattered light is then determined by measuring the frequency of the Ti:sapphire output. This is accomplished by photomixing the Ti:sapphire output with a stable reference beam of known frequency and detecting the beat frequency.

As employed the FM-FLS is a rather complicated technique. It utilizes a complicated, expensive laser system to generate a detectable Rayleigh scattered, modulated absorption signal. In addition, the photomixing technique relies on an additional laser of known and stable frequency. Nonetheless, the photomixing technique obviates the need to account for density and laser power fluctuations in the measurement probe volume, and provides a dynamic range that is limited only by the bandwidth of the photomixing detector. FM-FLS is a truly novel approach to a difficult problem.

The pDV technique, developed by Crafton et al. at Purdue University, is conceptually *identical* to the frequency-locked mode of the modulated filtered Rayleigh scattering (MFRS) technique that we are developing [35]. It differs only in respect to the laser source and the atomic vapor filter utilized; pDV utilized a 150 mW DBR laser at 852 nm in conjunction with a cesium vapor Faraday cell. The pDV technique has been employed to measure the velocity of a spinning disk and a smoke seeded subsonic jet.

Chapter 3: Modulated Filtered Rayleigh Scattering (MFRS)

3.1 Introduction

Laser velocimeters have become a substantial asset to experimental research in fluid mechanics. As discussed in the previous chapter, filtered Rayleigh scattering (FRS) is one of several established techniques used for measuring flow velocity with laser light. FRS is based on the Doppler effect, a phenomenon that is observed whenever there is relative motion between a radiating source and an observation point. In an FRS experiment, laser light incident on a probe volume in the flow under investigation is elastically scattered from some of the molecules (or atoms) in that volume. This scattered radiation is Doppler shifted in frequency from the perspective of some observation point if the molecules in the probe volume are moving with a bulk velocity relative to that observation point. In particular, when laser light at a centerline wavelength λ_o is scattered from a target with velocity V, it is Doppler shifted in frequency according to

$$\Delta\nu_D = \frac{V}{\lambda_o}\left[\hat{k}_V \bullet \left(\hat{k}_s - \hat{k}_o\right)\right]. \tag{3.1}$$

The unit vectors in the brackets define the geometry of the experiment: $\hat{k}_V, \hat{k}_s, \hat{k}_o$ are the unit vectors in the direction of the gas velocity, the scattered light (i.e. the observation direction), and the laser beam propagation respectively. (In Eq. 3.1 I simply recast the equation derived in Section 2.3 for the Doppler frequency shift; e.g. see Eq. 2.16). Figure 3.1 shows a generic FRS experimental setup.

FRS velocity measurements avoid the drawbacks associated with the introduction of a physical probe into the flow being interrogated. In addition, molecular Rayleigh scattering of laser light simplifies the measurement since it obviates the complications of flow seeding. It is the pW-level power that molecular Rayleigh scattering provides that presents the principal technical challenge for FRS experiments. All FRS velocimeters rely on flow seeding and/or relatively expensive high-power laser systems to obtain a detectable signal from Rayleigh scattering.

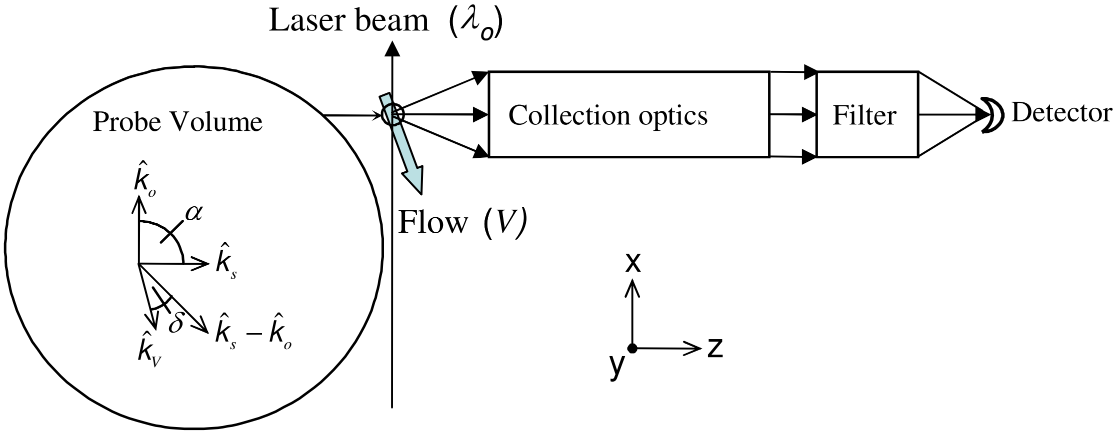

Figure 3.1 Generic FRS experimental setup

In the 1990's Dr. Varghese of the Department of Aerospace Engineering at the University of Texas conceived of a promising technique, which he termed modulated filtered Rayleigh scattering (MFRS), to improve detectability of the Doppler frequency shifted signal provided by molecular Rayleigh scattering in an FRS experiment. The MFRS technique is a novel variation of FRS, utilizing modulated absorption spectroscopy techniques to improve detectability of the weak Rayleigh scattered signal. As will be discussed in the next chapter, the MFRS velocimeter utilizes a relatively low-power, relatively inexpensive diode-based laser system to provide a weak Rayleigh scattered signal from a probe volume in the flow under investigation. The compact, rugged construction of semiconductor diode lasers is an attractive feature considering the environmental extremes encountered in many experiments, and their frequency tuning capability makes them ideally suited for implementation of homodyne detection using lock-in amplifiers.

To implement homodyne detection, the optical frequency of the diode-based laser beam interrogating the flow under investigation is modulated. The optical frequency of a stand-alone diode laser varies with injection current because of changes in the carrier density in the active layer and changes in temperature resulting from Joule heating. However, the temperature change is the dominant effect for time scales greater than approximately 1μs; i.e. changing the injection current is essentially a means of rapidly changing the cavity temperature. The diode laser frequency tunes with temperature because of the change in the optical path length of the cavity between the facets and a change in the index of refraction of the active layer, both resulting in a shift in the lasing mode wavelength [36,37]. The diode-based laser system developed for our experiment relies on feedback from an optical-frequency selective element to effect frequency tunability and is discussed in the next chapter.

The frequency modulation of the interrogating beam is imposed on the light scattered from the molecules present in the probe volume. This frequency-modulated Rayleigh scattered light is collected from the probe volume in the flow under investigation and transmitted through a rubidium (Rb) vapor filter before being detected. Alkali metal vapors have a high optical depth at modest vapor pressures, and their narrow linewidth is ideally suited for high-resolution velocimetry. In addition, 670 nm-850 nm is a popular wavelength range for commercially available diode lasers. Rubidium, in particular, has a strong absorption at 794.8 nm (D_1-line) and 780 nm (D_2-line). The detected modulated absorption signal is sent to a lock-in amplifier synchronized with the modulation frequency to provide high levels of background noise rejection [38]. The resulting lock-in signal provides a measure of the Doppler frequency shift of the Rayleigh scattered light due to a bulk velocity in the probe volume.

The aim of this chapter is to provide a realistic calculation of the expected signal-to-noise of the MFRS technique. The next three sections of this chapter – 3.2, 3.3, and 3.4 – will discuss the theoretical underpinnings of the MFRS technique: Rayleigh scattering, absorption spectroscopy, and modulated absorption spectroscopy, respectively. (Laser Doppler anemometry has already been discussed in Section 2.3, and the Doppler frequency shift affected by a bulk fluid velocity will not enter into our signal-to-noise calculations). An understanding of the theoretical details of each of these topics is necessary to calculate the expected signal when utilizing the MFRS technique – i.e. the lock-in signal. The general theoretical discussion of each of these three topics will be accompanied by experimental comparison. The experimental data provided in each section are not intended to simply validate the theory. All experimental data in this chapter were acquired using the same equipment utilized during frequency-locked MFRS velocity measurements – e.g. the same diode-based laser system, the same detectors, the same electronics, the same Rb vapor filters, and essentially the same optical designs. Comparison of the theory to these experimental data therefore allows for a more detailed description of the experimental apparatus that was ultimately used to make frequency-locked MFRS velocity measurements. The accuracy of the signal-to-noise calculation in this chapter ultimately depends on the number and validity of assumptions invoked. The experimental data provided in this chapter allow us to reduce the number of assumptions made pertaining to our specific experimental apparatus.

After developing a theoretical model describing the expected lock-in signal, I will turn my attention in Section 3.5 to a discussion of the noise components that corrupt MFRS measurements. Though much of the discussion in this section will be of general relevance to any laser-based measurement, the intent of this section is to accurately account for all noise that corrupts our specific experiment. For instance, the MFRS velocimeter as currently configured utilizes a photomultiplier tube (PMT) for detection of the modulated absorption signal in the scattering arm of the experiment, and any noise calculations must therefore account for PMT dark current. In addition, it is the high levels of background noise rejection provided by the lock-in amplifier utilized in the MFRS technique that ultimately improves detectability of the weak Rayleigh scattered signal. Only by accounting for this feature of the MFRS technique will the signal-to-noise calculations realistically represent MFRS measurements.

The theoretical signal-to-noise ratio for the MFRS velocimeter as configured during preliminary frequency-locked measurements will be calculated and compared to the signal-to-noise ratio for an optimized experimental arrangement in the final section of this chapter. I struggled to make frequency-locked MFRS measurements using molecular Rayleigh scattering from static air and from a jet of N_2. The signal-to-noise analysis concluding this chapter clearly demonstrates that with the MFRS velocimeter configured as it was during preliminary frequency-locked measurements the signal-to-noise ratio was simply too low to provide reliable measurements in a gas-phase flow. The signal-to-noise ratio of frequency-locked MFRS measurements could have been substantially improved by using a modulation index of m=2.3 and by using a z=100 mm Rb vapor cell heated to T=310 K in the scattering arm of the experiment.

3.2 Rayleigh Scattering

Rayleigh scattering describes the elastic scattering of light from atoms, molecules, and small particles with a circumference much less than the wavelength of the interrogating light. The theory used to describe Rayleigh scattering derives from a simple classical perspective: An oscillating electromagnetic field applied to an atom forces the electron “cloud” surrounding the nucleus of the atom to oscillate. From this perspective, Rayleigh scattering can be envisioned as originating from a classical linear electric dipole that consists of a negative charge ($-q$) linearly oscillating in a simple harmonic motion about an equal positive charge ($+q$).

First consider a linear electric dipole oriented along the y-axis, as shown in Figure 3.2, and oscillating at an angular frequency ω. The resulting time dependent electric dipole moment is,

$$\vec{p} = p_o \cos \omega t \hat{e}_y = qd \cos \omega t \hat{e}_y , \tag{3.2}$$

where d is the maximum charge separation and $\hat{e}_y$ is a unit vector oriented along the y-axis and describing the orientation of the electric dipole. The electric and magnetic fields generated by this oscillating linear electric dipole can be derived from Maxwell's equations. At a distance $R >> c/\omega$, in the so-called wave or radiation zone, we obtain the following expression for the electric field produced in vacuum by this oscillating linear electric dipole [39]:

$$\vec{E} = -\left(\frac{\omega}{c}\right)^2 \frac{p_o}{R} \sin\theta \exp\left[-\hat{\imath}\omega\left(t - R/c\right)\right]\hat{e}_\theta \ . \tag{3.3}$$

In Eq. 3.3 c is the speed of light in vacuum, θ is the angle between the dipole orientation and the direction of observed radiation, and $\hat{e}_\theta$ is a unit vector oriented along the electric field polarization of the observed radiation.

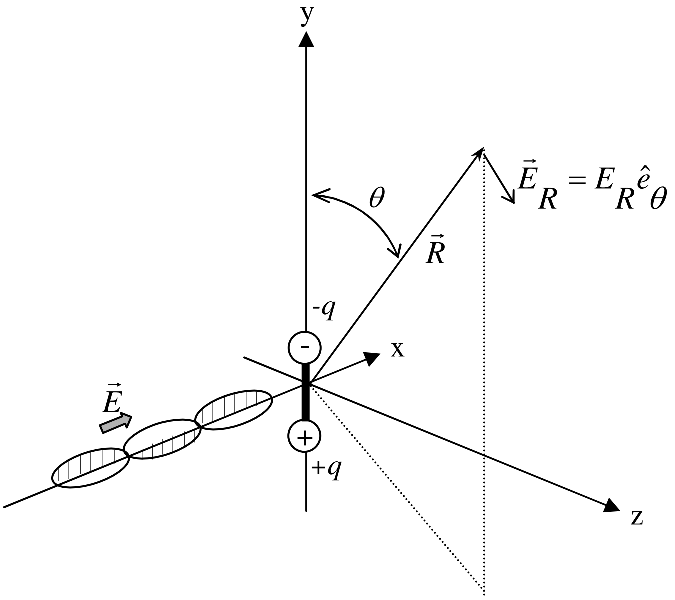

Figure 3.2 Linear electric dipole under the influence of an external electric field

Let us now regard a gas as consisting of atoms that are polarizable, and which therefore generate dipole oscillations under the influence of an external electric field, $\vec{E}$. (The discussion below is restricted to atoms and so-called nonpolar molecules, having no permanent dipole moment in the absence of an external field. In addition, we will confine our attention to isotropic, nonmagnetic gases). As a good approximation, we can assume that the electric dipole moment generated in a single polarizable atom under the influence of the electric field is proportional to that electric field,

$$\vec{p} = \alpha \vec{E}\,. \tag{3.4}$$

The proportionality constant, α, represents the mean polarizability of the atom. Referring now to Eqs. 3.2-3.4 as well as Figure 3.2, we find that the electric field generated by a single polarizable atom under the influence of an incident external electric field, $\vec{E} = E_o \cos(Kx + \omega t)\hat{e}_y$, oscillating at an angular frequency ω, propagating in the x-direction, and aligned (i.e. linearly polarized) along the y-direction is,

$$\vec{E}_R = -\left(\frac{\omega}{c}\right)^2 \frac{\alpha E_o}{R} \sin\theta \exp\left[\imath K(y + R)\right]\hat{e}_\theta\,. \tag{3.5}$$

Eq. 3.5 describes the classically derived electric field generated by atomic Rayleigh scattering of incident EM-radiation. The intensity of the Rayleigh scattered radiation is simply,

$$I_R = \left(\frac{\omega}{c}\right)^4 \left(\frac{\alpha}{R}\right)^2 \sin^2\theta\, I_o\ , \tag{3.6}$$

where I_o is the intensity of the light incident upon the atom. From Eq. 3.6 we see that the intensity of Rayleigh scattered radiation is proportional to ω^4. This is why the sky is blue; e.g. as the sun's visible light propagates through our atmosphere, Rayleigh scattering of blue light dominates Rayleigh scattering at the longer visible wavelengths. In addition, we see that there is an angular dependence to the Rayleigh scattered intensity that accounts for the fact that the scattered light is strongly polarized. For instance, no scattering is observed along the direction of the incident electric field polarization – i.e. if we neglect orientational and anisotropic scattering effects, no scattering is observed at $\theta = 0°$.

The Rayleigh scattering intensity is often written in terms of a differential scattering cross-section,

$$I_R = \left(\frac{\partial\sigma}{\partial\Omega}\right)\left(\frac{1}{R}\right)^2 I_o\,. \tag{3.7}$$

Comparing Eqs. 3.6 and 3.7 we find that the differential scattering cross-section is,

$$\left(\frac{\partial\sigma}{\partial\Omega}\right) = \left(\frac{\omega}{c}\right)^4 \alpha^2 \sin^2\theta\,. \tag{3.8}$$

The mean polarizability, α, of an atomic medium can be cast in terms of the index of refraction, n, of the medium using the Lorentz-Lorenz formula [39]:

$$\alpha = \frac{3}{4\pi N}\frac{n^2-1}{n^2+2}. \tag{3.9}$$

It is important to note that the mean polarizability defined in Eq. 3.9 is independent of number density, N: $N \propto \left(n^2-1\right)$ (this proportionality is derived in Appendix B using a classical kinetic model of the electric dipole [40] and Maxwell's equations) and the term $3/\left(n^2+2\right)$ is a field correction factor [41]. The number density introduced in the Eq. 3.9 is therefore understood to represent a reference number density associated with index of refraction measurements of a particular transmissive media in a particular thermodynamic state.

Inserting Eq. 3.9 into Eq. 3.8 and noting that $\omega/c = K = 2\pi/\lambda$, where λ is the wavelength of the light incident upon the atom, we arrive at the following expression for the differential scattering cross-section:

$$\left(\frac{\partial\sigma}{\partial\Omega}\right) = \frac{9\pi^2}{\lambda^4 N^2}\left(\frac{n^2-1}{n^2+2}\right)^2 \sin^2\theta. \tag{3.10}$$

For low density gases n~1 and the expression for the differential scattering cross-section in Eq. 3.10 can be approximated by,

$$\left(\frac{\partial\sigma}{\partial\Omega}\right) \approx \frac{4\pi^2}{\lambda^4}\left(\frac{n-1}{N}\right)^2 \sin^2\theta. \tag{3.11}$$

Rayleigh scattering experiments rely on the efficient collection of scattered radiation over a limited solid angle. From Eq. 3.7 we can derive the Rayleigh scattered power collected over a differential solid angle, $\partial\Omega = \mathrm{d}A/R^2$:

$$\partial P_{coll} = I_R \mathrm{d}A = I_o\left(\frac{\partial\sigma}{\partial\Omega}\right)\partial\Omega. \tag{3.12}$$

Integrating Eq. 3.12 over the collection solid angle, $\Delta\Omega$, yields the collected Rayleigh scattered power,

$$\Delta P_{coll} = I_o \int_{\Delta\Omega}\left(\frac{\partial\sigma}{\partial\Omega}\right)\partial\Omega. \tag{3.13}$$

Eq. 3.13 describes the radiant power collected over a solid angle $\Delta\Omega$ from a single polar atom driven into harmonic dipole oscillation by light of incident intensity I_o. Now, consider a laser beam of cross-sectional area A_o, wavelength λ, and intensity I_o that is incident on a gas of number density N_o consisting of a single atomic species. If the atoms were motionless, uniformly distributed, and of sufficiently high density, then the Rayleigh scattered radiation would coherently add in the direction of the propagating laser beam and cancel in all other directions [39]. In reality, the thermal motion of the atoms results in microscopic density fluctuations that randomize the interferences between the light scattered from each of the individual atoms [42]. As a consequence, the total scattered intensity from the ensemble of atoms is just the sum over individual intensities scattered from each atom, and from Eq. 3.13 we find that the total scattered power collected over a solid angle $\Delta\Omega$ from the ensemble of atoms is,

$$P_{coll} = I_o N_o V \int_{\Delta\Omega} \left(\frac{\partial\sigma}{\partial\Omega} \right) \partial\Omega = P_o N_o \ell \int_{\Delta\Omega} \left(\frac{\partial\sigma}{\partial\Omega} \right) \partial\Omega , \tag{3.14}$$

where $N_oV=N_oA_o\ell$ is the number of atoms within the probe volume $V=A_o\ell$ of length ℓ from which the scattering is collected and detected and $P_o=I_oA_o$ is the probe laser power. Combining Eqs. 3.11 and 3.14 we find that the Rayleigh scattered power collected from the ensemble of atoms is,

$$P_{coll} = \frac{4\pi^2}{\lambda^4} N_o P_o \ell \left(\frac{n-1}{N} \right)^2 \int_{\Delta\Omega} \sin^2\theta \, \partial\Omega \tag{3.15}$$

Let us assume that the laser beam interrogating the atomic gas propagates along the x-axis and is linearly polarized along the y-axis (i.e. vertically polarized) and that Rayleigh scattered radiation is collected along the z-axis (i.e. in a horizontal direction perpendicular to induced dipole moment). In addition, assume that the scattered light is collected by a fast, large diameter plano-convex lens of focal length f and diameter D. This arrangement is identical to the experimental configuration utilized by the MFRS velocimeter to collect the Rayleigh scattered radiation, and is depicted in Figure 3.3.

Most experiments that rely on Rayleigh scattered radiation to make quantitative measurements require fast collection of the scattered light. A large diameter, short focal length lens (i.e. low $F_\#$ lens) will collect more photons from the probe volume than a small diameter, long focal length lens (i.e. high $F_\#$ lens), but at the expense of aberrations introduced into the final image. The ideal collection optic for scattering experiments is a low $F_\#$ (for fast collection), long focal length (to provide sufficient stand-off distance for non-intrusive measurement), diffraction limited (to minimize aberrations) lens – e.g. a really large, really fast aspherical lens. Unfortunately, these lenses are not currently commercially available and are prohibitively expensive to have manufactured as single items. When money is an issue, a low $F_\#$, long focal length, plano-convex lens oriented with the planar side toward the probe volume is the next best alternative: It is commercially available, it is relatively inexpensive, and oriented back-to-back with another plano-convex lens such an optical system introduces fewer aberrations than a single bi-convex lens. For this reason, the optical design utilized during MFRS measurements relied upon a fast, large plano-convex lens for collection. (The next chapter discusses the specific optical designs utilized during MFRS measurements to balance the aberrations introduced by fast collection of the Rayleigh scattered light).

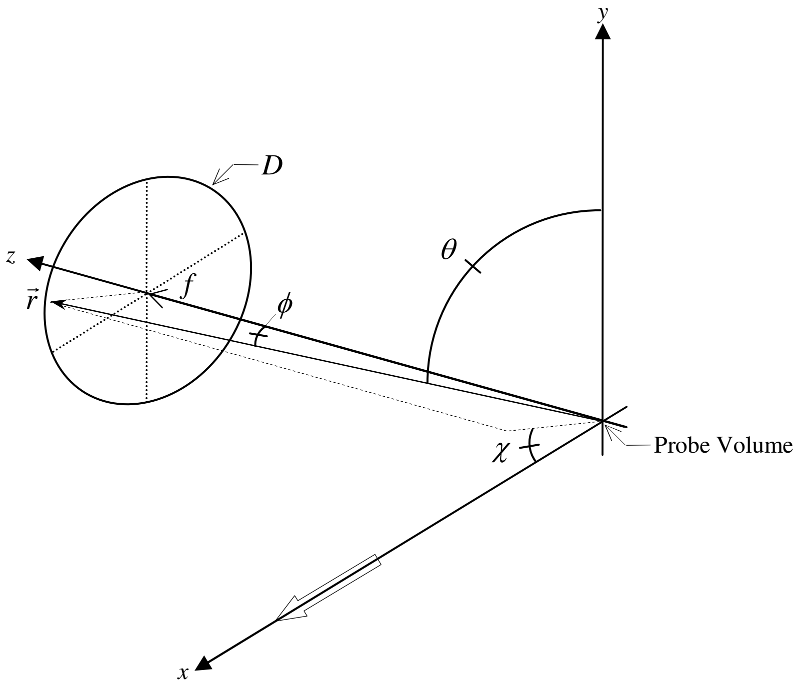

Figure 3.3 Illustration of the scattering geometry for the MFRS velocimeter

We can solve the integral in Eq. 3.15 for the scattering geometry illustrated in Figure 3.3 by casting the $\sin^2\theta$-term and differential solid angle, $\partial\Omega$, in terms of the spherical coordinates. Noting from Figure 3.3 that,

$$\vec{r} = r\hat{\mathrm{i}}_\mathrm{r} = r\left(\sin\phi\cos\chi\,\hat{\mathrm{i}} + \sin\phi\sin\chi\,\hat{\mathrm{j}} + \cos\phi\,\hat{\mathrm{k}}\right), \tag{3.16}$$

we find that,

$$\cos\theta = \hat{\mathrm{i}}_\mathrm{r}\cdot\hat{\mathrm{j}} = \sin\phi\sin\chi \tag{3.17}$$

and,

$$\sin^2\theta = 1 - \sin^2\phi\sin^2\chi \tag{3.18}$$

Expressing the differential solid angle in terms of spherical coordinates,

$$\partial\Omega = \sin\phi \mathrm{d}\phi \mathrm{d}\chi \tag{3.19}$$

and introducing Eqs. 3.18 and 3.19 into Eq. 3.15 we find,

$$\int_{\Delta\Omega} \sin^2\theta \, \partial\Omega = \int_{\chi=0}^{2\pi}\int_{\phi=0}^{\alpha_{\max}} \left(1-\sin^2\phi\sin^2\chi\right)\sin\phi \, \mathrm{d}\phi \, \mathrm{d}\chi \tag{3.20}$$

where,

$$\alpha_{\max} = \arctan\left(\frac{1}{2F_\#} \right) \tag{3.21}$$

and,

$$F_\# = \frac{f}{D} \tag{3.22}$$

is the F-number of the collection optic. Solving Eq. 3.20 we derive the following analytic expression for the collected Rayleigh scattered power:

$$P_{coll}\Big|_{R_V} = \frac{4\pi^3}{3\lambda^4} N_o P_o \ell \left(\frac{n-1}{N}\right)^2 \left\{4 - 3\cos\left[\arctan\left(\frac{1}{2F_\#}\right)\right] - \cos^3\left[\arctan\left(\frac{1}{2F_\#}\right)\right]\right\}. \tag{3.23}$$

It should be noted that the differential solid angle as it was derived above assumes collection from an infinitesimal point. This is a perfectly valid approximation when the spatial dimensions of the probe volume are much less than the diameter of the collection optic, which is generally the case for Rayleigh scattering experiments.

Eq. 3.23 is an expression for the scattered power collected from an ensemble of atoms utilizing vertically polarized light and the collection geometry illustrated in Figures 3.1-3.3. Scattering from an ensemble of molecules is complicated by the random orientation of the molecules with respect to the polarization of the incident radiation and the direction of the observed scattering. This results in depolarization of the elastically scattered radiation. Rigorous scattering calculations require averaging over the random orientations of the molecules to capture this effect.

Orientation averaging is accomplished by accounting for the anisotropy, γ, of the molecular constituents in calculations [42]. Consider the scattering geometry in Figures 3.1-3.3 – The laser light is linearly polarized in the y-direction, the beam propagates in the x-direction, and the scattered radiation is collected in the z-direction orthogonal to the polarization of the interrogating laser light. Again, this arrangement is identical to the experimental configuration utilized by the MFRS velocimeter to collect the Rayleigh scattered radiation. Orientation averaging results in the following differential scattering cross-section for this scattering geometry [43]:

$$\overline{\left(\frac{\partial\sigma}{\partial\Omega}\right)} = \frac{4\pi^2}{\lambda^4}\left(\frac{n-1}{N}\right)^2 \frac{1}{2+\rho_o}\left[2-\left(2-2\rho_o\right)\cos^2\theta\right]. \tag{3.24}$$

Referring to Figure 3.3, ρ_o is defined to be the ratio of the horizontally-to-vertically polarized light scattered in the z-direction if unpolarized light propagating in the x-direction – i.e. parallel to the horizontal plane – is incident on the probe volume. Note that the expression in Eq. 3.24 can be used to calculate the collected and subsequently detected Rayleigh scattered power only for experimental geometry illustrated in Figures 3.1-3.3 and only if the detector used in the experiment is insensitive to polarization. The MFRS velocimeter utilizes a photomultiplier tube (PMT) – which is essentially insensitive to polarization – to detect the collected Rayleigh scattered light.

The depolarization ratio is related to the anisotropy, γ, and the mean polarizability, α, of the molecular constituents in the probe volume [42]:

$$\rho_o = \frac{6\gamma^2}{45\alpha^2 + 7\gamma^2}. \tag{3.25}$$

Note that in the limit $\rho_o \to 0$, the differential scattering cross-section defined in Eq. 3.24 reduces to the expression derived previously, Eq. 3.11, for atomic scattering:

$$\rho_o \to 0 \Rightarrow \overline{\left(\frac{\partial\sigma}{\partial\Omega}\right)} \approx \frac{4\pi^2}{\lambda^4}\left(\frac{n-1}{N}\right)^2\left(1-\cos^2\theta\right) = \frac{4\pi^2}{\lambda^4}\left(\frac{n-1}{N}\right)^2 \sin^2\theta = \left(\frac{\partial\sigma}{\partial\Omega}\right). \tag{3.26}$$

The details of orientation averaging may be important for some diagnostic techniques that rely on Rayleigh scattering, but in our case it is not critical. For instance, the depolarization of 780 nm light scattered from air is ρ_o=0.028 [42, 44, 45]. The effect of neglecting orientation averaging is an overestimation of the collected and subsequently detected Rayleigh scattered power by <1% for our experimental configuration. The following analysis will therefore neglect orientation averaging.

In addition to anisotropy, molecules have rotational and vibrational degrees-of-freedom, and rotational and vibrational Raman bands contribute to the total scattering cross-section of a molecule. The vibrational Raman bands, corresponding to a change in the vibrational energy of the molecule, are the farthest removed from the probe laser wavelength. For instance, some of the preliminary MFRS experiments relied on molecular Rayleigh scattering from N_2. The vibrational Raman bands of N_2 are 2331 cm^{-1} (1 cm^{-1}=30 GHz) separated from the interrogating laser line [42], placing them well outside of the D_2-line of Rb employed during the experiment – i.e. The Doppler broadened D_2-line of Rb is O(10 GHz) in overall extent, and the vibrational Raman bands of N_2 did not contribute to the modulated absorption signal detected during preliminary MFRS experiments. Regardless of the specifics of a particular Rayleigh scattering experiment, vibrational Raman scattering is so weak that it is generally ignored.

Rotational Raman scattering consists of three branches. Inelastic rotational Raman scattering, corresponding to a change in the rotational energy of the molecule, contributes to the so-called Stokes and anti-Stokes branches. These branches are closer to the probe laser wavelength than the vibrational Raman bands, but still did not contribute to the detected modulated absorption signal during preliminary MFRS measurements. For instance, the closest rotational Raman lines in the Stokes and anti-Stokes branches of N_2 are ±11.94 cm^{-1} from the laser line [42]. The third branch is the so-called Raman Q-branch corresponding to a reorientation of the molecular rotation with no change in the internal energy of the molecule. This Raman Q-branch is unshifted in frequency from the coherent Rayleigh scattering defined in Eq. 3.23 – termed the Placzek trace scattering [46] – and therefore adds to the Placzek trace scattering. The sum of the Raman Q-branch scattering and the Placzek trace scattering defines the so-called Cabannes line [47].

Though a completely rigorous calculation of the expected signal-to-noise of MFRS measurements should include the Raman Q-branch, we will ignore this detail in our calculations. Considering the relative magnitude of the Q-branch compared to coherent Rayleigh scattering, this approximation will not significantly affect the results of the signal-to-noise calculations. For instance, Raman Q-branch scattering is <1% of the Placzek trace scattering from air at 780 nm [42, 44, 45, 48].

Eq. 3.23 realistically represents the Rayleigh scattered power collected during preliminary MFRS experiments. Calculations of the detected Rayleigh scattered power must account for reflection and transmission losses at all elements in the optical design utilized for collection. (Absorption losses through the rubidium vapor filter utilized during MFRS measurements will be discussed in the next and final section of this chapter). These losses are accounted for by introducing a parameter termed the collection efficiency, η, into the calculation of the detected Rayleigh scattered power,

$$P_{DET} = \eta P_{coll} . \tag{3.27}$$

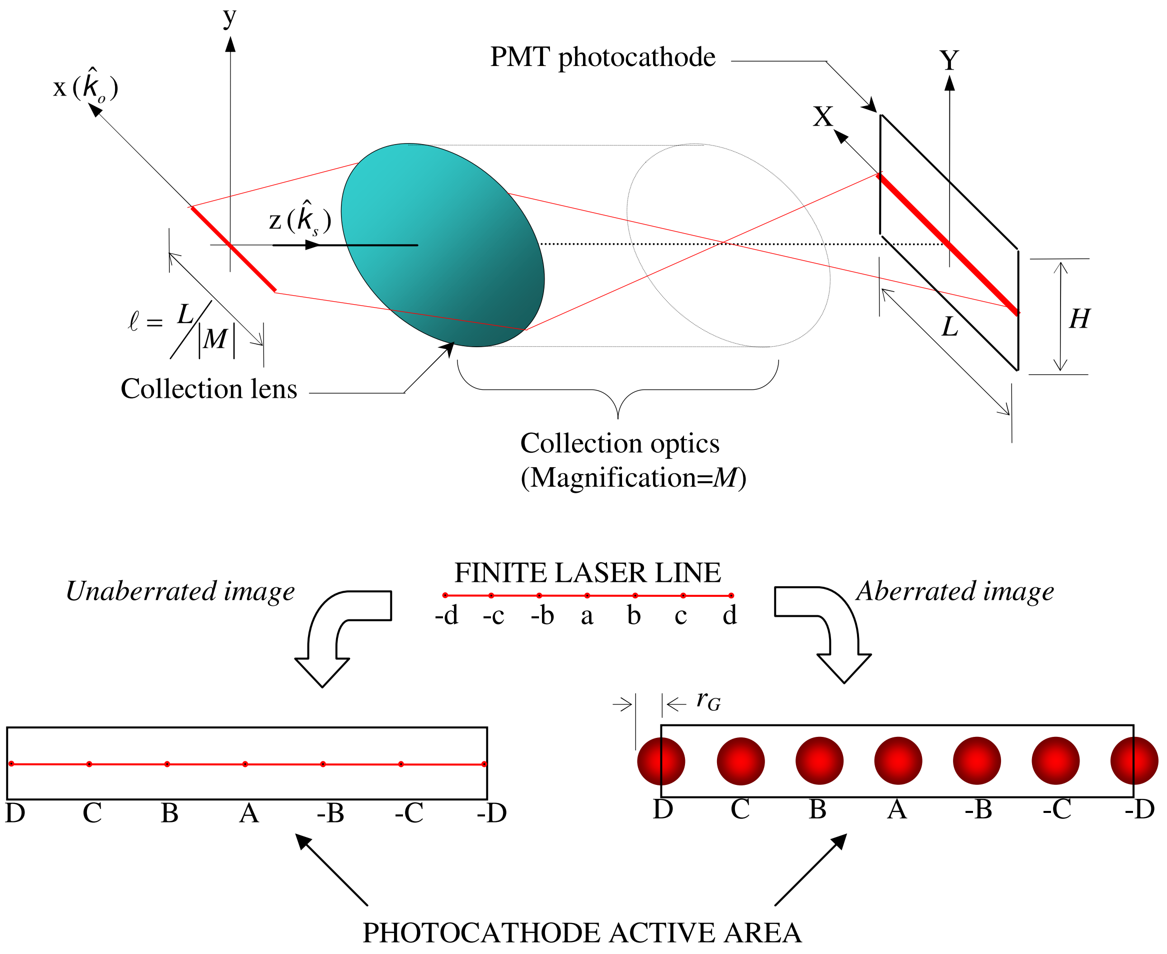

Figure 3.4 Illustrating the effects of aberrations on the detected Rayleigh scattered power

The aberrations introduced into the collected Rayleigh scattered light by the optical design utilized for collection must also be considered in calculations of the detected Rayleigh scattered light. Consider the scattering geometry illustrated in Figure 3.4. Let us imagine that a finite laser line of length $\ell = L/|M|$ oriented along the x-axis is imaged by the collection optics with a magnification M onto a photomultiplier tube (PMT) photocathode oriented parallel to the xy-plane and of length L parallel to the x-axis. (The rest of this section specifically considers PMT detection – i.e. preliminary MFRS experiments utilized a PMT to detect the Rayleigh scattering – but can be generalized to experiments utilizing any detector). Assume that the probe laser beam of finite length has an infinitesimal waist radius whose aberrated image does not overfill the Y-axis active area of the PMT photocathode and that the active area of the PMT exhibits completely uniform radiant sensitivity. We will neglect transmission losses for the time being and define the detected Rayleigh scattered power,

$$P_{DET} = \int_{-L/2}^{L/2} P'_{DET}(X)\mathrm{d}X \ , \tag{3.28}$$

where P'_{DET} is the detected power density along the X-axis the PMT photocathode. In the absence of any aberrations (and neglecting transmission losses) the detected power density at the PMT photocathode is uniform in X,

$$P'_{DET}(X) = P'_{DET} = \frac{P_{coll}}{L} \ , \tag{3.29}$$

and from Eq. 3.28 we find that the detected power is simply equal to the collected power,

$$P_{DET} = \int_{-L/2}^{L/2} \frac{P_{coll}}{L}\mathrm{d}X = P_{coll} \tag{3.30}$$

Aberrations result in a functional dependence, $P'_{DET} = f(X)$, of the detected power density near both edges of the photocathode when collecting scattered radiation from the finite laser line illustrated in Figure 3.4. For instance, half of the power collected from point *d* on the laser line in Figure 3.4 would not be detected since half of the aberrated image *D* falls outside of the photocathode active area. In other words, the detected power density at the edges of the photocathode is less than the detected power density near the center of the photocathode and $P_{DET}<P_{coll}$.

The probe laser beam utilized for MFRS measurements extends well beyond the measurement probe volume, however, and the superposition of aberrated blur spot images from points beyond *D* and *-D* in Figure 3.4, for instance, results in a uniform detected power density at both edges of the photocathode. In this case, aberrations effectively increase the field of view of the measurement along the x-axis. For instance, the geometric X-axis spatial resolution extends approximately two times the geometric blur spot radius, r_G, beyond that predicted when ignoring aberrations,

$$\ell_G = \frac{L}{|M|} + 2\frac{r_G}{|M|} \tag{3.31}$$

(This statement assumes that the length of the PMT photocathode along the x-axis – i.e. parallel to the laser line – establishes the x-axis spatial resolution. This assumption is valid for all optical designs utilized for collection of the Rayleigh scattered light during preliminary MFRS measurements). As an alternative to the geometric x-axis spatial resolution, a root-mean-square (RMS) x-axis spatial resolution could be defined by determining the contribution from those points near both edges of the x-axis geometric spatial extent toward the detected power at the respective edges of the PMT photocathode. (Note that the y-axis and z-axis geometric spatial resolutions are defined by the probe laser beam waist assuming that the image of the beam waist does not overfill the photocathode along the y-axis and that the spatial extent of the beam waist radius along the z-axis, $w_{o,z}$, is much smaller than the depth of field of the collection optics for the collection geometry illustrated in Figure 3.4).

The intent of this chapter is not to rigorously define the spatial resolution of our preliminary MFRS measurements, but rather to produce a realistic calculation of the expected MFRS signal-to-noise during those measurements. Toward this end, it is prudent to define an effective x-axis spatial resolution that accounts for the uniformity in response of the PMT photocathode along the X-axis, $U(X)$ (i.e. PMT cathodes exhibit a maximum – e.g. manufacture specified – radiant sensitivity only near the center of the active area. The radiant sensitivity quickly degrades near the edges of the active area):

$$\ell_{eff} = \frac{1}{|M|} \int_{-L/2}^{L/2} U(X)\,\mathrm{d}X \tag{3.32}$$

This effective x-axis spatial resolution will be utilized in all calculations of the detected Rayleigh scattered power that follow.

We now have an expression for the detected Rayleigh scattered power that realistically represents preliminary MFRS experiments. Let us combine Eqs. 3.23, 3.27, and 3.32 and summarize:

$$\boxed{P_{DET}\big|_{R_V} = \eta N_o P_o \ell_{eff} \frac{4\pi^3}{3\lambda^4}\left(\frac{n-1}{N}\right)^2 \left\{4 - 3\cos\left[\arctan\left(\tfrac{1}{2F_\#}\right)\right] - \cos^3\left[\arctan\left(\tfrac{1}{2F_\#}\right)\right]\right\}}\ , \tag{3.33}$$

where,

$\eta \equiv$ Collection efficiency

$N_o \equiv$ Number density of atoms or molecules in probe volume [m^{-3}]

$P_o \equiv$ Power of probe laser beam [W]

$\ell_{eff} = \frac{1}{|M|} \int_{-L/2}^{L/2} U(X)\,\mathrm{d}X \equiv$ Effective x-axis spatial resolution [m]

$M \equiv$ Magnification of optical design utilized for collection

$L \equiv$ Physical length of photocathode active area along X-axis [m]

$U(X) \equiv$ Photocathode uniformity along X-axis

$\lambda \equiv$ Centerline wavelength of probe laser beam [m]

$n \equiv$ Index of refraction of atomic or molecular gas in probe volume at a centerline wavelength λ and a reference number density N [m^{-3}]

$N \equiv$ Reference number density

$F_{\#} \equiv$ F-number of collection optic

and where we have assumed,

(i) The gas under investigation consists of atoms or molecules that are polarizable.

(ii) The gas is isotropic, nonpolar, and nonmagnetic.

(iii) The index of refraction of the gas is $n \sim 1$.

(iv) The probe laser beam is propagating in the x-direction and is linearly polarized in the y-direction and the Rayleigh scattered light is collected in the z-direction – i.e. orthogonal to the propagation direction and polarization of the probe laser beam – by a fast, large diameter plano-convex lens with the planar face directed toward the probe volume, as illustrated in Figures 3.1-3.4.

(v) The probe beam waist diameter along the y-axis is much smaller than the effective y-axis spatial resolution defined by the PMT,

$$h_{eff} = \frac{1}{|M|} \int_{-H/2}^{H/2} U(Y) \mathrm{d}Y \,, \tag{3.34}$$

where H is the length of the photocathode active area in the Y-direction, as illustrated in Figure 3.4. In other words, all photons collected from the y-axis spatial extent of the probe laser beam are detected by the PMT (neglecting transmission losses).

(vi) The probe beam waist radius along the z-axis, $w_{o,z}$, is much smaller than the depth of field of the optical design utilized for collection; e.g. The collected scattering from points displaced $\Delta z \ll w_{o,z}$ from the object plane aren't significantly more aberrated than the collected scattering from points on the object plane.

(vii) Orientation averaging and Raman Q-branch scattering can be neglected in the Rayleigh power calculations.

To reiterate, the assumptions employed in the derivation of Eq. 3.33 are applicable to calculations of the Rayleigh scattered power detected during all preliminary MFRS experiments.

I would now like to discuss an experiment that I conducted in February of 2006. The results of this experiment can be compared to calculations based on the theory described above and provides us with an estimate of the collection efficiency, η, of the optical designs utilized for collection of Rayleigh scattered light during preliminary MFRS experiments. The experiment also provides a realistic measure of the PMT dark current, ambient background radiation, and stray reflections that corrupted preliminary MFRS measurements. Before I delve into the details of the experiment, however, I would like to quickly discuss what motivated the experiment.

Having spent over three years developing a master oscillator power amplifer (MOPA) laser system for the MFRS velocimeter, in October of 2004 I was at long last convinced that I had a laser system that was up to the task of conducting frequency-locked MFRS experiments in a supersonic jet of N_2. With approximately 50 mW of power in the probe volume, an optical design that provided fast, efficient collection of the Rayleigh scattered radiation, and a PMT capable of sensitive detection of the collected scattering, my calculations indicated that measurements should be a breeze. And yet from October 2004 until May of 2005 I struggled to make any measurement from molecular Rayleigh scattering.

I initially suspected that the experimental instrument I had developed to conduct MFRS measurements was not performing as I had expected it would. I focused my initial concern on the PMT. The PMT utilized in our experiment has a GaAs photocathode with a damage threshold of only 16 nW at λ=780 nm. In addition, GaAs photocathodes tends to suffer from sensitivity degradation when exposed to high intensity light – even with the PMT powered off [49]. I had been extremely careful when handling the PMT, but that didn't rule out the possibility that damage had occurred.

Measurements of the PMT anode dark current as a function of supply voltage eventually led me to conclude that the PMT was not damaged. Not only were the measurements of the anode dark current similar to the manufacture specified dark current, but the dark current vs. supply voltage curve in the supply voltage range 1000 V<V_{PMT}<1500 V had a slope that was nearly identical to the manufacture specified gain vs. supply voltage curve. Within this supply voltage range, the dark current is dominated by thermionic emissions from the photocathode and as a result the aforementioned curves should follow the same slope (see Appendix C: Gain Characteristics of the R636-10 PMT).

Having convinced myself that the PMT was fine, I began to suspect that the optical design utilized in the scattering arm of the experiment was not efficiently collecting the Rayleigh scattered light. I decided to redesign the collection optics with the hope of improving the efficiency with which I was collecting Rayleigh scattered radiation. Though the redesigned optical system appeared to be slightly more effective at collecting Rayleigh scattered radiation, I was still unable to make a reliable, repeatable MFRS measurement from molecular Rayleigh scattering after implementing the change.

Having seemingly exhausted my options, in May of 2005 I decided to turn my attention from making measurements using molecular Rayleigh scattering and to making measurements in a condensing jet of CO_2. After some moderately successful preliminary measurements in a condensing jet of CO_2, I stepped away from the experiment to work on yet another redesign of the collection optics. The aim of this redesign was to accommodate an intermediate focus in the optical system utilized for collection. All previous optical designs utilized for collection relied upon the physical extent of the PMT photocathode to define the effective length of the probe volume along the x-axis, ℓ_{eff}, and were limited to a minimum effective x-axis spatial resolution of ~1.2 mm. A slit introduced at the intermediate focus of the redesigned collection optics would allow us to improve upon the x-axis spatial resolution, an improvement that Dr. Varghese and I felt warranted attention.

Unfortunately, when I returned to the experiment in December of 2005 the power had dropped out of the MOPA laser system; I suspect that the antireflection-coated (AR-coated) front facet of the broad area laser (BAL) amplifier was somehow damaged. With only half of the previously available power now at my disposal, Dr. Varghese and I decided it was time for me to graduate. However, after almost eight years in the graduate program I had failed to accomplish what my preliminary signal-to-noise calculations indicated was possible. I asked Dr. Paul Danehy, who had just published some impressive measurements that relied on Rayleigh scattering [50], for some advice. Dr. Danehy suggested that I conduct a simple Rayleigh scattering experiment without all of the complications of the MFRS technique – i.e. don't modulate the optical frequency of the interrogating laser beam, get rid of the rubidium (Rb) vapor filter and lock-in amplifier, and just collect and detect Rayleigh scattered light. The simple Rayleigh scattering experiment inspired by Dr. Danehy is illustrated in Figure 3.5.

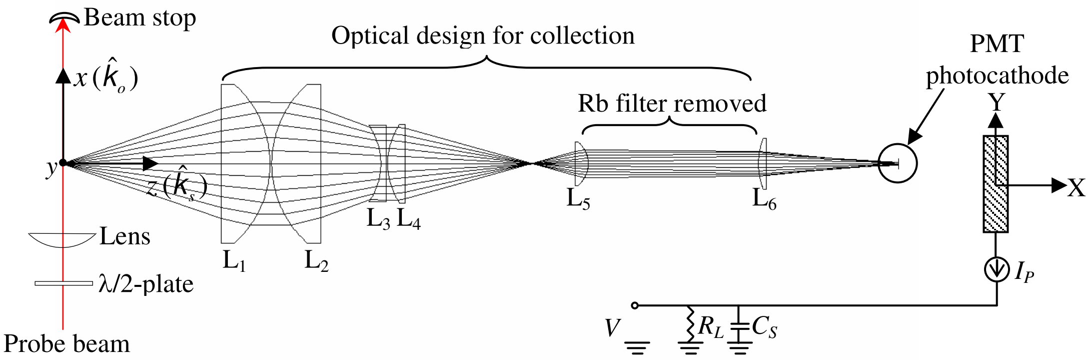

Figure 3.5 Simple Rayleigh scattering experiment

A laser beam of centerline wavelength λ=780 nm and average power P_o≈40 mW is incident on a volume of air at a temperature T=20°C and a pressure P=1 atm. (Note that P_o was the total probe laser power measured during the experiment, including ~12 mW of amplified spontaneous emissions (ASE) from the broad area laser (BAL). This convention changes later in the dissertation; i.e. P_o is defined as the frequency modulated probe laser power in the context of modulated absorption spectroscopy). Rayleigh scattered photons are collected using a plano-convex lens with a collection F-number of $F_\#$=1.445 and are imaged onto the PMT photocathode with an optical magnification of M=3. (These assertions are based on Zemax ray-tracing analysis of the optical design utilized for collection). The effective x- and y-axis spatial resolution defined by the PMT were calculated based on the manufacture specified photocathode uniformity, plotted in Figure 3.6:

$$\ell_{eff} = \frac{1}{|M|}\int_{-L/2}^{L/2} U(X)\mathrm{d}X \approx 1.2\,\mathrm{mm} \tag{3.35a}$$

$$h_{eff} = \frac{1}{|M|}\int_{-H/2}^{H/2} U(Y)\mathrm{d}Y \approx 3.8\,\mathrm{mm} \tag{3.35b}$$

The spatial intensity profile of the probe laser beam along the y- and z-axis is plotted in Figure 3.7. A ϕ=50 μm pinhole detector mounted on a translation stage was used to incrementally sweep along the y- and z-axis spatial beam profile. Measurements along the y-axis were made at the peak of the z-axis spatial intensity profile, and measurements along the z-axis were made at the peak of the y-axis spatial intensity profile. Both y- and z-axis measurements were made in the imaged probe volume, corresponding to x=0 in Figure 3.5. Figure 3.7 clearly shows that the y-axis spatial extent of the probe laser beam is approximately an order of magnitude less than the effective y-axis spatial resolution established by the PMT, h_{eff}. It is also possible to show that the z-axis spatial extent of the probe laser beam is well within the depth of field of the collection optics. (Zemax ray-tracing analysis indicates that the aberrated image of any infinitesimal field point lying within the imaged probe volume of the collection optics has an RMS radius of less than 600μm and a geometric radius of less than 1 mm – i.e. All photons scattered from the y- and z-axis spatial extent of the probe laser beam along a length ℓ_{eff} fall well within the Y-axis spatial extent of the PMT).

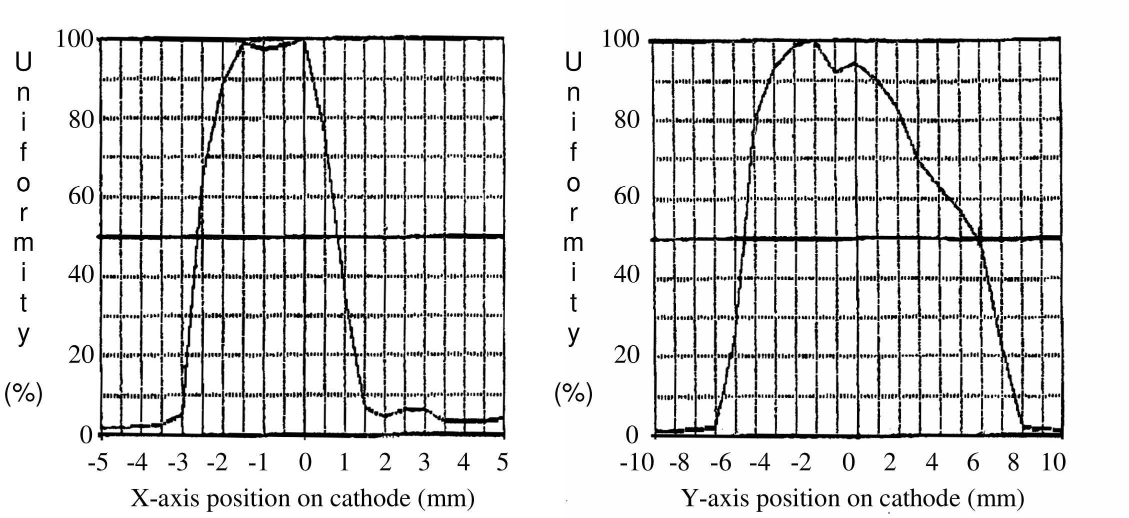

Figure 3.6 Manufacture specifications of uniformity of PMT radiant sensitivity along the X- and Y-axis of the PMT photocathode at V_{PMT}=90 V [51]

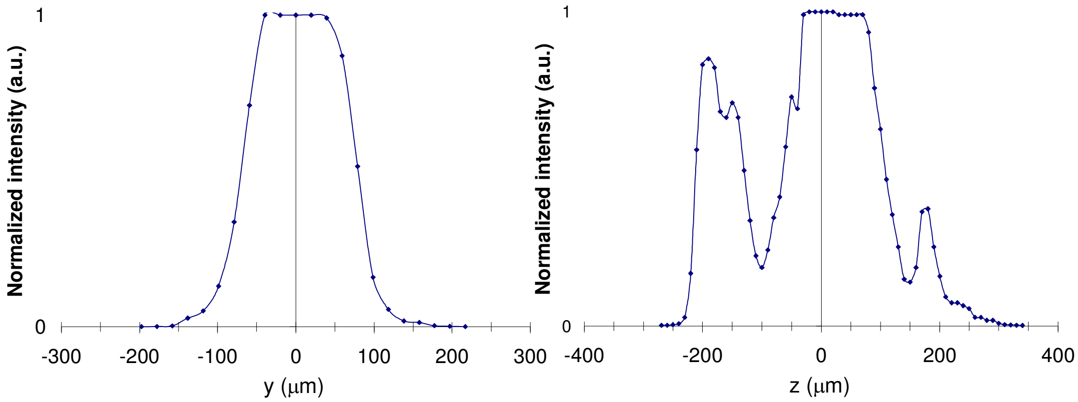

Figure 3.7 Measured y-axis and z-axis spatial intensity profiles of probe laser beam

The contribution from PMT dark current, ambient background radiation, and stray reflections to the detected signal were accounted for by making measurements with the probe laser beam horizontally polarized – i.e. with the probe laser polarization parallel to the optical axis of collection – and vertically polarized – i.e. with the probe laser polarization perpendicular to the optical axis of collection. (The probe laser polarization was flipped using a half-wave plate). PMT dark current, ambient background radiation, and stray reflections are not sensitive to the probe laser polarization. Therefore, subtracting the signal detected with horizontally polarized light from the signal detected with vertically polarized light provides a measure of the Rayleigh scattered light that is collected and detected.

Assume that an interrogating laser beam propagates along the x-axis and is linearly polarized along the z-axis and that Rayleigh scattered radiation is collected along the z-axis (i.e. in a direction parallel to induced dipole moment) by a fast plano-convex lens. It is possible to show, in a manner analogous to the derivation of Eq. 3.33, that the Rayleigh scattered light detected from this horizontally polarized beam is,

$$\left.P_{DET}\right|_{R_H} = \eta N_o P_o \ell_{eff} \frac{4\pi^3}{3\lambda^4}\left(\frac{n-1}{N}\right)^2 \left\{4-6\cos\left[\arctan\left(\frac{1}{2F_\#}\right)\right]+2\cos^3\left[\arctan\left(\frac{1}{2F_\#}\right)\right]\right\} \tag{3.36}$$

Subtracting the Rayleigh scattered power detected with horizontally polarized light, Eq. 3.36, from the Rayleigh scattered power detected with vertically polarized light, Eq. 3.33, we find,

$$\left.P_{DET}\right|_{R_V} - \left.P_{DET}\right|_{R_H} = \eta N_o P_o \ell_{eff} \frac{4\pi^3}{\lambda^4}\left(\frac{n-1}{N}\right)^2 \left\{\cos\left[\arctan\left(\frac{1}{2F_\#}\right)\right]-\cos^3\left[\arctan\left(\frac{1}{2F_\#}\right)\right]\right\} \tag{3.37}$$

The detected radiant power, P_{DET}, results in a PMT anode current,

$$i_P = \mu(V_{PMT})\cdot S_K(\lambda)\cdot P_{DET} \tag{3.38}$$

where $\mu(V_{PMT})$ is the PMT gain at a PMT supply voltage V_{PMT} and $S_k(\lambda)$ is the cathode radiant sensitivity to light at a wavelength λ (see Appendix C: Gain Characteristics of the R636-10 PMT). The detected voltage across a shunt resistor of resistance R_L is simply,

$$V = \mu(V_{PMT})\cdot S_K(\lambda)\cdot R_L \cdot P_{DET} \tag{3.39}$$

Combining Eqs. 3.37-3.39,

$$\begin{aligned} \left.V\right|_{D+B+S+R_V} - \left.V\right|_{D+B+S+R_H} &= \mu S_K R_L \eta N_o P_o \ell_{eff} \frac{4\pi^3}{\lambda^4}\left(\frac{n-1}{N}\right)^2 \cdot \\ &\left\{2\sin^2\left[\arctan\left(\frac{1}{2F_\#}\right)\right]+2\ln\left(\cos\left[\arctan\left(\frac{1}{2F_\#}\right)\right]\right)\right\} \end{aligned} \tag{3.40}$$

The subscripts on the left-hand side of the equation indicate that the individual voltage measurements, either made with the probe laser beam vertically polarized (*V*) or with the probe laser beam horizontally (*H*) polarized, include contributions from the PMT dark current (*D*), ambient background radiation (*B*), stray reflections (*S*), and Rayleigh scattered light (*R*). The functional dependence of the PMT gain and cathode radiant sensitivity on the PMT supply voltage and the wavelength of the detected light, respectively, have been dropped in Eq. 3.40.

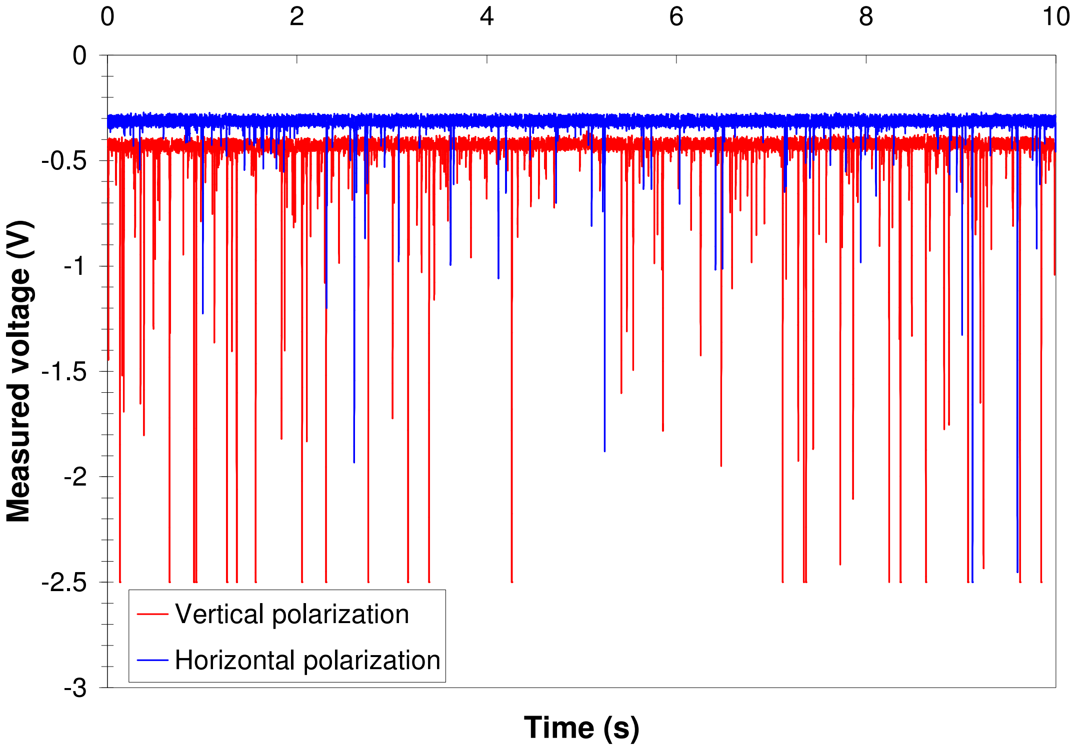

Figure 3.8 A sample of voltages measured with the probe laser beam vertically and horizontally polarized

Figure 3.8 is a plot of some sample voltage measurements made during the experiment illustrated in Figure 3.5 and discussed above. There were in fact eight total ten second scans recorded, four with vertically polarized light at the four different half-wave plate angles that maximized the recorded signal and four with horizontally polarized light at the four different half-wave plate angles that minimized the recorded signal. The measurements from the four scans with vertically polarized light were averaged to provide an average measured voltage with vertically polarized light, and the measurements from the four scans with horizontally polarized light were averaged to provide an average measured voltage with horizontally polarized light.

The intention of this approach was to average over any trends in the probe laser power during the course of experimentation. In addition, this approach helps account for the possibility of slightly different beam waist locations in the probe volume at different half-wave plate rotations.

EXPERIMENTAL PARAMETERS	
V_{PMT}	1200 V
λ	780 nm
$\mu(V_{PMT})$	$3.5\text{x}10^{5}$ at V_{PMT}=1200 V
$S_K(\lambda)$	62 mA/W at λ=780 nm
R_L	1 MΩ
N_o	$2.5\text{x}10^{25}$ m^{-3}
P_o	40 mW
ℓ_{eff}	1.2 mm
N	$2.55\text{x}10^{25}$ m^{-3}
n-1 [44,45]	$2.7516\text{x}10^{-4}$ for air at
	λ=780 nm, N=$2.55\text{x}10^{25}$ m^{-3}
$F_\#$	1.445

Table 3.1 Known or estimated experimental parameters for the simple Rayleigh scattering experiment illustrated in Figure 3.5 and discussed above

Table 3.1 is a list of estimated or known experimental parameters associated with the experiment illustrated in Figure 3.5 and discussed above. Plugging these numbers into Eq. 3.40 results in the following theoretical calculation:

$$\left| V\Big|_{D+B+S+R_V} - V\Big|_{D+B+S+R_H} \right|_{\text{THEORY}} = 102\,\text{mV}\,. \tag{3.41}$$

Comparing the theoretical calculation in Eq. 3.41 to the measurements,

$$\left| \overline{V}\Big|_{D+B+S+R_V} - \overline{V}\Big|_{D+B+S+R_H} \right|_{\text{MEASURED}} = \left| -420\,\text{mV} - \left(-321\,\text{mV}\right) \right| = 99\,\text{mV} \tag{3.42}$$

we find that the collection efficiency of the optical design utilized in this experiment is $\eta \approx 97\%$. (Note that the PMT anode output current is negative with respect to ground, and hence the measured voltages were negative).

Though this efficiency may seem unrealistically high, it is a direct reflection of the care with which the experimental parameters in Table 3.1 were defined. For instance, the collection F-number was defined based on ray-tracing analysis, which indicated that the F-stop of the collection optics is defined by the clear aperture of lens L_3 in Figure 3.5. Had we defined a collection F-number $F_\#$=1 based on the clear aperture of lens L_1, then comparison of the theoretical calculation in Eq. 3.41 to the measurements would have resulted in an estimate of $\eta \approx 66\%$ for the collection efficiency; i.e. The collection is less efficient in this case because of aperture truncation of the marginal collected rays at lens L_3. The experimental parameters as they are defined in Table 3.1 account for aberrations and truncation in the optical design utilized for collection. In this case, the collection efficiency merely determines the reflection and transmission losses in the optical design – e.g. There are twelve antireflection-coated (AR-coated) optical faces in the optical design used to collect the Rayleigh scattered light, each with an average reflectance of $R_{\text{avg}}<0.25\%$ at λ=780 nm [52].

I owe Dr. Danehy a debt of gratitude. The simple experiment he suggested I conduct essentially convinced me that the instrument I had developed to make MFRS measurements was performing up to my expectations: The laser power measurements could be trusted, the manufacture specifications for the PMT were realistic, and the optical designs utilized for collection of the Rayleigh scattered radiation during all preliminary MFRS experiments were efficient. (Though the optical design utilized for collection of the Rayleigh scattered light had been redesigned before conducting the simple Rayleigh scattering experiment, all collection optics utilized in preliminary MFRS experiments were designed and aligned with the same care). Undistracted by questions concerning the experimental apparatus, I was finally able to question the experiment itself. I had never doubted my calculations, but it became immediately obvious that my calculations had failed to predict reality.

Before we turn our attention back to a theoretical discussion of Rayleigh scattering, I would like to further discuss the measurements recorded during the simple Rayleigh scattering experiment outlined above; there are some additional points to be made concerning the measurements which have important implications for the practical implementation of the MFRS technique. Referring to Eqs. 3.33 and 3.39, we find that the scattering theory developed in this section predicts a voltage signal of $V\big|_{R_v} = 105\,\text{mV}$ resulting from the collected and detected Rayleigh scattering with the experimental parameters outlined in Table 3.1, a collection efficiency $\eta \approx 97\%$, and with vertically polarized light in the probe volume. Comparing this with the average voltage measured with vertically polarized light in the probe volume, $\left|V\big|_{D+B+S+R_V}\right|_{\text{MEASURED}} = 420\,\text{mV}$, we find that PMT dark current, ambient background radiation, and stray reflections account for 75% of the measured signal.

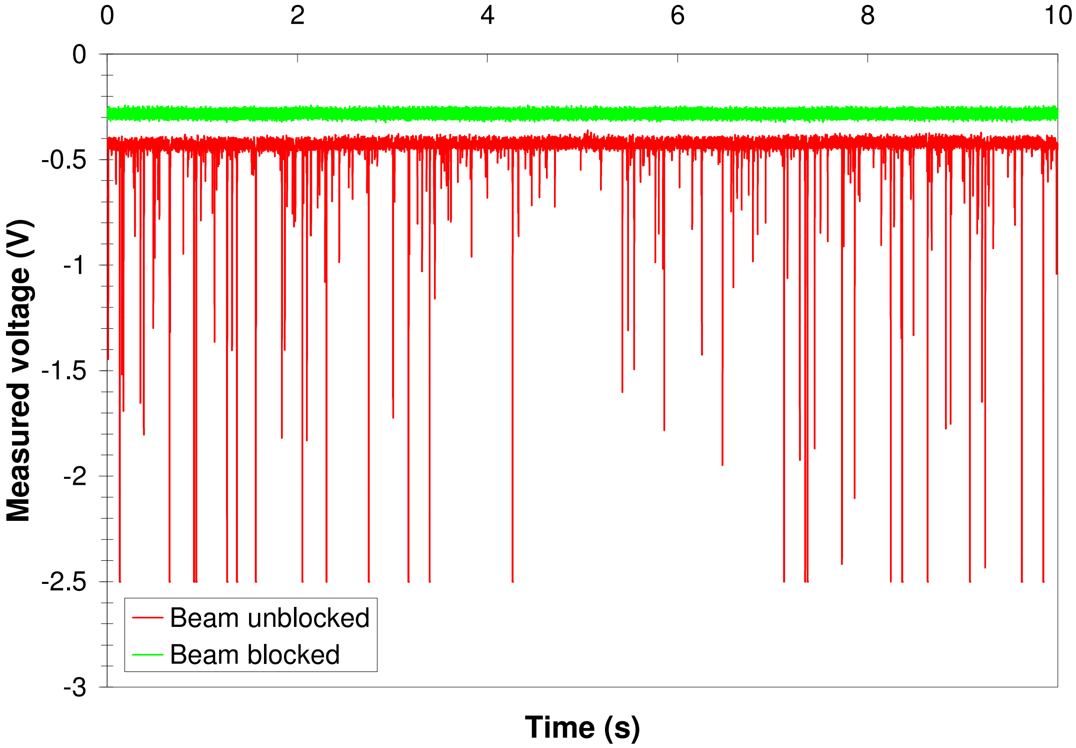

Figure 3.9 A sample of voltages measured with a vertically polarized probe laser beam blocked up beam of the probe volume versus unblocked

Figure 3.9 compares some sample voltage measurements made during the simple Rayleigh scattering experiment with vertically polarized light in the probe volume to some sample voltage measurements made with the laser beam blocked up-beam of the probe volume. The average voltage recorded with a PMT supply voltage of V_{PMT}=1200 V during the measurements made with the probe laser beam blocked was $\left. \left| V \right|_{D+B} \right|_{\text{MEASURED}} = 285\,\text{mV}$. This measured voltage is the result of PMT dark current (D) and detected ambient background radiation (B). The typical PMT dark current at a PMT supply voltage V_{PMT}=1200 V is ~0.3 nA, resulting in a voltage of ~0.3 mV across a R_L=1MΩ shunt resistor. This implies that ambient background radiation essentially accounts for the entire signal detected with the probe beam blocked.

Now, comparing the average voltage recorded during the simple Rayleigh scattering experiment with vertically polarized light in the probe volume, $\left. \left| V \right|_{D+B+S+R_V} \right|_{\text{MEASURED}} = 420\,\text{mV}$, to the average voltage measured with the probe beam blocked, $\left. \left| V \right|_{D+B} \right|_{\text{MEASURED}} = 285\,\text{mV}$, we find that the PMT dark current ($|V_D|\approx 0.3$ mV) accounts for <0.1% of the total signal detected with vertically polarized light in the probe volume, ambient background radiation ($|V_B|\approx 285$ mV) accounts for 68% of the signal, stray reflections ($|V_S|\approx 30$ mV) account for 7% of the signal, and collected and detected Rayleigh scattering ($\left|V_{R_V}\right|\approx 105$ mV) accounts for 25% of the signal.

Fortunately, the PMT dark current does not significantly contribute to the total detected signal – The dark current can be minimized with experimental care (e.g. waiting a while after turing on the PMT and avoiding placement of heat sources in the vicinity of the cathode), but is ever present. The ambient background radiation, however, contributes significantly to the detected signal. The experimental data in Figures 3.8 and 3.9 was acquired in an essentially dark room; the windows were blocked, the overhead room lights were off, and the only light that prevented me from tripping over the experiment was provided by a 40 W reading lamp and a computer monitor in a corner of the lab. Preliminary MFRS measurements were often made in a completely dark room with no reading lamp or computer monitor to light my way. Under these conditions, the minimum detected ambient background radiation was of the same order as the PMT dark current; the lowest recorded anode output current resulting from detected ambient background radiation with a PMT supply voltage of V_{PMT}=1200 V and with the room completely dark was ~0.3 nA, corresponding to 300 μV across a 1MΩ load resistor.

Preliminary MFRS experiments were intended to provide proof of the concept, not practical measurements. The point is that practical implementation of the MFRS velocimeter – i.e. in an environment that is not completely dark – would require optical filtering of the ambient background radiation. (We in fact purchased a narrow band optical filter centered at 780 nm to minimize detection of the broadband ambient background radiation. After every day that I struggled for signal, however, it became more and more apparent that I could not afford the ~25% transmission losses through the optical filter. I was throwing away collected Rayleigh scattered photons that I couldn't afford to throw away, and so I decided to stumble around in the dark, both literally and figuratively). Though the signal-to-noise certainly comes into play – i.e. the greater the detected ambient background radiation the greater the shot noise that corrupts the measurements – the real issue is with detector saturation. The PMT utilized during preliminary MFRS measurements, for instance, has an absolute maximum anode current of $I_P|_{MAX}$=1 μA. Before I completely blocked the windows in the lab, I relied on the cover of night to prevent PMT saturation in my measurements – With all the lights in the lab turned off, there was still enough sunlight seeping through the blinds on a cloudy afternoon to practically saturate the PMT. I would still classify the lab as dark before I covered the windows – it was hard to navigate without bumping into tables and chairs with the room lights off – but the PMT was practically at its damage threshold. Optical filtering of the ambient background radiation is essential to any practical MFRS velocimeter.

The whole point of the MFRS technique is to minimize the corrupting effects of noise sources such as dark current and ambient background radiation. Provided that the ambient background radiation does not saturate the detection electronics, for instance, homodyne detection utilizing a lock-in amplifier should effectively suppress its impact on the measurement. Any collected stray reflections, however, result in a detected modulated absorption signal that is not filtered by the lock-in amplifier. Since stray reflections are not Doppler frequency shifted due to the bulk velocity in the flow under investigation, any collected and detected stray reflections generally offset the velocity measurements – Stray reflections that are detected not only increase the shot noise in the measurement, but potentially affect the accuracy of the measurement itself.

The MFRS technique relies on experimental care to minimize the effect of stray reflections on the accuracy of velocity measurements. This is in fact the case for all FRS experiments. The general approach used to minimize detection of stray reflections in FRS experiments that utilize an optically thick atomic or molecular vapor filter is to stabilize the laser frequency to a strong absorption corresponding to an atomic or molecular resonance. A very strong resonant absorption suppresses the collected stray reflections, while the Doppler frequency shifted scattered light that is collected from the flow under investigation is partially transmitted. The Doppler frequency shift is calculated from the measured signal based on models that accurately predict the optical transmission through the filter as a function of optical frequency. For instance, the mercury [53] and iodine [54] absorption profiles in the vicinity of 254 nm (Ti:sapphire) and 532 nm (frequency doubled Nd:YAG), respectively, have been thoroughly investigated. Since these absorption profiles are well known, the detected scattering signal through either filter can be deconvolved, resulting in a measure of the Doppler frequency shift due to a bulk velocity (as well as the scattering lineshape and hence the temperature of the gas).

The frequency-locked mode of the MFRS velocimeter adopts a similar approach to minimize the effect of stray reflections on measurements. The laser frequency is stabilized to an absorption peak in the D_2-line of Rb. Even if there is incomplete attenuation of the stray reflections through the Rb vapor filter (and the stray reflections still contribute to the shot noise), the **1*f*** lock-in signal corresponding to the first Fourier component of the detected modulated absorption signal is zero at the peak of an atomic resonance. The stray reflections therefore do not contribute to the detected modulated absorption signal while conducting frequency-locked measurements. They do contribute to the detected calibration profile, however, and in this regard they affect the accuracy of MFRS velocity measurements. The MFRS velocimeter as currently developed cannot completely deal with stray reflections and relies on experimental care in order to minimize the detection of background scattering. The details of the frequency-locked mode of operation of the MFRS velocimeter will be discussed further in the next chapter.

PMT dark current, ambient background radiation, and stray reflections all present difficulties when trying to conduct MFRS measurements. By far the largest obstacle to meaningful MFRS measurements has yet to be discussed, however. Referring to Figures 3.8 and 3.9, we see that the voltage measured with both horizontally and vertically polarized light in the probe volume contains several strong peaks. There are fewer of these peaks with horizontally polarized light than with vertically polarized light, and the peaks are not present when the probe laser beam is blocked. These peaks correspond to collected and detected particle scattering from what can only be described as dust.

Dust is an enemy to any Rayleigh scattering experiment, and the MFRS velocimeter is no exception. The frequency-locked mode of the MFRS velocimeter accounts for scattering power fluctuations using a ratio-detection scheme, as will be discussed in the next chapter. The problem with dust is that, since the Rayleigh scattered power is proportional to the sixth power of the particle radius [55], the scattered power from a small piece of dust is so much larger than the molecular Rayleigh scattered power that the detected scattering signal from dust tends to saturate the detection electronics. For instance, the scattering signal detected from a single 1 μm radius piece of dust floating through a 1 mm^3 probe volume of air at STP is approximately two orders of magnitude more than the detected scattering signal resulting from all the air molecules in that probe volume. (Scattering from particles is complicated by optical interference effects, and is treated using Thomson/Mie scattering theory [56]. The differential scattering cross-section dependence on the sixth power of the particle radius, for instance, is only valid in the Rayleigh regime).

The detected signals from dust scattering in Figures 3.8 and 3.9 certainly saturate the PMT and frequently saturate the data acquisition electronics. The same holds true for MFRS measurements. The PMT and lock-in amplifiers in the scattering arm of the experiment are set up for sensitive detection of molecular Rayleigh scattering. Everything is working just fine when all of a sudden a piece of dust floats through the probe volume. The PMT saturates and the lock-in amplifiers, which don't have nearly enough dynamic reserve to deal with the sudden spike in signal, go to the rail. The ratio detection scheme is effective for small scattering power fluctuations, but the ratio of a saturated amplifier signal to a saturated amplifier signal is meaningless anyway you look at it. If now you consider the number of signal peaks in Figure 3.8 resulting from dust scattering and recorded during a ten second interval, you can almost imagine how difficult it was to record a repeatable calibration profile over a period of one-hundred seconds. (Scattering from dust was problematic throughout preliminary MFRS experiments, particularly while trying to acquire a repeatable calibration profile. The most recent experiments minimized the incidence of detected dust scattering by conducting all measurements, including measurements of the calibration profile, in the core of a jet flow. I still observed scattering from dust entrained into the shear layer and jet core, but the incidence of dust scattering was significantly less during these experiments than during preliminary experiments in static lab air).

The data acquired during the simple Rayleigh scattering experiment discussed in the previous paragraphs illustrates many of the difficulties associated with conducting MFRS measurements. PMT dark current is of minor concern compared to ambient background radiation and stray reflections. The detection of ambient background radiation during preliminary MFRS measurements was minimized by working in the dark and the detection of stray reflections was minimized with experimental care. Particle scattering from dust was detected during all preliminary MFRS measurements. Scattering from dust particles was effectively cancelled by the ratio detection scheme employed during frequency-locked MFRS measurements conducted in a condensing jet of CO_2 – the required detection sensitivity during those experiments was low enough that detected scattering rarely saturated the detection electronics – but plagued all measurements that relied on molecular Rayleigh scattering.

One of the assumptions invoked in all of my calculations was that the detected Rayleigh scattering was monochromatic. As will be discussed in Section 3.4, this assumption results in a gross overestimation of the theoretical lock-in signal. Rayleigh scattered light is in fact spectrally broadened by the motion of the atoms or molecules in the probe volume under investigation [13]. In the low-density limit, the uncorrelated thermal motion of the atoms or molecules inhomogeneously broadens the Rayleigh scattered light. This so-called Doppler broadened spectrum of the Rayleigh scattered light has a Gaussian lineshape,

$$f(\nu)=\frac{2}{\Delta\nu_T}\sqrt{\frac{\ln 2}{\pi}}\exp\left[-\frac{\ln 2(\nu-\nu_o)^2}{(\Delta\nu_T/2)^2}\right] \tag{3.43}$$

where,

$$\Delta\nu_T=\frac{|\vec{K}|}{2\pi}\sqrt{\frac{8kT\ln 2}{m}}=\frac{\nu_o}{c}\sqrt{\frac{8kT\ln 2}{m}}\cdot 2\sin\left(\frac{\alpha}{2}\right)=\frac{\nu_o}{c}\sqrt{\frac{8kT\ln 2}{m}}\cdot\left|\hat{k}_s-\hat{k}_o\right| \tag{3.44}$$

is the full-width at half-maximum (FWHM) of the Doppler broadened profile, *k* is Boltzmann's constant, *T* is the temperature of the gas in the probe volume, *m* is the atomic or molecular mass of the gas, ν_o is the centerline frequency of the Rayleigh scattered radiation, and *c* is the speed of light. Note that Eqs. 3.43 and 3.44 account for the scattering geometry of the experiment: As illustrated in Figure 3.1, α is the angle between the interrogating laser beam and the observed scattering direction, $\hat{k}_o$ is the unit vector in the direction of the laser beam propagation, and $\hat{k}_s$ is the unit vector in the direction of the scattered light (i.e. the observation direction).

Eq. 3.44 also introduces a wave vector,

$$\vec{K}=\frac{2\pi}{\lambda_o}\cdot 2\sin\left(\frac{\alpha}{2}\right)\frac{\left(\vec{k}_s-\vec{k}_o\right)}{\left|\vec{k}_s-\vec{k}_o\right|}=\frac{2\pi}{\lambda_o}\cdot\left(\hat{k}_s-\hat{k}_o\right), \tag{3.45}$$

which is directed orthogonal to the fringe patterns generated in the probe volume by interference between the incident laser light and the Rayleigh scattered radiation. The probe laser wavelength, λ_o, corresponds to the spatial frequency of the each of the various fringe patterns and the rest of the expression in Eq. 3.45 accounts for the scattering geometry. Each of the various fringe patterns in the probe volume correspond to a distinct frequency of scattered light. The spatial frequency of all fringe patterns is the same, but each fringe pattern is swept along the direction of the wave vector $\vec{K}$ at a rate proportional to the Doppler frequency-shift.

In a low density gas (e.g. high temperature gas), the mean free path between collisions is large compared to the spatial scale of the fringe pattern and the spectral profile of the scattered light just reflects the thermal motion of those particles traveling along with the corresponding fringe pattern. As the density of the gas increases (e.g. as the temperature of the gas drops), the mean free path between atomic or molecular collisions approaches the fringe spacing and minor density fluctuations resulting from acoustic waves propagating in the gas begin to contribute to the spectral profile of the scattered light. So-called Brillouin sidebands appear in the spectral profile of scattered light.

Gases in the Knudsen regime of gas kinetics – i.e. with a mean free path much greater than the fringe spacing – correspond to the thermal limit, and the spectral profile is Gaussian. High pressure gases – i.e. with a mean free path much less than the fringe spacing – correspond to the so-called hydrodynamic limit, and are treated with a continuum theory of gas dynamics (i.e. the Navier-Stokes equations). In the hydrodynamic limit the spectrum contains three sharply peaked Lorentzian profiles. The intermediate regime, or so-called kinetic regime, is described using kinetic theory.

Several models based on kinetic theory have been developed to quantify the relative magnitude of the uncorrelated thermal motion of the atoms or molecules in a gas to their correlated acoustic motion [57-61]. The Tenti six moment, or S6 model, based on the linerized Wang-Chang-Uhlenbeck equation from kinetic theory, is generally considered the most accurate [42]. The Tenti S6 model classifies the gas using a Y-parameter, which is essentially the ratio of the fringe spacing, λ_o, to the mean free path, ℓ_m,

$$Y \equiv \frac{\lambda_o}{2\pi\ell_m} \cong \frac{P}{\left|\vec{K}\right| v_P \eta} . \tag{3.46}$$

P is the pressure, v_P is the most probable speed of an atom or molecule of atomic or molecular mass m at a gas temperature T,

$$v_P = \sqrt{\frac{2kT}{m}} , \tag{3.47}$$

and η is the shear viscosity of the gas, which can be modeled with the Sutherland formula,

$$\eta = \eta_o \left(\frac{T}{T_o}\right)^{3/2} \left(\frac{T_o + S}{T + S}\right) . \tag{3.48}$$

For air m=4.8×10^{-26} kg, η_o=1.716×10^{-5} Ns/m^2, T_o=273 K, and S=111K, and combining Eqs. 3.45-48 the Y-parameter becomes,

$$Y = 0.230 \left[\frac{T(\mathrm{K}) + 111}{T^2(\mathrm{K})}\right] \left[\frac{P(\mathrm{atm}) \lambda_o(\mathrm{nm})}{\sin \alpha/2}\right] . \tag{3.49}$$

The data in Figures 3.8 and 3.9 corresponds to collected and detected Rayleigh scattered light from air at T=293 K, P=1 atm, λ_o=780 nm, and α=90°. We find from Eq. 3.49 that the Y-parameter in this case is Y=1.19.

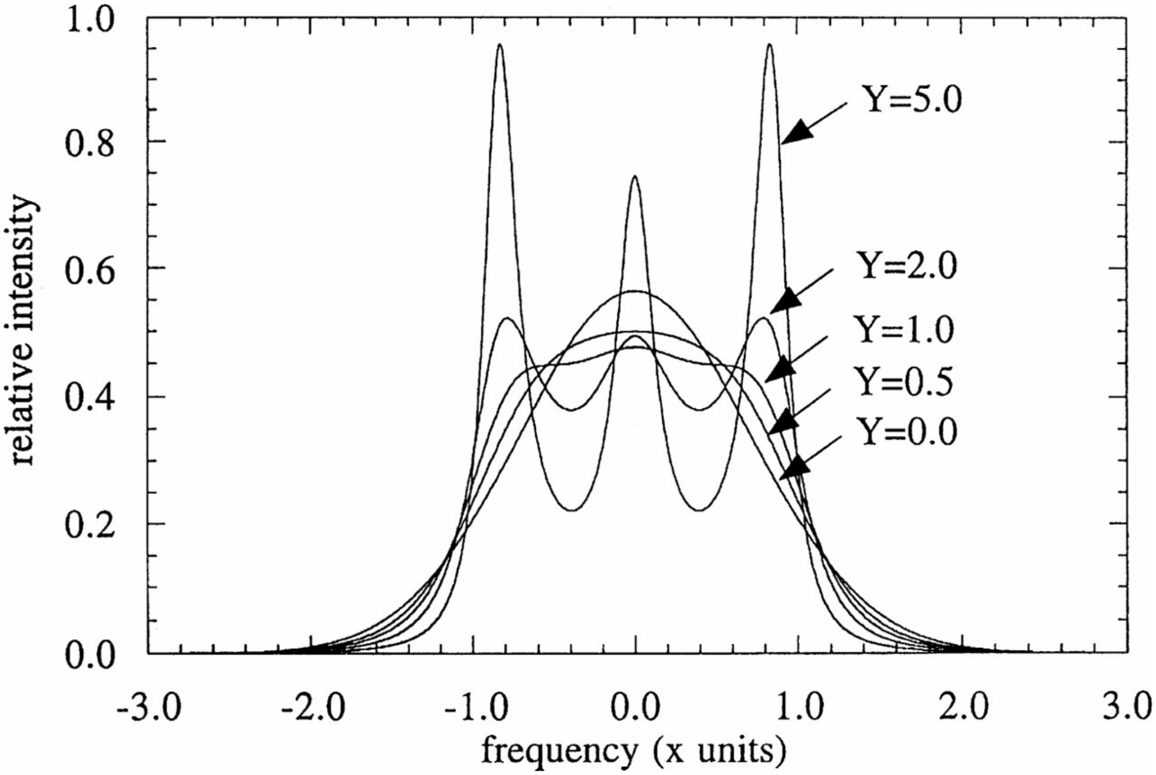

Figure 3.10 Spectral profiles of Rayleigh scattered light at various Y-parameters [10, 42, 62]

In the last section of this chapter we will calculate the theoretical signal-to-noise (S/N) during preliminary MFRS experiments in static air. To simplify these S/N calculations I will assume that the Rayleigh scattered light collected during these experiments has a Gaussian spectral lineshape. This is not strictly correct and will lead to a slightly optimistic prediction of the peak first- and second-harmonic lock-in signals detected during preliminary MFRS measurements utilizing molecular Rayleigh scattering from static air.

Figure 3.10 is a plot of the Rayleigh-Brillouin profiles calculated using the S6 model for various Y-parameters [10, 42, 62]. The frequency, ν, has been normalized in this plot in units of,

$$x = \frac{2\pi(\nu - \nu_o)}{|\vec{K}|v_p} \tag{3.50}$$

Looking at Figure 3.10 we find that the spectral lineshape of Rayleigh scattered light collected from static air (and characterized by a Y-parameter of approximately one) is in fact intermediate between the thermal limit and the acoustic limit. It exhibits faint acoustic sidebands and is flat and broad compared to the Gaussian Rayleigh lineshape in the thermal limit; i.e. the Rayleigh scattered power spectrum was more spread out in our preliminary experiments than a Rayleigh scattered power spectrum at the thermal limit.

It is intuitively obvious that ignoring the acoustic sidebands in the S/N calculations that conclude this chapter will lead to an optimistic calculation of the peak first- and second-harmonic lock-in signals detected during preliminary MFRS measurements. The acoustic sidebands in a Rayleigh-Brillouin spectrum are centered at a Doppler shifted frequency, ν_D, corresponding to the speed of sound in the scattering gas. It is possible to show that the acoustic sidebands in the Rayleigh scattered spectrum collected during preliminary MFRS measurements in static air are roughly centered at a Doppler shifted frequency $\nu_D = \pm 622$ MHz from the center of the spectrum.

Now, consider the first-harmonic lock-in signal detected while slowly sweeping the probe laser frequency across the $\boldsymbol{F}=3$ ground state transition of ^{85}Rb during preliminary MFRS experiments. The peaks (i.e. maximum positive and negative excursion) in the acquired **1*f***-profile roughly occur at frequencies corresponding to the half-width of the Doppler broadened absorption feature, which at lab temperature is roughly $\delta\nu_{1/2}= 256$ MHz for ^{85}Rb. Let us imagine a Rayleigh-Brillouin spectrum modulating about this point in the frequency domain. The central thermal peak in the spectrum modulates along the edge of the absorption feature, resulting in a modulated absorption signal. Simultaneously, one acoustic sideband modulates completely outside of the absorption feature, and contributes nothing to the modulated absorption signal, while the other acoustic sideband modulates from outside the absorption feature to inside the absorption feature, resulting in a modulated absorption signal that is 180° out-of-phase with the modulated absorption signal detected from central thermal peak. Acoustic sidebands obviously reduce the detected peak first-harmonic modulated absorption signal. Since they rob power from the central thermal peak, they also reduce the detected second-harmonic modulated absorption signal.

3.3 Absorption Spectroscopy

The modulated filtered Rayleigh scattering (MFRS) velocimeter utilizes a vapor cell filled with Rubidium (Rb) in natural isotopic abundance to determine the Doppler frequency shift affected by a bulk velocity in the flow under investigation. The aim of this section is to develop a realistic theoretical model for the absorption profile of the D_2-line of Rb (used exclusively as the optical frequency discriminator in all preliminary MFRS experiments). The section begins by introducing a semi-classical theory involving so-called Einstein coefficients used to describe the absorption of light resonant with an electronic transition of an atom. (A purely classical theory involving the so-called Lorentz atom is discussed in Appendix B).

A Rb vapor filter in natural isotopic abundance contains 72.2% ^{85}Rb and 27.8% ^{87}Rb. The D_1- and D_2-lines of both isotopes are the components of a fine-structure doublet that is the result of coupling between the orbital angular momentum of the outer electron, $\boldsymbol{L}$, and its spin angular momentum, $\boldsymbol{S}$. Within each of these lines there is additional hyperfine energy splitting that is the result of coupling between the total electron angular momentum, $\boldsymbol{J}=\boldsymbol{L}+\boldsymbol{S}$, and the total nuclear angular momentum, $\boldsymbol{I}$.

For the D_2-line both ^{85}Rb and ^{87}Rb can be excited from two allowable hyperfine ground state sublevels (i.e. the degeneracy of the ground state is two) into four allowable hyperfine excited state sublevels (i.e. the degeneracy of the excited state is four). Figure 3.11 is a plot of the Doppler broadened D_2-line of Rb in natural isotopic abundance acquired during a direct absorption experiment in the reference arm of the MFRS velocimeter. (The plot shows the signal detected down beam of the Rb vapor cell as the laser wavelength, λ, is slowly tuned through the line). The ground state hyperfine energy splitting of both ^{85}Rb and ^{87}Rb, corresponding to a total ground state atomic angular momentum, $\boldsymbol{F}=\boldsymbol{J}+\boldsymbol{I}$, of $\boldsymbol{F}$=2 and 3 and $\boldsymbol{F}$=1 and 2, respectively, are distinguishable. However, the excited state sublevels, $\boldsymbol{F'}$=1,2,3, and 4 and $\boldsymbol{F'}$=0,1,2, and 3, respectively, are obscured by thermal broadening.

To rigorously model the D_2-line of Rb, the hyperfine splitting must be accounted for. The model must accommodate the energy shift associated with each hyperfine sublevel from the unshifted fine structure center-of-gravity. In addition, the relative transition probability of each hyperfine component must be considered. Quantum theory can be used to determine the energy shift and transition probability of each hyperfine transition in the D_2-line of Rb. This section will not discuss the requisite quantum theory in detail, but will simply present and reference the pertinent results of the quantum calculations. By introducing these results into the semi-classical theory involving Einstein coefficients a realistic model of the D_2-line of Rb evolves that is in good agreement with experimental measurement.

We will conclude this section by developing a heuristic model of the Doppler broadened D_2-line of Rb that neglects the upper state hyperfine energy shifts. This heuristic model will benefit the discussion of modulated absorption spectroscopy in the next section by simplifying the math pertinent to that discussion. Though not completely rigorous, this heuristic model can still be used to reliably calculate the signal-to-noise ratio during MFRS experiments. (The heuristic model employed will in fact result in a slight over-prediction of the maximum positive and negative excursions in detected harmonic profiles; i.e. it will result in a slightly optimistic calculation of the expected lock-in signal).

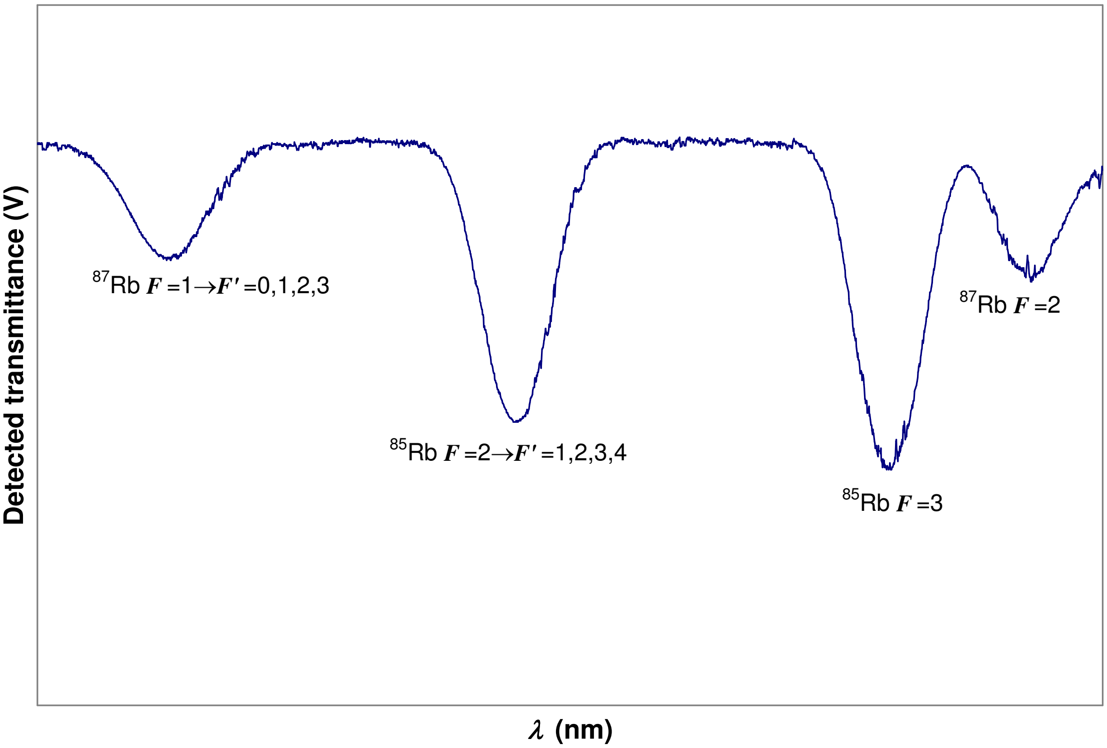

Figure 3.11 The Doppler broadened D_2-line of Rb in natural isotopic abundance at room temperature

3.3.1 The Einstein Coefficients

Consider the internal electronic energy of an atom modeled by the simple two-level system in Figure 3.12. Level 1 corresponds to a lower ground state of the atom and level 2 corresponds to an upper excited state. The internal electronic energy of the atom in its ground state and excited state is E_1 and E_2, respectively. Now, imagine that a photon of light with energy,

$$\varepsilon_P = h\nu_{1\to 2} = \left|E_2 - E_1\right|, \tag{3.51}$$

where h is Planck's constant and $\nu_{1\to 2}$ is the photon "frequency", is incident upon and absorbed by the atom. After the photon of light resonant with the electronic transition of the atom is absorbed, it will quickly be reemitted. The reemission can either be stimulated by a passing photon of equivalent energy or it can occur spontaneously. (The analysis below ignores collisional interactions; i.e. The quantum energy of the electronic transition is assumed to be large and the absorbing gas is assumed to be "cold"). All stimulated emissions are coherent with – i.e. travel in the same direction, have the same wavelength, and have a fixed phase relative to – the photon that stimulates the emission. Those photons that are stimulated to emit therefore do not contribute to an attenuation of the incoming light. On the other hand, spontaneous emissions are directionally isotropic. (The direction of spontaneously emitted radiation is in fact slightly dependent on the polarization of the absorbed radiation, but the assumption of isotropic emission is generally valid for a large ensemble of atoms). If we neglect the small portion of spontaneously emitted photons that do in fact follow the direction of the stimulated emissions we can say that all spontaneously emitted photons contribute to the attenuation of the incoming light,

$$\text{Light attenuation} = \text{Spontaneous emission} = \text{Induced absorption} - \text{Stimulated emission}\,. \tag{3.52}$$

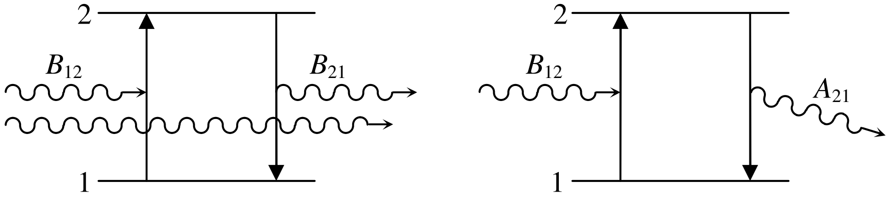

Induced absorption ⇒ Stimulated emission *Induced absorption ⇒ Spontaneous emission*

Figure 3.12 Generic two-level atomic transition

Eq. 3.52 can be cast in terms of the following constitutive relations describing the interaction of resonant light with an atomic media [40, 63],

$$N_1 B_{12}\rho_{\nu_{1\to 2}}(\nu) \equiv \text{Number of photons with resonant energy } h\nu_{1\to 2} = |E_2 - E_1| \text{ absorbed per unit vol. per unit time } [\text{m}^{-3}\text{s}^{-1}]. \tag{3.53a}$$

$$N_2 B_{21}\rho_{\nu_{1\to 2}}(\nu) \equiv \text{Number of absorbed photons stimulated to emit per unit vol. per unit time } [\text{m}^{-3}\text{s}^{-1}]. \tag{3.53b}$$

$$N_2 A_{21} \equiv \text{Number of absorbed photons spontaneously emitted per unit vol. per unit time } [\text{m}^{-3}\text{s}^{-1}]. \tag{3.53c}$$

where,

$$N_1 \equiv \text{Number of atoms in low lying energy level (e.g. ground state) per unit vol. } [\text{m}^{-3}]. \tag{3.54a}$$

$$N_2 \equiv \text{Number of atoms in upper energy level (e.g. excited state) per unit vol. } [\text{m}^{-3}]. \tag{3.54b}$$

$$B_{12} \equiv \text{Einstein coeff. of induced absorption } [\text{m}^3\text{Hz/Js}]. \tag{3.54c}$$

$$B_{21} \equiv \text{Einstein coeff. of stimulated emission } [\text{m}^3\text{Hz/Js}]. \tag{3.54d}$$

$$A_{21} \equiv \text{Einstein coeff. of spontaneous emission } [\text{s}^{-1}]. \tag{3.54d}$$

$$\rho_{\nu_{1\to 2}}(\nu) \equiv \text{Spectral energy density } [\text{J/m}^3\text{Hz}]. = \left(\frac{\text{Avg. energy of ensemble of resonant photons}}{\text{unit vol} \cdot \text{unit bandwidth}}\right) \tag{3.54e}$$

Referring to Eqs. 3.53a-c and the definitions in 3.54a-e we see that $B_{12}\rho_{\nu_{1\to 2}}(\nu)$ represents the probability per unit time that a photon with resonant energy $h\nu_{1\to 2}=|E_2-E_1|$ is absorbed by a single atom, $B_{21}\rho_{\nu_{1\to 2}}(\nu)$ represents the probability per unit time that a single excited atom will be stimulated to emit the absorbed photon, and A_{21} is the probability per unit time that a single excited atom will spontaneously emit the absorbed photon. Note that the probability of a spontaneous emission event is independent of the external radiation field.

Inserting the relations in Eqs. 3.53a-c into Eq. 3.52 we find that the photon attenuation per unit time per unit volume of an electromagnetic field incident upon and resonant with an atomic media is given by,

$$\frac{\text{Photon attenuation}}{\text{unit time} \cdot \text{unit vol.}} = N_2 A_{21} = (N_1 B_{12} - N_2 B_{21})\rho_{\nu_{1\to 2}}(\nu) \tag{3.55}$$

The formulation in Eq. 3.55 assumes that the ground state population, N_1, and the excited state population, N_2, are both in steady state and implies that the spectral energy density incident upon the absorbing media, $\rho_{\nu_{1\to 2}}(\nu)$, falls within the bandwidth of the resonant transition.

The equilibrium population distribution of the atomic media among the various energy levels, i, is given by the Boltzmann distribution at thermal equilibrium [64],

$$N_i = N\frac{g_i}{Z}\exp\left[-E_i\big/kT\right], \tag{3.56}$$

where N is the number density of the atomic media, g_i is the degeneracy of the i^{th} energy level, $Z = \sum_i g_i \exp\left[-E_i\big/kT\right]$ is the partition function (which acts as a normalizing factor; e.g. $N = \sum_i N_i$), E_i is the energy of the i^{th} level, k is Boltzmann's constant, and T is the equilibrium temperature of the gas.

The Einstein coefficients in Eq. 3.55 can be related to each other by considering the spectral energy density of thermal radiation [40]. Let us first solve Eq. 3.55 for the spectral energy density of the resonant light incident upon the absorbing gas. Noting from Eq. 3.56 that,

$$\frac{N_2}{N_1} = \frac{g_2}{g_1}\exp\left[-\left(E_2 - E_1\right)\big/kT\right] = \frac{g_2}{g_1}\exp\left[-h\nu_{1\to 2}\big/kT\right], \tag{3.57}$$

we find,

$$\begin{aligned}\rho_{\nu_{1\to 2}}(\nu) &= \frac{N_2 A_{21}}{N_1 B_{12} - N_2 B_{21}} \\ &= \frac{\frac{A_{21}}{B_{21}}}{\frac{N_1}{N_2}\frac{B_{12}}{B_{21}} - 1}\end{aligned}$$

$$\rho_{\nu_{1\to 2}}(\nu) = \frac{\frac{A_{21}}{B_{21}}}{\frac{g_1}{g_2}\frac{B_{12}}{B_{21}}\exp\left[h\nu_{1\to 2}\big/kT\right] - 1} \tag{3.58}$$

In 1900 M. Planck derived the now famous radiation law physicists use to describe the spectral energy density of thermal radiation [65]. Prior to Planck's derivation, the equipartition theorem of classical thermodynamics was used to describe thermal radiation as a continuum. The Rayleigh-Jeans law derived from this classical perspective diverged from observation toward the higher frequencies in the spectrum. Planck's epiphany was intuiting that absorptions and irradiative emissions are quantized; i.e. a radiation field can only emit or absorb discrete amounts of energy. Planck still relied upon the equipartition theorem in his derivation, but with this concept of quantized energy in mind he was able to derive an expression for the spectral energy density of thermal radiation that is completely consistent with observation,

$$\rho_\nu(\nu)\mathrm{d}\nu = \frac{8\pi\nu^2}{c^3}\frac{h\nu}{\exp\left(h\nu/kT\right)-1}\mathrm{d}\nu \tag{3.59}$$

Eqs. 3.58 and 3.59 are both consistent and valid expressions for the spectral energy density at any temperature and a particular frequency, and we can therefore relate the constant coefficients in those equations:

$$g_1B_{12} = g_2B_{21} \tag{3.60a}$$

$$A_{21} = \frac{8\pi\nu^3h}{c^3}B_{21} \tag{3.60b}$$

The Einstein *A*-coefficients for most atomic gases of interest have been determined experimentally (The Einstein *B*-coefficients follow from Eqs. 3.60a and 3.60b). There are quantum theoretical relations for the Einstein coefficients [63], but a number of reputable books with detailed spectroscopic data exist, and looking up the Einstein coefficients for a particular transition is a relatively straight-forward exercise (e.g. reference [66]).

Let us now introduce Eqs. 3.56 and 3.60a into Eq. 3.55:

$$\begin{aligned}
\frac{\text{Photon attenuation}}{\text{unit time}\cdot\text{unit vol.}} &= N_1B_{12}\left(1-\frac{N_2}{N_1}\frac{B_{21}}{B_{12}}\right)\rho_{\nu_{1\to2}}(\nu)\\
&= N\frac{g_1}{Z}\exp\left[-E_1/kT\right]B_{12}\left(1-\frac{N_2}{N_1}\frac{B_{21}}{B_{12}}\right)\rho_{\nu_{1\to2}}(\nu)\\
&= N\frac{g_1}{Z}\exp\left[-E_1/kT\right]B_{12}\left(1-\frac{g_1}{g_2}\frac{N_2}{N_1}\right)\rho_{\nu_{1\to2}}(\nu)\\
\frac{\text{Photon attenuation}}{\text{unit time}\cdot\text{unit vol.}} &= N\frac{g_1}{Z}\exp\left[-E_1/kT\right]B_{12}\left\{1-\exp\left[-h\nu_{1\to2}/kT\right]\right\}\rho_{\nu_{1\to2}}(\nu)
\end{aligned} \tag{3.61}$$

The Rb vapor cell employed during preliminary MFRS experiments was at lab temperatures and far from optical saturation; The saturation intensity of Rb is I_{sat}=O(mW/cm^2) [67], which is approximate nine-orders-of-magnitude greater than the intensity of collected Rayleigh scattered light that propagates through the Rb vapor cell in the scattering arm of the experiment, $I_{RAYLEIGH}$=O(10^{-9} mW/cm^2). It is therefore completely valid to employ the following approximations in our derivation of the Rb absorption profile utilized during preliminary MFRS measurements to determine the Doppler frequency shift affected by a bulk velocity in the flow under investigation:

(i) $Z \cong g_1$: What this assumption implies is that $E_1 << kT$ whereas $E_{i>1} >> kT$; i.e. The ground state is at a low lying energy level that is thermally populated:

$$Z = g_1 \underbrace{\exp\left[-E_1/kT\right]}_{\to 1} + g_2 \underbrace{\exp\left[-E_2/kT\right]}_{\to 0} + \ldots$$

(ii) $\exp\left[-\frac{h\nu_{1\to 2}}{kT}\right] \cong 0$: This assumption follows from the argument above. From Eqs. 3.56, 57, and 60a we find $N\frac{g_1}{Z}\exp\left[-E_1/kT\right]B_{12}\exp\left[-h\nu_{1\to 2}/kT\right] = N_2 B_{21}$. If we assume that the ground state is heavily populated at typical lab temperatures, $N_2 << N_1$, and knowing from Eq. 3.60a that $O(B_{12})=O(B_{21})$, then from Eq. 3.55 we can totally disregard stimulated emissions relative to induced absorption.

Under these approximations it follows from Eq. 3.61 that,

$$\frac{\text{Photon attenuation}}{\text{unit time} \cdot \text{unit vol.}} = NB_{12}\rho_{\nu_{1\to 2}}(\nu). \tag{3.62}$$

That is, the photon attenuation is simply equal to the induced absorption.

We can cast Eq. 3.62 describing the photon attenuation per unit time per unit volume of an electromagnetic field incident upon and resonant with an atomic media in terms of spectral irradiance by noting that,

$$I_\nu = \rho_\nu c \ , \tag{3.63}$$

where ρ_ν is the spectral energy density, c is the speed of light, and I_ν is the spectral irradiance – i.e. the irradiative power per unit area per unit frequency bandwidth (mks-units of $\frac{\text{J/s}}{\text{m}^2\text{Hz}}$) [63]:

$$\frac{\text{Photons absorbed}}{\text{unit time} \cdot \text{unit vol.}} = NB_{12}\frac{I_{\nu_{1\to 2}}(\nu)}{c}. \tag{3.64}$$

Noting from Eq. 3.51 that the energy per absorbed photon is $\varepsilon_P = h\nu_{1\to 2}$, we find from Eq. 3.64 that the resonant energy absorbed per unit time per unit volume is,

$$\frac{\text{Energy absorbed}}{\text{unit time} \cdot \text{unit vol.}} = \frac{\text{Power absorbed}}{\text{unit vol.}} = \frac{h\nu_{1\to 2}}{c} NB_{12} I_{\nu_{1\to 2}}(\nu), \qquad (3.65)$$

or alternatively,

$$\frac{\text{Incident irradiance absorbed}}{\text{unit length}} \equiv \frac{\Delta I}{\Delta z} = I_o \frac{h\nu_{1\to 2}}{c} NB_{12} Y_{\nu_{1\to 2}}(\nu). \qquad (3.66)$$

In Eq. 3.66, I_o is the incident irradiance (or incident intensity) – i.e. the incident irradiative power per unit area (mks-units of $\frac{\text{J/s}}{\text{m}^2}$) – of resonant light that is traveling in the positive *z*-direction through the absorbing gas and $Y_{\nu_{1\to 2}}(\nu)$ is the normalized lineshape function (mks-units of Hz^{-1}),

$$\int_{-\infty}^{\infty} Y_{\nu_{1\to 2}}(\nu) \mathrm{d}\nu = 1, \qquad (3.67)$$

of the absorption profile corresponding to the transition 1→2 at a centerline frequency $\nu_{1\to 2}$; the centerline frequency $\nu_{1\to 2}$ corresponds to the center-of-gravity of the fine structure component (e.g. the center-of-gravity of the D_2-line of Rb). We have thus far ignored line broadening in our analysis. The discussion above has implied that an atomic gas in thermal equilibrium with its surroundings only absorbs light at discrete frequencies, and that only light tuned to that discrete frequency will be absorbed on passage through the gas. In other words, we have essentially acted as though the normalized lineshape function defining the absorption is a delta function in frequency,

$$Y_{\nu_{1\to 2}}(\nu) = \delta(\nu - \nu_{1\to 2}) \,\text{Hz}^{-1}. \qquad (3.68)$$

The lineshape function is in fact never a delta function, but instead is a broadened absorption profile that reflects the kinetics of the atoms in the gas. For instance, the D_2-line of Rb at room temperature contains four Doppler broadened absorption profiles, as illustrated in Figure 3.11, reflecting the thermal motion of the atoms in the Rb gas. We will eventually account for this Doppler broadening in our model of the D_2-line, but for the time being let us simply recognize that $Y_{\nu_{1\to 2}}(\nu)$ is any normalized lineshape function that describes the absorption profile.

After traveling an infinitesimal distance Δz in the positive z-direction, the incident irradiance that is transmitted through the absorbing gas, $I(\Delta z)$, is simply the incident irradiance, I_o, minus the irradiance absorbed, $\Delta I(\Delta z)$. Referring to Eq. 3.66 we find,

$$I(\Delta z) = I_o\left[1 - \overline{\alpha}(\nu_{1\to 2}) \cdot \Delta z \cdot Y_{\nu_{1\to 2}}(\nu)\right] = I_o\left[1 - N \cdot \overline{\sigma}(\nu_{1\to 2}) \cdot \Delta z \cdot Y_{\nu_{1\to 2}}(\nu)\right] \qquad (3.69)$$

where $\overline{\alpha}(\nu_{1\to 2})$ is the spectrally integrated absorption constant and $\overline{\sigma}(\nu_{1\to 2})$ is the spectrally integrated absorption cross-section for the transition 1→2 at the centerline frequency $\nu_{1\to 2}$ (the terminology is sometimes confused in the literature):

$$\overline{\alpha}(\nu_{1\to 2}) = \int_{-\infty}^{\infty} N \frac{h\nu_{1\to 2}}{c} B_{12} Y_{\nu_{1\to 2}}(\nu)\mathrm{d}\nu = N \frac{h\nu_{1\to 2}}{c} B_{12} \quad \left[\mathrm{Hz}/\mathrm{m}\right] \tag{3.70a}$$

$$\overline{\sigma}(\nu_{1\to 2}) = \int_{-\infty}^{\infty} \frac{h\nu_{1\to 2}}{c} B_{12} Y_{\nu_{1\to 2}}(\nu)\mathrm{d}\nu = \frac{h\nu_{1\to 2}}{c} B_{12} \quad \left[\mathrm{m}^2\mathrm{Hz}\right] \tag{3.70b}$$

The spectrally integrated absorption constant and the spectrally integrated absorption cross-section are generally written in terms of the Einstein *A*-coefficient. Referring to Eq. 3.60, we can recast Eq. 3.70 in terms of the Einstein *A*-coefficient:

$$\begin{aligned}\overline{\alpha}(\nu_{1\to 2}) &= N \frac{h\nu_{1\to 2}}{c} B_{12} \\ &= N \frac{g_2}{g_1} \frac{h\nu_{1\to 2}}{c} B_{21}\end{aligned}$$

$$\overline{\alpha}(\nu_{1\to 2}) = N \frac{g_2}{g_1} \frac{c^2}{8\pi \nu_{1\to 2}^2} A_{21} \tag{3.71a}$$

Similarly,

$$\overline{\sigma}(\nu_{1\to 2}) = \frac{g_2}{g_1} \frac{c^2}{8\pi \nu_{1\to 2}^2} A_{21}. \tag{3.71b}$$

Eq. 3.69 describes the intensity of radiation within the bandwidth of an atomic transition that is transmitted after passing an *infinitesimal* distance through the absorbing gas. The incident irradiance absorbed and spontaneously emitted is lost to the radiation that continues its passage through the gas. This affects the cumulative intensity of radiation that is absorbed and spontaneously emitted through a finite distance. Referring to Eqs. 3.66 and 3.70a,

$$\frac{\partial I}{\partial z} = -I\overline{\alpha}(\nu_{1\to 2}) Y_{\nu_{1\to 2}}(\nu) \Rightarrow \int_{I_o}^{I(z)} \frac{\mathrm{d}I}{I} = -\int_0^z \overline{\alpha}(\nu_{1\to 2}) Y_{\nu_{1\to 2}}(\nu)\mathrm{d}z, \tag{3.72}$$

and we find that the intensity of light resonant with and incident upon an absorbing gas that is transmitted after passage a *finite* distance z through the gas is,

$$I(z) = I_o \exp\left[-\overline{\alpha}(\nu_{1\to 2}) \cdot z \cdot Y_{\nu_{1\to 2}}(\nu)\right] \tag{3.73a}$$

or in terms of the absorption cross-section,

$$I(z) = I_o \exp\left[-N \cdot \overline{\sigma}(\nu_{1\to 2}) \cdot z \cdot Y_{\nu_{1\to 2}}(\nu)\right]. \tag{3.73b}$$

Eq. 3.73 is simply Beer's law; Eq. 3.69 is an approximation for $\overline{\alpha}(\nu_{1\to 2})\cdot z\cdot Y_{\nu_{1\to 2}}(\nu)<<1$ (e.g. weak absorptions, short propagation path lengths, or broad absorption lineshapes).

The discussion thus far has described the resonant electromagnetic radiation, the spectral energy density, the spectral irradiance, and the lineshape function in units of frequency. Care must be taken when working in units other than frequency. For instance, defining the absorption constant or cross-section in units of angular frequency can not simply be derived from Eq. 3.71 by converting frequency, ν, to angular frequency, $\omega = 2\pi\nu$. It is important to recognize that the Einstein coefficients as defined above are also in terms of frequency. For instance, the Einstein *A*-coefficient in Eq. 3.71 is defined as the spontaneous emission probability in a unit frequency bandwidth. When working in angular frequency units, the *A*-coefficient as so defined must be multiplied by 2π :

$$A_{ki}^{\omega} = 2\pi A_{ki}^{\nu} \tag{3.74}$$

The superscripts in Eq. 3.74 correspond to the unit employed and the subscripts to the transition described. With this in mind we can write Eq. 3.73 in terms of angular frequency,

$$\boxed{I(z)=I_o\exp\left[-\overline{\alpha}(\omega_{1\to 2})\cdot z\cdot Y_{\omega_{1\to 2}}(\omega)\right]=I_o\exp\left[-N\cdot\overline{\sigma}(\omega_{1\to 2})\cdot z\cdot Y_{\omega_{1\to 2}}(\omega)\right]} \tag{3.75}$$

where,

$$\overline{\alpha}(\omega_{1\to 2}) = N\frac{g_2}{g_1}\frac{\pi}{2}\frac{c^2}{(2\pi\nu_{1\to 2})^2}A_{21}^{\omega}$$

$$= N\frac{g_2}{g_1}\frac{\pi}{2}\frac{c^2}{\omega_{1\to 2}^2}2\pi A_{21}^{\nu}$$

$$\boxed{\overline{\alpha}(\omega_{1\to 2}) = N\frac{g_2}{g_1}\frac{\pi^2 c^2}{\omega_{1\to 2}^2}A_{21}\quad \left[\mathrm{rad}/\mathrm{s\,m}\right]} \tag{3.76a}$$

and similarly,

$$\boxed{\overline{\sigma}(\omega_{1\to 2}) = \frac{g_2}{g_1}\frac{\pi^2 c^2}{\omega_{1\to 2}^2}A_{21}\quad [\mathrm{m}^2\,\mathrm{rad/s}]}. \tag{3.76b}$$

Note that the lineshape function in Eq. 3.75 is now defined in units of angular frequency (mks-units of s/rad). Keep in mind that $A_{21} = A_{21}^{\nu}$ in Eq. 3.76 is how the Einstein *A*-coefficient is most commonly defined in spectroscopic texts, but careful attention to the units associated with any quoted spectroscopic data is advisable. We will return to Eqs. 3.75 and 3.76 during the discussion that follows.

As mentioned in the introduction to this section, there are two dominant lines for Rb – the D_1-line at a center-of-gravity angular frequency $\omega_o\big|_{D_1} = 2\pi \cdot 377\text{THz}$ [68] and the D_2-line at $\omega_o\big|_{D_2} = 2\pi \cdot 384\text{THz}$ [69]. Within each of these fine structure components there is additional hyperfine splitting. Within the D_2-line of Rb in natural isotopic abundance, for instance, there are sixteen possible hyperfine transitions – eight for ^{85}Rb and eight for ^{87}Rb. (Of the eight possible hyperfine electronic transitions in the D_2-line of either isotope of Rb, only six are statistically probable as will be discussed in the next sub-section). When light resonant with one of these hyperfine electronic transitions passes through a vapor cell of Rb in natural isotopic abundance its intensity is attenuated.

Analysis from the perspective of Einstein coefficients does not distinguish between the different hyperfine transitions in an atomic line. Referring back to Eqs. 3.60, 3.66, and 3.71, analysis from the perspective of Einstein coefficients predicts that the attenuation in intensity of light resonant with an atomic transition $l \to u$ after passage an infinitesimal distance Δz is,

$$\Delta I = I_o N \frac{g_u}{g_l} \frac{\pi^2 c^2}{\omega_{l\to u}^2} A_{ul} \Delta z Y_{\omega_{l\to u}}(\omega) \propto \frac{1}{\omega_{l\to u}^2} \frac{g_u}{g_l} A_{ul} N \,, \tag{3.77}$$

The resonant angular frequency, $\omega_{l\to u}$, in Eq. 3.77 is associated with the line and not a particular hyperfine transition. In addition, the Einstein *A*-coefficient in Eq. 3.77 does not make a distinction between the excited state and ground state sublevels in the line – This is the convention adopted in most spectroscopic texts and adopted by us throughout our discussion. Noting that the Einstein *A*-coefficient, A_{ul}, of a particular transition $l \to u$ is related to the mean spontaneous lifetime, $\tau_{u\to l}$, of the transitions upper state (i.e. after a time τ the excited state population density would decrease to 1/e of its initial value if not repopulated),

$$A_{ul} = 1 \big/ \tau_{u\to l} \tag{3.78}$$

what this implies is that an atom of ^{85}Rb (or ^{87}Rb) that is excited into any of the four upper state hyperfine sublevels in the D_2-line is assumed to decay into any of the two lower ground state hyperfine sublevels in the D_2-line at the same rate regardless of the specific excited state and ground state sublevels involved.

We can interpret the ratio of the excited state degeneracy to the ground state degeneracy in Eq. 3.77 as accounting for the hyperfine structure in the line without making a distinction. Calculations from the perspective of Einstein coefficients assume that light resonant with a particular atomic transition $l \rightarrow u$ can be excited into any of the g_u upper state hyperfine sublevels; i.e. calculations from the perspective of Einstein coefficients sum over the hyperfine excited states:

$$\Delta I \propto g_u A_{ul} . \tag{3.79}$$

The spontaneous emissions from any excited states populated are then assumed to branch into the ground state sublevels with an equal probability; i.e. calculations from the perspective of Einstein coefficients average over the hyperfine ground states:

$$\Delta I \propto \frac{g_u}{g_l} A_{ul} . \tag{3.80}$$

By accounting for the hyperfine structure in a line, analysis from the perspective of Einstein coefficients effectively makes a distinction between the fine structure of an atom. Consider the D_1 and D_2 lines of Rb in natural isotopic abundance. Looking up the Einstein *A*-coefficient for Rb in any spectroscopic reference we in fact find two approximately equal but distinct values for the D-line – one for the D_1-line and one for the D_2-line. Looking further we find two approximately equal but distinct resonant frequencies for the D-line of Rb – one associated with the D_1-line and one associated with the D_2-line. Digging still deeper we find that, though the ground state degeneracy of the D_1-line is equal to the ground state degeneracy of the D_2-line, the upper excited state degeneracy of the D_1-line is half that of the D_2-line. Based on analysis from the perspective of Einstein coefficients (vis-à-vis Eq. 3.77) we would therefore conclude that the D_2-line is roughly twice as optically thick as the D_1-line, a conclusion that is consistent with observation. In other words, analysis from the perspective of Einstein coefficients makes a distinction between the different atomic lines.

At this point it is useful to refer back to Figure 3.11 plotting the Doppler broadened D_2-line of Rubidium in natural isotopic abundance. In the measured D_2-line, four Doppler broadened profiles can be resolved – two corresponding to the two ground state hyperfine transitions of ^{85}Rb in the D_2-line and two corresponding to the two ground state hyperfine transitions of ^{87}Rb in the D_2-line. But calculations from the perspective of Einstein coefficients do not distinguish between the hyperfine sublevels of Rb; i.e. analysis from the perspective of Einstein coefficients would predict a single broadened profile at the center-of-gravity angular frequency of the line that is a superposition of a single Doppler broadened profile corresponding to ^{85}Rb with a single Doppler broadened profile corresponding to ^{87}Rb.

We can begin to explain away this discrepancy between the analysis based on Einstein coefficients and observation if we wave our hands a bit. Looking up the ground state and excited state degeneracy of Rb is a spectroscopic reference, we find that the ground state degeneracy of both ^{85}Rb and ^{87}Rb is two and that excited state degeneracy of both isotopes is four in the D_2-line. As mentioned above, we therefore conclude that there are sixteen possible hyperfine transitions in the D_2-line of Rb in natural isotopic abundance – eight for ^{85}Rb and eight for ^{87}Rb – each corresponding to a slightly different resonant energy. Based on this information, we would therefore expect to see sixteen absorption features in the D_2-line of Rb in natural isotopic abundance. Noting from Figure 3.11 that there are in fact only four observable absorption features in the measured D_2-line, we intuit that the energy splitting between the excited state hyperfine sublevels is obscured by thermal broadening, but that we are able to resolve the energy splitting between the ground state hyperfine sublevels of both isotopes.

Now, we notice that the two Doppler broadened absorption profiles corresponding to ^{85}Rb are approximately three times the depth of the two profiles corresponding to ^{87}Rb. Though the lower and upper state degeneracies, center-of-gravity angular frequencies, and Einstein *A*-coefficients of ^{85}Rb and ^{87}Rb as defined are equivalent for the D_2-line, the natural isotopic abundance of ^{85}Rb is approximately three times the natural isotopic abundance of ^{87}Rb (i.e. the number density of ^{85}Rb is approximately three times the number density of ^{87}Rb in a Rb vapor filter of natural isotopic abundance). Referring to Eq. 3.77, we therefore expect a vapor filter of ^{85}Rb to absorb approximately three times more resonant photons than a vapor filter of ^{87}Rb all else equal.

Again, analysis from the perspective of Einstein coefficients assumes that an atom excited into any of its hyperfine upper state sublevels will decay into any of its hyperfine ground state sublevels with equal probability. Keeping the hand-waving argument above in mind, we therefore expect the analysis based on Einstein coefficients to predict four Doppler broadened absorption profiles offset from each other in the frequency domain – Two identical absorption profiles corresponding to ^{85}Rb that are approximately three times the depth of two identical profiles corresponding to ^{87}Rb.

Utilizing the absorption theory based on Einstein coefficients and waving our hands a bit we have been able at this point to theoretically justify the key features observed in the measured D_2-line of Rb. But the hand-waving argument only goes so far. For instance, the absorption profiles corresponding to each of the two isotopes are not identical as anticipated – e.g. the $\boldsymbol{F}$=3 ground state transition of ^{85}Rb is clearly more probable than the $\boldsymbol{F}$=2 ground state transition. In addition, we can't predict where the observed features lie relative to the fine structure center-of-gravity in the frequency domain. To make the theory derived from the perspective of Einstein coefficients consistent with and predictive of observations of the D$_2$-line of Rb, the hyperfine structure of the line must be incorporated into the analysis. The energy splitting between the different hyperfine sublevels must be quantified, and the relative transition probability of each transition incorporated into the model. These details will be discussed in the next sub-section.

3.3.2 The Hyperfine Structure of Rubidium

The D$_1$- and D$_2$-lines of Rb are the components of a fine-structure doublet that is the result of coupling between the orbital angular momentum of the outer electron, $\boldsymbol{L}$, and its spin angular momentum, $\boldsymbol{S}$. According to conventional quantum theory, the total electron angular momentum of a particular atomic state,

$$\boldsymbol{J}=\boldsymbol{L}+\boldsymbol{S}, \tag{3.81}$$

must lie within the range [70],

$$\left|\boldsymbol{L}-\boldsymbol{S}\right| \le \boldsymbol{J} \le \boldsymbol{L}+\boldsymbol{S} . \tag{3.82}$$

The outer electron in a ground state atom of either ^{85}Rb or ^{87}Rb has an orbital angular momentum of $\boldsymbol{L}$ = 0 and a spin angular momentum of $\boldsymbol{S}$ = 1/2. For the first excited state of both isotopes $\boldsymbol{L}'$ = 1 and $\boldsymbol{S}'$ = 1/2 [66]. (Any primed quantum number refers to an excited state in the discussion that follows). Therefore, according to Eq. 3.82 both ^{85}Rb and ^{87}Rb have a total electron angular momentum of $\boldsymbol{J}$ = 1/2 in the ground state and $\boldsymbol{J}'$= 1/2 or 3/2 in the first excited state. What this implies is that, since the energy of a particular state depends (among other things) on the total electron angular momentum, $\boldsymbol{J}$, of that state, the $\boldsymbol{L}$ = 0 ground state transition to the $\boldsymbol{L}'$= 1 excited state of either Rb isotope – i.e. the D-line transition of either isotope – is split into two components: The D$_1$-line corresponding to the $\boldsymbol{J} = 1/2 \rightarrow \boldsymbol{J}' = 1/2$ transition and the D$_2$-line corresponding to the $\boldsymbol{J} = 1/2 \rightarrow \boldsymbol{J}' = 3/2$ transition. In terms of conventional spectroscopic notation, the D$_1$-line corresponds to the $5^2P_{1/2} \leftarrow 5^2S_{1/2}$ transition and the D$_2$-line corresponds to the $5^2P_{3/2} \leftarrow 5^2S_{1/2}$ transition, where the first number in the energy level label is the principal quantum number of the outer electron, the superscript is 2$\boldsymbol{S}$+1, the letter refers to $\boldsymbol{L}$ (e.g. S $\leftrightarrow$ $\boldsymbol{L}$ = 0, P $\leftrightarrow$ $\boldsymbol{L}'$= 1, etc.), and the subscript is $\boldsymbol{J}$.

Within each fine structure component – i.e. within each line – there is additional hyperfine energy splitting that is the result of coupling between the total electron angular momentum, $\boldsymbol{J}=\boldsymbol{L}+\boldsymbol{S}$, and the total nuclear angular momentum, $\boldsymbol{I}$. Noting that the degeneracy, g, of a particular state is related to the total electron angular momentum, $\boldsymbol{J}$, of that state [70],

$$g = 2\boldsymbol{J} + 1, \tag{3.83}$$

and recalling that the total electron angular momentum of either isotope of Rb is $\boldsymbol{J}$ = 1/2 in the ground state, we expect the ground state of both ^{85}Rb and ^{87}Rb to have two hyperfine sublevels; i.e. the degeneracy of the ground state of either isotope is two. Similarly, we expect a degeneracy of two for the $5^2P_{1/2}$ excited state and four for the $5^2P_{3/2}$ excited state of either isotope of Rb. This isn't anything we didn't already know, but let's dig a bit deeper.

According to conventional quantum theory, the total atomic angular momentum of a particular atomic state,

$$\boldsymbol{F}=\boldsymbol{J}+\boldsymbol{I}, \tag{3.84}$$

must lie within the range [70],

$$\left|\boldsymbol{J} - \boldsymbol{I}\right| \le \boldsymbol{F} \le \boldsymbol{J} + \boldsymbol{I} . \tag{3.85}$$

The nuclear spin of ^{85}Rb is $\boldsymbol{I}$ = 5/2 and the nuclear spin of ^{87}Rb is $\boldsymbol{I}$ = 3/2 [66]. Referring to Eq. 3.85 we therefore find that both ^{85}Rb and ^{87}Rb do indeed have two hyperfine ground state sublevels – ^{85}Rb can have a total atomic angular momentum of $\boldsymbol{F}$ = 2 or 3 in its ground state and ^{87}Rb can have a total atomic angular momentum $\boldsymbol{F}$ = 1 or 2 in its ground state. Similarly, we find that an atom of ^{85}Rb in the $5^2P_{1/2}$ excited state can have a total atomic angular momentum of $\boldsymbol{F}'$= 2 or 3 and that an atom of ^{87}Rb in the $5^2P_{1/2}$ excited state can have a total atomic angular momentum of $\boldsymbol{F}'$= 1 or 2. For the $5^2P_{3/2}$ excited state, ^{85}Rb and ^{87}Rb can have a total atomic angular momentum of $\boldsymbol{F}'$= 1, 2, 3 or 4 and $\boldsymbol{F}'$= 0, 1, 2 or 3, respectively.

Whereas the fine structure energy splitting of Rb arises from differences in the total electron angular momentum of the $\boldsymbol{L}'$= 1 excited state, the hyperfine energy splitting within each fine structure component arises from (relatively smaller) differences in the total atomic angular momentum, $\boldsymbol{F}$, of each state in the corresponding line; i.e. the energy of a particular atomic state does not merely depend of the total electron angular momentum, $\boldsymbol{J}$, of the state, but the total atomic angular momentum, $\boldsymbol{F}$, of the state. The absorption theory developed from the perspective of Einstein coefficients does not account for this detail, but it is possible to incorporate this detail into the theory we have developed up to this point by referring to those quantum calculations used to quantify the hyperfine energy splitting and relative transition probabilities.

Let us first consider the quantum formalism used to describe the energy spitting between the hyperfine components. The hyperfine energy shifts relative to the unshifted fine structure center-of-gravity follow from the quantum derived Hamiltonian describing the hyperfine structure [70, 71],

$$\Delta E_{HFS} = \frac{1}{2} A_{HFS} K + B_{HFS} \frac{\frac{3}{2} K(K+1) - 2\boldsymbol{I}(\boldsymbol{I}+1)\boldsymbol{J}(\boldsymbol{J}+1)}{2\boldsymbol{I}(2\boldsymbol{I}-1)2\boldsymbol{J}(2\boldsymbol{J}-1)} = h\Delta\nu_{HFS} \tag{3.86}$$

where A_{HFS} is the magnetic dipole coupling constant of the atom, B_{HFS} is the electric quadrupole coupling constant, $\boldsymbol{I}$ is the nuclear spin, $\boldsymbol{J}$ is the total electron angular momentum, h=6.626 × 10^{-34} Js is Planck's constant, $\Delta\nu_{HFS}$ is the hyperfine frequency shift from the unshifted fine structure center-of-gravity, and

$$K = \boldsymbol{F}(\boldsymbol{F}+1) - \boldsymbol{I}(\boldsymbol{I}+1) - \boldsymbol{J}(\boldsymbol{J}+1) \tag{3.87}$$

where $\boldsymbol{F}$ is the total atomic angular momentum. The magnetic dipole and electric quadrupole coupling constants for each electronic state in the D_2-line of ^{85}Rb and ^{87}Rb are given in Table 3.2 along with the pertinent references. (Additional significant digits reported in the referenced articles for the magnetic dipole and electric quadrupole coupling constants of ^{87}Rb have been excluded from those values recorded in Table 3.2). Note that the electric quadrupole constant only applies to energy levels with $\boldsymbol{J}$ = 3/2 (i.e. excited states in the D_2-line).

	^{85}Rb	^{87}Rb
$A_{5^2S_{1/2}}$	$h \cdot 1.011911$ GHz [66]	$h \cdot 3.4173413$ GHz [73]
$A_{5^2P_{3/2}}$	$h \cdot 25.038$ MHz [72]	$h \cdot 84.719$ MHz [69]
$B_{5^2P_{3/2}}$	$h \cdot 26.011$ MHz [72]	$h \cdot 12.497$ MHz [69]

Table 3.2 Magnetic dipole and electric quadrupole coupling constants of the $5^2S_{1/2}$ ground state and the $5^2P_{3/2}$ excited state of ^{85}Rb and ^{87}Rb

Let's go through a sample calculation. Referring to Eq. 3.86 and the data in Table 3.2 let us determine the frequency shift of the $\boldsymbol{F}$ = 1 ground state (e.g. the $5^2S_{1/2}$ state) of ^{87}Rb from the fine structure center-of-gravity:

$$\left.\begin{array}{l} \boldsymbol{J} = \frac{1}{2}, \boldsymbol{I} = \frac{3}{2}, \boldsymbol{F} = 1 \Rightarrow K = -\frac{5}{2} \\ A_{5^2S_{1/2}} = h \cdot 3.417\,\text{GHz} \end{array}\right\} \Rightarrow \Delta E^{F=1}_{5^2S_{1/2}} = h \cdot (-4.272\,\text{GHz}) \tag{3.88}$$

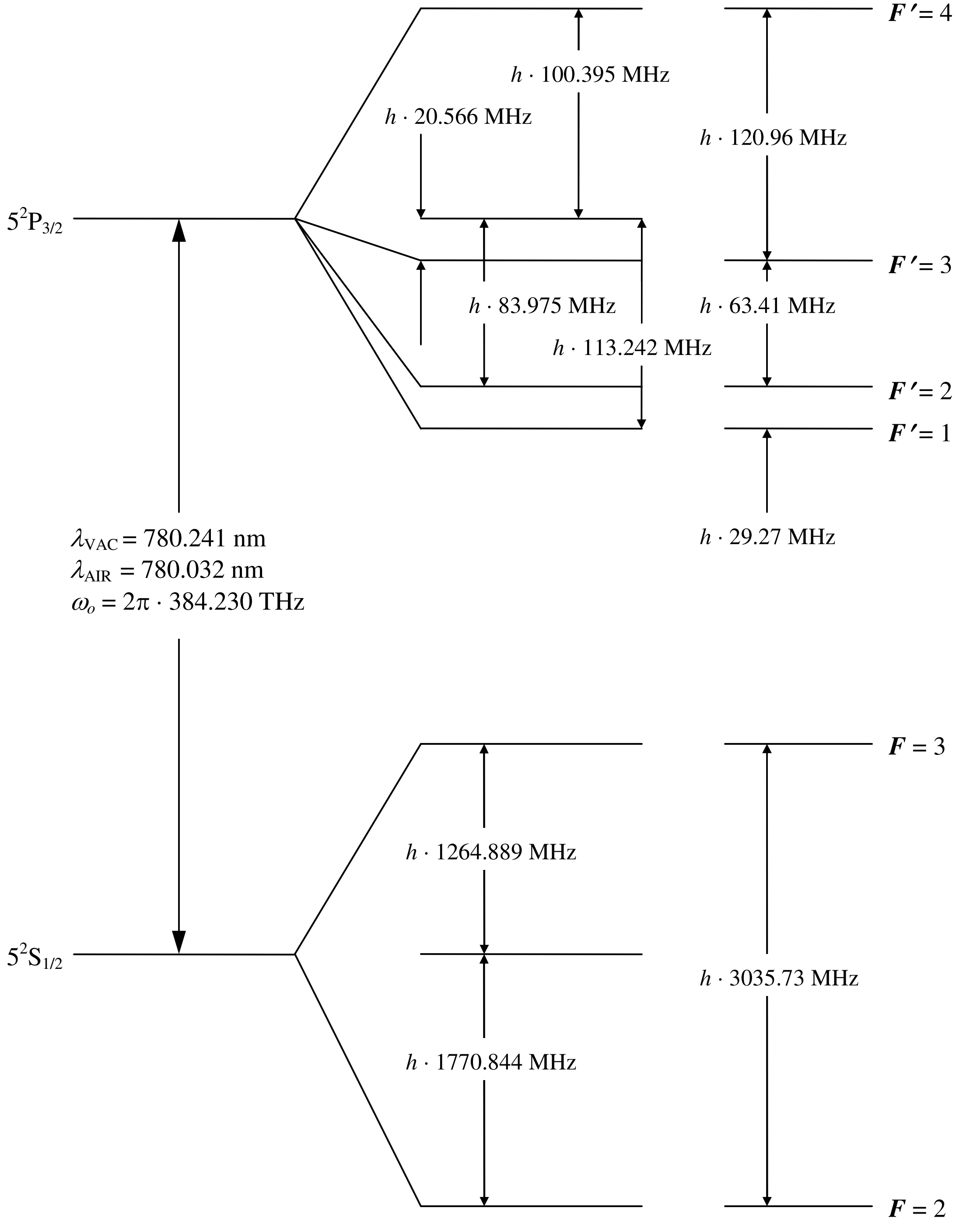

Figure 3.13 Hyperfine energy splitting within D_2-line of ^{85}Rb

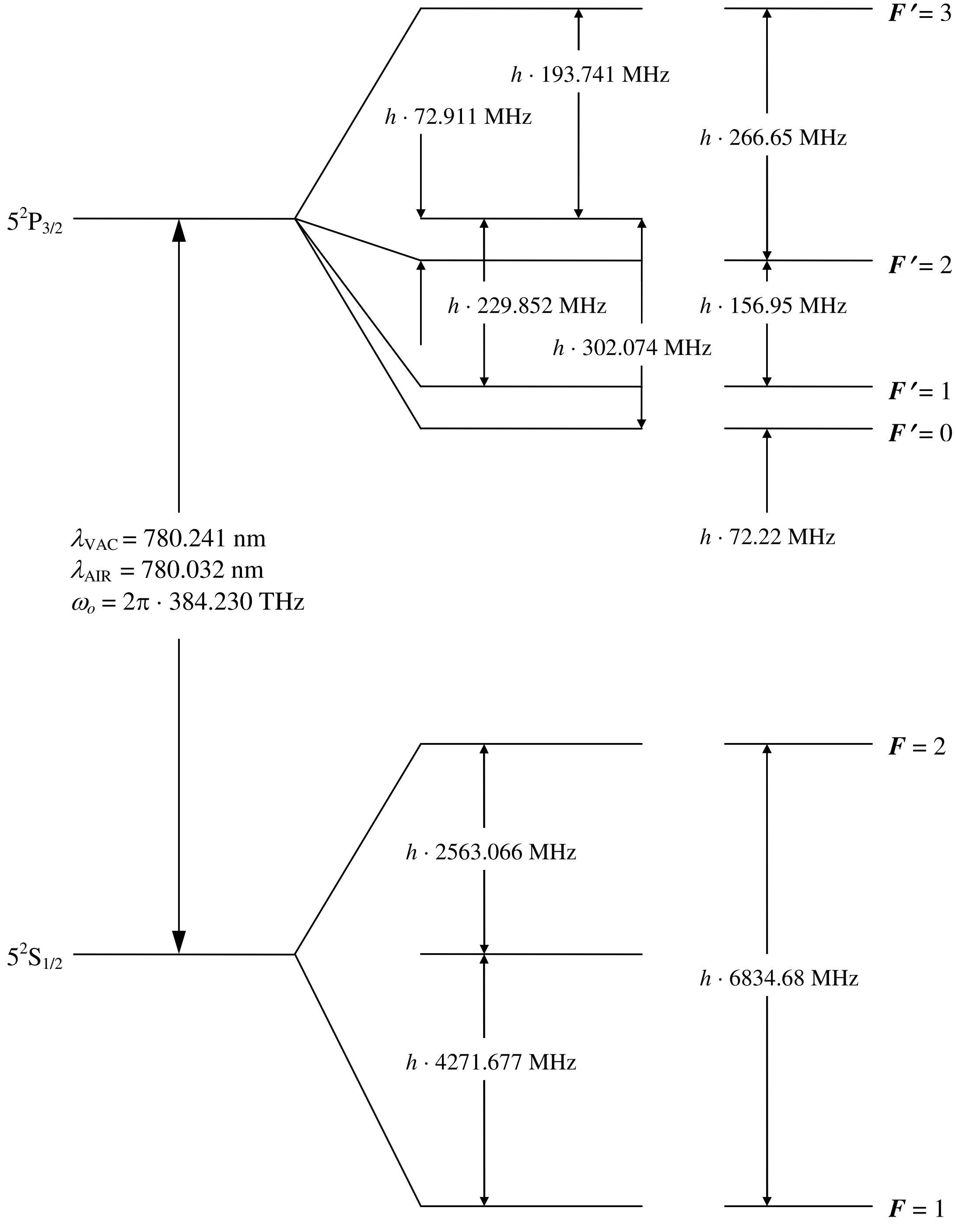

Figure 3.14 Hyperfine energy splitting within D_2-line of ^{87}Rb

Relative transition probability, $P_{F\to F'}$					
^{85}Rb			^{87}Rb		
	F=2	F=3		F=1	F=2
F′=1	33.33	0.00	F′=0	14.29	0.00
F′=2	43.21	12.35	F′=1	35.71	7.14
F′=3	34.57	43.21	F′=2	35.71	35.71
F′=4	0.00	100.00	F′=3	0.00	100.00

Normalized relative transition probability, $\overline{P}_{F\to F'}$					
^{85}Rb			^{87}Rb		
	F=2	F=3		F=1	F=2
F′=1	0.12	0.00	F′=0	0.06	0.00
F′=2	0.16	0.05	F′=1	0.16	0.03
F′=3	0.13	0.16	F′=2	0.16	0.16
F′=4	0.00	0.37	F′=3	0.00	0.44

Table 3.3 Transition probabilities for hyperfine transitions in the D_2-line of ^{85}Rb and ^{87}Rb [74]

A summary of the energy splitting between all hyperfine components in the D_2-line of ^{85}Rb and ^{87}Rb can be found in Figures 3.13 and 3.14, respectively. (Additional significant digits have been excluded from the numerical values in Figures 3.13 and 3.14). The numbers in the figures follow from Eq. 3.86 and Table 3.2 and will be used in the model that follows. For each of the hyperfine transitions depicted in Figures 3.13 and 3.14 there is an associated transition probability summarized in Table 3.3. The relative transition probability, $P_{F\to F'}$, for each hyperfine transition in the D_2-line of Rb is listed in Table 3.3. The numbers in Table 3.3 follow from quantum calculations and will be used in the model that follows [74]. The normalized relative transition probability, $\overline{P}_{F\to F'}$, of a particular hyperfine transition of a particular isotope in Table 3.3 is simply the ratio of the relative transition probability of that hyperfine transition of that isotope to the sum over all relative transition probabilities for the D_2-line of that isotope,

$$\overline{P}_{F\to F'} = \frac{P_{F\to F'}}{\sum P_{F\to F'}} \Rightarrow \sum \overline{P}_{F\to F'} = 1. \tag{3.89}$$

To summarize, the intensity of light transmitted after passage through a Rb vapor filter follows from Beer's law. According to Beer's law, the attenuation of light resonant with a hyperfine transition within the D_2-line of Rb depends upon the propagation path length through the Rb vapor cell, the number density of Rb atoms in the cell, the line broadening associated with the induced absorption, and the spectrally integrated absorption cross-section. Aside from a couple of details, we now know everything we need to know to develop a theoretical model of the D_2-line of Rb.

The propagation path length through the Rb vapor cell is a known experimental parameter, the number density of Rb atoms in the cell will be discussed in the beginning of the next sub-section, and we will assume that the induced absorption is Doppler broadened by the thermal motion of the Rb atoms in the model that follows. The spectrally integrated absorption cross-section was derived from the perspective of Einstein coefficients in sub-section 3.3.1. For a particular hyperfine transition, this spectrally integrated absorption cross-section is simply weighted by the normalized relative transition probability quoted in Table 3.3 for that hyperfine transition. In Table 3.3 we find that there are twelve probable hyperfine transitions in the D_2-line of Rb – six for ^{85}Rb and six for ^{87}Rb. The model of the D_2-line of Rb described in the next sub-section is simply a superposition of these twelve hyperfine transitions, each Doppler broadened according to the thermal motion of the atoms, of varying depth according to the relative transition probability of the transition and number density of the associated Rb isotope, and offset from each other in the frequency domain according to the hyperfine energy splitting depicted in Figures 3.13 and 3.14.

3.3.3 Theoretical Model of the D_2-Line of Rb in Natural Isotopic Abundance

The attenuation in power of light passing through an atomic gas and resonant with an electronic transition of that gas is given by Beer's law,

$$\boxed{P(z) = P_o \exp\left[-N \cdot \bar{\sigma}\left(\omega_{F \to F'}\right) \cdot z \cdot Y_{\omega_o}(\omega)\right]} \tag{3.90}$$

where P_o is the incident power within the bandwidth of the atomic transition and $P(z)$ is that power transmitted after passage a distance z through the gas. Beer's law, as written in Eq. 3.90, is the basis of the model we will presently develop for the D_2-line of Rb. In developing this model we will assume that each hyperfine electronic transition in the D_2-line of Rb is Doppler broadened by the thermal motion of the Rb atoms in the vapor cell – The Rb vapor cells in both the reference and scattering arm of the MFRS velocimeter utilized during preliminary experiments were at room temperature. This Doppler broadening is modeled by the following normalized Gaussian lineshape function [40],

$$\boxed{Y_{\omega_o}(\omega)=\frac{2}{\Delta\omega_T}\sqrt{\frac{\ln 2}{\pi}}\exp\left[-\frac{\ln 2(\omega-\omega_{F\to F'})^2}{(\Delta\omega_T/2)^2}\right]} \tag{3.91}$$

where,

$$\boxed{\Delta\omega_T=\frac{\omega_o}{c}\sqrt{\frac{8kT\ln 2}{m}}}, \tag{3.92}$$

is the full-width at half-maximum (FWHM) of the Gaussian profile, k is Boltzmann's constant, T is the equilibrium temperature of the Rb gas in the vapor cell, m is the atomic mass of either ^{85}Rb or ^{87}Rb, ω_o is the center-of-gravity angular frequency of the D$_2$-line, $\omega_{F\to F'}$ is the resonant angular frequency of the hyperfine transition $\boldsymbol{F\to F'}$, and c is the speed of light.

For the time being we will also assume that the linewidth of resonant light passing through the Rb vapor cell is much less than the Doppler width of the transitions; i.e. we will assume that the light is a delta function in instantaneous optical frequency. This is a good assumption for modeling the D$_2$-line measured in the reference arm of the MFRS velocimeter, but leads to a highly optimistic calculation of the expected lock-in signal in the scattering arm of the experiment. In general, neglecting the linewidth of light resonant with an atomic transition leads to an overestimation in the calculated optical attenuation through the absorption feature. In the reference arm of the experiment, a relatively narrow linewidth frequency tunable laser beam passes directly through a Rb vapor cell in natural isotopic abundance before detection, and the overestimation in optical attenuation is negligible. In the scattering arm, however, Rayleigh scattered light collected from a probe volume under investigation is transmitted through a Rb vapor cell before detection. This collected Rayleigh scattered light is spectrally broadened by the motion of the atoms or molecules in the probe volume under investigation, as discussed at the end of Section 3.2. As will be shown in the next section, this spectral broadening of the Rayleigh scattered light cannot be neglected in the analysis of the lock-in signal.

Finally, we will invoke the ideal gas approximation to calculate the number density, N, of Rb atoms in the vapor cell. From the ideal gas law, and employing Dalton's law of partial pressures, it follows that the number density of each isotope of Rb in the vapor cell can be calculated knowing the mole fraction, X, of each isotope in natural abundance, the cell temperature, and the equilibrium vapor pressure, $P_v(T)$, of Rb at that cell temperature (refer to Appendix D for a general discussion of vapor pressure):

$$\boxed{\left.\begin{aligned} N_{^{85}\mathrm{Rb}}(T) &= \frac{X_{^{85}\mathrm{Rb}}\, P_v(T)\big|_{\mathrm{Rb}}}{kT} \\ N_{^{87}\mathrm{Rb}}(T) &= \frac{X_{^{87}\mathrm{Rb}}\, P_v(T)\big|_{\mathrm{Rb}}}{kT} \end{aligned}\right\} \Rightarrow N_{\mathrm{Rb}}(T) = N_{^{85}\mathrm{Rb}}(T) + N_{^{87}\mathrm{Rb}}(T) = \frac{P_v(T)\big|_{\mathrm{Rb}}}{kT}} \tag{3.93}$$

Many measurements of the vapor pressure of Rb as a function of temperature have been made, but there is an unfortunate lack of consensus among these measurements. In the temperature range of 400K, for instance, the maximum reported number density for Rb is more than twice the minimum reported number density [75].

It is this author's opinion that the most reliable expressions for the vapor pressure of Rb were provided by Nesemeyanov, who arrived at two models for the vapor pressure of Rb – one for Rb vapor in equilibrium with its liquid phase and one for Rb vapor in equilibrium with its solid phase – by weighting an ensemble of vapor pressure measurements according to the assumed accuracy of those measurements [76]. His models for the vapor pressure of Rb are as follows, where the vapor pressure is in units of Torr and the temperature is expressed in K:

$$\boxed{\log_{10} P_v(T)\big|_{\mathrm{Rb}} = -\frac{4529.635}{T} - 2.99138\log_{10} T + 0.00058663T + 15.88253} \quad \text{(liquid phase)} \tag{3.94a}$$

$$\boxed{\log_{10} P_v(T)\big|_{\mathrm{Rb}} = -\frac{1961.258}{T} + 42.57526\log_{10} T - 0.037716T - 94.04826} \quad \text{(solid phase)} \tag{3.94b}$$

In addition to the sheer number of experiments considered by Nesemeyanov, his liquid phase model was essentially validated by Gallagher and Lewis [75], who made what this author considers the most careful and what appear to be the latest vapor pressure measurements for Rb in the temperature range of 330K. Having said this, the vapor pressure values calculated from Eq. 3.94 should be viewed as rough estimates only.

We now have everything we need to model the D_2-line of Rb: The transmitted power as a function of optical frequency follows from Beer's law, Eq. 3.90, the isotopic number density follows from Nesemeyanov's model for the vapor pressure of Rb, Eq. 3.94, and the ideal gas approximation, Eq. 3.93, the propagation path length through the Rb vapor cell is a known experimental parameter, and a normalized Gaussian lineshape function, Eqs. 3.91 and 3.92, is assumed in the model that follows. The spectrally integrated absorption cross-section of Rb was derived from the perspective of Einstein coefficients in sub-section 3.3.1. We simply need to modify Eq. 3.76 for the spectrally integrated absorption cross-section to account for the transition probability of each hyperfine component in the D_2-line of Rb,

$$\boxed{\overline{\sigma}\left(\omega_{F\to F'}\right) = \overline{P}_{F\to F'}\frac{2\boldsymbol{J}'+1}{2\boldsymbol{J}+1}\frac{\pi^2c^2}{\omega_o^2}A_{J\to J'}} \tag{3.95}$$

where $\overline{P}_{F\to F'}$ is the pertinent normalized relative transition probability from Table 3.3, $\boldsymbol{J}$ = 1/2 for Rb in the $5^2S_{1/2}$ ground state, and $\boldsymbol{J}'$ = 3/2 in the $5^2P_{3/2}$ excited state. Keeping in mind that the angular frequency, $\omega_{F\to F'}$, of each hyperfine component in the D_2-line is offset from the center-of-gravity, ω_o, of the line by the pertinent value in either Figure 3.13 or Figure 3.14, a model of the D_2-line then follows which is simply a superposition of all the hyperfine components in the line.

A numerical simulation was performed to model the D_2-line of Rb. This model is presented in Figure 3.15 along with an experimental measurement of the D_2-line made through a $z \cong 100$ mm cell at an equilibrium temperature of $T \cong 20.8$ °C. The measured profile was acquired by slowly tuning the optical frequency of a relatively narrow linewidth extended-cavity diode laser (ECDL) across the D_2-line of Rb and detecting the transmitted laser power down beam of the $z \cong 100$ mm Rb vapor cell in the reference arm of the MFRS velocimeter. The modeled profile utilizes the fundamental physical constants provided in Table 3.4 as well as those physical and optical properties of Rb provided in Table 3.5. Both the modeled and measured profiles in Figure 3.15 have been normalized to one outside of the bandwidth of a resonant transition. The frequency of each data point in the measured profile relative to the D_2-line's center-of-gravity was calculated by setting the relative frequency of the peak absorption detected while sweeping through the $\boldsymbol{F}$=3 ground state transition of ^{85}Rb to the theoretically determined value (i.e. from the simulated profile) of $\nu-\nu_o=-1.21$ and by setting the relative frequency of the peak absorption detected while sweeping through the $\boldsymbol{F}$=2 ground state transition of ^{85}Rb to the theoretically determined value of $\nu-\nu_o=1.7$ GHz. The relative frequency of every other data point in the measured profile was then interpolated by assuming that the optical frequency of the ECDL utilized during the measurement increased linearly with time while sweeping across the D_2-line.

The fit between the measured profile and the modeled profile in Figure 3.15 is pretty good. The measured signal is slightly more attenuated than the modeled signal between the $\boldsymbol{F}$=2 ground state transition of ^{87}Rb and the $\boldsymbol{F}$=3 ground state transition of ^{85}Rb, possibly because of the finite linewidth of the ECDL laser output – i.e. the modeled profile simulates absorption of a monochromatic laser beam – but practically lies on top of the modeled signal throughout the rest of the frequency domain.

Fundamental Physical Constants

Property	Label	Value
Speed of light	c	2.99792458×10^{8} m/s
Boltzmann's constant	k	$1.3806503 \times 10^{-23}$ J/K
Avagadro's number	N_A	6.0221367×10^{26} (kg mol)$^{-1}$
Universal gas constant	$\hat{R}$	8.314510 J/(mol·K)
Permittivity of free space	ε_o	$8.854187817 \times 10^{-12}$ C^2/Nm^2
Electron mass	m_e	$9.10928188 \times 10^{-31}$kg
Elementary charge	e	$1.602176462 \times 10^{-19}$ C
Plank's constant	h	$6.62606876 \times 10^{-34}$ J·s

Table 3.4 Fundamental physical constants [77]

Physical and Optical Properties of Rb

Property	^{85}Rb	^{87}Rb
Natural isotopic abundance (X) [78]	72.17%	27.83%
Molar mass ($\hat{M}$) [79]	84.912 kg/kmol	86.910 kg/kmol
Atomic mass (m)	1.410×10^{-25} kg	1.443×10^{-25} kg
Melting point temperature ™ [78]	39.31 °C	
Total nuclear angular momentum (I) [66]	5/2	3/2
Total atomic angular momentum [66]		
$5^2S_{1/2}$ ground state (F)	2 or 3	1 or 2
$5^2P_{1/2}$ excited state (F')	2 or 3	1 or 2
$5^2P_{3/2}$ excited state (F')	1,2,3 or 4	0,1,2 or 3
Degeneracy [66]		
$5^2S_{1/2}$ ground state ($g = 2J+1$)	2	
$5^2P_{1/2}$ excited state ($g' = 2J'+1$)	2	
$5^2P_{3/2}$ excited state ($g' = 2J'+1$)	4	
Center-of gravity angular frequency (ω_o)		
$5^2S_{1/2} \rightarrow 5^2P_{1/2}$ transition (D_1-line) [68]	$2\pi \cdot 377.107$ THz	
$5^2S_{1/2} \rightarrow 5^2P_{3/2}$ transition (D_2-line) [69]	$2\pi \cdot 384.230$ THz	
Einstein coefficient of spontaneous emission (A)		
$5^2S_{1/2} \rightarrow 5^2P_{1/2}$ transition (D_1-line) [80]	0.3610×10^{8} s^{-1}	
$5^2S_{1/2} \rightarrow 5^2P_{3/2}$ transition (D_2-line) [80]	0.3811×10^{8} s^{-1}	
Oscillator strength (f)		
$5^2S_{1/2} \rightarrow 5^2P_{1/2}$ transition (D_1-line)	0.3420	
$5^2S_{1/2} \rightarrow 5^2P_{3/2}$ transition (D_2-line)	0.6956	

Table 3.5 Physical and optical properties of Rb

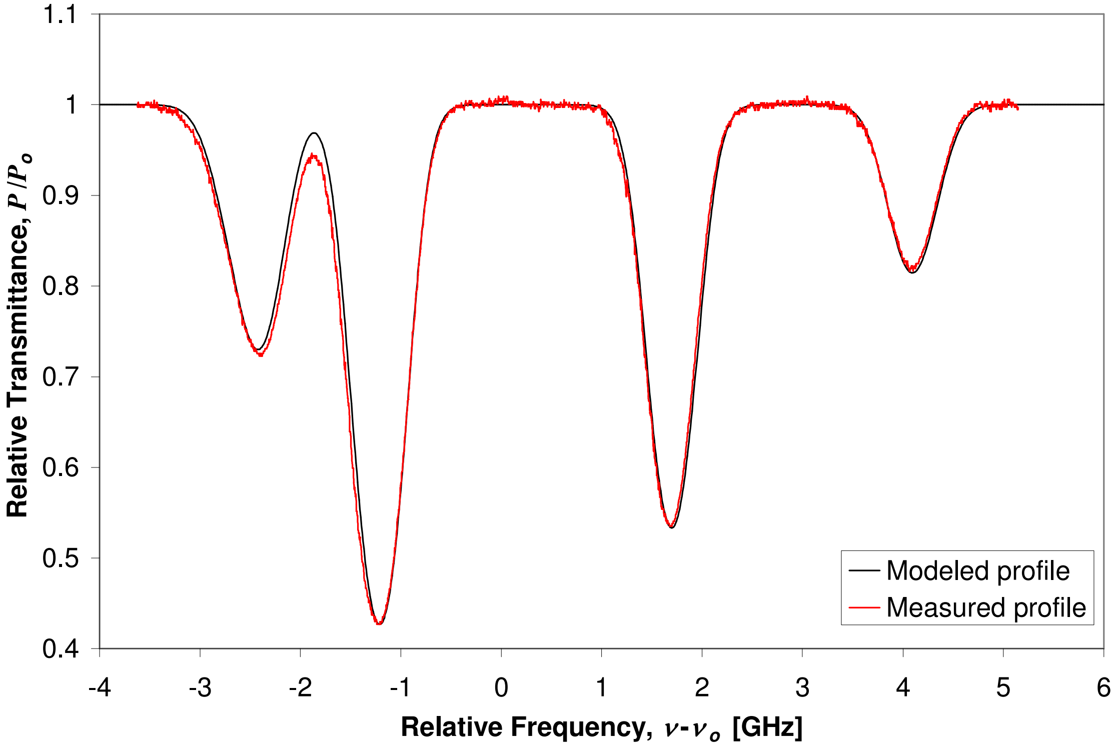

Figure 3.15 Direct absorption measurement of D_2-line of isotopic Rb made through z=100 mm vapor cell at T=20.8 °C compared to simulated D_2-line of isotopic Rb

3.3.4 A Heuristic Model of the Doppler Broadened *F*=3 Ground State Transition of ^{85}Rb in the D_2-Line of Rb in Natural Isotopic Abundance

Preliminary MFRS experiments in the frequency-locked mode of operation utilized calibration profiles to determine the Doppler frequency shift of the collected Rayleigh scattered light and hence the velocity of the flow under investigation. These calibration profiles were acquired by slowly tuning the centerline laser frequency, and hence the centerline frequency of the Rayleigh scattered light, through a Doppler broadened absorption profile in the D_2-line of Rb while simultaneously and rapidly modulating the laser frequency about its instantaneous centerline frequency. The first and second Fourier components of the modulated absorption signal detected in the scattering arm of the experiment – the 1*f* and 2*f* modulated absorption profiles – were measured using a lock-in amplifier and the ratio of these two harmonic profiles was then calculated, resulting in a calibration profile that was insensitive to minor fluctuations in the scattered power collected from the probe volume.

Consider Figure 3.16 illustrating a laser line centered on the edge of an absorption feature whose optical frequency is rapidly modulated between the absorption peak and no absorption at all. The modulated absorption signal illustrated in Figure 3.16 increases as the optical depth of the absorption feature increases. It is for this reason that preliminary MFRS measurements in the frequency-locked mode of operation utilized a calibration profile constructed from modulated absorption measurements of the ***F***=3 ground state transition of ^{85}Rb in the D_2-line. The Doppler broadened ***F***=3 ground state transition of ^{85}Rb exhibits the greatest optical depth out of the four Doppler broadened absorption features in the D_2-line of Rb in natural isotopic abundance, and therefore affords the maximum possible modulated absorption signal in the D_2-line. (The widths of the four Doppler broadened absorption features resolved in the D_2-line of Rb are approximately equal. For a given modulation depth the maximum modulated absorption signal therefore increases with the optical depth of the absorption feature measured in the D_2-line). In addition, by stabilizing the laser frequency to the absorption peak of the Doppler broadened ***F***=3 ground state transition of ^{85}Rb during frequency-locked MFRS velocity measurements, the detection of stray reflections collected in the scattering arm of the MFRS velocimeter is minimized by the relatively strong attenuation of the transition.

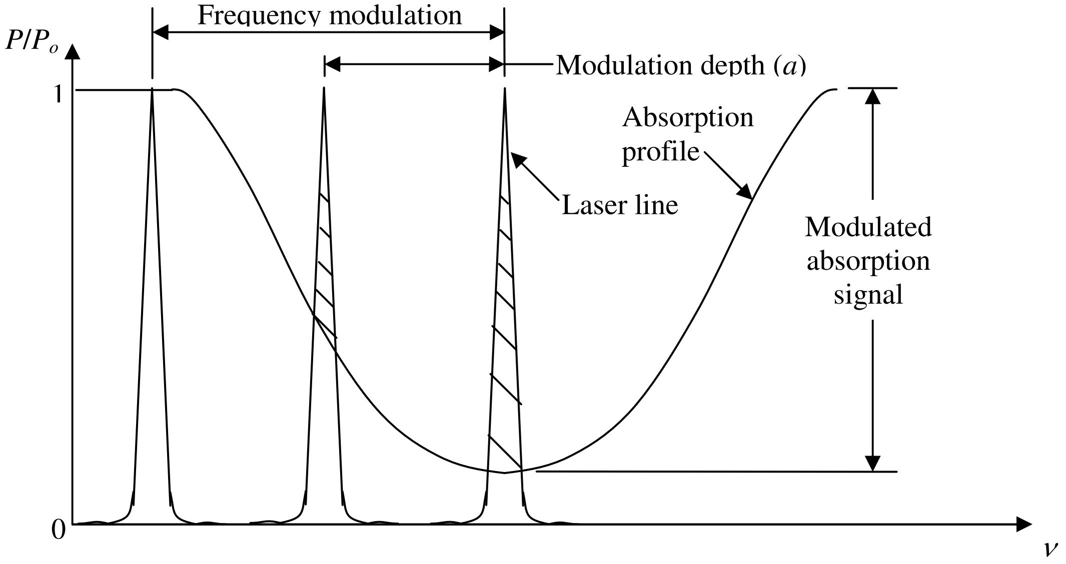

Figure 3.16 Pictorial description of maximum modulated absorption signal

In this sub-section we will develop a heuristic model of the Doppler broadened ***F***=3 ground state transition of ^{85}Rb that neglects the upper state hyperfine energy shifts. In collapsing the three probable excited states of the ***F***=3 ground state transition of ^{85}Rb into one energy level, we expect a modeled absorption feature that is more highly peaked than the measured absorption feature. Referring again to Figure 3.16, this overestimation in the optical depth of the Doppler broadened ***F***=3 ground state transition of ^{85}Rb will ultimately result in a slight overestimation of the peak modulated absorption signal calculated in the following section. Nevertheless, the heuristic model developed in this sub-section will greatly benefit the discussion of modulated absorption spectroscopy in the next section by simplifying the math pertinent to that discussion.

Our heuristic model of the Doppler broadened ***F***=3 ground state transition of ^{85}Rb is in many ways unchanged from the model developed in the previous sub-section. The attenuation of resonant laser power still follows from Beer's law, Eq. 3.90. We will continue to calculate the isotopic number density by assuming the Rb gas is ideal and by using the appropriate Nesemeyanov model, either Eq. 3.94a or Eq. 3.94b, to calculate the vapor pressure as a function of temperature. And we will continue to use a normalized Gaussian lineshape function, Eqs. 3.91 and 3.92, to model the assumed Doppler broadened profile. In neglecting the excited state splitting in the ***F***=3 ground state transition of ^{85}Rb, however, our previous formulation for the spectrally integrated absorption cross-section, Eq. 3.95, is slightly simplified:

$$\begin{aligned}\bar{\sigma}\left(\omega_{F=3\rightarrow F'=2,3,4}\right) &= \bar{P}_{F=3\rightarrow F'=2,3,4}\,\frac{2\boldsymbol{J}'+1}{2\boldsymbol{J}+1}\frac{\pi^2c^2}{\omega_o^2}A_{J\rightarrow J'} \\ &= \frac{2\boldsymbol{F}+1}{2(2\boldsymbol{I}+1)}\,\frac{2\boldsymbol{J}'+1}{2\boldsymbol{J}+1}\frac{\pi^2c^2}{\omega_o^2}A_{J\rightarrow J'} \\ \bar{\sigma}\left(\omega_{F=3\rightarrow F'=2,3,4}\right) &= 6.767\times10^{-6}\ \mathrm{m}^2\,\frac{\mathrm{rad}}{\mathrm{s}}\,. \end{aligned} \tag{3.96}$$

An analytic solution for the normalized relative ground state transition probability has been introduced in Eq. 3.96 [81],

$$\bar{P}_{F=3\rightarrow F'=2,3,4} = \frac{2\boldsymbol{F}+1}{2(2\boldsymbol{I}+1)} = 0.583 \tag{3.97}$$

where ***F***=3 is the ground state total atomic angular momentum we are presently concerned with and ***I***=5/2 is the total nuclear angular momentum of ^{85}Rb. The normalized relative transition probability of the ***F***=3 ground state transition of ^{85}Rb in Eq. 3.97 is numerically equivalent to the sum over the three normalized relative transition probability in Table 3.3 associated with the three probable hyperfine energy transitions from the ***F***=3 ground state of ^{85}Rb. Finally, the numerical calculation of the absorption cross-section associated with the ***F***=3 ground state transition of ^{85}Rb in Eq. 3.96 follows from the values outlined in Tables 3.4 and 3.5 for the ground state and excited state total electron angular momentum, ***J*** and ***J'***, respectively, the speed of light, *c*, the center-of-gravity angular frequency of the D$_2$-line, ω_o, and the Einstein coefficient of spontaneous emission, $A_{J\rightarrow J'}$.

Introducing Eq. 3.96, defining the spectrally integrated absorption cross-section of our heuristic model and Eq. 3.91, defining the normalized Gaussian lineshape function into Beer's law, Eq. 3.90, we arrive at the following expression for the transmitted power as a function of frequency:

$$\begin{aligned}\left.\frac{P(\omega,T,z)}{P_o}\right|_{^{85}\mathrm{Rb}_{\mathrm{F=3}}} &= \exp\left[-N_{^{85}\mathrm{Rb}}\cdot\bar{\sigma}\left(\omega_{F=3\rightarrow F'=2,3,4}\right)\cdot Y_{\omega_o}(\omega)\cdot z\right] \\ &= \exp\left\{-N_{^{85}\mathrm{Rb}}\cdot 6.767\times10^{-6}\ \mathrm{m}^2\,\frac{\mathrm{rad}}{\mathrm{s}}\cdot\frac{2}{\Delta\omega_T}\sqrt{\frac{\ln 2}{\pi}}\exp\left[-\frac{\ln 2\left(\omega-\omega_{F=3\rightarrow F'=2,3,4}\right)^2}{\left(\Delta\omega_T/2\right)^2}\right]\cdot z\right\} \\ &= \exp\left[-\alpha(\omega)\cdot z\right] \\ \left.\frac{P(\omega,T,z)}{P_o}\right|_{^{85}\mathrm{Rb}_{\mathrm{F=3}}} &= \exp\left\{-3.179\times10^{-6}\,\frac{N_{^{85}\mathrm{Rb}}}{\delta\omega_{1/2}}\exp\left[-\frac{\ln 2\left(\omega-\omega_o\right)^2}{\delta\omega_{1/2}{}^2}\right]\cdot z\right\} \qquad (3.98)\end{aligned}$$

We recognize from our discussion in the previous sub-section that the ***F***=3 ground state transition of ^{85}Rb is offset from the center-of-gravity angular frequency of the D$_2$-line, ω_o. We will neglect this subtlety in our heuristic model, however, and simply center the ***F***=3 ground state transition of ^{85}Rb at ω_o. This slight simplification will not affect our analysis in the following sections of this chapter, and will benefit our discussion of modulated absorption spectroscopy in the next section by reducing the number of variables we need to keep track of. I have ever-so-slightly simplified the expression in 3.150 further by writing the normalized Gaussian lineshape function in terms of the Doppler broadened half-width at half-maximum (HWHM),

$$\delta\omega_{1/2} = \frac{\omega_o}{c}\sqrt{\frac{2kT\ln 2}{m}} \qquad (3.99)$$

The heuristic model developed in this sub-section and described by Eq. 3.98 is compared to a measurement of the ***F***=3 ground state transition of ^{85}Rb in Figure 3.17. The measured absorption profile was acquired by slowly tuning the optical frequency of the ECDL utilized during preliminary MFRS experiments through the Doppler broadened absorption features associated with the ***F***=2 and ***F***=3 ground state transitions of ^{85}Rb. (The stability of the ECDL deteriorates as the range of optical frequencies across which it is tuned increases. Since there was no need to tune across the entire D_2-line to measure the Doppler broadened ***F***=3 ground state transition of ^{85}Rb, I limited the sweep during this round of experiments). A small fraction of the laser power (<1%) was diverted to the reference arm of the MFRS velocimeter, and the transmitted laser power down beam of a $z \cong 100$ mm Rb vapor cell at a cell temperature of $T \cong 22.2$ °C was detected. (The laser intensity diverted through the Rb cell in the reference arm was far from the saturation intensity of Rb during all preliminary MFRS experiments).

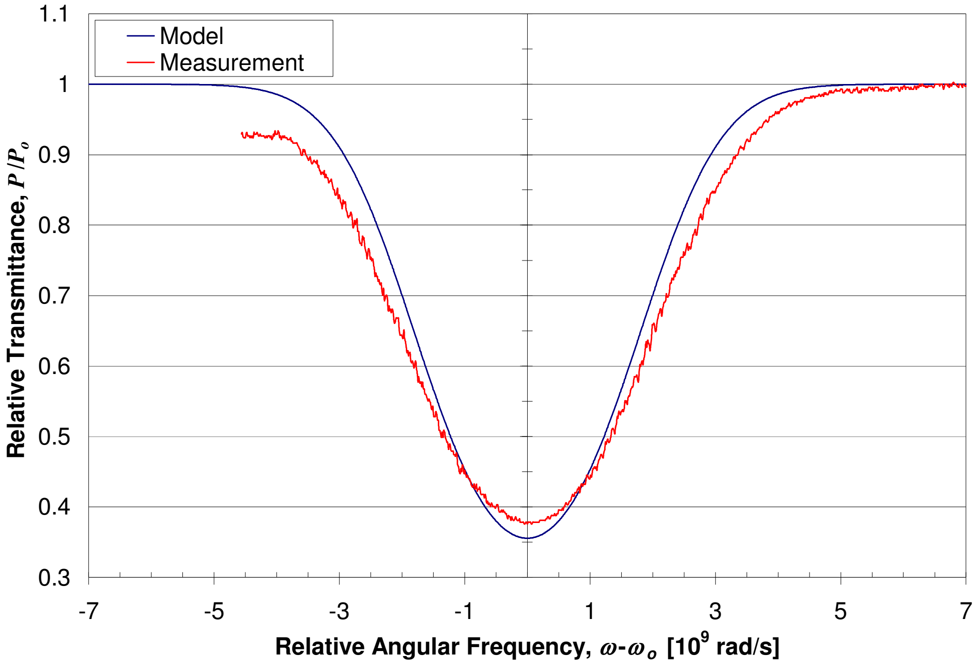

*Figure 3.17 A measurement of the **F**=3 ground state transition of ^{85}Rb through a $z \cong 100$mm cell of Rb vapor in natural isotopic abundance at $T \cong 22.2$ °C compared to our heuristic model*

Figure 3.18 shows twenty profiles measured consecutively in this fashion over the course of 100 s. Each profile consists of 2500 data points acquired during a five second interval. The twenty profiles illustrated in Figure 3.18 are in fact the result of ten triangle-wave sweeps of the laser frequency. The ten profiles in Figure 3.18a were measured as the ECDL was slowly tuned from a lower to a higher optical frequency – as the triangle-wave voltage input to the ECDL was increasing – and the ten counterpart profiles in Figure 3.18b were measured as the ECDL was tuned from a higher to lower frequency – as the triangle-wave voltage input to the ECDL was decreasing.

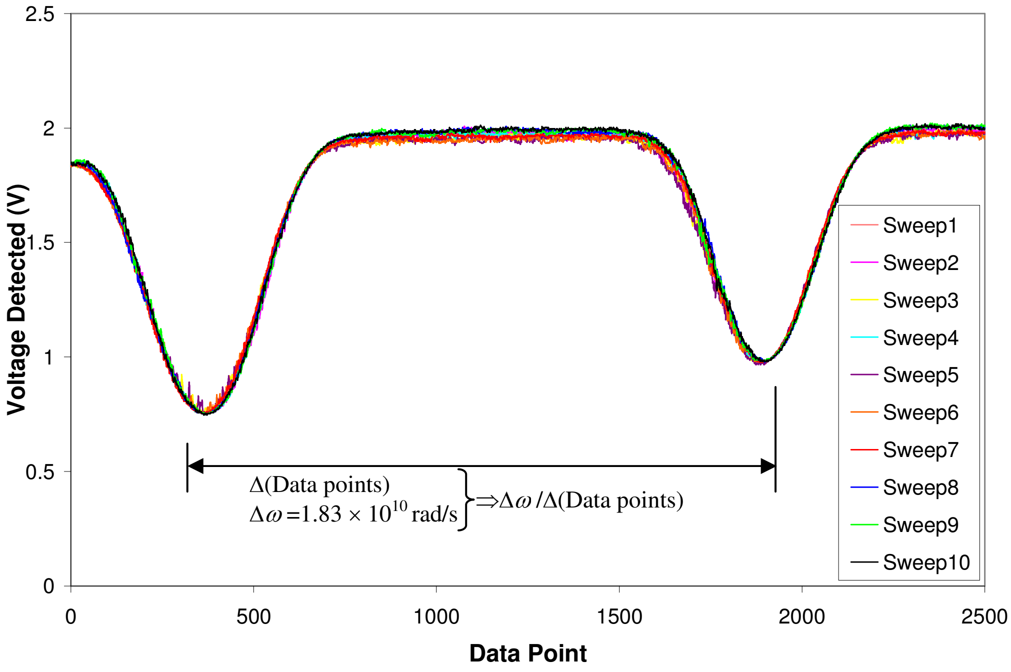

a. Ten sweeps with positive going frequency

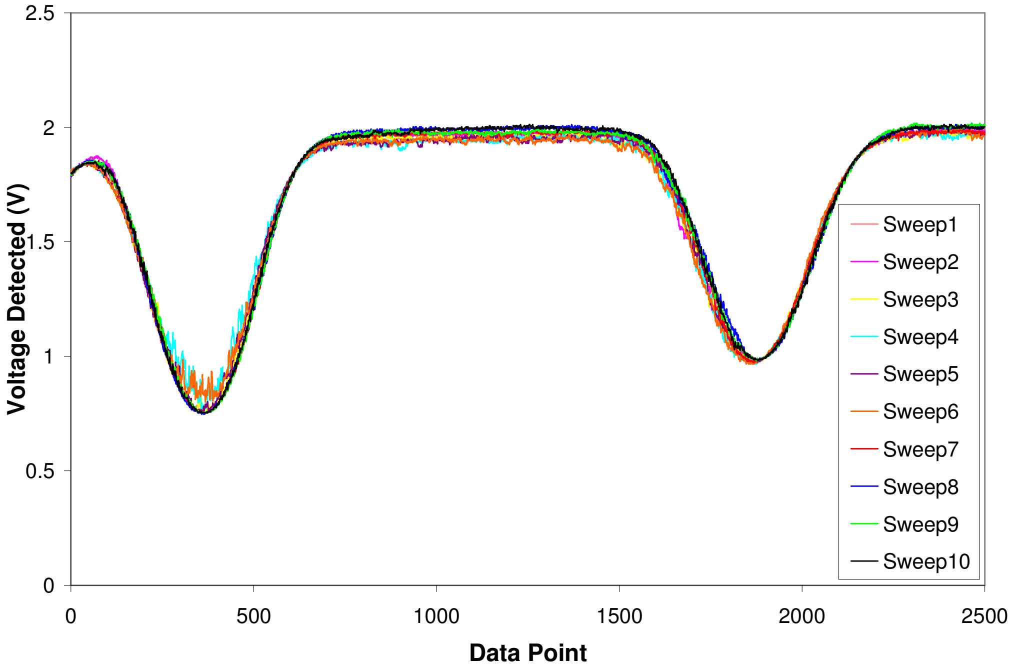

b. Ten sweeps with negative going frequency

*Figure 3.18 Twenty consecutive measurements of the **F**=2 and **F**=3 ground state transitions of ^{85}Rb through a $z \cong 100$mm cell of Rb vapor in natural isotopic abundance at $T \cong 22.2$ ℃*

The ten measured profiles in Figure 3.18b exhibit a pronounced spike within the absorption feature we're trying to model. I don't know the specific cause of this spike in the data, but I intuit that it may originate in the laser system. Another possible explanation is that the pronounced spikes within the Doppler broadened absorption profiles measured during these 10 sweeps are in fact cross-over resonances within the ***F***=3 ground state transition of ^{85}Rb resolved during the measurements. A cross-over resonance occurs within an atomic spectrum when the Doppler widths of two hyperfine transitions sharing the same ground state overlap and is located exactly between the centerline frequencies of the two hyperfine transitions involved. It requires two counter-propagating laser beams to resolve, however, such as in a saturated absorption spectroscopy experiment: A pumping beam that excites those atoms at the cross-over frequency and a probing beam that resolves the cross-over resonance. The ground state population density of the absorbing atoms is reduced by the pumping beam at the cross-over frequency, resulting in less attenuation of the probe beam by the absorbing at the cross-over frequency (i.e. a spike in transmitted probe power). It is possible that reflections from the detector could have set up just such a scenario. Regardless of the cause, the ten profiles that exhibited a pronounced spike were disqualified from further consideration. Of the ten relatively repeatable, relatively smooth profiles in Figure 3.18a, I chose that profile that visually exhibited the smoothest lineshape for comparison to our heuristic model.

The measured profile in Figure 3.17 was normalized to one outside of the absorption (a linear detector response with power is assumed). The angular frequency of each measured point in the profile relative to point of maximum absorption – i.e. the absorption peak – was determined by first measuring the peak-to-peak separation of the ***F***=2 and ***F***=3 profiles in data points and then utilizing the peak-to-peak angular frequency separation of $\Delta\omega_{F=2\rightarrow F=3}=1.828 \times 10^{10}$ rad/s between the ***F***=2 and ***F***=3 absorption features – determined from the theoretical model developed in the previous sub-section – to calculate a data point-to-angular frequency conversion. This approach is illustrated in Figure 3.18a.

We see from Figure 3.17 that our heuristic model of the Doppler broadened ***F***=3 ground state transition of ^{85}Rb predicts reality reasonably well. The model profile is slightly more peaked than the measured profile, as we had expected. The model and measurement begin to diverge at lower frequencies as a result of contributions from the ***F***=2 ground state transition of ^{87}Rb to the measured profile. To illustrate, I have plotted the Doppler broadened ***F***=2 ground state transition of ^{85}Rb predicted by the heuristic model,

$$\left.\frac{P(\omega,T,z)}{P_o}\right|_{^{85}\mathrm{Rb}_{\mathrm{F=2}}} = \exp\left\{-2.270\times10^{-6}\,\frac{N_{^{85}\mathrm{Rb}}}{\delta\omega_{1/2}}\exp\left[-\frac{\ln 2(\omega-\omega_o)^2}{\delta\omega_{1/2}{}^2}\right]\cdot z\right\}, \quad (3.100)$$

against a measurement of the ***F***=2 absorption profile in Figure 3.19.

The measured profile in Figure 3.19 was acquired during the same sweep as the measured profile in Figure 3.17, was normalized to one outside of the absorption, and utilizes the same data point-to-angular frequency conversion used to plot the measured profile in Figure 3.17. Since the ***F***=2 ground state transition of ^{85}Rb is far removed from the other ground state transitions in the D$_2$-line, the measured ***F***=2 absorption profile is relatively symmetric about its peak. In addition, the maximum hyperfine splitting between the probable excited states in the ***F***=2 ground state transition of ^{85}Rb is $(\Delta\nu_{F'=3} - \Delta\nu_{F'=1})$ = 92.68 MHz compared to a maximum hyperfine splitting of $(\Delta\nu_{F'=4} - \Delta\nu_{F'=2})$ = 184.37 MHz between the probable excited states in the ***F***=3 ground state transition. The fit between the measurement and model is therefore better for the ***F***=2 ground state transition of ^{85}Rb.

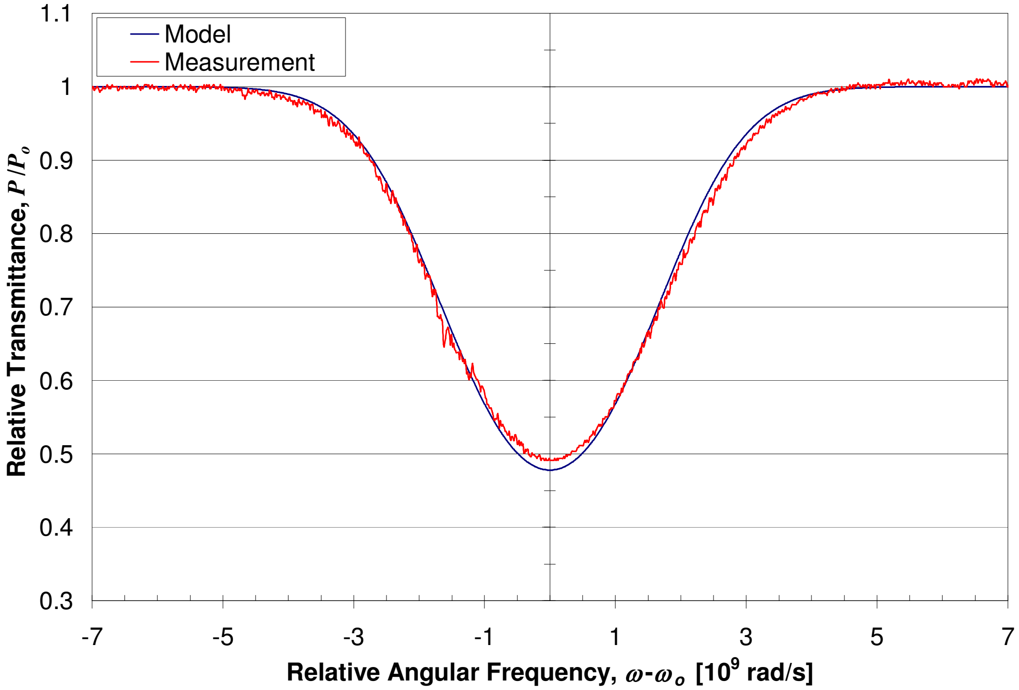

*Figure 3.19 A measurement of the **F**=2 ground state transition of ^{85}Rb through a z ≅ 100mm cell of Rb vapor in natural isotopic abundance at T ≅ 22.2 °C compared to our heuristic model*

3.4 A Description of Modulated Absorption Spectroscopy from the Temporal Perspective

Modulated absorption spectroscopy techniques are frequently utilized to improve the detectability of weak absorptions corresponding to trace species in a gas sample [82-91]. The wavelength of a probe laser beam is slowly tuned across an absorption line of the species being investigated in the gas sample. The wavelength is simultaneously and rapidly modulated about the mean (and slowly varying) laser wavelength. This wavelength modulation results in a modulated absorption signal as the probe laser beam is tuned through the absorption line. Homodyne detection of the resulting modulating photocurrent at the original modulation frequency or some related Fourier component dramatically reduces the noise that would otherwise corrupt the measurement by limiting the equivalent noise bandwidth of the measurement. In addition, detection at the relatively high frequency corresponding to modulation reduces the impact of laser source noise on the measurement.

The harmonic absorption profiles (**n*f***-profiles) that are recorded (utilizing the process described above) as the wavelength is scanned across the absorption feature can be used to determine flow parameters – e.g. temperature, pressure, number density, and velocity– provided that the requisite spectroscopic data for the species under investigation are known [92,93]. We are concerned with the measurement of flow velocities in this dissertation, but the theory discussed in this section is the basis for deriving those mathematical transforms required to relate recorded harmonic absorption profiles to the absorption features scanned and hence the thermodynamic properties of the species under investigation.

Modulated absorption spectroscopy emerged as a practical and potentially powerful diagnostic technique some thirty years ago [94-99]. During the 1980's a semantic distinction was made based on the modulation frequency employed. The technique is referred to as wavelength modulation spectroscopy (WMS) when the modulation frequency, ω_m, is much less than the half-width-at-half-maximum (HWHM), $\delta\omega_{1/2}$, of the absorption feature being investigated; i.e. WMS corresponds to $\omega_m << \delta\omega_{1/2}$. (WMS is alternatively referred to as harmonic detection or derivative spectroscopy). The technique is referred to as frequency modulation spectroscopy (FMS) when the modulation frequency is greater than the HWHM of the absorption feature under investigation; i.e. FMS corresponds to $\omega_m > \delta\omega_{1/2}$ [100-102]. The distinction made between WMS and FMS was more than semantic; the theories used to describe WMS and FMS evolved from two different perspectives.

WMS is generally described from a temporal perspective. From this perspective, the carrier frequency is sinusoidally modulated as a function of time between two extrema separated by the modulation depth from the instantaneous centerline wavelength [102]. This description is suitable provided that the instantaneous centerline wavelength of the laser is essentially constant on the characteristic time scale, τ, of the atomic or molecular transition being scanned,

$$\omega_m << \frac{1}{\tau} = \Delta\omega_T = 2\delta\omega_{1/2} \Rightarrow \omega_m << \delta\omega_{1/2} \qquad (3.101)$$

FMS is described from a spectral perspective. From this perspective, the modulation broadens the laser spectrum creating sidebands around the instantaneous centerline wavelength that are equally spaced in frequency by the modulation frequency [102]. The spectral perspective is the most general and involves an examination of the probe laser electric field rather than the probe laser intensity, as is the case with the temporal perspective. By considering the electric field, the spectral perspective retains phase information, captures both absorption and dispersion, and can investigate the effects of amplitude modulation (AM). Joel Silver has found that the theoretical results from both the temporal and spectral perspective are essentially identical for $\omega_m \leq 0.1\delta\omega_{1/2}$ [100].

The discussion below introduces a theoretical description of WMS from the temporal perspective. We were limited by our laser system to the WMS-region of modulation frequencies during all MFRS measurements, and so this perspective provides a perfectly suitable description of our preliminary experiments. In addition, I find that the temporal perspective is mathematically more intuitive than the spectral perspective. (The spectral perspective is a generalization of the temporal theory and as such provides a richer representation of the modulated absorption signal. I have therefore included a brief theoretical discussion of FMS in Appendix E).

Trace species detection involves looking for a small change –i.e. a weak absorption – in a potentially large signal. Implementation of the MFRS technique involves looking for a relatively large change – i.e. a relatively strong absorption – in a small signal. In both cases, wavelength modulation spectroscopy (WMS) techniques are employed to dramatically improve detection sensitivity. Consider the experimental schematic of the scattering arm of the MFRS velocimeter depicted in Figure 3.20. Rayleigh scattering from a probe volume in some flow under investigation is collected, transmitted through a rubidium (Rb) vapor filter, and detected by a PMT. Detection of the O(100nA) absorption signal resulting from the collected Rayleigh scattered light is dramatically improved by employing homodyne detection of a modulated absorption. (The O(100nA) Rayleigh scattered signal follows from the analysis in Section 3.2, and was typical of all preliminary MFRS experiments). To implement this WMS technique, the probe laser frequency is rapidly modulated about its instantaneous centerline wavelength as it is slowly tuned across an absorption feature in the D_2-line of Rb. This modulation is imposed on the Rayleigh scattered light that is collected, transmitted through the Rb vapor filter, and detected by the PMT. Homodyne detection of the resulting modulated absorption signal output from the PMT in the scattering arm is accomplished with a lock-in amplifier.

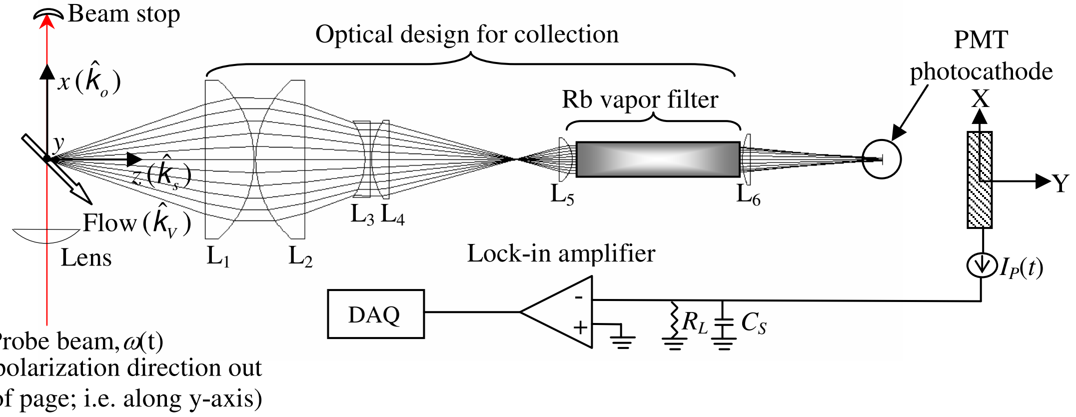

Figure 3.20 Experimental schematic of MFRS scattering arm

In this section I will endeavor to derive a mathematical model for WMS – e.g. for the process described above. In particular, I will focus on the development of mathematical models for the ***1f***- and ***2f***-profiles of a Doppler broadened absorption feature; The calibration profile utilized during preliminary MFRS experiments in the frequency-locked mode of operation consisted of a ratio of the first-to-second Fourier components of the modulated absorption signal detected while slowly tuning through a Doppler broadened absorption feature in the D_2-line of Rb. Initially, a monochromatic light source will be assumed in the development of these mathematical models. This is a relatively good assumption when considering harmonic profile measurements in the reference arm of the MFRS velocimeter; in the reference arm of the experiment, a relatively narrow linewidth frequency tunable laser beam passes directly through a

Rb vapor cell in natural isotopic abundance before detection. The mathematical model of the **1*f***- and **2*f***-profiles developed under this assumption will therefore be compared to experimental measurements of the **1*f***- and **2*f***-profiles made in the reference arm of the instrument. The intent of this comparison is to validate the mathematical models developed and to provide a few more details concerning the experimental apparatus that was used during preliminary MFRS measurements.

Having established confidence in the mathematical models, I will conclude this section with a theoretical calculation of the lock-in signal detected using frequency modulated Rayleigh scattered light. To effectively model the harmonic profiles detected in the scattering arm during preliminary MFRS experiments, the line-broadening of the Rayleigh scattered light must be accounted for in the analysis. From Eq. 3.44 (at the end of Section 3.2) we find that the Doppler width of light scattered from air at a temperature of T=293 K and collected orthogonal to a probe laser beam with a centerline wavelength of λ_o=780 nm is $\Delta\nu_T$= 1.2 GHz. When compared to the Doppler width of an absorption feature in the D_2-line of ^{85}Rb at the same temperature, $\Delta\nu_T$= 511 MHz, it is obvious that the Rayleigh lineshape cannot be neglected in the signal-to-noise analysis. A sharp spike in scattered power that is modulated across an absorption feature will result in a significantly larger modulated absorption signal than if the scattered power is spread out over a broad spectrum extending approximately two-times the frequency extent of the absorption feature. This section will conclude with a comparison of the theoretically derived harmonic profiles in the scattering arm of the experiment to some experimentally measured profiles recorded in the scattering arm.

To begin the theoretical description of WMS, let us model the optical frequency modulation with the following time-varying angular frequency,

$$\omega(t) = \omega + a\cos\omega_m t\,, \tag{3.102}$$

where ω is the mean instantaneous optical frequency that is slowly tuned across the absorption feature, a is the modulation amplitude (or modulation depth), and ω_m is the modulation frequency. (Note that during measurements of the bulk flow velocity the mean optical frequency of the Rayleigh scattered light is Doppler frequency shifted from the mean optical frequency of the probe laser beam. Though this is worth keeping in mind, it will not enter into the analysis that follows). The resulting time-varying absorption constant,

$$\alpha(\omega(t)) = \alpha(\omega + a\cos\omega_m t) \tag{3.103}$$

is a 2π-periodic function, and as such can be expanded in a Fourier series if we assume that the mean optical frequency is constant during one modulation period, $\omega \cong$ constant [102, 103]. The validity of this assumption depends on the rate at which the mean optical frequency is scanned through the absorption feature under investigation. This deserves a few words of explanation.

The scan rates during all MFRS measurements – including the modulated absorption experiments described in this section – were chosen such that a decrease in the scan rate did not visually affect the shape of the harmonic profiles recorded while an increase in the scan rate resulted in noticeable distortion of the recorded profiles. In other words, the optical frequency of the interrogating laser beam was scanned through the pertinent absorption profiles as fast as possible without distorting the harmonic profiles recorded during all MFRS experiments. During preliminary MFRS experiments in the frequency-locked mode of operation this optimized scan rate had two practical purposes. Preliminary frequency-locked velocity measurements utilizing the MFRS technique relied on a calibration profile acquired while slowly scanning the optical frequency of the interrogating laser beam, and hence the Rayleigh scattered light, through an absorption feature in the D_2-line of Rb. Any distortion in the harmonic profiles recorded during this calibration phase of the experiment would compromise the accuracy of velocity measurements made with the scan turned off and the interrogating laser stabilized at a single frequency – i.e. fast scans compromised the accuracy of frequency-locked velocity measurements. On the other hand, excessively slow scan rates were avoided to prevent system instabilities from corrupting the acquired profile. During preliminary measurements in the scattering arm of the MFRS velocimeter, lock-in integration times of τ_L = 1s were typically required to provide any signal-to-noise and scan periods less than O(100s) resulted in profile distortion. Though longer scan periods would have provided distortion-free harmonic profiles, the stability of the laser system during excessively long periods of time was a practical concern that prevented me from employing excessively long scan periods – i.e. excessively slow scans compromised acquisition of the calibration profiles.

Now, the implication of a distortion-free harmonic profile is that the mean optical frequency of the interrogating light is essentially constant during the lock-in integration time employed during the measurement. The experimentally acquired harmonic profiles presented in this section were measured with a lock-in integration time of τ_L=10 ms. Distortion-free profiles were acquired by scanning across the pertinent absorption feature(s) in the D_2-line of Rb at a rate of 2-10 s/scan while simultaneously modulating at a frequency of ω_m = 2.090 kHz. Since the modulation period is approximately two orders-of-magnitude less than the integration time constant and the harmonic profiles used to validate the theory in this section are not distorted, it is perfectly valid if we assume that the mean optical frequency of the interrogating laser beam is constant during one modulation period in the analysis that follows.

Let's continue. The heuristic model we developed at the end of the previous section predicts the following absorption constant for the Doppler broadened **F** = 2 ground state transition of ^{85}Rb,

$$\alpha(\omega,T) = \bar{\sigma} N_{^{85}\text{Rb}} \frac{1}{\delta\omega_{1/2}} \sqrt{\frac{\ln 2}{\pi}} \exp\left[-\frac{\ln 2(\omega-\omega_o)^2}{\delta\omega_{1/2}{}^2} \right]$$

$$= 4.833\times 10^{-6} \frac{N_{^{85}\text{Rb}}}{\delta\omega_{1/2}} \sqrt{\frac{\ln 2}{\pi}} \exp\left[-\frac{\ln 2(\omega-\omega_o)^2}{\delta\omega_{1/2}{}^2} \right]$$

$$\alpha(\omega,T) = 2.270\times 10^{-6} \frac{N_{^{85}\text{Rb}}}{\delta\omega_{1/2}} \exp\left[-\frac{\ln 2(\omega-\omega_o)^2}{\delta\omega_{1/2}{}^2} \right], \qquad (3.104)$$

where $\bar{\sigma}$ is the spectrally integrated absorption cross-section derived from the perspective of Einstein coefficients, $N_{^{85}\text{Rb}}$ is the number density of ^{85}Rb atoms, $\delta\omega_{1/2}$ is the HWHM of the Doppler broadened **F** = 2 and **F** = 3 ground state transitions in the D_2-line of ^{85}Rb, and ω_o is the angular frequency at the center of the absorption profile, defined as the center-of-gravity angular frequency of the D_2-line of Rb in our heuristic model. Similarly, for the **F** = 3 ground state of ^{85}Rb we derived the following heuristic model for the absorption constant:

$$\alpha(\omega,T) = 3.179\times 10^{-6} \frac{N_{^{85}\text{Rb}}}{\delta\omega_{1/2}} \exp\left[-\frac{\ln 2(\omega-\omega_o)^2}{\delta\omega_{1/2}{}^2} \right]. \qquad (3.105)$$

Let us express Eqs. 3.104 and 3.105 in a more general form,

$$\alpha(\omega,T) = \zeta(T)\alpha'(\omega,T). \qquad (3.106)$$

Eq. 3.106 is in fact a general expression for the absorption constant of any ground state atomic transition. For a specific atomic transition ζ is a function of the gas temperature T only. The angular frequency dependence associated with the Doppler broadened lineshape is defined by the simplified function α'. Comparing Eq. 3.106 to Eqs. 3.104 and 3.105 we define,

$$\zeta(T) = 2.270\times 10^{-6} \frac{N_{^{85}\text{Rb}}}{\delta\omega_{1/2}} \; (\boldsymbol{F} = 2) \qquad (3.107a)$$

$$\zeta(T) = 3.179\times10^{-6}\frac{N_{^{85}\mathrm{Rb}}}{\delta\omega_{1/2}}\ (\boldsymbol{F}=3) \tag{3.107b}$$

for the Doppler broadened $\boldsymbol{F}$=2 and $\boldsymbol{F}$=3 ground state transitions in the D$_2$-line of ^{85}Rb and,

$$\alpha'(\omega,T) = \exp\left[-\frac{\ln 2(\omega-\omega_o)^2}{\delta\omega_{1/2}{}^2}\right]. \tag{3.108}$$

Let us now insert Eq. 3.102 describing the optical frequency modulation into Eq. 3.108,

$$\alpha'(\omega(t)) = \exp\left\{-\ln 2\left[\frac{(\omega-\omega_o)}{\delta\omega_{1/2}}+\frac{a}{\delta\omega_{1/2}}\cos\omega_m t\right]^2\right\}. \tag{3.109}$$

If we recast this equation in terms of the following dimensionless parameters,

$$m = \frac{a}{\delta\omega_{1/2}} \equiv \text{modulation index} \tag{3.110a}$$

$$x = \frac{\omega-\omega_0}{\delta\omega_{1/2}} \equiv \text{normalized relative angular frequency}, \tag{3.110b}$$

we derive the following 2π-periodic even function,

$$\alpha'(x,m,t) = \exp\left[-\ln 2(x+m\cos\omega_m t)^2\right], \tag{3.111}$$

which can be expanded in a cosine Fourier series,

$$\alpha'(x,m,t) = \frac{H_0{}'(x,m)}{2}+\sum_{\mathrm{n}=1}^{\infty}H_{\mathrm{n}}{}'(x,m)\cos \mathrm{n}\omega_m t. \tag{3.112}$$

The Fourier coefficients in Eq. 3.112 are defined,

$$H_{\mathrm{n}}{}'(x,m) = \frac{2}{\pi}\int_0^{\pi}\exp\left[-\ln 2(x+m\cos\varphi)^2\right]\cos(\mathrm{n}\varphi)\mathrm{d}\varphi. \tag{3.113}$$

Now consider the detected modulated absorption signal,

$$i_P(t) = i_o\exp\left[-\zeta\alpha'(\omega(t))z\right] \tag{3.114}$$

where i_o is the anode (or cathode) output current detected outside the bandwidth of an atomic transition. Eq. 3.114 follows from Beer's law and represents the time-varying anode output current, i_P, that results from the modulated absorption of light within the bandwidth of an atomic transition detected after passage a distance z through the atomic gas. Homodyne detection of this sinusoidal signal is accomplished with a lock-in amplifier. The lock-in amplifier mixes the detected modulated absorption signal with a reference sinusoidal signal oscillating at an integer multiple, n – corresponding to the Fourier component being recorded – of the modulation frequency [38],

$$R^{\mathrm{n}}(t) = 2\cos(\mathrm{n}\omega_m t + \theta) \quad (\mathrm{n} = 1,2,3,...)\,. \tag{3.115}$$

The relative phase, θ, of the reference signal $R^{\mathrm{n}}(t)$ to the detected signal $i_P(t)$ can be adjusted to accommodate detection of either the modulated absorption signal or the modulated dispersion signal. A low pass filter blocks the AC-component in the mixed signal, and a DC-signal proportional to the detected harmonic signal amplitude is output from the lock-in (see Appendix A: A General Discussion of Lock-in Amplifiers).

Homodyne detection can be mathematically modeled if we expand Eq. 3.114 in a Taylor series,

$$i_p(t) = i_o\left\{1 - \zeta\alpha'(\omega(t))z + \frac{1}{2!}[\zeta\alpha'(\omega(t))z]^2 - \frac{1}{3!}[\zeta\alpha'(\omega(t))z]^3 + \text{...h.o.t.s}\right\} \tag{3.116}$$

Defining,

$$H_{\mathrm{n}}(x,m) = \zeta H_{\mathrm{n}}{}'(x,m) \tag{3.117}$$

and referring to Eqs. 3.106 and 3.112, we can recast Eq. 3.116 in terms of the Fourier components of the detected modulated absorption signal:

$$i_p = i_o\begin{Bmatrix} 1 - \left[\dfrac{H_0 z}{2} + H_1 z\cos\omega_m t + H_2 z\cos 2\omega_m t + H_3 z\cos 3\omega_m t + ...\right] \\ + \dfrac{1}{2!}\left[\dfrac{H_0 z}{2} + H_1 z\cos\omega_m t + H_2 z\cos 2\omega_m t + H_3 z\cos 3\omega_m t + ...\right]^2 \\ - \dfrac{1}{3!}\left[\dfrac{H_0 z}{2} + H_1 z\cos\omega_m t + H_2 z\cos 2\omega_m t + H_3 z\cos 3\omega_m t + ...\right]^3 \\ + \text{...h.o.t.s} \end{Bmatrix} \tag{3.118}$$

Utilizing the trigonometric identity,

$$\cos(x \pm y) = \cos x\cos y \mp \sin x\sin y\,, \tag{3.119}$$

we can now calculate the DC-component of the mixed signal,

$$S_M^{\mathrm{n}} = i_o\exp[-\zeta\alpha'(\omega(t))z]\cdot 2\cos(\mathrm{n}\omega_m t + \theta)\,, \tag{3.120}$$

passed by the lock-in amplifier. The lock-in amplifier output signals for first- and second-harmonic detection calculated from the temporal perspective described above follow:

$$
\begin{aligned}
S_L^1 = \frac{i_o R_L G}{\sqrt{2}} \cos\theta \Bigg\langle \quad & -zH_1 \\
& + \frac{z^2}{2}\left(H_0H_1 + H_1H_2 + H_2H_3 + H_3H_4 + H_4H_5 + H_5H_6 + \ldots\right) \\
& - \frac{z^3}{6}\Bigg\{ \frac{3}{4}H_0{}^2H_1 \\
& \qquad + \frac{3}{4}\Big[H_1{}^2\left(H_1 + H_3\right) + H_2{}^2\left(H_3 + H_5\right) + H_3{}^2\left(H_5 + H_7\right) \\
& \qquad\quad + H_4{}^2\left(H_7 + H_9\right) + H_5{}^2\left(H_9 + H_{11}\right) + \ldots\Big] \\
& \qquad + \frac{3}{2}H_1\left(H_2{}^2 + H_3{}^2 + H_4{}^2 + H_5{}^2 + H_6{}^2 + H_7{}^2 + H_8{}^2 + \ldots\right) \\
& \qquad + \frac{3}{2}H_0\left(H_1H_2 + H_2H_3 + H_3H_4 + H_4H_5 + H_5H_6 + \ldots\right) \\
& \qquad + \frac{3}{2}H_1\left(H_2H_4 + H_3H_5 + H_4H_6 + H_5H_7 + H_6H_8 + \ldots\right) \\
& \qquad + \frac{3}{2}H_2\left[H_3\left(H_4 + H_6\right) + H_4\left(H_5 + H_7\right) + H_5\left(H_6 + H_8\right) + \ldots\right] \\
& \qquad + \frac{3}{2}H_3\left[H_4\left(H_6 + H_8\right) + H_5\left(H_7 + H_9\right) + H_6\left(H_8 + H_{10}\right) + \ldots\right] \\
& \qquad + \frac{3}{2}H_4\left[H_5\left(H_8 + H_{10}\right) + H_6\left(H_9 + H_{11}\right) + H_7\left(H_{10} + H_{12}\right) + \ldots\right] \\
& \qquad + \ \ldots \ \Bigg\} + \ldots\text{h.o.t.s} \quad \Bigg\rangle
\end{aligned}
\tag{3.121}
$$

$$
\begin{aligned}
S_L^2 = \frac{i_o R_L G}{\sqrt{2}} \cos\theta \Bigg\langle & -zH_2 \\
& + \frac{z^2}{2}\left[\frac{{H_1}^2}{2} + \left(H_0 H_2 + H_1 H_3 + H_2 H_4 + H_3 H_5 + H_4 H_6 + \ldots \right) \right] \\
& - \frac{z^3}{6} \Bigg\{ \frac{3}{4} {H_0}^2 H_2 \\
& \qquad + \frac{3}{4}\Big[{H_1}^2 \left(H_0 + H_4 \right) + {H_2}^2 \left(H_2 + H_6 \right) + {H_3}^2 \left(H_4 + H_8 \right) \\
& \qquad\quad + {H_4}^2 \left(H_6 + H_{10} \right) + {H_5}^2 \left(H_8 + H_{12} \right) + \ldots \Big] \\
& \qquad + \frac{3}{2} H_2 \left({H_1}^2 + {H_3}^2 + {H_4}^2 + {H_5}^2 + {H_6}^2 + {H_7}^2 + {H_8}^2 + \ldots \right) \\
& \qquad + \frac{3}{2} H_0 \left(H_1 H_3 + H_2 H_4 + H_3 H_5 + H_4 H_6 + H_5 H_7 + \ldots \right) \\
& \qquad + \frac{3}{2} H_1 \left[H_2 \left(H_3 + H_5 \right) + H_3 \left(H_4 + H_6 \right) + H_4 \left(H_5 + H_7 \right) + \ldots \right] \\
& \qquad + \frac{3}{2} H_2 \left(H_3 H_7 + H_4 H_8 + H_5 H_9 + H_6 H_{10} + H_7 H_{11} + \ldots \right) \\
& \qquad + \frac{3}{2} H_3 \left[H_4 \left(H_5 + H_9 \right) + H_5 \left(H_6 + H_{10} \right) + H_6 \left(H_7 + H_{11} \right) + \ldots \right] \\
& \qquad + \frac{3}{2} H_4 \left[H_5 \left(H_7 + H_{11} \right) + H_6 \left(H_8 + H_{12} \right) + H_7 \left(H_9 + H_{13} \right) + \ldots \right] \\
& \qquad + \frac{3}{2} H_5 \left[H_6 \left(H_9 + H_{13} \right) + H_7 \left(H_{10} + H_{14} \right) + H_8 \left(H_{11} + H_{15} \right) + \ldots \right] \\
& \qquad + \ \ldots \Bigg\} + \ldots \text{h.o.t.s} \Bigg\rangle
\end{aligned}
\tag{3.122}
$$

In Eqs. 3.121 and 3.122, i_o is the current detected outside the bandwidth of an atomic transition, R_L is the shunt resistance at the input of the lock-in amplifier that converts the detected current signal into a voltage signal, G is the gain imposed by the lock-in on the detected harmonic signal, and the multiplicative constant $1/\sqrt{2}$ accounts for the fact that the lock-in amplifier utilized in all preliminary MFRS experiments outputs the RMS-amplitude of the detected sinusoidal voltage signal. (To simplify the analytic expressions leading up to Eq. 3.119, I did not introduce these variables earlier). A relative phase of $\theta = 0°$ or $180°$ optimizes detection of the modulated absorption signal and is used throughout the simulations that follow. I have tried to retain enough terms in each sub-series in the expressions above to clearly establish the pattern within each of these sub-series. The ellipses at the end of each sub-series represent a patterned continuation of the series. Finally, it is worth mentioning that the formulations for the first- and second-harmonic lock-in signals in Eqs. 3.121 and 3.122, respectively, are appropriate for any absorption lineshape. The Fourier coefficients, H_n', are defined in Eq 3.113 for a Gaussian profile, but we could just as easily determine the Fourier coefficients associated with a Lorentz or Voigt profile.

Formulations of the first- and second-harmonic lock-in signals derived from the temporal perspective are significantly simplified when modeling homodyne detection of weak absorptions – e.g. corresponding to trace species in a gas sample [101]. Referring to Eq. 3.116, only the first-order term in the Taylor series representation of Beer's law needs to be retained when $\zeta\alpha' z << 1$,

$$i_p(t) \cong i_o\left[1 - \zeta\alpha'(\omega(t))z\right]. \tag{3.123}$$

If we now expand $\alpha'(\omega(t))$ in a Taylor series about the mean instantaneous optical frequency we find,

$$\begin{aligned} i_p(t) &= i_o\left\{1 - \zeta z\left[\alpha'(\omega) + \left.\frac{\partial\alpha'}{\partial\omega}\right|_{\omega}(\omega - \omega(t)) + \frac{1}{2!}\left.\frac{\partial^2\alpha'}{\partial\omega^2}\right|_{\omega}(\omega - \omega(t))^2\right.\right. \\ &\qquad \left.\left. + \frac{1}{3!}\left.\frac{\partial^3\alpha'}{\partial\omega^3}\right|_{\omega}(\omega - \omega(t))^3 + \ldots\text{h.o.t.s}\right]\right\} \\ &= i_o\left[1 - \zeta z\alpha'(\omega) - \zeta z\left.\frac{\partial\alpha'}{\partial\omega}\right|_{\omega} a\cos\omega_m t - \frac{\zeta z}{2!}\left.\frac{\partial^2\alpha'}{\partial\omega^2}\right|_{\omega}(a\cos\omega_m t)^2\right. \\ &\qquad \left. - \frac{\zeta z}{3!}\left.\frac{\partial^3\alpha'}{\partial\omega^3}\right|_{\omega}(a\cos\omega_m t)^3 + \ldots\text{h.o.t.s}\right] \end{aligned}$$

$$
\begin{aligned}
i_p(t) = i_o\Bigg[1 - \zeta z\alpha'(x) - \zeta z\left.\frac{\partial\alpha'}{\partial x}\right|_x m\cos\omega_m t - \frac{\zeta z}{2!}\left.\frac{\partial^2\alpha'}{\partial x^2}\right|_x m^2\cos^2\omega_m t \\
- \frac{\zeta z}{3!}\left.\frac{\partial^3\alpha'}{\partial x^3}\right|_x m^3\cos^3\omega_m t + \ldots\text{h.o.t.s}\Bigg]
\end{aligned}
\tag{3.124}
$$

where the final expression in Eq. 3.124 is written in terms of the dimensionless parameters defined in Eq. 3.110. Expanding the $\cos^2\omega_m t$ and $\cos^3\omega_m t$ terms using the trigonometric identity in Eq. 3.120 we find,

$$
\begin{aligned}
i_p(t) = i_o\Bigg[1 - \zeta z\alpha'(x) - \zeta z\left.\frac{\partial\alpha'}{\partial x}\right|_x m\cos\omega_m t - \frac{\zeta z}{2!}\left.\frac{\partial^2\alpha'}{\partial x^2}\right|_x m^2\frac{1}{2}\left(1+\cos 2\omega_m t\right) \\
- \frac{\zeta z}{3!}\left.\frac{\partial^3\alpha'}{\partial x^3}\right|_x m^3\frac{1}{4}\left(3\cos\omega_m t + \cos 3\omega_m t\right) + \ldots\text{h.o.t.s}\Bigg]
\end{aligned}
\tag{3.125}
$$

Eq. 3.125 is completely analogous to the expression in Eq. 3.118 for the detected modulated current signal truncated after the first-order term,

$$
\begin{aligned}
i_p &= i_o\left\{1 - \left[\frac{H_o z}{2} + H_1 z\cos\omega_m t + H_2 z\cos 2\omega_m t + H_3 z\cos 3\omega_m t + \ldots\right]\right\} \\
&= i_o\left[1 - \frac{H_o z}{2} - H_1 z\cos\omega_m t - H_2 z\cos 2\omega_m t - H_3 z\cos 3\omega_m t - \ldots\right]
\end{aligned}
$$

$$
i_p = i_o\left[1 - \zeta z\frac{H_o{}'}{2} - \zeta z H_1{}'\cos\omega_m t - \zeta z H_2{}'\cos 2\omega_m t - \zeta z H_3{}'\cos 3\omega_m t - \ldots\right] \tag{3.126}
$$

A particularly clear connection between the derivative profiles in Eq. 3.125 and the Fourier coefficients in Eq. 3.126 is established in the limit of $m << 1$. In this limit the n$^{\text{th}}$-harmonic lock-in signal is simply proportional to the n$^{\text{th}}$-derivative of the absorption profile with angular frequency (or normalized relative angular frequency, x); i.e. all higher-order terms modulating at a particular integer frequency nω_m can be neglected. (Hence WMS is commonly referred to as derivative spectroscopy). Referring to Eqs. 3.120, 3.125 and 3.126 we derive the following theoretical lock-in signals describing the first- and second-harmonic profiles detected while lightly modulating and simultaneously sweeping through a weak absorption:

$$
\begin{aligned}
S_L^1(x) &= -\frac{i_o R_L G}{\sqrt{2}}\cos\theta\cdot\zeta z m\left.\frac{\partial\alpha'}{\partial x}\right|_x = -\frac{i_o R_L G}{\sqrt{2}}\cos\theta\cdot\zeta z H_1{}' \\
&= -\frac{i_o R_L G}{\sqrt{2}}\cos\theta\cdot z m\left.\frac{\partial\alpha}{\partial x}\right|_x = -\frac{i_o R_L G}{\sqrt{2}}\cos\theta\cdot z H_1
\end{aligned}
\tag{3.127a}
$$

$$\begin{aligned} S_L^2(x) &= -\frac{i_o R_L G}{\sqrt{2}} \cos\theta \cdot \zeta z \frac{m^2}{4} \left.\frac{\partial^2 \alpha'}{\partial x^2}\right|_x = -\frac{i_o R_L G}{\sqrt{2}} \cos\theta \cdot \zeta z H_2{}' \\ &= -\frac{i_o R_L G}{\sqrt{2}} \cos\theta \cdot z \frac{m^2}{4} \left.\frac{\partial^2 \alpha}{\partial x^2}\right|_x = -\frac{i_o R_L G}{\sqrt{2}} \cos\theta \cdot z H_2 \end{aligned} \tag{3.127b}$$

A Rb cell temperature of $T \cong 20$ °C – i.e. room temperature – was typical for all preliminary MFRS experiments; the cell temperature measured during the experiments presented in this section to validate our theoretical calculations was specifically $T = 20.2$ °C. The Rb cells in the reference and scattering arms of the MFRS velocimeter were 100 mm and 75 mm long, respectively, during all preliminary experiments; the experiments conducted in this section to validate the theory were conducted in the reference arm. Now, the heuristic model for the Doppler broadened $\boldsymbol{F}=3$ ground state transition of ^{85}Rb developed at the end of the previous section predicts a maximum intensity attenuation of approximately 57% after resonant light incident upon a Rb vapor cell at a temperature of $T = 20.2$ °C passes a distance $z = 100$ mm through this cell. If we were to retain only the first-order term in the Taylor series expansion of Beer's law in Eq. 3.116 the predicted peak intensity attenuation would be 48% greater than the peak intensity attenuation predicted by the analytic expression of Beer's law in Eq. 3.114; i.e. by our heuristic model. If we retain the second-order term there is a resulting underestimation in peak attenuation of 14%, but retaining the third-order term results in an overestimation in peak attenuation of only 3%. A small overestimation in peak attenuation results in a smaller still overestimation of the peak theoretical lock-in signals. I therefore decided to truncate my expressions for the first- and second-harmonic lock-in signals after the third-order terms.

Referring back to Eqs. 3.122 and 3.123 we find a sub-series associated with the second-order term and several sub-series associated with the third-order term in both the first- and second-harmonic lock-in signals. These sub-series involve a summation over patterned terms which consist of Fourier coefficients that are multiplied together. The Fourier coefficients that are multiplied together are associated with higher and higher harmonics of the cosine Fourier series as each sub-series unfolds. Fortunately, for the temperatures and modulation depths typical of preliminary frequency-locked MFRS experiments the Fourier coefficients associated with higher harmonics of the Fourier expansion quickly approach zero.

Figure 3.21 shows the first twelve Fourier coefficients in the cosine Fourier series of Eq. 3.112. These Fourier coefficients follow from Eq. 3.113 and were numerically calculated as a function of the normalized relative angular frequency, x, using a Gaussian quadrature-based integration routine. The calculation was conducted at a temperature of T = 20.2 °C – with a corresponding HWHM of $\delta\omega_{1/2} = 1.607 \times 10^9$ rad/s – and a modulation index of $m = 0.571$. The first five Fourier coefficients in the cosine Fourier series – H_0', H_1', H_2', H_3', and H_4'– are visually relevant terms in Figure 3.21 and were retained during numerical simulations of the first- and second-harmonic lock-in signals. The specific expressions I utilized for my simulations follow:

$$\begin{aligned}
S_L^1 &= \frac{i_o R_L G}{\sqrt{2}} \cos\theta \cdot \bar{S}_L^1 \\
&= \frac{i_o R_L G}{\sqrt{2}} \cos\theta \Bigg\langle -z\zeta H_1' + \frac{z^2\zeta^2}{2}\left(H_0' H_1' + H_1' H_2' + H_2' H_3' + H_3' H_4'\right) - \frac{z^3\zeta^3}{6}\bigg\{\frac{3}{4} H_0'^2 H_1' \\
&\quad + \frac{3}{4}\Big[H_1'^2\left(H_1' + H_3'\right) + H_2'^2\left(H_3' + H_5'\right) + H_3'^2\left(H_5' + H_7'\right) + H_4'^2\left(H_7' + H_9'\right)\Big] \\
&\quad + \frac{3}{2} H_1'\left(H_2'^2 + H_3'^2 + H_4'^2\right) + \frac{3}{2} H_0'\left(H_1' H_2' + H_2' H_3' + H_3' H_4' + H_4' H_5'\right) \\
&\quad + \frac{3}{2} H_1'\left(H_2' H_4' + H_3' H_5'\right) + \frac{3}{2} H_2'\Big[H_3'\left(H_4' + H_6'\right) + H_4'\left(H_5' + H_7'\right)\Big] \\
&\quad + \frac{3}{2} H_3' H_4'\left(H_6' + H_8'\right) + \frac{3}{2} H_4' H_5'\left(H_8' + H_{10}'\right)\bigg\} \Bigg\rangle
\end{aligned} \tag{3.128}$$

$$\begin{aligned}
S_L^2 &= \frac{i_o R_L G}{\sqrt{2}} \cos\theta \cdot \bar{S}_L^2 \\
&= \frac{i_o R_L G}{\sqrt{2}} \cos\theta \Bigg\langle -z\zeta H_2' + \frac{z^2\zeta^2}{2}\left[\frac{H_1'^2}{2} + \left(H_0' H_2' + H_1' H_3' + H_2' H_4' + H_3' H_5'\right)\right] \\
&\quad - \frac{z^3\zeta^3}{6}\bigg\{\frac{3}{4} H_0'^2 H_2' + \frac{3}{4}\Big[H_1'^2\left(H_0' + H_4'\right) + H_2'^2\left(H_2' + H_6'\right) + H_3'^2\left(H_4' + H_8'\right) \\
&\quad + H_4'^2\left(H_6' + H_{10}'\right)\Big] + \frac{3}{2} H_2'\left(H_1'^2 + H_3'^2 + H_4'^2 + H_5'^2\right) + \frac{3}{2} H_0'\Big(H_1' H_3' + H_2' H_4' \\
&\quad + H_3' H_5'\Big) + \frac{3}{2} H_1'\Big[H_2'\left(H_3' + H_5'\right) + H_3'\left(H_4' + H_6'\right) + H_4'\left(H_5' + H_7'\right) \\
&\quad + H_5'\left(H_6' + H_8'\right)\Big] + \frac{3}{2} H_2'\left(H_3' H_7' + H_4' H_8' + H_5' H_9'\right) + \frac{3}{2} H_3'\Big[H_4'\left(H_5' + H_9'\right) \\
&\quad + H_5'\left(H_6' + H_{10}'\right)\Big] + \frac{3}{2} H_4' H_5'\left(H_7' + H_{11}'\right)\bigg\} \Bigg\rangle
\end{aligned} \tag{3.129}$$

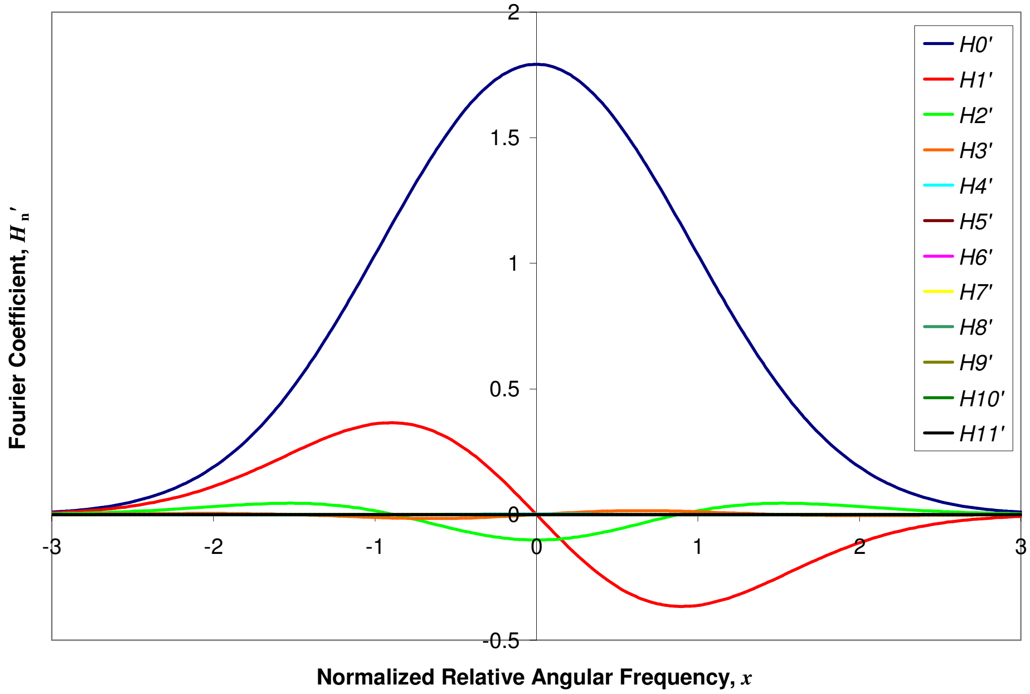

Figure 3.21 Fourier coefficients at T=20.2 °C and m=0.571
as a function of normalized relative angular frequency

Let us now turn our attention to some experimental data. The data from three separate but related experiments will be discussed in the following pages. First, the results from an "absorption" experiment will be discussed. An absorption profile acquired during this experiment will be used to define instrumental parameters required of our theory: The mean anode output current detected outside the bandwidth of an atomic transition, the tuning rate of the extended-cavity diode laser (ECDL), and the theoretical modulation depth employed during WMS measurements. Next, the results of a modulated absorption experiment conducted to validate our theoretical expressions for the first- and second-harmonic lock-in signals will be discussed. The **1*f***- and **2*f***-profiles acquired during this "validation" experiment will be compared to theoretical **1*f***- and **2*f***-profiles simulated using Eqs. 3.128 and 3.129, respectively, utilizing the instrumental parameters deduced from the "absorption" experiment. Finally, we will consider the results of a second modulated absorption experiment conducted to investigate a discrepancy between the measured and modeled harmonic profiles. The **1*f***-profiles acquired during this "resonance" experiment will be used to illustrate the source of this discrepancy. In presenting the results of both the "validation" and "resonance" experiments my intention is to establish confidence that the calculations concluding this section accurately predict the lock-in signal detected from molecular Rayleigh scattering during preliminary frequency-locked MFRS measurements.

Let us first refer to Figure 3.22 showing a portion of the Doppler broadened D_2-line of isotopic Rb measured in the reference arm of the MFRS velocimeter. The profile measured during this “absorption” experiment consists of 2500 data points acquired while slowly tuning the optical frequency of the ECDL utilized during preliminary MFRS experiments through the Doppler broadened absorption features associated with the $\boldsymbol{F}$=2 and $\boldsymbol{F}$=3 ground state transitions of ^{85}Rb. A small fraction of the laser power (<1%) was diverted to the reference arm and the laser power transmitted through a $z \cong 100$ mm vapor cell of isotopic Rb at a temperature of $T \cong$ 20.2 °C was detected. The temperature was monitored using a thermocouple placed in the vicinity of the vapor cell. The current signal output from the silicon photodiode detector in the reference arm was converted to a voltage signal using a R_L=1 MΩ shunt resistor at the front-end of the data acquisition board.

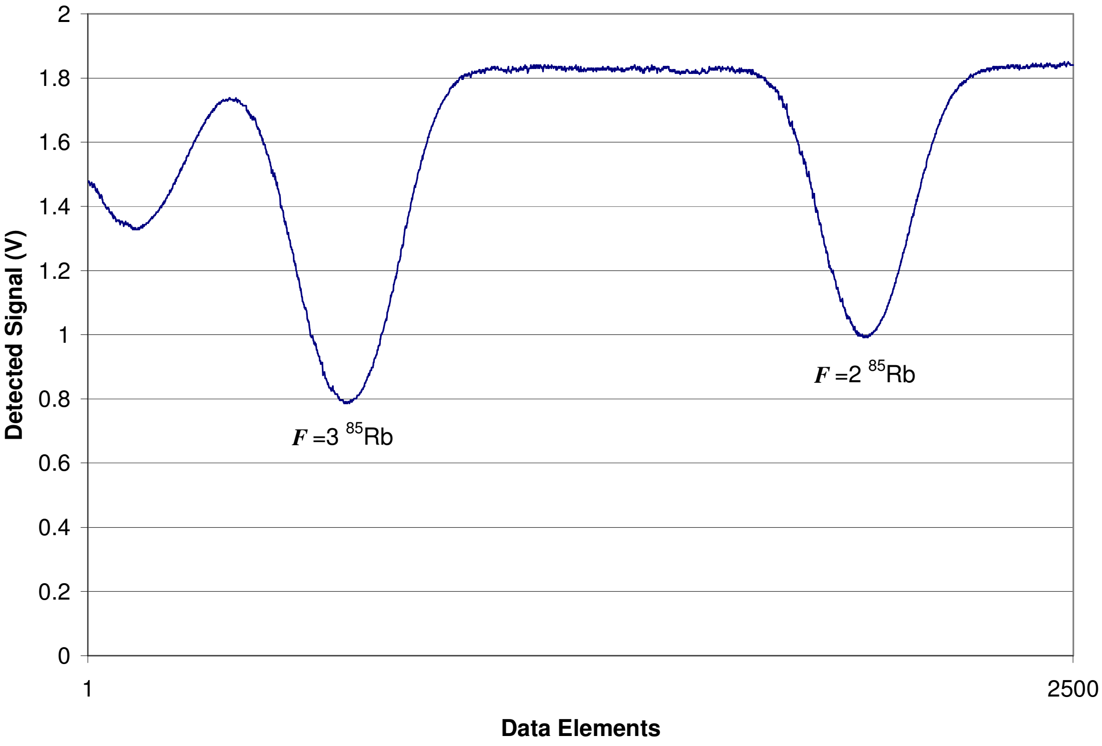

Figure 3.22 A portion of the D_2-line measured by detecting the probe laser power after passage through a z=100 mm cell of Rb in natural isotopic abundance at T=20.2 °C

Figure 3.23 shows the measured profile in Figure 3.22 normalized to one outside the bandwidth of the detected Doppler broadened absorption features. As illustrated in this figure, a data element-to-angular frequency conversion was calculated from the acquired profile by first determining the peak-to-peak separation in data elements between the measured **F**=2 and **F**=3 Doppler broadened absorption features and then utilizing the theoretical peak-to-peak angular frequency separation of $\Delta\omega_{F=2\rightarrow F=3}=1.828 \times 10^{10}$ rad/s between these features (the peak-to-peak angular frequency separation between the Doppler broadened **F**=2 and **F**=3 ground state transitions in the D_2-line of ^{85}Rb follows from the theoretical model described in sub-section 3.3.3):

$$\frac{\Delta\omega}{\Delta(\text{Data Element})} = \frac{1.828\times10^{10}\,\text{rad/s}}{(1973-659)\text{Data Element}} = 1.391\times10^{7}\,\frac{\text{rad/s}}{\text{Data Element}}\,. \qquad (3.130)$$

A similar approach was utilized during all preliminary MFRS measurements to determine the data element-to-frequency conversion; the zero-crossings in acquired **1*f***-profiles correspond to peaks in the Doppler broadened absorption profiles and were occasionally referenced to calculate the conversion.

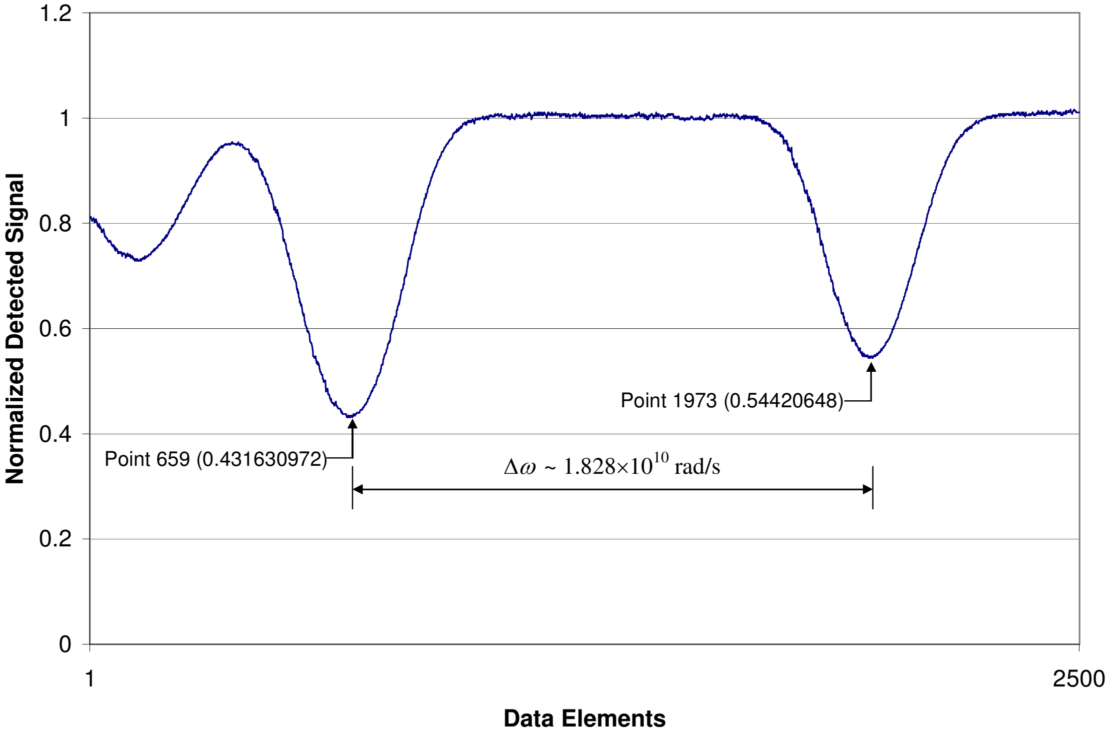

Figure 3.23 Measured D_2-line normalized to one outside the bandwidth of an atomic transition

Immediately after acquiring the absorption profile illustrated in Figure 3.22, I made a few modifications to the instrument and measured some first- and second-harmonic modulated absorption profiles. The injection current to the ECDL, the sweep rate and amplitude, and the data acquisition settings were left unchanged during this "validation" experiment, but an ν_m=2.090 kHz modulation was imposed upon the slowly varying optical frequency of the ECDL. To implement homodyne detection, the output from the detector in the reference arm was fed into two digital lock-in amplifiers: Lock-in #1 was set to detect the first-harmonic of the modulated absorption signal and lock-in #2 was set to detect the second-harmonic of the modulated absorption signal. A shunt resistance of R_L=50 Ω was used to convert the detector output current to a voltage signal, which was AC-coupled into the front-end of both lock-in amplifiers. The input sensitivity of lock-in #1 was set to $S_{L,\mathbf{1f}} = 20$ μVrms and the input sensitivity of lock-in #2 was set to $S_{L,\mathbf{2f}} = 5$ μVrms. Both lock-in amplifiers employed an integration time of $\tau_L = 10$ ms.

To compare the theoretical first-and second-harmonic lock-in signals in Eqs. 3.128 and 3.129 to the **1*f***- and **2*f***-profiles acquired using the instrument settings described above and utilized throughout the "validation" experiment, we need to know the shunt resistance at the front-end of the lock-in amplifier, R_L, the relative phase between the lock-in reference signal and the detected harmonic signal, θ, the mean detector output current outside the bandwidth of a ground state transition, i_o, the lock-in gain, G, the length of the Rb vapor cell, z, the temperature of the Rb gas in the vapor cell, T, and the modulation index, m. The shunt resistance at the front-end of the lock-in amplifiers was R_L=50 Ω during all modulated absorption experiments presented in the following figures. A relative phase of $\theta = 0°$ or 180° was used in all simulations – i.e. the phase of each lock-in reference signal, $R^{\mathrm{n}}(t)$, was adjusted for optimal detection of the first- and second-harmonic modulated absorption signals during acquisition of all but one of the harmonic profiles presented below. (One out-of phase measurement was made to demonstrate that the in-phase measurements were truly in-phase). The detector output current outside the bandwidth of a ground state transition, i_o, follows from Figure 3.22 if we recall that the data in this figure was acquired using an R_L=1 MΩ shunt resistor to convert the detected output current to a voltage signal and if we assume that the laser output power during the "validation" experiment was unchanged from the laser output power during the "absorption" experiment– i.e. since the injection current to the ECDL was unchanged from one experiment to the next. Relying on this assumption and referring to Figure 3.22 we find,

$$i_o \cong \frac{1.821\,\mathrm{V}}{1\,\mathrm{M\Omega}} = 1.821\times 10^{-6}\ \mathrm{A} \tag{3.131}$$

during the "absorption" and "validation" experiments. The gain, G, in Eqs. 3.128 and 3.129 is simply the full scale output of the lock-in amplifier, 10Vrms, divided by the full scale input sensitivity of the lock-in amplifier,

$$G = \frac{10\mathrm{Vrms}}{S_L}\,. \tag{3.132}$$

For the harmonic profile measurements illustrated in the following figures the gain of lock-in #1 was,

$$G_{L,\mathbf{1}f} = \frac{10\mathrm{Vrms}}{20\,\mu\mathrm{Vrms}} = 5\times 10^5 \tag{3.133a}$$

and the gain of lock-in #2 was,

$$G_{L,\mathbf{2}f} = \frac{10\mathrm{Vrms}}{5\,\mu\mathrm{Vrms}} = 2\times 10^6\,. \tag{3.133b}$$

A Rb vapor cell of length $z \cong 100$ mm was utilized in the reference arm of the MFRS velocimeter during all modulated absorption measurements. The temperature of the Rb gas in this vapor cell fluctuated between $T \cong 20.1$ °C - 20.2 °C during the "validation" experiment. A temperature of T=20.2 °C was assumed in all simulations of the harmonic profiles detected during the "validation" experiment.

We now need only determine the modulation depth employed during the "validation" experiment to know everything required of our model. Preliminary estimates of the modulation amplitudes employed during acquisition of the harmonic profiles presented below were made by first determining the tuning rate of the ECDL – i.e. the Littrow laser cavity. Recall that the absorption profile in Figure 3.22 was acquired by slowly scanning the optical frequency of the ECDL through a portion of the D_2-line of Rb. This scan in optical frequency is the result of a triangle-wave voltage signal input to the piezoelectric transducer attached to the tuning arm of the Littrow laser cavity. The profile illustrated in Figure 3.22 was acquired during the positive-going portion of the triangle-wave sweep in voltage – i.e. while scanning from the minimum triangle-wave voltage (minimum optical frequency) to the maximum triangle-wave voltage (maximum optical frequency).

During all preliminary frequency-locked MFRS experiments, including the absorption and modulated absorption experiments presented in this section, a 9Vpp triangle-wave voltage signal was input to a regulated high-voltage amplifier, which output a triangle-wave voltage signal of $126 \cdot G_s$ Vpp to the piezoelectric transducer attached to the tuning arm of the Littrow laser cavity. (Details concerning the Littrow laser cavity and electronics are provided in the next chapter of this dissertation). The regulated high-voltage amplifier offers a sweep gain of G_s = 0-1; e.g. a sweep gain of $G_s = 0$ was employed during frequency-locked measurements. During the measurement of the absorption profile in Figure 3.22, as well as the ***1f***- and ***2f*** -profiles acquired during the "validation" experiment, a sweep gain of $G_s = 0.125$ was employed, resulting in a peak-to-peak triangle-wave voltage scan of 15.75 Vpp at the input of the piezoelectric transducer. Referring back to the data element-to-angular frequency conversion in Eq. 3.130 and noting that 2500 data points were acquired in Figure 3.22 during the positive-going portion of the triangle-wave voltage scan, we find that the output optical frequency of the Littrow laser cavity changes at a rate of 2.21×10^9 rad/s per volt applied to the piezoelectric transducer:

$$\begin{aligned} \left.\frac{\Delta\omega}{\Delta V}\right|_{\text{LITTROW}} &= \frac{\Delta\omega}{\Delta(\text{Data Element})}\cdot\frac{\Delta(\text{Data Element})}{\Delta V} \\ &= 1.391\times10^{7}\,\frac{\text{rad/s}}{\text{Data Element}}\cdot\frac{2499\text{ Data Elements}}{15.75\text{ V}} \\ \left.\frac{\Delta\omega}{\Delta V}\right|_{\text{LITTROW}} &= 2.21\times10^{9}\,\frac{\text{rad/s}}{\text{V}}. \end{aligned} \tag{3.134}$$

Having determined the tuning rate of the Littrow laser cavity, the modulation amplitudes and corresponding modulation indices employed during the "validation" experiment could be theoretically calculated. Frequency modulation of the Littrow laser cavity is implemented by inputting a sinusoidal voltage signal to the piezoelectric transducer attached to the tuning arm of the Littrow laser cavity. During all preliminary frequency-locked MFRS experiments, including the absorption and modulated absorption experiments presented in this section, a 680 mVpp sinusoidal voltage signal was input to a regulated high-voltage amplifier, which output a sinusoidal voltage signal of $317 \cdot G_m$ mVpp to the piezoelectric transducer. The regulated high-voltage amplifier offers a modulation gain of G_m = 0-1; e.g. a modulation gain of $G_m = 0$ was employed during the absorption measurements illustrated in Figure 3.22. During ***ALL*** preliminary frequency-locked MFRS experiments a modulation gain of $G_m = 0.5$ was employed, resulting in a sinusoidal voltage signal of amplitude $A = 79.3$ mV at the input of the piezoelectric transducer attached to the tuning arm of the Littrow laser cavity. Using the tuning rate of the

Littrow laser cavity defined by Eq. 3.134 we find for G_m = 0.5 that the theoretical modulation amplitude is,

$$\begin{aligned} a &= A \cdot \left.\frac{\Delta\omega}{\Delta V}\right|_{\text{LITTROW}} \\ &= 159\, G_m \text{ mV} \cdot 2.21 \times 10^9 \frac{\text{rad/s}}{\text{V}} \\ a &= 1.75 \times 10^8 \text{rad/s @ } G_m = 0.5\,. \end{aligned} \tag{3.135}$$

At a Rb gas temperature of T = 20.2 °C (observed during the "validation" experiment) the HWHM of the Doppler broadened $\boldsymbol{F}$=2 and $\boldsymbol{F}$=3 ground state transitions in the D_2-line of ^{85}Rb is $\delta\omega_{1/2} = 1.607 \times 10^9$ rad/s, and the modulation index corresponding to a modulation amplitude of $a = 1.75 \times 10^8$ rad/s is $m = a\,/\delta\omega_{1/2} = 0.11$.

We now know everything required to calculate theoretical first-and second-harmonic lock-in signals for comparison to the harmonic profiles detected during the "validation" experiment. The question is where to begin? The harmonic profile simulations presented below rely on our heuristic model of the Doppler broadened features in the D_2-line of Rb. The more closely the heuristic model resembles the measured absorption feature the more closely the simulated lock-in signal will resemble the detected lock-in signal. Whereas the neighboring Doppler broadened $\boldsymbol{F}$=2 ground state transition of ^{87}Rb contributes to the Doppler broadened $\boldsymbol{F}$=3 ground state transition of ^{85}Rb, the neighboring Doppler broadened $\boldsymbol{F}$=1 ground state transition of ^{87}Rb does not contribute to the Doppler broadened $\boldsymbol{F}$=2 ground state transition of ^{85}Rb. In addition, referring back to Figure 3.13 we see that the excited state energy splitting of ^{85}Rb results in a maximum separation of $\Delta\nu_{\boldsymbol{F}=2\rightarrow\boldsymbol{F}'=1,2,3}$=92.68 MHz between the hyperfine components in the Doppler broadened $\boldsymbol{F}$=2 ground state transition of ^{85}Rb compared to a maximum separation of $\Delta\nu_{\boldsymbol{F}=3\rightarrow\boldsymbol{F}'=2,3,4}$=184.37 MHz between the hyperfine components in the Doppler broadened $\boldsymbol{F}$=3 ground state transition of ^{85}Rb. Recalling that the heuristic model neglects the excited state energy splitting in each ground state transition of Rb, we therefore expect the heuristic model to more closely resemble the measured Doppler broadened $\boldsymbol{F}$=2 ground state transition of ^{85}Rb than the measured Doppler broadened $\boldsymbol{F}$=3 ground state transition of ^{85}Rb… even in the absence of ^{87}Rb. We will therefore begin by considering those harmonic profiles measured during the "validation" experiment that correspond to the Doppler broadened $\boldsymbol{F}$=2 ground state transition in the D_2-line of ^{85}Rb.

Figure 3.24 shows a comparison between the measured Doppler broadened ***F***=2 ground state transition of ^{85}Rb illustrated in Figure 3.22 and our heuristic model of the Doppler broadened ***F***=2 ground state transition of ^{85}Rb calculated at T=20.2 °C. The measured profile was normalized to one outside the bandwidth of the transition, as illustrate in Figure 3.23, and the angular frequency of each measured point relative to the absorption peak was determined from the data element-to-angular frequency conversion derived in Eq. 3.130. The comparison between the measurement and the model is practically perfect. We would therefore expect a **1*f***-profile simulation utilizing the heuristic model of the Doppler broadened ***F***=2 ground state transition of ^{85}Rb and the instrumental parameters describing the "validation" experiment to closely resemble the **1*f***-profiles corresponding to the Doppler broadened ***F***=2 ground state transition of ^{85}Rb that were measured during that experiment.

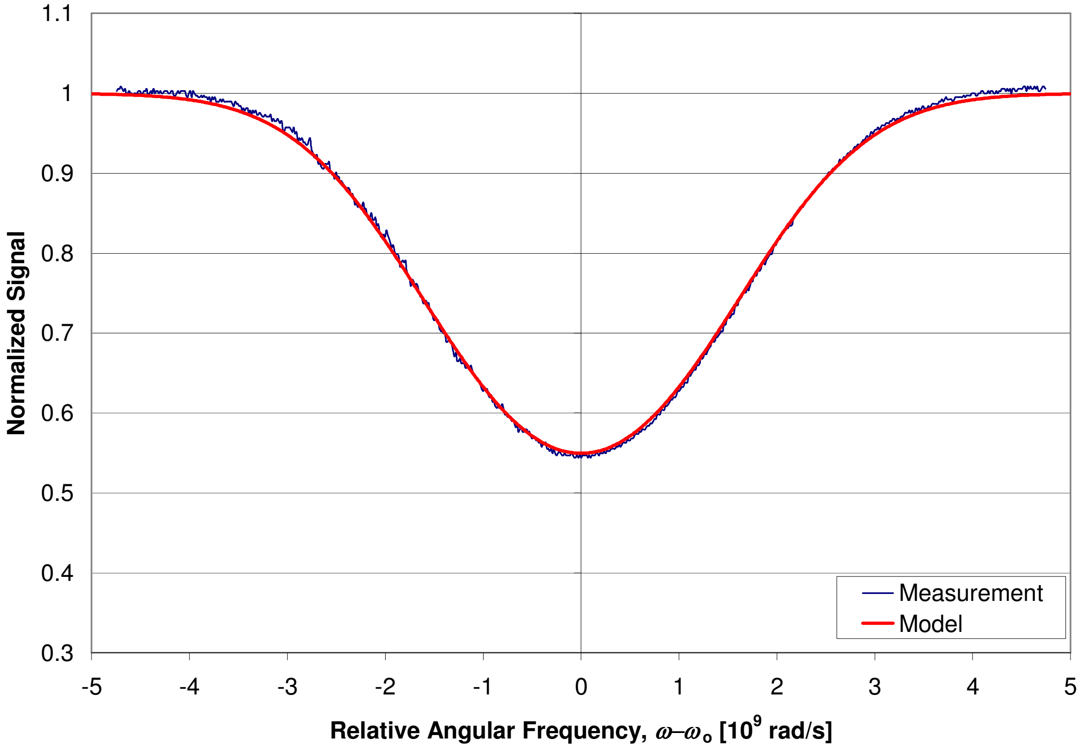

*Figure 3.24 Measured Doppler broadened **F**=2 ground state transition in the D_2-line of ^{85}Rb compared to the heuristic model of this transition at T=20.2 °C*

Figure 3.25 shows two such measured profiles. Both measurements were made with the modulation gain of the regulated high voltage amplifier set to G_m = 0.5. One measurement was made with the lock-in amplifier in phase with the first-harmonic of the detected modulated absorption signal – i.e. the phase of the reference signal internal to the lock-in amplifier, ϕ_L, was equal to the phase of the first-harmonic of the detected modulated absorption signal – and the other measurement was made with the lock-in amplifier out of phase with the first-harmonic of the detected modulated absorption signal - i.e. the phase of the reference signal internal to the lock-in amplifier was shifted ±90° from the phase of the first-harmonic of the detected modulated absorption signal. (To ensure that the phase of the lock-in reference signal matched the phase of the detected modulated absorption signal during preliminary frequency-locked MFRS measurements, the lock-in phase was first adjusted to minimize the detected signal and then modified by ±90°, as illustrated in Figure 3.25). Both measured profiles were plotted against the normalized relative angular frequency, x, by utilizing the data element-to-angular frequency conversion in Eq. 3.130 – i.e. the sweep rate and amplitude during the "validation" experiment were unchanged from the sweep rate and amplitude employed during the "absorption" experiment – and by assuming a temperature of T=20.2 °C when calculating the theoretical HWHM of the Doppler broadened $\boldsymbol{F}$=2 ground state transition of ^{85}Rb. Visually comparing the in-phase measurement to the out-of-phase measurement leads to the following simple conclusion: The in-phase measurement was truly in-phase.

Also in Figure 3.25 are two simulated **1*f***-profiles corresponding to the $\boldsymbol{F}$=2 ground state transition in the D$_2$-line of ^{85}Rb. Both simulations follow from Eq. 3.128 with i_o = 1.821 μA, R_L = 50 Ω, $G = 5\times10^5$, θ = 180°, z = 100 mm, and T=20.2 °C. One simulation was performed using a modulation index of m = 0.11, the other with a modulation index of m = 0.476. The modulation index m = 0.476 provides the best fit between the measured **1*f***-profile peak amplitude and the simulated **1*f***-profile peak amplitude. As discussed above, the modulation index m = 0.11 is the estimated modulation amplitude at a modulation gain of G_m = 0.5 – i.e. $a = 1.75 \times 10^8$ rad/s – divided by the Doppler broadened half-width of ^{85}Rb at a gas temperature of T=20.2 °C – i.e. $\delta\omega_{1/2} = 1.607 \times 10^9$ rad/s.

Looking at Figure 3.25, we see a large discrepancy between the in phase measurement of the first-harmonic modulated absorption profile and the simulated **1*f***-profile computed using the estimated modulation index m = 0.11. If left unexplained this discrepancy would ultimately undermine our confidence in the calculations that conclude this section. We must therefore dedicate some time and attention toward explaining the source of the observed discrepancy.

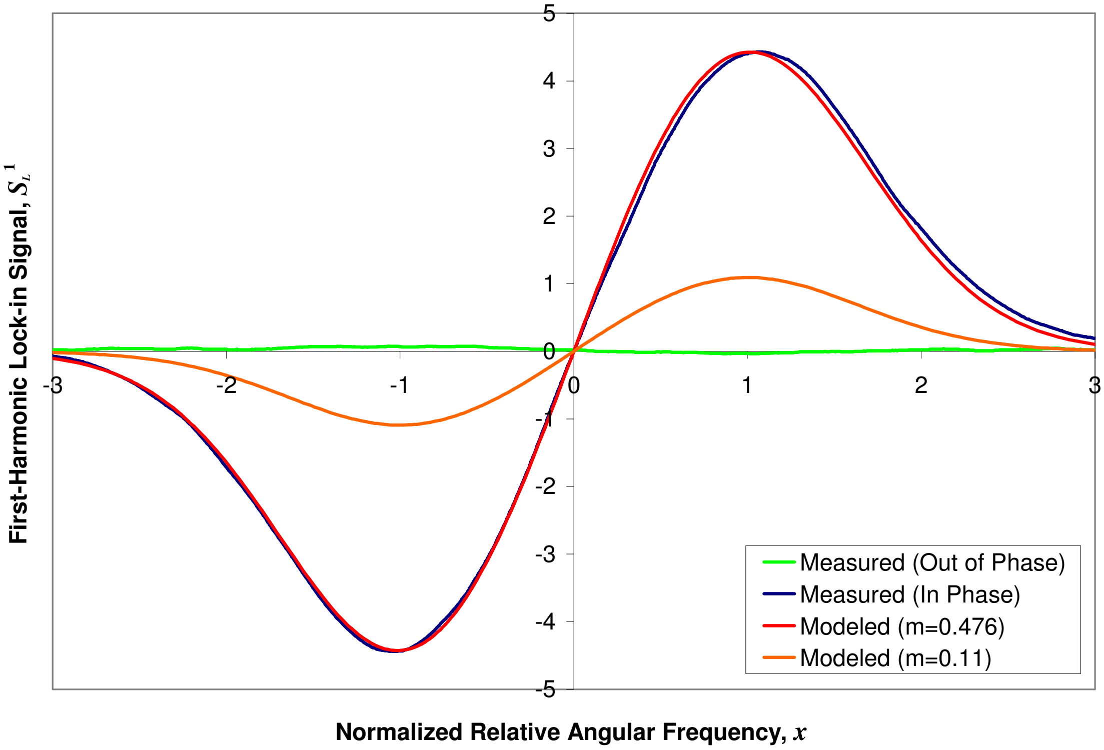

Figure 3.25 Measured ***1f****-profiles corresponding to the Doppler broadened* ***F****=2 ground state transition in the D_2-line of ^{85}Rb compared to* ***1f****-simulations at m=0.11 and m=0.476 (T=20.2 °C)*

Figure 3.26 shows some **1*f***-profiles measured during a "resonance" experiment I conducted to investigate the source of the discrepancy. The measurements illustrated were made with a constant probe laser power through a $z \cong 100$ mm cell of Rb in natural isotopic abundance at a recorded temperature of $T \cong 20.8$ °C. The optical frequency of the probe laser was tuned across a portion of the D_2-line at a rate of 2 s/scan and a modulated absorption signal was detected by simultaneously dithering about the mean instantaneous optical frequency. Lock-in #1 – i.e. the lock-in configured for first-harmonic detection of the modulated absorption signal – was used to implement homodyne detection of the modulated absorption signal. A shunt resistance of $R_L =$ 50 Ω was used to convert the detector output current to a voltage signal, which was AC-coupled into the front-end lock-in #1 with an input sensitivity of $S_{L,\mathbf{1}f} = 20$ µVrms. The lock-in employed an integration time of $\tau_L = 10$ ms.

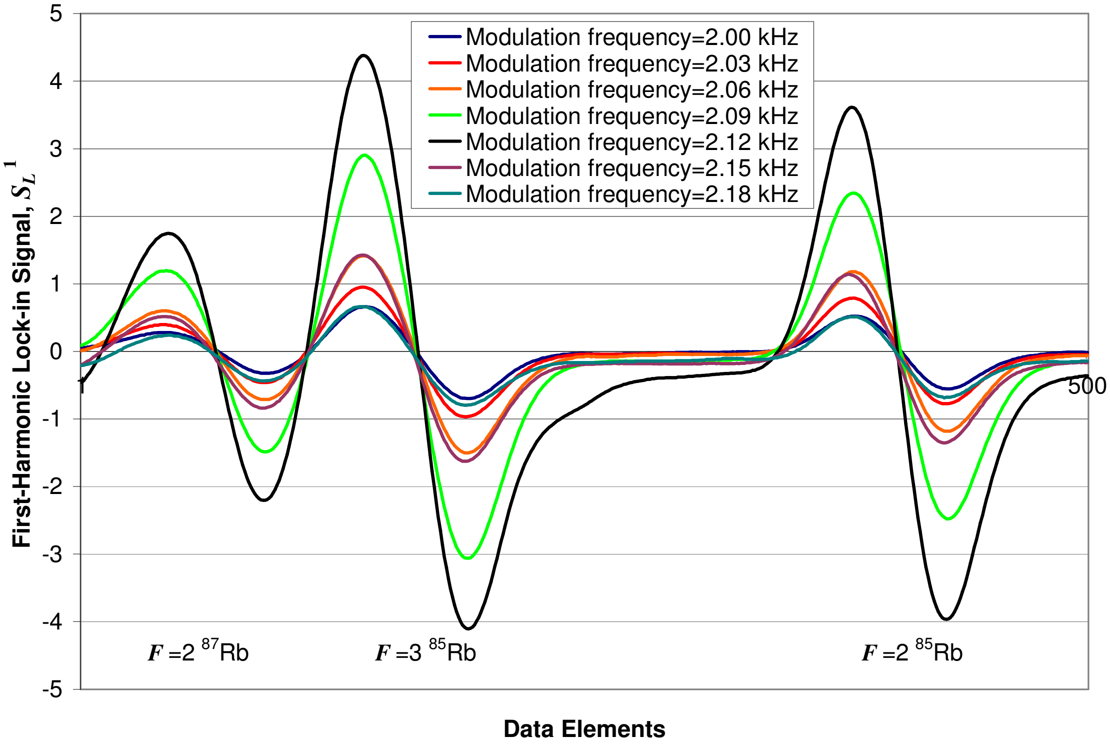

Figure 3.26 ***1f****-profiles covering the* ***F****=2 and* ***F****=3 ground state transitions in the D_2-line of ^{85}Rb measured with modulation frequencies ranging from ν_m=2.00 kHz-2.18 kHz*

The sweep and modulation amplitudes were not changed while acquiring the **1*f***-profiles illustrated in Figure 3.26: A sweep gain of G_s = 0.135 and a modulation gain of G_m = 0.3 were used for all measurements in Figure 3.26. In fact, the only parameters modified during the course of the "resonance" experiment were the modulation frequency – **1*f***-profiles were acquired at modulation frequencies of ν_m = 1.98 kHz-2.21 kHz in increments of $\Delta\nu_m$=10 Hz – and the lock-in reference phase – phase adjustments were required to maximize the peak amplitudes in the measured **1*f***-profiles. Assuming that the mean optical frequency is constant during one modulation period, the theoretical formulations for the first- and second-harmonic lock-in signals are independent of the modulation frequency employed. In addition, we don't expect a phase shift in the detected modulated absorption signal. In other words, with all else constant we expect the **1*f***-profiles acquired at modulation frequencies of ν_m = 1.98kHz-2.21kHz to have a constant phase and an identical amplitude profile. Looking at Figure 3.26 we must therefore conclude that all else was not constant during the course of the measurements. The only reasonable explanation for the observed increase in **1*f***-profile amplitudes in the vicinity of ν_m = 2.12 kHz is that there was a dramatic increase in the modulation depth brought about by a system resonance at ~2.12 kHz; the regulated high-voltage amplifier, piezoelectric transducer, and/or Littrow laser cavity has a resonance in the vicinity of ν_m = 2.12 kHz. Large fluctuations in the laser power and cell temperature were not observed during the measurements and the detection electronics were not modified during the experiment. This conclusion is practically irrefutable if we consider resonance theory.

A simple theoretical description of first-order resonance can be derived from the driven, damped harmonic oscillator model in Figure 3.27 [104]. (The theory that follows is derived by considering a mechanical harmonic oscillator, but can also be derived by considering an electrical harmonic oscillator – i.e. an RLC-circuit. The mechanical harmonic oscillator model was utilized in the derivation because it provides a simple description of the modulating tuning arm in the Littrow laser cavity (which I suspect is resonating) – e.g. The flexure joint provides both a restoring and damping force to the relatively massive tuning arm and the piezoelectric transducer provides a driving force). Summing the forces on the mass, m – the restoring force provided by the spring, the damping force provided by the damper, and the driving force provided by the sinusoidal excitation – we find,

$$\sum F = m\frac{\mathrm{d}^2 x}{\mathrm{d}t^2} = F_o \sin \omega t - Kx - b\frac{\mathrm{d}x}{\mathrm{d}t} \tag{3.136}$$

where b is the damping constant, K is the spring constant, F_o is the amplitude of the sinusoidal driving force, and ω is the angular frequency of the sinusoidal driving force. Eq. 3.136 can be recast in terms of the undamped natural frequency of the harmonic oscillator,

$$\omega_o = \sqrt{\frac{K}{m}} \tag{3.137}$$

and the mass-reduced damping constant (or damping coefficient),

$$\gamma = \frac{b}{m}\,. \tag{3.138}$$

Inserting Eqs. 3.137 and 3.138 into Eq. 3.136 and rearranging we find,

$$\ddot{x} + \gamma\dot{x} + \omega_o^2 x = \frac{F_o}{m}\sin \omega t\,. \tag{3.139}$$

The steady-state solution to Eq. 3.139 is,

$$x(t) = A(\omega)\sin[\omega t - \phi(\omega)] \tag{3.140}$$

where the oscillation amplitude, $A(\omega)$, as a function of driving frequency is,

$$A(\omega) = \frac{F_o / m}{\left[\left(\omega_o^2 - \omega^2 \right)^2 + \gamma^2 \omega^2 \right]^{1/2}} \tag{3.141}$$

and the phase, $\phi(\omega)$, as a function of driving frequency is,

$$\phi(\omega) = \arctan\left(\frac{\gamma\omega}{\omega_o^2 - \omega^2} \right). \tag{3.142}$$

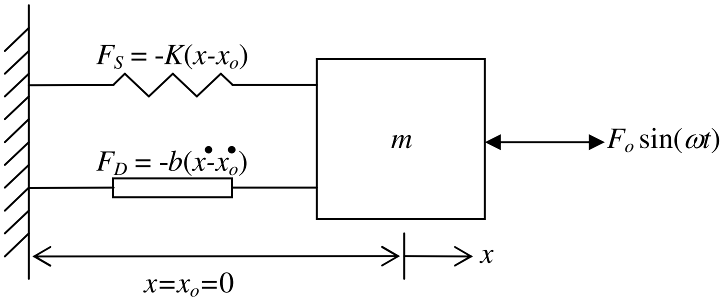

Figure 3.27 Illustration of driven, damped mechanical harmonic oscillator

Setting the derivative of the oscillation amplitude $A(\omega)$ with respect to the driving frequency ω equal to zero we find that the amplitude is a maximum,

$$\frac{\mathrm{d}A(\omega)}{\mathrm{d}\omega} = 0 \Rightarrow A\big|_{\mathrm{MAX}} = A(\omega = \omega_R) \tag{3.143}$$

at the resonant frequency ω_R of the damped harmonic oscillator,

$$\omega_R = \omega_o \sqrt{1 - \frac{\gamma^2}{2\omega_o^2}} \tag{3.144}$$

Let us now consider the driven, under-damped harmonic oscillator – i.e. corresponding to a damping ratio much less than one,

$$\frac{\gamma}{\omega_o} << 1. \tag{3.145}$$

Referring to Eqs. 3.144 and 3.145, we find that the resonant frequency of an under-damped harmonic oscillator is approximately equal to the undamped natural frequency of the harmonic oscillator,

$$\left.\begin{array}{l} \omega_R = \omega_o \sqrt{1 - \dfrac{\gamma^2}{2\omega_o^2}} \\[2ex] \dfrac{\gamma}{\omega_o} << 1 \end{array}\right\} \Rightarrow \omega_R \cong \omega_o \, . \tag{3.146}$$

Inserting Eq. 3.146 into Eq. 3.141, we find that the maximum oscillation amplitude – i.e. the oscillation amplitude on resonance – of an under-damped harmonic oscillator is approximately,

$$A(\omega_R \cong \omega_o) = {F_o}\big/{m\gamma\omega_o} \, . \tag{3.147}$$

From Eqs. 3.141 and 3.147 we can now formulate an expression for the driving frequencies at the half-maximum oscillation amplitude:

$$\frac{A(\omega)}{A(\omega_R \cong \omega_o)} = \frac{\gamma\omega_o}{\left[\left(\omega_o^2 - \omega^2\right)^2 + \gamma^2\omega^2\right]^{1/2}} = \frac{1}{2} \Rightarrow \omega^4 + \left(\gamma^2 - 2\omega_o^2\right)\omega^2 + \left(\omega_o^4 - 4\gamma^2\omega_o^2\right) = 0 \, . \tag{3.148}$$

Solving Eq. 3.148,

$$\omega^2 = \frac{\left[2 - \left(\dfrac{\gamma}{\omega_o}\right)^2\right] \pm \dfrac{\gamma}{\omega_o}\sqrt{12 + \left(\dfrac{\gamma}{\omega_o}\right)^2}}{\dfrac{2}{\omega_o^2}} \tag{3.149}$$

and in the limit of an under-damped harmonic oscillator – $\gamma / \omega_o << 1$ – we find,

$$\omega^2 \cong \omega_o^2 \pm \sqrt{3}\gamma\omega_o \Rightarrow \omega \cong \omega_o\left(1 \pm \sqrt{3}\gamma\omega_o\right)^{1/2} . \tag{3.150}$$

The expression in Eq. 3.150 for the driving frequencies at half-maximum oscillation amplitude can be simplified further in the limit of an under-damped harmonic oscillator by expanding the expression in a Taylor series about $\gamma / \omega_o = 0$:

$$\begin{aligned} \omega &\cong \omega_o\left[1 \pm \frac{\sqrt{3}}{2}\frac{\gamma}{\omega_o} \mp \frac{1}{2!}\frac{\sqrt{3}}{4}\left(\frac{\gamma}{\omega_o}\right)^2 \pm \frac{1}{3!}\frac{\sqrt{3}}{8}\left(\frac{\gamma}{\omega_o}\right)^3 + \text{...h.o.t.s}\right] \\ &\cong \omega_o\left[1 \pm \frac{\sqrt{3}}{2}\frac{\gamma}{\omega_o}\right] \\ \omega &\cong \omega_o \pm \frac{\sqrt{3}}{2}\gamma \, . \end{aligned} \tag{3.151}$$

From Eq. 3.151 we find that the full-width at half-maximum (FWHM) of the resonance profile corresponding to a driven, under-damped harmonic oscillator – i.e. the plot of oscillation amplitude, $A(\omega)$, versus driving frequency, ω, in the vicinity of the resonance frequency, ω_o – is simply proportional to the mass reduced damping constant, γ, in units of rad/s:

$$2(\omega-\omega_o)=\sqrt{3}\gamma\ . \tag{3.152}$$

Let us now reconsider the **1*f***-profiles measured during the "resonance" experiment, a few of which were illustrated in Figure 3.26. In Figure 3.28 I have plotted the peak amplitudes in the measured **1*f***-profiles corresponding to the ***F***=2 ground state transition in the D_2-line of ^{85}Rb against the modulation frequency employed during the measurement. This plot of the **1*f***-profile peak amplitude versus modulation frequency is conspicuously similar to the resonance profile of a driven, under-damped harmonic oscillator. (Referring back to Figure 3.26, we see that the **1*f***-profiles recorded near resonance are slightly biased toward negative voltages; e.g. outside the bandwidth of the Doppler broadened features the **1*f***-profiles near resonance exhibit a negative voltage. This bias increases as the modulation frequency approaches resonance and is likely the result of a detected amplitude modulation. WMS theory does not accommodate amplitude modulation – the topic is discussed in Appendix E on FMS – and therefore the peak amplitude of each acquired **1*f***-profile corresponding to the ***F***=2 ground state transition of ^{85}Rb was calculated by averaging the maximum positive and negative excursion in the profile).

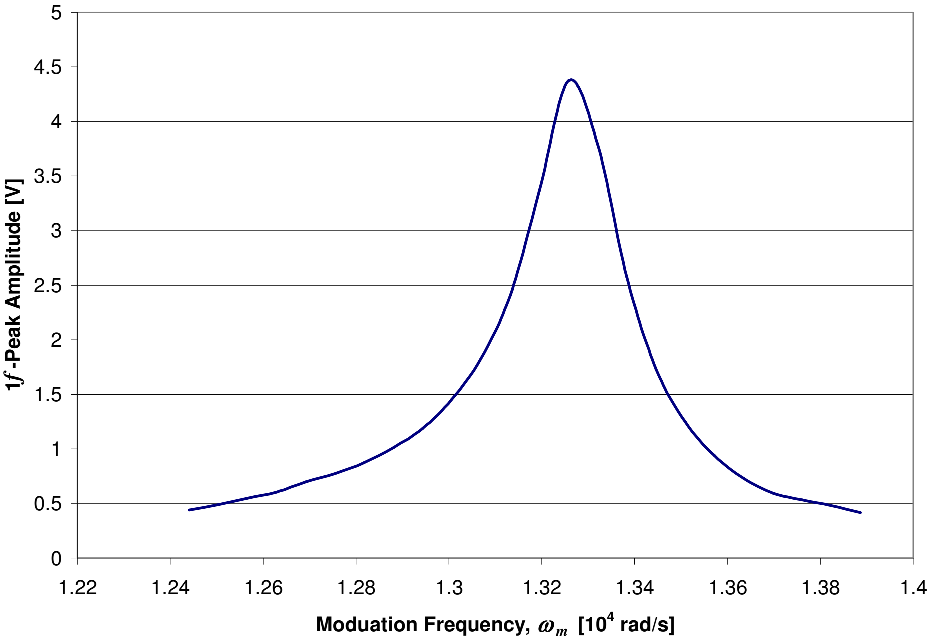

*Figure 3.28 Peak amplitude in measured **1f**-profile corresponding to **F**=2 ground state transition in D_2-line of ^{85}Rb versus modulation frequency employed during measurement*

The amplitude of the modulated absorption signal increases almost linearly with increasing modulation index, *m*, for the relatively small modulation indices employed during the "validation" and "resonance" experiments. In addition, the modulation index is linearly proportional to the modulation depth, *a*, at a given Rb gas temperature. Finally, the modulation depth is linearly proportional to the displacement amplitude of the tuning arm. (This will be shown in the next chapter). In other words, if the displacement amplitude of the tuning arm doubles – e.g. either because the amplitude of the sinusoidal excitation voltage driving the piezoelectric transducer attached to the tuning arm doubles or because the oscillation amplitude of the tuning arm itself doubles due to a system resonance – then we expect the first-harmonic lock-in signal (including the peak signal) to approximately double.

Let us assume that the latter case is illustrated in Figure 3.28. In particular, let us assume that the tuning arm of the Littrow laser cavity behaves like an under-damped harmonic oscillator that is being driven into oscillation by the piezoelectric transducer. In addition, let us assume there is a resonance at $\nu_o \cong 2.112$ kHz ($\omega_o = 1.327\times10^4$ rad/s) corresponding to the interpolated peak of the amplitude versus modulation frequency plot in Figure 3.28. Under these assumptions, the mass-reduced damping constant of the tuning arm follows from Eq. 3.152 and Figure 3.28: The plot of peak **1*f***-profile amplitude versus modulation frequency in Figure 3.28 has a FWHM of ~302 rad/s and from Eq. 3.152 it follows that $\gamma \cong 174$ rad/s.

Figure 3.29 shows a theoretical plot of the normalized oscillation amplitude,

$$\frac{A(\omega)}{A(\omega_R \cong \omega_o)} = \frac{\gamma\omega_o}{\left[\left(\omega_o^2 - \omega^2\right)^2 + \gamma^2\omega^2\right]^{1/2}} \tag{3.153}$$

versus driving frequency, ω, for an under-damped harmonic oscillator with a resonant frequency of $\omega_R \cong \omega_o = 1.327\times10^4$ rad/s and a mass-reduced damping constant of $\gamma \cong 174$ rad/s. The plot of **1*f***-profile peak amplitude versus modulation frequency from Figure 3.28 has been normalized by the interpolated maximum amplitude at $\omega_m = 1.327\times10^4$ rad/s and plotted in Figure 3.29 as well. In Figure 3.30, a theoretical plot of phase versus driving frequency for a under-damped harmonic oscillator with a resonant frequency of $\omega_R \cong \omega_o = 1.327\times10^4$ rad/s and a mass-reduced damping constant of $\gamma \cong 174$ rad/s has been plotted. The plot follows from Eq. 3.142. The phase of each first-harmonic modulated absorption signal measured during the "resonance" experiment relative to the phase on resonance is also plotted in Figure 3.30 against the modulation frequency employed during the measurement. The fit between the plot based on theory and the plot based on measurement is favorable in both Figure 3.29 and 3.30– It is impossible to deny that there is a system resonance in the vicinity of $\omega_m = 1.327\times10^4$ rad/s.

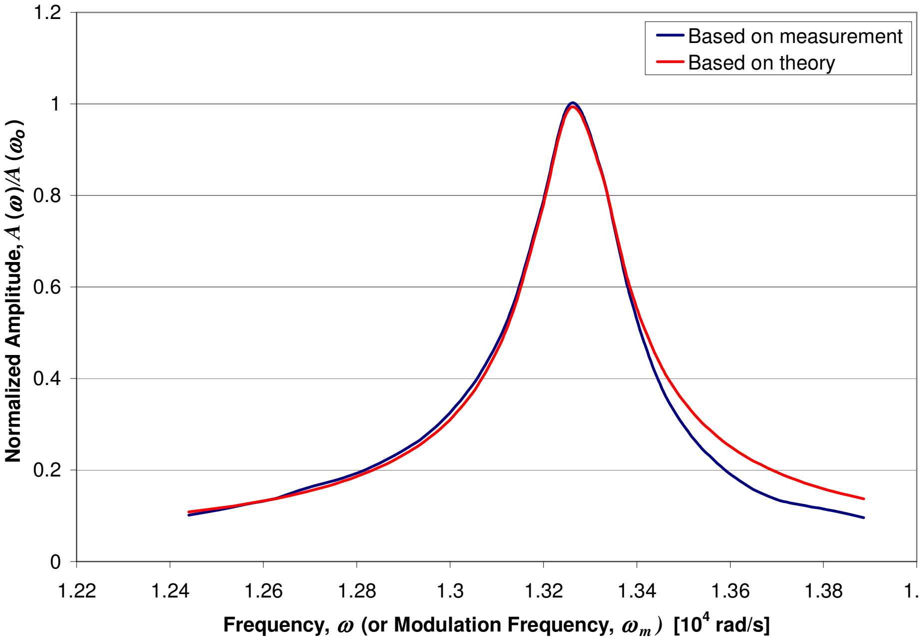

Figure 3.29 Normalized oscillation amplitude versus modulation (i.e. driving) frequency

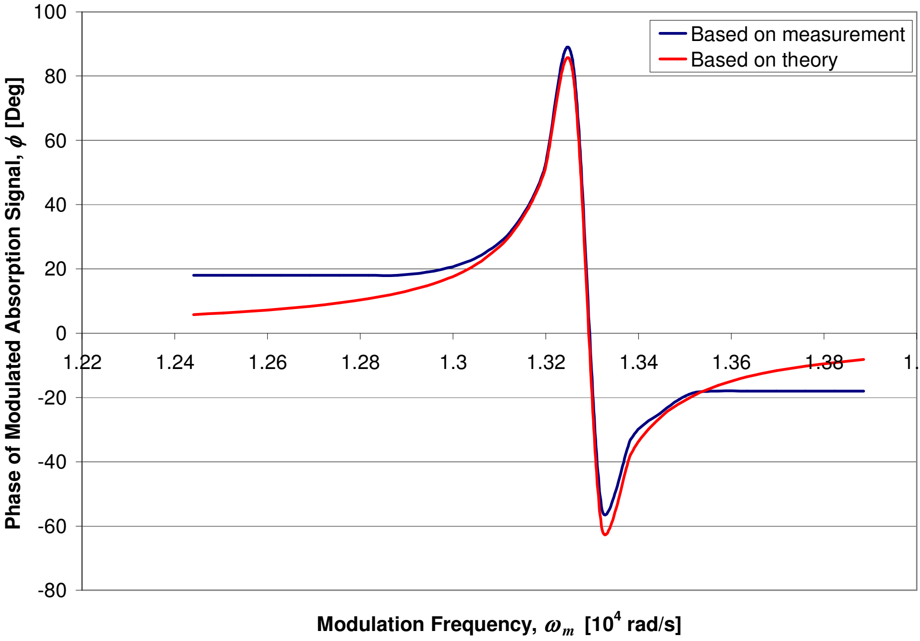

Figure 3.30 Phase of modulated absorption signal versus modulation (i.e. driving) frequency

There are three possible sources of the observed resonance: The regulated high-voltage amplifier, the piezoelectric transducer, or the Littrow laser cavity. The regulated high-voltage amplifier may be resonating, but it is rare for a circuit to ring at O(kHz) frequencies and rarer still for an electronic resonance to overshoot the driving signal by four-times its amplitude – The only circuit I can think of that exhibits this degree of overshoot is a tuned LC-circuit. In addition, I see no evidence of circuit resonance when I monitor the regulated high-voltage output. Having said this, I have not made a single measurements that conclusively supports my claim that the regulated high-voltage amplifier does not ring at O(kHz) frequencies – this claim is based on simple observation. The piezoelectric transducer attached to the tuning arm of the Littrow laser cavity may be resonating, but the small mass of the piezoelectric crystal would tend to inhibit an O(kHz) resonance. In fact, the piezoelectric stack utilized in the Littrow laser cavity has a manufacture specified resonance at a fundamental frequency of 138 kHz. Again, I have not made a single measurement that conclusively supports my claim that the piezoelectric transducer attached to the tuning arm of the Littrow laser cavity does not resonate at O(kHz) frequencies – my claim is based on intuition and faith in the manufacture specifications. The Littrow tuning arm is the most likely source of the resonance. Not only is the tuning arm relatively massive, but it was intentionally constructed for compliance; i.e. it was machined out of a relatively elastic aluminum-bronze alloy to accommodate a flexure joint in the design. Compliance in a mechanical system tends to encourage bending and twisting resonances.

I would certainly like to know the specific cause of the observed resonance at ω_m = 1.327×10^4 rad/s, but whether it originates in the electronics, the piezoelectric transducer, or the Littrow laser cavity really has no bearing on our discussion. I am less concerned with the source of this resonance than with how it affects the aim of all our analysis. I have discussed the theories of Rayleigh scattering, absorption spectroscopy, and WMS will one specific aim in mind – to provide a realistic calculation of the first- and second-harmonic lock-in signals detected from frequency modulated molecular Rayleigh scattering during preliminary frequency-locked MFRS measurements in the scattering arm of the experiment. I have introduced some experimental results along the way to provide a detailed description of the experimental apparatus that was used during these preliminary measurements as well as to establish confidence in our ability to predict reality using the developed theory. For instance, ***ALL*** preliminary frequency-locked MFRS measurements were conducted using a modulation frequency of ν_m = 2.090 kHz (ω_m = 1.313×10^4 rad/s). The results from the “resonance” experiment therefore provide a very important detail concerning the experimental apparatus utilized during preliminary frequency-locked MFRS measurements – The modulation frequency employed during all preliminary frequency-locked MFRS measurements is within the bandwidth of a system resonance. Determining the modulation depth employed during preliminary frequency-locked MFRS experiments is difficult in light of this revelation.

I don't trust the data in Figure 3.28 enough to draw any conclusions from it concerning the modulation index employed during preliminary MFRS experiments. The discrepancy in Figure 3.30 between the theoretical phase of the harmonic oscillator and the measured phase of the modulated absorption signal at a modulation frequency (or driving frequency) of ν_m=1.98 kHz leads me to believe that the **1*f***-profile amplitudes – including the peak amplitude – measured at this modulation frequency during the "resonance" experiment are low. In addition, the data was acquired using a modulation gain of G_m=0.3 (compared to a modulation gain of G_m=0.5 utilized during preliminary MFRS experiments). A reasonable estimate of the modulation depth employed during preliminary frequency-locked MFRS experiments is still possible, however, if we proceed along an empirical line of reasoning.

A sinusoidal voltage signal of amplitude A = 79.3 mV – corresponding to a modulation gain of G_m = 0.5 – was input to the piezoelectric transducer attached to the tuning arm of the Littrow laser cavity during ***ALL*** preliminary frequency-locked MFRS experiments. This same modulation signal was input to the piezoelectric transducer during the **1*f***-profile measurement illustrated in Figure 3.25. In addition, a modulation frequency of ν_m = 2.090 kHz (ω_m = 1.313×10^4 rad/s) was used during ***ALL*** preliminary frequency-locked MFRS experiments. And this same modulation frequency was employed during the **1*f***-profile measurement illustrated in Figure 3.25. In other words, the modulation amplitude employed during ***ALL*** preliminary frequency-locked MFRS experiments is identical to the modulation amplitude employed during the **1*f***-profile measurement illustrated in Figure 3.25. To determine the modulation amplitude employed during the **1*f***-profile measurement illustrated in Figure 3.25, let us continue along an empirical line of reasoning.

The Rb vapor cell utilized in the scattering arm during ***ALL*** preliminary frequency-locked MFRS experiments was at room temperature. Granted some days were warmer than others, but a temperature of T = 20.2 °C is as good an estimate as any for the Rb cell temperature during preliminary frequency-locked MFRS measurements. (I failed to keep rigorous account of the lab temperature during preliminary frequency-locked measurements). Since this was the temperature of the Rb cell in the reference arm of the MFRS experiment during the **1*f***-profile measurement illustrated in Figure 3.25 and since the modulation amplitude employed during ***ALL*** preliminary MFRS measurements is identical to the modulation amplitude employed during the **1*f***-profile measurement illustrated in Figure 3.25 we might draw the following simple conclusion: The modulation index employed during ***ALL*** preliminary frequency-locked MFRS experiments is that modulation index that optimizes the fit between peak amplitudes of the measured and modeled **1*f***-profile in Figure 3.25, $m = 0.476$.

This is certainly a reasonable estimate for the modulation index employed during all preliminary frequency-locked measurements, and will be utilized in the calculations concluding this section. It should be noted that the harmonic profile simulations up to this point have assumed that the laser linewidth, $\delta\omega_L$, is infinitesimally small. It can be shown that this assumption is valid in the limit of $a=m\delta\omega_{1/2}>>\delta\omega_L$ [101]; i.e. a laser linewidth of $\delta\omega_L<<121$ MHz will not affect the **1*f***-simulation in Figure 3.25 calculated using $m = 0.476$. It is my conjecture that the Littrow laser linewidth is in fact at this limit. This deduction follows from Figure 3.31 which compares a **2*f***-profile measured during the “validation” experiment and corresponding to the ***F***=2 ground state transition in the D_2-line of ^{85}Rb to a couple simulated **2*f***-profiles corresponding to the ***F***=2 ground state transition. The modeled profiles follow from Eq. 3.129, and were computed using the instrumental parameters recorded during second-harmonic “validation” measurements: $i_o = 1.821$ μA, $R_L = 50\ \Omega$, $G = 2\times10^6$, $\theta = 0°$, $z = 100$ mm, and $T = 20.2$ °C.

Looking at Figure 3.31 we see a large discrepancy between the measured **2*f***-profile and the **2*f***-profile simulated using our preliminary estimate of the modulation index, $m = 0.11$, corresponding to a modulation gain G_m=0.5 and a Rb gas temperature of T ≅ 20.2 °C. In light of the “resonance” experiment this discrepancy is reassuring. We also see that the fit between the measured **2*f***-profile in Figure 3.31 and the **2*f***-profile simulated with $m = 0.476$ is quite favorable. If the linewidth of the Littrow laser enters critically into our first- and second-harmonic lock-in simulations, then it is possible to show that the resulting reduction in lock-in signal is more pronounced for second-harmonic detection. In other words, if the laser linewidth entered critically into the analysis we would expect the **2*f***-profile simulation in Figure 3.31 that assumes an infinitesimal laser linewidth and uses a modulation index of m =0.476 to overestimate the measurement.

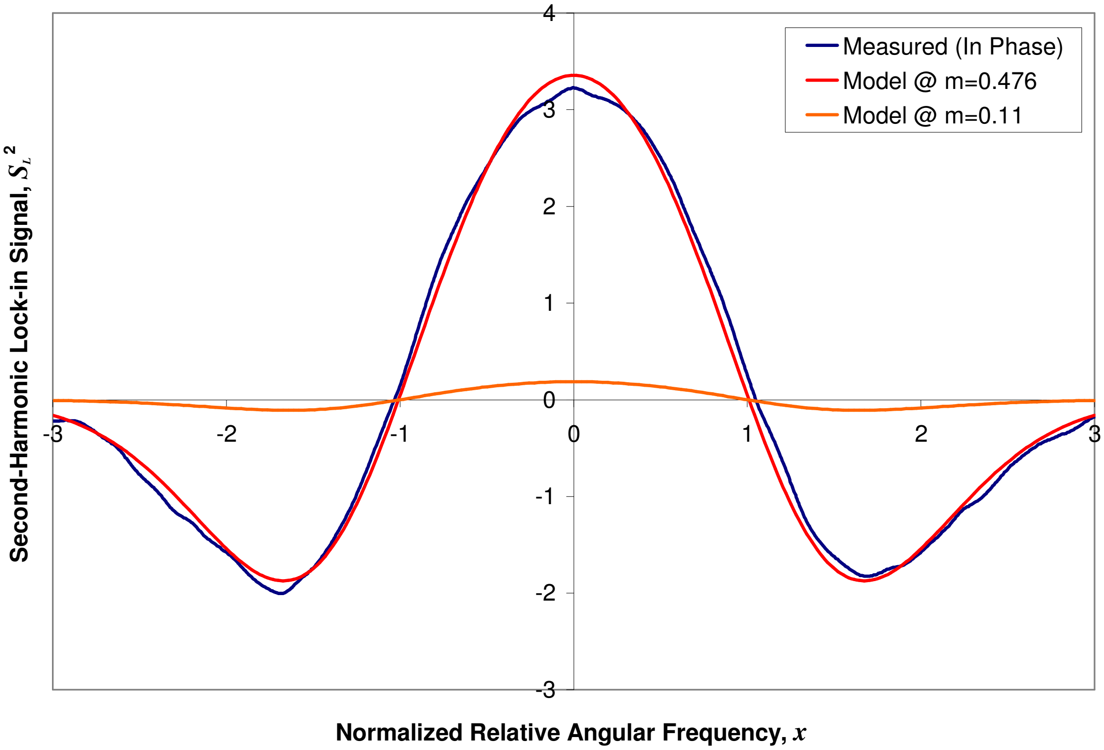

Figure 3.31 ***2f****-profile corresponding to* ***F****=2 Doppler broadened ground state transition in* D_2*-line of* ^{85}*Rb measured during "validation" experiment at* ν_m*=2.09 kHz and* G_m*=0.5 compared to several* ***2f****-profile simulations*

Preliminary MFRS experiments in the frequency-locked mode of operation utilized first- and second-harmonic lock-in measurements associated with the ***F***=3 ground state transition in the D_2-line of ^{85}Rb; the Doppler broadened ***F***=3 ground state transition of ^{85}Rb exhibits the greatest optical depth out of the four Doppler broadened absorption features in the D_2-line of Rb in natural isotopic abundance, and therefore affords the maximum possible modulated absorption signal in the D_2-line. We first considered the harmonic profiles associated with the ***F***=2 ground state transition of ^{85}Rb because our heuristic model of this absorption feature almost perfectly fit the measured absorption profile. Let us now check whether the ***1f***- and ***2f***-profiles measured during the "validation" experiment and associated with the ***F***=3 ground state transition in the D_2-line of ^{85}Rb are accurately modeled by the ***1f***- and ***2f***-profile simulations associated with the ***F***=3 ground state transition of ^{85}Rb and calculated from Eqs. 3.128 and 3.129, respectively, utilizing the experimental parameters recorded during the "validation" experiment.

Figure 3.32 shows such a comparison. The figure includes a **1*f***-profile and a **2*f***-profile measured during the "validation" experiment and corresponding to the ***F***=3 ground state transition in the D$_2$-line of ^{85}Rb. These measured profiles were plotted against the normalized relative angular frequency, *x*, by utilizing the data element-to-angular frequency conversion in Eq. 3.130. Both profiles were measured concurrently and during the same scan across the D$_2$-line of ^{85}Rb that produced the **1*f***- and **2*f***-profiles associated with the ***F***=2 ground state transition of ^{85}Rb illustrated in Figures 3.25 and 3.31, respectively. These profiles were acquired using a modulation gain of G_m = 0.5 and a modulation frequency of ν_m = 2.090 kHz. Also plotted in Figure 3.32 is a **1*f***-profile simulation and a **2*f***-profile simulation corresponding to the ***F***=3 ground state transition in the D$_2$-line of ^{85}Rb. These simulations follow from Eq. 3.128 and 3.129, respectively, using i_o = 1.821 μA, R_L = 50 Ω, $G_{1f} = 5\times10^5$ and $G_{2f} = 2\times10^6$, θ_{1f} = 180° and θ_{2f} = 0°, z = 100 mm, and T=20.2 °C.

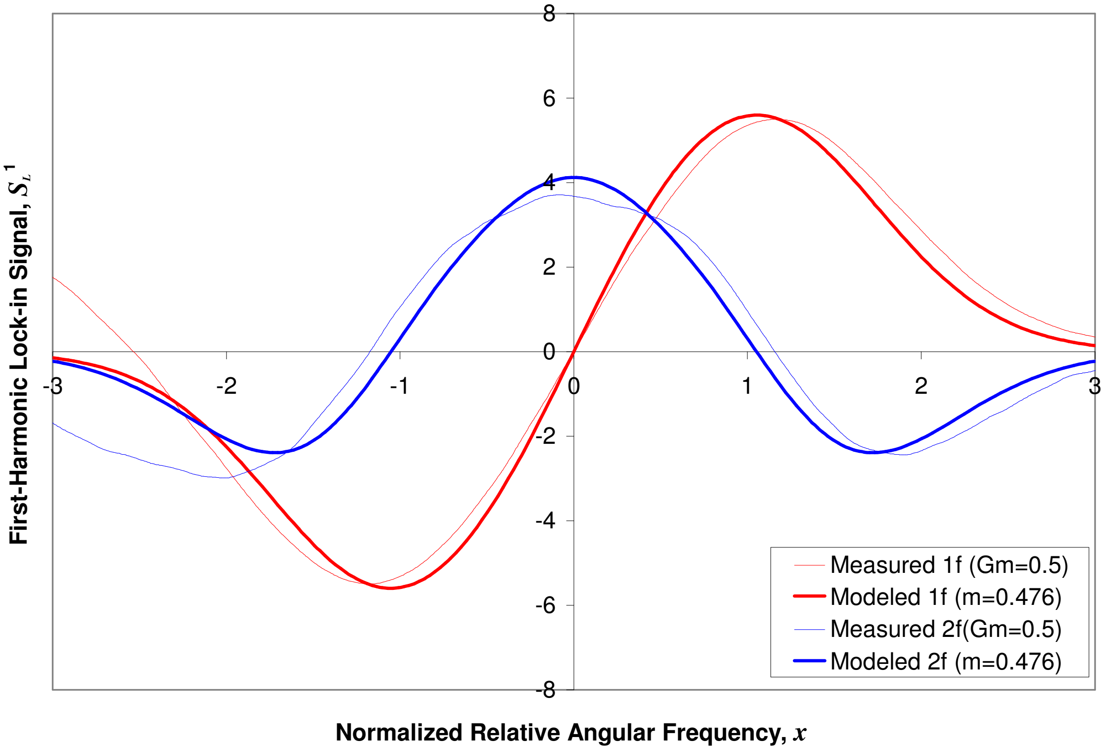

*Figure 3.32 **1f**- and **2f**-profiles measured during the "validation" experiment with ν_m=2.09 kHz and G_m=0.5 and corresponding to **F**=3 Doppler broadened ground state transition in D$_2$-line of ^{85}Rb versus comparable **1f**- and **2f**-profiles simulated at T=20.2 °C and m=0.476*

The comparison between the measured and modeled harmonic profiles corresponding to the ***F***=3 ground state transition of ^{85}Rb is less favorable than the comparison between the measured and modeled harmonic profiles corresponding to the ***F***=2 ground state transition of ^{85}Rb. This is no surprise. First, we expect our heuristic model of the Doppler broadened ***F***=3 ground state transition of ^{85}Rb to diverge from the measured absorption profile at lower frequencies as a result of contributions from the ***F***=2 ground state transition of ^{87}Rb to the measured profile. This is illustrated in Figure 3.33, which compares a Doppler broadened ***F***=3 ground state transition of ^{85}Rb measured during the "absorption" experiment to our heuristic model of the Doppler broadened ***F***=3 ground state transition of ^{85}Rb at T=20.2 °C. Since our harmonic profile simulations rely on our heuristic model, we therefore expect the measured and modeled harmonic profiles corresponding to the ***F***=3 ground state transition of ^{85}Rb to diverge at lower frequencies. This is evidenced in Figure 3.32.

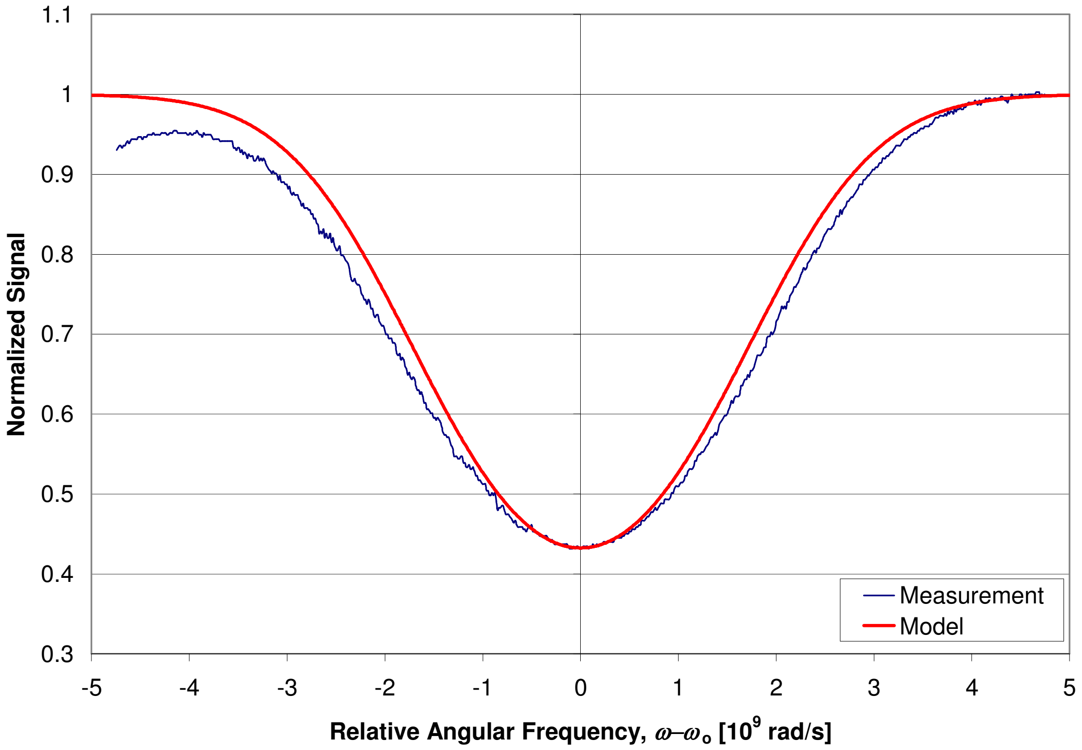

*Figure 3.33 Measured **F**=3 Doppler broadened ground state transition in D_2-line of ^{85}Rb compared to heuristic model of this transition at T=20.2 °C*

In addition, the maximum frequency separation between the hyperfine components in the ***F***=3 ground state transition of ^{85}Rb is twice the maximum frequency separation between the hyperfine components in the ***F***=2 ground state transition of ^{85}Rb. Since our heuristic model neglects the excited state energy splitting in each ground state transition, we therefore expect the measured Doppler broadened profile corresponding to the ***F***=3 ground state transition of ^{85}Rb to be broader than the profile predicted by our heuristic model. Again, this is illustrated in Figure 3.33. The peaks in the ***1f***-profile – i.e. the maximum positive and negative excursions in the profile – approximately correspond to the inflection points in the associated Doppler broadened absorption profile. Since the measured absorption profile corresponding to the ***F***=3 ground state transition of ^{85}Rb is broader than the modeled absorption profile, and since our harmonic profile simulations rely on the modeled absorption profile, we expect a greater separation in frequency between the peaks in the measured ***1f***-profile corresponding to the ***F***=3 ground state transition of ^{85}Rb than between the peaks in the ***1f***-profile simulation. Similarly, the peaks in the ***2f***-profile approximately correspond to the inflection points in the associated ***1f***-profile and the zero-crossings in the ***2f***-profile correspond to the peaks in the associated ***1f***-profile. Since the measured ***1f***-profile is "broader" than the simulated ***1f***-profile, we therefore expect a greater separation in frequency between the peaks and zero-crossings in the measured ***2f***-profile than between the peaks and zero-crossings in the ***2f***-profile simulation. Our expectations are confirmed in Figure 3.32.

The amplitudes of the modeled profiles are the primary concern of the signal-to-noise analysis that follows. If we ignore the left side of the plot in Figure 3.32, because of the contributions from the ***F***=2 ground state transition of ^{87}Rb, we see that the peak amplitudes of the simulated ***1f***- and ***2f***-profiles are a little optimistic compared to the peak amplitudes of the measured ***1f***- and ***2f***-profiles. The simulated harmonic profiles in Figure 3.32 would undoubtedly reflect reality more accurately if we included contributions from the ***F***=2 ground state transition of ^{87}Rb to the harmonic profiles associated with the ***F***=3 ground state transition of ^{85}Rb. A completely rigorous model would also account for the hyperfine splitting in both ground state transitions.

Realistic calculations of the harmonic profiles detected in the scattering arm during preliminary frequency-locked MFRS experiments must account for the spectral broadening of Rayleigh scattered light. In the analysis that follows, calculations neglecting the line-broadening of the Rayleigh scattered light will be compared to the realistic calculations accounting for the line-broadening to clearly illustrate the impact of spectral broadening on the detected harmonic profiles. The line broadening of the Rayleigh scattered light collected during preliminary MFRS experiments is accounted for as follows.

Consider the theoretical first-harmonic lock-in signal illustrated in Figure 3.34, $\bar{S}_L^1$, corresponding to the ***F***=3 ground state transition in the D$_2$-line of ^{85}Rb. The plot was numerically calculated using Eq. 3.128 assuming a path length through the Rb vapor cell of *z*=75 mm, a Rb gas temperature of *T*=20.2°C, a modulation index of *m*=0.476, and a multiplicative constant of one by definition; i.e. referring back to Eq. 3.128,

$$\frac{i_o R_L G}{\sqrt{2}} = 1 \Rightarrow \bar{S}_L^1 = S_L^1 . \tag{3.154}$$

Contributions from the Doppler broadened ***F***=2 ground state transition of ^{87}Rb to the lock-in signal were neglected in the calculation, as was the line broadening of the frequency modulated radiation passing through the Rb vapor cell.

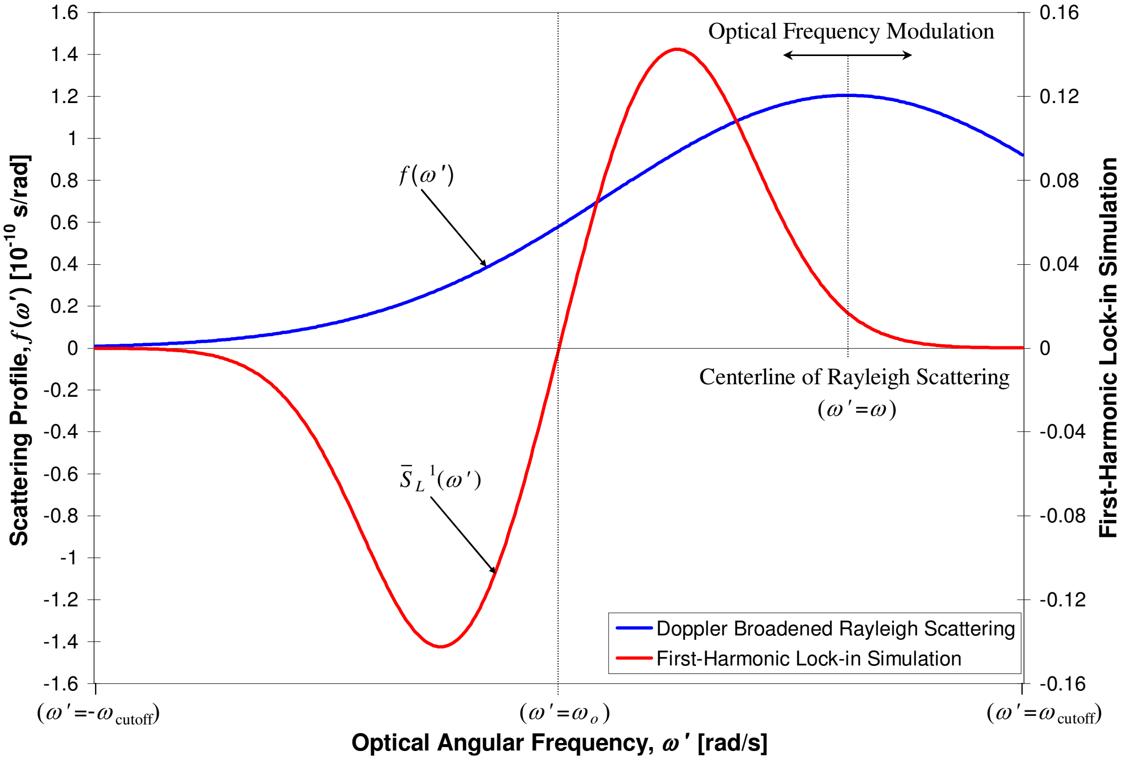

*Figure 3.34 Normalized Gaussian lineshape used to model the spectral broadening of frequency modulated Rayleigh scattered radiation collected during preliminary MFRS experiments compared to a **1f**-profile simulation neglecting spectral line broadening*

The line broadening of the frequency modulated Rayleigh scattered radiation collected and detected during preliminary MFRS experiments is also illustrated in Figure 3.34. This line broadening obviously must be accounted for if we intend to accurately calculate the lock-in signals detected during preliminary frequency-locked MFRS experiments in the scattering arm. The spectral lineshape, $f(\omega')$, plotted in Figure 3.34 simulates molecular Rayleigh scattering of monochromatic incident radiation at a wavelength of λ=780.032 nm – corresponding to the center-of-gravity of the D_2-line of Rb – from air at a pressure of P = 1 atm and an equilibrium temperature of T_{air}=20.2°C that is collected orthogonal to the incident radiation. This simulated lineshape assumes that the Rayleigh scattering is Doppler broadened about the centerline angular frequency, ω, of the collected radiation – i.e. I will neglect acoustic broadening and the associated Brillouin wings in the analysis that follows. Referring back to Eqs. 3.43 and 3.44 we find that the normalized Gaussian lineshape describing this spectral broadening is,

$$f(\omega') = \frac{1}{\delta\omega_{1/2}\big|_{\text{air}}} \sqrt{\frac{\ln 2}{\pi}} \exp\left[-\frac{\ln 2 (\omega' - \omega)^2}{\delta\omega_{1/2}\big|_{\text{air}}^2} \right] \tag{3.155}$$

in terms of angular frequency where,

$$\delta\omega_{1/2}\big|_{\text{air}} = \frac{\omega_o}{c} \sqrt{\frac{2kT_{\text{air}} \ln 2}{m_{\text{air}}}} \cdot \left| \hat{k}_s - \hat{k}_o \right| \tag{3.156}$$

is the half-width at half-maximum (HWHM) of the Doppler broadened Rayleigh scattered radiation from air, k is Boltzmann's constant, T_{air} is the equilibrium air temperature, m_{air} is the molecular mass of air, and c is the speed of light. In Eq. 3.156 I have approximated the Doppler half-width of the Rayleigh scattered radiation at a centerline angular frequency ω by assuming $\omega \sim \omega_o$, where ω_o is the center-of-gravity angular frequency of the D_2-line of Rb. For the experimental geometry described above and utilized in the scattering arm during preliminary MFRS experiments – i.e. the Rayleigh scattered radiation is collected in a direction, $\hat{k}_s$, that is orthogonal to the direction of the incident probe laser beam, $\hat{k}_o$ – the last term in Eq. 3.156 is $\left| \hat{k}_s - \hat{k}_o \right| = \sqrt{2}$.

Now, imagine that frequency modulated monochromatic laser light at a centerline angular frequency ω interrogates a volume of static air. As illustrated in Figure 3.20, MFRS measurements involve collecting the Rayleigh scattered radiation from the probe volume under investigation and transmitting the collected radiation through a Rb vapor filter before detection.

If we assume that the Rayleigh scattered light is Doppler broadened by the thermal motion of the air molecules, than the collected scattering can be described by a Gaussian power spectrum centered at and modulating about an optical angular frequency ω, as illustrated in Figure 3.34. A modulated absorption will be detected down beam of the Rb vapor filter if this modulating power spectrum lies even partially within the bandwidth of an absorption feature over the course of one modulation cycle. This is clearly the case for the modulating power spectrum illustrated in Figure 3.34.

The detected modulated absorption results in a first-harmonic lock-in signal, $s_l^1(\omega)$, at the centerline angular frequency, ω, of the modulating Rayleigh scattered power spectrum. This lock-in signal can be modeled as a superposition of lock-in signals calculated assuming an infinitesimal spectral linewidth (vis-à-vis Eqs. 3.128 and 3.129) and weighted by the Rayleigh scattered power density – i.e the Rayleigh scattered power per angular frequency bandwidth. In mathematical terms,

$$s_l^{\,1}(\omega) = \int_{-\infty}^{\infty} S_L^{\,1}(\omega')f(\omega')\mathrm{d}\omega'$$

$$= \sum_{\omega'=-\omega_{\text{cuttoff}}}^{\omega_{\text{cuttoff}}} S_L^{\,1}(\omega')f(\omega')\mathrm{d}\omega'$$

$$s_l^{\,1}(\omega) = \frac{i_o R_L G}{\sqrt{2}}\cos\theta \sum_{\omega'=-\omega_{\text{cuttoff}}}^{\omega_{\text{cuttoff}}} \overline{S}_L^{\,1}(\omega')f(\omega')\mathrm{d}\omega' \qquad (3.157)$$

where $S_L{}^1(\omega')$ is the theoretical first-harmonic lock-in signal at an angular frequency ω' calculated from Eq. 3.128 assuming an infinitesimal spectral linewidth, $f(\omega')$ is the Rayleigh scattered power density at an angular frequency ω' calculated from Eq. 3.155 describing the normalized Gaussian lineshape of scattered radiation modulating about a centerline angular frequency of $\omega'=\omega$, and $\mathrm{d}\omega'$ is the angular frequency bandwidth. Similarly, the second-harmonic lock-in signal, $s_l^2(\omega)$, can be modeled as,

$$s_l^{\,2}(\omega) = \int_{-\infty}^{\infty} S_L^{\,2}(\omega')f(\omega')\mathrm{d}\omega'$$

$$= \sum_{\omega'=-\omega_{\text{cuttoff}}}^{\omega_{\text{cuttoff}}} S_L^{\,2}(\omega')f(\omega')\mathrm{d}\omega'$$

$$s_l^{\,2}(\omega) = \frac{i_o R_L G}{\sqrt{2}}\cos\theta \sum_{\omega'=-\omega_{\text{cuttoff}}}^{\omega_{\text{cuttoff}}} \overline{S}_L^{\,2}(\omega')f(\omega')\mathrm{d}\omega' \qquad (3.158)$$

where $S_L{}^2(\omega')$ is the theoretical second-harmonic lock-in signal at an angular frequency ω' calculated from Eq. 3.129 assuming an infinitesimal spectral linewidth. The summations in Eqs. 3.157 and 3.158 are carried out over the angular frequency range ω':[$-\omega_{\text{cutoff}}$, $+\omega_{\text{cutoff}}$] outside of which the lock-in signals – i.e. $\overline{S}_L^1$ and $\overline{S}_L^2$ – go to zero, as illustrated in Figure 3.34. In the limit of $d\omega' \ll \delta\omega_{1/2}$, where $\delta\omega_{1/2}$ is the HWHM of the absorption feature utilized during the modulated absorption measurement, this summation accurately approximates the integrated response expressed in the first line of both Eqs. 3.157 and 3.158 that analytically describes the lock-in signal.

We are now in a position to predict the first- and second-harmonic lock-in signals corresponding to the $\boldsymbol{F}=3$ ground state transition in the D_2-line of ^{85}Rb detected during preliminary frequency-locked MFRS experiments. The heuristic model of the Doppler broadened absorption features in the D_2-line of ^{85}Rb and the theoretical formulations for the first- and second-harmonic lock-in signals, which rely on this heuristic model, appear to predict reality reasonably well. I will incorporate the spectral line broadening of Rayleigh scattered radiation into the theoretical formulations for the first- and second-harmonic lock-in signals using Eqs. 3.157 and 3.158.

Table 3.6 provides a summary of the theoretical models that will be utilized to predict the first- and second-harmonic lock-in signals detected during preliminary MFRS experiments. The table includes a brief description of each formula as well as the location in the text of this dissertation from which each formula was pulled. The unit of each calculated variable is also included in the table – The calculations described in Table 3.6 were carried out exclusively in MKS-units. As a reminder, the formula for the detected Rayleigh scattered power in Table 3.6 was derived assuming that the scattered radiation is collected in a direction that is orthogonal to the polarization and propagation direction of a linearly polarized probe laser beam, as illustrated in Figure 3.20.

We now need only determine the instrumental parameters utilized during preliminary frequency-locked experiments to predict the lock-in signals detected during those experiments. I struggled to make reliable measurements utilizing molecular Rayleigh scattering from both static air and a supersonic expansion of dry nitrogen during preliminary frequency-locked experiments. During the latter experiments, the rapid expansion of the nitrogen through the regulator attached to the gas cylinder cooled the gas exiting the cylinder. Frost slowly accumulated on the hose leading from the regulator to the stagnation chamber of the nozzle and the stagnation temperature recorded during the course of the experiment slowly dropped. The static temperature of the gas dropped further as the nitrogen expanded from the stagnation chamber to the nozzle exit. A minute or so into the measurements the temperature of the nitrogen exiting the nozzle was near freezing and a sudden explosion in signal was observed. (To prevent saturation of and potential damage to the detector and detection electronics I reduced the PMT supply voltage and the lock-in amplifier gain during the course of these experiments). The only logical explanation for this dramatic increase in signal is that H_2O entrained into the jet core condensed and the scattering from this condensate was collected. (I will present a sample of sweep-mode velocity measurements made in a supersonic expansion of N_2 in the next chapter to illustrate this point).

Even if we had developed a theoretical description of condensate scattering, I wouldn't know enough about the condensate entrained into the jet core to make accurate predictions based on this theory. In addition, I set out to make MFRS measurements utilizing molecular Rayleigh scattering. Scattering from condensate may still lie within the Rayleigh regime, but I feel that classifying condensate scattering as Rayleigh scattering is a stretch. In the analysis that follows I will therefore focus my attention of calculating the harmonic profiles detected during preliminary frequency-locked MFRS experiments utilizing molecular Rayleigh scattering from static air. These experiments were more tractable than the experiments conducted in a supersonic expansion of dry nitrogen, and the instrumental parameters associated with these experiments are therefore more easily defined.

Table 3.7 provides a summary of the instrumental parameters I recorded during preliminary MFRS measurements utilizing molecular Rayleigh scattering from air. Only those instrumental parameters required of the theoretical models in Table 3.6 are listed in Table 3.7.

A shunt resistance of R_L=50 Ω was attached to the front-end of the lock-in amplifier during all preliminary MFRS experiments and all modulated absorption measurements were AC-coupled into the front-end of the lock-in amplifier to prevent the DC-offset in the measured signal from "soaking-up" the dynamic reserve (see Appendix A). Note that if the dynamic reserve of the lock-in amplifier is insufficient to handle the front-end noise, then increasing the shunt resistance helps. Dynamic reserve was generally not a problem during preliminary MFRS measurements.

The lock-in amplifier gain, *G*, has practical relevance in that it provides a signal that is large enough for resolvable analog-to-digital conversion. The particular lock-in gain employed during preliminary MFRS measurement does not affect the calculated signal-to-noise, however, and a lock-in amplifier gain of one will therefore be assumed in the analysis that follows. In phase measurement of the first- and second harmonic lock-in signals was ensured during all preliminary MFRS measurements and will be modeled in the analysis that follows by setting the lock-in reference phase to zero, $\theta = 0°$.

Description	**Theoretical Formula**	**Reference Eqn.**
First-harmonic lock-in signal accounting for spectral broadening of scattered radiation [V]	$s_l^{\,1}(\omega) = \dfrac{i_o R_L G}{\sqrt{2}} \sum_{\omega' = -\omega_{\text{cuttoff}}}^{\omega_{\text{cuttoff}}} \bar{S}_L^{\,1}(\omega') f(\omega') \mathrm{d}\omega'$	3.157
Second-harmonic lock-in signal accounting for spectral broadening of scattered radiation [V]	$s_l^{\,2}(\omega) = \dfrac{i_o R_L G}{\sqrt{2}} \sum_{\omega' = -\omega_{\text{cuttoff}}}^{\omega_{\text{cuttoff}}} \bar{S}_L^{\,2}(\omega') f(\omega') \mathrm{d}\omega'$	3.158
PMT anode current detected outside the bandwidth of a resonant absorption [A]	$i_o = i_p = \mu S_k P_k$	C.11
PMT gain	$\mu = 4.52 \times 10^{-14} V_{PMT}^{\;6.12} + 3.64 \times 10^{-18} V_{PMT}^{\;7.12}$	C.12
Rayleigh scattered power detected orthogonal to probe laser polarization and direction [W]	$P_k = P_{DET}\big\vert_{R_V} = \eta N_o P_o \ell_{eff} \dfrac{4\pi^3}{3\lambda^4} \left(\dfrac{n-1}{N} \right)^2 \left\{ 4 - 3\cos\alpha_{\max} - \cos^3 \alpha_{\max} \right\}$ $\alpha_{\max} = \arctan(1/2F_{\#})$	3.33
Number density of atoms or molecules in probe volume assuming gas is ideal [m^{-3}]	$N_o = \dfrac{p_o}{kT_o}$	Ideal gas eqn.
Reduced first-harmonic lock-in signal assuming infinitesimal spectral linewidth	$\bar{S}_L^1 = -z\zeta H_1^{\,\prime} + \dfrac{z^2 \zeta^2}{2} \left(H_0^{\,\prime} H_1^{\,\prime} + H_1^{\,\prime} H_2^{\,\prime} + \ldots \right) - \ldots \text{ h.o.t.s}$	See eq. 3.128 for full formula
Reduced second-harmonic lock-in signal assuming infinitesimal spectral linewidth	$\bar{S}_L^2 = -z\zeta H_2^{\,\prime} + \dfrac{z^2 \zeta^2}{2} \left[\dfrac{H_1^{\,\prime 2}}{2} + \left(H_0^{\,\prime} H_2^{\,\prime} + \ldots \right) \right] - \ldots \text{ h.o.t.s}$	See eq. 3.129 for full formula
Rb gas temperature dependent coefficient for ***F*** =3 ground state transition of ^{85}Rb [m^{-1}]	$\zeta = 3.179 \times 10^{-6} \dfrac{N_{^{85}\text{Rb}}}{\delta\omega_{1/2}\big\vert_{^{85}\text{Rb}}}$	3.107
Number density of ^{85}Rb atoms in Rb vapor cell calculated assuming gas is ideal [m^{-3}]	$N_{^{85}\text{Rb}} = \dfrac{X_{^{85}\text{Rb}} P_v\big\vert_{\text{Rb}}}{kT_{\text{Rb}}}$	3.93
Vapor pressure of Rb from Nesemeyanov's solid phase model [Pa]	$P_v\big\vert_{\text{Rb}} = 133.322368421 \cdot 10^{-94.04826 - \frac{1961.258}{T_{\text{Rb}}} - 0.037716\, T_{\text{Rb}} + 42.57526 \log_{10} T_{\text{Rb}}}$	3.94
Doppler half-width (HWHM) of ^{85}Rb gas [rad/s]	$\delta\omega_{1/2}\big\vert_{^{85}\text{Rb}} = \dfrac{\omega_o}{c} \sqrt{\dfrac{2kT_{\text{Rb}} \ln 2}{m_{^{85}\text{Rb}}}}$	3.99
Fourier coefficients for Doppler broadened absorption profile	$H_{\text{n}}^{\,\prime} = \dfrac{2}{\pi} \int_0^{\pi} \exp\left[-\ln 2 (x + m\cos\varphi)^2 \right] \cos(\text{n}\varphi) \mathrm{d}\varphi$	3.113
Normalized relative angular frequency	$x = \dfrac{\omega - \omega_0}{\delta\omega_{1/2}\big\vert_{^{85}\text{Rb}}}$	3.11
Lineshape function for Doppler broadened Rayleigh scattered radiation from air [s/rad]	$f(\omega') = \dfrac{1}{\delta\omega_{1/2}\big\vert_{\text{air}}} \sqrt{\dfrac{\ln 2}{\pi}} \exp\left[-\dfrac{\ln 2 (\omega' - \omega)^2}{\delta\omega_{1/2}\big\vert_{\text{air}}^2} \right]$	3.155
Doppler half-width (HWHM) of Rayleigh scattered radiation from air [rad/s]	$\delta\omega_{1/2}\big\vert_{\text{air}} = \dfrac{\omega_o}{c} \sqrt{\dfrac{2kT_{\text{air}} \ln 2}{m_{\text{air}}}} \cdot \left\vert \hat{k}_s - \hat{k}_o \right\vert$	3.156

Table 3.6 Summary of theoretical models used to predict the first- and second-harmonic lock-in signals detected from molecular Rayleigh scattering during preliminary MFRS experiments

Description	**Symbol**	**Value**
Shunt resistance at front-end of lock-in amplifier	R_L	$50\,\Omega$
Lock-in amplifier gain	G	1
Phase of reference signal internal to lock-in amplifier	θ	0°
Voltage applied across PMT	V_{PMT}	1200 V
Radiant sensitivity of PMT photocathode	S_k	62 mA/W
Collection efficiency	η	82%
Probe laser power	P_o	50 mW
Effective spatial resolution along direction of probe laser beam	ℓ_{eff}	3.8 mm
Probe laser centerline wavelength	λ	780.032 nm
Index of refraction of air minus one	$n-1$	2.7516×10^{-4}
Reference number density for index of refraction quoted above	N	2.55×10^{25} m^{-3}
Collection F-number	$F_{\#}$	1.445
Pressure of gas in probe volume	$p_o = p_{\text{air}}$	101325 Pa
Temperature of gas in probe volume	$T_o = T_{\text{air}}$	293.35 K
Atomic/Molecular mass of gas in probe volume	$m_o = m_{\text{air}}$	4.8×10^{-26} kg
Path length through Rb vapor cell in scattering arm	z	75 mm
Temperature of Rb vapor cell in scattering arm	T_{Rb}	293.35 K
Mole fraction of ^{85}Rb in Rb vapor cell	$X_{^{85}\text{Rb}}$	72.17%
Atomic mass of ^{85}Rb	$m_{^{85}\text{Rb}}$	1.41×10^{-25} kg
Center-of-gravity angular frequency of D$_2$-line of Rb	ω_o	$2\pi\cdot384.23$ THz
Modulation index	m	0.476
Modulus of unit vector in scattering direction minus unit vector in probe laser direction	$\left\lvert \hat{k}_s - \hat{k}_o \right\rvert$	$\sqrt{2}$

Table 3.7 Instrumental parameters describing preliminary frequency-locked MFRS measurements utilizing molecular Rayleigh scattering from air

The collection F-number listed in Table 3.7 follows from Zemax ray-tracing analysis of the optical designs utilized for collection of Rayleigh scattered radiation. In Section 3.2 we arrived at an estimate for the efficiency with which the Rayleigh scattered radiation is collected in the scattering arm of the MFRS velocimeter, $\eta \cong 97\%$. This collection efficiency was calculated by comparing the theoretical formulation for the detected Rayleigh scattered power to the Rayleigh scattered power detected during a simple scattering experiment conducted using an optical design for collection that exhibits similar performance to those designs utilized during preliminary MFRS experiments. There are two critical differences between the scattering arm as it was configured during the simple scattering experiment conducted to arrive at this estimate for the collection efficiency and the scattering arm as it was configured during preliminary MFRS experiments.

First, a Rb vapor cell was utilized in the scattering arm during all preliminary MFRS measurements. This Rb vapor cell is simply an uncoated glass cylinder approximately 1 inch in diameter and 3 inches in length. The Rayleigh scattered light collected in the scattering arm was collimated before passing through the cell to minimize the effect of dispersion on the propagating wavefront as the optical frequency of the collected light was tuned across an atomic resonance. The collimated light enters one end of the cylindrical cell and exits the other end, passing across and approximately orthogonal to four air-glass interfaces in the process. Cumulatively these four air-glass interfaces result in an approximately 15% reflection loss that must be accounted for in our estimate of the collection efficiency during preliminary MFRS experiments; our estimate of $\eta \cong 97\%$ only accounts for reflection losses from the anti-reflection coated lenses utilized in the optical design for collection.

Second, during preliminary MFRS experiments the PMT photocathode was rotated 90° from the orientation utilized during the simple Rayleigh scattering experiment discussed in Section 3.2. As illustrated in Figure 3.20, during preliminary MFRS experiments the long dimension of the photocathode was oriented along the x-axis, parallel to the direction of the probe laser beam, in order to maximize the effective x-axis spatial resolution of the measurement, ℓ_{eff}, and hence the number of photons collected from the laser line; i.e. during preliminary MFRS experiments the effective x-axis spatial resolution of the measurement was $\ell_{eff} \approx 3.8\,\text{mm}$ compared to an effective x-axis spatial resolution of $\ell_{eff} = 1.2\,\text{mm}$ for the measurements made with the PMT photocathode oriented as it was during the simple Rayleigh scattering experiment discussed in Section 3.2 and illustrated in Figure 3.5. During the simple scattering experiment illustrated in Figure 3.5 the long dimension of the PMT photocathode was intentionally oriented along the y-axis, orthogonal to the laser line, so that the effective y-axis spatial resolution of the measurement was much greater than the probe laser beam waist diameter along that axis. This simplified our calculation of the detected Rayleigh scattered light by allowing us to assume that all photons collected from the y-axis spatial extent of the probe laser beam were effectively imaged onto the PMT photocathode during the experiment; i.e. losses due to aberrations along the y-axis were negligible with the PMT oriented as it was during the simple scattering experiment. With the PMT oriented as it was during preliminary MFRS experiments, this assumption is of questionable validity; i.e. during preliminary MFRS experiments the effective y-axis spatial resolution of the measurement was $h_{eff} \approx 1.2\,\text{mm}$ compared to an effective y-axis spatial resolution of

$h_{eff} = 3.8\,\text{mm}$ for the measurements made with the PMT photocathode oriented as it was during the simple scattering experiment.

It is possible that I lost photons to aberrations along the y-axis during preliminary MFRS experiments, but in the analysis that follows I will assume that the aberrated blur spot image of the Rayleigh scattering radiation collected during preliminary MFRS measurements did not overfill the PMT photocathode along the y-axis and use an estimate of $\eta = 0.97{\cdot}(0.96)^4 = 82\%$ for the efficiency with which Rayleigh scattered photons were collected during preliminary frequency-locked experiments.

A reasonable estimate for the probe laser power recorded during preliminary frequency-locked MFRS experiments –i.e. P_o=50 mW – is listed in Table 3.7. By increasing the injection current to the power amplifier in the master oscillator power amplifier (MOPA) laser system utilized during preliminary frequency-locked experiments, probe laser powers greater than 50 mW were possible. Beyond probe laser powers of P_o ~ 50 mW, however, amplified spontaneous emissions from the power amplifier dramatically increased resulting in a dramatic increase in the shot noise from the detected Rayleigh scattered light as well as from stray reflections. In addition, when the irradiative power of spontaneous emissions exceeded 10 mW, the stability of the master oscillator – i.e. the Littrow laser cavity – was compromised by excessive feedback from the power amplifier. This generally occurred beyond probe laser powers of P_o ~ 50 mW.

The first- and second-harmonic profiles plotted respectively in Figures 3.35 and 3.36 were calculated by introducing the instrumental parameters listed in Table 3.7 into the theoretical formulations summarized in Table 3.6. The profiles plotted in both figures correspond to the Doppler broadened ***F***=3 ground state transition in the D_2-line of ^{85}Rb, and were simulated using our heuristic model of this Doppler broadened absorption feature at an assumed Rb gas temperature of T_{Rb}=20.2 °C. The simulated profiles neglect contributions from the ***F***=2 ground state transition of ^{87}Rb to the lock-in signal, and are plotted against the normalized relative angular frequency, *x*. (The corresponding relative angular frequency follows from Eq. 3.110b). Only half of the simulated profiles are plotted in Figures 3.35 and 3.36 – The half farthest removed in the frequency domain from the ***F***=2 ground state transition of ^{87}Rb. In the absence of ^{87}Rb the first-harmonic profile simulation in Figure 3.35 is symmetric about the origin of the plot and the second-harmonic profile simulation in Figure 3.36 is symmetric about the ordinate axis of the plot. In the presence of ^{87}Rb this symmetry is lost.

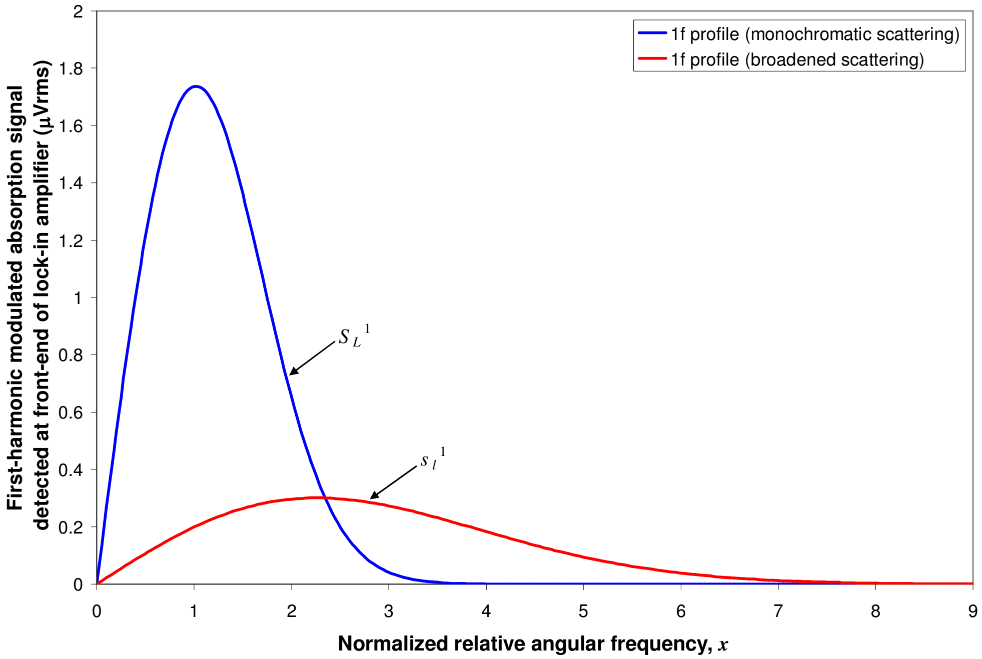

Figure 3.35 ***1f****-profile corresponding to the* ***F****=3 ground state transition in the D_2-line of ^{85}Rb and simulated assuming monochromatic Rayleigh scattered radiation compared to simulation incorporating thermal broadening of scattered radiation*

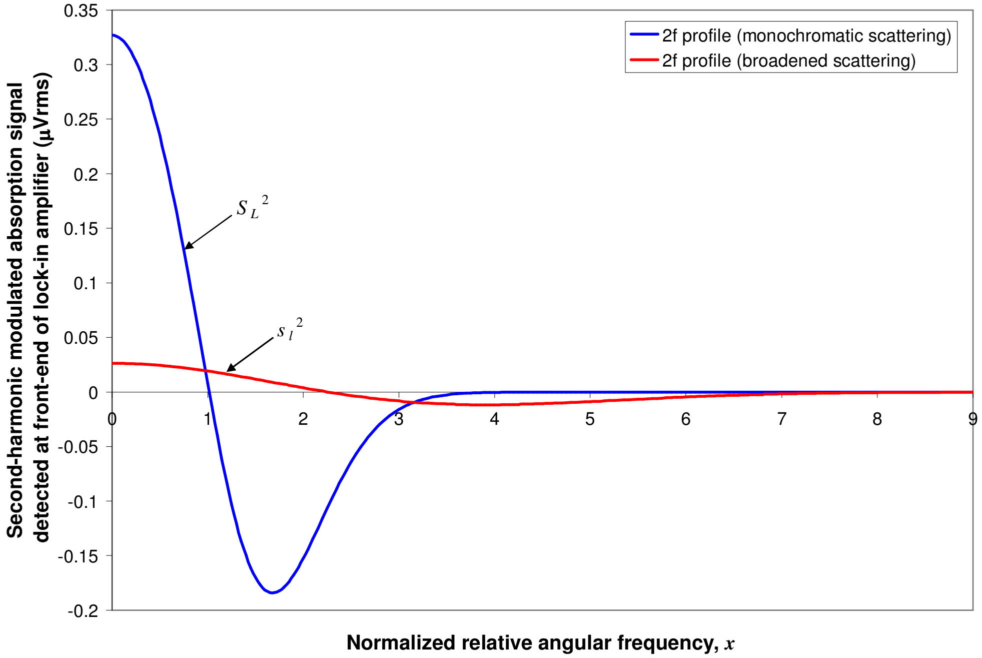

Figure 3.36 ***2f****-profile corresponding to the* ***F****=3 ground state transition in the D_2-line of ^{85}Rb and simulated assuming monochromatic Rayleigh scattered radiation compared to simulation incorporating thermal broadening of scattered radiation*

In Figure 3.35, a ***1f***-profile simulation assuming monochromatic Rayleigh scattered power is compared to a ***1f***-profile simulation assuming a Doppler broadened Rayleigh scattered power spectrum. In Figure 3.36, a ***2f***-profile simulation assuming monochromatic Rayleigh scattered power is compared to a ***2f***-profile simulation assuming a Doppler broadened Rayleigh scattered power spectrum. The Doppler broadened Rayleigh scattered power spectrum was incorporated into the first- and second-harmonic lock-in simulations according to Eqs. 3.157 and 3.158, respectively. The summation described in each of these equations was carried out over a normalized relative angular frequency range $x' = [-4,4]$ – corresponding to a relative angular frequency range of $(\omega_{\text{cutoff}} - \omega_o) = [-6.4 \times 10^9 \text{ rad/s}, +6.4 \times 10^9 \text{ rad/s}]$ and a relative frequency range of $(\nu_{\text{cutoff}} - \nu_o) = [-1 \text{ GHz}, +1 \text{ GHz}]$. Outside of this domain the lock-in signals $\bar{S}_L^1$ and $\bar{S}_L^2$ go to zero, as illustrated in Figures 3.35 and 3.36. A normalized angular frequency bandwidth of $dx' = 0.01$ – corresponding to an angular frequency bandwidth of $\mathrm{d}\omega' = 1.6 \times 10^7$ rad/s$<< \delta\omega_{1/2}\big|_{^{85}\text{Rb}} = 1.6 \times 10^9$ rad/s – was utilized in the summation.

In general, the thermal broadening of Rayleigh scattered light results in a broadened, flattened harmonic profile when compared to the harmonic profile simulated assuming monochromatic scattering. In both figures we see a dramatic reduction in peak harmonic profile signals when the spectral broadening of Rayleigh scattered light is incorporated into the simulation. The ***1f***-profile peak amplitude in the simulation accounting for the thermal broadening of Rayleigh scattered radiation is only 17% the ***1f***-profile peak amplitude in the simulation assuming monochromatic scattering. The ***2f***-profile peak amplitude in the simulation accounting for the thermal broadening of Rayleigh scattered radiation is only 8% the ***2f***-profile peak amplitude in the simulation assuming monochromatic scattering.

The first- and second-harmonic profiles plotted in Figures 3.35 and 3.36 that account for the spectrally broadened Rayleigh scattered radiation realistically represent the lock-in signals detected in the scattering arm during preliminary frequency-locked MFRS experiments while slowly sweeping the probe laser frequency across the ***F***=3 ground state transition of ^{85}Rb – i.e while acquiring the calibration profiles utilized during frequency-locked velocity measurements. I was never able to acquire reliable, repeatable calibration profiles utilizing molecular Rayleigh scattering from air – the detected lock-in signal was simply insufficient. I will illustrate this point at the end of this chapter by calculating the theoretical signal-to-noise during preliminary frequency-locked measurements utilizing molecular Rayleigh scattering from air and the instrumental parameters listed in Table 3.7. In the next section we will discuss the noise sources that corrupted the measurements. Before we proceed, however, I would like to compare a spectrally broadened **1*f***-profile simulation to some noise-contaminated **1*f***-profile measurements I acquired utilizing molecular Rayleigh scattering from air.

I have chosen what I consider to be the best harmonic profiles acquired utilizing molecular Rayleigh scattering from air for comparison to the developed theory. The experimentally acquired **1*f***-profiles presented below were selected based on two criteria: the collected Rayleigh scattered light contributed significantly to the detected modulated absorption signal and the acquired profiles resemble theoretical **1*f***-profiles.

Two sample **1*f***-profiles acquired in the scattering arm of the MFRS velocimeter utilizing molecular Rayleigh scattering from air at room temperature are plotted in Figure 3.37. One profile was acquired with vertically polarized light in the probe volume – i.e. with the probe laser polarization perpendicular to the direction of the collected scattering – and the other profile was acquired with horizontally polarized light in the probe volume – i.e. with the probe laser polarization parallel to the direction of the collected scattering. With the exception of the PMT supply voltage and lock-in amplifier gain, the instrumental parameters utilized while acquiring both profiles were similar to those outlined in Table 3.7; A PMT supply voltage of V_{PMT}=1050 V and a lock-in amplifier gain of $G = 5 \times 10^5$ (corresponding to a lock-in input sensitivity of S_L=2 μV) was utilized during both measurements. The profiles were acquired using a lock-in integration time constant of τ_L = 10 ms while slowly sweeping across the ***F***=2 and ***F***=3 ground state transitions of ^{87}Rb and ^{85}Rb, respectively.

I would like to reemphasize that the data illustrated in Figure 3.37 represents my most successful attempt to measure harmonic profiles utilizing molecular Rayleigh scattering from static room air. Though riddled with noise, the measurement made with vertically polarized light in the probe volume clearly resembles a first-harmonic profile. In addition, the harmonic profile detected with horizontally polarized light in the probe volume is noticeably less peaked than the harmonic profile detected with vertically polarized light; i.e. collected stray reflections certainly contributed to the detected profiles, but collected Rayleigh scattering is clearly evident.

The two profiles illustrated in Figure 3.37 each represent one of twenty successive profiles that were consecutively acquired during the experiment. In Figure 3.38 I have plotted an average of the twenty successive **1*f***-profile measurements made with vertically polarized light in the probe volume and an average of the twenty successive **1*f***-profile measurements made with horizontally polarized light in the probe volume. These averaged profiles were normalized by the lock-in amplifier gain employed during the measurement, $G = 5 \times 10^5$, and effectively represent those first-harmonic profiles that would have been acquired utilizing a lock-in integration time constant of τ_L=0.2 s and a lock-in amplifier gain of G=1. As expected, these averaged profiles are noticeably less noisy than the raw profiles illustrated in Figure 3.37 that were acquired with a lock-in integration time of τ_L=10 ms; i.e. the RMS-noise that corrupts a measurement is proportional to the square root of the equivalent noise bandwidth (ENBW) which in turn is inversely proportional to the integration time of a lock-in measurement. Only that portion of the averaged profiles corresponding to the frequency domain of the Doppler broadened ***F***=3 ground state transition of ^{85}Rb that was utilized in the simulations illustrated in Figures 3.35 and 3.36 has been plotted in Figure 3.38.

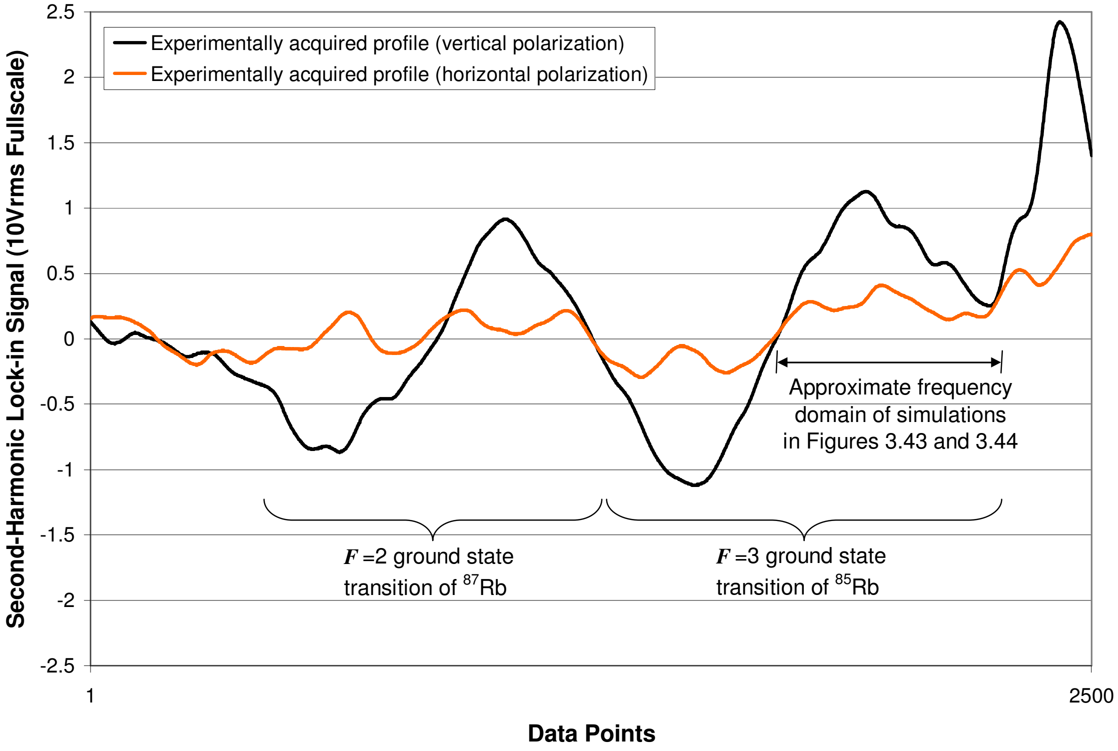

*Figure 3.37 **1f**-profiles corresponding to the Doppler broadened **F**=2 and **F**=3 ground state transitions in the D_2-line of ^{87}Rb and ^{85}Rb, respectively, detected utilizing frequency modulated molecular Rayleigh scattering collected from a probe volume of static air at lab temperature and standard pressure using vertically and horizontally polarized probe laser light*

Also plotted in Figure 3.38 is a **1*f***-profile simulation corresponding to the ***F***=3 ground state transition in the D_2-line of ^{85}Rb. With the exception of the PMT supply voltage this simulated profile was, like the spectrally broadened harmonic profile simulations illustrated in Figures 3.35 and 3.36, calculated using the instrumental parameters outlined in Table 3.7; A PMT supply voltage of V_{PMT}=1050 V was utilized in the simulation illustrated in Figure 3.38. A Doppler broadened Rayleigh scattered power spectrum was assumed in the simulation and contributions from the ***F***=2 ground state transition of ^{87}Rb were neglected.

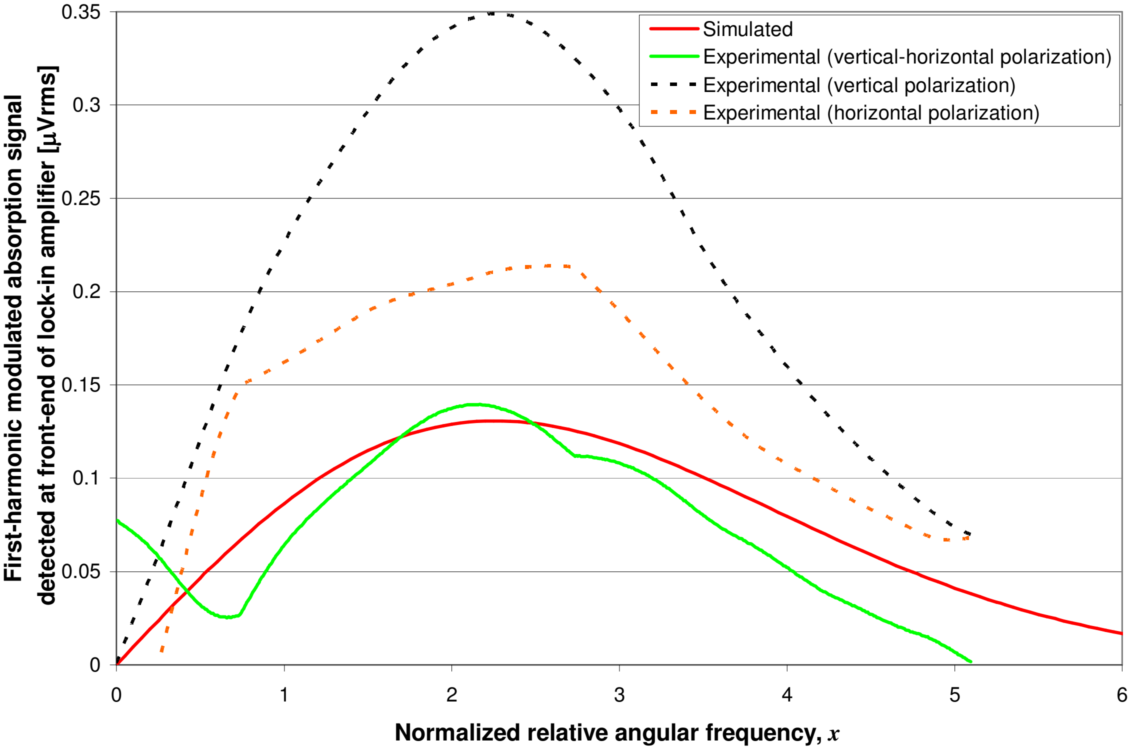

Figure 3.38 Experimentally acquired ***1f****-profiles corresponding to the Doppler broadened* ***F****=3 ground state transition of* ^{85}*Rb versus comparable spectrally broadened 1f-profile simulation*

As mentioned above, stray reflections collected in the scattering arm while acquiring the harmonic profiles illustrated in Figure 3.37 contributed to the detected lock-in signal. The spectrally broadened **1*f***-profile simulation plotted in Figure 3.38 only models the optical frequency-dependent first-harmonic lock-in signal detected from collected Rayleigh scattering, however, and does not include contributions from collected stray reflections. Fortunately, the contributions from stray reflections to the detected lock-in signal is insensitive to the probe laser polarization and the Rayleigh scattered power collected with horizontally polarized light is much less than the scattered power collected with vertically polarized light. Therefore, simply subtracting the lock-in signal detected with horizontally polarized light from the lock-in signal detected with vertically polarized light provides a reasonably accurate measure of the lock-in signal detected from Rayleigh scattering using vertically polarized light in the probe volume. The difference between the averaged **1*f***-profiles acquired using vertically polarized light in the probe volume and the averaged **1*f***-profiles acquired using horizontally polarized light has been plotted in Figure 3.38 for comparison to the theoretical **1*f***-profile. The comparison is surprisingly favorable.

Based on Figure 3.38 I am confident making the following claim: The first- and second-harmonic profile simulations developed in this section that account for the thermal broadening of the radiation collected during preliminary MFRS experiments utilizing molecular Rayleigh scattering from air are reasonably accurate models of the first- and second-harmonic calibration profiles that would have been measured in the absence of any noise during those experiments. Of course, noise is present in every measurement and must be accounted for when sizing up an experiment. We will consider the noise sources that corrupted preliminary MFRS measurements in the next section.

3.5 Noise

In this section we turn our attention to the noise sources that corrupt homodyne detection of a modulated absorption signal utilizing a photomultiplier tube (PMT) and a lock-in amplifier. The noise components accounted for in the following discussion are shot noise, Johnson noise, residual amplitude modulation (RAM) noise, and laser excess noise. The SR830 digital lock-in amplifier utilized during all preliminary MFRS measurements in the scattering arm has a manufacture specified RMS input noise of $6\,\mathrm{nVrms}/\sqrt{\mathrm{Hz}}$. I will include this lock-in amplifier input noise in the signal-to-noise calculations that conclude this chapter. The flicker noise generated by the shunt resistor attached to the front-end of the lock-in amplifier is, even for the worst case of a carbon-composition resistor, about two-orders-of-magnitude less than the Johnson noise generated by the same resistor at typical operating temperatures. I will therefore neglect flicker noise in the signal-to-noise calculations that conclude this chapter. In addition, the following discussion assumes that the experiment was configured with enough care that capacitive, inductive, and resistive coupling – i.e. ground loops – were avoided and stray reflections collected in the scattering arm during preliminary MFRS experiments were negligible. (The latter assumption is undeniably optimistic. For instance, collected stray reflections accounted for approximately 60% of the first-harmonic modulated absorption signal detected with vertically polarized light in the probe volume – i.e. with the probe laser polarization perpendicular to the direction of the collected scattering – while acquiring that data plotted in Figure 3.38). In other words, the signal-to-noise calculations that conclude this section reflect the best case scenario.

3.5.1 Shot Noise

As discussed in Appendix C, a PMT consists of a photocathode, several intermediate dynode stages, and an anode [105]. Photons that strike the PMT photocathode result in a secondary emission of photoelectrons. The cathode current generated by these photoelectrons, i_K, depends on the power of light incident upon the photocathode, P_K, and the wavelength dependent radiant sensitivity of the photocathode to the incident light, $S_K(\lambda)$. An electric field applied between the PMT cathode and anode accelerates the photoelectrons ejected from the cathode to the first of several dynode stages. Typically, for each electron that hits the dynode several are ejected and accelerated to the next dynode. This electron amplification continues until the electrons are collected by the anode and output to the measurement electronics. The total amplification of the cathode photocurrent is accounted for by the PMT gain, μ, which is a function of the voltage applied across the PMT, V_{PMT}:

$$i_P = \mu i_K = \mu S_K P_K \,. \tag{3.159}$$

Shot noise describes the statistical fluctuations in the secondary emission of photoelectrons from the photocathode and the resulting non-uniformity in electron flow. The root-mean-square (RMS) shot noise, $\boldsymbol{i_K}|_{\mathrm{SN}}$, or cathode current noise is defined [106],

$$\boldsymbol{i_K}\big|_{\mathrm{SN}} = \left(2 \cdot e \cdot i_K \cdot B\right)^{1/2} \tag{3.160}$$

where e is the electron charge and B is the equivalent noise bandwidth (ENBW) of the measurement system. (High levels of background noise rejection are possible by implementing homodyne detection utilizing a lock-in amplifier. In this case, the ENBW of the measurement system is established by the low-pass filter internal to the lock-in amplifier. The ENBW for the one-, two-, three-, and four-pole low-pass RC-filters internal to the SR830 lock-in amplifier utilized during preliminary MFRS measurements in the scattering arm are listed in Table A.1 of Appendix A). For PMT detection the cathode current noise in Eq. 3.160 is amplified by the intermediate dynode stages according to Eq. 3.159. The resulting RMS anode current noise, $\boldsymbol{i_P}|_{\mathrm{SN}}$, that corrupts the measurements is,

$$\boldsymbol{i_P}\Big|_{\mathrm{SN}} = \mu(2 \cdot e \cdot i_K \cdot B \cdot NF)^{1/2} = (2 \cdot e \cdot \mu \cdot i_P \cdot B \cdot NF)^{1/2}. \qquad (3.161)$$

The noise factor, $NF > 1$, accounts for the fact that the PMT gain, μ, exhibits fluctuations due to statistical fluctuations in the secondary emission of electrons from the intermediate dynode stages [106]. For a PMT with n dynode stages the noise factor can be calculated from,

$$NF = \frac{1}{\alpha}\left(1 + \frac{1}{\delta_1} + \frac{1}{\delta_1\delta_2} + \ldots + \frac{1}{\delta_1\delta_2\ldots\delta_n}\right), \qquad (3.162)$$

where α is the PMT collection efficiency and δ_i is the secondary-emission ratio for the i$^{\text{th}}$-dynode – i.e. for each electron incident on the i$^{\text{th}}$-dynode δ_i electrons are ejected. As discussed in Appendix C, the socket assembly used to interface the PMT voltage supply and detection electronics to the R636-10 PMT utilized during all preliminary MFRS experiments has a built-in voltage divider that equally distributes the PMT supply voltage between the nine dynodes within the R636-10 PMT [105]. In this case, the secondary emission ratio from each dynode is the same, $\delta_i = \delta$, and the noise factor described by Eq. 3.162 can be approximated with the following expression:

$$NF \cong \frac{1}{\alpha}\left(\frac{\delta}{\delta - 1}\right). \qquad (3.163)$$

There are five sources of shot noise that corrupt MFRS measurements utilizing a PMT: shot noise due to the signal measured (including amplitude modulation), shot noise due to contributions from amplified spontaneous emissions (ASE) to the signal measured, shot noise due to PMT dark current, shot noise due to collected and detected ambient background radiation, and shot noise due to collected and detected stray reflections. I will include stray reflections in the analysis below but, as mentioned above, we will neglect stray reflections in the calculations that conclude this section.

To begin, let us consider the shot noise arising from the frequency modulated Rayleigh scattered light collected and detected in the scattering arm during preliminary MFRS measurements. Referring to Eq. 3.159 and Eq. 3.33 (in Section 3.2) we find that the mean anode current, i_o, output from the PMT in the scattering arm as a result of collected and detected frequency modulated Rayleigh scattered light is,

$$i_o = \mu S_K \eta P_{coll} = \mu S_K \eta \cdot N_o P_o \ell_{eff} \frac{4\pi^3}{3\lambda^4}\left(\frac{n-1}{N}\right)^2 \cdot \\ \left\{4 - 3\cos\left[\arctan\left(\frac{1}{2F_\#}\right)\right] - \cos^3\left[\arctan\left(\frac{1}{2F_\#}\right)\right]\right\} \tag{3.164}$$

where η is the collection efficiency, N_o is the number density of scattering molecules in the probe volume, P_o is the frequency modulated mean probe laser power, ℓ_{eff} is the effective spatial resolution of the measurement along the propagation direction of the probe laser beam, N is a reference number density associated with index of refraction, n, of air at a probe laser wavelength, λ, and $F_\#$ is the collection F-number. Eq. 3.164 describes the PMT anode current signal detected in the absence of absorption or frequency modulation. To be completely rigorous, the signal-to-noise calculations that conclude this chapter must account for absorption and frequency modulation. Scanning the optical frequency of the probe laser beam through an absorption feature in the D_2-line of Rb results in an optical frequency dependent attenuation of the collected Rayleigh scattered light upon passage through the Rb vapor filter in the scattering arm of the MFRS velocimeter and modulating the optical frequency of the probe laser beam results in an amplitude modulation that contributes to the detected PMT anode current. The PMT anode current detected in the presence of absorption and frequency modulation is,

$$\begin{aligned} i_{\text{SIGNAL}}(\omega) &= i_o\left[1 + M\sin(\omega_m t + \psi)\right]\left[1 + M\sin(\omega_m t + \psi)\right]^* \exp\left[-\alpha(\omega)z\right] \\ &= i_o\left[1 + 2M\sin(\omega_m t + \psi) + M^2\sin^2(\omega_m t + \psi)\right]\exp\left[-\alpha(\omega)z\right] \end{aligned} \tag{3.165}$$

where M is the amplitude modulation index, ψ is the phase difference between the amplitude modulation and the frequency modulation, ω_m is the modulation frequency, α is absorption constant, and z is the propagation distance of the collected frequency modulated Rayleigh scattered light through the Rb vapor cell in the scattering arm. (Eq. 3.165 follows from Eqs. E.7 and E.28 in Appendix E). Noting that,

$$\left\langle \sin x \right\rangle_\tau = \frac{1}{\tau}\int_{t-\tau/2}^{t+\tau/2} \sin x \, \mathrm{d}x \xrightarrow{\tau>>1} 0 \tag{3.166a}$$

$$\left\langle \sin^2 x \right\rangle_\tau = \frac{1}{\tau}\int_{t-\tau/2}^{t+\tau/2} \sin^2 x \, \mathrm{d}x \xrightarrow{\tau>>1} \frac{1}{2}, \tag{3.166b}$$

then from Eq. 3.165 we see that for typical measurement integration times, $\tau >> 2\pi/\omega_m$, the mean anode current detected in the scattering arm is simply,

$$\langle i_{\text{SIGNAL}} \rangle_{\tau} \xrightarrow{\tau >> 2\pi/\omega_m} i_o \left(1 + \frac{M^2}{2}\right) \exp(-\alpha z) \tag{3.167}$$

and from Eq. 3.161 we find that the RMS anode current noise arising from the frequency modulated Rayleigh scattered light collected and detected in the scattering arm during preliminary MFRS measurements is,

$$\boldsymbol{i}_{\text{SIGNAL}}(\omega) = \left\{ 2 \cdot e \cdot \mu \cdot i_o \left(1 + \frac{M^2}{2}\right) \exp[-\alpha(\omega) z] \cdot B \cdot NF \right\}^{1/2} \tag{3.168}$$

In the discussion above, the parameter P_o was defined as the frequency modulated mean probe laser power. There is an additional component to the probe laser power that increases the shot noise while contributing nothing to the detected modulated absorption signal - amplified spontaneous emissions (ASE). The master oscillator power amplifier (MOPA) laser system utilized during all preliminary frequency-locked MFRS experiments consists of a master oscillator – i.e. the Littrow laser cavity – and a power amplifier – i.e. an anti-reflection coated broad area diode laser (AR-coated BAL). The output from the Littrow laser cavity is coupled into the BAL junction, is amplified within the junction, and passes back out of the junction. In addition to this amplified output beam, ASE is also emitted from the BAL junction. Whereas the amplified output beam from the BAL spectrally tracks the Littrow laser beam and was ultimately used to interrogate the probe volume during preliminary frequency-locked MFRS measurements, ASE is a broadband emission from the AR-coated BAL that only served to increase the shot noise of those measurements.

The RMS anode current noise that results from Rayleigh scattered ASE collected during preliminary MFRS measurements is,

$$\boldsymbol{i}_{\text{ASE}} = \{2 \cdot e \cdot \mu \cdot i_{\text{ASE}} \cdot B \cdot NF\}^{1/2} \tag{3.169}$$

where,

$$i_{\text{ASE}} = \mu S_K \eta N_o P_{ASE} \ell_{eff} \frac{4\pi^3}{3\lambda^4} \left(\frac{n-1}{N}\right)^2 \left\{ 4 - 3\cos\left[\arctan\left(1/2F_{\#}\right)\right] - \cos^3\left[\arctan\left(1/2F_{\#}\right)\right] \right\} \tag{3.170}$$

and P_{ASE} is the contribution from ASE to the total probe laser power, $P_{PROBE}=P_o+P_{ASE}$. Comparing Eq. 3.169 to Eq. 3.168 we see that there is no optical frequency dependence to the ASE induced shot noise – i.e. ASE is broadband – and amplitude modulation does not contribute to the ASE induced shot noise – i.e. ASE does not spectrally track the Littrow laser cavity.

The RMS anode current noise that results from collected and detected background radiation is,

$$\boldsymbol{i}_{\text{BACK}} = \{2 \cdot e \cdot \mu \cdot i_{\text{BACK}} \cdot B \cdot NF\}^{1/2} \tag{3.171}$$

where i_{BACK} is the mean anode current output from the PMT as a result of collected and detected background radiation. Similarly, the RMS anode current noise that results from the PMT dark current is,

$$\boldsymbol{i}_{\text{DARK}} = \{2 \cdot e \cdot \mu \cdot i_{\text{DARK}} \cdot B \cdot NF\}^{1/2} \tag{3.172}$$

where i_{DARK} is the mean PMT anode dark current resulting from the thermionic emission of electrons from the photocathode. Finally, the RMS anode current noise that results from collected and detected stray reflections is,

$$\boldsymbol{i}_{\text{STRAY}}(\omega) = \{2 \cdot e \cdot \mu \cdot i_{\text{STRAY}} \exp[-\alpha(\omega)z] \cdot B \cdot NF\}^{1/2} \tag{3.173}$$

where i_{STRAY} is the mean PMT anode current resulting from collected stray reflections detected outside the bandwidth of an absorption feature. Notice that scanning the optical frequency of the probe laser beam through an absorption feature in the D_2-line of Rb results in an optical frequency dependent attenuation of the collected stray reflections upon passage through the Rb vapor filter in the scattering arm of the MFRS velocimeter. This effect has been accounted for in Eq. 3.173.

Combining Eqs. 3.168, 3.169, 3.171, 3.172, and 3.173 and noting that the squared amplitudes of uncorrelated noise sources – e.g. shot noise – add we find that the shot noise that corrupts MFRS measurements utilizing a PMT is,

$$\boldsymbol{i}_{\text{SN}}(\omega) = \sqrt{2 \cdot e \cdot \mu \cdot B \cdot NF \cdot \left\{ \left[i_o \left(1 + \frac{M^2}{2} \right) + i_{\text{STRAY}} \right] \exp(-\alpha z) + i_{\text{ASE}} + i_{\text{BACK}} + i_{\text{DARK}} \right\}} \tag{3.174}$$

or alternatively,

$$\boldsymbol{V}_{\text{SN}}(\omega) = R_L \sqrt{2 \cdot e \cdot \mu \cdot B \cdot NF \cdot \left\{ \left[i_o \left(1 + \frac{M^2}{2} \right) + i_{\text{STRAY}} \right] \exp(-\alpha z) + i_{\text{ASE}} + i_{\text{BACK}} + i_{\text{DARK}} \right\}} \tag{3.175}$$

where R_L is the shunt resistance at the front-end of the lock-in amplifier.

3.5.2 Johnson Noise

Johnson noise results from thermal fluctuations in the electron density within a resistor, and gives rise to an open-circuit RMS noise current. The shunt resistor, R_L, attached to the front-end of the lock-in amplifier during preliminary MFRS measurements generates an RMS Johnson noise current [105],

$$\boldsymbol{i}_{\mathrm{JN}} = \sqrt{\frac{4kT_{eff}B}{R_L}} \tag{3.176}$$

or alternatively,

$$\boldsymbol{V}_{\mathrm{JN}} = \sqrt{4R_L kT_{eff}B} \tag{3.177}$$

where k is Boltzmann's constant and T_{eff} is the effective temperature of the load resistor.

3.5.3 RAM-Induced Noise

Referring to Eq. 3.175 we see that the amplitude modulation (AM) accompanying frequency modulation (FM) increases the shot noise in the measured signal. In addition, residual amplitude modulation (RAM) contributes an independent noise term to MFRS measurements that is associated with variations in the collected Rayleigh scattered power. The RAM-induced lock-in signal,

$$S_l^{\mathrm{n}}\Big|_{\mathrm{RAM}} = \sqrt{2}i_o R_L G R^{\mathrm{n}}(M) \tag{3.178}$$

where G is the lock-in amplifier gain and the amplitude modulation functions $R^{\mathrm{n}}(M)$ for first- and second-harmonic lock-in detection are,

$$R^1(M) = M\sin(\theta - \psi), \tag{3.179a}$$

and,

$$R^2(M) = \frac{M^2}{4}\cos(\theta - 2\psi + \pi). \tag{3.179b}$$

(Refer to Appendix E for a derivation of Eqs. 3.178 and 3.179). Noting from Eq. 3.164 that the mean frequency modulated anode output current detected by the PMT in the scattering arm, i_o, is proportional to the frequency modulated Rayleigh scattered power collected in the scattering arm, P_{coll}, then from Eq. 3.178 we find that,

$$S_l^{\mathrm{n}}\Big|_{\mathrm{RAM}} \propto \sqrt{2}P_{coll}R_L G R^{\mathrm{n}}(M) \tag{3.180}$$

or,

$$\left\langle S_l^{\mathrm{n}}\Big|_{\mathrm{RAM}}\right\rangle + \Delta S_l^{\mathrm{n}}\Big|_{\mathrm{RAM}} \propto \sqrt{2}R_L G R^{\mathrm{n}}(M)\left[\langle P_{coll}\rangle + \Delta P_{coll}\right] \tag{3.181}$$

where $\left\langle S_l^{\mathrm{n}}\Big|_{\mathrm{RAM}}\right\rangle$ and $\langle P_{coll}\rangle$ are the mean RAM-induced lock-in signal and the mean frequency modulated power collected in the scattering arm and $\Delta S_l^{\mathrm{n}}|_{\mathrm{RAM}}$ is the deviation in the RAM-induced lock-in signal from the mean as a result of a deviation ΔP_{coll} in the collected frequency modulated Rayleigh scattered power from the mean,

$$\Delta S_l^{\mathrm{n}}\Big|_{\mathrm{RAM}} \propto \sqrt{2}R_L G R^{\mathrm{n}}(M)\left\langle(\Delta P_{coll})^2\right\rangle^{1/2} = \sqrt{2}R_L G R^{\mathrm{n}}(M)\sigma_{coll} \tag{3.182}$$

(Note that $R^{\mathrm{n}}(M)$ accounts for the deviation from $\langle P_{coll}\rangle$ associated with the frequency modulation; i.e. the FM induced AM is included in $R^{\mathrm{n}}(M)$. The ΔP_{coll} term in Eq. 3.182 is a deviation in the collected power resulting from variations in the number density of scattering molecules and from variations in the probe laser power not specifically associated with the FM). In Eq. 3.182, σ_{coll} is the standard deviation in the collected frequency modulated Rayleigh scattered power within the equivalent noise bandwidth (ENBW) of the lock-in amplifier. For MFRS measurements, fluctuations in collected Rayleigh scattered power can arise from fluctuations in the number density of scattering molecules in the probe volume or from fluctuations in the probe laser power. Combining Eqs. 3.164 and 3.182 we find that the RAM-induced noise current that corrupts measurements in the scattering arm of the MFRS velocimeter is,

$$\begin{aligned}\boldsymbol{i}^{\mathrm{n}}_{\mathrm{RAM}} = \sqrt{2}G R^{\mathrm{n}}(M)\mu S_K \eta \ell_{eff}\,\frac{4\pi^3}{3\lambda^4}\left(\frac{n-1}{N}\right)^2 \cdot \\ \left\{4 - 3\cos\left[\arctan\left(\tfrac{1}{2F_\#}\right)\right] - \cos^3\left[\arctan\left(\tfrac{1}{2F_\#}\right)\right]\right\}\sigma_{N_{PROBE}}\sigma_{P_o}\end{aligned} \tag{3.183}$$

or alternatively,

$$\begin{aligned}\boldsymbol{V}^{\mathrm{n}}_{\mathrm{RAM}} = \sqrt{2}R_L G R^{\mathrm{n}}(M)\mu S_K \eta \ell_{eff}\,\frac{4\pi^3}{3\lambda^4}\left(\frac{n-1}{N}\right)^2 \cdot \\ \left\{4 - 3\cos\left[\arctan\left(\tfrac{1}{2F_\#}\right)\right] - \cos^3\left[\arctan\left(\tfrac{1}{2F_\#}\right)\right]\right\}\sigma_{N_{PROBE}}\sigma_{P_o}\end{aligned} \tag{3.184}$$

where $\sigma_{N_{PROBE}}$ and σ_{P_o} represent the standard deviation in the number density of molecules within the probe volume and the standard deviation in the frequency modulated probe laser power, respectively, within the ENBW of the lock-in amplifier.

3.5.4 Laser Excess Noise

Whereas shot noise and Johnson noise are broadband, Gaussian, white noise components, laser excess noise is pink noise; i.e. it approximately has a 1/*f*-spectrum [3,107]. Specifically, laser excess noise is described by the following expression when employing PMT detection of the MFRS signal:

$$\boldsymbol{i}_{\mathrm{EX}} = \mu S_K \eta N_o \ell_{eff} \frac{4\pi^3}{3\lambda^4}\left(\frac{n-1}{N}\right)^2 \cdot \left\{4-3\cos\left[\arctan\left(\frac{1}{2F_\#}\right)\right]-\cos^3\left[\arctan\left(\frac{1}{2F_\#}\right)\right]\right\}\sqrt{\frac{2\pi B}{\omega_m^b}}\sigma_{\mathrm{EX}} \tag{3.185}$$

Joel Silver has pointed out that the modulation frequency exponent, *b*, generally ranges from 0.8-1.5 [100]. The parameter σ_{EX} is defined as the laser excess noise within a 1 Hz frequency bandwidth at a frequency of 1 Hz.

Eq. 3.185 clearly shows that homodyne detection at high modulation frequencies has the distinct advantage that laser excess noise is minimized. In particular, there is a general consensus in the literature that laser excess noise is negligible at modulation frequencies $f_m = \frac{\omega_m}{2\pi} > 100\,\mathrm{MHz}$. Preliminary measurements made in the scattering arm with the MFRS technique were far from this limit – e.g. all preliminary frequency-locked MFRS measurements employed a modulation frequency of f_m = 2.090 kHz – so laser excess noise should not be neglected in the signal-to-noise (S/N) analysis. However, calculations indicate that the laser excess noise was ~10^{-2} the shot noise during preliminary frequency-locked measurements. In addition, the broadband noise in the MOPA laser output was not measured before it failed; i.e. it is impossible for me to quantitatively define the laser excess noise detected during preliminary MFRS measurements. I will therefore neglect laser excess noise in the calculations that conclude this chapter.

3.6 Theoretical Signal-to-Noise Ratio of Preliminary MFRS Measurements

Table 3.7 of Section 3.4 provides a summary of the instrumental parameters recorded during preliminary frequency-locked MFRS experiments and used in the signal-to-noise calculations presented below. The first- and second-harmonic profiles plotted in Figures 3.35 and 3.36 that account for the spectrally broadened Rayleigh scattered radiation were derived using these instrumental parameters and realistically represent the lock-in signals detected utilizing molecular Rayleigh scattering from air during preliminary MFRS experiments while slowly sweeping the probe laser frequency across the ***F***=3 ground state transition of ^{85}Rb – i.e while acquiring the calibration profiles utilized during frequency-locked velocity measurements. The noise detected during preliminary MFRS experiments follows from the discussion in Section 3.5 and will be considered in the following paragraphs.

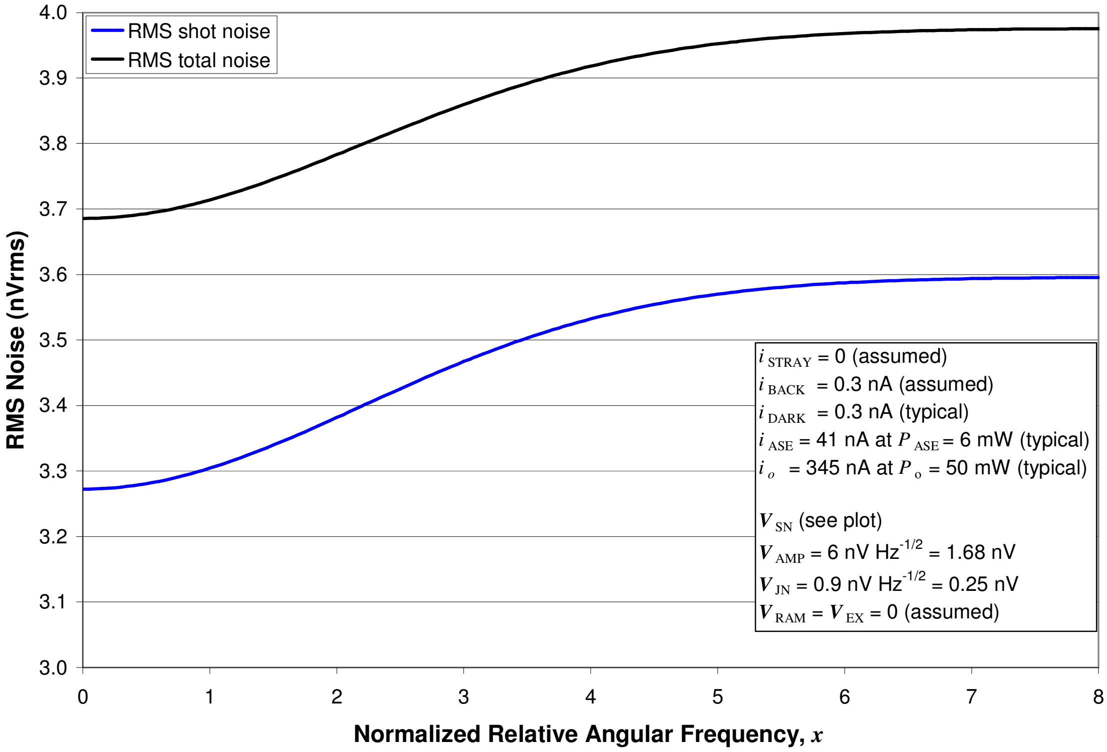

Figure 3.39 RMS noise detected in the scattering arm during preliminary frequency-locked MFRS measurements utilizing molecular Rayleigh scattering from air

Let us first consider the shot noise that corrupted preliminary frequency-locked measurements. Figure 3.39 shows a plot of the theoretical RMS shot noise detected during preliminary MFRS measurements utilizing molecular Rayleigh scattering from air as a function of normalized relative angular frequency,

$$x = \frac{\omega - \omega_o}{\delta\omega_{1/2}}, \tag{3.186}$$

where ω_o and $\delta\omega_{1/2}$ are the centerline angular frequency and Doppler half-width of the $\boldsymbol{F}$=3 ground state transition of ^{85}Rb, respectively. The theoretical RMS shot noise was calculated from Eq. 3.175.

From Table A.1 in Appendix A we find that employing the four-pole RC-filter internal to the SR830 digital lock-in limits the equivalent noise bandwidth to,

$$B = \frac{5}{64\tau_L} = 0.078\,\text{Hz} \tag{3.187}$$

when employing a lock-in integration time of τ_L=1 s. From Appendix C and Eq. 3.163 we find that the R636-10 PMT exhibits a gain of $\mu = 3.5\times10^5$ and a noise factor of $NF \approx 1.54$ at a PMT supply voltage of $V_{PMT} = 1200$ V. A mean PMT dark current of i_{DARK}=0.3 nA at a PMT supply voltage of V_{PMT}=1200 V is typical for the R636-10 PMT and was assumed in the calculation. A mean PMT anode current of only $i_{\text{BACK}} = 0.3$ nA resulting from collected and detected ambient background radiation was also assumed in the calculation and collected and detected stray reflections were completely neglected (i.e. $i_{\text{STRAY}} = 0$). The mean anode current, $i_{\text{ASE}} = 41$ nA, output from the PMT in the scattering arm as a result of collected and detected Rayleigh scattered amplified spontaneous emissions (ASE) was calculated from Eq. 3.170, where it was assumed that ASE contributes $P_{ASE} = 6$ mW of power to a total probe laser power of $P_{PROBE} = P_o + P_{ASE} = 56$ mW. (ASE typically accounted for approximately 10% of the total probe laser power during preliminary MFRS experiments). The mean anode current, $i_o = 345$ nA, output from the PMT in the scattering arm as a result of collected and detected frequency modulated Rayleigh scattered light was calculated from Eq. 3.164, where it was assumed that a frequency modulated amplified output power of $P_o = 50$ mW contributes to the total probe laser power.

The attenuation of this frequency modulated Rayleigh scattered light upon passage through the Rb vapor filter in the scattering arm was incorporated into the calculated RMS shot noise according to Eq. 3.175. The spectral broadening of the Rayleigh scattered radiation was also incorporated into the calculation, as it was into the simulated harmonic profiles, by neglecting acoustic broadening and assuming that the Rayleigh scattered power spectrum is described by a normalized Gaussian lineshape function. Specifically, the frequency dependent RMS shot noise resulting from collected and detected frequency modulated Rayleigh scattered light was calculated as follows,

$$\boldsymbol{i}_{\mathrm{SIGNAL}}(\omega) = \left\{ 2 \cdot e \cdot \mu \cdot i_o(\omega) \left(1 + \frac{M^2}{2} \right) \cdot B \cdot NF \right\}^{1/2}, \tag{3.188}$$

where,

$$i_o(\omega) = \sum_{\omega' = -\omega_{\mathrm{cutoff}}}^{\omega_{\mathrm{cutoff}}} i_o f(\omega') \exp[-\alpha(\omega') z] \mathrm{d}\omega' \tag{3.189}$$

The absorption constant in Eq. 3.189 follows from our heuristic model of Doppler broadened $\boldsymbol{F}$=3 ground state transition of ^{85}Rb described by Eq. 3.105.

Referring again to Figure 3.39 we find a listing of the other noise components that corrupted preliminary frequency-locked MFRS experiments and that were incorporated into the signal-to-noise calculations that follow, and a plot of the total theoretical RMS noise detected during preliminary MFRS measurements,

$$\boldsymbol{V}_{\mathrm{TOTAL}} = \sqrt{\boldsymbol{V}_{\mathrm{SN}}{}^2 + \boldsymbol{V}_{\mathrm{AMP}}{}^2 + \boldsymbol{V}_{\mathrm{JN}}{}^2 + \boldsymbol{V}_{\mathrm{RAM}}{}^2 + \boldsymbol{V}_{\mathrm{EX}}{}^2} \tag{3.190}$$

Amplitude modulation and laser excess noise were completely neglected in the following signal-to-noise calculations. The lock-in amplifier input noise and Johnson noise were not. The SR830 digital lock-in amplifier in the scattering arm has a manufacture specified RMS input noise of $\boldsymbol{V}_{\mathrm{AMP}} = 6\,\mathrm{nVrms}\big/\sqrt{B}$. The Johnson noise generated by the shunt resistor attached to the input of each lock-in amplifier, $\boldsymbol{V}_{\mathrm{JN}} = 0.9\,\mathrm{nVrms}\big/\sqrt{B}$, was calculated from Eq. 3.177 by assuming that the effective temperature of each resistor was simply the lab temperature – i.e. $T_{eff} = T_{air}$.

The theoretical first-harmonic RMS lock-in signal-to-RMS noise ratio and the theoretical second-harmonic RMS lock-in signal-to-RMS noise ratio are both plotted in Figure 3.40 as a function of normalized angular frequency. The first-harmonic signal-to-noise ratio was calculated by dividing the spectrally broadened **1*f***-profile plotted in Figure 3.35 by the total RMS noise plotted in Figure 3.39 and simulates the **1*f***-signal-to-noise detected with a τ_L = 1 s lock-in integration time during preliminary frequency-locked MFRS experiments in static air while slowly sweeping the modulating optical frequency of the probe laser beam across half of the Doppler broadened $\boldsymbol{F}$=3 ground state transition of ^{85}Rb. The simulated **1*f***-signal-to-noise profile predicts a maximum signal-to-noise ratio for first-harmonic detection of $\mathrm{S/N_{max}}|_{\boldsymbol{1f}}$ = 79 at a normalized relative angular frequency of $x = 2.20$, with the signal-to-noise only dropping into the single digits near the center of the Doppler broadened absorption feature ($x = 0$) and in the wings of the **1*f***-profile ($x > 6$). Based on the simulated **1*f***-signal-to-noise profile plotted in Figure 3.40, measuring a reliable, repeatable **1*f***-profile with a $\tau_L = 1$ s lock-in integration time and the MFRS configured as it was during preliminary experimentation appears to be theoretically possible. The measurements will be noisy at the zero-crossing and in the wings of the **1*f***-profile, but assuming that a S/N>10 is sufficient we could expect to acquire reliable, repeatable **1*f***-profiles in the normalized angular frequency range $x \approx [0.2:6.0]$. For the MFRS velocimeter as it was configured during preliminary frequency-locked measurements this corresponds to a velocity range of V≈[30 m/s:830 m/s].

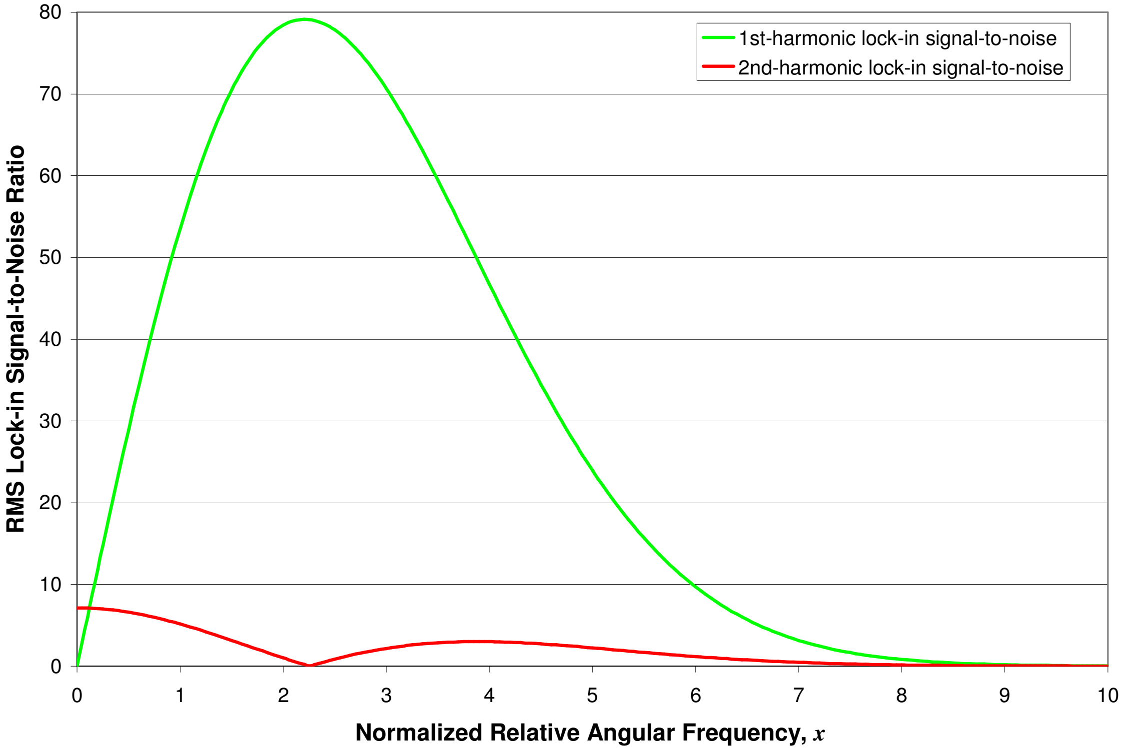

*Figure 3.40 Theoretical 1^{st}- and 2^{nd}- harmonic lock-in signal-to-noise detected with a τ_L=1 s lock-in integration time during preliminary MFRS measurements in static air while sweeping the modulating probe laser frequency across half of the **F**=3 ground state transition of ^{85}Rb*

The second-harmonic signal-to-noise ratio plotted in Figure 3.40 was calculated by dividing the spectrally broadened **2*f***-profile plotted in Figure 3.36 by the total RMS noise plotted in Figure

3.39 and simulates the **2*f***-signal-to-noise detected with a τ_L = 1 s lock-in integration time during preliminary MFRS experiments in static air while slowly sweeping the modulating optical frequency of the probe laser beam across half of the Doppler broadened ***F***=3 ground state transition of ^{85}Rb. The simulated **2*f***-signal-to-noise profile predicts a signal-to-noise in the single digits across the entire **2*f***-profile with a maximum signal-to-noise ratio for second-harmonic detection of only $S/N_{max}|_{2f} = 7$ at a normalized relative angular frequency of $x = 0$, corresponding to the center of the absorption feature. Based on the simulated **2*f***-signal-to-noise profile plotted in Figure 3.40, measuring a reliable, repeatable **2*f***-profile using molecular Rayleigh scattering from air with a lock-in integration time of τ_L = 1 s and the MFRS configured as it was during preliminary experimentation is improbable.

Due to scattering power fluctuations, the simultaneous detection of two different Fourier components of the modulated absorption signal is required to effectively conduct MFRS velocity measurements in the frequency-locked mode of operation. Because peak lock-in signals decrease at higher harmonics, I chose to employ first- and second-harmonic lock-in detection during all preliminary MFRS measurements in the frequency-locked mode of operation. Although I was occasionally able to measure a noisy **1*f***-profile utilizing molecular Rayleigh scattering from air (e.g. the **1*f***-profiles plotted in Figures 3.37 and 3.38), I never successfully measured a **2*f***-profile. All **2*f***-profile measurements in air were completely covered up by noise. Looking at the simulated **2*f***-signal-to-noise profile in Figure 3.40 I'm not surprised. Without a reliable **2*f***-profile I was unable to calculate a calibration profile corresponding to the Doppler broadened ***F***=3 ground state transition of ^{85}Rb that accurately modeled the optical-frequency dependent **1*f*:2*f*** signal detected in air. Without this calibration profile frequency-locked MFRS velocity measurements in air were impossible with the MFRS velocimeter configured as it was during preliminary experiments.

Analysis indicates the signal-to-noise ratio could be substantially improved by increasing the modulation depth and heating the Rb vapor cell in the scattering arm. In Figures 3.41 and 3.42 I have plotted the normalized first- and second-harmonic lock-in signals, $\overline{S}_L^{\,1}$ and $\overline{S}_L^{\,2}$, versus normalized relative angular frequency, x, for a number of modulation indices, m=1.4 - 2.4 (Δm=0.1). The normalized lock-in signals were calculated from Eqs. 3.128 and 3.129, respectively, assuming a Rb cell temperature of T_{Rb}=293.35 K (20.2 °C) and a Rb cell length z=100 mm and simulate the normalized **1*f***- and **2*f***-profiles detected while slowly sweeping across the Doppler broadened ***F***=3 ground state transition of ^{85}Rb. Contributions from the Doppler broadened $\boldsymbol{F}$=2 ground state transition of ^{87}Rb were neglected in the simulation, and a monochromatic, frequency modulating, resonant source was assumed.

From the plotted profiles in Figures 3.41 and 3.42 we find that first-harmonic detection is optimized with a modulation index of $m_{\mathrm{opt},\boldsymbol{1f}}$=1.7 and that second-harmonic detection is optimized with a modulation index of $m_{\mathrm{opt},\boldsymbol{2f}}$=2.3. (Note that the spectral width of the collected Rayleigh scattered radiation very likely affects these optimum modulation indices). At a modulation index of $m_{\mathrm{opt},\boldsymbol{1f}}$=1.7, the peak **1*f***-signal is 60.0% the maximum centerline attenuation through the Doppler broadened feature; i.e. at a Rb cell temperature of T_{Rb}=293.35 K and cell length of z=100 mm, the maximum attenuation at the resonant centerline of the Doppler broadened $\boldsymbol{F}$=3 ground state transition of ^{85}Rb is ~57% whereas the peak excursions in the corresponding normalized **1*f***-profile calculated with m=1.7 are ~±0.34. At a modulation index of $m_{\mathrm{opt},\boldsymbol{2f}}$=2.3, the peak **2*f***-signal is 47.2% the maximum centerline attenuation through the Doppler broadened feature – the peak excursion in the normalized **2*f***-profile is ~0.27 – and the peak **1*f***-signal is 58.4% the maximum centerline attenuation. (These values compare favorably to Joel Silver's predictions: $m_{\mathrm{opt},\boldsymbol{1f}}$=1.6 with a peak **1*f***-signal ~57.4% the maximum attenuation and $m_{\mathrm{opt},\boldsymbol{2f}}$=2.1 with a peak **2*f***-signal ~49.8% the maximum attenuation [100]).

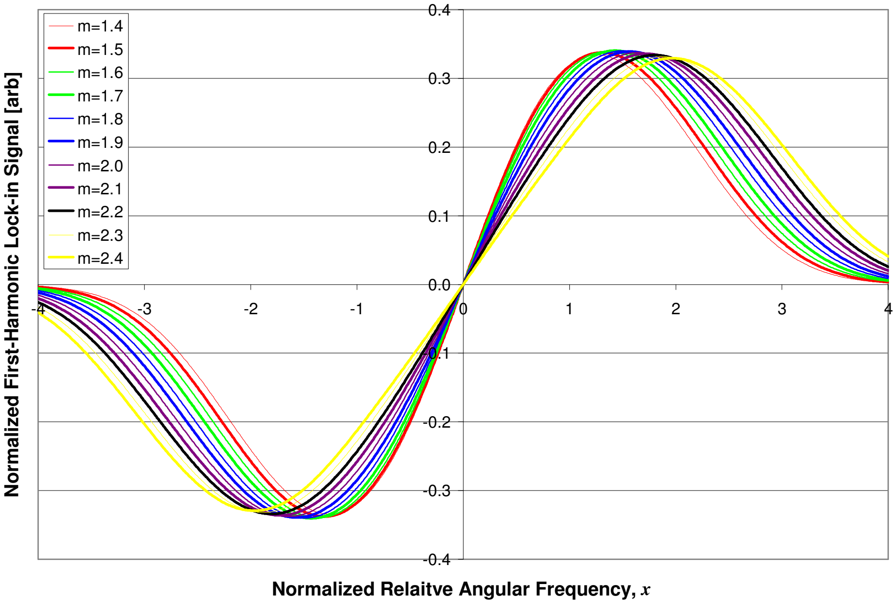

*Figure 3.41 Normalized 1st-harmonic lock-in signals calculated with m=1.4-2.4 and z=100 mm and corresponding to Doppler broadened **F**=3 ground state transition of ^{85}Rb at T_{Rb}=293.35 K*

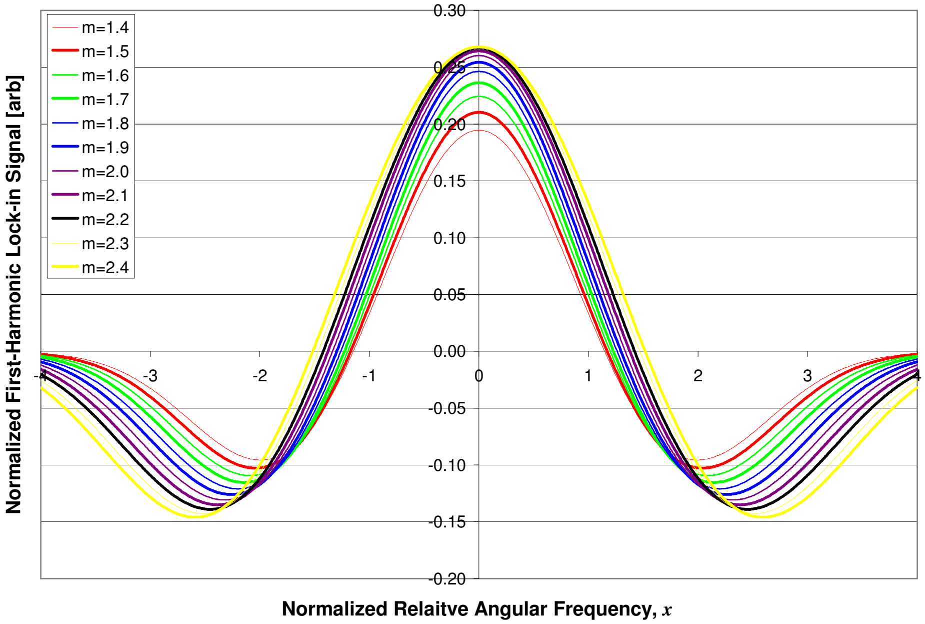

Figure 3.42 Normalized 2^{nd}*-harmonic lock-in signals calculated with m=1.4-2.4 and z=100 mm and corresponding to Doppler broadened* ***F****=3 ground state transition of* ^{85}*Rb at* T_{Rb}*=293.35 K*

Figure 3.43 shows the theoretical first- and second-harmonic lock-in signal-to-noise (S/N) ratio with the modulation index optimized for second harmonic detection, $m = m_{\mathrm{opt},\mathbf{2}f} = 2.3$, and with a Rb cell of length z=100 mm in the scattering arm. With the exception of the modulation index and cell length, the optimized S/N plotted in Figure 3.43 was calculated with exactly the same parameters used to calculate the S/N during preliminary frequency-locked MFRS experiments at the end of Chapter 3 (see Table 3.7). The theoretical S/N during preliminary MFRS experiments – i.e. utilizing a modulation index of m=0.476 and a Rb cell of length z=75 mm in the scattering arm – has been included in Figure 3.43 for comparison.

Based on what I see in Figure 3.43, MFRS velocity measurements in a gas phase flow are theoretically possible with a z=100 mm Rb vapor cell in the scattering arm and a modulation index optimized for second-harmonic detection. By implementing these changes I could expect the peak second-harmonic lock-in signal-to-noise ratio to increase by ~24-times and the peak first-harmonic lock-in signal-to-noise ratio to increase by ~8-times. I had moderate success acquiring a **1*f***-profile utilizing molecular Rayleigh scattering from static room air with the MFRS velocimeter configured as it was during preliminary experimentation (refer back to Figure 3.38). Had I optimized the modulation depth and swapped the Rb vapor cells, my chances of acquiring not only a **1*f***-profile but also a **2*f***-profile from molecular Rayleigh scattering would have substantially improved. I'm not saying that these measurements would have been trivial, but it certainly would have been easier to see past the noise.

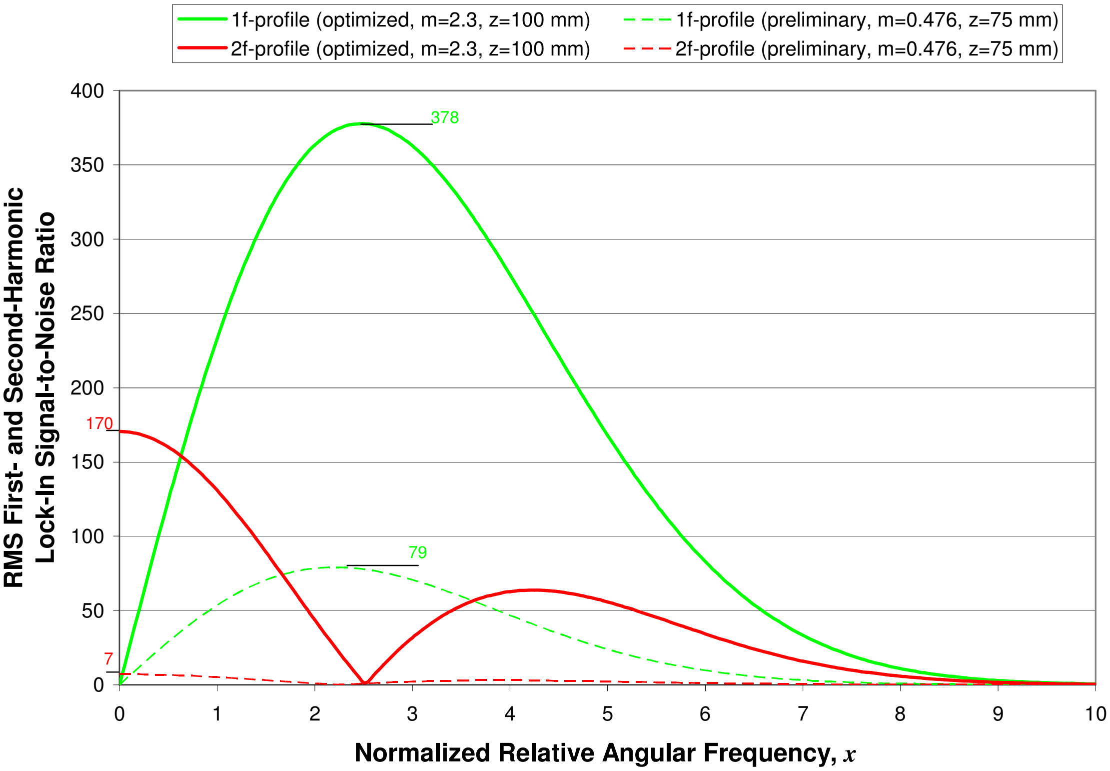

Figure 3.43 Theoretical 1st- and 2nd-harmonic lock-in S/N detected from static room air with the modulation index optimized for second harmonic detection versus the experimentally legitimate modulation index utilized during preliminary frequency-locked measurements

I could have further improved the S/N ratio by heating the Rb vapor cell in the scattering arm of the experiment. Let us consider the theoretical S/N ratio with a cell temperature of T_{Rb}=310 K. Recall that the simulated lock-in signals – such as those in Figure 3.41 and 3.42 – model Beer's law with a third-order Taylor series expansion. At a Rb cell temperature of T_{Rb}=293.35 K and a Rb cell length of z=100 mm, this series expansion of Beer's law overestimates the maximum attenuation at the resonant centerline of the Doppler broadened ***F***=3 ground state transition of ^{85}Rb by ~3%. At T_{Rb}=310 K we would need to expand the Taylor series to tenth-order just to see it converge, and to thirteenth order for it to accurately approximate Beer's law.

To estimate the effect the Rb cell temperature has on the peak first- and second-harmonic lock-in signal-to-noise, recall that with the modulation index optimized for second-harmonic detection, $m_{\text{opt},\boldsymbol{2f}}$=2.3, the peak **2*f***-signal is 47.2% the maximum centerline attenuation through the corresponding Doppler broadened absorption feature and the peak **1*f***-signal is 58.4% the maximum centerline attenuation. At a Rb cell temperature of T_{Rb}=293.35 K, the peak attenuation in the D_2-line is 56.76% at the resonant centerline of the Doppler broadened ***F***=3 ground state transition of ^{85}Rb. (This discussion assumes the vapor cell contains Rb in natural isotopic abundance). At a Rb cell temperature of T_{Rb}=310 K, the peak attenuation is 98.72%. Increasing the Rb cell temperature from T_{Rb}=293.35 K to T_{Rb}=310 K should therefore result in a 74% increase in the peak first-harmonic lock-in signal and a 74% increase in the peak second-harmonic lock-in signal. This translates to an approximate increase of 74% in the peak first- and second-harmonic lock-in signal-to-noise. (The shot noise due to the detected modulated absorption signal and stray reflections should decrease due to the increased absorption at T_{Rb}=310 K. You have to be careful of heat sources in the vicinity of a PMT, however; radiant sources close to a PMT cathode can result in a dramatic increase in thermionic emissions).

Referring to Figure 3.43 and the reasoning above, if I had employed a modulation index optimized for second-harmonic detection, $m_{\text{opt},\boldsymbol{2f}}$=2.3, and a z=100 mm Rb vapor cell heated to T_{Rb}=310 K in the scattering arm during preliminary frequency-locked experiments, I could have expected a peak first-harmonic lock-in signal-to-noise ratio detected from static room air of ~657 and a peak second-harmonic lock-in signal-to-noise ratio of ~296 with a lock-in integration time of τ_L=1 s and an effective spatial resolution of $\ell_{eff} = 3.8$ mm along the probe laser beam.

Minimizing the collection and detection of stray reflections and ambient background radiation is critical to the success of any Rayleigh scattering experiment. The preceeding S/N estimates assume that stray reflections are negligible and that minimal background radiation is collected and detected. If an MFRS experiment can be configured so that this is in fact the case – the detection of ambient background radiation can be minimized by attaching a narrow pass optical filter to the input to the detector, but I feel that stray reflection will always plague MFRS experiments – the shot noise limited signal-to-noise ratio is (essentially) proportional to the square root of the frequency modulating probe laser power, the effective spatial resolution, and the lock-in integration time, S/N$\propto\sqrt{P_o \ell_{eff} \tau_L}$. By utilizing this proportionality, we can estimate the best spatial and temporal resolution that could reasonably be expected during MFRS measurements with P_o=50 mW of frequency modulating laser power in the probe volume, a modulation index optimized for second-harmonic detection, and a z=100 mm Rb vapor cell heated to T_{Rb}=310 K in the scattering arm of the experiment. With this experimental configuration, for instance, one could realistically expect the peak shot noise limited first-harmonic lock-in signal-to-noise ratio detected from static room air to be ~238 and the peak shot noise limited second-harmonic lock-in signal-to-noise ratio detected from static room air to be ~107 when collecting photons from an effective spatial resolution of $\ell_{eff} = 500\,\mu\text{m}$ along the probe laser beam and when employing a lock-in integration time of τ_L=1s (or when employing an effective spatial resolution of $\ell_{eff} = 1\,\text{mm}$ and a lock-in integration time of τ_L=500 ms).

Chapter 4: Practical Implementation of the MFRS Velocimeter

4.1 Introduction

This chapter will discuss the results of two MFRS velocity measurements: One made in a sweep mode of operation and one made in a frequency-locked mode of operation. The feasibility of the MFRS technique was demonstrated in 1998 by making a two-component velocity measurement in a condensing jet of CO_2 utilizing the sweep mode of operation [108,109]. Ambient light collected in the scattering arm during these preliminary MFRS measurements resulted in gain saturation of the photomultiplier tube (PMT), which prevented sufficient amplification of the collected scattered signal. A narrow pass optical filter was subsequently attached to the PMT input, and in 2000 I made velocity measurements in a supersonic expansion using collected scattering from a jet of N_2. In Section 4.2 I will discuss the results of this sweep mode measurement.

Due to its limited temporal resolution, development of the sweep mode of operation was quickly abandoned and development of the frequency-locked mode of operation was taken-up. The frequency-locked mode of operation is an attractive alternative to the sweep mode because its temporal resolution is limited only by the required lock-in time constant. However, successful implementation of the frequency-locked mode of operation is complicated by the need to account for scattering intensity fluctuations and to frequency stabilize the interrogating laser beam. In addition, providing sufficient laser power to the probe volume is a constant concern when conducting Rayleigh scattering experiments. Section 4.3 begins with a discussion of the frequency-locked mode of operation and the steps I took toward its successful implementation. A ratioed detection scheme was developed to normalize out scattering intensity fluctuations, a proportional-integral-differential (PID) controller was designed and built to provide feedback for optical frequency stabilization based on an error signal in the reference arm of the experiment, and an extended-cavity diode laser master oscillator power amplifier (ECDL-MOPA) system was constructed to provide relatively narrow linewidth, frequency tunable, frequency stable probe laser power at 780 nm. I will conclude Section 4.3 and this chapter by discussing the results of some frequency-locked MFRS velocity measurements I made in a condensing jet of CO_2.

The results I will present in this chapter represent my most successful attempts to measure the velocity of an unseeded flow using the MFRS technique. The sweep mode measurements I will present in this chapter have an effective spatial resolution of $\ell_{eff} = 3.8$ mm along the probe laser beam. The spatial resolution of the frequency-locked measurements was $\ell_{eff} = 5$ mm. The sweep mode measurements have a temporal resolution of 10 s, and the frequency-locked measurements have an only slightly improved temporal resolution of 1 s. Finally, though the sweep mode and frequency-locked velocity measurements presented in this chapter were both made in an unseeded flow, both measurements relied on condensate scattering to provide an adequate signal-to-noise: The sweep mode measurements relied on scattering from water vapor entrained into the jet and the frequency-locked measurements relied on scattering from CO_2 condensate.

4.2 The Sweep Mode of Operation

In the sweep mode of operation, the optical frequency of a stand-alone diode laser is tuned relatively slowly across a portion of the D_2-line of Rb by sweeping the injection current of the diode. (A commercially available stand-alone diode laser was utilized during all sweep mode measurements). Detectability of the weak Rayleigh scattered signal is improved by simultaneously dithering the diode frequency (i.e. diode injection current) and implementing homodyne detection using a lock-in amplifier, as discussed in Appendix A. The optical frequency modulation of the probe laser beam is imposed on the Rayleigh scattered light, which is collected from a probe volume in the flow under investigation, transmitted through a Rb vapor cell, and focused onto a PMT in a scattering arm of the experiment. The detected modulated absorption signal is fed to a lock-in amplifier that is synchronized with the function generator driving the rapid frequency modulation, resulting in a sharp, strong, well-understood harmonic absorption profile corresponding to the Rb D_2-line. (Second-harmonic detection was employed during all preliminary sweep mode experiments). To determine the Doppler frequency shift of the scattered radiation, and hence the bulk velocity of the flow under investigation, the ***2f***-profile acquired in the scattering arm is cross-correlated to a ***2f***-profile that is simultaneously acquired from the unscattered laser output in the reference arm of the experiment.

The experimental setup for the MFRS velocimeter operated in the sweep mode of operation is shown in Figure 4.1. A single-mode GaAlAs diode laser (Hitachi HL7851), mounted in a diode laser head (ILX Lightwave LDM-4420), is excited with an ultra-low noise current controller (ILX Lightwave LDX-3620) that is specified to be stable to ≤10 ppm over 10-30 minutes. The temperature of the diode is controlled with a spectroscopic grade thermoelectric temperature controller (ILX Lightwave LDT-5910B) with a long-term stability of less than ±0.01°C. The diode emits approximately P_o=25 mW of power at λ=780 nm (i.e. the center-of-gravity wavelength of the Rb D_2-line) when operated at an injection current of approximately 125 mA and a temperature of approximately -3°C, and has a linear tuning rate of approximately -2.1 GHz/mA. (Dry nitrogen was bled into the laser head to prevent condensation on the diode).

A triangular ramp current signal of amplitude <5 mA is used to scan the optical frequency of the diode laser repetitively across the D_2-line, which covers approximately 10 GHz at Doppler limited resolution, and a sine wave current signal is used to modulate the diode frequency. The optimal modulation depth for implementing second-harmonic modulated absorption spectroscopy is theoretically about 2.2 times the half width at half maximum (HWHM) of the feature being resolved [103]. As discussed in Section 3.3, the Doppler-broadened HWHM of ^{85}Rb is approximately $\delta\nu_T$=256 MHz at room temperature. Therefore, optimal ***2f***-profile resolution is achieved with a modulation current amplitude of ~0.27 mA. The modulation sine wave and triangular sweep are produced by separate function generators (Exact 200MSP and Stanford Research Systems DS345) which are combined in a summing amplifier (Stanford Research Systems SR560) and input to the diode current driver.

The output beam from the diode laser is collimated and a small portion (< 1%) of the beam is split off to a reference arm. This reference beam passes through a 100 mm long room temperature cell containing Rb vapor in natural isotopic abundance (72.2% ^{85}Rb and 27.8% ^{87}Rb) before being recorded by an avalanche photodiode (Hamamatsu C5460). The majority of the laser beam passes to the probe volume. A series of six anti-reflection coated lenses collect the Rayleigh scattered light from the probe volume, relay it through a 75 mm long Rb vapor cell and a ±1 nm narrow-band optical filter with 75% peak transmittance at λ=780 nm (Barr Associates), and focus it onto a side-looking PMT (Hamamatsu R636-10). The PMT is biased at V_{PMT}~1000 V to give good radiant sensitivity while maintaining a linear response.

For these preliminary experiments I chose standard off-the-shelf lenses for the scattering arm optics. The lenses were chosen with the help of OSLO LT freeware, with a design objective of filling the PMT photocathode with high transmission efficiency. This was accomplished by using a combination of positive and negative lenses to balance spherical aberrations introduced by the fast collection optics; $F_\#$~1.2 collection was achieved using a pair of ϕ=100mm diameter, f=120.8

mm focal length plano-convex lenses (Melles Griot LPX215/076). (The Melles Griot product catalog contains a succinct introduction to aberration balancing [110]. A more detailed discussion of spherical aberrations and the Seidel formulas used to describe them can be found in the texts by O'Shea and Malacara *et al.* [111, 112]).

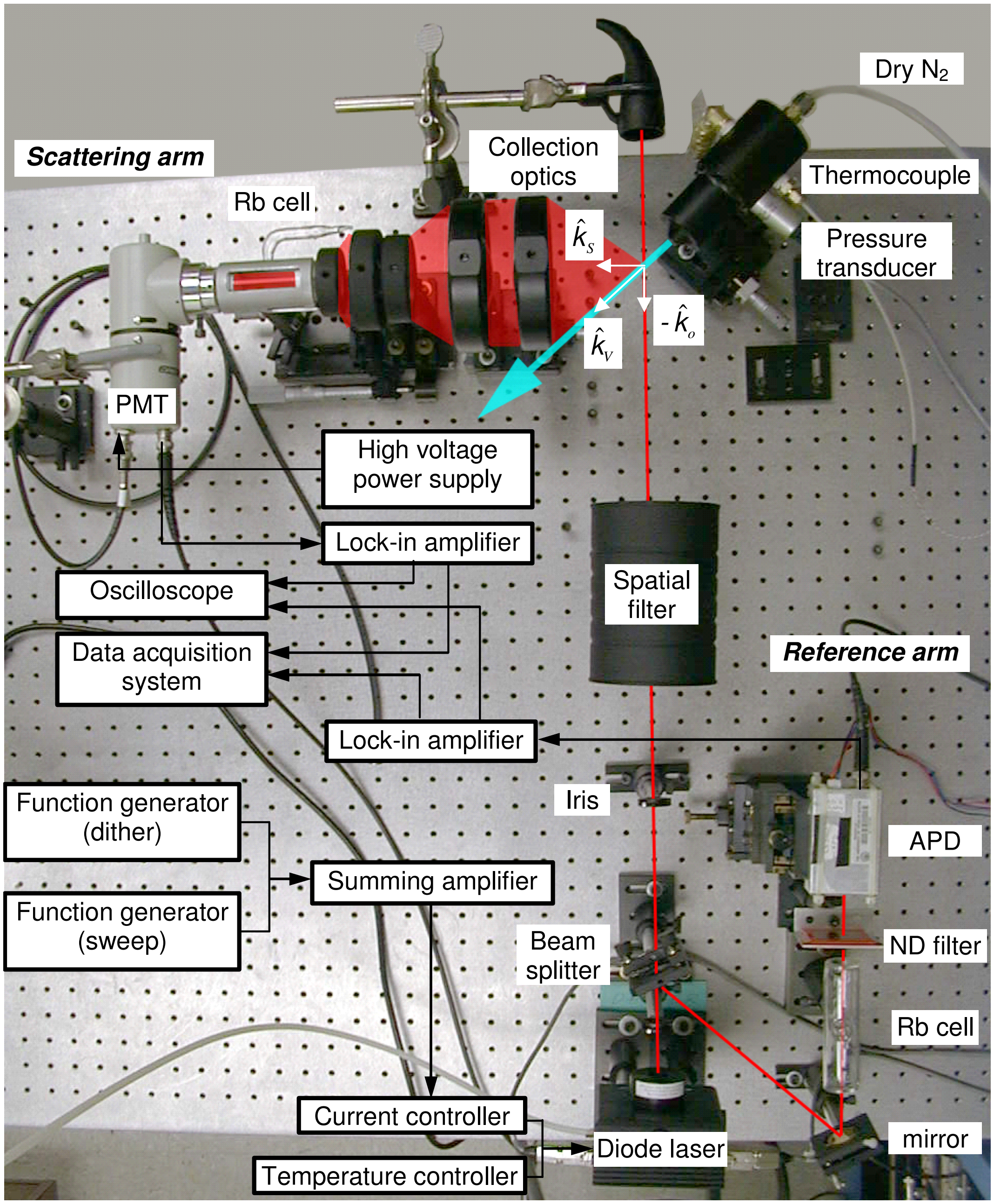

Figure 4.1 Experimental setup for the MFRS velocimeter in the sweep mode of operation

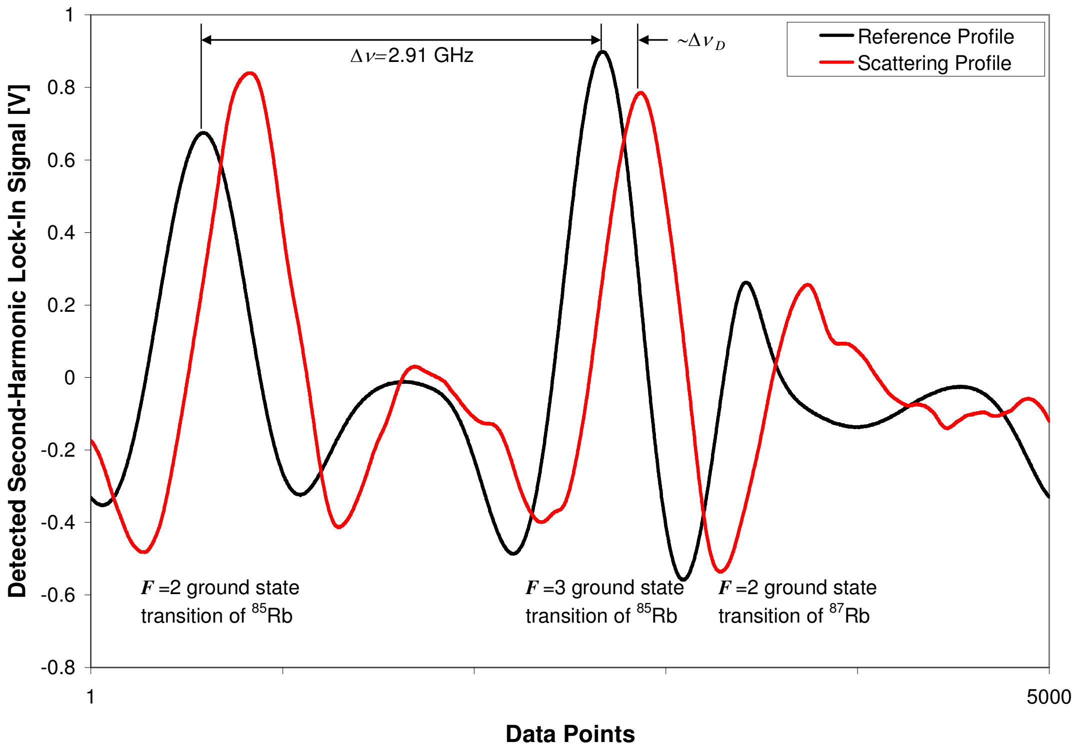

*Figure 4.2 Doppler-shifted **2f**-profile acquired in the scattering arm from a supersonic jet of N_2 compared to an unshifted **2f**-profile acquired in the reference arm*

The modulated absorption signals detected in the reference and scattering arms are sent to two digital lock-in amplifiers (Stanford Research Systems SR830) synchronized with the modulation frequency and set to extract the second harmonic of the detected signal. The second harmonic lock-in signals are digitized with a 1.25 Msample/s, 12-bit National Instruments data acquisition board (PCI-MIO-16E-1). A virtual instrument (VI) was developed with National Instruments LabView G-programming language to trigger acquisition and save the acquired ***2f***-profiles to a binary file. Figure 4.2 shows a sample of the ***2f***-profiles acquired in the scattering and reference arms during a single sweep. The Doppler shifted ***2f***-profile acquired in the scattering arm reflects the bulk velocity of the jet under investigation. Both profiles were acquired by sweeping the optical frequency of the diode laser at a rate of 10 s across approximately 5 GHz - thereby covering the two Doppler broadened absorption features in the D_2-line of ^{85}Rb – and simultaneously dithering the optical frequency of the diode laser at a modulation frequency of ν_m=2 kHz. The reduced sweep range results in less profile distortion for a given sweep rate. A frequency modulation amplitude of approximately a=570 MHz was employed to optimize detection of the second-harmonic signal, and the lock-in integration time constant was set to τ_L=100 ms to provide adequate signal-to-noise.

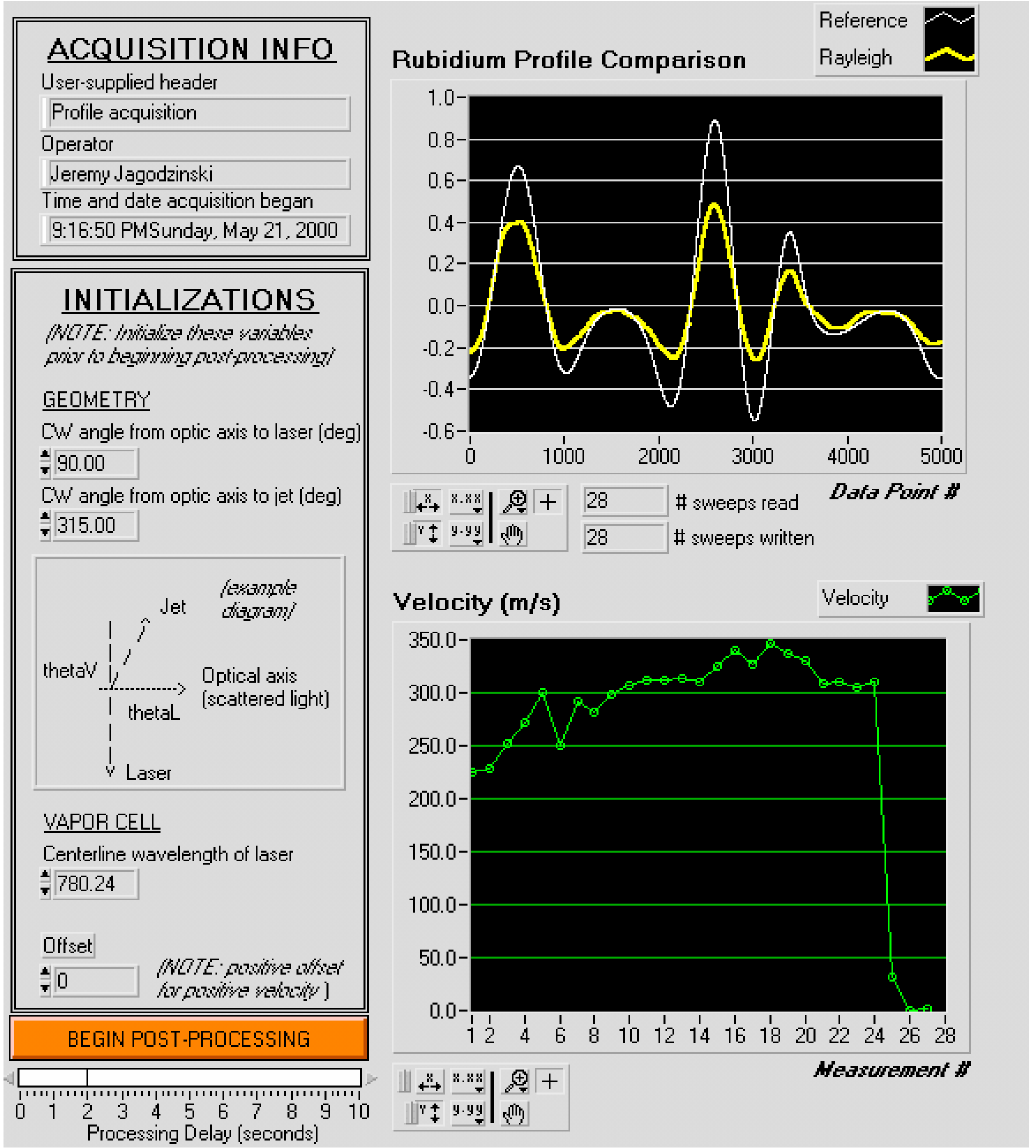

ACQUISITION INFO

User-supplied header: Profile acquisition

Operator: Jeremy Jagodzinski

Time and date acquisition began: 9:16:50 PMSunday, May 21, 2000

INITIALIZATIONS

(NOTE: Initialize these variables prior to beginning post-processing!)

GEOMETRY

CW angle from optic axis to laser (deg): 90.00

CW angle from optic axis to jet (deg): 315.00

VAPOR CELL

Centerline wavelength of laser: 780.24

Offset: 0

(NOTE: positive offset for positive velocity)

28 # sweeps read

28 # sweeps written

Figure 4.3 Sample post-processing VI

A post-processing VI was written to cross-correlate the reference and scattering profiles, and to convert the calculated Doppler frequency shift to a velocity measurement. This post-processing VI first employs a peak finding algorithm to determine the separation in data elements between the two strong peaks in the reference **2*f***-profile. These peaks correspond to the resonant centerline frequencies of the Doppler broadened ***F***=2 and ***F***=3 ground state transitions of ^{85}Rb, with a known frequency separation of $\Delta\nu$ =2.91GHz, and are therefore used to calculate a data element-to-frequency conversion. The Doppler frequency shift, $\Delta\nu_D$, of the scattered signal due to a bulk velocity in the probe volume is then determined by cross-correlating the Doppler-shifted ***2f*** scattering profile to the ***2f*** reference profile, and the velocity is calculated according to Eq. 3.1. Figure 4.3 shows a sample screen from this VI after post-processing the measurements presented below.

A converging nozzle with an exit diameter of ~3.1 mm (1/8-inch) was designed and machined to provide all preliminary MFRS experiments with a well-characterized jet flow. A relatively rapid acceleration is provided by a ~12.5 mm (1/2-in) radius of curvature up to the throat, and isentropic expansion is assumed in the core flow. The maximum theoretical velocity of the jet, expanding isentropically to atmospheric pressure, P_{atm}, is readily calculated from the stagnation pressure P_o and temperature T_o measured in the plenum just upstream of the nozzle,

$$V = \left[\frac{2\gamma R T_o}{\gamma - 1} \left\{ 1 - \left(\frac{P_{atm}}{P_o} \right)^{\gamma-1/\gamma} \right\} \right]^{1/2}, \tag{4.1}$$

where γ is the ratio of specific heats and R is the gas constant (e.g. $\gamma = 1.4$ and $R = 297$ J/kg K for N_2). As shown in Figure 4.1, the experimental geometry is set to collect the scattered radiation at right angles to the laser beam, with the jet axis bisecting this angle. From Eq. 3.1 we find that with this geometry the velocimeter measures the axial velocity of the jet.

Figure 4.4 summarizes the results of twenty-eight consecutive velocity measurements made nominally 9 nozzle exit diameters (~28 mm) downstream from the nozzle exit in a supersonic expansion of N_2. The plenum pressure and temperature were recorded manually for each laser sweep and are also displayed on Figure 4.4, as is the maximum jet core velocity, calculated from Eq. 4.1 assuming isentropic expansion from the stagnation pressure to the recorded atmospheric pressure of P_{atm}= 98 kPa. In these preliminary sweep mode experiments the effective imaged length of the probe volume was $\ell_{eff} = 3.8$ mm. The velocity measurements therefore average over flow gradients and cannot be directly compared to a calculated jet core velocity.

Referring to Figure 4.4 we find that the first velocity measurement is approximately 120 m/s less than the maximum theoretical velocity calculated assuming isentropic expansion. As the pressure in the settling chamber increases and as the temperature in the settling chamber decreases we see that the measured velocity tends toward the maximum theoretical velocity; e.g. the nineteenth velocity measurement is only 30 m/s less than the calculated maximum. The first question I would like to address is why the measured velocity changed so dramatically during the three minutes that transpired from the end of the first velocity measurement to the beginning of the nineteenth velocity measurement.

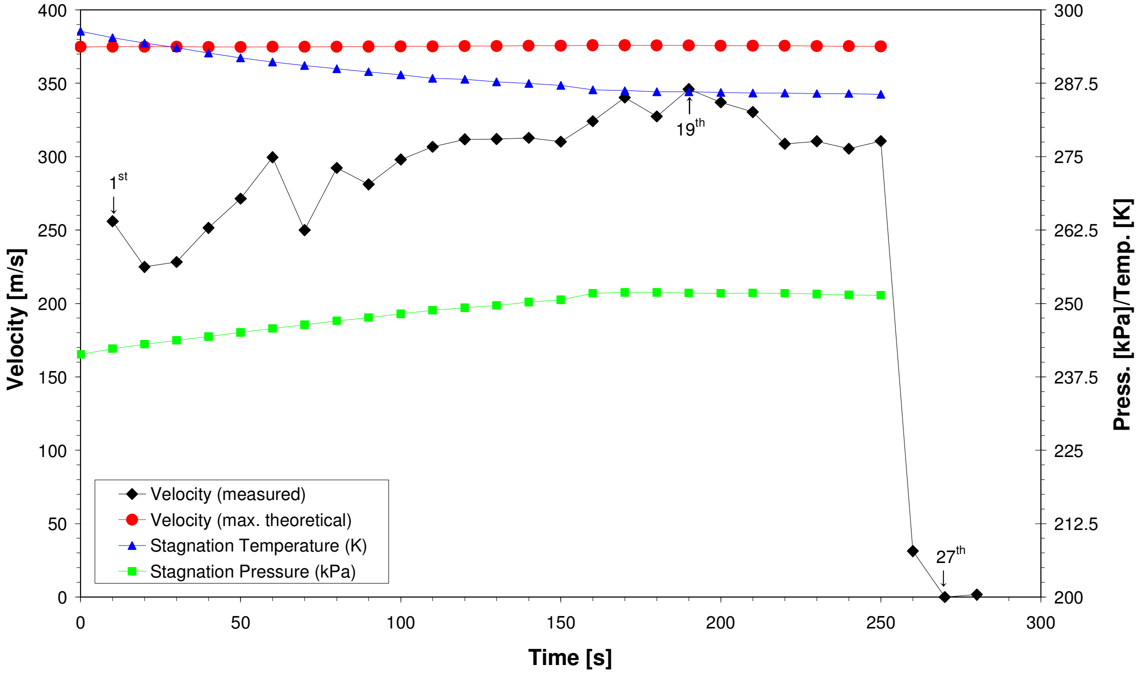

Figure 4.4 MFRS sweep mode velocity measurements in a supersonic expansion of N_2

All of the "scattering" profiles acquired during the sweep mode measurements discussed in this section are a superposition of an unshifted **2*f***-profile resulting from collected and detected stray reflections, a Doppler-shifted **2*f***-profile resulting from collected and detected molecular Rayleigh scattering, and a Doppler-shifted **2*f***-profile resulting from collected and detected condensate scattering; i.e. H_2O entrained into the shear layer and core of the nitrogen jet condensed, and scattering from this condensate provided a detectable modulated absorption signal. The calculated temperature of the jet core during the first velocity measurement is $T \approx 250$ K. Referring to Figure 4.5 illustrating the reference and scattering profiles that were cross-correlated to determine the first, nineteenth, and twenty-seventh measured velocities we find that the peak amplitudes in the scattering profile associated with the first velocity measurement are approximately two-times less than the corresponding peak amplitudes in the scattering profile associated with the nineteenth velocity measurement. (I increased the lock-in sensitivity in the reference arm from $S_L|_{\mathrm{REF}}$=500 μV to $S_L|_{\mathrm{REF}}$=200 μV after the fifteenth sweep. The peak amplitudes in the reference profiles associated to the first fifteen velocity measurements are therefore approximately two-and-one-half-times less than the corresponding peak amplitudes in the remaining reference profiles; e.g. compare the first reference profile in Figure 4.5 to the nineteenth and twenty-seventh reference profiles. Though I didn't record the specific lock-in sensitivity utilized in the scattering arm of the experiment, there is no indication in my notes that it changed during the sweep mode measurements discussed in this section).

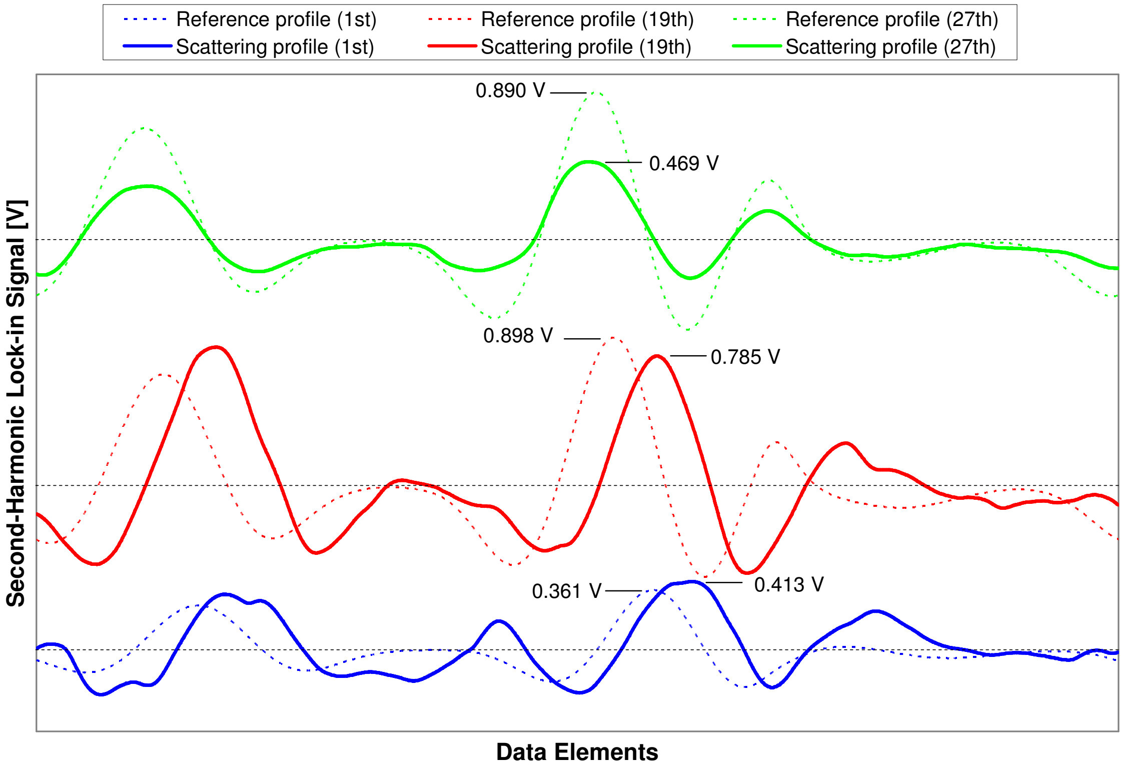

Figure 4.5 Reference and scattering profiles corresponding to the first, nineteenth, and twenty-seventh velocity measurements illustrated in Figure 4.4

It is my opinion that only minor condensate scattering was collected and detected during the first velocity measurement, that the contributions from molecular Rayleigh scattering to the first scattering profile are only slightly greater than the contributions from stray reflections, and that the first velocity measurement fails to accurately reflect the jet velocity because of the relatively significant contribution from stray reflections to the acquired scattering profile. The scattering profile associated with the first velocity measurement is relatively noisy and it is also possible that the cross correlation of this scattering profile with its corresponding reference profile therefore failed to accurately predict the Doppler frequency shift affected by the bulk flow velocity. Looking at the nineteenth scattering profile, I suspect that the contributions from molecular Rayleigh scattering to this profile are again only slightly greater than the contributions from stray reflections. It is my opinion, however, that there was a marked increase in collected and detected condensate scattering and that the nineteenth velocity measurement is a reasonably accurate reflection of the actual jet velocity because the increased condensate scattering minimized the corrupting effect of stray reflections on the velocity measurement – i.e. the Doppler-shifted profile resulting from scattering contributes significantly to the scattering profile associated with the nineteenth velocity measurement whereas collected and detected stray reflections contribute relatively little.

Beyond the nineteenth velocity measurement the measured velocities begin to trend away from the maximum theoretical velocity. The scattering profiles associated with these measurements exhibit good S/N and a slight increase in amplitude, and it is difficult for me to say with any certainty why there was a marked decrease in the measured velocities. I don't suspect that there was a dramatic change in the jet flow structure during the sweep mode measurements, but I haven't any data to support this claim; the highly under-expanded flow emanating from the nozzle is complex, and there is a very real possibility that its structure was highly sensitive to the relatively minor changes in temperature and pressure recorded during the run. It is possible that the contribution from stray reflections to the scattering profile increased after the nineteenth velocity measurement – e.g. condensate scattering from within the jet reflected off of the nozzle and was collected and detected – or that I was beginning to collect and detect secondary scattering from outside the object plane (and hence the jet) – i.e. condensate scattering from within the jet led to a secondary scattering event outside of the jet that was within the depth of field of the collection optics – but again, I don't have any corroborating evidence. Finally, it is possible that frost that had accumulated near the jet exit by this point in the run was redirecting the core flow; i.e. the nozzle was completely covered in frost by the end of the run, and it is possible that this frost obstructed the flow emanating from the ~3.1 mm nozzle exit. If an obstruction at the nozzle exit did redirect the core flow, then I was no longer measuring the axial component of the jet core velocity and I would expect a decrease in the measured velocity.

After making the twenty-fifth velocity measurement I turned off the jet flow. Let us consider one final velocity measurement – the twenty-seventh – before we proceed. We know that H_2O is no longer being entrained into and is no longer condensing within the jet flow during the twenty-seventh velocity measurement – i.e. the jet is off. We therefore expect the twenty-seventh acquired scattering profile to simply reflect collected and detected stray reflections as well as molecular Rayleigh scattering from air. Now, if the scattering profile associated with the nineteenth velocity measurement truly reflected molecular Rayleigh scattering from the nitrogen jet, we would expect the scattering profile associated with the twenty-seventh velocity measurement to exhibit only slightly reduced peak amplitudes: The probe laser power associated with the twenty-seventh velocity measurement was approximately equivalent to the probe laser power associated with the nineteenth velocity measurement, the scattering cross-section of air is only ~4% less than the scattering cross-section from N_2, and the ambient probe volume number density is only ~17% less than the number density in the measured jet core. In other words, if the scattering profile associated with the nineteenth velocity measurement truly reflected molecular Rayleigh scattering from the nitrogen jet we would expect its peak amplitudes to be ~26% greater than the corresponding peak amplitudes in the twenty-seventh scattering profile. What we observe in Figure 4.5, however, are peak amplitudes in the nineteenth scattering profile that are ~67% greater than the corresponding peak amplitudes in the twenty-seventh scattering profile. Again, it is my opinion that condensate scattering contributed to the profiles acquired with the jet on – significantly so in the case of the nineteenth scattering profile. Though I don't have enough data to corroborate my opinion, I also believe that condensate scattering contributed to the scattering profile associated with the twenty-seventh velocity measurement; i.e. the probe volume was only ~1 inch from what was essentially a block of ice by this point (i.e. the nozzle) and was likely saturated with water vapor. As I have previously illustrated, Rayleigh scattering experiments are extremely sensitive to ambient effects – e.g dust, dew, etc.

With P_o~50 mW of laser power in the probe volume during preliminary frequency-locked measurements I was unable to acquire a reliable, repeatable **2*f***-profile utilizing molecular Rayleigh scattering from air. And yet, with only P_o~25 mW of laser power in the probe volume during preliminary sweep mode measurements I had moderate success acquiring **2*f***-profiles from molecular Rayleigh scattering. I attribute this success to the modulation depth employed during these measurements. In Figure 4.6 I have plotted the theoretical second-harmonic lock-in signal-to-noise resulting from frequency modulated molecular Rayleigh scattering collected and detected during preliminary sweep mode measurements. This theoretical S/N is plotted versus normalized relative angular frequency and corresponds to the Doppler broadened $\boldsymbol{F}$=3 ground state transition of ^{85}Rb. It was calculated using the rigorous analysis presented in the previous chapter with parameters that realistically reflect the performance of the sweep mode experiment discussed in this section – e.g. a lock-in integration time of τ_L=100 ms, a probe laser power of P_o=25 mW, an effective spatial resolution of $\ell_{eff} = 3.8\,\text{mm}$ along the probe laser beam, a collection F-number of $F_\#$=1.445, a jet core temperature of $T_{\mathrm{N_2}}$ = 250 K, a Rb cell temperature of T_{Rb}=296.35 K (corresponding to the first stagnation temperature measurement in Figure 4.4), and a collection efficiency of η = 56% (which accounts for the ~25% transmission loss through the narrow pass optical filter). Looking at Figure 4.6 we find that the maximum second-harmonic lock-in signal-to-noise is theoretically $\mathrm{S/N}|_{\mathrm{max}}$~15 with the modulation index optimized for second-harmonic detection, m=2.2, as it was during preliminary sweep mode measurements. With a modulation index of m=0.476, utilized during preliminary frequency-locked measurements, the maximum second-harmonic lock-in signal-to-noise is theoretically only $\mathrm{S/N}|_{\mathrm{max}}$~1.

Preliminary sweep mode measurements were promising. In particular, this operational mode is less sensitive to noise and profile distortion than the frequency-locked mode of operation; i.e. the cross-correlation effectively averages out noise and is unaffected by *minor* profile distortion. Unfortunately, the temporal resolution of sweep mode measurements is severely limited by the need to sweep. To prevent harmonic profiles acquired while sweeping across an absorption feature from exhibiting gross distortion the sweep period needs be much longer (and the modulation period need to be much less) than the lock-in integration time constant. During my preliminary investigations of the sweep mode of operation, a lock-in time constant of at least τ_L=100 ms was required to measure a relatively reliable scattering profile. With a time constant of τ_L=100 ms, I observed that sweep periods less than 10 s resulted in significant harmonic profile distortion – e.g. a large reduction in peak amplitudes, highly asymmetric harmonic profiles, etc. In other words, the temporal resolution of all preliminary sweep mode measurements was limited to ~10 s. Accordingly, development of the sweep mode of operation was abandoned and development of the frequency-locked mode of operation was taken-up.

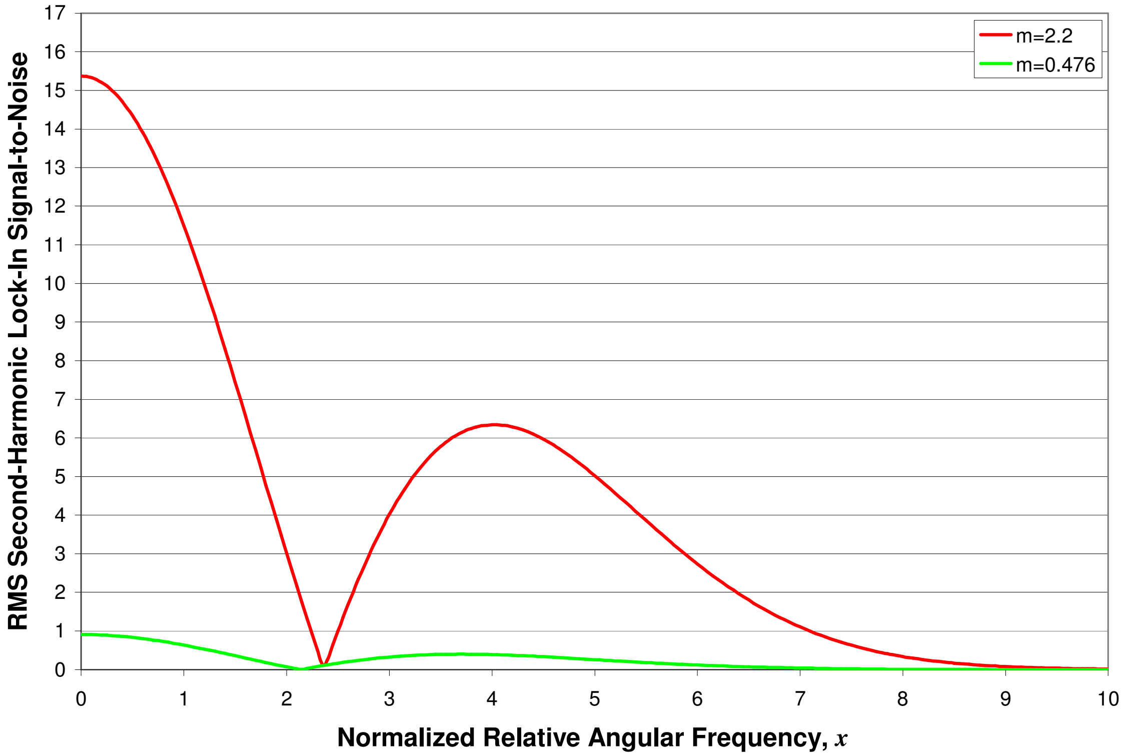

Figure 4.6 Theoretical 2^{nd}-harmonic lock-in signal-to-noise corresponding to the Doppler broadened ***F****=3 ground state transition of* ^{85}*Rb and resulting from molecular Rayleigh scattering collected and detected during preliminary sweep mode measurements with the experimentally legitimate modulation index m=2.2 versus m=0.476*

4.3 The Frequency-Locked Mode of Operation

The frequency-locked mode of operation is an attractive alternative to the sweep mode of operation because its temporal resolution is limited only by the required lock-in time constant. In the frequency-locked mode of operation the laser source is tuned to, stabilized to, and modulated about the centerline frequency of one of the Doppler broadened components in the D_2-line of Rb. A shift in the Rayleigh scattered frequency due to a Doppler frequency shift results in a change in absorption and thus in the magnitude of the detected modulated absorption signal in the scattering arm. By correlating the detected signal to the frequency shift of the collected Rayleigh scattered light, and knowing the geometry of the experiment, we are able to calculate the velocity in the probe volume according to Eq. 3.1. In particular, a calibration profile is acquired in the scattering arm prior to conducting frequency-locked velocity measurements by sweeping (and simultaneously modulating) the probe laser frequency across a pertinent portion of the D_2-line. This calibration profile is used to calculate the bulk velocity in the probe volume as a function of the measured modulated absorption signal.

In the frequency-locked mode of operation, variations in the collected Rayleigh scattering intensity would be misinterpreted as a Doppler frequency shift of the Rayleigh scattered light, and attributed to a change in flow velocity. As discussed in Section 3.2 (see Eq. 3.33), the Rayleigh scattered power, and therefore the amplitude of the Doppler shifted Rayleigh scattered signal detected in the scattering arm, is directly proportional to the density of the fluid in the probe volume, N_o, and the laser power interrogating the probe volume, P_o. In the sweep mode of operation, if the mean density in the probe volume and the mean power of the probe laser beam are constant, then any fluctuations in these parameters are effectively averaged-out provided that the time constant of the lock-in amplifier is sufficiently large. The frequency-locked mode of operation was developed to improve the temporal resolution of velocity measurements, however, and long lock-in time constants defeat this objective. For high-resolution frequency-locked measurements, the velocity can only be correlated to the amplitude of the Doppler shifted Rayleigh scattered signal provided that density and probe laser beam power fluctuations are normalized out. Dr. Philip Varghese and I developed a ratioed detection scheme for the frequency-locked mode of operation that provides a frequency dependent, scattering intensity independent reference for the Rayleigh scattered signal. This ratioed detection scheme will be discussed in sub-section 4.3.1.

As was the case for fluctuations in the Rayleigh scattering intensity, a drift in the laser frequency would be misinterpreted as a Doppler frequency shift of the Rayleigh scattered signal and attributed to a change in the bulk velocity in the probe volume. In the frequency-locked mode of operation the reference arm is therefore used to stabilize the laser frequency. Toward this end, I constructed a proportional-integral-differential (PID) controller to provide closed-loop feedback for frequency stabilization based on a **1*f*** error signal generated in the reference arm. During preliminary frequency-locked velocity measurements I generally chose the zero crossing in the **1*f***-profile corresponding to the ***F***=3 ground state transition of ^{85}Rb as the frequency set-point for stabilization. The zero-crossings in the **1*f***-profile correspond to the resonant centerline frequencies of the Doppler broadened features in the D_2-line. The frequency at each zero-crossing in the **1*f***-profile is therefore independent of the temperature in the Rb vapor cell, and though temperature fluctuations in the cell change the slope of the error signal to the PID, the resulting changes in stabilization feedback gain due to ambient temperature fluctuations is negligible. In addition, the ***F***=3 ground state transition of ^{85}Rb exhibits the greatest attenuation in the D_2-multiplet and tuning to its centerline frequency provides an effective means of minimizing the detection of collected stray reflections during frequency-locked velocity measurements. (Note that there is in fact one zero-crossing in the **1*f***-profile that does not correspond to a resonant centerline frequency of Rb – The zero-crossing that lies between the ***F***=2 ground state transition of ^{87}Rb and the ***F***=3 ground state transition of ^{85}Rb. While acquiring the frequency-locked velocity measurements presented below, I mistakenly stabilized the MOPA laser system to this zero-crossing in the **1*f***-profile. Since fluctuations in the temperature of the Rb vapor cell affect the frequency of this zero-crossing, I would not advise utilizing it as a frequency set-point during future investigations).

In the frequency-locked mode of operation the laser source must exhibit an acceptable level of frequency-stability determined by the magnitude of velocities being measured. I initially attempted to frequency stabilize a commercially available, stand-alone diode laser, but observed unacceptable levels of short-term and long-term drift. In addition, frequent mode-hops completely unlocked the frequency stabilization. To avoid the difficulties associated with my preliminary attempts to frequency stabilize a stand-alone diode, I designed and built an extended-cavity diode laser (ECDL) in the Littrow configuration; the feedback levels for frequency stabilization of an ECDL are more reasonable than the O(1 μV) proportional feedback voltages required for frequency stabilization of a stand-alone diode. In sub-section 4.3.2 I will describe the PID circuit, the Littrow laser cavity, and the associated electronics that I designed and built to ensure frequency stable probe laser power during preliminary frequency-locked MFRS velocity measurements.

The Littrow laser demonstrates good spectral qualities and an acceptable level of frequency stability, but provides only 12 mW of output power. With only 12 mW of power available in the probe volume, the lock-in time constant required to measure a reliable calibration profile in the scattering arm would have been prohibitively long. As a result, I spent considerable time trying to amplify the optical power from the Littrow cavity with a 1.5 W broad area laser (BAL). Sub-section 4.3.3 will briefly discuss the extended-cavity diode laser master oscillator power amplifier (ECDL-MOPA) system that I developed for preliminary frequency-locked MFRS measurements. The best performance I was able to attain from the ECDL-MOPA system was P_o ~ 73 mW of frequency modulated probe laser power on a background of P_{ASE} ~ 20 mW of amplified spontaneous emissions (ASE); the 73 mW of amplified output power spectrally tracks the Littrow laser cavity, and the 20 mW of ASE does not.

I will conclude this chapter by discussing the results of some frequency-locked MFRS velocity measurements in sub-section 4.3.4. These measurements were made in a supersonic expansion of CO_2 and relied on scattering from CO_2 condensate to provide sufficient S/N. The calibration profile acquired in the scattering arm prior to the velocity measurements also relied on condensate scattering from the CO_2 jet. By measuring the calibration profile in the jet flow, it not only exhibited better S/N, but also provided a more reliable standard – i.e. it reflected the thermodynamics of the jet flow – and was less susceptible to dust scattering from the ambient lab environment.

4.3.1 The Ratioed Detection Scheme

Figure 4.7 shows a schematic of the MFRS velocimeter configured for frequency-locked measurements. The laser source for the experiment is an extended-cavity diode laser master oscillator power amplifier (ECDL-MOPA) system. The master oscillator (MO) is an ECDL in the Littrow configuration, which provides frequency tunable lasing for implementation of homodyne detection. Optical power amplification of the Littrow laser output is provided by a 1.5 W, anti-reflection coated (AR coated) broad area laser (BAL). A small portion (<1%) of the collimated output from the ECDL-MOPA is split off to a reference arm, and passes through a 100 mm long room temperature cell containing rubidium (Rb) vapor in natural isotopic abundance (72.2% ^{85}Rb and 27.8% ^{87}Rb) before being recorded by a silicon photodiode (Thorlabs DET110). A high frequency modulation is imposed on the laser source, and results in a modulated absorption through the Rb filter in the reference arm. The detected modulated absorption is fed to a lock-in amplifier synchronized with the function generator that drives the modulation. A drift in the laser frequency results in a change in the modulated absorption signal output by the lock-in. This error signal is sent to a PID, which provides closed-loop feedback to the regulated high voltage amplifier that powers the piezoelectric transducer controlling the Littrow laser frequency.

The majority of the laser beam passes to the probe volume under investigation. A series of six anti-reflection coated lenses collect the scattered light from the probe volume, relay the collected light through a 75 mm long Rb vapor cell, and focus it onto a side-looking PMT (Hamamatsu R636-10); a narrow-pass optical filter was not utilized in the scattering arm during preliminary frequency-locked measurements. The high frequency modulation of the probing laser is imposed on the Rayleigh scattered light, and results in a modulated absorption through the Rb filter in the scattering arm. To account for scattering intensity fluctuations from the probe volume, we implement a ratioed detection scheme. The Doppler frequency shift, and hence the velocity in the probe volume, is extrapolated from the frequency dependent, scattering-intensity independent signal provided by this ratioed detection scheme.

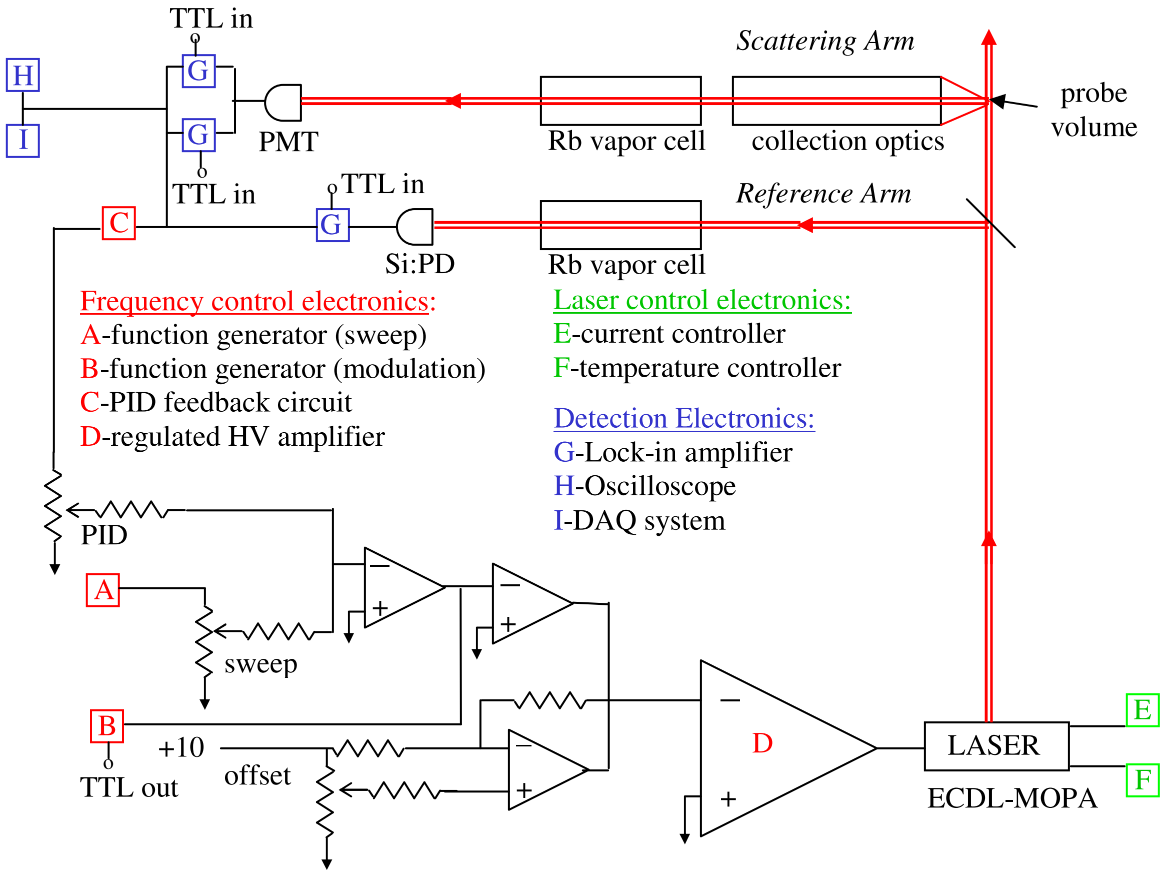

Figure 4.7 The MFRS velocimeter in the frequency-locked mode of operation

To implement the ratioed detection scheme, the Rayleigh scattered signal detected by the photomultiplier tube (PMT) in the scattering arm is fed to two separate lock-in amplifiers. The outputs from the lock-in amplifiers, each set to extract a different harmonic of the modulated signal from the PMT, are ratioed, resulting in a frequency dependent, scattering-intensity independent signal. In essence, we extract different Fourier components of the detected modulated absorption signal and ratio them. Because peak **n*f***-profile signals decrease at higher harmonics, I chose to implement first- and second-harmonic lock-in detection during preliminary frequency-locked measurements. The resulting ratio profiles also provide the largest continuous dynamic range.

To illustrate the ratio detection scheme, let us consider the mean PMT anode current resulting from Rayleigh scattered light detected in the scattering arm during preliminary MFRS experiments,

$$i_p = i_o \exp\left[-\bar{\alpha} z Y_{\omega_o}(\omega)\right] = \mu S_k P_{DET} \exp\left[-\bar{\alpha} z Y_{\omega_o}(\omega)\right], \tag{4.2}$$

where $i_o = \mu S_k P_{DET}$ is the PMT anode current detected outside the bandwidth of a Doppler broadened absorption feature in the D_2-line, μ is the PMT gain, S_k is the PMT photocathode sensitivity, $P_{DET} = f\,(N_o, P_o)$ is the Rayleigh scattered power (which is a function of the probe volume number density, N_o, and interrogating probe laser power, P_o), $\bar{\alpha}$ is the spectrally integrated absorption constant (derived from the perspective of Einstein coefficients in Section 3.3), z is the path length of the collected Rayleigh scattered light through the Rb vapor cell in the scattering arm, and $Y_{\omega_o}(\omega)$ is the normalized lineshape function describing the frequency-dependent attenuation associated with an absorption feature in the D_2-line of Rb. The frequency modulation imposed on the collected Rayleigh scattered light results in a detected modulated absorption signal in the scattering arm. Let us approximate the first- and second-harmonics of this detected modulated absorption signal with the derivative profiles described by Eq. 3.127; As discussed in Section 3.4, the shape of an **n*f***-profile resembles the nth-derivative of the detected absorption feature provided the absorption is weak, the frequency modulation amplitude is small, the detected **n*f***-profile is undistorted by excessively fast sweep rates, and the Rayleigh scattered light is monochromatic. Relying on this approximation it is easy to show that the ratio of the first-harmonic lock-in signal to the second harmonic lock-in signal is independent of the collected Rayleigh scattered power, and hence the number density and laser power in the probe volume:

$$\left.\begin{aligned} S_L^1(\omega) &= -\frac{i_o R_L G_{1f}}{\sqrt{2}} \cos\theta_{1f} \cdot \bar{\alpha} z a \left.\frac{\partial Y_{\omega_o}}{\partial \omega}\right|_{\omega} \\ S_L^2(\omega) &= -\frac{i_o R_L G_{2f}}{\sqrt{2}} \cos\theta_{2f} \cdot \bar{\alpha} z \frac{a^2}{4} \left.\frac{\partial^2 Y_{\omega_o}}{\partial \omega^2}\right|_{\omega} \end{aligned}\right\} \Rightarrow \left.\frac{S_L^1}{S_L^2}\right|_{\omega} = \frac{4}{a}\frac{G_{1f}}{G_{2f}}\frac{\cos\theta_{1f}}{\cos\theta_{2f}}\frac{Y_{\omega_o}{}'(\omega)}{Y_{\omega_o}{}''(\omega)}. \tag{4.3}$$

In Eq. 4.3, a is the frequency modulation amplitude in units of angular frequency, G_{1f} and G_{2f} are the lock-in gains applied to the first- and second-harmonic signals, respectively, and θ_{1f} and θ_{2f}

account for the phase difference between the detected harmonic signal and the synchronized reference signal internal to each lock-in.

Though the ratio signal described by Eq. 4.3 was derived assuming monochromatic scattering, a weak absorption, and a small frequency modulation amplitude, it is possible to derive a ratio profile that incorporates the spectral broadening of scattered radiation and accommodates strong absorptions and large frequency modulation amplitudes. Referring to Eqs. 3.157 and 3.158 we find that the ratio of the first-harmonic lock-in signal to the second-harmonic lock-in signal can be expressed by the following general expression,

$$
\begin{aligned}
\left.\frac{s_l^1}{s_l^2}\right|_{\omega} &= \frac{\int_{-\infty}^{\infty} S_L^{1}(\omega') f(\omega') \mathrm{d}\omega'}{\int_{-\infty}^{\infty} S_L^{2}(\omega') f(\omega') \mathrm{d}\omega'} \\
&= \frac{\frac{i_o R_L G_{1f}}{\sqrt{2}} \cos\theta_{1f} \int_{-\infty}^{\infty} \bar{S}_L^{1}(\omega') f(\omega') \mathrm{d}\omega'}{\frac{i_o R_L G_{2f}}{\sqrt{2}} \cos\theta_{2f} \int_{-\infty}^{\infty} \bar{S}_L^{2}(\omega') f(\omega') \mathrm{d}\omega'}
\end{aligned}
$$

$$
\left.\frac{s_l^1}{s_l^2}\right|_{\omega} \cong \frac{G_{1f} \cos\theta_{1f}}{G_{2f} \cos\theta_{2f}} \frac{\sum_{\omega'=-\omega_{\text{cuttoff}}}^{\omega_{\text{cuttoff}}} \bar{S}_L^{1}(\omega') f(\omega') \mathrm{d}\omega'}{\sum_{\omega'=-\omega_{\text{cuttoff}}}^{\omega_{\text{cuttoff}}} \bar{S}_L^{2}(\omega') f(\omega') \mathrm{d}\omega'}, \tag{4.4}
$$

where $f(\omega')$ is the Rayleigh-Brillouin lineshape function centered at an angular frequency ω. For the Doppler broadened absorption features in the D_2-line of Rb, $\bar{S}_L^{1}$ and $\bar{S}_L^{2}$ are described by Eqs. 3.128 and 3.129, respectively. As with the ratio in Eq. 4.3, the ratio in Eq. 4.4 is independent of the collected Rayleigh scattered power.

Though the ratio signals in Eqs. 4.3 and 4.4 are independent of the collected scattering intensity, there is a frequency-dependence to the ratio signal that can be illustrated by assuming a normalized Gaussian lineshape (e.g. representing the Doppler broadened absorption features in the D_2-line of Rb),

$$
Y_{\omega_o}(\omega) = \frac{1}{\delta\omega_{1/2}} \sqrt{\frac{\ln 2}{\pi}} \exp\left[-\frac{\ln 2 (\omega - \omega_o)^2}{\delta\omega_{1/2}^{\;2}} \right], \tag{4.5}
$$

in calculating the ratio defined by Eq. 4.3. Inserting Eq. 4.5 into Eq. 4.3 we find,

$$\left.\frac{S_L^1}{S_L^2}\right|_{\omega} = \frac{4}{a}\frac{G_{1f}}{G_{2f}}\frac{\cos\theta_{1f}}{\cos\theta_{2f}}\cdot\frac{\omega-\omega_o}{1-\frac{2\ln 2}{\delta\omega_{1/2}^2}(\omega-\omega_o)^2} \tag{4.6}$$

Figure 4.8 shows an example of the ***1f*/*2f*** and ***2f*/*1f*** ratio profiles acquired by direct modulated absorption through the Rb vapor cell in the reference arm of the MFRS velocimeter. These ratio profiles provide the largest continuous dynamic range of all possible ratios. Notice that, though the dynamic range of the ***mf*/*nf*** ratio profile is limited by zero-crossings of the ***nf*** profile, it can be extended by simply inverting the ratio. The *x*-axis velocity in Figure 4.8 was calculated for measurements made utilizing the experimental geometry in Figure 4.1, with the frequency set-point at the zero-crossing in the ***1f***-profile corresponding to the ***F***=3 ground state transition of ^{85}Rb.

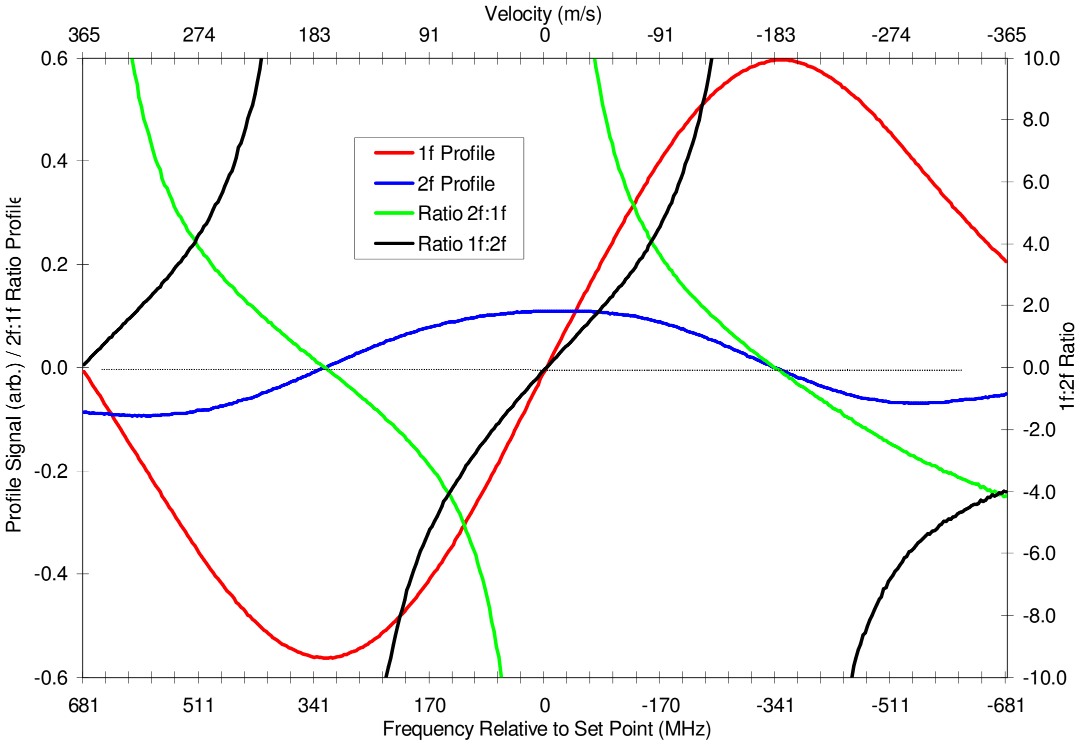

Figure 4.8 Frequency dependent, scattering intensity independent ratio profiles

4.3.2 Frequency Stabilization

Figures 4.9 and 4.10 show the proportional-integral-differential (PID) circuit that I designed and built to provide closed-loop feedback control for frequency stabilization based on an error signal in the reference arm of the experiment. The optional inverter accommodates stabilization on either the positive or negative slope of a harmonic profile (or absorption feature), and the user-defined voltage offset allows for frequency stabilization at any point along this slope. The error signal is amplified by an adjustable gain circuit that allows the user to effectively select the level of feedback provided by the PID. The resistors and capacitors in the proportional, integral, and differential feedback circuits were chosen based on the anticipated slope of the error signal and the tuning characteristics of the laser.

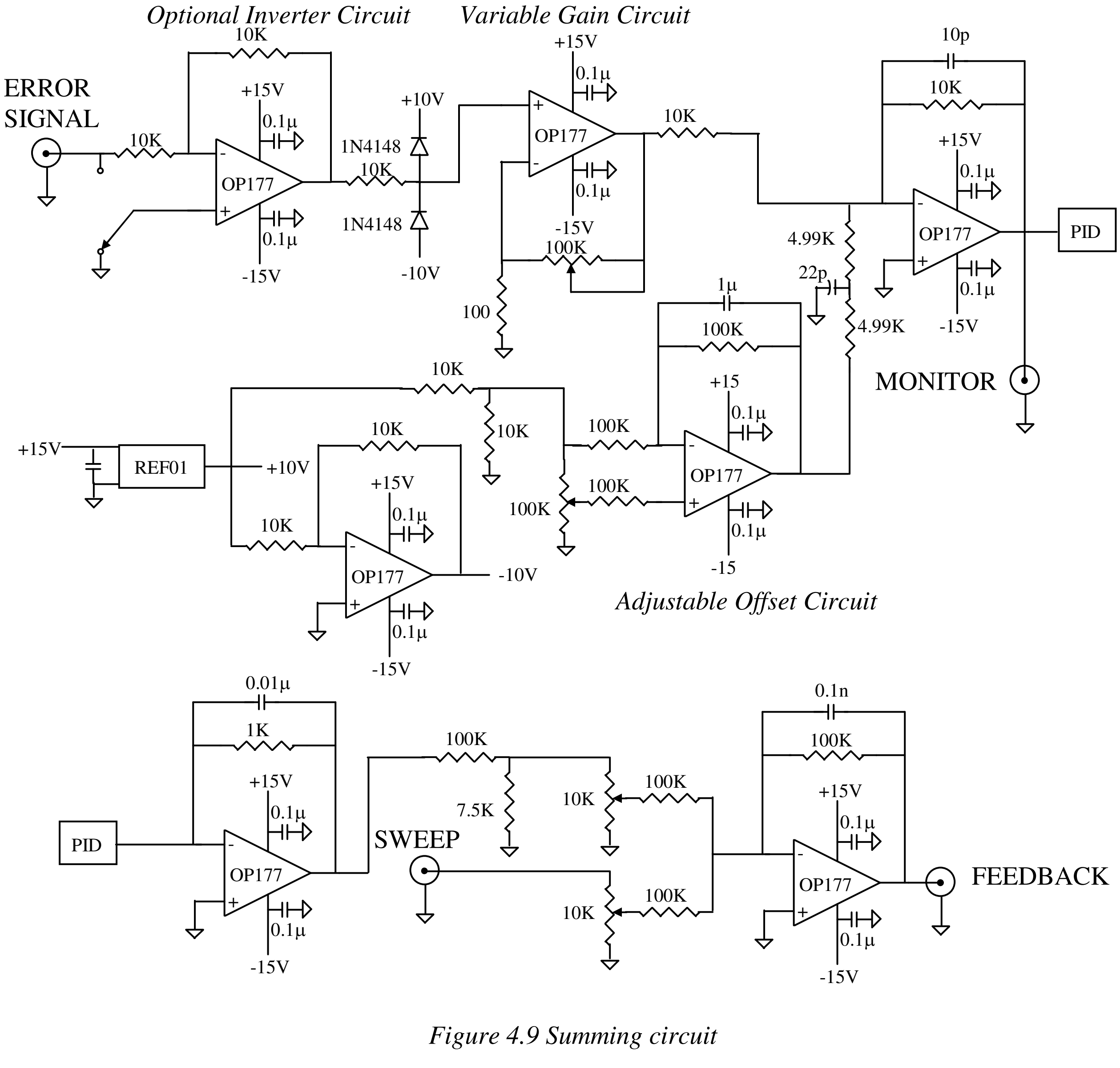

Figure 4.9 Summing circuit

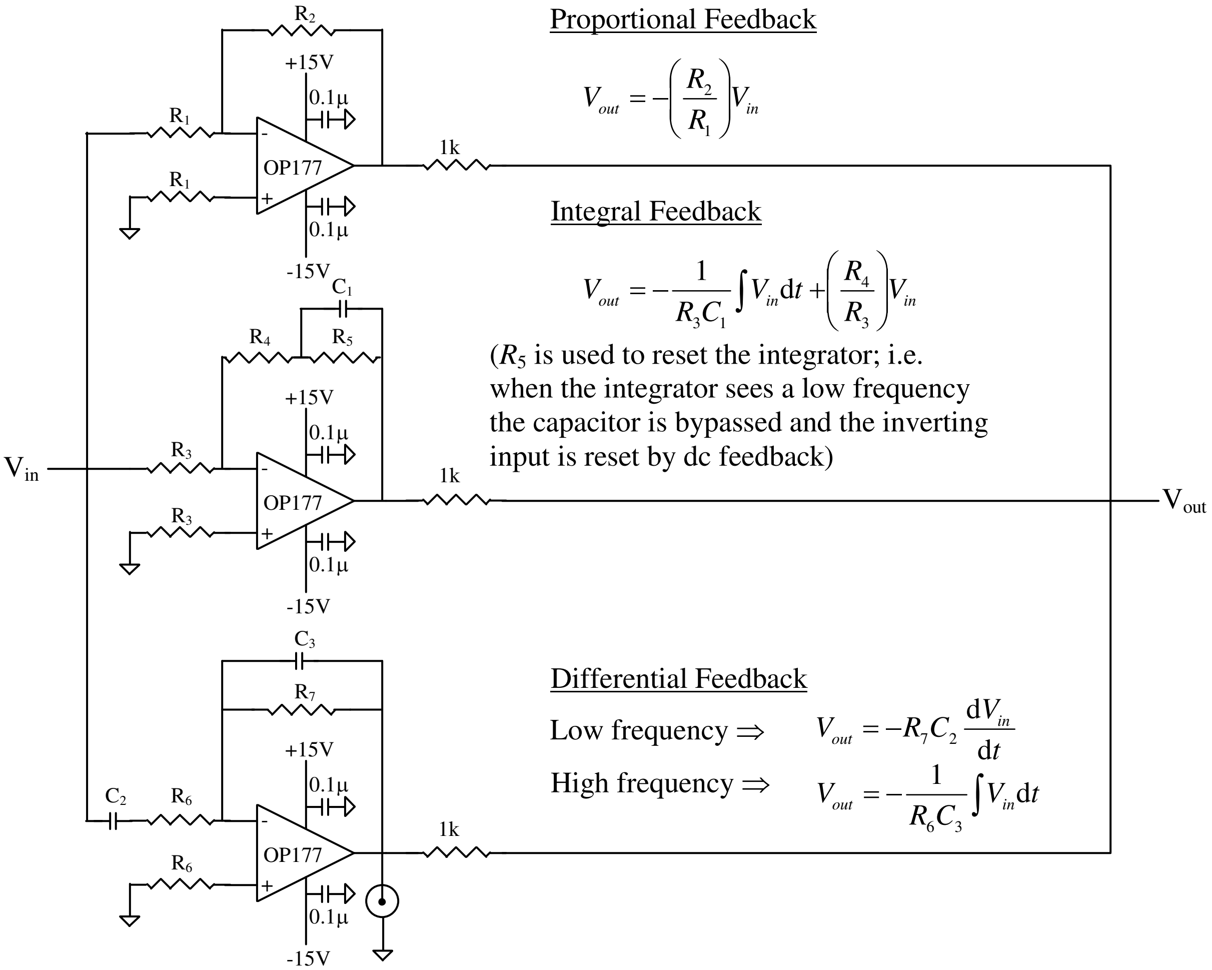

Proportional Feedback

$$V_{out} = -\left(\frac{R_2}{R_1}\right)V_{in}$$

Integral Feedback

$$V_{out} = -\frac{1}{R_3C_1}\int V_{in}\mathrm{d}t + \left(\frac{R_4}{R_3}\right)V_{in}$$

(R_5 is used to reset the integrator; i.e. when the integrator sees a low frequency the capacitor is bypassed and the inverting input is reset by dc feedback)

Differential Feedback

Low frequency ⇒ $V_{out} = -R_7C_2\frac{\mathrm{d}V_{in}}{\mathrm{d}t}$

High frequency ⇒ $V_{out} = -\frac{1}{R_6C_3}\int V_{in}\mathrm{d}t$

Figure 4.10 PID circuit

To investigate the performance of the PID I initially tried to stabilize a free-running commercially available diode. I was unable to obtain satisfactory frequency stability from any of the diodes utilized during these preliminary investigations. A 60 Hz ripple, resulting from the ac-line voltage powering the diode current controller, was noticeable when the diode was tuned to the edge of a harmonic profile. The PID provided unacceptable suppression of this ripple. When the current controller was powered from its internal batteries, the short-term frequency stability improved, but large long-term drifts in the laser frequency were observed and frequent mode-hops of the diode frequency completely destabilized the laser. Naturally, the specifics of PID design must account for the dynamics of the error signal and the circuit itself. However, these specifics can be ignored when illustrating the deficiencies associated with stabilization of a free-running diode via feedback to the current controller.

If an accuracy of 10 cm/s is demanded in our velocity measurements, for instance, then a maximum drift in laser frequency of 180 kHz is tolerable (assuming that the sensitivity vector is aligned with the bulk fluid velocity vector). Laser diodes tune with injection current at a rate of approximately −2 GHz/mA. Proportional current feedback of O(100 nA) is therefore required to correct for an 180 kHz drift in diode laser frequency. Feedback control was implemented through the external modulation input of the ILX Lightwave LDX-3620 current controller used during these preliminary investigations. The external modulation input of the LDX-3620 current controller has a transfer function of 100 mA/V. Proportional voltage feedback of O(1 μV) was therefore necessary to correct for an 180 kHz drift in laser frequency during my preliminary attempts to frequency stabilize a stand-alone diode laser. At these signal levels, any noise coupled into the external modulation input of the current controller overwhelmed the feedback signal. The ultraprecision OP177EZ operational amplifier used in the PID, for instance, has an input noise voltage of 118 nVrms and an input offset voltage drift of 100 nV/°C. There are ten of these op-amps in the feedback circuit, as seen in Figures 4.9 and 4.10.

An extended-cavity diode laser (ECDL) was built to avoid the difficulties associated with stabilization of a free-running diode; the feedback levels for frequency stabilization of an ECDL are significantly larger than those required to stabilize a free-running diode. ECDLs use a wavelength selective element (e.g. etalon, prism, grating) to provide optical feedback to the laser junction [36, 37]. Specifically, I built an ECDL in the Littrow configuration [113-117], as shown in Figure 4.11. The rear facet of the diode forms one end of the cavity and the diode junction provides gain. A grating at the Littrow angle to the rear facet forms the other end of the cavity, with the 1st-order diffraction providing optical feedback to the diode junction and the 0th-order diffraction exiting the cavity.

Optical feedback from the grating into the laser diode junction is characterized by the feedback ratio,

$$\rho = E_g \eta \,, \tag{4.7}$$

where E_g is the 1st-order diffraction efficiency of the grating and η is a geometrical factor describing the coupling of the diffracted light into the diode laser optical guide [37]. The spectral effects of the optical feedback from the grating can be classified according to the level of feedback, as described in Eq. 4.7.

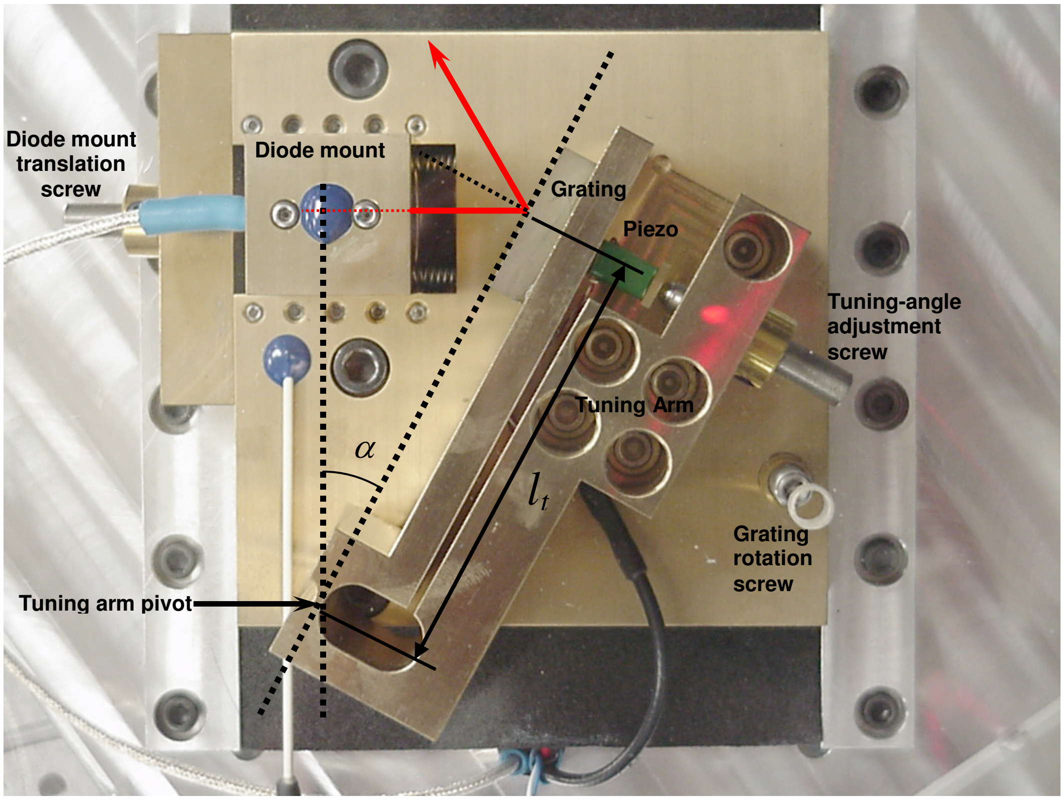

Figure 4.11 The Littrow laser cavity

In the low feedback regime ($\rho <$ -40 dB) the feedback efficiency is measured by

$$X = \frac{L_{ex}}{n \cdot l} \frac{1-R}{\sqrt{R}} \sqrt{\rho\left(1+\alpha^2\right)}, \tag{4.8}$$

where L_{ex} is the distance from diode output facet to the grating, n is the refractive index of the active layer in the diode junction, l is the distance between the facets of the diode, R is the diode output facet reflectivity, and α is the line broadening factor (typically 4-7;see below). Three distinct regions lie within the low feedback regime [37]:

For $X < 1$, single-mode operation is obtained, but the linewidth is unpredictably broadened or narrowed.

For X = 1-5, the laser frequency tends to jump quickly between several external-cavity modes, but a narrowed linewidth is achieved.

For X = 5-10, single-frequency lasing is obtained with a narrowed linewidth.

The advantage of laser diode systems utilizing low optical feedback is that they do not require an anti-reflection (AR) coating on the diode output facet. Many higher power (>15 mW) commercial diodes already have reduced reflectance coatings on the output facet and high reflectance coatings on the back facet, and this is sufficient for use in systems utilizing low optical feedback. These systems are not truly extended-cavity lasers since lasing occurs without feedback, but the system can be configured so that the external feedback dominates the Fabry-Perot cavity modes maintained inside the diode junction by the relatively low reflectance output facet. Several grating feedback ECDLs have been built that use commercial diodes [36, 118, 119].

Medium optical feedback levels (-30dB < ρ < -10dB) result in coherence collapse. The feedback field strongly perturbs the laser amplitude and the carrier density. The amplitude resonance peaks are enhanced significantly and the laser output is chaotic. This regime of optical feedback must be avoided because the coherence length is greatly reduced and the laser output is very unstable.

At high levels of optical feedback (ρ > -10dB), the laser diode system is truly in an extended-cavity configuration. In order to attain such high levels of optical feedback, the output facet of the diode laser has to be AR coated. With perfect AR-coating on the output facet the diode emits but does not lase, and when introduced into an external cavity acts merely as an optical amplifier, with the external cavity providing wavelength selectivity for lasing.

With perfect AR-coating on the output facet of the diode it is theoretically possible to tune an external cavity across the entire gain profile of the laser without mode-hops. In practice, residual reflectivity of the output facet affects both single frequency operation and the tuning range of extended-cavity laser systems. If the residual reflectivity of the AR-coating is too high, the internal oscillations of the laser diode may dominate the external cavity modes when the cavity is tuned far from the gain peak. In addition, whereas there is no clear connection between diode structure and single frequency operation in an extended cavity, AR-coating is a parameter that clearly affects the single frequency behavior. With poor AR-coating, the emission can become periodically multi-mode while tuning the wavelength selector, staying multi-mode until the diode mode hops to the successive external-cavity mode. It has been observed that 5% residual reflectivity regularly leads to multi-mode behavior, whereas single-mode behavior dominates with a residual reflectivity of 1% [37]. Harvey *et al.* [119] estimated that the reflectivity on the front facet of a Sharp LTO24MD GaAlAs diode (780 nm, 40 mW) is between

2%-10%. This manufacturing spread is typical for commercial diodes, and introduces considerable uncertainty into the performance of ECDLs that use them.

The use of AR coated diodes is critical for the design of a predictable, user-friendly, tunable laser system. Without AR-coating, wavelength tuning is an intricate balance between the gain profile of the active region of the diode, the diode cavity modes, and the external cavity modes. AR-coating lends predictability to the ECDL, allowing the operator to essentially ignore oscillations in the diode cavity. Our Littrow laser uses an AR coated diode (Sacher-Laser SAL-780-40) with a quoted front facet reflectivity of $R<1.9\times10^{-6}$ and a rated power of 40 mW before AR coating. The diode is mounted in a collimation tube with an f=11.0 mm focal length, 0.25NA aspheric collimation optic (Thorlabs LT220P-B). The collimation tube is mounted in a metal block that can be translated along the optical axis of the laser beam, allowing the rear facet of the diode laser to be correctly positioned with respect to the grating pivot, as discussed below. An 80-pitch screw (New Focus 9301-K) provides adjustment.

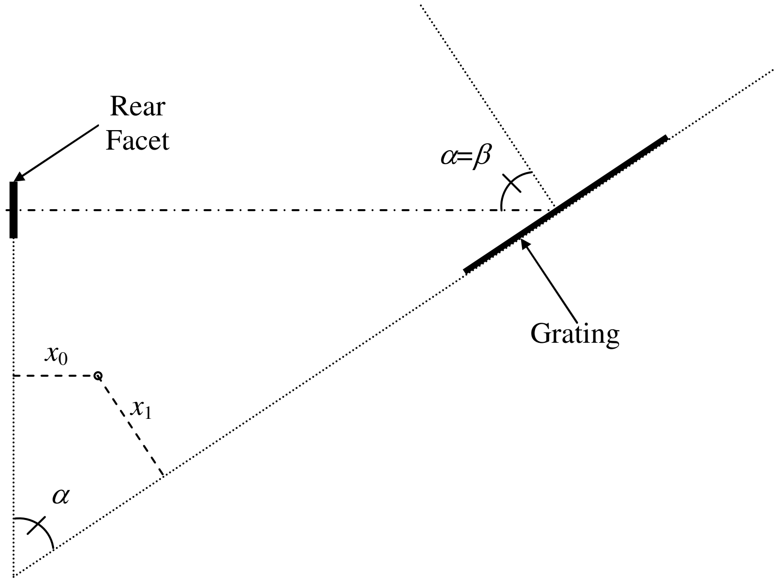

Figure 4.12 Basic Littrow configuration

The basic geometry of a Littrow laser is dictated by the grating equation,

$$d(\sin\alpha_o + \sin\beta_o) = m\lambda_o, \tag{4.9}$$

where d is the groove spacing (0.83 μm for the 1200 lines/mm grating I used in our cavity), m is the diffraction order (our Littrow laser utilizes 1st-order diffraction from the grating), λ_o is the centerline wavelength of the diffracted beam, α_o is the angle of the incident beam relative to the grating normal, and β_o is the angle of the diffracted beam at λ_o relative to the grating normal. Placing the grating at the Littrow angle we find $\alpha_o = \beta_o = 27.9°$ for operation at $\lambda_o = 780$ nm.

The cavity is tuned in frequency by changing the grating angle. For continuous wavelength tuning, the external-cavity mode structure has to synchronously track changes in the feedback frequency; i.e. as the grating angle is changed, generating a change in the feedback frequency, the phase in the external cavity formed by the rear facet of the diode and the grating must remain unchanged for synchronous tuning. The optimal configuration for synchronous tuning can be derived using scalar diffraction theory by considering the phase accrual in the external cavity [39].

Consider the generic Littrow laser cavity in Figure 4.12, with a grating pivot located a distance x_0 from the plane of the diode rear facet and a distance x_1 from the grating plane. From scalar diffraction theory we find that the phase accrued in the external cavity formed by the diode rear facet and grating is (to within an additive constant),

$$\psi = 4\pi \bar{\nu}\left(x_0 + x_1 \cos\alpha\right) \tag{4.10}$$

where $\bar{\nu}$ is the wavelength in wavenumbers. Let us now expand Eq. 4.10 about the centerline wavelength, $\bar{\nu}_o$. Assuming that the centerline wavelength is much greater than half of the desired tuning range, $\bar{\nu}_o >> \Delta\bar{\nu}$,

$$\psi\left(\bar{\nu} + \Delta\bar{\nu}\right) \approx \psi\left(\bar{\nu}_o\right) + \left.\frac{\partial\psi}{\partial\bar{\nu}}\right|_{\bar{\nu}_o} \Delta\bar{\nu} = \psi\left(\bar{\nu}_o\right) + \Delta\psi \ , \tag{4.11}$$

where from Eq. 4.10,

$$\left.\frac{\partial\psi}{\partial\bar{\nu}}\right|_{\bar{\nu}_o} = 4\pi\left(x_0 + x_1\cos\alpha_o\right) - 4\pi\bar{\nu}_o x_1 \sin\alpha_o \left.\frac{\mathrm{d}\alpha}{\mathrm{d}\bar{\nu}}\right|_{\bar{\nu}_o} \tag{4.12}$$

and from Eq. 4.9,

$$\left.\frac{\mathrm{d}\alpha}{\mathrm{d}\bar{\nu}}\right|_{\bar{\nu}_o} = -\frac{\tan\alpha_o}{\bar{\nu}_o} \ . \tag{4.13}$$

Combining Eqs. 4.11-4.13 we find,

$$\Delta\psi = 4\pi\left[x_0 + x_1\cos\alpha_o\left(1 + \tan^2\alpha_o\right)\right]\Delta\bar{\nu} \ . \tag{4.14}$$

From Eq. 4.14 we see that placing the grating rotation pivot at the intersection of diode rear facet and the grating plane, as in Figure 4.11, automatically minimizes phase changes in the cavity [120]. Eq. 4.14 also provides a measure of the tolerance with which the pivot must be located for synchronous tuning over a specified frequency range. A change of 2π in the roundtrip phase shifts the cavity mode structure one free-spectral range relative to the feedback frequency, and results in a mode-hop in the amplified optical feedback frequency. Even a small phase change can shift a neighboring cavity mode into the gain profile of the grating feedback, resulting in bimodal operation. Therefore, to ensure quasi single-mode operation we want the roundtrip phase change to be a fraction of 2π while tuning over the specified frequency range. For instance, assume that we want to tune 11 GHz in frequency ($\Delta\bar{\nu} = \pm 0.183\ \mathrm{cm}^{-1}$) with a maximum roundtrip phase shift in the cavity of $\Delta\psi < 2\pi/10$:

$$\left.\begin{aligned}\Delta\psi = 4\pi\left[x_0 + x_1 \cos\alpha_o\left(1+\tan^2\alpha_o\right)\right]\Delta\bar{\nu} &< {}^{2\pi}\!/_{10}\\ \Delta\bar{\nu} &= 0.18\overline{3}\ \mathrm{cm}^{-1}\\ \alpha_o &= 27.9^\circ\end{aligned}\right\} \Rightarrow x_0 + 1.1x_1 < 2.7\ \mathrm{mm} \tag{4.15}$$

In addition to designing for synchronous tuning, I minimized the external cavity length l_c with the intention of increasing the free spectral range of the cavity. This minimizes the sensitivity of the cavity to any phase changes that do occur and improves the chances of mode-hop free, single-mode, synchronous tuning. A minimum cavity length of l_c = 31.75 mm was chosen to avoid obstruction of the output beam by the diode mount.

Index guided diode lasers are polarized perpendicular to the fast optical axis of the output beam. To maximize the resolution of the grating I was therefore forced to use the grating in the S-plane (i.e. with the polarization parallel to the rulings). A relatively inexpensive, gold-coated, ruled grating (1200 lines/mm) from Edmund-Scientific (NT43-848) with an S-plane 1st-order efficiency of approximately 55% was chosen to provide sufficient levels of optical feedback to the diode junction. The grating is mounted to a tuning arm, with coarse angle tuning provided by an 80-pitch adjustment screw (New Focus 9301-K) and fine adjustment provided by a piezoelectric transducer (Thorlabs AE0505D08), as illustrated in Figure 4.11. The tuning arm is mounted to a baseplate. A vertical adjustment screw (New Focus 9313-K) in the baseplate allows for adjustment of the grating plane angle relative to the tuning arm axis. On a recommendation from Windell Oskay and Daniel Steck, then with the Atom Optics Group at The University of Texas at Austin, I used flexure joints for the tuning arm and baseplate pivots [113,121] and machined the cavity from 954 Aluminum-Bronze, a relatively elastic alloy with a high thermal mass.

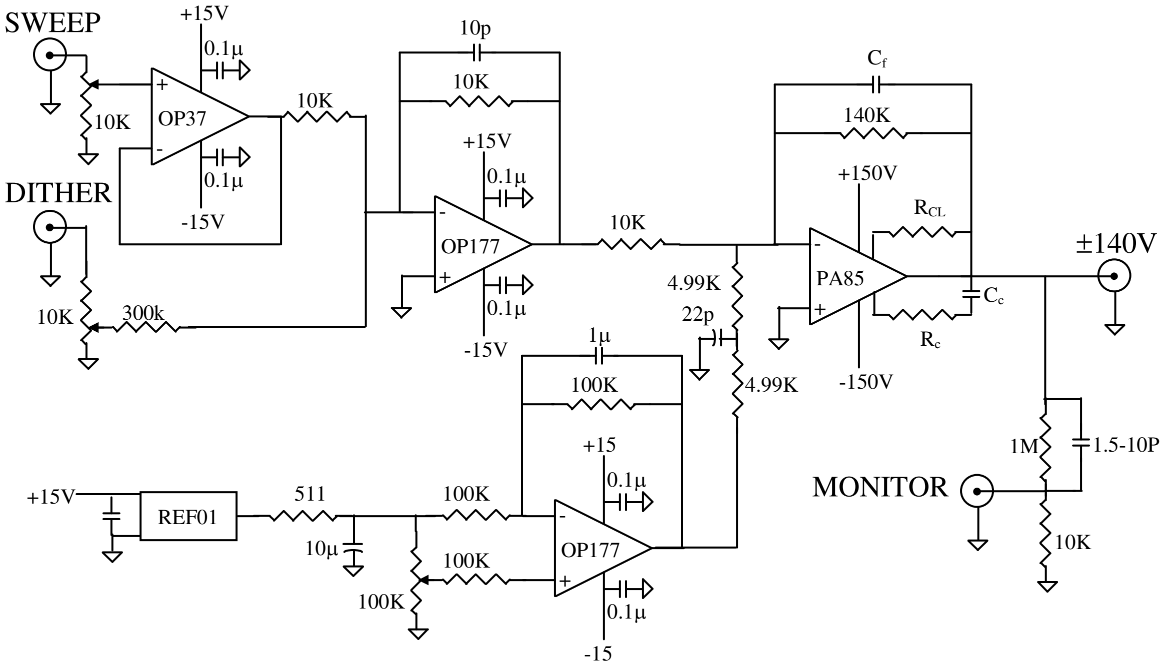

Figure 4.13 Regulated high-voltage amplifier

A low-noise current controller (ILX Lightwave LDX-3620) provides power to the AR coated diode in the cavity, and a spectroscopic grade thermoelectric temperature controller (ILX Lightwave LDT-5910B) provides temperature control to a 30 W thermoelectric cooler (Marlow Industries ST3353) mounted to the baseplate of the cavity. Temperature control is based on a 10 K NTC thermistor (Omega 44006). An amplified sweep voltage and modulation voltage are applied to the piezo attached to the tuning arm to sweep and dither the frequency of the Littrow laser. A function generator provides a sawtooth sweep voltage and one of the lock-in amplifiers in the experiment provides a sine wave modulation voltage, both of which are amplified by a ±140 V, 45 mA regulated high-voltage amplifier. Figure 4.13 is a schematic of the regulated high-voltage circuit that I constructed, and which was based on a circuit design by Leo Hollberg. (Several support components are included in the actual circuit to prevent destruction of the PA85 op-amp due to an overvoltage condition at its input or due to transients from its power supplies. Refer to the PA85 application notes [www.apexmicrotech.com]. Acceptable values for the feedback capacitor (C_f), the current clamping resistor (R_{CL}), the compensation capacitor (C_c), and the compensation resistor (R_c) can also be found in the application notes).

The Littrow laser is frequency stabilized by slowly reducing the sweep amplitude while simultaneously adjusting the offset voltage of the high voltage amplifier, as shown in Figure 4.14. With the sweep completely turned off, the PID is turned on to provide feedback based on an error signal in the reference arm of the experiment.

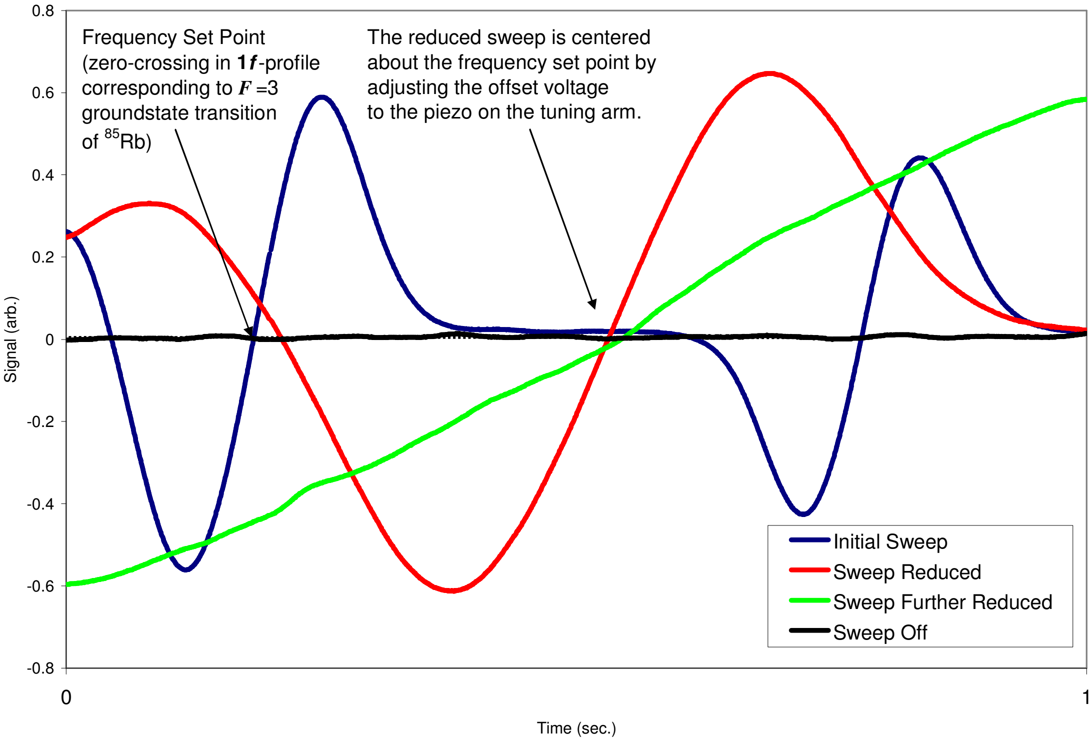

*Figure 4.14 Illustrating how the Littrow laser is stabilized to a zero-crossing in the **1f**-profile*

Operating the grating in 1st-order at the Littrow angle, Eq. 4.9 can be recast as

$$\sin\alpha_o = \frac{\lambda_o}{2d}, \tag{4.16}$$

from which the tuning performance of the Littrow laser is easily derivable,

$$\frac{\Delta\lambda}{\Delta\alpha} = -\lambda_o \cot\alpha_o . \tag{4.17}$$

For the fine angle tuning provided by the piezoelectric transducer attached to the tuning arm of the cavity,

$$\Delta\alpha \cong \frac{D_V V}{l_t} \tag{4.18}$$

where D_V is the axial displacement of the piezo stack per unit voltage (approximately 61 nm/V according to manufacture specifications), V is the voltage applied to the piezo stack, and l_t is the length from the grating pivot to the optical axis of the diode beam along the grating plane (approximately 67.8 mm), as shown in Figure 4.11. Combining Eq. 4.17 and Eq. 4.18, and noting that

$$\Delta \nu = -\frac{c}{\lambda_o^2}\Delta\lambda\,, \tag{4.19}$$

we find that the Littrow cavity tunes in frequency with voltage applied to the piezo according to the following equation:

$$\left.\frac{\Delta \nu}{V}\right|_{\text{ECDL}} \cong \frac{D_V}{l_t}\nu_o \cot\alpha_o\,. \tag{4.20}$$

Operating at a centerline frequency of $\nu_o = 3.85\times10^{14}$ Hz with a corresponding Littrow angle of α_o = 27.9°, the calculated tuning performance for the Littrow cavity is theoretically $\left.{}^{\Delta\nu}\!/\!{}_{\Delta V}\right|_{\text{ECDL}} \cong 0.6$ GHz/V. (Compare this to the experimentally measured tuning rate in Eq. 3.134, $\left.{}^{\Delta\nu}\!/\!{}_{\Delta V}\right|_{ECDL} \approx 0.4\,\text{GHz/V}$). Reconsidering our previous example, if an accuracy of 10 cm/s is demanded in our velocity measurements then a maximum drift in laser frequency of $\Delta\nu_{\text{error}}$ = 180 kHz is tolerable. In this case, the level of proportional feedback to the tuning arm of the Littrow cavity is,

$$\Delta V_{\text{feedback}} = \text{O}\left({}^{\Delta\nu_{\text{error}}}\Big/ {}_{\left.\frac{\Delta\nu}{\Delta V}\right|_{\text{ECDL}}} \right) = \text{O}(0.3\,\text{mV})\,. \tag{4.21}$$

These feedback levels are about two orders of magnitude higher than the O(1 μV) levels required to stabilize the free-running diode laser and are well above noise levels; this is the primary reason why I built the Littrow cavity.

Figure 4.15 shows the first-harmonic lock-in signal detected in the reference arm with the Littrow laser frequency modulating about a zero-crossing in the **1*f***-profile and with the sweep turned off. A modulation frequency of ν_m=2.09 kHz and the lock-in time constant of τ_L=3 ms were employed during the measurement. The blue line shows the **1*f*** signal with the PID turned off and the red line shows the signal with the PID providing proportional feedback to the piezo stack attached to the tuning arm. With only proportional feedback, the Littrow laser exhibits frequency stability to <±5 MHz.

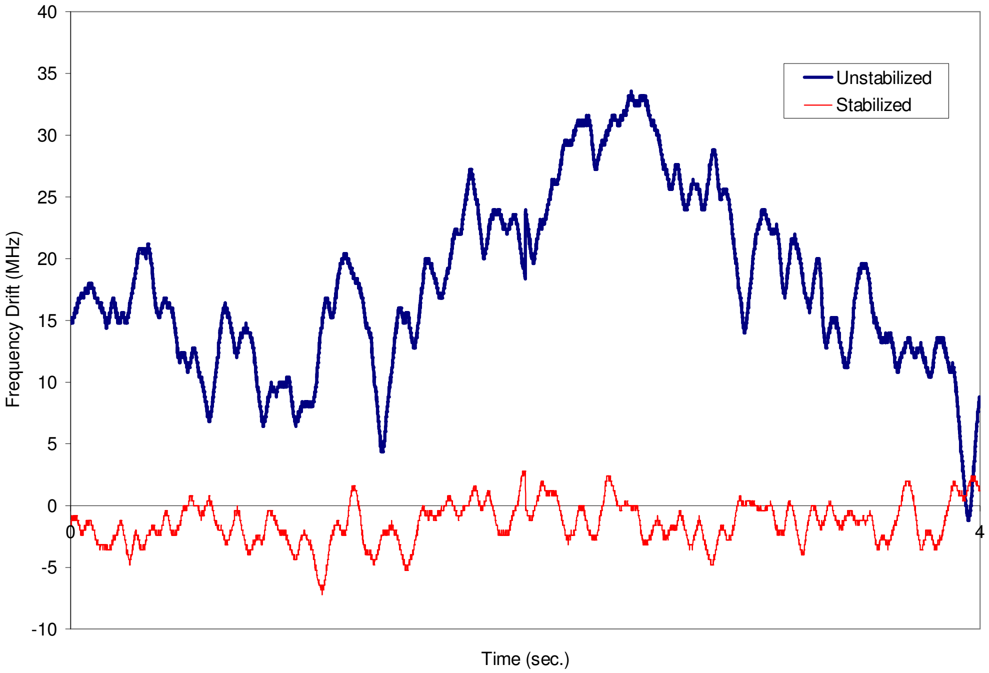

Figure 4.15 Comparing the first-harmonic lock-in signal detected in the reference arm with the Littrow laser cavity unstabilized versus stabilized with proportional feedback

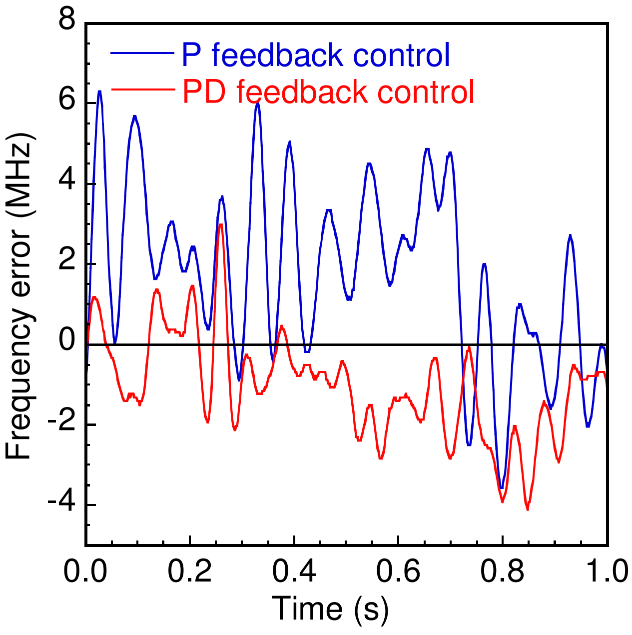

Figure 4.16 First-harmonic lock-in signal detected in the reference arm with the Littrow laser stabilized by proportional (P) feedback versus proportional and differential (PD) feedback

Incorporating the differentiator improves the short-term stability. Figure 4.16 shows the frequency stability attained with proportional and differential feedback versus the frequency stability attained with only proportional feedback. Again, with only proportional feedback, the Littrow laser exhibits frequency stability to <±5 MHz. Adding differential feedback improves the short-term frequency stability to <±3 MHz. (Introducing integration into the feedback signal improves the long-term stability).

4.3.3 Optical Power Amplification

The Littrow laser provides the required spectral performance for MFRS velocity measurements, but only outputs 12 mW of optical power. Rigorous S/N calculations indicate that with only 12 mW available in the probe volume, a modulation depth optimized for second-harmonic detection, and an effective x-axis spatial resolution of $\ell_{eff} = 3.8\,\text{mm}$ (along the probe laser beam) the lock-in time constant required to measure a reliable, repeatable calibration profile utilizing molecular Rayleigh scattering would need to be O(1s). The same holds true for the frequency-locked velocity measurements that rely on this calibration profile. In other words, with only 12 mW of frequency-modulated laser power in the probe volume we would expect the temporal resolution of frequency-locked velocity measurements to be only slightly better than the temporal resolution of the preliminary sweep mode measurements made with 25 mW of probe laser power.

The whole point of developing the frequency-locked mode of operation was to dramatically improve the temporal resolution of MFRS velocity measurements. I therefore spent considerable time trying to amplify the optical power of the Littrow laser output. Two systems were considered to amplify the optical power from the Littrow laser cavity – an injection-locked laser system and a master oscillator power amplifier (MOPA) system– both relying on a broad area laser (BAL) to provide optical power amplification. The output power of index-guided single-mode AlGaAs/GaAs semiconductor diode lasers, such as the diode utilized in the Littrow laser cavity, is limited by the onset of catastrophic-optical-facet damage at an intensity of ~1 MW/cm^2. Gain guided AlGaAs/GaAs BALs are fabricated with an increased stripe length perpendicular to the diode junction, which permits them to operate at higher optical powers before the onset of facet damage. The higher optical power afforded BALs comes at a price, however; the broad junction of the BAL supports higher order spatial modes, which in turn support multiple longitudinal modes. As a consequence, BALs exhibit poor spatial and spectral performance.

I initially considered optically injecting a commercially available BAL with the output from the Littrow laser cavity. As a result of their residual front facet reflectivity, commercially available BALs behave like saturable regenerative amplifiers when optically injected– i.e. an injection-locked BAL doesn't act merely as a power amplifier, but rather as an eigenmode selective amplifier – which imposes a limit on the continuous frequency tunability of injection-locked BALs [121-126]. To tune across the D_2-line of Rb, for instance, the injection current to the BAL would need to be controlled so that the eigenmode frequencies sustained in the BAL junction by the front facet reflectivity synchronously track the frequency of the injected light. Dr. Varghese and I decided that such an injection-locked laser system would be unnecessarily complicated.

Self-oscillation of semiconductor diode lasers is effectively suppressed (except at the highest injection currents) by antireflection coating (AR-coating) one or both facets of the laser [127, 128]. Single-pass diode amplifiers (e.g. tapered semiconductor amplifiers) have both facets AR coated, whereas double-pass diode amplifiers have an AR coated front facet. Though they exhibit lower extraction efficiency than double-pass amplifiers, single-pass amplifiers are less susceptible to thermal- and carrier-induced variations in their index of refraction. Therefore, not only is the optical arrangement required to effectively mode-match the beam from the master oscillator (MO) into a single-pass amplifier more predictable, the amplified output beam from a single-pass amplifier generally exhibits better spatial qualities as well. Unfortunately, we were unable to convince any manufacture or vendor to sell us a tapered amplifier. We therefore purchased a BAL with a $w_{\|}$=100μm stripe width and an AR-coated front facet (R~1.1x10^{-6}; λ=785 nm and $P_{\max}$=1.5 W – before AR-coating – at I=1.67A, T=25 °C), and turned our attention to the development of a double-pass BAL MOPA system.

Double-pass BAL amplifiers exhibit small-signal gain when the input optical power coupled into the BAL is low; for a given optical power coupled into the BAL, the small-signal gain linearly increases with the BAL injection current until amplified spontaneous emissions (ASE) saturate at increasing injection currents. With front facet reflectivities of R ~ 5x10^{-3} and R ~ 4.5x10^{-4}, Goldberg *et al.* reported small-signal gains of 15-20 dB before the gain was clamped by ASE [129,130].

Figure 4.17 The essential components of a BAL MOPA system

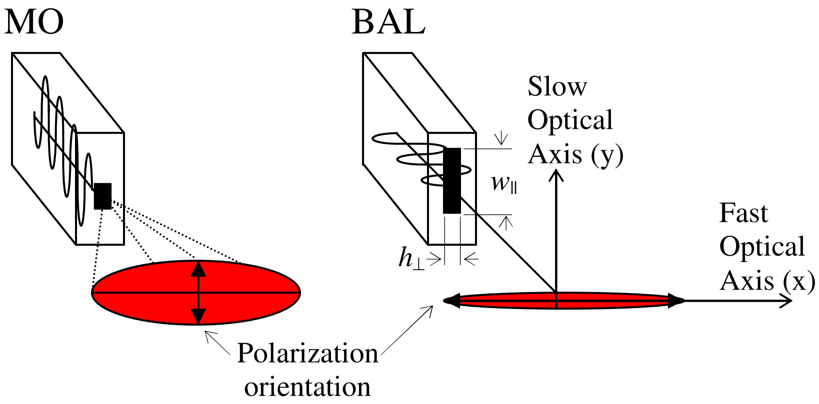

Figure 4.18 Comparing index-guided diodes (MO) to gain-guided diodes (BAL)

Figure 4.17 shows the essential components of the BAL MOPA system: The MO in the MOPA laser system is the Littrow ECDL, providing 12 mW of frequency tunable, frequency stable, relatively narrow linewidth lasing at 780 nm; a Faraday rotator provides isolation between the MO and the BAL; a λ/2-plate is used to match the polarization of the input beam to the BAL polarization; and an optical system was designed to efficiently couple the input beam into the BAL junction. As illustrated in Figure 4.18, index-guided single-mode diodes are linearly polarized parallel to the junction (along the junction width, $w_{\|}$), whereas gain-guided BALs are linearly polarized perpendicular to the junction (along the junction height, $h_{\perp}$). I initially felt that coupling the input beam into the BAL would most easily be accomplished by preserving the junction orientation between the MO and the BAL, as shown in Figure 4.18; i.e. I assumed that the fast optical axis of the collimated Littrow laser beam could be focused to a beam waist at the BAL front facet that was smaller than the BAL junction height, $h_{\perp}$. Unfortunately, multi-spatial modes supported along the fast optical axis of the Littrow laser beam prevented me from effectively coupling the input beam into the BAL junction with this arrangement; i.e. I couldn't attain a tight enough focus along the fast optical axis of the input beam. Having observed that the spatial intensity profile along the slow optical axis of the Littrow laser beam is relatively Gaussian, I eventually rotated the preliminary BAL orientation 90°, expanded the slow optical axis of the collimated input beam, and focused this expanded, relatively single-mode axis to a beam waist at the BAL front facet that didn't overfill the BAL junction height. The development of the coupling optics for the BAL MOPA laser system is discussed in greater detail in Appendix G.

Figure 4.19 is a picture of the fourth (and final) BAL MOPA system I desgined. An *f*=60 mm focal length positive cylindrical lens (Melles Griot 01LCP021) and an *f*=–19 mm negative cylindrical lens (Melles Griot 01LCN002) were configured as a Galilean telescope to compress the fast axis of the Littrow laser beam for passage through the isolator. An *f*=–25.4 mm negative cylindrical lens (Melles Griot 01LCN003) and an *f*=60 mm positive cylindrical lens (Melles Griot 01LCP021) were configured as a Galilean telescope to expand the slow optical axis of the Littrow laser beam after passage through the isolator.

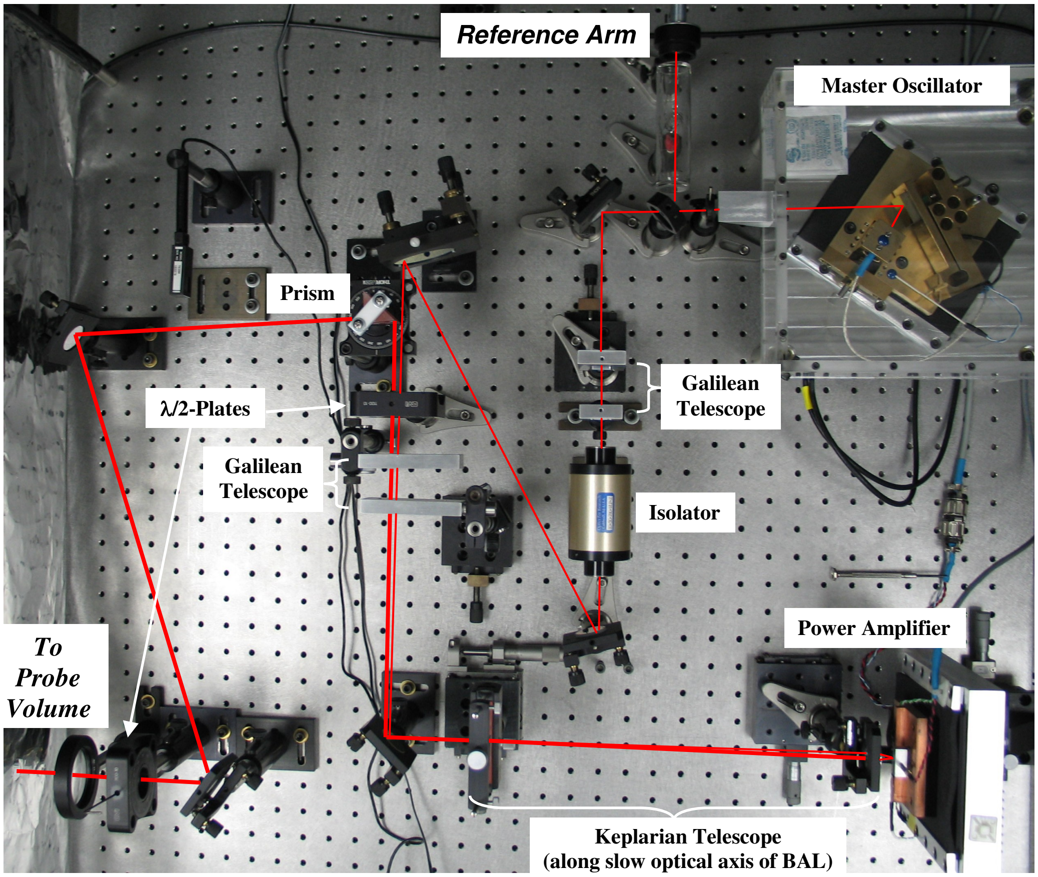

Figure 4.19 The fourth (and final) BAL MOPA system

The expanded slow optical axis of the Littrow laser beam was tightly focused at the BAL front facet, along the fast optical axis of the BAL, by an $F_{\#}$=1, f=8 mm focusing/collimating optic (Melles Griot 06GLC002). An f =300 mm plano-convex cylindrical lens (Melles Griot 01LCP019) and the final focusing/collimating optic were configured as an afocal (Keplarian) telescope along the compressed fast optical axis of the Littrow laser beam (which corresponds to the slow optical axis of the BAL), and an injection angle was introduced along the slow optical axis of the BAL by translating the f =300 mm positive cylindrical lens parallel to the BAL junction width (i.e. up the page). Two mica λ/2-plates were used in this final BAL MOPA system: One to align the polarization of the input beam to the BAL polarization and one to ensure that the amplified output diverted to the experiment is polarized perpendicular to the optical axis in the scattering arm. An AR coated right-angle prism was used to divert the amplified output from the BAL to the experiment.

The highest small signal gain I ever measured with the BAL MOPA system illustrated in Figure 4.19 was ~9.6 dB; i.e. with a measured power in the final focused spot at the front facet of the BAL of P_i~8 mW and operating the BAL at an injection current of I~520 mA and a temperature of T=14.4 °C, I measured an amplified output power P_o~73 mW on a background of P_{ASE}~20 mW of ASE. Unfortunately, the Littrow laser output was unstable during this measurement. For all BAL MOPA systems, I observed that a small fraction of the ASE always coupled into the Littrow laser cavity. Above ASE powers of P_{ASE}~10 mW this generally resulted in frequent mode-hops of the Littrow laser output. To ensure stable operation of the MOPA laser system, I therefore resigned myself to operating the BAL at lower injection currents. When operating the fourth BAL MOPA system with a BAL injection current of I~480-500 mA, for instance, I was generally able to measure a small signal gain of ~8-9 dB with ASE powers less than P_{ASE}~10 mW; i.e. with a measured power in the final focused spot of P_i~7-8 mW and operating the BAL at an injection current of I~480 mA, I typically measured an amplified output power P_o~50-55 mW on a background of P_{ASE}~5-10 mW of ASE.

The gain profile of our BAL has a calculated centerline wavelength of λ=787 nm at an injection current of I~500 mA and a temperature of T=25 °C. The gain curve of most GaAlAs/GaAs semiconductor diode lasers shifts with temperature at a rate of ~0.25 nm/°C. This implies that I would have needed to operate our BAL at T~ −3 °C to center its gain curve at λ=780 nm. I observed that the performance of the BAL MOPA laser system did in fact slightly improve as the BAL junction temperature was decreased. Unfortunately, there was a practical limit to how far I could reduce the BAL junction temperature – I regularly measured a dew point temperature in the lab of 5 °C, and observed condensation on the BAL at junction temperatures as high as T=17 °C.

4.3.4 Frequency-Locked MFRS Velocity Measurements in a Supersonic Expansion of CO_2

The frequency-locked measurements presented below were made using the fourth BAL MOPA system (illustrated in Figure 4.19), with P_o~45 mW of frequency-modulated probe laser power on a background of P_{ASE}~7 mW of ASE. During both phases of the experiment – while acquiring the calibration profile and while measuring the jet velocity – condensate scattering from a supersonic expansion of CO_2 was collected in the scattering arm of the experiment. The same converging nozzle utilized during the sweep mode measurements discussed in Section 4.2 was utilized during the frequency-locked measurements presented below, and was again oriented so that the jet axis direction coincided with the sensitivity vector. Condensate scattering was collected from a probe volume approximately 20 mm (~6-7 nozzle exit diameters) from the nozzle exit. The optical design used to collect the condensate scattering from the jet probe volume, to relay the collected scattering through the z=75 mm Rb cell in the scattering arm, and to focus the collected scattering onto the R636-10 PMT is illustrated in Figure 4.20. With help from the Zemax ray-tracing program, a total of six AR coated optics were chosen to balance aberrations introduced into the final focused image by the relatively fast collection: L_1 and L_2 are both f=120.8 mm, $F_\#$=1.2 plano-convex spherical lenses (Melles Griot 01LPX215/076), L_3 is a f=–75 mm, $F_\#$=–1.52 plano-concave spherical lens (Melles Griot 01LPK033/076), L_4 is a f=80 mm, $F_\#$=1.78 plano-convex spherical lens (Ross Optical L-PCX282/335), L_5 is a f=–50 mm, $F_\#$=–1.69 plano-convex spherical lens (Melles Griot 01LPK019/076), and L_6 is a f=80 mm, $F_\#$=2.96 plano-concave spherical lens (Melles Griot 01LPX153/084). The PMT cathode was oriented with its long dimension parallel to the probe laser beam and the illustrated optical design has a magnification of M=2.3, resulting in an effective spatial resolution of $\ell_{eff} = 5$ mm along the direction of the probing laser beam (refer to Eq. 3.35b of Section 3.2). All scattering measurements were made with an aluminum and cloth shroud surrounding the scattering arm of the experiment and with the PMT biased to V_{PMT}=900 V.

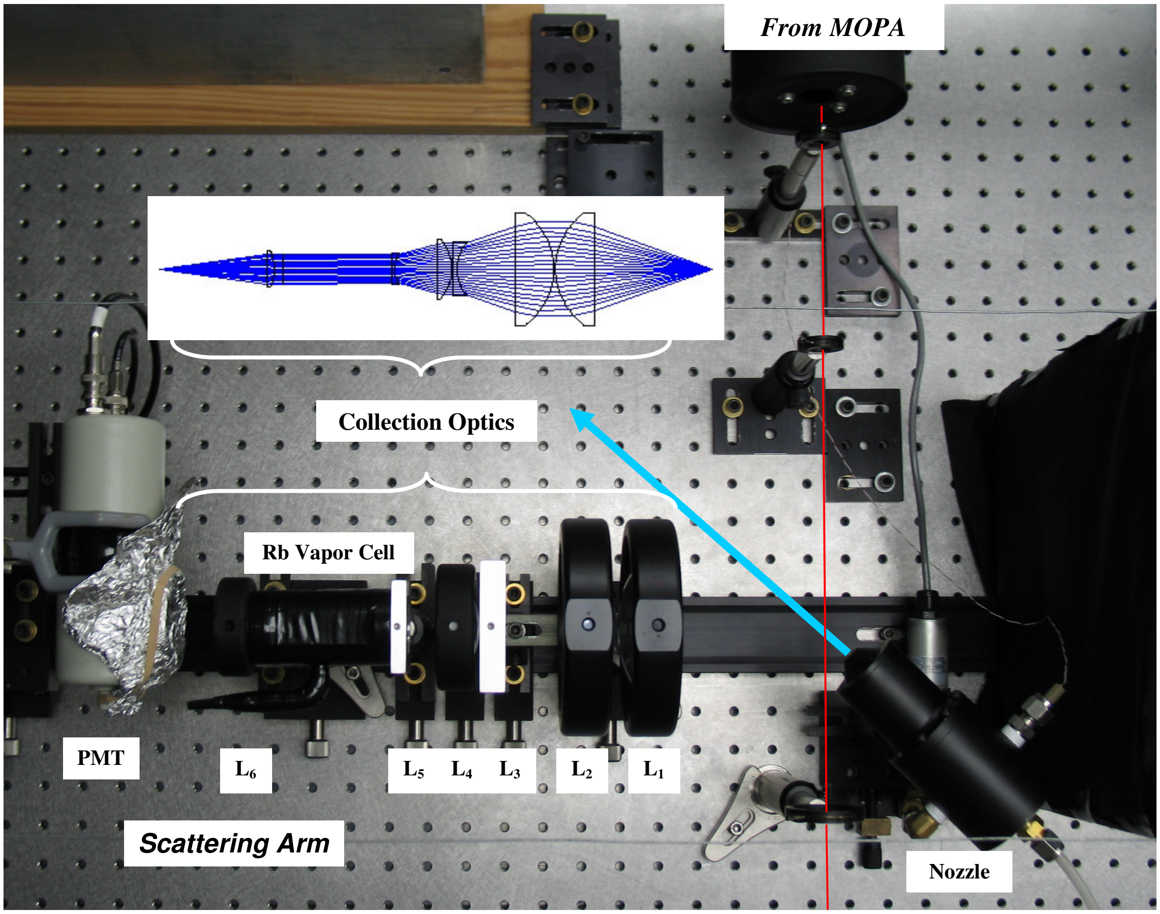

Figure 4.20 Scattering arm as configured during preliminary frequency-locked experiments

The measurements in the reference and scattering arms were made with a lock-in integration time of τ_L=1 s. The reference signals internal to each lock-in were synchronized with the modulation frequency, ν_m=2.09 kHz, and the phase of each synchronized reference signal was selected to optimize detection of the extracted harmonic. During the calibration phase of the experiment, the optical frequency of the probing laser beam was swept across the Doppler broadened ***F***=3 and ***F***=2 ground state transitions of ^{85}Rb and ^{87}Rb, respectively. Each sweep in optical frequency had a 100 s period and was the result of a triangle-wave voltage signal input to the piezoelectric transducer attached to the tuning arm of the Littrow laser cavity. Each 100 s triangle wave sweep of the grating angle resulted in the acquisition of two calibration profiles: One acquired while scanning from the minimum triangle-wave voltage (minimum optical frequency) to the maximum triangle-wave voltage (maximum optical frequency) and the other acquired while scanning from the maximum triangle-wave voltage back to the minimum triangle-wave voltage. A total of three triangle wave sweeps were acquired during the calibration phase resulting in a total of six calibration profiles.

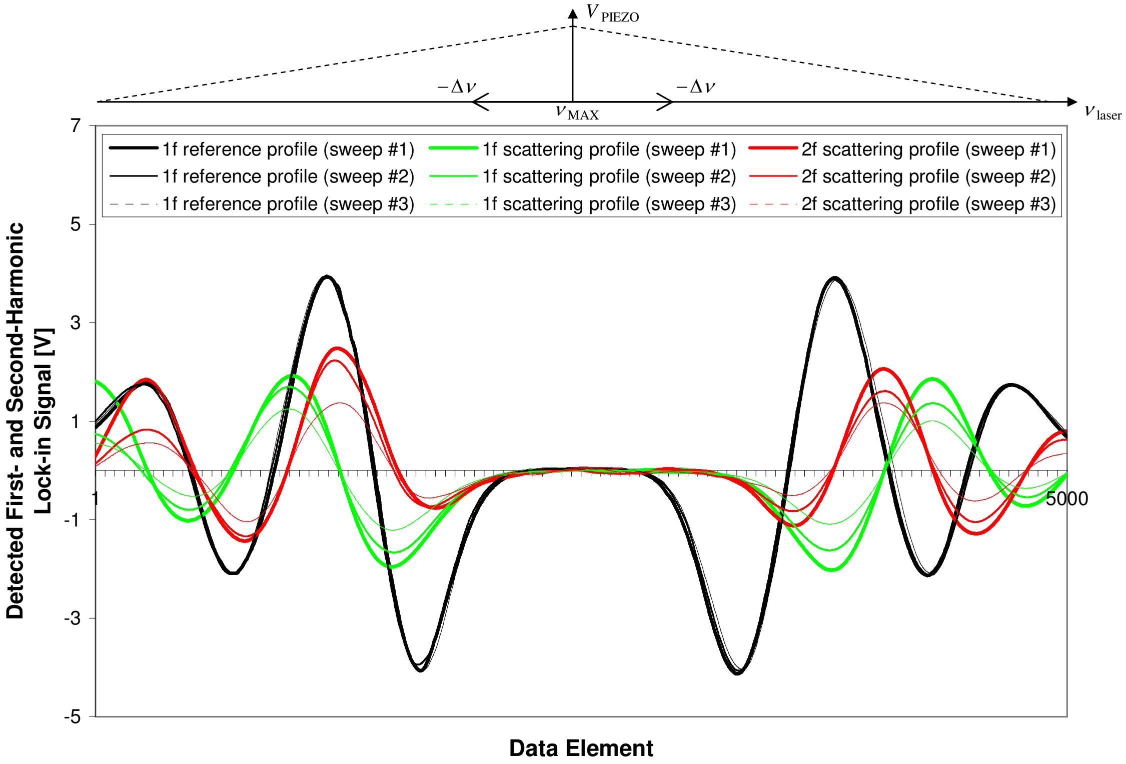

*Figure 4.21 Raw **1f** reference profiles and **1f** and **2f** scattering profiles acquired during the calibration phase of the frequency-locked experiment*

Figure 4.21 shows the raw **1*f***-profiles acquired in the reference arm during the calibration phase of the experiment and the raw **1*f***- and **2*f***-profiles simultaneously acquired from condensate scattering. The **1*f***-profiles in the reference arm were acquired with a lock-in sensitivity of $S_{L,ref}$ =500 µV and the **1*f***- and **2*f***-profiles in the scattering arm were acquired with lock-in sensitivities of $S_{L,\mathbf{1}f}$=500 µV and $S_{L,\mathbf{2}f}$=100 µV, respectively. First note that the peak first-harmonic lock-in signal detected in the scattering arm during the calibration phase is O(1.6 V). If I was only collecting and detecting frequency-modulated molecular Rayleigh scattering from gas phase CO$_2$, then with the experiment configured as it was during the calibration phase we would expect a peak theoretical first-harmonic signal of only O(6.5 mV) – i.e. I was obviously collecting condensate scattering. Notice also that the profiles acquired in the scattering arm are shifted relative to the profiles acquired in the reference arm, but that the shift is not symmetric about the center of the acquired reference profile (i.e. the peak in the triangle wave signal). The scattering profiles should in fact be Doppler frequency shifted relative to the corresponding reference profile due to the bulk velocity of the CO_2 jet, but since the jet is relatively steady we would expect the shifted profile acquired during the positive-going scan in frequency to mirror the shifted profile acquired during the negative-going scan in frequency; i.e. we would expect the shift to be symmetric about the center of the sweep.

There is a simple explanation for the observed asymmetry: The analog lock-in amplifier utilized in the reference arm during the experiment integrates measurements differently than the digital lock-in amplifiers utilized in the scattering arm, resulting in an offset in time between the profile measured in the reference arm and the corresponding profiles measured in the scattering arm. As illustrated in Figure 4.22, this offset can be accounted for by cross-correlating the **1*f***-profiles acquired in the reference and scattering arms during the positive-going and negative-going scans in frequency. Subtracting the calculated shift between the **1*f***-profiles acquired during the positive-going scan, ΔS_p, from the calculated shift between the **1*f***-profiles acquired during the negative-going scan, ΔS_n, results in a measure of the average Doppler frequency shift, $\Delta \nu_D$, during the triangle-wave sweep in frequency. Adding the calculated shift between the **1*f***-profiles acquired during the positive-going scan to the calculated shift between the **1*f***-profiles acquired during the negative-going scan results in a measure of the measurement offset, ΔO.

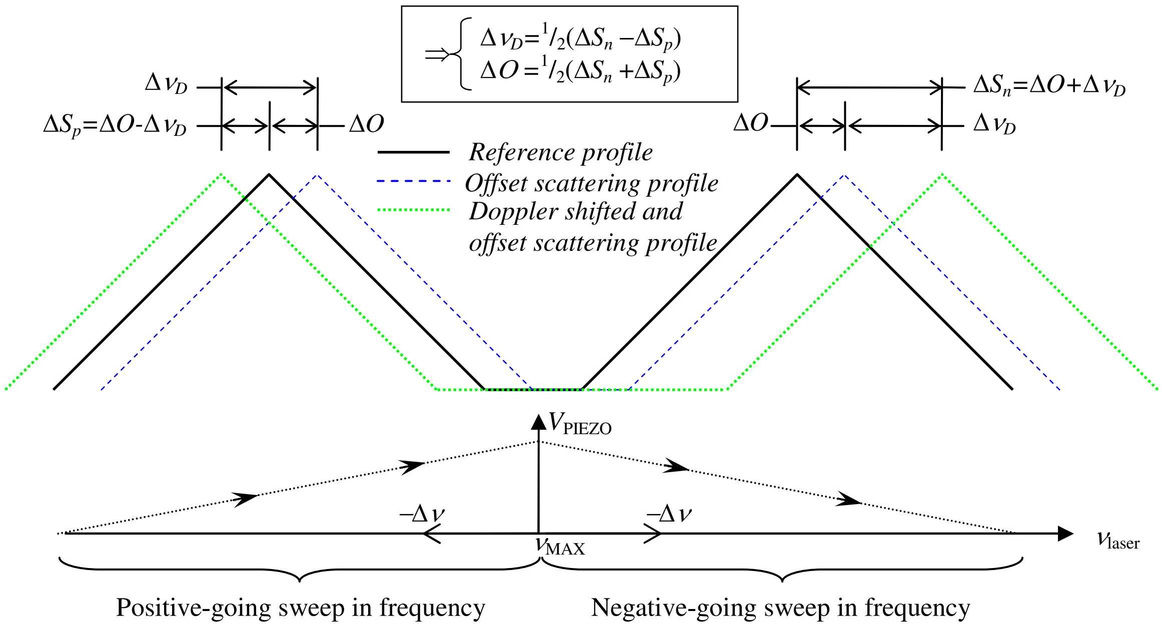

Figure 4.22 Accounting for the different data update rates of analog versus digital lock-ins

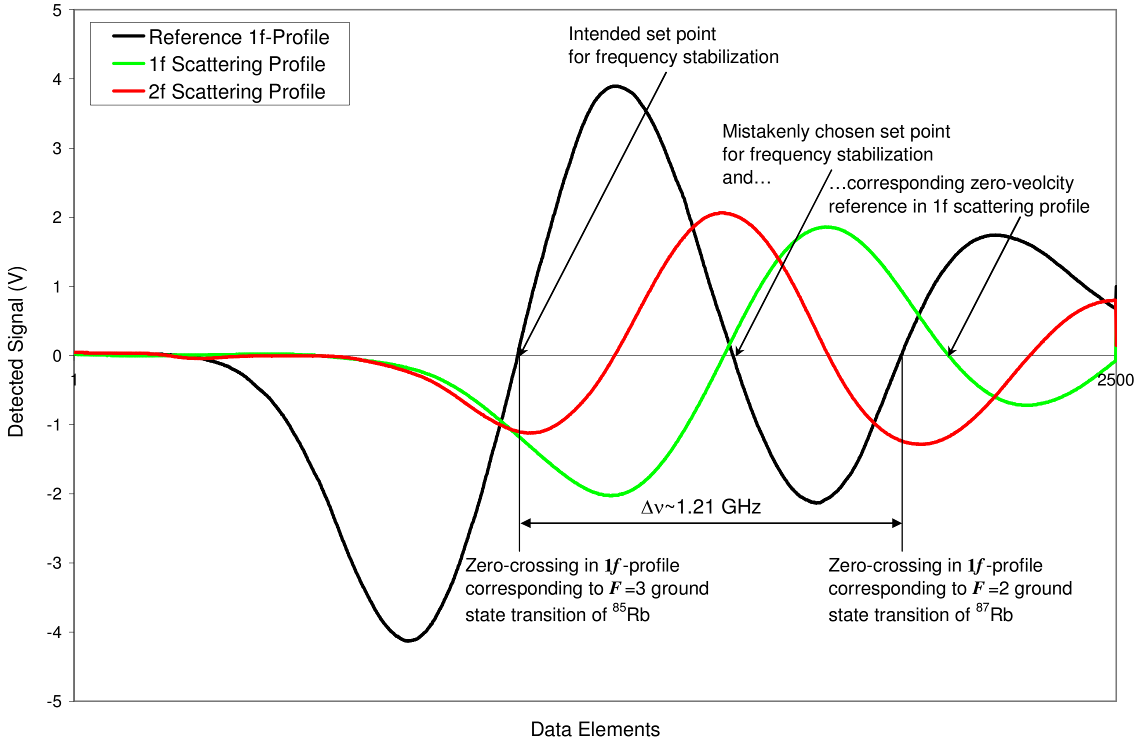

Figure 4.23 A sample of the 1f-profile acquired in the reference arm and the 1f- and 2f-profiles simultaneously acquired in the scattering arm during a single negative-going calibration scan

Using the procedure described above and illustrated in Figure 4.22, I calculated the average Doppler shift in data elements resulting from the bulk velocity in the CO_2 jet during each of the three calibration sweeps. I also calculated an average data element-to-frequency conversion for each sweep by measuring the separation in data elements between the zero-crossings in the reference **1*f***-profiles. As illustrated in Figure 4.23, the zero-crossings in the acquired **1*f*** -profiles correspond to the resonant centerlines of the Doppler broadened ***F***=2 and ***F***=3 ground state transitions of ^{87}Rb and ^{85}Rb, respectively, and have a known frequency separation of 1.21 GHz. The data element-to-frequency conversions calculated for the positive-going and negative-going scans in frequency were averaged for each sweep, resulting in an average data element-to-frequency conversion for each calibration sweep. Knowing the geometry of the experiment and having calculated the average Doppler shift in data elements for each sweep, I was then able to calculate the average velocity measured in the CO_2 jet during each of the three calibration sweeps: $\overline{V}_{measured}\big|_{\text{sweep \#1}} = 219.28$ m/s, $\overline{V}_{measured}\big|_{\text{sweep \#2}} = 214.32$ m/s, and $\overline{V}_{measured}\big|_{\text{sweep \#3}} = 212.18$ m/s.

(Note that this procedure is practically identical to the procedure employed during the sweep mode measurements discussed in Section 4.2. The analog lock-in amplifier was not employed during sweep mode measurements, however, and I did not observe a measurement offset between the data acquired in the reference arm and the data acquired in the scattering arm).

The stagnation pressure and temperature in the nozzle plenum were measured and manually recorded at the beginning – $P_o|_i$= 39.28 psi = 270.83 kPa, $T_o|_i$= −11 °C– and end – $P_o|_f$= 38.80 psi = 267.52 kPa, $T_o|_f$= −8.1 °C – of the calibration phase, and the maximum theoretical jet core velocities (corresponding to isentropic expansion to atmospheric pressure) at the beginning and end of the calibration phase were calculated from Eq. 4.1: $\overline{V}_{theoretical}\Big|_{\max,i}$ =296.24 m/s and $\overline{V}_{theoretical}\Big|_{\max,f}$ =296.33 m/s. (I attribute the temperature increase at the end of the calibration phase to the reduced expansion of CO_2 through the two stage regulator attached to the cylinder of CO_2 when the cylinder approached depletion). The velocity measurements presented in this sub-section average over flow gradients and cannot be directly compared to a calculated jet velocity field. Since the measurement probe volume extends into the shear layer of the under-expanded flow we would, however, expect all measured velocities to be less than the maximum theoretical jet core velocity. In addition, the sweep mode velocity measurements I made during the calibration phase of the experiment can be compared to the frequency-locked velocity measurements made during the measurement phase of the experiment to ensure that those measurements are reasonable.

A VI was developed with National Instruments LabView G-programming language to process the measured calibration profiles: The six **1*f***- and **2*f***-profiles that were simultaneously acquired in the scattering arm were ratioed, resulting in six **1*f*:2*f*** and six corresponding **2*f*:1*f*** ratio profiles; A data element-to-frequency conversion was calculated from each of the six **1*f***-profiles acquired in the reference arm according to the procedure discussed above; A data element-to-velocity conversion was then calculated for each **1*f*:2*f*** (and corresponding **2*f*:1*f***) ratio profile according to Eq. 3.1; Finally, the zero velocity reference for each ratio profile was defined at the interpolated zero-crossing in the shifted **1*f*** scattering profile corresponding to the frequency set-point in the unshifted **1*f*** reference profile, as illustrated in Figure 4.23. Figure 4.24 shows the six **1*f*:2*f*** ratio profiles as well as the corresponding **2*f*:1*f*** ratio profiles processed from the raw data in Figure 4.21.

Notice that none of the ratio profiles in Figure 4.24 coincide. The offsets between the six **1*f*:2*f*** ratio profiles increase in the vicinity of the **2*f*** zero-crossing and the offsets between the six **2*f*:1*f*** ratio profiles are relatively consistent across the plotted velocity range. For the exceedingly long sweep period employed during the calibration phase, there are several possible explanations for the observed offsets between the plotted ratio profiles: changes in the jet thermodynamics during the calibration phase resulted in a change in the spectral linewidth of collected scattered radiation; unsteadiness in the jet velocity resulted in a change in the Doppler frequency shift of collected scattered radiation; fluctuations in the temperature of the Rb cell in the scattering arm resulted in slight changes to the detected modulated absorption signal; and so forth. Though I failed to measure a repeatable calibration profile, I decided to conduct some velocity measurements with what I had; i.e. I measured the jet velocity in a supersonic expansion of CO_2 by correlating the **1*f*:2*f*** and **2*f*:1*f*** ratio signals detected in the scattering arm during frequency-locked measurements to the ratio profiles in Figure 4.24.

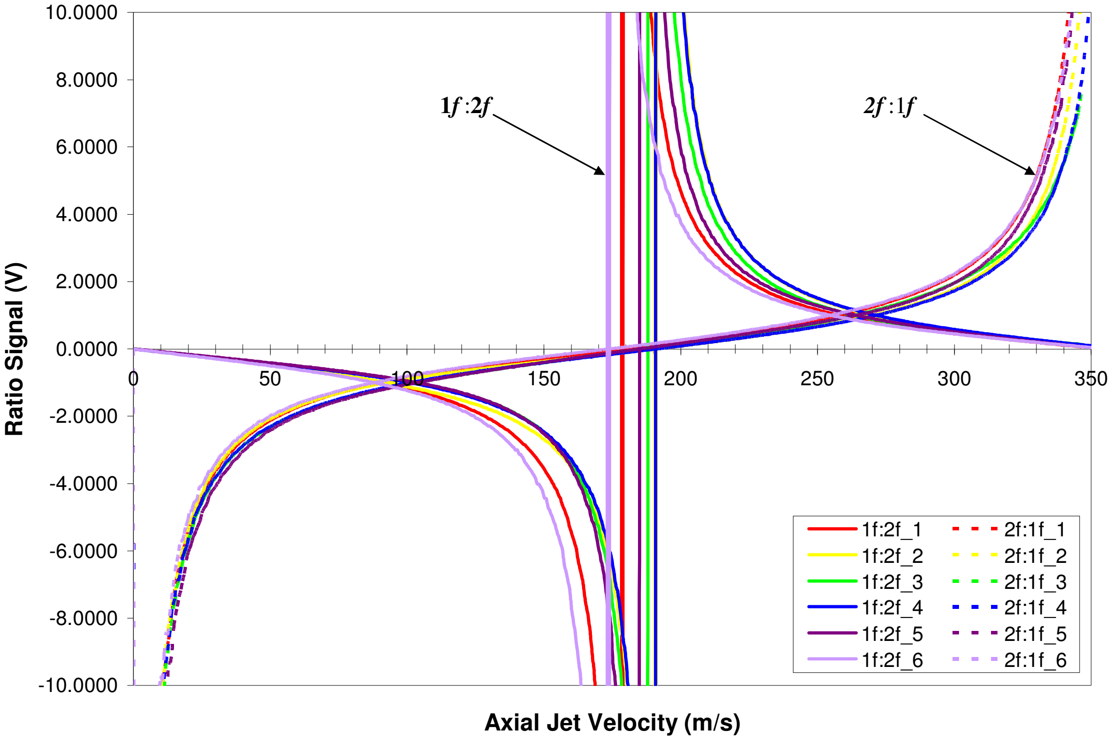

Figure 4.24 1f:2f and 2f:1f calibration profiles derived from the raw scattering profiles acquired during the calibration phase of the frequency-locked experiment

Figure 4.25 shows some raw first harmonic-to-second harmonic and second harmonic-to-first harmonic ratio signals detected in the scattering arm while conducting frequency-locked measurements in a supersonic expansion of CO_2. Included in the figure are the jet stagnation pressures and stagnation temperatures that I manually recorded during the data run, as well as the first-harmonic lock-in signal detected in the reference arm of the experiment. Based on the error signal in the reference arm, the Littrow laser cavity exhibited a short-term frequency drift of ±1.8 MHz (corresponding to a velocity error of ±0.9 m/s) during the data run. (This assertion neglects the possibility of a drift in the set point frequency due to a drift in the reference arm Rb cell temperature, as described below).

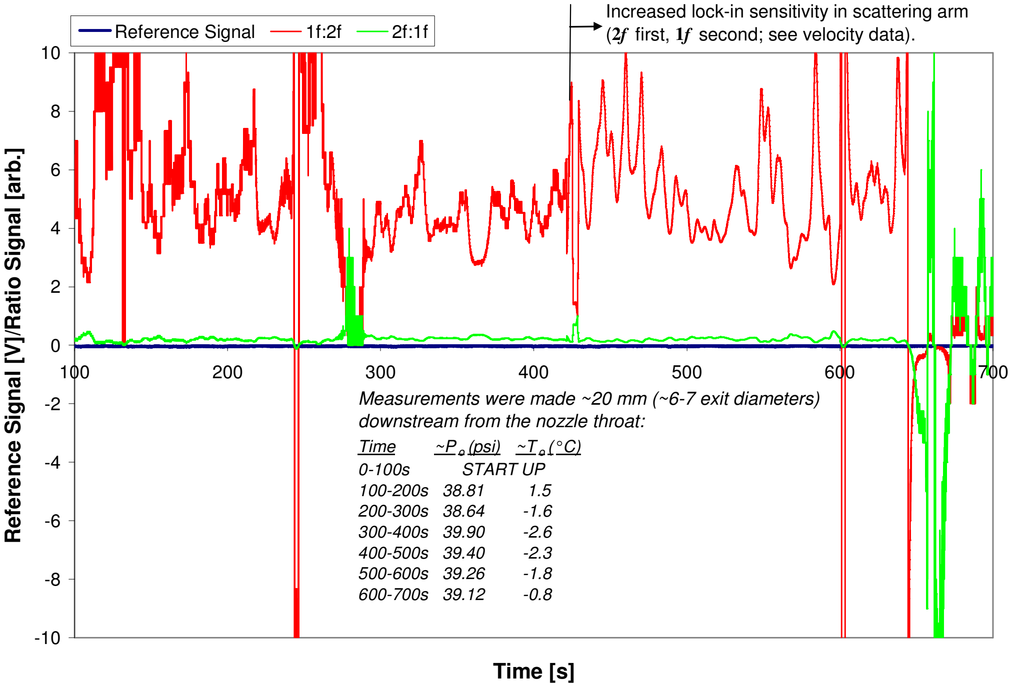

Measurements were made ~20 mm (~6-7 exit diameters) downstream from the nozzle throat:

Time	*~P_o (psi)*	*~T_o (°C)*
0-100s	*START UP*	
100-200s	*38.81*	*1.5*
200-300s	*38.64*	*-1.6*
300-400s	*39.90*	*-2.6*
400-500s	*39.40*	*-2.3*
500-600s	*39.26*	*-1.8*
600-700s	*39.12*	*-0.8*

Figure 4.25 Raw first harmonic-to-second harmonic and second harmonic-to-first-harmonic lock-in ratios detected in the scattering arm during the measurement phase of the experiment

Figure 4.26 shows a sample of the jet velocities measured during the data run. The plotted velocities correspond to the raw **1*f*:2*f*** and **2*f*:1*f*** signals in Figure 4.25 that were measured from *t*=400 s to *t*=500 s into the run, and were calculated using the ratio profiles illustrated in Figure 4.24. The large, almost top-hat spike observed in the plotted velocities is the result of a change that I made mid-run to the lock-in amplifiers in the scattering arm: I increased the second-harmonic lock-in sensitivity from $S_{L,2f}$=100 μV to $S_{L,2f}$=10 μV and then immediately increased the first-harmonic lock-in sensitivity from $S_{L,1f}$=500 µV to $S_{L,1f}$=50 µV. Notice that before I made this instrumental change there were no significant spikes in the plotted velocities, and that after I increased the lock-in sensitivities regular spikes began to appear in the data. I suspect that these spikes were the result of a momentary over-voltage at the front-end of one or both of the lock-in amplifiers in the scattering arm due to a marked increase in the collected and detected scattering intensity (e.g. either from dust entrained into the jet, a momentary increase in condensate, etc.).

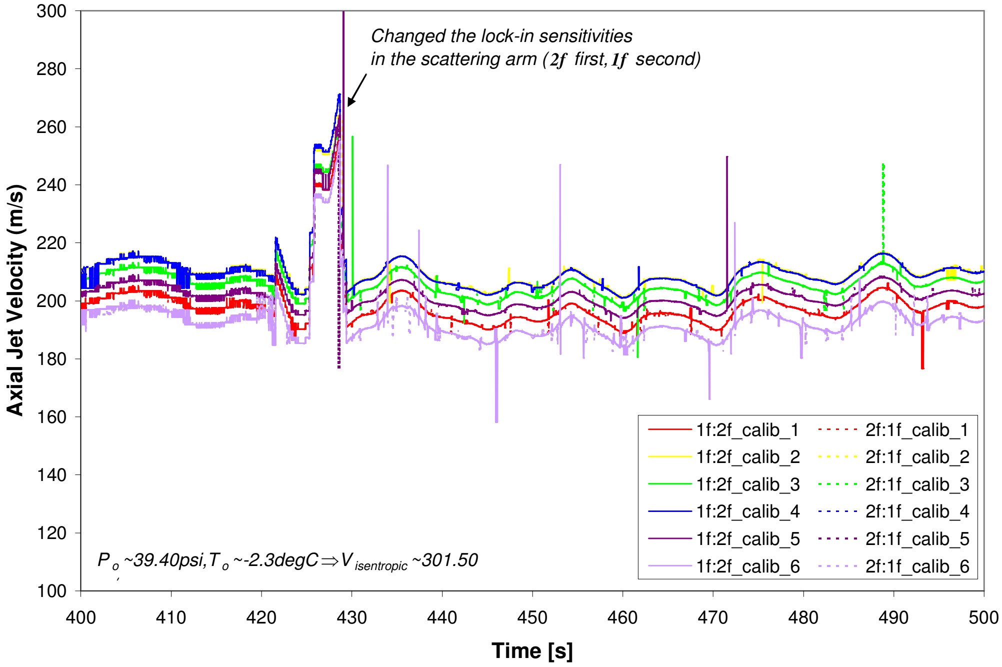

Figure 4.26 Some frequency-locked velocity measurements

The average measured velocity in Figure 4.26, calculated from all six ratio profile, is ~204 m/s. The offset between the ratio profiles in Figure 4.24 results in a velocity offset of ~17 m/s between the average maximum velocity, $\overline{V}_{measured}\big|_{\max} \approx$ 211 m/s, and the average minimum velocity, $\overline{V}_{measured}\big|_{\min} \approx$ 194 m/s. Based on the stagnation pressure and temperature recorded during this portion of the data run, the maximum theoretical jet core velocity (calculated from Eq. 4.1) was $\overline{V}_{theoretical}\big|_{\max} =$ 301 m/s.

I had intended on stabilizing to the Littrow laser cavity at the zero-crossing in the **1*f*** reference profile associated with the ***F***=3 ground state transition of ^{85}Rb. I mistakenly stabilized the Littrow laser cavity at the zero-crossing between the ***F***=3 ground state transition of ^{85}Rb and the ***F***=2 ground state transition of ^{87}Rb, as illustrated in Figure 4.23. Consequently, any drift in the reference cell temperature during the frequency-locked measurements presented below resulted in a slight change in the stabilized laser frequency. In addition, if the spectral width of the collected condensate scattering was appreciably larger than the laser linewidth, then we would expect the **1*f***-profile acquired in the scattering arm to be "broader" than the **1*f***-profile acquired in the reference arm; i.e. we would expect the zero-crossing between the ***F***=3 ground state transition of ^{85}Rb and the ***F***=2 ground state transition of ^{87}Rb to lie at a lower frequency in the **1*f*** scattering profile than in the **1*f*** reference profile. With the zero velocity reference for each ratio profile defined as it was, this would result in frequency-locked velocity measurements that over-predict the jet velocity.

Chapter 5: Conclusions

When I started building the ECDL-MOPA laser system, there was no commercially available system like it. Sacher Lasertechnik now offers a 1050mW diode-based laser system at 780 nm that exhibits mode-hop free tuning up to 15 GHz, a single-mode spectral linewidth of ~1MHz, a circular spatial mode profile with an M-square of $M^2 < 1.7$ (sufficient for fiber coupling), and side-mode suppression >50dB (the TEC-300-0780-1000~$26,000). Provided collection and detection of stray reflections and ambient background radiation is effectively suppressed, with P_o=1 W of frequency modulating laser power in the probe volume, a modulation index optimized for second-harmonic detection, and a z=100 mm Rb vapor cell heated to T_{Rb}=310 K in the scattering arm of the experiment the rigourous theoretical model developed in Chapter 3 predicts a peak first-harmonic lock-in signal-to-noise ratio detected from static room air of ~107 and a peak second-harmonic lock-in signal-to-noise ratio detected from static room air of ~48 with a lock-in integration time of only τ_L=10 ms and an effective spatial resolution of only $\ell_{eff} = 500\,\mu\text{m}$ along the probe laser beam.

I feel that the MFRS velocimeter could be developed into a useful scientific tool. However, a significant experimental and theoretical effort would be required to take the MFRS velocimeter out of the lab and into the field. In any environment other than a dust-free facility there is simply too much dust (or particle matter) floating around to measure a reliable calibration profile using molecular Rayleigh scattering. MFRS velocity measurements made outside of the lab would require a priori knowledge of the calibration profile corresponding to the flow under investigation. This calibration profile would need to be measured in a dust-free lab environment utilizing Rayleigh scattering from a gas with identical composition, temperature, and pressure to the flow under investigation. As an alternative, one could develop a model for the detected first- and second-harmonic profiles as a function of gas composition, temperature, and pressure and laser linewidth and make enough measurements in the lab to instill confidence in the developed model. The theory described in Chapter 3 provides a starting point for the development of such a model, and the measurements described in Chapter 4 provide significant experimental insight into MFRS velocimetry. With a trust-worthy model, MFRS velocity measurements could be conducted in an ambient environment by simply ignoring saturated measurements resulting from collected and detected dust scattering.

Appendix A: A General Discussion of Lock-In Amplifiers

A.1 Introduction

Homodyne detection of the modulated absorption signal measured during preliminary MFRS experiments was accomplished with a lock-in amplifier. As illustrated in Figure A.1, a digital lock-in consists of a front-end amplifier, an analog-to-digital (A/D) converter, a phase sensitive detector (PSD), a low pass RC-filter, and a back-end amplifier [38]. Consider a detected modulated absorption signal oscillating at a primary angular frequency ω_{sig} and output to the lock-in. The signal is first amplified at the front-end of the lock-in to provide adequate resolution for analog-to-digital conversion. The digital signal from the A/D converter enters the PSD, which mixes it with an internal reference signal synchronized with a harmonic of the detected modulated absorption signal – e.g. for first harmonic detection, the internal reference is simply synchronized with the primary angular frequency, ω_{sig}, of the detected modulated absorption signal. A DC-component of the mixed signal proportional to the amplitude of the corresponding detected harmonic is passed by the low pass filter and then amplified at the back-end of the lock-in up to a full scale voltage of ±10 V.

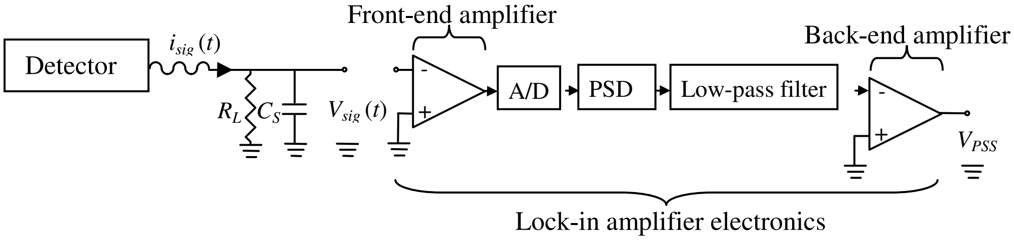

Figure A.1 Simple schematic of a digital lock-in amplifier

The discussion below begins with a simple mathematical description of homodyne detection utilizing lock-in amplifiers. The primary advantage of homodyne detection is the extremely low equivalent noise bandwidth (ENBW) that lock-in amplifiers offer. This appendix will conclude with a definition and mathematical derivation of the lock-in amplifier ENBW.

A.2 Simple Description of Homodyne Detection Utilizing a Lock-In Amplifier

Consider a laser beam that is slowly swept in frequency across an absorption feature, as illustrated in Figure A.2. If the laser frequency is simultaneously dithered at a rapid rate then a modulated absorption signal is generated at the dither frequency, ω_{sig}. Homodyne detection – i.e. single frequency detection – of the measured modulated absorption signal is accomplished using a lock-in amplifier that is configured for detection of a specific harmonic, n=1, 2, 3,…, of the modulating signal. The phase sensitive detector (PSD) inside of the lock-in performs the essential task of multiplying the modulated absorption signal,

$$V_{sig}(t) = A_{sig}^{1}\sin\left(\omega_{sig}t + \theta_{sig}^{1}\right) + A_{sig}^{2}\sin\left(2\omega_{sig}t + \theta_{sig}^{2}\right) + \ldots + A_{sig}^{\mathrm{n}}\sin\left(\mathrm{n}\omega_{sig}t + \theta_{sig}^{\mathrm{n}}\right) + \ldots \qquad \text{(A.1)}$$

by an internal reference signal synchronized for detection of a specific harmonic,

$$V_{ref}(t) = \frac{2}{\sqrt{2}}G\sin\left(\omega_{ref}t + \theta_{ref}\right);\ \omega_{ref} = \mathrm{n}\omega_{sig},\ \mathrm{n} = 1, 2, 3\ldots\ , \qquad \text{(A.2)}$$

In Eq. A.1, A_{sig}^{n} and $\theta_{sig}^{\mathrm{n}}$ are the amplitude and phase, respectively, of the nth-Fourier component of the modulated absorption signal. In Eq. A.2, θ_{ref} is the selectable phase of the internal reference signal, $\omega_{ref} = \mathrm{n}\omega_{sig}$ is the angular frequency of the reference signal with the lock-in configured for detection of the nth-harmonic of the modulated absorption signal, and G represents the overall gain – front-end and back-end – applied to the detected harmonic signal. A multiplicative constant of two was included in Eq. A.2 to accommodate the mathematical analysis below. The $1/\sqrt{2}$ multiplicative constant accounts for the fact that, as a general rule, lock-in amplifiers output the root-mean-square (RMS) amplitude of the detected Fourier component of the modulated signal [38].

Consider 1st-harmonic detection, for instance:

$$V_{PSD} = \frac{2}{\sqrt{2}}GA_{sig}^{1}\sin\left(\omega_{sig}t + \theta_{sig}^{1}\right)\sin\left(\omega_{ref}t + \theta_{ref}\right). \qquad \text{(A.3)}$$

With the reference signal synchronized with the first harmonic of the modulated absorption signal, $\omega_{ref} = \omega_{sig}$, the mixed signal in Eq. A.3 contains both a DC-component and an AC-component. Utilizing the trigonometric identity,

$$\cos(x \pm y) = \cos x \cos y \mp \sin x \sin y \qquad \text{(A.4)}$$

we find,

$$V_{PSD} = G\frac{A_{sig}^{1}}{\sqrt{2}}\left\{\underbrace{\cos\left[\left(\omega_{sig}-\omega_{ref}\right)t+\left(\theta_{sig}-\theta_{ref}\right)\right]}_{\text{DC-component}}+\underbrace{\cos\left[\left(\omega_{sig}+\omega_{ref}\right)t+\left(\theta_{sig}+\theta_{ref}\right)\right]}_{\text{AC-component}}\right\}. \qquad \text{(A.5)}$$

All AC-components in the mixed signal – including noise – that are outside of the ENBW of the RC-low pass filter are essentially extinguished; A lock-in amplifier is effectively an extremely narrow-pass filter centered at the synchronized reference frequency, thereby providing high levels of background noise rejection. The DC-component in the mixed signal is passed by the filter. This phase sensitive signal, V_{PSS}, is directly proportional to the RMS-amplitude of the detected harmonic signal:

$$V_{PSS} = G\frac{A_{sig}^{1}}{\sqrt{2}}\cos\left(\theta_{sig}-\theta_{ref}\right) \xrightarrow{\text{select } \theta_{ref}=\theta_{sig}} V_{PSS} = G\frac{A_{sig}^{1}}{\sqrt{2}}. \qquad \text{(A.6)}$$

It is the phase sensitive signal (or lock-in signal) defined in Eq. A.6 that we're after.

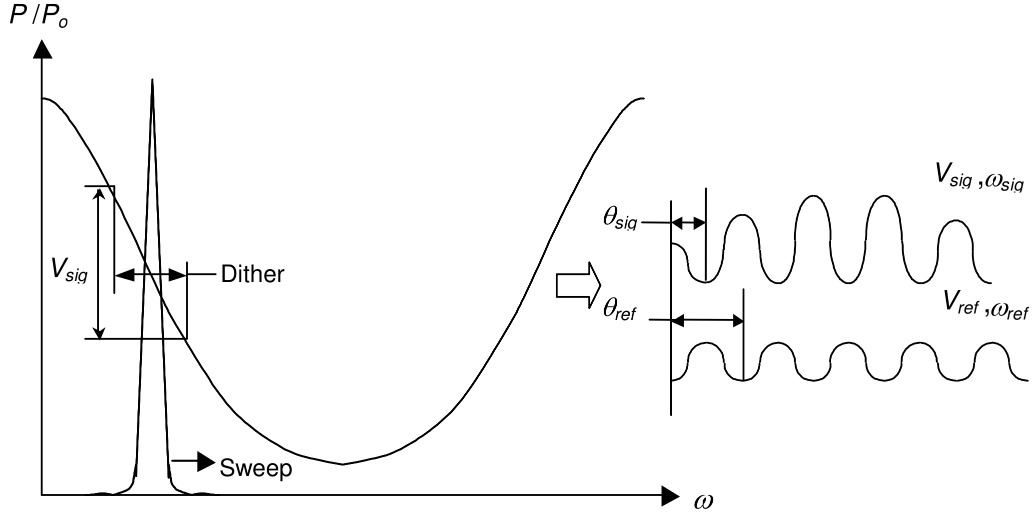

Figure A.2 Simple illustration of modulated absorption spectroscopy

A.3 Equivalent Noise Bandwidth (ENBW) of a Lock-In Amplifier

Let us return to Figure A.1 illustrating the lock-in detection electronics. A modulating current signal, $I_{sig}(t)$, output from the detector is fed into the front end of a lock-in amplifier. A shunt resistor, R_L, across the front end of the lock-in converts this modulating current signal into a modulating voltage signal, $V_{sig}(t) \propto I_{sig}(t)R_L$. In addition, this load resistance and the total electrostatic capacitance of the detector anode (or cathode) to all other electrodes, C_S, form a single-pole low-pass RC-filter. (Stray wiring capacitance is generally the predominant contributor to C_S. The capacitance of a coaxial cable is typically 30 pF per foot, for instance).

The impedance of this filter is,

$$Z_{RC} = \frac{1}{1/R_L + \hat{\imath}\omega C_S} \tag{A.7}$$

where $\hat{\imath} = \sqrt{-1}$ is an imaginary number and ω is the angular frequency of the signal driving the capacitor [107]. (A capacitor is a linear reactive component which essentially behaves like a frequency-dependent resistance). Let us represent the sinusoidal voltage at the input of the lock-in amplifier with the following complex equation,

$$V_{sig} = I_{sig} Z_{RC} = \frac{I_{sig}}{1/R_L + \hat{\imath}\omega C_S} \tag{A.8}$$

We recognize, however, that the actual voltage signal is real. (The imaginary component of the complex voltage contains information concerning the phase of the signal). Multiplying the complex voltage in Eq. A.8 by its complex conjugate we find,

$$\left|V_{sig}\right| = \left(V_{sig} \cdot V_{sig}^{\;*}\right)^{1/2} = \frac{I_{sig} R_L}{\left(1 + \omega^2 R_L^{\;2} C_S^{\;2}\right)^{1/2}}\,. \tag{A.9}$$

Eq. A.9 represents the voltage signal passed by the single-pole RC-filter at the input of the lock-in amplifier as a function of the angular frequency of that signal – e.g. a DC-signal would pass without attenuation, an RF-signal would pass with significant attenuation. This low-pass filter establishes the equivalent noise bandwidth (ENBW) of the detector output circuit leading into the front-end of the lock-in amplifier. (Calculating the ENBW at the input of the lock-in amplifier is necessary to determine the dynamic reserve limitations of the lock-in electronics – i.e. to determine the largest tolerable noise signal to the expected full scale input voltage. See sub-section A.4).

It is common to find the ENBW defined at the -3dB breakpoint(s) of a filter – i.e. the frequency (or frequencies in the case of a narrow pass filter) at which the signal passed by the filter has dropped to -3dB (or $1/\sqrt{2}$) of the input signal to the filter [107]. For the single-pole low-pass RC-filter defined by Eq. A.9, for instance, it is common to find the ENBW defined,

$$B = f_{-3\mathrm{dB}} = \frac{1}{2\pi RC}[\mathrm{Hz}]\,. \tag{A.10}$$

(Note that $f = \omega/2\pi$ is frequency). A more rigorous definition for the ENBW seen by random, incoherent, Gaussian white noise (i.e. any noise with a flat frequency spectrum – meaning there is the same noise power in each hertz of frequency bandwidth – and a Gaussian amplitude distribution) follows from calculations of the equivalent "brick-wall" noise bandwidth [107]. For instance, from this perspective the ENBW of the single-pole low-pass RC-filter described above is defined as the width in the frequency domain of a perfect "brick-wall" low pass filter that lets through the same mean square noise voltage as the RC-filter. This equivalent "brick-wall" filter is illustrated in Figure A.3.

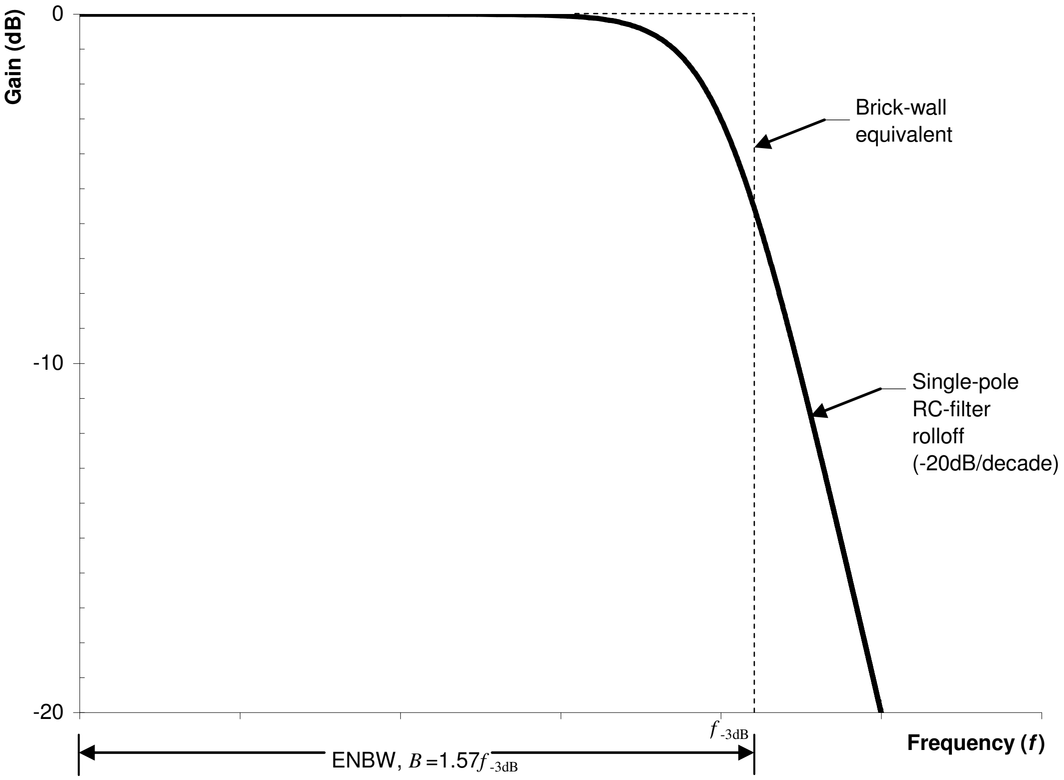

Figure A.3 Pictorial description of equivalent "brick-wall" noise bandwidth for single-pole low-pass RC-filter

From a mathematical viewpoint,

$$B = \int_0^\infty H(f)^2 \, df \tag{A.11}$$

where,

$$H(f) = \left[1 + (2\pi fRC)^2\right]^{-1/2} \tag{A.12}$$

for a single-pole low-pass RC-filter. Eq. A.12 follows from Eq. A.9 and the definition of the equivalent "brick-wall" noise bandwidth. Inserting Eq. A.12 into Eq. A.11 and rearranging some of the terms we find,

$$B = \int_0^\infty \frac{f_{-3\mathrm{dB}}{}^2}{f_{-3\mathrm{dB}}{}^2 + f^2}\, df \tag{A.13}$$

where $f_{-3\mathrm{dB}}$ is defined in Eq. A.10. The integrand in Eq. A.13 is an even function, and therefore the integral lends itself nicely to solution by residues [131]. The solution is illustrated in Figure A.4. We find that the ENBW for a single-pole low-pass RC-filter is,

$$\left.\begin{aligned} B &= \frac{\pi}{2} f_{-3\mathrm{dB}} \\ f_{-3\mathrm{dB}} &= (2\pi RC)^{-1} \end{aligned}\right\} \Rightarrow B = \frac{1}{4RC}\,. \tag{A.14}$$

Eq. A.14 represents the ENBW of the detector output circuit leading into the front-end of the lock-in amplifier, and defines the bandwidth of broadband, Gaussian, white noise passed *into* the lock-in amplifier. Calculating the ENBW at the input of the lock-in amplifier is necessary if we want to determine the theoretical signal-to-noise at the front-end of the lock-in. Calculations of the theoretical signal-to-noise at the front-end of the lock-in amplifier are necessary to determine potential dynamic reserve limitations of the lock-in electronics.

The dynamic reserve of a lock-in amplifier represents the largest tolerable noise signal to the full scale signal in decibels [38]. (It is worth noting that absolute-noise amplitudes up to five times the RMS-noise amplitude of Gaussian white noise are observed in broadband spectrums). For a digital lock-in the dynamic reserve is primarily limited by circuit overload. Operating below the dynamic reserve implies that the detected noise passed into the front-end of the lock-in amplifier will not cause an overload anywhere in the instrument – not in the input signal amplifier, A/D converter, PSD, low pass filter, or DC output amplifier. When running at high dynamic reserve, for instance, the input signal gain of the lock-in is automatically set very low to prevent the noise from overloading the A/D converter, PSD, or low pass filter. After the low pass filter eliminates a significant portion of the noise, the DC output amplifier provides the remaining amplification to the full scale output (typically ±10 Vrms). (The input noise of the A/D converter may plague high-sensitivity measurements at high dynamic reserve; i.e. The low analog gain at high dynamic reserve may prevent the A/D converter from properly resolving the measured signal when the full scale RMS-amplitude of that signal is small. In other words, the lock-in can only do so much. Looking for a 5 μVrms signal within O(100 mVrms) of broadband noise may be asking too much. The SR830 digital lock-in utilized during preliminary MFRS experiments can still make the measurement if we set the input sensitivity to S=5 μVrms and the dynamic reserve to 100dB, it's just that the measurement won't be very good unless we integrate a good long time).

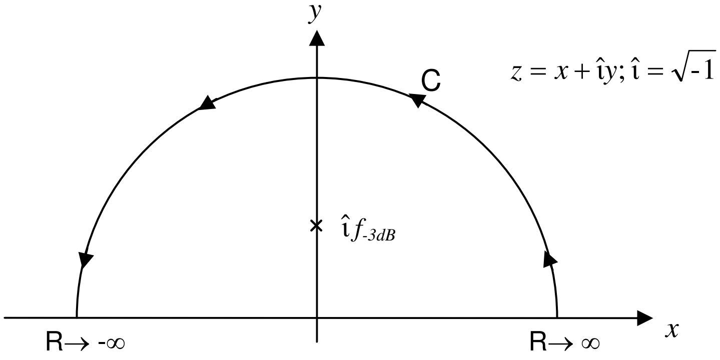

$$\underbrace{\oint \frac{f_{-3\mathrm{dB}}{}^2}{f_{-3\mathrm{dB}}{}^2 + z^2}\mathrm{d}z}_{\|} = 2B + \underbrace{\int_C \frac{f_{-3\mathrm{dB}}{}^2}{f_{-3\mathrm{dB}}{}^2 + z^2}\mathrm{d}z}_{\|}$$

$$\oint \frac{f_{-3\mathrm{dB}}{}^2}{\left(z + \hat{\imath}f_{-3\mathrm{dB}}\right)\left(z - \hat{\imath}f_{-3\mathrm{dB}}\right)}\mathrm{d}z \qquad \mathrm{O}\left(\frac{f_{-3\mathrm{dB}}{}^2}{R^2}\cdot \pi R\right) = \mathrm{O}\left(\frac{f_{-3\mathrm{dB}}{}^2}{R}\right) \xrightarrow{R\to\infty} 0$$

There is a simple pole at $z = \hat{\imath}f_{-3\mathrm{dB}}$ within contour. According to the residue theorem,

$$\oint \frac{f_{-3\mathrm{dB}}{}^2}{\left(z + \hat{\imath}f_{-3\mathrm{dB}}\right)\left(z - \hat{\imath}f_{-3\mathrm{dB}}\right)}\mathrm{d}z = 2\pi\hat{\imath} \lim_{z\to\hat{\imath}f_{-3\mathrm{dB}}} \left(z - \hat{\imath}f_{-3\mathrm{dB}}\right)\frac{f_{-3\mathrm{dB}}{}^2}{\left(z + \hat{\imath}f_{-3\mathrm{dB}}\right)\left(z - \hat{\imath}f_{-3\mathrm{dB}}\right)}$$

$$= 2\pi\hat{\imath} \lim_{z\to\hat{\imath}f_{-3\mathrm{dB}}} \frac{f_{-3\mathrm{dB}}{}^2}{\left(z + \hat{\imath}f_{-3\mathrm{dB}}\right)}$$

$$= 2\pi\hat{\imath}\frac{f_{-3\mathrm{dB}}{}^2}{2\hat{\imath}f_{-3\mathrm{dB}}}$$

$$\oint \frac{f_{-3\mathrm{dB}}{}^2}{\left(z + \hat{\imath}f_{-3\mathrm{dB}}\right)\left(z - \hat{\imath}f_{-3\mathrm{dB}}\right)}\mathrm{d}z = \pi f_{-3\mathrm{dB}}$$

Putting it all together we find that the ENBW for a single-pole low-pass RC-filter is,

$$B = \frac{\pi}{2}f_{-3\mathrm{dB}}; f_{-3\mathrm{dB}} = \frac{1}{2\pi RC}$$

Figure A.4 Calculating ENBW of single-pole low-pass RC-filter

It may be simpler to think of dynamic reserve in the following manner: No interfering signal can exceed the input range of a lock-in amplifier, which for the SR830 digital lock-in utilized in the scattering arm of all preliminary MFRS experiments is 1 Vrms. If the expected full scale RMS-signal voltage is 1 Vrms – e.g. if the harmonic signal has an expected maximum RMS-amplitude of 1 Vrms – we would set the full scale input sensitivity to $S=1$ Vrms. In this case, the dynamic reserve of the lock-in amplifier is automatically limited to 0dB, and any noise signal whose absolute amplitude exceeds 1 V will saturate the electronics. If the full-scale RMS-signal voltage is 1 μVrms, the dynamic reserve of the lock-in is automatically set to 100dB. Again, any interfering signal whose absolute amplitude exceeds 1 V will saturate the electronics.

Assuming that the lock-in amplifier has sufficient dynamic reserve to handle that noise in the detected output signal passed to the front-end, the signal is processed by the lock-in electronics in the manner described in sub-sections A.1 and A.2: The signal (including the noise) is amplified, this amplified analog signal is digitized, and this digitized signal is mixed with a synchronized reference signal. The resulting mixed signal has an AC-component that is extinguished by the low-pass filter internal to the lock-in and a DC-component – proportional to the RMS-amplitude of the detected harmonic signal – that is passed by the low-pass filter. It is the low pass filter internal to lock-in amplifiers that ultimately establishes the ENBW of homodyne detection utilizing lock-ins; i.e. not only does it extinguish the AC-component of the mixed signal, but it defines the bandwidth of broadband, Gaussian, white noise passed *by* the lock-in amplifier.

I used an SR830 digital lock-in amplifier from Stanford Research Systems during all preliminary MFRS measurements in the scattering arm of the experiment. This lock-in amplifier offers four low-pass RC-filter options: a one-pole, a two-pole, a three-pole, or a four-pole low-pass RC-filter [38]. The time constant for each of these filters is defined by the lock-in integration time, $\tau_L = RC$. For instance, referring to Eq. A.14 we find that the ENBW for homodyne detection utilizing a lock-in amplifier with a one-pole low-pass RC-filter is,

$$B = \frac{1}{4\tau_L}\ [\text{Hz}]. \tag{A.15}$$

If we integrate our measurements for $\tau_L=1$ s the equivalent noise bandwidth is B=0.25Hz. If we integrate our measurements for $\tau_L=10$s the equivalent noise bandwidth is B=0.025Hz. (Lock-in integration represents digital signal averaging. The SR830 digital lock-in affords integration times up to 30ks. Though it is tempting to consider only the bandwidth narrowing associated with a given lock-in measurement when trying to determine the feasibility that measurement, it is important to also consider the stability of the measurement system if long-integration times are employed. For instance, the instrument developed for preliminary MFRS measurements was never stable for 30 ks).

Table A.1 lists the ENBW for the one-, two-, three-, and four-pole low-pass RC-filters internal to the SR830 lock-in amplifier. The ENBW is tabulated both in terms of the -3dB breakpoint of the corresponding filter as well as the lock-in integration time constant, τ_L. Calculations of the ENBW for the two-, three-, and four-pole low-pass RC-filters assumed that the cascaded RC-filters are buffered to prevent circuit loading. The filter rolloff in Table A.1 is the decibel change in signal amplitude passed by the corresponding RC-filter when a signal frequency beyond the -3dB breakpoint is doubled (-6dB/octave=-20dB/decade).

	Rolloff	$f_{\text{-3dB}}$	ENBW, B=f($f_{\text{-3dB}}$)	ENBW, B=f(τ_L)
1-pole	-6dB/oct	$\frac{1}{2\pi RC}$	$\frac{\pi}{2} f_{-3\text{dB}}$	$\frac{1}{4\tau_L}$
2-pole	-12dB/oct	$\frac{\sqrt{2^{1/2}-1}}{2\pi RC}$	$\frac{\pi}{4\sqrt{2^{1/2}-1}} f_{-3\text{dB}}$	$\frac{1}{8\tau_L}$
3-pole	-18dB/oct	$\frac{\sqrt{2^{1/3}-1}}{2\pi RC}$	$\frac{3\pi}{16\sqrt{2^{1/3}-1}} f_{-3\text{dB}}$	$\frac{3}{32\tau_L}$
4-pole	-24dB/oct	$\frac{\sqrt{2^{1/4}-1}}{2\pi RC}$	$\frac{5\pi}{32\sqrt{2^{1/4}-1}} f_{-3\text{dB}}$	$\frac{5}{64\tau_L}$

Table A.1 ENBWs of one-, two-, three-, and four-pole low-pass RC-filters

Appendix B: Classical Theory of Atomic Absorption

In the 19th century J. C. Maxwell derived four equations that unified the theories of electricity and magnetism [132,133]. A description of light as a propagating electromagnetic wave naturally followed, a description that is both consistent with physical observation and also beautifully simple. Maxwell's equations are discussed in great detail in a great number of optics texts (e.g. my understanding of Maxwell's equations derives primarily from references [14,39,41]). The following paragraphs will therefore not discuss Maxwell's equations in detail, but will instead focus on the description, derived from Maxwell's equations, of how light interacts with a transmissive, isotropic, dielectric (i.e. nonconductive) material.

Let us first consider the propagation of an electromagnetic wave (e.g. light) in a vacuum. Assuming that the free charge density, ρ_f, and free current, J_f, in this vacuum are zero, Maxwell's four equations reduce to two wave equations describing the propagation of the electric field, $\vec{E}$, and the magnetic field, $\vec{B}$, that constitute the electromagnetic wave:

$$\nabla^2 \vec{E} = \mu_o \varepsilon_o \frac{\partial^2 \vec{E}}{\partial t^2} \tag{B.1a}$$

$$\nabla^2 \vec{B} = \mu_o \varepsilon_o \frac{\partial^2 \vec{B}}{\partial t^2} \tag{B.1b}$$

By inspection, we see that the propagation speed of both the electric field and the magnetic field are equivalent. This propagation speed is the speed of light in vacuum,

$$c = (\mu_o \varepsilon_o)^{-1/2} \tag{B.2}$$

where ε_o is the permittivity of free space (8.8542×10^{-12} C^2/Nm^2) and μ_o is the permeability of free space ($4\pi \times 10^{-7}$ Ns^2/C^2). The permittivity of free space can be thought of as the resistance of a vacuum to an electric field and the permeability of free space its resistance to a magnetic field. The inverse square root of their product is the *observed* speed of light in a nonconductive ($\rho_f = J_f = 0$) vacuum.

Let us now consider light that is traveling through a transmissive, isotropic, dielectric material – e.g. a neutral atomic gas. Compared to propagation through a vacuum, the speed that light travels through any dielectric material, v, is slower (we won't distract ourselves with anomalous dispersion),

$$v = (\mu \varepsilon)^{-1/2} < (\mu_o \varepsilon_o)^{-1/2} = c \tag{B.3}$$

where the permittivity, ε, and the permeability, μ, of the dielectric material are defined,

$$\varepsilon = \varepsilon_o\left(1+\chi_e\right) > \varepsilon_o \Rightarrow \frac{\varepsilon}{\varepsilon_o} = K_e = \left(1+\chi_e\right) \tag{B.4a}$$

$$\mu = \mu_o\left(1+\chi_m\right) \cong \mu_o \Rightarrow \frac{\mu}{\mu_o} = K_m = \left(1+\chi_m\right) \tag{B.4b}$$

In Eq. B.4 I have introduced some new material constants: χ_e is the electric susceptibility of the material, χ_m is its magnetic susceptibility, K_e is the relative permittivity of the material (also called the dielectric constant), and K_m is its relative permeability.

Most transmissive, dielectric materials of interest – including Rb – are "nonmagnetic", meaning that the magnetic susceptibility is effectively zero, $\chi_m \cong 0$:

$$\mu \cong \mu_0 \Rightarrow K_m \cong 1. \tag{B.5}$$

In this case, the absolute index of refraction, n, of the material – i.e. the ratio of the speed of electromagnetic wave propagation in a vacuum to the speed in the material – is given by Maxwell's relation:

$$n = \frac{c}{v} = \sqrt{\frac{\varepsilon}{\varepsilon_o}} = \sqrt{K_e}\ . \tag{B.6}$$

There is a not-so-clear connection between the material constants introduced above and what physically happens when light interacts with a dielectric material. Physical insight at the microscopic level is necessary to make the connection. In particular, a microscopic perspective is necessary to understand two important phenomenon that occur when light interacts with matter – dispersion (i.e. the dependence of the electromagnetic phase velocity, or alternatively the index of refraction, on frequency) and absorption – where an understanding of the latter phenomenon is of particular importance for the MFRS practitioner and the hopeful intention of this section. Dispersion and absorption are both microscopic phenomena that cannot be understood from Maxwell's description of interacting fields. We must give a microscopic meaning to the material constants discussed above and used to describe the interaction of light with matter from the perspective of Maxwell's equations if we intend to understand dispersion and absorption in the context of classical theory.

From a microscopic perspective, when an electromagnetic wave is incident upon a transmissive, dielectric medium, the atoms (or molecules) that constitute that medium experience time-varying forces under the influence of the time-varying electric and magnetic fields associated with the electromagnetic wave. This is the same microscopic perspective utilized in the previous section to classically describe Rayleigh scattering. The forces induced by the magnetic field, $\vec{F}_m$, are generally negligible compared to the forces induced by the electric field, $\vec{F}_e$, and can effectively be ignored:

$$\left.\begin{array}{l} \vec{F}_m = q\vec{v}_q \times \vec{B} \\ \vec{F}_e = q\vec{E} = qc\vec{B} \\ \left|\bar{v}_q\right| \equiv \text{Speed of charge} << \text{c} \end{array}\right\} \Rightarrow \left|\vec{F}_m\right| << \left|\vec{F}_e\right| \tag{B.7}$$

The forces induced by the electric field result in a redistribution of charge in the dielectric medium – Positive charges, +*q*, are separated from negative charges,-*q*, in the media. Each pair of separated charges is termed an electric dipole. If the dielectric medium is composed of polar molecules – i.e. molecules with a permanent electric dipole resulting from an unequal sharing of valence electrons – the incident electric field will align the permanent dipoles that constitute the medium. If the dielectric is composed of ionic molecules, the incident electric field will shift the positive and negative ions with respect to each other and induce dipoles in the dielectric. Finally, the electric field can simply distort the electron "cloud" of an atom (or molecule), thereby creating a dipole.

Regardless of the specific mechanism involved, the dipoles aligned or induced in the dielectric material by the incident electric field contribute to that field. Under the influence of a harmonic electric field, for instance, the permanent or induced dipoles are forced into oscillation. These oscillating electric dipoles create time-varying electric fields which in turn create time varying magnetic fields according to Maxwell's equations – light begets light.

The dipole induced electric field is termed the polarization field (or the material or electric polarization), $\vec{P}$, and is classically defined in terms of the electric susceptibility,

$$\vec{P} = \varepsilon_o \chi_e \vec{E} \,. \tag{B.8}$$

The polarization field is simply the charge density (mks-units of C/m^2) in the dipole induced electric field. The derivative of the polarization field with respect to time is the current density (mks-units of $\frac{\text{C}}{\text{s m}^2} = \frac{\text{A}}{\text{m}^2}$) of the dipole induced electric field. This current density induced in the dielectric material adds to the displacement current density, J_D, defined by Maxwell for EM-propagation in a vacuum,

$$\vec{J}_D = \varepsilon_o \frac{\partial \vec{E}}{\partial t} \Rightarrow \vec{J}_D \Big|_{\text{DIELECTRIC}} = \vec{J}_D + \frac{\partial \vec{P}}{\partial t}$$

$$= \varepsilon_o \frac{\partial \vec{E}}{\partial t} + \varepsilon_o \chi_e \frac{\partial \vec{E}}{\partial t}$$

$$= \varepsilon_o (1 + \chi_e) \frac{\partial \vec{E}}{\partial t}$$

$$\vec{J}_D \Big|_{\text{DIELECTRIC}} = \varepsilon_o K_e \frac{\partial \vec{E}}{\partial t}. \tag{B.9}$$

From this perspective we find that the electric susceptibility, χ_e, is simply a measure of the contribution from the induced dipoles in a dielectric material to the incident electric field.

The definition of the polarization field from a microscopic perspective allows us to extend this field concept to the atomic domain, and therefore to give microscopic meaning to the electric susceptibility. From a microscopic perspective, the polarization field is defined as the induced dipole moment per unit volume,

$$\vec{P} = \lim_{\Delta V \to 0} \frac{1}{\Delta V} \sum_{i=1}^{N\Delta V} \vec{p}_i \tag{B.10}$$

where ΔV is the volume element, N is the number density of atoms in the transmissive dielectric, and $\vec{p}_i$ is the induced electric dipole moment of atom-*i* [63]. Rewriting Eq. 3.2 from Section 3.2 we find,

$$\vec{p}_i(t) = q_i x_i(t) \hat{e}_i \tag{B.11}$$

where x is the charge separation and $\hat{e}_i$ is a unit vector that defines the dipole orientation. A temporal dependence has been included in Eq. B.11 to accommodate the time-varying influence of an oscillating electric field on the induced dipole. Equating Eqs. B.8 and B.10 with reference to Eq. B.11 and dropping the vector notation we find,

$$P(t) = \varepsilon_o \chi_e E(t) = Nqx(t). \tag{B.12}$$

At the end of the 19th century, the usefulness of Eq. B.12 became immediately apparent when H.A. Lorentz developed a model that captured the essence of the interaction of light with an ensemble of atoms [134]. (Predictions made using the Lorentz atom are not strictly correct, but the model has been "tweaked" over the years to allow predictions that are consistent with observation and quantum theory. We will discuss one such modification – i.e. oscillator strengths – at the end of this appendix). The Lorentz atom models the induced dipole oscillation of the negatively charged electron "cloud" under the influence of an oscillating electric field about the positively charged (and relatively massive) atomic nucleus as a driven damped harmonic oscillator (anharmonic effects can also be modeled, one of many "tweaks" to the Lorentz atom as originally conceived); The electron "cloud" is modeled as an electron of mass m_e and charge $-q=-1.6 \times 10^{-19}$ C that is connected to the atomic nucleus of mass $m_n >> m_e$ and charge $+q$ by a spring of spring constant K (e.g. representing the binding energy) and a damper with a damping coefficient γ (e.g. representing a loss mechanism). Note that the damping coefficient is inversely proportional to the natural lifetime of a driven, resonant, harmonic oscillation, $\gamma=1/\tau$. The Lorentz atom is illustrated in Figure B.1.

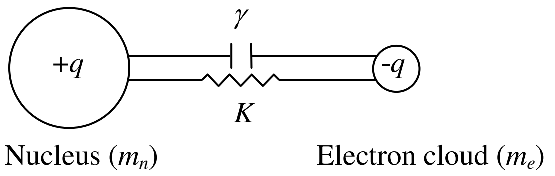

Figure B.1 The Lorentz atom

Under the influence of an electric field, $\vec{E}(t)=\vec{E}_o \exp[\hat{\imath}\omega t]$, oscillating at an angular frequency ω, the electron in the Lorentz atom experiences a force $q\vec{E}$ that drives it into oscillation. Lorentz modeled this driven damped harmonic oscillation of the electron with the following equation from Newtonian mechanics:

$$m_e \frac{\partial^2 \vec{x}}{\partial t^2} + m_e \gamma \frac{\partial \vec{x}}{\partial t} + K\vec{x} = q\vec{E}_o \exp[\hat{\imath}\omega t]. \tag{B.13}$$

Noting that the resonant oscillation frequency of this system in the absence of damping is,

$$\omega_o = \sqrt{\frac{K}{m_e}} \tag{B.14}$$

and dropping the vector notation (with the understanding that the material polarization – i.e. the induced dipole moment – is aligned with the incident, oscillating electric field), we can recast Eq. B.13:

$$\ddot{x} + \gamma \dot{x} + \omega_o^2 x = \frac{q}{m_e} E_o \exp[\hat{\imath}\omega t]. \tag{B.15}$$

Defining the equilibrium electron position as $x(t=0)=0$ and the initial electron velocity as $\dot{x}(t=0)=0$ we find that the temporal response of the electron to the incident electric field is,

$$\vec{x}(t) = \frac{q}{m_e\left(\omega_o^2 - \omega^2 + \hat{\imath}\gamma\omega\right)} \vec{E}_o \exp[\hat{\imath}\omega t]. \tag{B.16}$$

Referring now to Eq. B.12, an ensemble of *N* such Lorentz atoms per unit volume results in an induced dipole moment per unit volume – i.e. a polarization field – of,

$$P = \varepsilon_o \chi_e E(t) = \frac{Nq^2}{m_e\left(\omega_o^2 - \omega^2 + \hat{\imath}\gamma\omega\right)} E(t) \tag{B.17}$$

from which it follows,

$$\chi_e = \frac{Nq^2}{\varepsilon_o m_e\left(\omega_o^2 - \omega^2 + \hat{\imath}\gamma\omega\right)}. \tag{B.18}$$

Combining Eqs. B.4a and B.6 we find (for a non-magnetic dielectric material) that,

$$K_e = n^2 = 1 + \chi_e \tag{B.19}$$

and inserting Eq. B.18 into Eq. B.19,

$$n^2 - 1 = (n+1)(n-1) = \frac{Nq^2}{\varepsilon_o m_e\left(\omega_o^2 - \omega^2 + \hat{\imath}\gamma\omega\right)}. \tag{B.20}$$

The index of refraction is close to unity for dielectric gases at relatively low pressure, and the accuracy of the analysis that follows is therefore not significantly affected if we employ the following approximation:

$$n^2 - 1 \cong 2(n-1) \Rightarrow n = 1 + \frac{Nq^2}{2\varepsilon_o m_e\left(\omega_o^2 - \omega^2 + \hat{\imath}\gamma\omega\right)}$$

$$= 1 + \frac{Nq^2}{2\varepsilon_o m_e\left[\left(\omega_o^2 - \omega^2\right) + \hat{\imath}\gamma\omega\right]} \cdot \frac{\left[\left(\omega_o^2 - \omega^2\right) - \hat{\imath}\gamma\omega\right]}{\left[\left(\omega_o^2 - \omega^2\right) - \hat{\imath}\gamma\omega\right]}$$

$$n = 1 + \frac{Nq^2}{2\varepsilon_o m_e} \frac{\omega_o^2 - \omega^2}{\left[\left(\omega_o^2 - \omega^2\right) + (\gamma\omega)^2\right]} - \hat{\imath} \frac{Nq^2}{2\varepsilon_o m_e} \frac{\gamma\omega}{\left[\left(\omega_o^2 - \omega^2\right) + (\gamma\omega)^2\right]}. \tag{B.21}$$

In Eq. B.21 we have separated the real and imaginary parts of the complex index of refraction,

$$n = n_R - \hat{\imath} n_I. \tag{B.22}$$

Now, consider an electromagnetic wave of angular frequency ω passing in the *z*-direction through a dielectric material with an index of refraction *n*. An important concept to keep in mind when discussing the interaction of light with matter is that the angular frequency (or frequency, ν) of the light is not affected by the interaction. We have shown, however, that the speed of the light, v – and therefore its wavelength, λ – is affected by the interaction:

$$\left.\begin{aligned} \lambda &= \frac{v}{\nu} \\ &= \frac{v}{c}\frac{c}{\nu} \\ \lambda &= \frac{1}{n}\lambda_{\mathrm{VAC}} \end{aligned}\right\} \Rightarrow \left|\vec{K}\right| = \frac{2\pi}{\lambda} = n\frac{2\pi}{\lambda_{\mathrm{VAC}}} = n\left|\vec{K}_{\mathrm{VAC}}\right| \tag{B.23}$$

In Eq. B.23, λ_{VAC} is the vacuum wavelength and $\left|\vec{K}_{\mathrm{VAC}}\right| = \frac{2\pi}{\lambda_{\mathrm{VAC}}}$ is the vacuum wave number.

Referring to Eq. B.23, we can describe the electric field component of an electromagnetic wave of angular frequency ω propagating in the z-direction through a dielectric material of index of refraction n with the following scalar equation:

$$\begin{aligned} E &= E_o \exp\left[\hat{\imath}\left(\omega t\text{-}Kz\right)\right] \\ &= E_o \exp\left[\hat{\imath}\left(\omega t\text{-}nK_{\mathrm{VAC}}z\right)\right] \\ &= E_o \exp\left\{\hat{\imath}\left[\omega t\text{-}\left(n_R - \hat{\imath}n_I\right)K_{\mathrm{VAC}}z\right]\right\} \end{aligned}$$

$$E = E_o \exp\left[\text{-}\, n_I K_{\mathrm{VAC}}z\right]\exp\left[\hat{\imath}\left(\omega t\text{-}n_R K_{\mathrm{VAC}}z\right)\right]. \tag{B.24}$$

Noting that the intensity (or irradiance) of an electromagnetic wave, I, is proportional to the product of the electric field, E, and the complex conjugate of the electric field, E^*,

$$I = \frac{\varepsilon v}{2} E E^* \tag{B.25}$$

and that,

$$I_0 = \frac{\varepsilon v}{2} E_o E_o^* \tag{B.26}$$

we find that the incident intensity, I_o, of the propagating electromagnetic wave discussed above decreases with the distance z traveled as,

$$I(z) = I_o \exp\left[-2n_I K_{\mathrm{VAC}}z\right]. \tag{B.27}$$

This expression is completely analogous to Beer's law describing the intensity of light resonant with an atomic (or molecular) gas that is transmitted after passage a distance z through that gas,

$$I(z) = I_o \exp\left[-\alpha(\omega)z\right], \tag{B.28}$$

where $\alpha(\omega)$ is the absorption constant,

$$\alpha(\omega) = \bar{\alpha}(\omega) Y_{\omega_{1\to 2}}(\omega) \tag{B.29}$$

In other words, the imaginary part, $n_I(\omega)$, of the complex index of refraction describes absorption. Comparing Eqs. B.27 and B.28 and referring to Eqs. B.21 and B.22, we find that the Lorentz atom predicts an absorption constant of,

$$\begin{aligned}\alpha(\omega) &= \frac{4\pi}{\lambda_{\text{VAC}}} n_I \\ &= \frac{2\omega}{c} n_I \\ \alpha(\omega) &= \frac{Nq^2\omega}{c\varepsilon_o m_e} \frac{\gamma\omega}{\left(\omega_o^2-\omega^2\right)^2+(\gamma\omega)^2}\,. \end{aligned} \tag{B.30}$$

Since our focus in this appendix is to describe a classical theory of atomic absorption, I only mention that the real part, $n_R(\omega)$, of the complex index of refraction describes dispersion. Referring to Eqs. B.21 and B.22, we find that the frequency dependence of the material index of refraction defined by the Lorentz atom is,

$$n(\omega) = n_R(\omega) = 1 + \frac{Nq^2}{2\varepsilon_o m_e} \frac{\omega_o^2-\omega^2}{\left(\omega_o^2-\omega^2\right)^2+(\gamma\omega)^2}\,. \tag{B.31}$$

Eqs. B.30 and B.31 are referred to as the Kramers-Kronig relations.

We are interested in this appendix in describing the absorption associated with an atomic resonance; i.e. We want to know what happens to light on passage through an atomic gas when the spectral irradiance of that light falls within the bandwidth of a resonant transition of the gas. In other words, we are considering light whose angular frequency is within the bandwidth of an atomic transition,

$$\omega \cong \omega_o = \omega_{1\to2} = \frac{|E_2-E_1|}{\hbar};\hbar = \frac{h}{2\pi}\,. \tag{B.32}$$

Assuming that the linewidth of the absorption profile – defined by $Y_{\omega_{1\to2}}(\omega)$ – is much less than the resonant frequency, ω_o, we can invoke the following approximation in our analysis:

$$\omega+\omega_o \cong 2\omega \Rightarrow \omega^2-\omega_o^2 \cong 2\omega(\omega-\omega_o)\,. \tag{B.33}$$

This approximation simplifies the expression in Eq. B.30 for the absorption constant:

$$\alpha(\omega) = \underbrace{\frac{Ne^2\pi}{2\varepsilon_o m_e c}}_{\bar{\alpha}(\omega_{1\to2})} \underbrace{\frac{1}{\pi} \frac{\gamma/2}{(\omega-\omega_{1\to2})^2+\left(\gamma/2\right)^2}}_{Y_{\omega_{1\to2}}(\omega)} \tag{B.34}$$

To review, Eq. B.34 is the absorption constant predicted using the Lorentz atom in the vicinity of the resonant atomic transition 1→2: N is the number density of atoms in the absorbing gas, e=1.6 × 10^{-19} C is the electron charge, ε_o=8.8542 × 10^{-12} $\frac{\mathrm{C}^2}{\mathrm{Nm}^2}$ is the permittivity of free space, m_e=9.11 × 10^{-31} kg is the electron mass, $\gamma=1/\tau$ is the damping coefficient, and $\omega_{1\to 2}$ is the centerline angular frequency of the atomic transition. We see from Eq. B.34 that the spectrally integrated absorption constant predicted by the Lorentz atom is,

$$\boxed{\overline{\alpha}(\omega_{1\to 2})=\frac{Ne^2\pi}{2\varepsilon_o m_e c}} \tag{B.35}$$

and that the absorption constant defined in Eq. B.34 is simply this spectrally integrated absorption constant multiplied by the normalized Lorentzian lineshape function associated with the natural lifetime, $\tau_{1\to 2}$ (i.e. the mean spontaneous lifetime), of the transition,

$$Y_{\omega_{1\to 2}}(\omega)=l(\omega)=\frac{1}{\pi}\frac{1/2\tau_{1\to 2}}{(\omega-\omega_{1\to 2})^2+\left(1/2\tau_{1\to 2}\right)^2}\Rightarrow\int_{-\infty}^{\infty}l(\omega)\mathrm{d}\omega=1\,. \tag{B.36}$$

It is important to keep in mind that analysis from the perspective of the Lorentz atom does not account for the hyperfine or fine structure of an atom, and as a result is grossly inconsistent with observation in and of itself. To bring the theory developed by Lorentz more in line with observation – i.e. with the analysis based on Einstein coefficients – the concept of oscillator strengths was introduced. This concept effectively unifies the theory as developed by Lorentz with the theory based on Einstein coefficients. Let us equate the spectrally integrated absorption constant derived from the perspective of Einstein coefficients, Eq. 3.76a, with the spectrally integrated absorption constant in Eq. B.35 derived using the Lorentz atom,

$$N\frac{g_u}{g_l}\frac{\pi^2c^2}{\omega_{l\to u}^2}A_{ul}=f_{lu}\cdot\frac{Ne^2\pi}{2\varepsilon_o m_e c} \tag{B.37}$$

where f_{lu} is the oscillator strength. Solving Eq. B.37 for the oscillator strength we find,

$$f_{lu}=\frac{2\pi\varepsilon_o m_e c^3}{e^2\omega_{l\to u}^2}\frac{g_u}{g_l}A_{ul}\,. \tag{B.38}$$

Appendix C: Gain Characteristics of the R636-10 PMT

I employed the R636-10 PMT from Hamamatsu Corp. for sensitive detection in the scattering arm of all preliminary MFRS experiments. This PMT has relatively high quantum efficiency in the near-infrared, and was therefore ideally suited for all preliminary MFRS experiments – All preliminary MFRS measurements utilized the D_2-line of Rb at λ =780 nm as a frequency discriminator. In this appendix I will derive an expression for the anode output current of the R636-10 PMT as a function of the supply voltage applied across the PMT and the power of light in the vicinity of $\lambda \cong$ 780 nm incident upon the PMT. This expression was used exclusively in the analysis of Chapter 3 to model the detection sensitivity in the scattering arm of the MFRS velocimeter.

A photomultiplier tube (PMT) consists of a photocathode, a series of intermediate dynode stages, and an anode [105]. When light irradiates the photocathode, electrons are emitted from it and focused onto the first dynode. These photoelectrons are multiplied at the first dynode by means of a secondary emission of electrons. This secondary emission of electrons is repeated at each successive dynode until the multiplied secondary electrons ejected from the final dynode stage are finally collected by the anode.

Ultimately, light incident upon the PMT photocathode results in an anode output current. This anode current depends on the power, P_K, and wavelength, λ, of the incident light, the sensitivity of the photocathode at that wavelength of light, $S_K(\lambda)$ (i.e. how many photoelectrons are ejected from the cathode for a given power and wavelength of incident light), the efficiency with which the ejected photoelectrons are focused onto the first dynode, α, and the secondary electron emission ratio of each dynode, δ.

The collection efficiency, α, and secondary emission ratio, δ, both depend on the voltage applied across the PMT. (Photoelectrons ejected from the cathode are effectively collected by the first dynode if the resulting secondary electron emission from the first dynode can be multiplied at each successive dynode stage without diverting from a favorable trajectory – i.e. toward the next dynode and ultimately the anode). For instance, Figure C.1 shows the collection efficiency vs. photocathode-to-first dynode voltage for a ϕ=28 mm side-on PMT (such as the R636-10 PMT) with a 3 mm × 15 mm light spot incident upon the photocathode [106]. This figure is representative of the collection efficiency we could expect from the R636-10 PMT employed in the scattering arm of all preliminary MFRS experiments, and indicates that a photocathode-to-first dynode voltage of at least 100 V should be employed to optimize the collection efficiency of the R636-10 PMT. (The collection efficiency also affects the photocathode uniformity, defined as the variation in output sensitivity with respect to the photocathode position. If the supply voltage is too low, the resulting degradation in collection efficiency adversely affects the uniformity. It is therefore recommended that >100 V be applied across the cathode-to-first dynode and >50 V be applied between all successive dynodes).

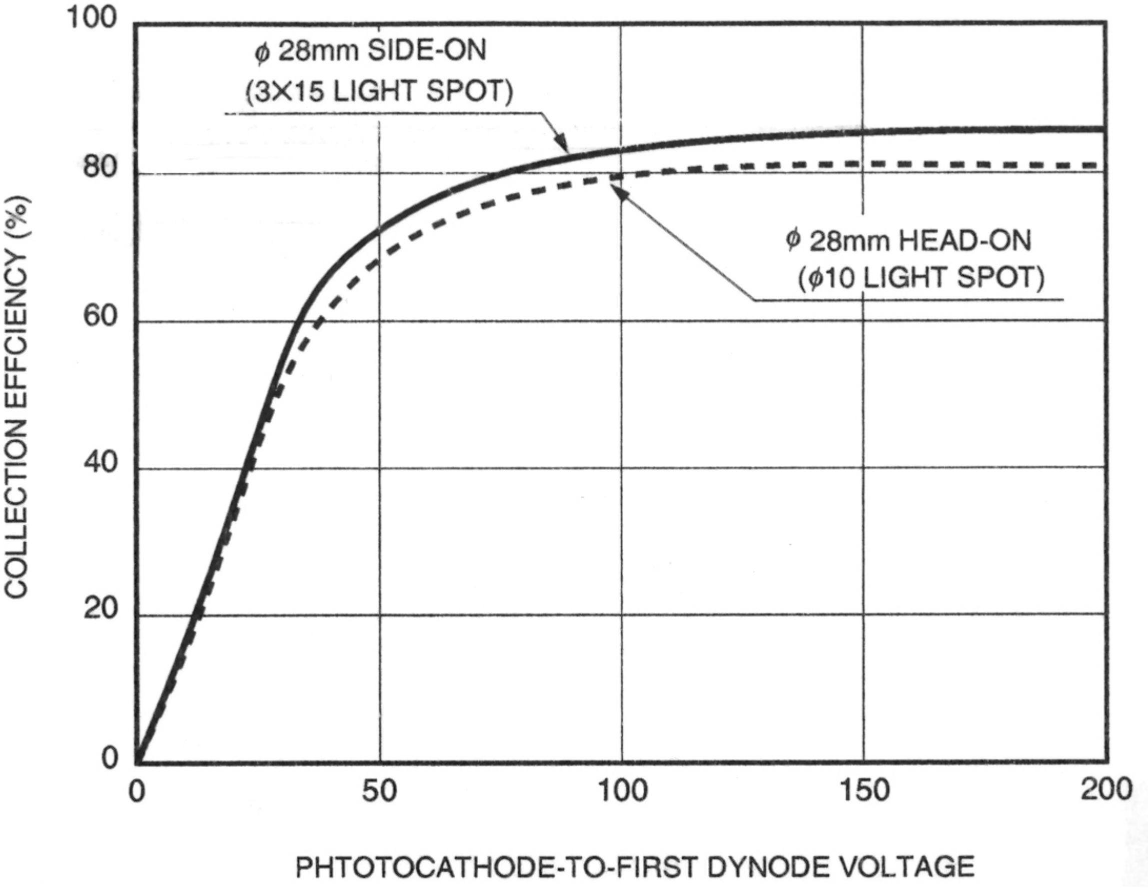

Figure C.1 Typical collection efficiency vs. photocathode-to-first dynode voltage for side-looking PMT [106]

An E717-63 socket assembly was used to interface the PMT voltage supply and detection electronics to the R636-10 PMT during all preliminary MFRS experiments. This socket assembly has a built in voltage divider that equally distributes the PMT supply voltage, V_{PMT} – i.e. the photocathode-to-anode voltage – between the nine dynodes within the R636-10 PMT, as illustrated in Figure C.2 [105]. Referring again to Figure C.1, this implies that the collection efficiency of the R636-10 PMT utilizing the E717-63 socket is optimized in the PMT supply voltage range $1000 < V_{PMT} < 1500 = V_{PMT}|_{\mathrm{MAX}}$. (In this voltage range, the dark current is dominated by thermionic emissions. At lower supply voltages the dark current is dominated by ohmic-leakage – i.e. current leakage from the anode. Beyond the maximum supply voltage electrons emitted from the PMT electrodes under the influence the strong electric field inside the PMT dramatically increase the dark current. Although thermionic emissions occur from both the photocathode and the dynodes, thermionic emissions from the former are dominant). The following approximate linear expression for the collection efficiency in this PMT supply voltage range was derived from Figure C.1:

$$\alpha(V_{PMT}) \cong 77.5 + 0.00625V_{PMT}[\%];1000 < V_{PMT} < 1500 \quad \text{(C.1)}$$

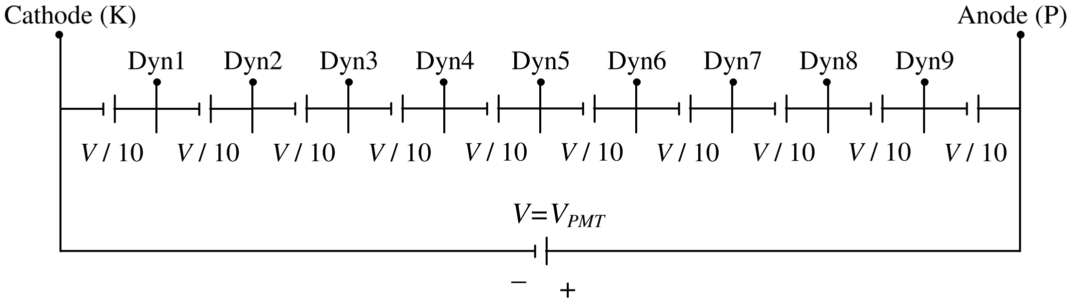

Figure C.2 Schematic of R636-10 PMT utilizing E717-63 socket

The secondary emission ratio from dynode ζ is defined by the following expression [106],

$$\delta_\zeta = aE_\zeta{}^k \quad \text{(C.2)}$$

where a and k are constant for each dynode and E_ζ is the voltage between dynodes ζ-1→ζ (or between the cathode and first dynode, K→ζ=1, or between the last dynode and anode, ζ=9→P). For the R636-10 PMT utilizing the E717-63 socket this inter-dynode voltage is simply,

$$E_\zeta = \frac{V_{PMT}}{n+1} \quad \text{(C.3)}$$

where n=9 is the number of dynodes. From Eqs. C.2 and C.3 it follows that the secondary emission ratio for the R636-10 PMT utilizing the E717-63 socket is,

$$\delta_\zeta = \delta = a\left(\frac{V_{PMT}}{n+1}\right)^k \quad \text{(C.4)}$$

for all n=9 dynodes.

The functional dependence of the secondary emission ratio of the R636-10 PMT on the supply voltage can be determined – i.e. the constants a and k in Eq. C.4 can be determined – if we consider the gain vs. supply voltage curve for the R636-10 PMT plotted in Figure C.3 [135]. The PMT gain is defined as the ratio of the current output from the anode, i_P, to the photocurrent output from the cathode, i_K,

$$\mu = {}^{i_P}\!/_{i_K} , \tag{C.5}$$

where,

$$i_K = S_K P_K . \tag{C.6}$$

(The maximum cathode photocurrent and anode output current specified for the R636-10 PMT is i_K=1 nA and i_P=1 μA, respectively [135]). In Eq. C.6 describing the photocurrent output from the cathode, P_K is the power of light incident upon the photocathode and S_K is the cathode radiant sensitivity,

$$S_K = n(\lambda)\frac{\lambda e}{hc} , \tag{C.7}$$

where λ is the wavelength of the incident light, e is the electron charge, h is Plank's constant, c is the speed of light, and $n(\lambda)$ is the quantum efficiency – i.e. the ratio of the rate of photoelectron production to the photon flux. (Note that the term hc/λ in Eq. C.7 is simply the photon energy (m.k.s. units of [J]). Eq. C.7 is simply an expression of the rate of electron production times the electron charge – i.e. output photocurrent – as a function of the incident photon flux times the photon energy – i.e. the incident power). For the GaAs photocathode employed in the R636-10 PMT, the quantum efficiency is $n(\lambda$=780 nm) ≅ 10% at λ=780 nm. From Eq. C.7 we therefore find that the cathode radiant sensitivity of the R636-10 PMT at λ=780 nm is $S_K(\lambda$=780 nm) ≅ 62 mA/W [135]. (To reiteratre, λ≅780 nm corresponds to the laser wavelength utilized throughout all preliminary MFRS experiments).

Returning to Eq. C.5, we see that the gain is defined as the current amplification that occurs across the n-dynodes within the PMT,

$$\mu = \alpha\delta_1\delta_2\delta_3\delta_4 \ldots \delta_n . \tag{C.8}$$

Inserting Eq. C.4 describing the secondary emission ratio of the R636-10 PMT utilizing the E717-63 socket into Eq. C.8 we find that the gain of the R636-10 as configured during preliminary MFRS measurements is simply,

$$\begin{aligned}\mu &= \alpha\delta^n \\ &= \alpha\left[\frac{a}{(n+1)^k}\right]^n V_{PMT}{}^{nk}\end{aligned}$$

$$\mu = \alpha \cdot A \cdot V_{PMT}{}^{nk}; A = \left[\frac{a}{(n+1)^k}\right]^n . \qquad \text{(C.9)}$$

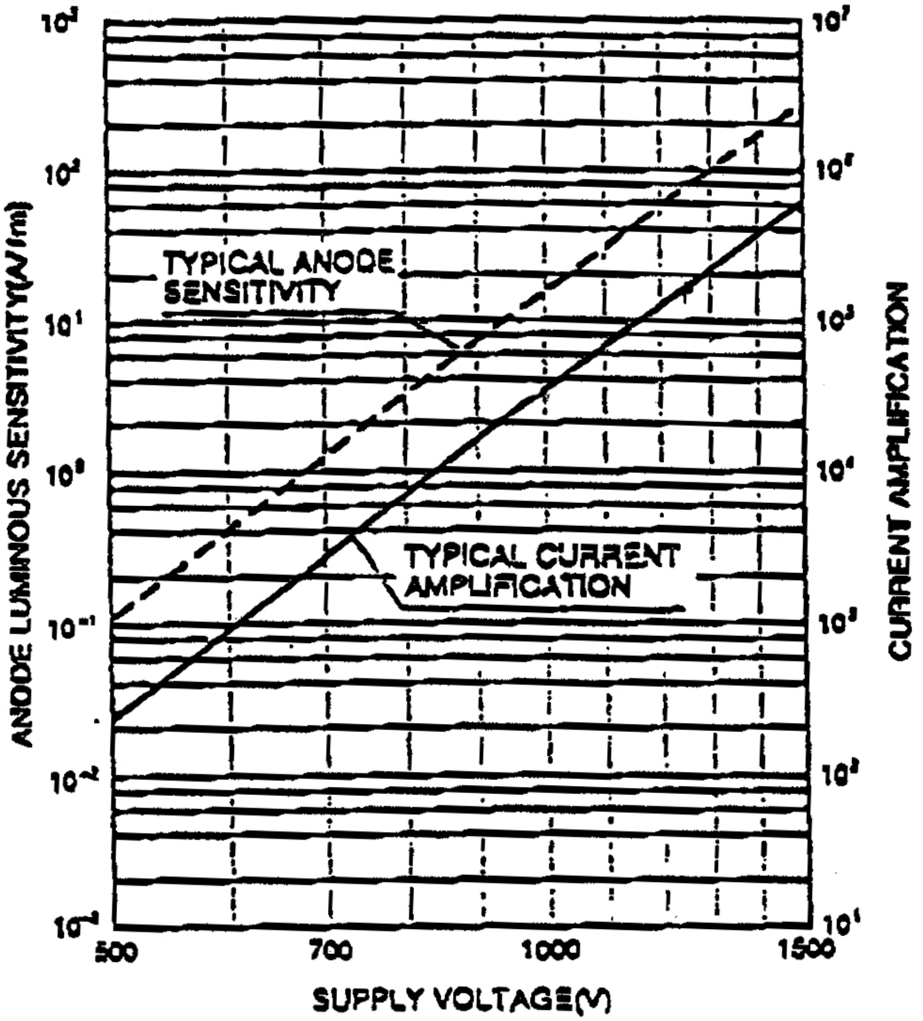

Figure C.3 Manufacture specified gain vs. PMT supply voltage curve for R636-10 PMT [135]

The gain vs. supply voltage curve in Figure C.3 is plotted on a log-log scale. Taking the common logarithm of both sides of Eq. C.9,

$$\log \mu = \log \alpha + \log A + nk \log V_{PMT} , \tag{C.10}$$

we find that the slope of the plot in Figure C.3 is simply equal to *nk* if we assume that $\alpha = \mathrm{f}(V_{PMT})$ ≈ constant. From Eq. C.1 we see that this is a perfectly valid assumption in the PMT supply voltage range $1000 < V_{PMT} < 1500$, but it is easy enough to account for the slight collection efficiency dependence on supply voltage:

$$nk = \frac{\log\left({}^{\mu_2}\!\!\diagup_{\alpha_2} \right) - \log\left({}^{\mu_1}\!\!\diagup_{\alpha_1} \right)}{\log\left(V_{PMT}\big|_2 \right) - \log\left(V_{PMT}\big|_1 \right)} . \tag{C.11}$$

From the plot in Figure C.3 and Eq. C.1 we find $\mu_2 \cong 1.4 \times 10^6$ and $\alpha_2 \cong 86.875\%$ at $V_{PMT}|_2$=1500 V. Similarly $\mu_1 \cong 4.5 \times 10^5$ and $\alpha_1 \cong 85.3125\%$ at $V_{PMT}|_1$=1250 V. Inserting these values into Eq. C.11 and recalling that the R636-10 has n=9 dynode stages we calculate $k \cong 0.68$. Referring back to Eq. C.10 we find – with $\mu \cong 1.4 \times 10^6$ and $\alpha \cong 86.875\%$ at V_{PMT}=1500 V and $k \cong 0.68$ – that $A \cong 5.646 \times 10^{-14}$ and from Eq. C.9 it follows that $a \cong 0.162$.

To summarize, the anode output current of the R636-10 PMT as configured during preliminary MFRS experiments as a function of the incident light power P_K and PMT supply voltage V_{PMT} is,

$$i_p = \mu S_k P_k , \tag{C.12}$$

where,

$$\mu = 4.52 \times 10^{-14} V_{PMT}{}^{6.12} + 3.64 \times 10^{-18} V_{PMT}{}^{7.12} \tag{C.13}$$

is the PMT gain and $S_K(\lambda$=780 nm$) \cong 62$ mA/W is the cathode radiant sensitivity to light in the vicinity of λ=780 nm.

Appendix D: Vapor Pressure

The equilibrium vapor pressure refers to that vapor pressure measured when the rate of condensation or deposition from the gas phase to the liquid or solid phase, respectively, is in dynamic equilibrium with the rate of evaporation or sublimation from the liquid or solid phase, respectively, to the gas phase. Phase transitions occur at constant temperature, *T*, and constant pressure, *P*, and since the vapor pressure is measured when the two phase are in equilibrium the difference in Gibbs free energy between the phases is zero,

$$G = H - TS \Rightarrow \Delta G = \Delta H - T\Delta S = 0\,. \tag{D.1}$$

Solving Eq. D.1, we find that the change in entropy, Δ*S*, from one phase to the other is simply the ratio of the difference in enthalpy, Δ*H*, between the phases to the temperature of the equilibrium two phase system,

$$\Delta S = \frac{\Delta H}{T}\,. \tag{D.2}$$

We are interested in knowing the vapor pressure dependence on temperature. Using Euler's chain relation between variables *x*, *y*, and *z*,

$$\left.\frac{\partial x}{\partial y}\right|_z = -\frac{\left.{}^{\partial z}\!/_{\partial y}\right|_x}{\left.{}^{\partial z}\!/_{\partial x}\right|_y} \tag{D.3}$$

we can solve for the change in vapor pressure with temperature along the phase line,

$$\left.\frac{\partial P}{\partial T}\right|_{\Delta G} = -\frac{\left.{}^{\partial \Delta G}\!/_{\partial T}\right|_P}{\left.{}^{\partial \Delta G}\!/_{\partial T}\right|_T} \tag{D.4}$$

by noting from Gibbs relation,

$$\mathrm{d}G = V\mathrm{d}P - S\mathrm{d}T \tag{D.5}$$

that,

$$\left.\frac{\partial \Delta G}{\partial T}\right|_P = -\Delta S \tag{D.6a}$$

$$\left.\frac{\partial \Delta G}{\partial P}\right|_T = \Delta V \tag{D.6b}$$

Inserting Eqs. D.2 and D.6 into Eq. D.4 we find,

$$\left.\frac{\partial P}{\partial T}\right|_{\Delta G} = \frac{\Delta H}{T\Delta V}\,. \tag{D.7}$$

Assuming that the change in enthalpy is constant in temperature and that the volume of gas is much greater than the volume of either liquid or solid,

$$\Delta V = V_{\text{gas}} - V_{\text{liquid}} \approx V_{\text{gas}} - V_{\text{solid}} \approx V_{\text{gas}} = \frac{n\hat{R}T}{P} \tag{D.8}$$

we arrive at the following integral equation,

$$\int \frac{\mathrm{d}P_v}{P_v} = \int \frac{\Delta\hat{H}_v}{\hat{R}T^2}\mathrm{d}T\,. \tag{D.9}$$

Integrating Eq. D.9 we find,

$$\ln P_v(T) = -\frac{\Delta\hat{H}_v}{\hat{R}T} + \text{constant}\,. \tag{D.10}$$

Eq. D.10 is referred to as the Clausius-Clapeyron equation, where $\hat{R} = 8314\frac{\mathrm{J}}{\mathrm{kmol}\cdot\mathrm{K}}$ is the universal gas constant and $\Delta\hat{H}_v$ is called the standard enthalpy change of vaporization (or the heat of vaporization). The heat of vaporization is the enthalpy difference per unit mole between the two phases – gas and liquid or gas and solid – when they are in dynamic equilibrium with each other, and can be thought of as the energy required per unit mole to overcome the intermolecular interactions in the liquid or solid, resulting in evaporation or sublimation, respectively.

(According to the Clausis-Clapeyron equation, Eq. D.10, the vapor pressure exponentially increases with temperature. Referring to Beer's law, Eq. 3.90, we find that the attenuation in power of light resonant with an atomic transition therefore increases exponentially with the exponential increase in vapor pressure with temperature. It is rubidium's relatively low heat of vaporization, resulting in a strong resonant absorption at modest temperature, which makes it an ideal candidate for high resolution MFRS velocimetery).

A more refined expression for the vapor pressure dependence on temperature follows if we account for the (relatively minor) temperature dependence of the heat of vaporization,

$$\Delta\hat{H}_v(T) = \Delta\hat{H}_v(T_1) + \int_{T_1}^{T} \Delta\hat{C}_p \mathrm{d}T \tag{D.11}$$

as well as the (even smaller) change in heat capacities with temperature,

$$\Delta\hat{C}_p = \mathrm{f}(T)\,. \tag{D.12}$$

Inserting Eqs. D.11 and D.12 into Eq. D.9 and integrating results in an expression of the form,

$$\ln P_v(T) = \frac{C_1}{T} + C_2 \ln T + C_3 T + C_4 \tag{D.13}$$

or in terms of common logarithms,

$$\log_{10} P_v(T) = \frac{c_1}{T} + c_2 \log_{10} T + c_3 T + c_4 \,. \tag{D.14}$$

Eq. D.14 is generally how the vapor pressure for Rb is defined in scientific literature, with values for the constants c_1, c_2, c_3, and c_4 chosen so that the vapor pressure as a function of temperature is consistent with measurement.

Appendix E: A Description of Modulated Absorption Spectroscopy from the Spectral Perspective

Frequency modulation spectroscopy (FMS) is described from the spectral perspective. The FMS theory outlined below is a generalization of the WMS theory described in Section 3.4 and provides a completely valid description of WMS as well as FMS. Joel Silver wrote what I consider to be the seminal paper describing FMS [100]. My intention in this sub-section is to lend a little more mathematical insight into FMS while briefly summarizing the poignant theoretical discussion contained in Dr. Silver's paper.

From the spectral perspective, the electric field being transmitted through an absorptive and dispersive medium is investigated. The frequency modulation imposed on an electric field of amplitude E_o modulating about a mean optical frequency ω,

$$E(t) = E_o \exp[\hat{\imath}\omega t + \hat{\imath}\phi(t)] \,, \tag{E.1}$$

is captured by a time-dependent phase shift,

$$\phi(t) = \beta \sin(\omega_m t) \,. \tag{E.2}$$

In Eq. E.2 describing the time-dependent phase shift β is the so-called frequency modulation index (FM index) and ω_m is the modulation frequency.

Note that the instantaneous frequency of the electric field described in Eq. E.1 is defined as the time rate-of-change of the phase [101],

$$\omega(t) = \frac{\mathrm{d}}{\mathrm{d}t}\left[\omega t + \beta \sin(\omega_m t)\right] = \omega + \beta\omega_m \cos(\omega_m t) \,. \tag{E.3}$$

This instantaneous frequency is completely analogous to the time-varying optical frequency used to describe modulation from the temporal perspective. Comparing Eq. E.3 to Eq. 3.102 from the Section 3.4 we find,

$$a = \beta\omega_m \,. \tag{E.4}$$

In other words, $\beta\omega_m$ is equivalent to the amplitude of the frequency modulation, a – i.e. the maximum excursion from the mean laser optical frequency. The frequency modulation index, β, therefore defines the number of multiples of ω_m – i.e. the number of sidebands – that the modulation encompasses.

Recasting Eq. E.4 in terms of the following dimensionless parameters,

$$m = \frac{a}{\delta\omega_{1/2}} \equiv \text{modulation index} \qquad \text{(E.5a)}$$

$$x_m = \frac{\omega_m}{\delta\omega_{1/2}} \equiv \text{normalized modulation frequency ,} \qquad \text{(E.5b)}$$

we find that the FM index is related to the modulation index according to the following equation:

$$m = \beta x_m \, . \qquad \text{(E.6)}$$

For WMS measurements the modulation frequency is relatively low ($\omega_m << \delta\omega_{1/2} \Rightarrow x_m << 1$) and the modulation signal consists of contributions from many closely spaced sidebands at $\omega_o \pm \text{n}\omega_m$. For FMS measurements the modulation frequency is relatively high ($\omega_m > \delta\omega_{1/2} \Rightarrow x_m > 1$) and the modulation index is typically less than one, $m < 1$ [101]. In this case the modulation signal is dominated by the strong carrier and likely receives contributions from only one set of sidebands.

In real laser systems an amplitude modulation (AM) of the electric field occurs in conjunction with the optical frequency modulation (FM). Combining Eqs. E.1 and E.2 and introducing a term to account for this amplitude modulation we find,

$$E(t) = E_o\left[1 + M\sin(\omega_m t + \psi)\right]\exp\left[\hat{\imath}\omega t + \hat{\imath}\beta\sin(\omega_m t)\right]. \qquad \text{(E.7)}$$

The parameter ψ introduced in Eq. E.7 is the phase difference between the AM and the FM. Noting that the intensity is proportional to the square of the electric field we find that the amplitude modulation index (AM index), M, introduced in Eq. E.7 is related to the change in intensity while modulating about the mean optical frequency; i.e. solving Eq. E.7 for the total light intensity,

$$I(t) \propto I_o\left[1 + 2M\sin(\omega_m t)\right] \qquad \text{(E.8)}$$

we find,

$$M \propto \frac{\left|I_o - I_{MAX}\right|}{2I_o} \qquad \text{(E.9)}$$

where I_o is the intensity detected at the mean optical frequency, ω, and I_{MAX} is the intensity detected at $\omega \pm a$.

Since the optical frequency of diode lasers can be rapidly modulated via the injection current they are typically employed in WMS and FMS experiments. In this case the AM index in Eq. E.9 is defined by the slope efficiency of the diode employed; e.g. for near-IR diodes the slope efficiency is essentially linear (i.e. the output laser intensity linearly increases with injection current). The phase difference between the AM associated with the diode slope efficiency and the FM has been found to have a value of ψ ≅ π/2 for commercially available diodes [100].

Though it increases experimental complexity, using electro optic modulators to impose modulation sidebands on a laser electric field has the distinct advantage that residual amplitude modulation (RAM) in the detected signal is minimized. During all MFRS experiments in the frequency-locked mode of operation optical frequency modulation was implemented via a wavelength selective element. A master oscillator power amplifier (MOPA) system provided the laser beam used during these investigation. The spectral characteristics of this laser beam were defined by the master oscillator – an extended-cavity diode laser (ECDL) in the Littrow configuration – and optical frequency modulation was implemented by dithering the Littrow grating angle; i.e. an ECDL in the Littrow configuration uses a grating to provide wavelength selective feedback to the diode laser in the cavity. In this case, the dependence of grating diffraction efficiency on the wavelength and incident angle of the light re-circulating within the cavity results in an amplitude modulation. In addition, power amplification of the Littrow laser beam was provided by an anti-reflection coated broad area laser (BAL). Littrow laser cavities suffer from beam steer – i.e. the propagation direction of a Littrow laser output beam depends on the grating angle – and since we implemented modulation by dithering the grating angle this beam steer affects the efficiency with which the Littrow laser beam is coupled into and amplified within the BAL junction.

Let's continue with the theoretical analysis of FMS by first expanding the amplitude modulation term in Eq. E.7 in terms of exponentials,

$$\begin{aligned}1+M\sin(\omega_m t+\psi) &= 1+\frac{M}{2\mathrm{j}}\left\{\exp\left[\hat{\imath}(\omega_m t+\psi)\right]-\exp\left[-\hat{\imath}(\omega_m t+\psi)\right]\right\}\\ &= 1+\frac{M}{2\mathrm{j}}\exp(\hat{\imath}\psi)\exp(\hat{\imath}\omega_m t)-\frac{M}{2\mathrm{j}}\exp(-\hat{\imath}\psi)\exp(-\hat{\imath}\omega_m t)\end{aligned}$$

$$1+M\sin(\omega_m t+\psi)=c_0+c_1\exp(\hat{\imath}\omega_m t)+c_{-1}(-\hat{\imath}\omega_m t)\,. \tag{E.10}$$

In Eq. E.10,

$$c_0=1 \tag{E.10a}$$

and,

$$c_{\pm 1}=\pm\frac{M}{2\hat{\imath}}\exp(\pm\hat{\imath}\psi) \tag{E.10b}$$

accounts for the amplitude modulation.

We can expand the other term in Eq. E.7 in terms of Bessel functions of the first kind. Consider the generating function,

$$g(z,t) = \exp\left[\frac{z}{2}\left(t - \frac{1}{t}\right)\right] \tag{E.11}$$

Expanding this generating function in a Taylor series we find,

$$\exp\left[\frac{z}{2}\left(t - \frac{1}{t}\right)\right] = \exp\left(\frac{z}{2}t\right)\exp\left(-\frac{z}{2t}\right)$$

$$= \sum_{r=0}^{\infty}\left(\frac{z}{2}\right)^r \frac{t^r}{r!}\sum_{s=0}^{\infty}(-1)^s\left(\frac{z}{2}\right)^s \frac{t^{-s}}{s!}$$

$$\exp\left[\frac{z}{2}\left(t - \frac{1}{t}\right)\right] = \sum_{r,s}\left(\frac{z}{2}\right)^{r+s}(-1)^s \frac{1}{r!s!}t^{r-s}\ . \tag{E.12}$$

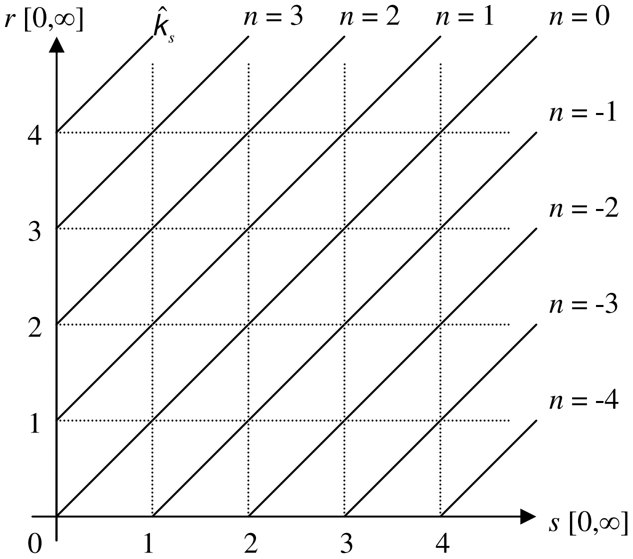

Figure E.1 Pictorial description of variable definition in Eq. E.13

Let’s introduce the following change of variables,

$$n = r - s \Rightarrow \exp\left[\frac{z}{2}\left(t - \frac{1}{t}\right)\right] = \sum_{n=-\infty}^{\infty} t^n \sum_{s=s_{\min}}^{\infty}\left(\frac{z}{2}\right)^{2s+n}(-1)^s \frac{1}{s!(s+n)!} \tag{E.13}$$

where from Figure E.1 we can see,

$$s_{\min} = \begin{cases} 0 & n \geq 0 \\ -n & n < 0 \end{cases} \tag{E.14}$$

Rewriting Eq. E.13,

$$\exp\left[\frac{z}{2}\left(t-\frac{1}{t}\right)\right]=\sum_{n=0}^{\infty}t^n\sum_{s=0}^{\infty}\left(\frac{z}{2}\right)^{2s+n}(-1)^s\frac{1}{s!(s+n)!} + \sum_{n=-\infty}^{-1}t^n\sum_{s'=n}^{\infty}\left(\frac{z}{2}\right)^{2s'-n}(-1)^{s'}\frac{1}{s'!(s'-n)!} \tag{E.15}$$

and introducing yet another change of variables we find,

$$s=s'-n\Rightarrow\exp\left[\frac{z}{2}\left(t-\frac{1}{t}\right)\right]=\sum_{n=0}^{\infty}t^n\sum_{s=0}^{\infty}\left(\frac{z}{2}\right)^{2s+n}(-1)^s\frac{1}{s!(s+n)!} + \sum_{n=-\infty}^{-1}t^n\sum_{s=0}^{\infty}\left(\frac{z}{2}\right)^{2s+n}(-1)^{s+n}\frac{1}{s!(s+n)!} \tag{E.16}$$

From the definition of the Bessel function of first kind,

$$J_n(z)=\sum_{s=0}^{\infty}\frac{(-1)^s}{s!(s+n)!}\left(\frac{z}{2}\right)^{2s+n} \tag{E.17}$$

and noting that,

$$J_{-n}(z)=(-1)J_n(z) \tag{E.18}$$

we find, after combining Eqs. E.16-E.18, that the generating function introduced in Eq. E.11 can be written in terms of a series expansion of Bessel functions:

$$\exp\left[\frac{z}{2}\left(t-\frac{1}{t}\right)\right]=\sum_{n=-\infty}^{\infty}J_n(z)t^n \tag{E.19}$$

Introducing one final change of variables,

$$t=\exp(\hat{\imath}\theta)\Rightarrow t-\frac{1}{t}=2\hat{\imath}\sin\theta \tag{E.20}$$

into Eq. E.19 we find,

$$\exp(\hat{\imath}z\sin\theta)=\sum_{n=-\infty}^{\infty}J_n(z)\exp(\hat{\imath}n\theta) \tag{E.21}$$

or,

$$\exp(\hat{\imath}\beta\sin\omega_m t)=\sum_{l=-\infty}^{\infty}J_l(\beta)\exp(\hat{\imath}l\omega_m t) \tag{E.22}$$

Recasting Eq. E.7 in terms of the expansions in Eqs. E.10 and E.22,

$$E(t)=E_o\exp(\hat{\imath}\omega t)\left\{\sum_{l=-\infty}^{\infty}c_oJ_l(\beta)\exp(\hat{\imath}l\omega_m t)+\sum_{l'=-\infty}^{\infty}c_{\pm1}J_{l'}(\beta)\exp[\hat{\imath}(l'\pm1)\omega_m t]\right\} \tag{E.23}$$

and introducing the following change of variables,

$$l=l'\pm1 \tag{E.24}$$

we find,

$$E(t) = E_o \exp(\hat{\imath}\omega t)\left\{ \sum_{l=-\infty}^{\infty} c_o J_l(\beta)\exp(\hat{\imath} l \omega_m t) + \sum_{l=-\infty}^{\infty} c_{\pm 1} J_{l\mp 1}(\beta)\exp(\hat{\imath} l \omega_m t) \right\} \qquad \text{(E.25)}$$

or alternatively,

$$E(t) = E_o \exp(\hat{\imath}\omega t)\sum_{l=-\infty}^{\infty} r_l \exp(\hat{\imath} l \omega_m t) \qquad \text{(E.26)}$$

where,

$$r_l = \sum_{k=-1}^{1} c_k J_{l-k}(\beta)\left(c_o = 1\,;\, c_{\pm 1} = \pm\frac{M}{2\hat{\imath}}\exp(\pm\hat{\imath}\psi)\right). \qquad \text{(E.27)}$$

If the optical frequency modulated electric field described by Eq. E.26 is passed through a medium exhibiting absorption, then the transmitted intensity is a sum of Fourier components at integer multiples of the modulation frequency, nω_m. The attenuation experienced by each optical sideband on passage a distance z through an absorbing medium is again expressed by Beer's law,

$$I_t(\omega, z, t) = \frac{c\varepsilon}{2}\left[E(t)\exp\left(-\frac{\alpha(\omega)z}{2}\right)\right]\left[E^*(t)\exp\left(-\frac{\alpha(\omega)z}{2}\right)\right] \qquad \text{(E.28)}$$

where c is the speed of light, ε is the permittivity of the medium, and $\alpha(\omega)$ is the frequency-dependent absorption constant. A superscript asterisk is used to denote the complex conjugate of the electric field in Eq. E.28 and will be used in the discussion that follows to denote the complex conjugate of the associated parameter. Inserting Eq. E.26 describing the optical frequency modulated electric field into Eq. E.28 describing the intensity of light within the bandwidth of an absorption feature transmitted after passage a distance z through the absorbing gas we find,

$$\begin{aligned}
I_t(\omega, z, t) = {} & I_o\left\{ \sum_{l=-\infty}^{\infty} r_l \exp(\hat{\imath} l\omega_m t)\exp\left[-\frac{z}{2}\alpha(\omega + l\omega_m)\right]\right\}\cdot\left\{ \sum_{l=-\infty}^{\infty} r_l^* \exp(-\hat{\imath} l\omega_m t)\exp\left[-\frac{z}{2}\alpha(\omega + l\omega_m)\right]\right\} \\
= {} & I_o\left\{ \ldots r_{-2}\exp(-\hat{\imath}2\omega_m t)\exp\left[-\frac{z}{2}\alpha(\omega - 2\omega_m)\right] + r_{-1}\exp(-\hat{\imath}\omega_m t)\exp\left[-\frac{z}{2}\alpha(\omega - \omega_m)\right]\right. \\
& + r_0\exp\left[-\frac{z}{2}\alpha(\omega)\right] + r_1\exp(\hat{\imath}\omega_m t)\exp\left[-\frac{z}{2}\alpha(\omega + \omega_m)\right] \\
& \left. + r_2\exp(\hat{\imath}2\omega_m t)\exp\left[-\frac{z}{2}\alpha(\omega + 2\omega_m)\right]\ldots\right\}\cdot\left\{ \ldots r_{-2}^*\exp(\hat{\imath}2\omega_m t)\exp\left[-\frac{z}{2}\alpha(\omega - 2\omega_m)\right]\right. \\
& + r_{-1}^*\exp(\hat{\imath}\omega_m t)\exp\left[-\frac{z}{2}\alpha(\omega - \omega_m)\right] + r_0^*\exp\left[-\frac{z}{2}\alpha(\omega)\right] \\
& \left. + r_1^*\exp(-\hat{\imath}\omega_m t)\exp\left[-\frac{z}{2}\alpha(\omega + \omega_m)\right] + r_2^*\exp(-\hat{\imath}2\omega_m t)\exp\left[-\frac{z}{2}\alpha(\omega + 2\omega_m)\right]\ldots\right\}
\end{aligned}$$

$$
\begin{aligned}
I_t(\omega,z,t) = I_o\Big\{ & ..r_{-2}r_{-2}^{*}\exp[-\alpha(\omega-2\omega_m)z] + r_{-1}r_{-1}^{*}\exp[-\alpha(\omega-\omega_m)z] + r_0r_0^{*}\exp[-\alpha(\omega)z] \\
& + r_1r_1^{*}\exp[-\alpha(\omega+\omega_m)z] + r_2r_2^{*}\exp[-\alpha(\omega+2\omega_m)z] + ... \\
& ... + r_{-2}r_{-1}^{*}\exp(-\hat{\imath}\omega_m t)\exp\left[-\frac{z}{2}\alpha(\omega-2\omega_m) - \frac{z}{2}\alpha(\omega-\omega_m)\right] \\
& + r_{-1}r_{-2}^{*}\exp(\hat{\imath}\omega_m t)\exp\left[-\frac{z}{2}\alpha(\omega-2\omega_m) - \frac{z}{2}\alpha(\omega-\omega_m)\right] \\
& + r_{-1}r_0^{*}\exp(-\hat{\imath}\omega_m t)\exp\left[-\frac{z}{2}\alpha(\omega-\omega_m) - \frac{z}{2}\alpha(\omega)\right] \\
& + r_0r_{-1}^{*}\exp(\hat{\imath}\omega_m t)\exp\left[-\frac{z}{2}\alpha(\omega-\omega_m) - \frac{z}{2}\alpha(\omega)\right] \\
& + r_0r_1^{*}\exp(-\hat{\imath}\omega_m t)\exp\left[-\frac{z}{2}\alpha(\omega) - \frac{z}{2}\alpha(\omega+\omega_m)\right] \\
& + r_1r_0^{*}\exp(\hat{\imath}\omega_m t)\exp\left[-\frac{z}{2}\alpha(\omega) - \frac{z}{2}\alpha(\omega+\omega_m)\right] \\
& + r_1r_2^{*}\exp(-\hat{\imath}\omega_m t)\exp\left[-\frac{z}{2}\alpha(\omega+\omega_m) - \frac{z}{2}\alpha(\omega+2\omega_m)\right] \\
& + r_2r_1^{*}\exp(\hat{\imath}\omega_m t)\exp\left[-\frac{z}{2}\alpha(\omega+\omega_m) - \frac{z}{2}\alpha(\omega+2\omega_m)\right] + ...\Big\}
\end{aligned}
\tag{E.29}
$$

where I_o is the intensity of light incident upon the absorbing medium.

In the absence of homodyne detection the attenuation of the individual sidebands generated by the optical frequency modulation would be detected directly. This is modeled for instance by the first five terms in Eq. E.29. The Fourier components, such as the eight first-harmonic terms included at the end of Eq. E.29, would essentially average out to zero for typical measurement integration times, $\tau >> 1/\omega_m$:

$$
\begin{aligned}
\left\langle e^{\hat{\imath}\omega_m t}\right\rangle_\tau &= \frac{1}{\tau}\int_{t-\tau/2}^{t+\tau/2} e^{\hat{\imath}\omega_m t'}\,dt' \\
&= \frac{1}{\hat{\imath}\omega_m\tau}\left[e^{\hat{\imath}\omega_m(t+\tau/2)} - e^{\hat{\imath}\omega_m(t-\tau/2)}\right] \\
&= \left(\frac{\sin \omega_m\tau/2}{\omega_m\tau/2}\right)e^{\hat{\imath}\omega_m t}
\end{aligned}
$$

$$
\left\langle e^{\hat{\imath}\omega_m t}\right\rangle_\tau = \operatorname{sinc}\frac{\omega_\mathrm{m}\tau}{2}\cdot e^{\hat{\imath}\omega_m t} \xrightarrow{\tau >> \frac{1}{\omega_m}} 0\,. \tag{E.30}
$$

If we implement homodyne detection using a lock-in amplifier, however, only the pertinent Fourier component of the transmitted intensity contributes to the signal. For first-harmonic detection, for instance, the lock-in amplifier mixes the detected modulated absorption with a reference sinusoidal signal oscillating at the modulation frequency,

$$R^1(t) = 2\cos\left(\mathrm{n}\omega_m t + \theta\right). \tag{E.31}$$

In this case, only those terms similar to the last eight terms in Eq. E.29 modeling the transmitted intensity contribute to the detected lock-in signal. Noting that,

$$XY^* = \left(X^* Y\right)^* \tag{E.32}$$

and that,

$$\mathrm{Re}\left(Z\right) = \mathrm{Re}\left(Z^*\right) \tag{E.33a}$$

$$\mathrm{Im}\left(Z\right) = -\,\mathrm{Im}\left(Z^*\right) \tag{E.33b}$$

and retaining only the first-harmonic terms, we can rewrite Eq. E.29 as follows:

$$\begin{aligned}
I_t(\omega, z, t) = I_o \Bigg\{ & \ldots \left[r_{-1} r_{-2}^* \exp\left(\hat{\imath}\omega_m t\right) + \left(r_{-1} r_{-2}^*\right)^* \exp\left(-\hat{\imath}\omega_m t\right)\right] \exp\left[-\frac{z}{2}\alpha\left(\omega - \omega_m\right) - \frac{z}{2}\alpha\left(\omega - 2\omega_m\right)\right] \\
& + \left[r_0 r_{-1}^* \exp\left(\hat{\imath}\omega_m t\right) + \left(r_0 r_{-1}^*\right)^* \exp\left(-\hat{\imath}\omega_m t\right)\right] \exp\left[-\frac{z}{2}\alpha\left(\omega\right) - \frac{z}{2}\alpha\left(\omega - \omega_m\right)\right] \\
& + \left[r_1 r_0^* \exp\left(\hat{\imath}\omega_m t\right) + \left(r_1 r_0^*\right)^* \exp\left(-\hat{\imath}\omega_m t\right)\right] \exp\left[-\frac{z}{2}\alpha\left(\omega + \omega_m\right) - \frac{z}{2}\alpha\left(\omega\right)\right] \\
& + \left[r_2 r_1^* \exp\left(\hat{\imath}\omega_m t\right) + \left(r_2 r_1^*\right)^* \exp\left(-\hat{\imath}\omega_m t\right)\right] \exp\left[-\frac{z}{2}\alpha\left(\omega + 2\omega_m\right) - \frac{z}{2}\alpha\left(\omega + \omega_m\right)\right] + \ldots \Bigg\}
\end{aligned}$$

$$\begin{aligned}
I_t(\omega, z, t) = I_o \Bigg\{ & \ldots \left[2\,\mathrm{Re}\left(r_{-1} r_{-2}^*\right)\cos\left(\omega_m t\right) - 2\,\mathrm{Im}\left(r_{-1} r_{-2}^*\right)\sin\left(\omega_m t\right)\right] \exp\left[-\frac{z}{2}\alpha\left(\omega - \omega_m\right) - \frac{z}{2}\alpha\left(\omega - 2\omega_m\right)\right] \\
& + \left[2\,\mathrm{Re}\left(r_0 r_{-1}^*\right)\cos\left(\omega_m t\right) - 2\,\mathrm{Im}\left(r_0 r_{-1}^*\right)\sin\left(\omega_m t\right)\right] \exp\left[-\frac{z}{2}\alpha\left(\omega\right) - \frac{z}{2}\alpha\left(\omega - \omega_m\right)\right] \\
& + \left[2\,\mathrm{Re}\left(r_1 r_0^*\right)\cos\left(\omega_m t\right) - 2\,\mathrm{Im}\left(r_1 r_0^*\right)\sin\left(\omega_m t\right)\right] \exp\left[-\frac{z}{2}\alpha\left(\omega + \omega_m\right) - \frac{z}{2}\alpha\left(\omega\right)\right] \\
& + \left[2\,\mathrm{Re}\left(r_2 r_1^*\right)\cos\left(\omega_m t\right) - 2\,\mathrm{Im}\left(r_2 r_1^*\right)\sin\left(\omega_m t\right)\right] \exp\left[-\frac{z}{2}\alpha\left(\omega + 2\omega_m\right) - \frac{z}{2}\alpha\left(\omega + \omega_m\right)\right] \\
& + \ldots \Bigg\}.
\end{aligned} \tag{E.34}$$

Consider the scattering arm of the MFRS velocimeter (see Figure 3.20 in Section 3.4). Rayleigh scattered photons from an optical frequency modulated probe laser beam are collected, transmitted through a Rb vapor cell, and detected by a photomultiplier tube (PMT). Referring to Eq. E.34, if we assume that the collected Rayleigh scattered light is monochromatic then the first-harmonic modulated absorption signal detected by the PMT as the probe laser beam frequency, ω, is slowly tuned across a Doppler broadened absorption feature in the D_2-line is,

$$\begin{aligned} i_p(\omega,z,t) = i_o \Big\{ & \ldots \left[2\operatorname{Re}\left(r_{-1}r_{-2}^*\right)\cos(\omega_m t) - 2\operatorname{Im}\left(r_{-1}r_{-2}^*\right)\sin(\omega_m t)\right]\exp\left[-\frac{z}{2}\alpha(\omega-\omega_m) - \frac{z}{2}\alpha(\omega-2\omega_m)\right] \\ & + \left[2\operatorname{Re}\left(r_0 r_{-1}^*\right)\cos(\omega_m t) - 2\operatorname{Im}\left(r_0 r_{-1}^*\right)\sin(\omega_m t)\right]\exp\left[-\frac{z}{2}\alpha(\omega) - \frac{z}{2}\alpha(\omega-\omega_m)\right] \\ & + \left[2\operatorname{Re}\left(r_1 r_0^*\right)\cos(\omega_m t) - 2\operatorname{Im}\left(r_1 r_0^*\right)\sin(\omega_m t)\right]\exp\left[-\frac{z}{2}\alpha(\omega+\omega_m) - \frac{z}{2}\alpha(\omega)\right] \\ & + \left[2\operatorname{Re}\left(r_2 r_1^*\right)\cos(\omega_m t) - 2\operatorname{Im}\left(r_2 r_1^*\right)\sin(\omega_m t)\right]\exp\left[-\frac{z}{2}\alpha(\omega+2\omega_m) - \frac{z}{2}\alpha(\omega+\omega_m)\right] \\ & + \ldots \Big\} \end{aligned} \tag{E.35}$$

where i_o is the PMT anode current detected outside the bandwidth of a Doppler broadened absorption feature. Noting that,

$$\cos x \cos y = \frac{1}{2}\left[\cos(x+y) + \cos(x-y)\right] \tag{E.36a}$$

$$\sin x \cos y = \frac{1}{2}\left[\sin(x+y) + \sin(x-y)\right] \tag{E.36b}$$

it follows that the DC-component of the mixed first-harmonic signal,

$$S_M^1 = i_p(\omega,z,t)\cdot R^1(t), \tag{E.37}$$

passed by the lock-in amplifier is,

$$\begin{aligned} S_l^1 = \frac{2 i_o R_L G}{\sqrt{2}} \Big\{ & \ldots \left[\operatorname{Re}\left(r_{-1}r_{-2}^*\right)\cos\theta + \operatorname{Im}\left(r_{-1}r_{-2}^*\right)\sin\theta\right]\exp\left[-\frac{z}{2}\alpha(\omega-\omega_m) - \frac{z}{2}\alpha(\omega-2\omega_m)\right] \\ & + \left[\operatorname{Re}\left(r_0 r_{-1}^*\right)\cos\theta + \operatorname{Im}\left(r_0 r_{-1}^*\right)\sin\theta\right]\exp\left[-\frac{z}{2}\alpha(\omega) - \frac{z}{2}\alpha(\omega-\omega_m)\right] \\ & + \left[\operatorname{Re}\left(r_1 r_0^*\right)\cos\theta + \operatorname{Im}\left(r_1 r_0^*\right)\sin\theta\right]\exp\left[-\frac{z}{2}\alpha(\omega+\omega_m) - \frac{z}{2}\alpha(\omega)\right] \\ & + \left[\operatorname{Re}\left(r_2 r_1^*\right)\cos\theta + \operatorname{Im}\left(r_2 r_1^*\right)\sin\theta\right]\exp\left[-\frac{z}{2}\alpha(\omega+2\omega_m) - \frac{z}{2}\alpha(\omega+\omega_m)\right] \\ & + \ldots \Big\}. \end{aligned} \tag{E.38}$$

In Eq. E.38 R_L is the shunt resistance at the input of the lock-in amplifier that converts the detected current signal into a voltage signal, G is the gain imposed by the lock-in on the detected harmonic signal, and the multiplicative constant $1/\sqrt{2}$ accounts for the fact that the lock-in amplifier utilized in all preliminary MFRS experiments outputs the RMS-amplitude of the detected sinusoidal voltage signal.

Following the logic above it is possible to show that lock-in detection of any harmonic, $\mathrm{n}\omega_m$, of the modulated absorption results in the following signal [100-104,136],

$$S_l^{\mathrm{n}} = \sqrt{2}\, i_o R_L G\left[\mathrm{Re}\left(\xi^{\mathrm{n}}\right)\cos\theta + \mathrm{Im}\left(\xi^{\mathrm{n}}\right)\sin\theta\right] \qquad \text{(E.39)}$$

where,

$$\xi^{\mathrm{n}} = \sum_l r_l r_{l-\mathrm{n}}^* \exp\left\{-\frac{z}{2}\alpha\left(\omega + l\omega_m\right) - \frac{z}{2}\alpha\left[\omega + \left(l-\mathrm{n}\right)\omega_m\right]\right\}. \qquad \text{(E.40)}$$

If we include dispersion, $\varphi(\omega)$, in our derivation of the **n*f***-signal we find,

$$\begin{aligned}\xi^{\mathrm{n}} = \sum_l r_l r_{l-\mathrm{n}}^* \exp&\left\{-\frac{z}{2}\alpha\left(\omega + l\omega_m\right) - \frac{z}{2}\alpha\left[\omega + \left(l-\mathrm{n}\right)\omega_m\right]\right\} \\ &\cdot \exp\left\{-\hat{\imath} z\varphi\left(\omega + l\omega_m\right) + \hat{\imath} z\varphi\left[\omega + \left(l-\mathrm{n}\right)\omega_m\right]\right\}\end{aligned} \qquad \text{(E.41)}$$

The relative phase, θ, of the reference signal $R^{\mathrm{n}}(t)$ to the detected signal $i_P(t)$ can be adjusted to accommodate detection of either the modulated absorption signal or the modulated dispersion signal. Inserting Eq. E.41 in Eq. E.39 and referring to Eq. E.27 we find that the in-phase component – i.e. detected with $\theta = 0$ or π – corresponds to the modulated absorption signal and that the quadrature component – i.e. detected with $\theta = \pm\pi/2$ – corresponds to the modulated dispersion signal. Joel Silver has pointed out that for WMS the modulated dispersion signal may only be $O(10^{-4})$ of the modulated absorption signal. This is evidenced in Eq. E.41: Each dispersion term in the summation contains a pair of exponentials of opposite sign whose values quickly approach each other as the modulation frequency (i.e. the frequency sideband separation) decreases. In light of this and referring back to Eq. E.27 we find that since $J_{-n}(z)=(-1)^{\mathrm{n}}J_n(z)$ the dispersion signal becomes vanishingly small as $\omega_m \rightarrow 0$.

Joel Silver's paper on the subject of FMS presents many experimentally relevant insights into the theory discussed above [100]. I never intended on discussing all of Dr. Silver's insights in this appendix – any researcher interested in attaining optimal detection sensitivities from WMS and FMS techniques should read (and re-read) the paper for him/herself – but I would like to discuss one insight that is relevant to the signal-to-noise calculations in Section 3.6: In the absence of absorption and dispersion, the detected lock-in signal is non-zero.

This background signal is termed residual amplitude modulation (RAM) and can be derived from the mathematical formalism developed above. Inserting Eq. E.27 into Eq. E.41 we find that in the absence of absorption or dispersion [137],

$$\begin{aligned}\alpha,\varphi=0\Rightarrow\xi^{\mathrm{n}}&=\sum_l r_l r_{l-\mathrm{n}}\\&=\sum_{k=-1}^{1}\sum_{j=-1}^{1}\left[c_k c_j^*\sum_l J_{l-k}(\beta)J_{l-j-\mathrm{n}}^*(\beta)\right]\\&=\sum_{k=-1}^{1}\sum_{j=-1}^{1}c_k c_j^* J_{k-j-\mathrm{n}}(0)\end{aligned}$$

$$\xi^{\mathrm{n}}=\sum_{k=-1}^{1}\sum_{j=-1}^{1}c_k c_j^* J_{k-j-\mathrm{n}}(0);\,k-j-\mathrm{n}=0\ . \tag{E.42}$$

For first-harmonic detection,

$$\begin{aligned}\alpha,\varphi=0,\mathrm{n}=1\Rightarrow\xi^1&=c_1c_0^*+c_0c_{-1}^*\\&=-\hat{\imath}M\exp(\hat{\imath}\psi)\end{aligned}$$

$$\xi^1=-\hat{\imath}M\cos\psi+M\sin\psi\ . \tag{E.43}$$

Inserting Eq. E.43 into Eq. E.39 and referring to Eq. E.27 we find that the first-harmonic lock-in signal detected in the absence of absorption or dispersion is,

$$\begin{aligned}S_l^1\Big|_{\mathrm{RAM}}&=\sqrt{2}i_oR_LG(-M\sin\psi\cos\theta+M\sin\theta\cos\psi)\\&=\sqrt{2}i_oR_LGM(\sin\theta\cos\psi-\sin\psi\cos\theta)\end{aligned}$$

$$S_l^1\Big|_{\mathrm{RAM}}=\sqrt{2}i_oR_LGR^1(M);\,R^1(M)=M\sin(\theta-\psi). \tag{E.44}$$

Similarly, for second-harmonic detection,

$$\begin{aligned}\alpha,\varphi=0,\mathrm{n}=2\Rightarrow\xi^2&=c_1c_{-1}^*\\&=-\frac{M^2}{4}\exp(\hat{\imath}2\psi)\end{aligned}$$

$$\xi^2=-\frac{M^2}{4}\cos2\psi-\hat{\imath}\frac{M^2}{4}\sin2\psi \tag{E.45}$$

and,

$$
\begin{aligned}
S_l^2\Big|_{\mathrm{RAM}} &= \sqrt{2}\,i_o R_L G\left(-\frac{M^2}{4}\cos\theta\cos 2\psi - \frac{M^2}{4}\sin\theta\sin 2\psi\right)\\
&= \frac{i_o R_L G M^2}{2\sqrt{2}}\left(-\cos\theta\cos 2\psi - \sin\theta\sin 2\psi\right)
\end{aligned}
$$

$$
S_l^2\Big|_{\mathrm{RAM}} = \sqrt{2}\,i_o R_L G R^2(M);\, R^2(M) = \frac{M^2}{4}\cos(\theta - 2\psi + \pi). \qquad \text{(E.46)}
$$

As a reminder ψ is the phase difference between the AM and the FM and θ is the relative phase between the lock-in reference signal and the detected harmonic of the modulated absorption signal.

As discussed in the Section 3.5, the amplitude modulation associated with modulated absorption spectroscopy techniques not only increases the shot noise of the measurement, but any variation in the amplitude modulation, associated with a variation in the laser power or the collected Rayleigh scattered power, for instance, also corrupts the measurement. This noise term is different from laser excess noise – RAM-induced noise results from and tracks the frequency modulation whereas excess laser noise is 1/*f* broadband noise.

Appendix F: Laser Beam Propagation and Transformation

F.1 Mathematical Representation of a Propagating Laser Beam

Consider a monochromatic electromagnetic wave (EM-wave),

$$E(x,y,z,t)=\tilde{E}(x,y,z)\exp(-\hat{\imath}\omega t) \qquad \text{(F.1)}$$

propagating through a uniform, isotropic, non-conducting medium. The dependence of the electric field amplitude $\tilde{E}(x,y,z)$ on the spatial coordinates *x*, *y*, and *z* is governed by a time-independent scalar wave equation (i.e. the Helmholtz equation) [39],

$$\left[\nabla^2+K^2\right]\tilde{E}(x,y,z)=0\,, \qquad \text{(F.2)}$$

where ∇^2 is the Laplacian and $K={}^{2\pi}\!/\!_{\lambda}$. In the following analysis we will assume that the EM-wave is propagating primarily along the *z*-axis, and that the primary spatial dependence of $\tilde{E}(x,y,z)$ is therefore a $\exp(-\hat{\imath}Kz)$ variation. Let us define,

$$\tilde{E}(x,y,z)\equiv\tilde{u}(x,y,z)\exp(-\hat{\imath}Kz) \qquad \text{(F.3)}$$

where $\tilde{u}(x,y,z)$ is a complex scalar wave amplitude describing the transverse profile of the propagating EM-beam as a function of *z*. Substituting Eq. F.3 into Eq. F.2 we find,

$$\frac{\partial^2\tilde{u}}{\partial x^2}+\frac{\partial^2\tilde{u}}{\partial y^2}+\frac{\partial^2\tilde{u}}{\partial z^2}-2\hat{\imath}K\frac{\partial\tilde{u}}{\partial z}=0\,. \qquad \text{(F.4)}$$

Eq. F.4 describes the spatial variation of $\tilde{u}$ due to diffraction effects. One of the fundamental assumptions of paraxial analysis is that the *z*-variation of $\tilde{u}$ occurs much more slowly than transverse variations due to the finite width of the propagating EM-beam [39]. That is,

$$\left|\frac{\partial}{\partial z}\left(\frac{\partial\tilde{u}}{\partial z}\right)=\frac{\partial^2\tilde{u}}{\partial z^2}\right|<<\left|\frac{\partial\tilde{u}}{\partial z}\right|,\left|\frac{\partial^2\tilde{u}}{\partial x^2}\right|,\text{ and}\left|\frac{\partial^2\tilde{u}}{\partial y^2}\right|. \qquad \text{(F.5)}$$

Inserting Eq. F.5 into F.4 leads to the following time-independent scalar wave equation,

$$\nabla_t^{\,2}\tilde{u}(s,z)-2\hat{\imath}K\frac{\partial\tilde{u}(s,z)}{\partial z}=0\,, \qquad \text{(F.6)}$$

which I will call the paraxial scalar wave equation. In Cartesian coordinates *s*=(*x*,*y*) and $\nabla_t^{\,2}=\frac{\partial^2}{\partial x^2}+\frac{\partial^2}{\partial y^2}$. In cylindrical coordinates *s*=(r,θ) and $\nabla_t^{\,2}=\frac{1}{r}\frac{\partial}{\partial r}\left(r\frac{\partial}{\partial r}\right)+\frac{1}{r^2}\frac{\partial^2}{\partial\theta^2}$.

A general solution to the Helmholtz equation in Eq. F.2 is,

$$\tilde{E}(r,r_o)=\frac{1}{\rho(r,r_o)}\exp[-\hat{\imath}K\rho(r,r_o)] \tag{F.7}$$

where in Cartesian coordinates,

$$\rho(r,r_o)=\sqrt{(x-x_o)^2+(y-y_o)^2+(z-z_o)^2} \tag{F.8}$$

Eq. F.7 physically represents the electric field amplitude at a point *r* due to a uniform spherical wave originating at a source point r_o, as illustrated in Figure F.1. Now consider a uniform spherical wave originating at some source point r_o close to the *z*-axis and propagating to another point *r* also close to the *z*-axis. In this case,

$$\begin{aligned}\rho(r,r_o)&=(z-z_o)\left[1+\frac{(x-x_o)^2+(y-y_o)^2}{(z-z_o)^2}\right]^{1/2}\\&\cong(z-z_o)\left[1+\frac{1}{2}\frac{(x-x_o)^2+(y-y_o)^2}{(z-z_o)^2}+\text{h.o.t.s}\right]\end{aligned}$$

$$\rho(r,r_o)\cong(z-z_o)+\frac{(x-x_o)^2+(y-y_o)^2}{2(z-z_o)}+\text{h.o.t.s} \tag{F.9}$$

and we can apply the Fresnel approximation to Eq. F.7. The Fresnel approximation involves only retaining those terms in Eq. F.9 through quadratic-order when expressing the phase factor in Eq. F.7, $\exp[-\hat{\imath}K\rho(r,r_o)]$, and retaining only the first-order term in Eq. F.9 when expressing the $1/\rho$-term in Eq. F.7 [39]:

$$\tilde{E}(x,y,z)\cong\frac{1}{(z-z_o)}\exp\left[-\hat{\imath}K(z-z_o)-\hat{\imath}K\frac{(x-x_o)^2+(y-y_o)^2}{2(z-z_o)}\right]. \tag{F.10}$$

As before, let us define

$$\tilde{E}(x,y,z)\equiv\tilde{u}(x,y,z)\exp[-\hat{\imath}K(z-z_o)]. \tag{F.11}$$

Comparing Eqs. F.10 and F.11 we find,

$$\tilde{u}(x,y,z)\cong\frac{1}{(z-z_o)}\exp\left[-\hat{\imath}K\frac{(x-x_o)^2+(y-y_o)^2}{2(z-z_o)}\right]. \tag{F.12}$$

Whereas Eq. F.7 is a general solution to the scalar wave equation in Eq. F.2, Eq. F.12 is a general solution to the paraxial scalar wave equation in Eq. F.6.

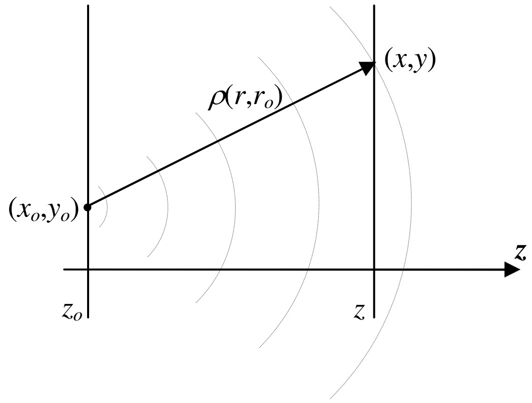

Figure F.1 Pictorial diagram of a spherical wave

The paraxial spherical wave solution in Eq. F.12 describes the complex scalar wave amplitude at some point $r=(x,y,z)$ due to a uniform spherical wave originating at a point $r_o=(x_o,y_o,z_o\approx z)$. We will now discuss how an EM-wavefront propagating primarily along the z-axis evolves. To describe wavefront propagation I will use an integral approach employing Huygens' Principle.

Huygens' Principle is a physically intuitive notion. Let us imagine that there is some known electric field distribution $\tilde{E}_o(x_o,y_o,z_o)$ on a closed surface, S_o, as illustrated in Figure F.2. Huygens' Principle regards each point on S_o as a source of uniform spherical waves which radiate from that point, and considers the total field at any other point inside or beyond S_o to be a superposition of all the Huygens' wavelets from S_o [14]. Huygens' Principle is expressed mathematically by the following integral, the Huygens' integral [39]:

$$\tilde{E}(x,y,z)=\frac{\hat{\imath}}{\lambda}\int_{x_o}\int_{y_o}\tilde{E}_o(x_o,y_o,z_o)\frac{\exp[-\hat{\imath}K\rho(r,r_o)]}{\rho(r,r_o)}\cos\theta(r,r_o)\,\mathrm{d}x_o\mathrm{d}y_o\,. \tag{F.13}$$

In Eq. F.13, $\frac{\hat{\imath}}{\lambda}$ is a normalization factor (which is also necessary for correct near field descriptions) and $\cos\theta\,(r,r_o)$ is the obliquity factor [39]. Employing the Fresnel approximation to Eq. F.13, and noting that the obliquity factor approaches one in the paraxial limit we find,

$$\tilde{E}(x,y,z)=\frac{\hat{\imath}}{\lambda}\frac{\exp[-\hat{\imath}K(z-z_o)]}{(z-z_o)}\int_{x_o}\int_{y_o}\tilde{E}_o(x_o,y_o,z_o)\exp\left[-\hat{\imath}K\frac{(x-x_o)^2+(y-y_o)^2}{2(z-z_o)}\right]\mathrm{d}x_o\mathrm{d}y_o \tag{F.14}$$

and referring to Eq. F.11,

$$\boxed{\tilde{u}(x,y,z)=\frac{\hat{\imath}}{\lambda}\frac{1}{(z-z_o)}\int_{x_o}\int_{y_o}\tilde{u}_o(x_o,y_o,z_o)\exp\left[-\hat{\imath}K\frac{(x-x_o)^2+(y-y_o)^2}{2(z-z_o)}\right]\mathrm{d}x_o\mathrm{d}y_o} \tag{F.15}$$

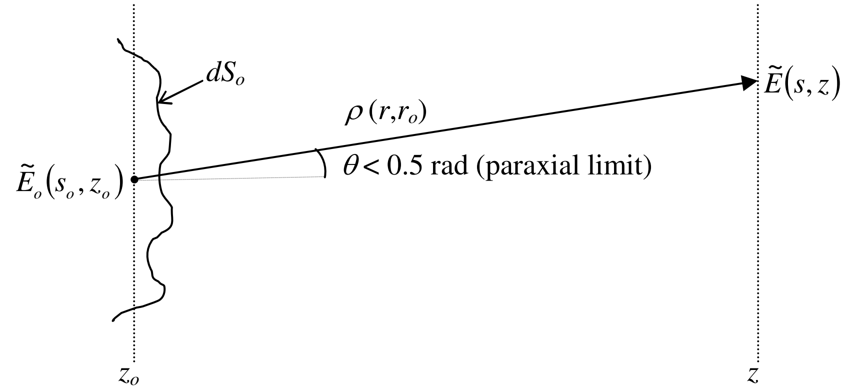

Figure F.2 Pictorial diagram of propagating wavefront

$\tilde{u}(x,y,z)$ defines the transverse profile of an EM-beam propagating primarily in the z-direction and the Huygens-Fresnel integral in Eq. F.15 describes how this transverse profile evolves in the paraxial limit. Let us consider a basic spatial mode ideal (BSMI) Gaussian laser beam propagating along the z-axis. The paraxial spherical wave solution given in Eq. F.12 is not in and of itself sufficient to describe the wavefront propagation of a BSMI Gaussian beam. In particular, the amplitude of the spherical wave solution does not fall of with transverse distance from the optical axis as a Gaussian beam does; i.e. The wavefront irradiance distribution of a BSMI Gaussian beam is symmetric and varies radially as,

$$I(r)=I_o\exp\left[-2\left(\frac{r}{w}\right)^2\right] \tag{F.16}$$

where w is the beam radius, defined as the radius, $r=w$, where the wavefront intensity has dropped to $1/e^2$ of the wavefront intensity on the beam axis, I_o. We can capture the physical nature of a propagating BSMI Gaussian beam, however, by introducing the so-called Gaussian spherical wave solution into the Huygens-Fresnel integral in Eq. F.15.

There are at least four ways to derive the Gaussian spherical wave (and the higher mode extensions). I refer you to Siegman [3, pp. 637-655] for the details of two such derivations resulting in the following normalized Gaussian spherical wave describing the fundamental mode of a laser beam propagating along the z-axis:

$$\tilde{u}(x,y,z)=\left(\frac{2}{\pi}\right)^{1/2}\left(\frac{\tilde{q}_o}{\omega_o\tilde{q}(z)}\right)\exp\left[-\hat{\imath}K\frac{(x-x_o)^2+(y-y_o)^2}{2\tilde{q}(z)}\right]. \tag{F.17}$$

In Eq. F.17 $K={}^{2\pi}\!/_{\lambda}$, $w_o=w(z_o=0)$ is the beam waist radius – i.e. the minimum beam radius of a continuously propagating BSMI Gaussian beam – assumed to reside at $z=z_o=0$ and associated with a wavefront radius of curvature $R(z_o=0)=\infty$, $\tilde{q}_o=\tilde{q}(z=z_o=0)$ is the complex source point, and

$$\tilde{q}(z)=R(z)+\tilde{q}_o=z+\tilde{q}_o \tag{F.18}$$

is the complex radius of curvature, which is defined by the following mathematical expression,

$$\frac{1}{\tilde{q}(z)}\equiv\frac{1}{R(z)}-\hat{\imath}\frac{\lambda}{\pi w(z)^2}. \tag{F.19}$$

Note from Eq. F.19 that,

$$\frac{1}{\tilde{q}(z=z_o)}=\frac{1}{R(z_o)}-\hat{\imath}\frac{\lambda}{\pi w(z_o)^2}\Rightarrow\frac{1}{\tilde{q}_o}=-\hat{\imath}\frac{\lambda}{\pi w_o^{\;2}}. \tag{F.20}$$

That is,

$$\tilde{q}_o=\hat{\imath}\frac{\pi w_o^{\;2}}{\lambda}=\hat{\imath}z_R \tag{F.21}$$

where z_R is the Rayleigh range typically used to define the extent of the beam waist region. Inserting Eq. F.21 into Eq. F.18 we find,

$$\tilde{q}(z)=z+\hat{\imath}z_R. \tag{F.22}$$

Setting $x_o=y_o=0$, inserting Eqs. F.19 and F.21 into Eq. F.17, and rearranging terms we find,

$$\tilde{u}(x,y,z)=\left(\frac{2}{\pi}\right)^{1/2}\frac{1}{w(z)}\exp[-\hat{\imath}\Psi(z)]\exp\left[\underbrace{-\hat{\imath}K\frac{x^2+y^2}{2R(z)}}_{\text{spherical wave}}-\underbrace{\frac{x^2+y^2}{w(z)^2}}_{\text{Gaussian transverse variation}}\right] \tag{F.23}$$

where,

$$\Psi(z)=\arctan\left(\frac{z}{z_R}\right) \tag{F.24}$$

is the Guoy phase shift.

I have ignored much of the math in deriving Eq. F.23, but the point is that the Gaussian spherical wave described by this equation is still an exact mathematical solution to either the paraxial scalar wave equation (Eq. F.6) or the Huygens-Fresnel integral (Eq. F.15). It also mathematically describes the physical nature of a BSMI Gaussian beam: It has a Gaussian amplitude profile in the transverse direction, it carries finite power across the beam cross-section, and it remains complex Gaussian in profile at all z-planes [3]. With the complex source point defined as it is in Eq. F.19 and described as it is in Eq. F.22, for instance, two observed physical properties of a propagating BSMI Gaussian beam are implied:

$$\left.\begin{aligned} \frac{1}{\tilde{q}(z)} &\equiv \frac{1}{R(z)} - \hat{\imath}\frac{\lambda}{\pi w(z)^2} \\ \frac{1}{\tilde{q}(z)} &= \frac{1}{z+\hat{\imath}z_R} = \frac{z}{z^2+z_R^2} - \hat{\imath}\frac{z_R}{z^2+z_R^2} \end{aligned}\right\} \Rightarrow$$

$$\Rightarrow R(z) = z\left[1+\left({}^{z_R}\!\!/_{z}\right)^2\right] \tag{F.25}$$

and,

$$\left.\begin{aligned} &\Rightarrow w(z)^2 = \frac{\lambda}{\pi} z_R\left[1+\left({}^{z}\!/_{z_R}\right)^2\right] \\ &z_R = \frac{\pi w_o^2}{\lambda} \end{aligned}\right\} \Rightarrow w(z) = w_o\left[1+\left({}^{z}\!/_{z_r}\right)^2\right]^{1/2}. \tag{F.26}$$

We are now in a position to analyze the unimpeded propagation of a BSMI Gaussian beam. Let's consider the unimpeded propagation of a BSMI Gaussian beam from its beam waist at z_o=0. From Eqs. F. 23 and F.24 we find that the input field is simply,

$$\tilde{u}_o(x_o, y_o, z_o) = \left(\frac{2}{\pi}\right)^{1/2} \frac{1}{w_o} \exp\left(-\frac{x_o^2+y_o^2}{w_o^2}\right). \tag{F.27}$$

(To simplify the analysis, I have assumed that the propagating BSMI Gaussian beam has a circular beam profile. An elliptic beam profile can be analyzed by simply defining the beam waist radius on two orthogonal axes; e.g. $w_o|_x$ along the x-axis and $w_o|_y$ along the y-axis). The Huygens-Fresenl integral provides a relatively straight-forward way of propagating this Gaussian wavefront to any other z-plane. Inserting Eq. F.27 into Eq. F.15 we find,

$$\begin{aligned}\tilde{u}(x,y,z) &= \frac{\hat{\imath}}{\lambda z}\sqrt{\frac{2}{\pi}}\frac{1}{w_o}\int_{x_o}\int_{y_o}\exp\left[-\frac{x_o^2+y_o^2}{w_o^2}\right]\exp\left[-\hat{\imath}\frac{\pi}{\lambda}\frac{(x-x_o)^2+(y-y_o)^2}{z}\right]\mathrm{d}x_o\mathrm{d}y_o \\ &= \frac{\hat{\imath}}{\lambda z}\sqrt{\frac{2}{\pi}}\frac{1}{w_o}\int_{x_o}\exp\left[-\frac{x_o^2}{w_o^2}\right]\exp\left[-\hat{\imath}\frac{\pi}{\lambda}\frac{(x-x_o)^2}{z}\right]\mathrm{d}x_o\int_{y_o}\exp\left[-\frac{y_o^2}{w_o^2}\right]\exp\left[-\hat{\imath}\frac{\pi}{\lambda}\frac{(y-y_o)^2}{z}\right]\mathrm{d}y_o \\ &= \frac{\hat{\imath}}{\lambda z}\sqrt{\frac{2}{\pi}}\frac{1}{w_o}\left\{\exp\left[-\frac{x_o^2}{w_o^2}\right]*\exp\left[-\hat{\imath}\frac{\pi}{\lambda}\frac{x_o^{\,2}}{z}\right]\right\}\cdot\left\{\exp\left[-\frac{y_o^2}{w_o^2}\right]*\exp\left[-\hat{\imath}\frac{\pi}{\lambda}\frac{y_o^{\,2}}{z}\right]\right\} \\ \tilde{u}(x,y,z) &= \frac{\hat{\imath}}{\lambda z}\sqrt{\frac{2}{\pi}}\frac{1}{w_o}\left\langle\Im\left\{\Im^{-1}\left[\exp\left(-\frac{x_o^2}{w_o^2}\right)\right]\cdot\Im^{-1}\left[\exp\left(-\hat{\imath}\frac{\pi}{\lambda}\frac{x_o^{\,2}}{z}\right)\right]\right\}\right\rangle\cdot \\ &\qquad\left\langle\Im\left\{\Im^{-1}\left[\exp\left(-\frac{y_o^2}{w_o^2}\right)\right]\cdot\Im^{-1}\left[\exp\left(-\hat{\imath}\frac{\pi}{\lambda}\frac{y_o^{\,2}}{z}\right)\right]\right\}\right\rangle\end{aligned} \tag{F.28}$$

where I made use of the convolution theorem in going from the third expression to the fourth expression [131]. Evaluating Eq. F.28 we find that the BSMI Gaussian field distribution at z_o=0 – i.e. the field distribution at the beam waist – evolves into the following BSMI Gaussian field distribution upon propagation to an arbitrary z-plane,

$$\tilde{u}(x,y,z) = \sqrt{\frac{2}{\pi}}\frac{1}{w_o\left[1-\hat{\imath}\left(z/z_R\right)\right]}\exp\left[-\hat{\imath}\Phi(z)\right]\exp\left[-\frac{x^2+y^2}{w(z)^2}\right] \tag{F.29}$$

where,

$$\Phi(z) = \frac{\pi}{\lambda}\frac{\left(x^2+y^2\right)}{R(z)}. \tag{F.30}$$

The beam radius $w(z)$ in Eq. F.29 evolves according to Eq. F.26 and the radius of curvature $R(z)$ in Eq. F.30 evolves according to Eq. F.25.

Solving the convolution integral in Eq. F.28 is by no means trivial and you may be asking yourself why I went to the trouble. After all, the complex scalar wave amplitude described by Eqs. F.23 and F.24 (i.e. the Gaussian spherical wave solution) is *identical* to the complex scalar wave amplitude derived from the Huygens-Fresnel integral and described by Eqs. F.29 and F.30. Solving the Huygens-Fresnel integral for the unimpeded propagation of a BSMI Gaussian beam could be considered big waste of time – The problem has already been well studied and the solution is well known. My intention in the analysis above, however, was to simply demonstrate one possible approach for evaluating the integral. The Huygens-Fresnel integral does after all have utility.

The Huygens-Fresnel integral can be used to mathematically represent the wavefront propagation of any laser beam. It is particularly well suited for analyzing the effects of aperture truncation and higher-order spatial modes on the propagation (and transformation) of a laser beam. For instance, assume that a BSMI Gaussian beam is truncated by a circular aperture of radius R_A at its waist. We can determine the effect of this aperture truncation on the propagating wavefront by numerically solving the following Huygens-Fresnel integral (I know of no analytic solution to the integral in Eq. F.31):

$$\tilde{u}(x, y, z) = \frac{\hat{\imath}}{\lambda z}\sqrt{\frac{2}{\pi}}\frac{1}{w_o}\int_{r_o=0}^{R_A} \exp\left(-\frac{r_o^2}{w_o^2}\right)\exp\left[-\hat{\imath}\frac{\pi}{\lambda}\frac{(r-r_o)^2}{z}\right]\mathrm{d}r_o \tag{F.31}$$

As mentioned in sub-section 4.3.3, most optical ray-tracing programs offer a fast and effective means of analyzing the effects of aperture truncation on a propagating BSMI Gaussian beam. The Zemax ray-tracing program, for instance, simulates diffraction by numerically solving Huygens integral. One need only define a Gaussian input field, an optical arrangement that realistically represents the optical design under investigation, and an image plane for Zemax to effectively calculate the diffraction limited spot size on the image plane. In other words, we appear to have reached a point in our plug-and play world where the mathematical details of single-mode Gaussian beam are superfluous.

This may be the case, but I have found that most semiconductor diode laser classified as "single-mode" in fact exhibit multiple spatial modes (particularly along the fast optical axis of the output beam) and that the Huygens-Fresnel integral can be a handy tool for evaluating the diffraction behavior of these multi-spatial-mode laser beams. For instance, consider the spatial intensity profiles in Figure F.3 measured along the slow and fast optical axes of the collimated Littrow laser beam. I had initially assumed that the Littrow laser beam was single-mode when designing the coupling optics for the master oscillator power amplifier (MOPA) laser system, and had configured the preliminary MOPA laser system with the fast optical axis of the PA (i.e. the broad area laser (BAL)) aligned to the fast optical axis of the MO (i.e. the Littrow laser). This was a bad choice. Referring to Figure F.3, we see that the spatial intensity profile along the slow optical axis of the Littrow laser beam is relative Gaussian whereas the fast optical axis clearly contains multiple spatial modes. I was now faced with a difficult decision: Do I try to focus the non-diffraction limited fast optical axis of the Littrow laser beam to the O(2μm) beam waist radius required for efficient coupling along the fast optical axis of the BAL or do I redesign the MOPA laser system such that the slow optical axis of the Littrow laser beam is aligned with the fast optical axis of the BAL? Based on intuition I felt that focusing a non-diffraction-limited beam to an O(2μm) waist radius was impossible, but faced with a relatively complicated redesign of the MOPA coupling optics I decided to pursue a conclusive answer. Unaware of any commercially available software with higher-spatial-mode modeling capabilities, I began studying laser beam propagation and transformation intent on finding a way to mathematically represent the diffraction behavior of multi-mode laser beams.

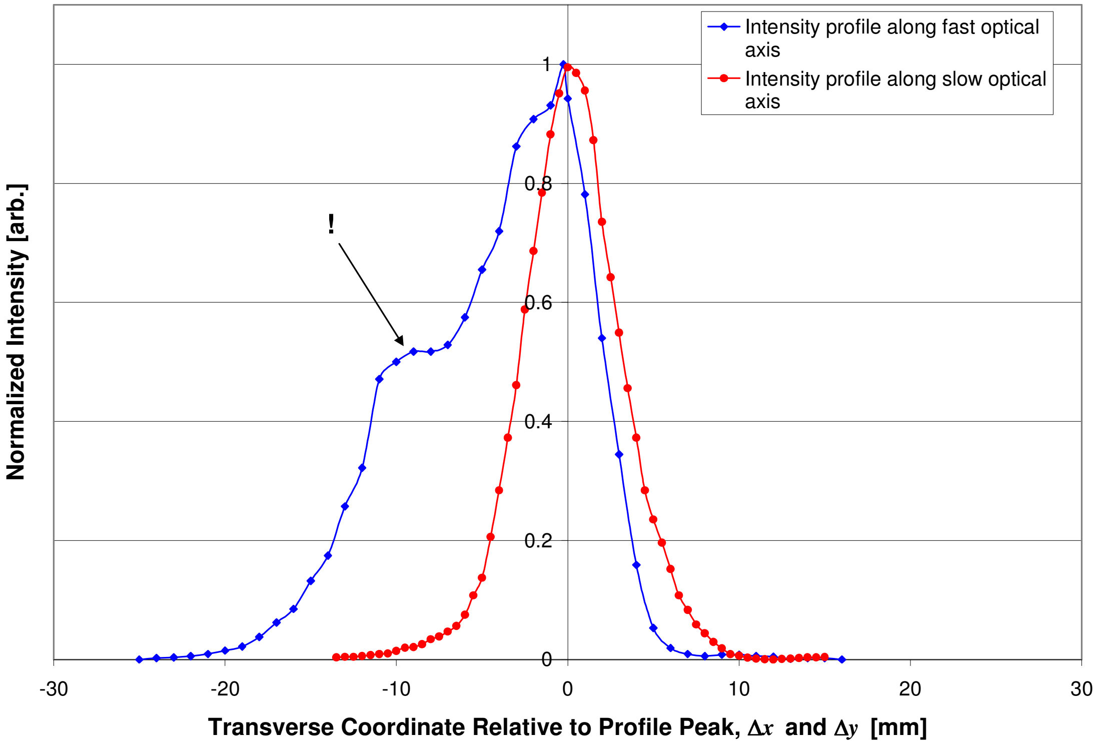

Figure F.3 Spatial intensity profiles measured along the slow and fast optical axes of the collimated Littrow laser beam

The Huygens-Fresnel integral provides a straight-forward means of calculating the diffraction behavior of higher-order spatial modes. These higher-order spatial modes are generally modeled by Hermite-Gaussian functions [3, pp. 642-648, 685-697],

$$\tilde{u}_n(x,z)=\left(\frac{2}{\pi}\right)^{1/4}\left(\frac{1}{2^n n! w_o}\right)^{1/2}\left[\frac{\tilde{q}_o}{\tilde{q}(z)}\right]^{1/2}\left[\frac{\tilde{q}_o}{\tilde{q}_o^{*}}\frac{\tilde{q}(z)^{*}}{\tilde{q}(z)}\right]^{n/2} H_n\left(\frac{\sqrt{2}x}{w(z)}\right)\exp\left[-\hat{\imath}\frac{\pi}{\lambda}\frac{x^2}{\tilde{q}(z)}\right], \qquad \text{(F.32)}$$

where n is the spatial mode order and H_n is the Hermite polynomial of order n,

$$H_{n+1}(x)=2xH_n(x)-2nH_{n-1}(x);H_o(x)=1,H_1(x)=2x\,. \qquad \text{(F.33)}$$

The Hermite-Gaussian functions in Eq. F.32 are orthonormal – e.g. $\int_{-\infty}^{\infty} \tilde{u}_\alpha(x,z)^* \tilde{u}_\beta(x,z)\mathrm{d}x = \delta_{\alpha\beta}$ – and therefore provide a complete basis set; i.e. the field distribution of any arbitrary optical beam $\tilde{u}(x,y,z)$ can be expanded in the form,

$$\tilde{u}(x,y,z) = \sum_n \sum_m c_{nm} \tilde{u}_n(x,z) \tilde{u}_m(y,z) \tag{F.34}$$

where $\tilde{u}_n(x,z)$ and $\tilde{u}_m(y,z)$ are the orthonormal Hermite-Gaussian functions defined along two orthogonal transverse coordinates according to Eq. F.32. The Hermite-Gaussian functions are also the closest approximation to the actual higher-order modes of finite-mirror stable resonator and have the same normalized shape as they propagate [3]; i.e. they change in transverse scale like $w(z)$ and acquire spherical wavefront curvature $R(z)$ but their amplitude profiles remain unchanged in shape.

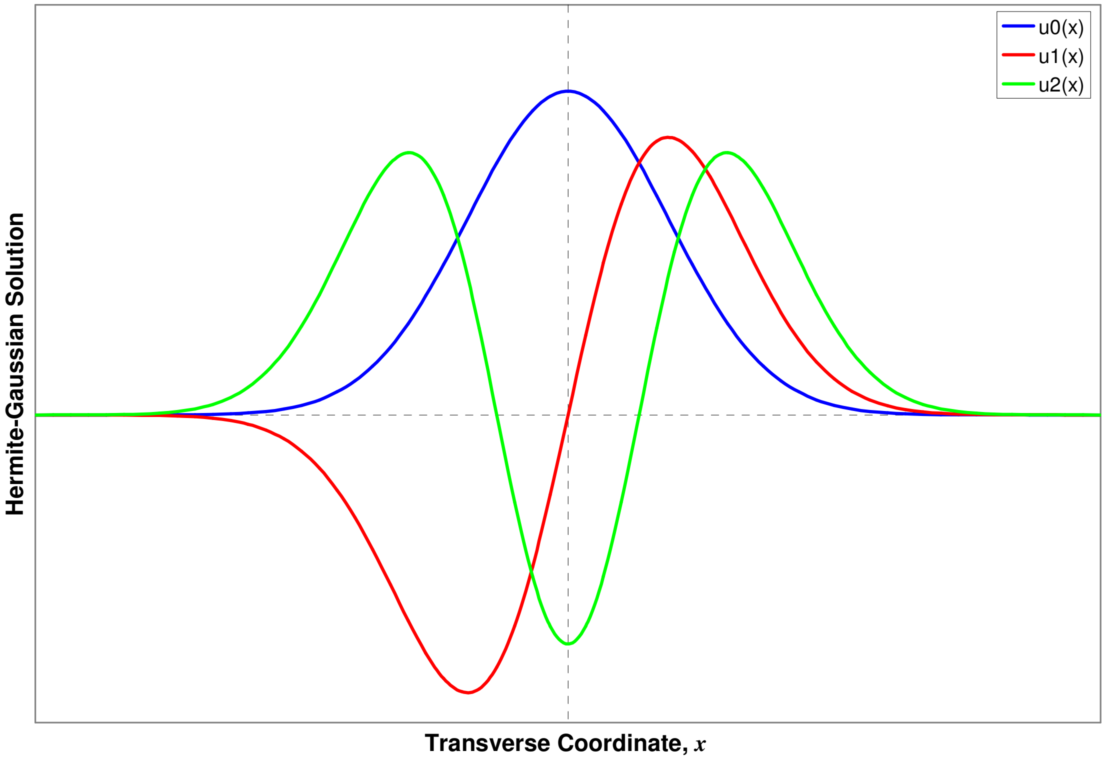

Figure F.4 The lowest-, first-, and second-order Hermite-Gaussian functions

Referring to Figure F.4 illustrating the lowest-, first-, and second-order Hermite Gaussian functions and noting that $I(x,z) \propto |u(x,z)|^2$ we might logically conclude that the spatial intensity profile in Figure F.3 measured along the fast optical axis of the collimated Littrow laser beam at the very least contains the lowest-, first-, and second-order transverse spatial modes,

$$I(x,z) \propto \left|\tilde{u}(x,z)\right|^2 ; \tilde{u}(x,z) = c_0 u_0(x,z) + c_1 u_1(x,z) + c_2 u_2(x,z) \tag{F.35}$$

where for a "collimated" beam (i.e. corresponding to $R(z_o)=\infty$ for all spatial modes),

$$\tilde{u}_0(x,z) = \left(\frac{2}{\pi}\right)^{1/4} \left(\frac{1}{w_o}\right)^{1/2} \exp\left[-\frac{x^2}{w_o^2}\right] \tag{F.36a}$$

$$\tilde{u}_1(x,z) = \left(\frac{2}{\pi}\right)^{1/4} \left(\frac{1}{2w_o}\right)^{1/2} \left(\frac{2\sqrt{2}x}{w_o}\right) \exp\left[-\frac{x^2}{w_o^2}\right] \tag{F.36b}$$

$$\tilde{u}_2(x,z) = \left(\frac{2}{\pi}\right)^{1/4} \left(\frac{1}{8w_o}\right)^{1/2} \left(\frac{8x^2}{w_o^2} - 2\right) \exp\left[-\frac{x^2}{w_o^2}\right] \tag{F.36c}$$

This is in fact how I modeled the field distribution along the fast optical axis of the Littrow laser output. Defining c_0, c_1, c_2, and w_o as floating parameters, I was able to obtain a relatively good fit between the measured intensity profile and the modeled intensity profile. Using the Huygens-Fresnel integral, I was then able to calculate the smallest theoretical beam waist possible with the modeled field distribution and to conclusively show that focusing the fast optical axis of the Littrow laser output to an O(2 μm) beam waist was impossible, at least with commercially available optics. (The calculation assumed that the "collimated" beam waist of the Littrow laser coincided with and filled a ϕ=8 mm diameter, f= 6.5 mm focal length, $F_\#$=0.813 focusing lens (e.g. the Melles Griot 06GLC001 focusing optic), that the focusing lens was diffraction limited and infinitesimally thin, and that aperture truncation was negligible).

We will now turn our attention to a paraxial, thin-lens theory describing Gaussian beam transformation. I used the results of this simple theory extensively while designing the optical system used to couple the Littrow laser output beam into the BAL junction. Although the MOPA coupling optics were ultimately analyzed using Zemax, the paraxial, thin-lens theory of Gaussian beam transformation helped me to develop a starting point for all designs; i.e. like Huygens' Principle, the paraxial, thin-lens theory of Gaussian beam transformation described in the next sub-section provided invaluable insight into the design of the MOPA laser system.

F.2 Thin-Lens, Paraxial Theory of Gaussian Beam Transformation

The lowest order spatial mode supported by an optical resonator is the basic spatial mode ideal (BSMI) Gaussian mode. A BSMI Gaussian beam in free space diverges from or converges to a region where the beam diameter is a minimum, called the beam waist. This is the result of diffraction, and is mathematically represented by the following set of equations derived in the previous sub-section from the perspective of the Gaussian spherical wave solution and repeated here for convenience [3]:

$$w(z)=w_o\left[1+\left(\frac{\lambda z}{\pi w_o^2}\right)^2\right]^{1/2} \tag{F.37a}$$

$$R(z)=z\left[1+\left(\frac{\pi w_o^2}{\lambda z}\right)^2\right] \tag{F.37b}$$

Eq. F.37 describes the evolution of a BSMI Gaussian beam in free space that is propagating in the z-direction. $w(z)$ represents the variation of the beam radius a distance z from the beam waist, w_o is the $1/e^2$ beam radius at the beam waist, λ is the wavelength of the beam, and $R(z)$ represents the variation of the wavefront radius of curvature a distance z from the beam waist. The extent of the waist region is characterized by the Rayleigh range, z_R,

$$z_R=\frac{\pi w_o^2}{\lambda}. \tag{F.38}$$

At a distance $z= z_R$ from the beam waist the beam radius is,

$$w(z_R)=\sqrt{2}w_o \tag{F.39}$$

and the wavefront radius of curvature, $R(z)$, is a minimum. Note that $z_R \propto w_o^2$; i.e. a long Rayleigh range is associated with a large beam waist. The extent of the beam divergence (convergence) is measured with a half-angle beam divergence, θ, which is the half-angle subtended by the $1/e^2$ radius from the beam axis in the far-field (i.e. when $z >> z_R$), as shown in Figure F.5:

$$\left.\begin{aligned} w(z>>z_R)&\cong\frac{\lambda z}{\pi w_o}\\ \theta&\cong\frac{w(z>>z_R)}{z}(\text{paraxial limit})\end{aligned}\right\}\Rightarrow\theta\approx\frac{\lambda}{\pi w_o}. \tag{F.40}$$

Notice from Eq. F.40 that for a given beam wavelength the product $w_o\theta$ is constant. This has two implications: For a small focused spot size the divergence must be large (e.g. a fast optic must be used) and for a highly collimated beam (i.e. small θ) the beam waist must be large (e.g. this is the primary motivation for commercial beam expanders).

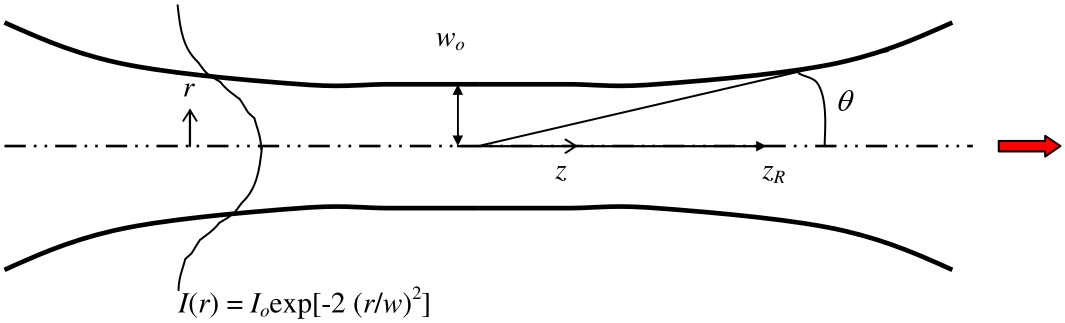

Figure F.5 Parameters defining the free space propagation of a BSMI Gaussian beam

A paraxial, thin-lens theory describing the transformation of a BSMI Gaussian beam by refractive components can be derived from the previous conclusions concerning the free space propagation of Gaussian beams by referring to the lensmakers' equation from geometrical optics,

$$\frac{1}{s_o} + \frac{1}{s_i'} = \frac{1}{f}\,. \tag{F.41}$$

The physical implication of Eq. F.41 is that a thin, spherical lens of focal length f introduces a change in the wavefront radius of curvature from the input to the output side of the lens according to the following formula [138]:

$$\frac{1}{R} - \frac{1}{R'} = \frac{1}{f} \Rightarrow \frac{1}{R'} = \frac{1}{R} - \frac{1}{f}\,. \tag{F.42}$$

This is represented pictorially in Figure F.6. (This little insight is indispensable. For instance, it is the key to modeling the transformation of any laser beam by a relatively thin optical element from the perspective of Huygens' Principle). Note that a prime was used to differentiate the output side from the input side of the refractive element. This convention will be adopted in the following discussion. In addition, when propagating a Gaussian beam through an optical system, all distances are measured from the waist location, as shown in Figure F.7.

Combining Eq.s F.37, F.40, and F.42, and noting that for a thin lens $w(s_o)=w'(-s_i')=w'(s_i')$, the following thin-lens, paraxial equations describing the transformation of a BSMI Gaussian beam by a refractive element of focal length f can be derived:

$$m=\frac{w_o'}{w_o}=\frac{|f|}{\left[(s_o-f)^2+z_R^2\right]^{1/2}} \tag{F.43a}$$

$$z_R'=m^2 z_R \tag{F.43b}$$

$$s_i'=f+m^2(s_o-f) \tag{F.43c}$$

Referring to Figure F.7 we see that m is the ratio of the waist radius on the output side of the refractive element, w_o', to the waist radius on the input side, w_o (i.e. m is the magnification), s_o is the distance from the beam waist on the input side to the refractive element, z_R is the Rayleigh range on the input side, z_R' is the Rayleigh range on the output side, and s_i' is the distance from the refractive element to the beam waist on the output side.

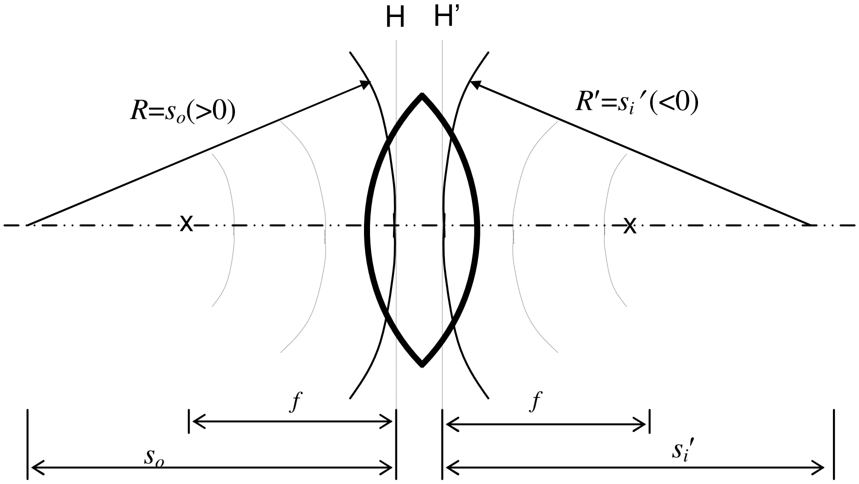

Figure F.6 Illustrating the thin-lens formula from geometric optics

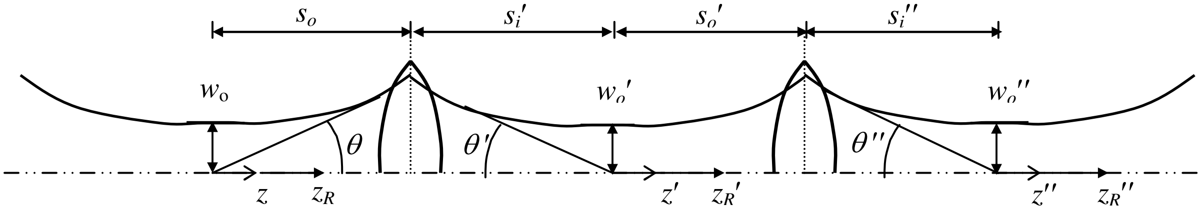

Figure F.7 Nomenclature used in thin-lens, paraxial calculations with Gaussian beams

As mentioned in the previous sub-section, the spatial intensity profile of a real laser beam generally deviates from Gaussian. From the perspective of the thin-lens, paraxial theory of Gaussian beams this deviation is accounted for by a parameter called the *M*-square (M^{2}); Semiconductor diode lasers advertised as single-mode generally have an M^2 of 1.1-1.7 [139]. The M^{2} accounts for the fact that higher-order spatial modes effectively increase the beam divergence and decrease the Rayleigh range of real laser beams,

$$\theta = M^{2}\frac{\lambda}{\pi w_{o}} \Rightarrow z_{R} = \frac{\pi w_{o}^{2}}{M^{2}\lambda}. \tag{F.44}$$

The M^{2} is an observational parameter that effectively quantifies the focal shift and increased focused spot size of a real laser beam relative to the calculated focal position and focused spot size of a BSMI Gaussian beam [139]. This can be seen by incorporating the M^{2} of real laser beams into the transformation equations in Eqs. F.43a-c,

$$m = \frac{w_{o}'}{w_{o}} = \frac{\left(\frac{M^{2}\,'}{M^{2}}\right)\left|f\right|}{\left\{\left(s_{o}-f\right)^{2} + z_{R}^{2} + \left[\left(\frac{M^{2}\,'}{M^{2}}\right)^{2} - 1\right]\frac{z_{R}}{\left(s_{o}^{2}+z_{R}^{2}\right)}\right\}^{1/2}} \tag{F.45a}$$

$$z_{R}' = m^{2} z_{R} \tag{F.45b}$$

$$\frac{1}{s_{o} + \frac{z_{R}^{2}}{\left(s_{o}-f\right)}} + \frac{1}{s_{i}} - \frac{\left[\left(\frac{M^{2}\,'}{M^{2}}\right)^{2} - 1\right]\left(\frac{z_{R}^{2}}{f}\right)}{\left(s_{o}^{2}+z_{R}^{2}\right)\left(s_{o}^{2} - s_{o}f + z_{R}\right)} = \frac{1}{f} \tag{F.45c}$$

where z_R follows from Eq. F.44. $M^{2}\,' \neq M^{2}$ accounts for the fact that beam truncation through a lens (or iris) effectively increase the *M*-square factor [140]. Aperture truncation can have a non-negligible effect when the ratio of the aperture radius to the beam radius is less than $R_A/w < 2.2$ [3].

Appendix G: Development of the Coupling Optics for the BAL MOPA System

The coupling optics for all revisions of the broad area laser master oscillator power amplifier (BAL MOPA) system were chosen based on three design criteria: Focusing the input beam along the fast optical axis of the BAL to a beam waist that just fills BAL junction height; focusing the input beam along the slow optical axis of the BAL to a beam waist that underfills the BAL junction width; and focusing the input beam along the slow optical axis of the BAL at a slight angle, θ, to the BAL front facet normal (in a plane parallel to the junction width). It has been shown that the coupling efficiency is maximized when $\theta \approx 3°–5°$, and when the full width at half maximum (FWHM) of the spatial intensity profile along the slow optical axis of the focused input beam is approximately half the stripe width, $\frac{1}{2}w_{\|}$, as shown in Figure G.1. Basically, the BAL junction is more uniformly filled by the double passing beam when the input beam is focused at an angle onto half of the BAL junction. This helps suppress ASE, decreases the effects of thermal lensing and filamentation, and results in a narrower (near diffraction limited) lobe in the far-field of the amplified output [121, 123, 129]. Appreciable side-lobes and ASE are then only observed when the BAL is operated at relatively high injection currents. In addition, focusing into the BAL at an angle allows the amplified output from the BAL to be spatially segregated from the input beam.

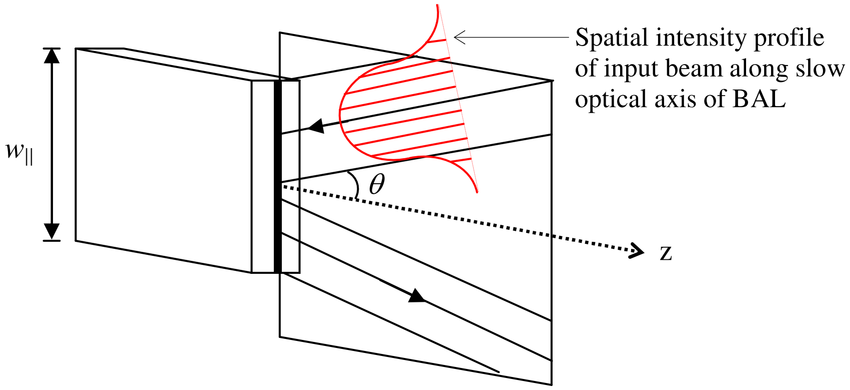

Figure G.1 An illustration of efficient coupling

I chose the coupling optics for the preliminary BAL MOPA system using the thin-lens, paraxial theory of Gaussian beam transformation that is discussed in the Appendix F. A beam waist was assumed to reside on the front facet of the MO diode. The waist radius on the front facet was calculated along both the fast optical axis (perpendicular to the diode junction) and the slow optical axis (parallel to the diode junction) by assuming that the output beam diverges from the front facet at the angles specified by the laser vendor with a spatial intensity profile that deviates only slightly from Gaussian. This deviation was accounted for by assuming an M-square of M^2 = 1.1-1.7:

$$\begin{aligned} w_o\big|_f &= {M^2\lambda}\big/{\pi\theta_\perp} \\ w_o\big|_s &= {M^2\lambda}\big/{\pi\theta_\parallel} \end{aligned} \tag{G.1}$$

$\theta_\perp \approx 13.5°$ and $\theta_\parallel \approx 9°$are the half angle divergences specified by the laser vendor along the fast optical axis and the slow optical axis, respectively, and the centerline wavelength of the MO is λ=780 nm.

The output beam from the MO diode is collimated by an f=11 mm focal length, $F_\#$=2 collimation optic, L_1, in the Littrow cavity. Having calculated the waist radius of the output beam with Eq G.1, and assuming that L_1 is positioned for far-field collimation (i.e. s_o=f), I then applied the thin-lens, paraxial theory discussed in Appendix F to determine the transformation imposed on the output beam by L_1. The coupling optics for the preliminary BAL MOPA system were chosen based on this calculated collimated output beam. Based on thin-lens, paraxial calculations, the coupling optics shown in Figure G.2 provide a final focused 1/e^2 waist radius along the slow and fast optical axes of the BAL of $w_o|_s''''$=20 - 38 μm and $w_o|_f''''$=2 - 3.4 μm, respectively, for an M^2 = 1.1-1.7.

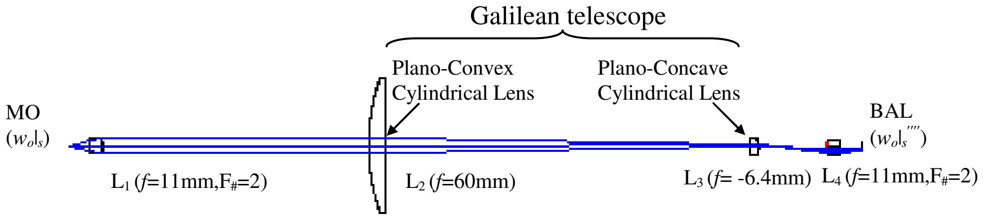

(a) Slow optical axis of BAL

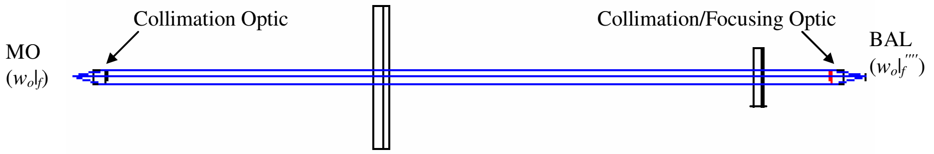

(b) Fast optical axis of BAL

Figure G.2 Optical system for preliminary BAL MOPA system

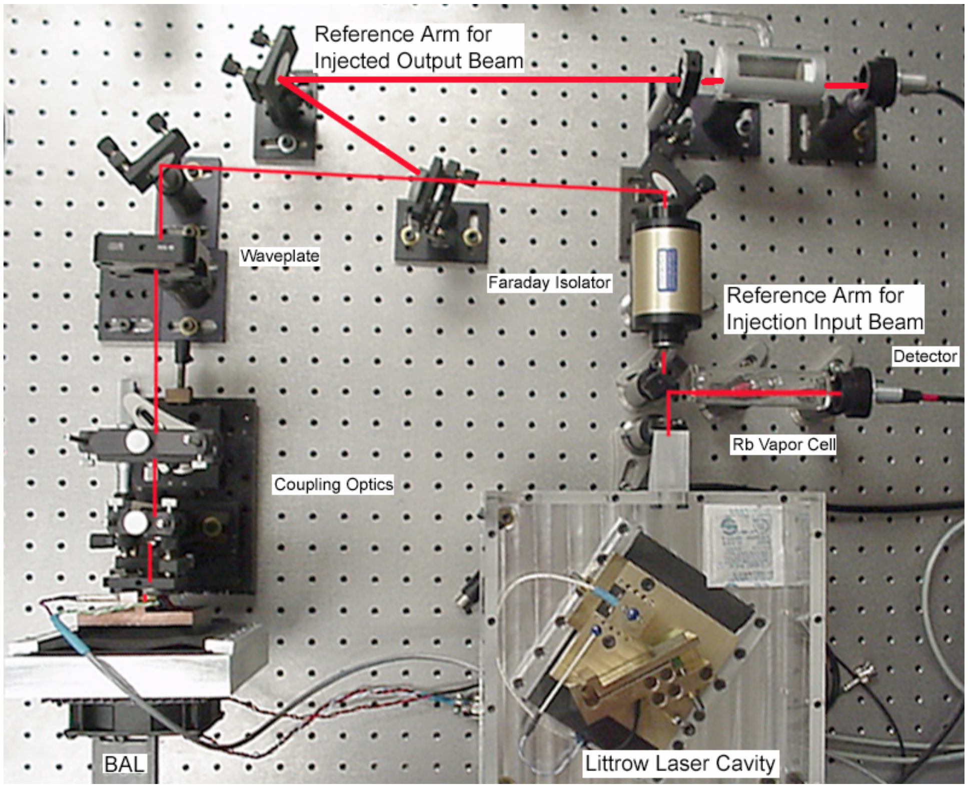

Figure G.3 The preliminary BAL MOPA system

Figure G.3 is a picture of the preliminary BAL MOPA system. A small portion (<1%) of the Littrow output is split off to a reference arm, and passes through a Rb vapor cell before being recorded by a Si photodiode (Thorlabs DET110); The reference arm enables us to tune the Littrow cavity to the D_2-line of Rb. A Faraday isolator (Optics for Research IO-5C-780-VLP-Z) provides 42 dB of isolation between the Littrow laser and the BAL. After passing through the isolator, the collimated Littrow laser beam is guided through a λ/2-wave plate and the three coupling optics shown in Figure G.2 – an f=60 mm positive cylindrical lens, an f=–6.4 mm negative cylindrical lens, and an f=11 mm aspheric collimation optic (Melles Griot 01LCP005/077, 01LCN000/077, and Thorlabs 350220-B, respectively) – which focus the collimated input beam into the BAL junction. An injection angle is introduced by translating the positive cylindrical lens, L_2, along the slow optical axis of the BAL (i.e. out of the picture). The BAL is mounted to a Cu cold plate, which is mounted to a 30 W thermoelectric cooler (TEC) (Marlow Industries ST3353). A spectroscopic grade temperature controller (ILX Lightwave LDT-5910B) provides temperature control to the TEC based on a signal from a 10 K NTC thermistor (Omega 44006). A 5 A low-noise current controller (Wavelength Electronics PLD5000) provides power to the BAL. A portion of the injected output is picked off by an Al mirror, transmitted through a Rb cell, and detected by a Si photodiode (Thorlabs DET110).

I was unable to demonstrate amplification with this preliminary BAL MOPA system. I lost nearly 80% of the 12 mW of optical power output from the Littrow laser to the optical system. 34% of the power was lost to the rotator – 13% to losses within the isolator and 21% to beam truncation along the fast optical axis. I also used four Al mirrors in the preliminary setup, which have a reflectance of only 75-80% at 780 nm. Aperture truncation through the final focusing/collimating optic, L_4 (with a diameter of ϕ_4=5.5mm), resulted in a loss of ~13%. Finally, we lost a few percent to all the AR-coated optics. With a measured input power in the final focused spot of P_i ~2.6 mW I was only able to demonstrate an (un)amplified output power of P_o~1.2 mW from the BAL when operated at an injection current of I=497 mA, just above the threshold current (I_{th}=377 mA). Above I~500 mA ASE began to dominate.

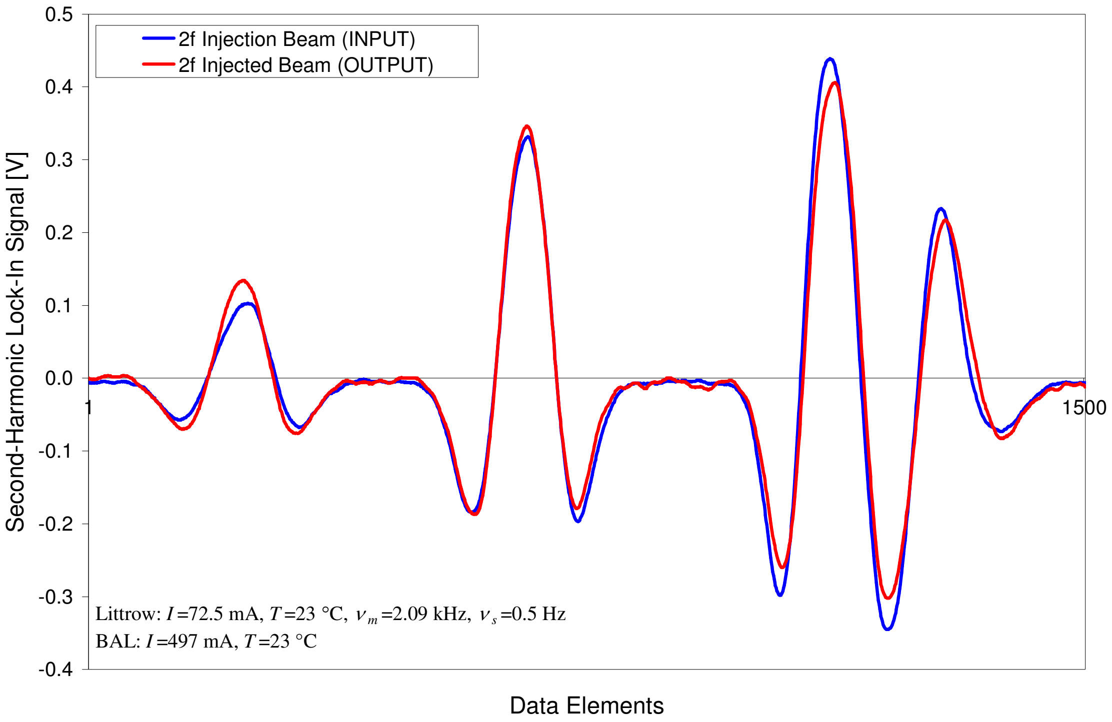

*Figure G.4 **2f**-profiles acquired by direct modulated absorption of the input beam (i.e. Littrow output beam) and (un)amplified BAL output beam*

I was able to demonstrate that the (un)amplified output from the BAL tracked the spectral characteristics of the Littrow laser. Figure G.4 shows a ***2f***-profile acquired by direct modulated absorption of the input beam (i.e. the output beam from the Littrow laser cavity) and a ***2f***-profile acquired by direct modulated absorption of the output beam from the preliminary BAL MOPA system. The modulation frequency was ν_m=2.09 kHz, the sweep frequency was ν_s=0.5 Hz, and the time constant of both lock-in amplifiers was τ_L=3 ms. The BAL was operated at a constant injection current of 497 mA; sweep and modulation of the injected input frequency were imposed by sweeping and modulating of the Littrow laser frequency. Figure G.4 clearly demonstrates that the injected output is tracking the spectral performance of the Littrow laser. The BAL used in the MOPA laser system has a quoted spectral width of 2 nm, or approximately 1 THz. This is more than three orders-of-magnitude broader than the spectral width of the Doppler broadened multiplets in the D_2-line of Rb; the multi-mode spectral output from the BAL would not be able to resolve the absorption features of the D_2-line. Differences in the profiles are likely the result of power fluctuations in the output beam from the BAL, which our ratioed detection scheme would compensate for. The asymmetries in the ***2f***-profile acquired using the BAL output may be the result of residual amplitude modulation (RAM).

There are two ways to get more power from a BAL amplifier: To increase the power injected into the junction or to increase the current across the junction. With the preliminary MOPA system, increasing the injection current to the BAL simply resulted in increased ASE. The dominance of ASE at relatively low injection currents implied that I was not effectively coupling the input beam into the BAL junction; i.e. ASE should be suppressed when the injected input fills that BAL junction. I therefore turned my attention to improving the efficiency with which the input beam was coupled into the BAL junction.

The thin-lens, paraxial theory that I used to select the coupling optics for the preliminary BAL MOPA system neglects the effects of beam truncation on the focused waist radius. Beam truncation through an aperture effectively increases the M^2 of a laser beam, and can have non-negligible effects when the ratio of the aperture radius to the $1/e^2$ beam radius $r/w(z)<2.2$ [3]. The truncation along the slow optical axis of the preliminary BAL MOPA system was weak and did not have an appreciable effect on the final slow axis waist radius, $w_o|_s''''$. However, the truncation along the fast optical axis was strong; I lost 21% of the optical power output from the Littrow laser to fast axis truncation by the isolator apertures and ~13% to fast axis truncation by the final focusing/collimating optic, L_4 (ϕ_4=5.5mm). This strong beam truncation results in an increase in the M^2 along the fast optical axis, which effectively increases the final focused beam waist along the fast optical axis. Since I needed to focus to a final fast axis waist radius of $w_o|_f^{''''}$~2μm I decided to investigate how the observed fast axis beam truncation specifically affected the final fast axis waist.

There are some analytical expressions available that account for weak beam truncation [140], but none that I know of that account for strong beam truncation. I spent some time trying to formulate an analytical expression based on Huygens' principle to account for strong beam truncation, and eventually derived a Huygens-Fresnel integral expression that I felt would model the effects of aperture truncation. I was able to derive the thin-lens, paraxial theory of Gaussian beam transformation from my integral formulation, but I could not analytically solve the convolutions required to account for aperture truncation. For instance, the x-axis field distribution of a basic spatial mode ideal (BSMI) Gaussian beam propagating in the z-direction evolves according to the following integral if the beam is truncated along its x-axis by a rectangular aperture $2R$-wide at its waist,

$$E(x,z)=\sqrt{\frac{\hat{i}}{\lambda z}}\left(\frac{2}{\pi}\right)^{1/4}\frac{1}{\sqrt{w_o}}\int_{-\infty}^{\infty}\mathrm{rect}\left(\frac{x_o}{2R}\right)\exp\left[-\left(\frac{x_o}{w_o}\right)^2\right]\exp\left[-\hat{i}\,\frac{\pi}{\lambda z}(x-x_o)^2\right]dx_o \tag{G.2}$$

where w_o is the beam waist radius. Eq. G.2 follows from the discussion in Appendix F.

Fortunately, optical ray-tracing programs numerically solve the required convolutions. I therefore ran a simulation in Zemax to determine the effect the fast axis beam truncation had on the final fast axis waist radius. The optics used in our preliminary BAL MOPA system were positioned to realistically reflect system performance, and the simulation assumed a Gaussian spatial intensity profile from the MO. The final focused spot size predicted by Zemax without aperture truncation was practically identical to the final focused spot size predicted by the thin-lens, paraxial theory used to design the preliminary BAL MOPA system. Apertures were then inserted into the simulation to realistically represent beam truncation in the preliminary MOPA system. Inserting the apertures did not affect the final focused spot size along the slow optical axis, but did affect the final focused spot size along the fast optical axis.

Figure G.5 shows the fraction of encircled energy in the final focused fast axis (x-axis) waist as a function of distance from its optical axis. From it I inferred that, as a result of fast axis aperture truncation in our preliminary MOPA system, the final focused spot grossly overfilled the BAL perpendicular to its junction (i.e. the BAL junction height, $h_{\perp}|_{\mathrm{BAL}}$). I modified the optical design of the preliminary BAL MOPA system to avoid beam truncation along the fast optical axis and to achieve a smaller fast axis waist at the front facet of the BAL. Aperture truncation through the isolator was prevented with a pair of Galilean telescopes on the fast optical axis. An *f*=60 mm focal length positive cylindrical lens (Melles Griot 01LCP021) and an *f*=–19 mm negative cylindrical lens (Melles Griot 01LCN002) were configured as a Galilean telescope to compress the fast axis for passage through the isolator. An *f*=–25.4 mm negative cylindrical lens (Melles Griot 01LCN003) and an *f*=60 mm positive cylindrical lens (Melles Griot 01LCP021) were configured as a Galilean telescope to re-expand the fast axis after passage through the isolator. Note that due to the difference in the negative cylindrical lenses, the waist radius along the fast optical axis is minified after passage through the pair of Galilean telescopes ($M \approx 19/25.4$). The fast axis was intentionally minified to minimize fast axis beam truncation through the final focusing/collimating optic, L_4.

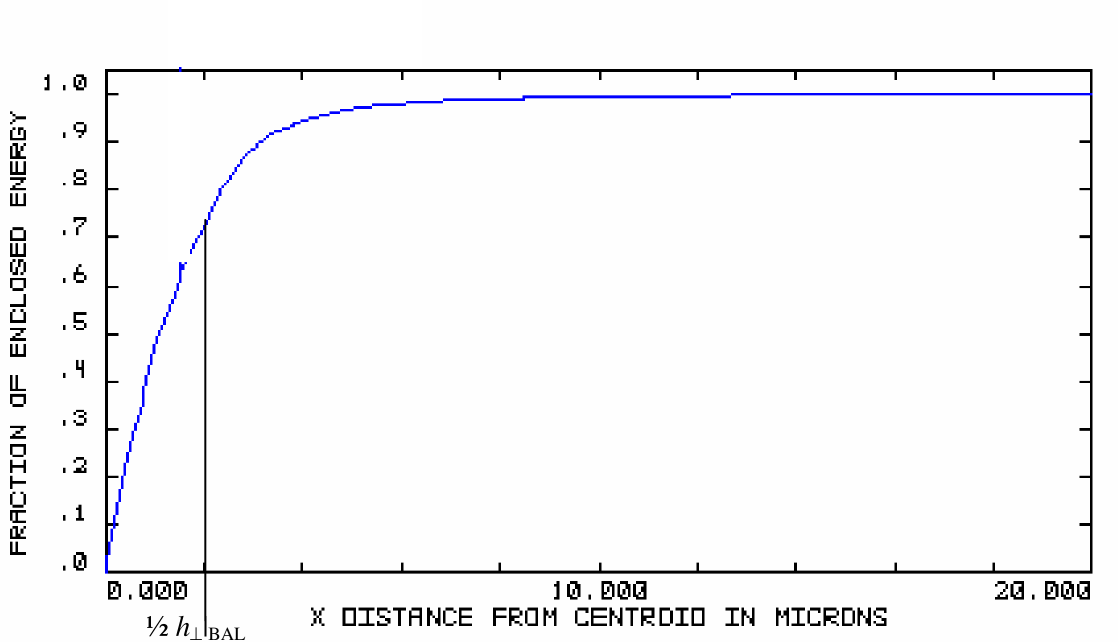

Figure G.5 Huygens' diffraction fast axis (x-axis) encircled energy calculated using a Zemax simulation of the preliminary MOPA system

I also replaced the final focusing/collimating optic in our preliminary BAL MOPA system, L_4, with a faster *f*=8 mm, $F_\#=1$ focusing/collimating optic (Melles Griot 06GLC002). The *f*=60 mm plano-convex cylindrical lens in the preliminary BAL MOPA system, L_2, was replaced with an *f*=150 mm plano-convex cylindrical lens (Melles Griot 01LCP013) to accommodate this change to L_4. Selection of the appropriate replacement was made with reference to the thin lens, paraxial theory of Gaussian beam transformation since this lens affects a change along the slow optical axis and weak beam truncation along the slow optical axis was determined to be negligible. This optical design was checked with Zemax, which predicted a final focused waist radius along the slow optical axis of the BAL of ~16μm, with 100% of the power along the slow optical axis enclosed within 20 μm from the slow axis centroid. Zemax also predicted a final focused beam waist radius along the fast optical axis of ~2 μm, as shown in Figure G.6. Having effectively removed the fast axis beam truncation and by using an $F_{\#}$=1 focusing/collimating optic, Zemax predicted that approximately 90% of the power in the input beam was being coupled into the BAL junction.

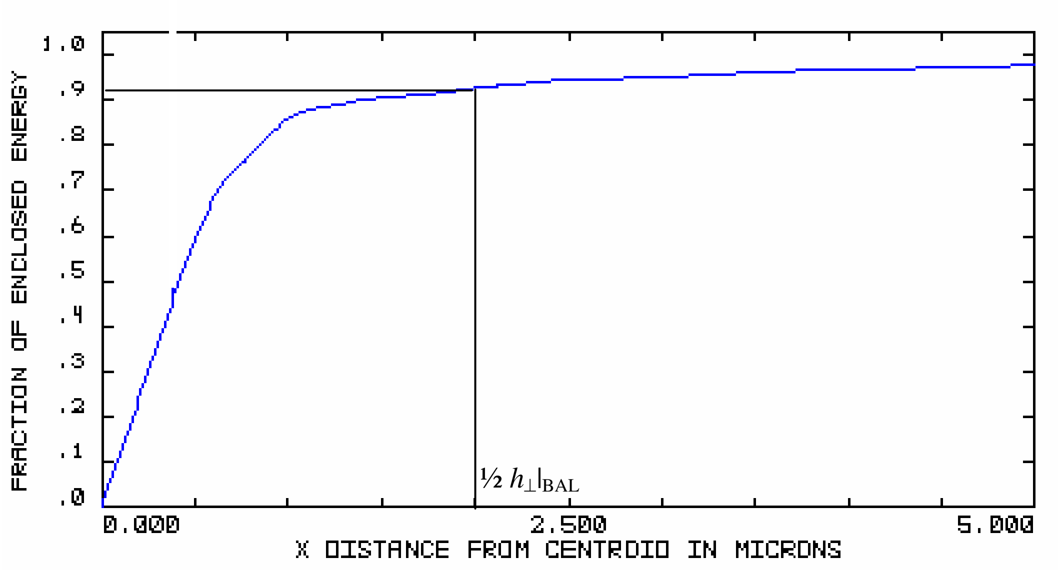

Figure G.6 Fast axis (x-axis) encircled energy for redesigned BAL MOPA system

I was able to demonstrate amplification with the redesigned BAL MOPA system. By avoiding beam truncation through the isolator apertures and L_4, and having replaced the four Al mirrors previously used with a gold mirror, a silver mirror, and two dielectric mirrors, I reduced the losses in the optical system by 50%. With a measured power in the final focused spot of P_i ~ 7 mW, I was able to demonstrate 6 dB of amplification. The greatest amplification was observed when operating the BAL slightly above threshold, at an injection current of I~500 mA. When the injection current to the BAL was increases above I~600 mA, the power in the amplified output began to drop and ASE began to dominate. At these injection currents I also noticed a slight temperature dependence to the amplified output power: The amplified output power was a maximum (by ~ 1 mW) at BAL temperature intervals of ~0.5°C. I attributed this behavior to the minimal residual front facet reflectivity of the BAL. There was no observed dependence of the amplified output power on injection angle, and the amplified output was again observed to track the spectral characteristics of the Littrow laser cavity.

Though amplification was demonstrated with the redesigned BAL MOPA system, I was still a long way from the hoped for 15-20 dB of small-signal gain. The designs for both optical systems utilized up to this point to couple the Littrow laser beam into the BAL junction were based upon a *calculated* collimated output beam from the Littrow laser cavity. This calculated collimated output beam relied upon the slow and fast axis divergences that the vendor had specified for the laser diode in the Littrow cavity; i.e. if the vendor specifications were incorrect, than the calculated collimated output beam from the Littrow laser cavity would fail to reflect reality.

I now decided to measure the spatial beam profile of the collimated output from the Littrow laser cavity. A ϕ=50 μm diameter pinhole detector mounted on a translation stage was incrementally swept across the fast and slow axis spatial beam profiles. Measurements across the fast optical axis were made along the peak of the slow axis profile, and measurements across the slow optical axis were made along the peak of the fast axis profile. The spatial intensity profiles along both axes were measured between the Faraday rotator and L_2 at two longitudinal positions, z_1 and $z_2 = z_1 + \Delta z$, with Δz=447.6 mm. The measured spatial intensity profiles are shown in Figure G.7.

The beam radii at z_1 and z_2, $w(z_1)$ and $w(z_2)$, were inferred from the $1/e^2$ amplitude points of the measured spatial intensity profiles, and the beam waist radius between the isolator and L_2, w_o', was numerically calculated along both optical axes as a function of M^2. Referring to Appendix F,

$$\left.\begin{aligned} w(z_2) = w_o'\left[1+\left(z_2 \big/ z_R\right)^2\right]^{1/2} &\Rightarrow \left\{\left[\frac{w(z_2)}{w_o'}\right]^2 - 1\right\}^{1/2} = \frac{M^2\lambda}{\pi w_o'^2}\left(z_1 + \Delta z\right) \\ w(z_1) = w_o'\left[1+\left(z_1 \big/ z_R\right)^2\right]^{1/2} &\Rightarrow \left\{\left[\frac{w(z_1)}{w_o'}\right]^2 - 1\right\}^{1/2} = \frac{M^2\lambda}{\pi w_o'^2} z_1 \end{aligned}\right\}\Rightarrow$$

$$\Rightarrow\left\{\left[\frac{w(z_2)}{w_o'}\right]^2-1\right\}^{1/2}-\left\{\left[\frac{w(z_1)}{w_o'}\right]^2-1\right\}^{1/2}-\frac{M^2\lambda}{\pi w_o'^2}\Delta z=0 \qquad \text{(G.3)}$$

The lens separations were then measured, and the final focused spot size was calculated using the thin-lens, paraxial theory of Gaussian beam transformation; having effectively removed beam truncation in the optical system, I felt that the thin-lens, paraxial theory of Gaussian beam transformation would provide an accurate prediction of the final focused spot size. The calculation assumed that the beam entering L_2 was well collimated (i.e. $s_o' << z_R' \Rightarrow w_o' \approx w'$ at L_2) and predicted a final focused slow axis waist radius that is essentially independent of the slow axis M^2, and a final focused fast axis waist radius that is directly proportional to the fast axis M^2: $w_o''''|_s \approx 13.5$ µm and $w_o''''|_f = 1.0M^2$ µm.

I decided to compare the calculated focused spot size to a measured focused spot size. The BAL was removed from the optical path and the spatial intensity profile of the beam diverging from the final focused waist was measured. The spatial intensity profiles along both the slow and fast optical axes were measured downbeam of the final focus at two longitudinal positions, z_1 and $z_2 = z_1 + \Delta z$, with $\Delta z = 10$ mm. The measured spatial intensity profiles are shown in Figure G.8.

Since the beam profiles were measured in the far-field of the focused spot (i.e. $z_1, z_2 >> z_R''''$), the final focused waist radius along each optical axis could be calculated analytically. Referring to Appendix F,

$$\left.\begin{aligned} w''''(z >> z_R'''') &\cong w_o'''' = M^2\frac{\lambda z}{\pi w_o} \\ \theta = \frac{|w(z_2)-w(z_1)|}{\Delta z} &\cong \frac{w(z)}{z} \end{aligned}\right\} \Rightarrow w_o'''' \cong M^2\frac{\lambda}{\pi}\frac{\Delta z}{|w(z_2)-w(z_1)|} \qquad \text{(G.4)}$$

The waist radii calculated using the spatial intensity measurements of the beam diverging from the final focus were practically identical to the waist radii calculated using the spatial intensity measurements of the collimated input to L_2:

Collimated beam calculations$\Rightarrow$ $w_o''''|_s \approx 13.5$ µm and $w_o''''|_f = 1.0M^2$ µm.

Diverging beam calculations $\Rightarrow$ $w_o''''|_s = 13.7\,M^2$ µm and $w_o''''|_f = 1.1M^2$ µm.

From the measurements and calculations just discussed, I concluded that $M^2 \approx 1$ along the slow optical axis, and that an $M^2 < 2$ along the fast optical axis would result in an acceptable final focused waist along that axis.

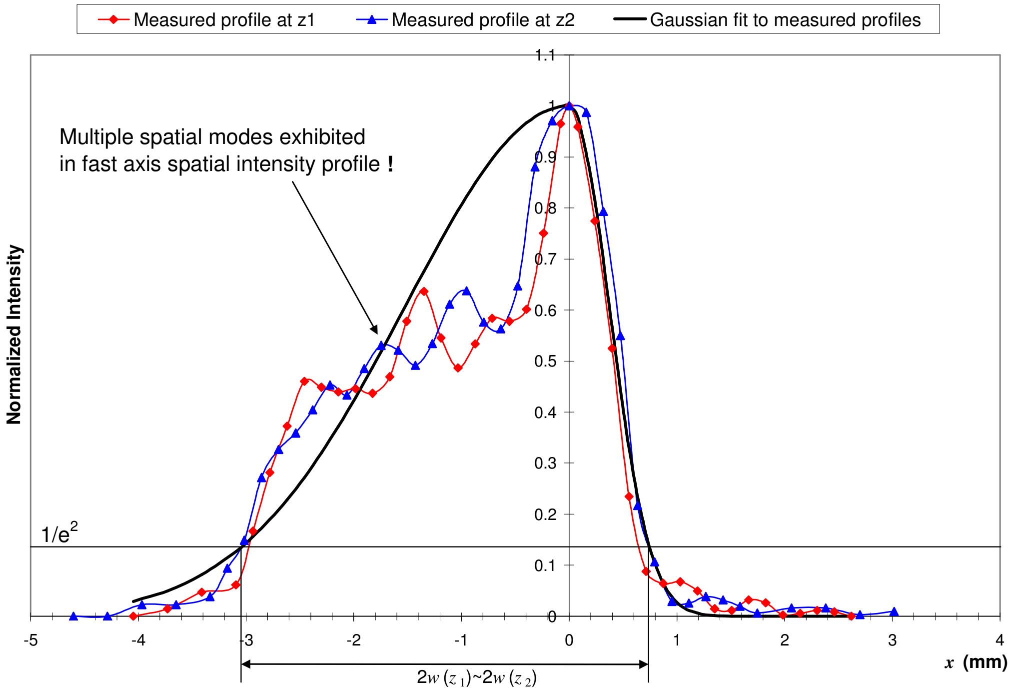

(a) Fast optical axis

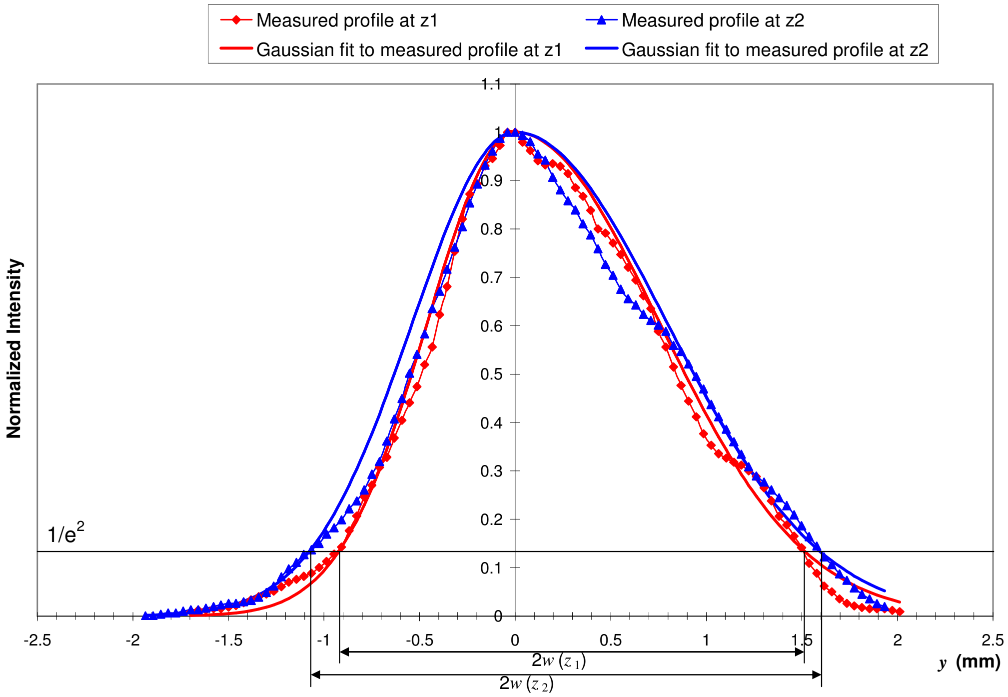

(b)Slow optical axis

Figure G.7 Spatial intensity profiles for the collimated beam entering lens L_2

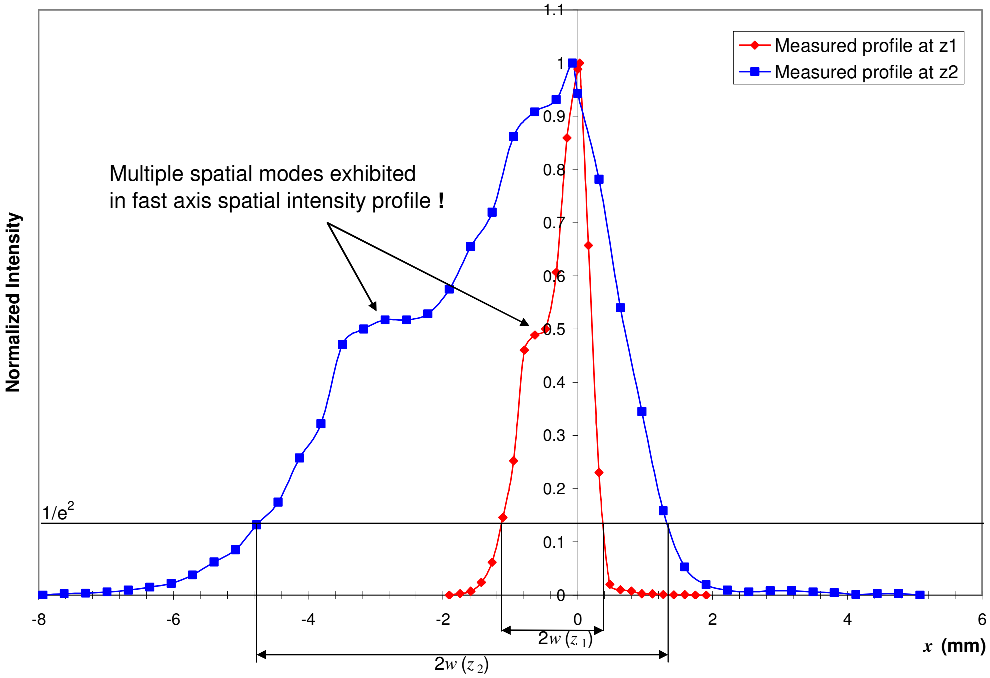

(a) Fast optical axis

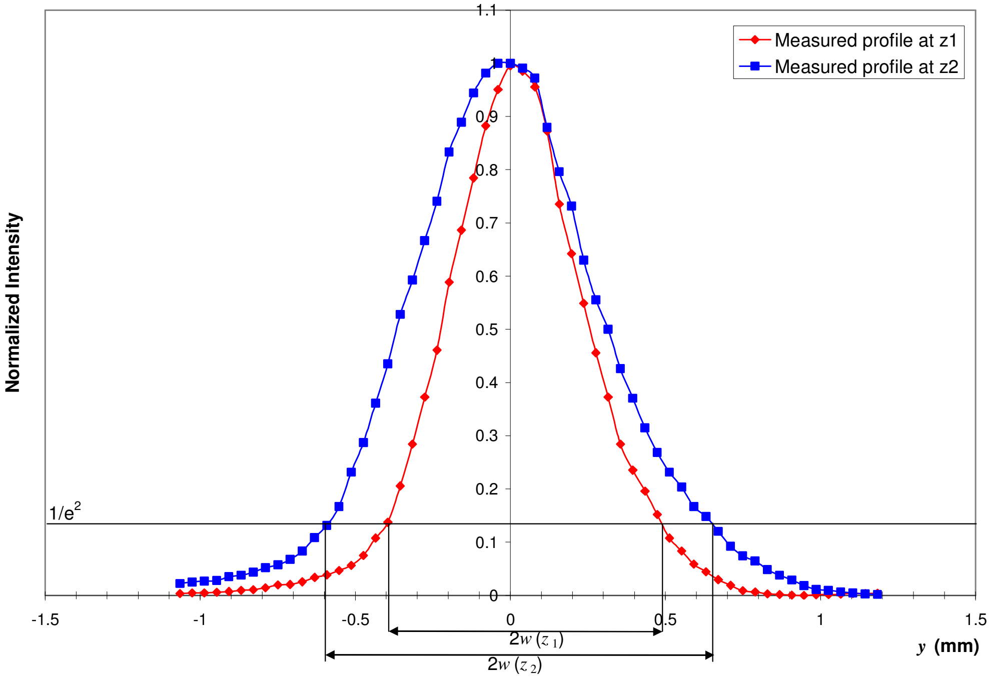

(b) Slow optical axis

Figure G.8 Spatial intensity profiles for the beam diverging from the final focus

In addition to calculating the waist radii along each optical axis, I also calculated the approximate final focus waist location for each optical axis from the measured spatial intensity profiles of the beam diverging from the final focus. This calculation pointed to a problem with both optical designs that I had utilized up to this point: The final focus provided by both designs was highly astigmatic. With the BAL front facet placed at the fast axis focus, the wavefront radius of curvature along the slow axis was ~ −2 mm. To effectively mode-match into an optical waveguide (which a BAL junction essentially is), the beam waist should be at the entrance to the waveguide along both optical axes; i.e. there should be a planar wavefront entering the waveguide. In particular, a negative radius of curvature at the BAL entrance would magnify the detrimental effects of thermal lensing.

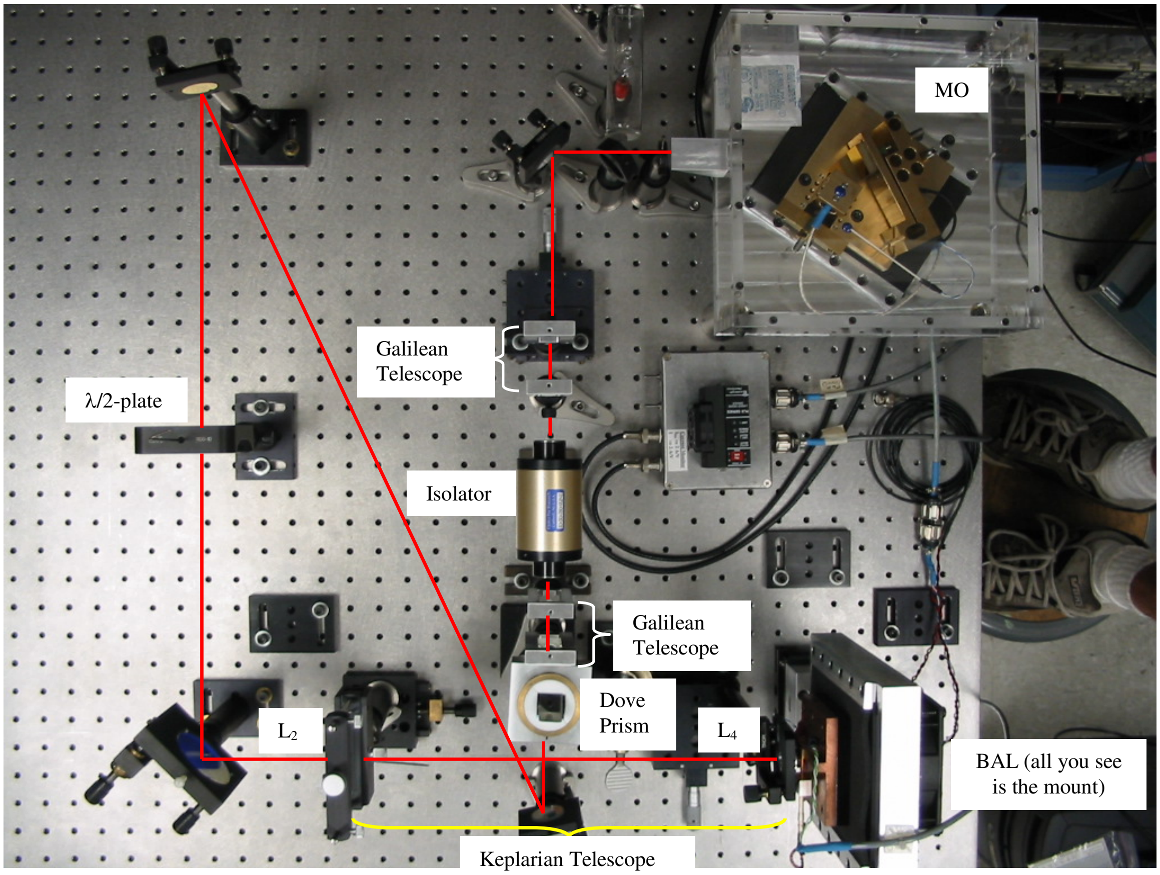

Figure G.9 The third BAL MOPA system

I modified the coupling optics along the slow optical axis to remove the astigmatism in the final focused spot size. Figure G.9 is a picture of this redesigned BAL MOPA system. The negative cylindrical lens, L_3, was removed and an f=300 mm focal length plano-convex cylindrical lens (Melles Griot 01LCP019), L_2, and the final focusing/collimating optic (Melles Griot 06GLC002), L_4, were configured as an afocal (Keplarian) telescope; this was the optical design utilized in all papers reviewed. An injection angle was introduced along the slow optical axis of the BAL by translating the positive cylindrical lens, L_2, parallel to the BAL junction width (i.e. out of the page). The amplified output was diverted to the experiment using a dove prism.

With this third MOPA design, a maximum gain in optical power of 8.3 dB was measured in the amplified output from the BAL; i.e. with a measured power in the final focused spot of P_i=7 mW and operating the BAL at an injection current of I~560 mA, I measured an amplified output power P_o=48 mW on a background of P_{ASE}=28 mW of ASE. The general performance of the third BAL MOPA system was identical to the previous MOPA systems: there was no observed dependence of the output power on injection angle; at high injection currents ASE dominated and a minor temperature dependence was observed in the amplified output power; and the amplified output was observed to spectrally track the Littrow laser cavity.

Though the third BAL MOPA system performed better than the previous two designs, I still felt that I was not effectively coupling the Littrow laser beam into the BAL junction. The third MOPA system exhibited reasonable small signal gain, but also exhibited relatively high levels of ASE. I was concerned that these relatively high levels of ASE would prevent stable operation of the MOPA system; even with 42 dB of isolation between the MO and BAL, the Littrow laser would frequently mode-hop due to ASE coupled into its external cavity. In addition, looking back at Figures G.7a and G.8a we see that the spatial intensity profile along the fast optical axis of the Littrow laser beam exhibits several peaks. The multiple peaks in the measured profile imply that the Littrow laser beam supports multiple spatial modes along its fast optical axis. My intuition told me that these higher order spatial modes along the fast optical axis of the input beam prevented me from attaining a tight enough focus perpendicular to the BAL junction (i.e. along the fast optical axis of the BAL). The final focusing/collimating optic utilized in the third BAL MOPA system is a diffraction limited multiplet that that should be able to focus a collimated BSMI Gaussian beam to a 2.2 μm waist radius. The problem is that that the Littrow laser beam is far from "diffraction limited" along its fast optical axis; i.e. it exhibits multimode behavior.

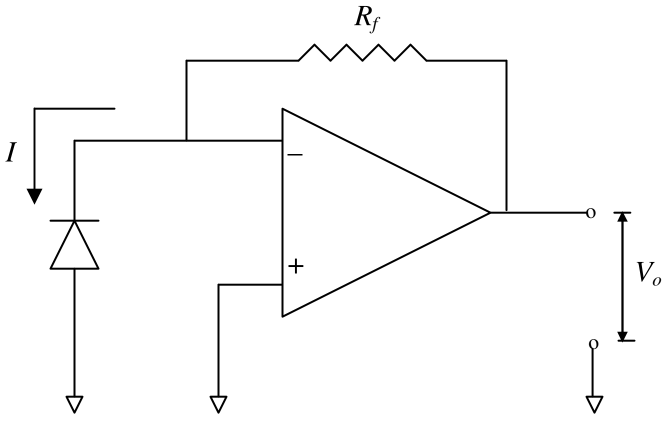

Figure G.10 Trans-impedance amplifier

I considered using the BAL as a photovoltaic detector in order to quantitatively determine the fraction of power at the BAL front facet that was in fact being coupled into the junction; i.e. to determine whether I was overfilling the BAL along its fast optical axis. Optical power input into the BAL generates a current across the p-n junction. I planned on detecting this current using an operational amplifier in a negative feedback trans-impedance configuration, as shown in Figure G.10. The op-amp maintains the BAL at near zero voltage bias, thereby minimizing the dangers of reverse bias breakdown across the BAL junction. The feedback circuit converts the output current from the BAL to a voltage that is directly proportional to the optical power in the BAL junction,

$$V_o = \frac{R_f P}{\eta_D} \tag{G.5}$$

The differential quantum efficiency, η_D, can calculated from the manufacture specified slope efficiency of the BAL, and the feedback resistor is chosen to provide measurable voltage signal (based on the anticipated BAL output current).

I never carried out this investigation – I was afraid of damaging the $1200 BAL – and instead decided to theoretically investigate how the multimode behavior along the fast optical axis of the Littrow laser beam affected the final focused waist radius along this axis. As described in Appendix F, I modeled the higher-order modes measured in the fast axis spatial intensity profile with Hermite-Gaussian functions. After some effort, I was able to derive a relatively good model of the measured spatial intensity profiles, and using the Huygens-Fresnel integral I was then able to analytically calculate the transformed spatial intensity profile at the focused beam waist. This calculation indicated that focusing the fast optical axis of the Littrow laser output to the O(2 μm) beam waist radius required for effective coupling along the fast optical axis of the BAL was simply impossible (or at least highly impractical).

To corroborate this theoretical conclusion I decided to image the front facet of the BAL using the two-lens imaging technique shown in Figure G.11. A pellicle was inserted slightly upbeam from the final focusing/collimating multiplet, L_4, and a lens of focal length F was positioned $2F$ from the focusing/collimating multiplet along the path of the reflected output beam. This configuration resulted in a magnified image of the NF (i.e. the front facet of the BAL) a distance F behind the lens at the plane labeled NF in Figure G.11. In addition, a one-to-one image of the field at L_4 was produced a distance $2F$ behind the lens at the plane labeled FF in Figure G.11.

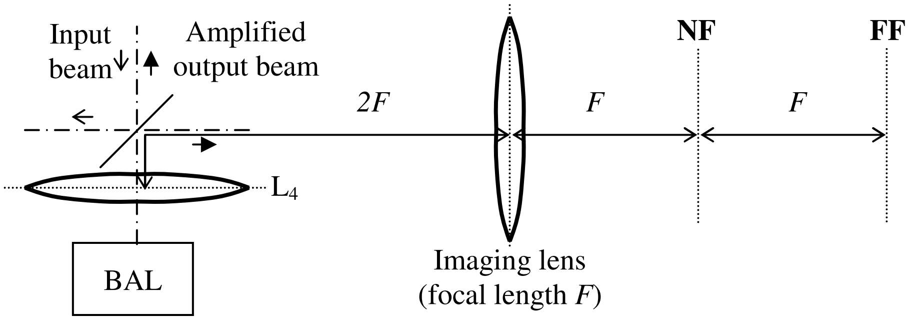

Figure G.11 Two-lens imaging technique

The near-field image that I observed with the two-lens imaging technique clearly indicated that the final focus along the fast axis of the input beam was overfilling the BAL junction height. For instance, with the Littrow laser on and the BAL off, there was a thin, dark stripe with a spot of light surrounding its center in the NF image; the thin, dark stripe is the AR coated front facet of the BAL, and the spot of light is the input beam overfilling the facet height and reflecting off of the BAL mount. The far-field image indicated that I was not effectively mode matching into the BAL junction. With the Littrow laser output coupled into the BAL junction and with the BAL operated at its threshold current, the output beam from the BAL exhibited several amplified lobes on a background of ASE; a strong single lobe with minimal power in ASE should be observed when the input beam is effectively mode matched into the BAL junction [121].

Looking back at Figures G.7b and G.8b we see that the spatial intensity profile along the slow optical axis of the Littrow laser beam is relatively Gaussian. The theoretical and experimental investigations described above convinced me to flip the orientation of the BAL junction 90°, to expand the relatively Gaussian slow optical axis of the collimated Littrow laser beam, and to try and focus this expanded, relatively Gaussian spatial intensity profile to the O(2 μm) waist required for efficient coupling along the fast optical axis of the BAL. The fourth (and final) BAL MOPA system is described in sub-section 4.3.3 (see Figure 4.19).

References

1. E. Mach and P. Salcher, Optische Untersuchung der Luftstrahlen, V98, Sitzungsber. Akad. Wiss. Wien., 1889, pp. 1303-8.
2. H. Sun, “Thin lens equation for a real laser beam with weak lens aperature truncation,” *Opt. Eng.* **37** (11), 1998, pp. 2906-13.
3. A.E. Siegman, Lasers, 1st ed, University Science Books, 1985, pp. 665-7.
4. P. Buchave, “Particle image velocimetry,” in Optical Diagnostics for Flow Processes, Plenum Press, 1994, pp. 247-69.
5. B. S. Rinkevichius, Laser Diagnostics in Fluid Mechanics, 1st ed, Begell House, Inc., 1998, pp. 205-209.
6. R. D. Keane, “Correlation methods of PIV analysis,” in Optical Diagnostics for Flow Processes, Plenum Press, 1994, pp. 271-89.
7. R. J. Adrian, “Image shifting techniques to resolve directional ambiguity in double-pulsed velocimetry,” *Appl. Optics* **25**, 1986, pp. 3855-58.
8. C. C. Landreth and R. J. Adrian, “Electro-optical image shifting for particle image velocimetry,” *Appl. Optics* **27**, 1988, pp. 4216-19.
9. R. D. Keane and R. J. Adrian, “Optimization of particle image velocimeters, Part I. Double pulsed systems,” *Meas. Sci. Technol.* **1**, 1990, pp. 1202-15.
10. R. B. Miles and D. M. Nosenchuck, “Three-dimensional quantitative flow diagnostics,” in Lecture Notes in Engineering 45, Springer:Verlag, 1989, pp. 33-107.
11. S. Watanabe and H. Kato, “Stereo PIV applications to large-scale low-speed windtunnels,” AIAA Paper 2003-0919, 41st AIAA Aerospace Sciences Meeting, Reno, NV, 2003.
12. K. D. Hirsch, “Three dimensional particle velocimetry,” in Optical Diagnostics for Flow Processes, Plenum Press, 1994, pp. 303-18.
13. R. B. Miles and W. R. Lempert, “Quantitative flow visualization in unseeded flows,” *Annu. Rev. Fluid Mech.* **29**, 1997, pp. 285-326.
14. E. Hecht, Optics, 4th ed, Addison Wesley, 2002, pp 56-58,65-66, 86-90, 62-63, 421-425.
15. Ch. Doppler, Abhanglungen, Verlag von W. Endelman, Leipzig, 1907.
16. Y. Yea and H. Cummins, “Localized fluid flow measurements with a He-Ne laser spectrometer,” *Appl. Phys. Lett.* **4**, 1964, pp. 176-78.
17. A. T. Forrester, R. A. Gudmundsen, and P. O. Johnson, “Photo-electric mixing of incoherent light, ” *Phy. Rev.* **99**, 1955, p. 1691.
18. B. S. Rinkevichius, Laser Diagnoztics in Fluid Mechanics, 1st ed, Begell House, Inc., 1998, pp. 101-108.
19. B. S. Rinkevichius, “Analysis of optical Doppler velocimeter operation,” in Physical Optics: Collected Papers if the Moscow Power Engineering Institute, MEI Press, Moscow, 1972, pp. 48-56.
20. B. S. Rinkevichius, Fundamental Principles of Laser Diagnostics of Flow, Dissertation, FIAN, Moscow, 1979.
21. Y. N. Dubnitchev and B. S. Rinkevichius, Methods of Laser Doppler Anemometry, Nauka, Moscow, 1982 (Russian).
22. R. V. Edwards (Ed.), “Report on the special panel on statistical particle bias problems in laser anemometry,” *J. Fluids Eng.* **109**, 1987, pp. 89-93.
23. W. K. George and J. L. Lumley, “The laser Doppler velocimeter and its application to the measurement of turbulence,” *J. Fluid Mech.* **60**, 1973, pp. 312-62.

24. M. Hercher, "The spherical mirror Fabry-Perot interferometer," *Appl. Optics* **5** (7), 1968, pp. 951-66.
25. B. S. Rinkevichius, Laser Diagnoztics in Fluid Mechanics, 1st ed, Begell House, Inc., 1998, pp. 262-65.
26. B. S. Rinkevichius and A. V. Tolkachev, "Optical Doppler flowmeter for gases," *Sov. J. Quantum Electron.* **4** (5), 1975, pp. 1061-63.
27. K. B. Yüceil, M. V. Ötügen, and E. Arik, "Interferometric Rayleigh scattering and PIV measurements in the near field of underexpanded sonic jets," AIAA Paper 2003-0917, 41st AIAA Aerospace Sciences Meeting, Reno, NV, 2003.
28. D. Bivolaru, M. V. Ötügen, A. Tzes, and G. Papadopoulos, "Image processing for interferometric Mie and Rayleigh scattering velocity measurements," *AIAA Journal* **37** (6), 1999.
29. R. G. Seasholtz, J. Panda, and K. A. Elam, "Rayleigh scattering diagnostics for dynamic measurement of velocity fluctuations in high speed jets," AIAA Paper 2001-0847, 39th AIAA Aerospace Sciences Meeting, Reno, NV, 2001.
30. R. S. Clancy and M. Samimy, "Multiple-component velocimetry in high speed flow using planar Doppler velocimetry," AIAA Paper 97-0497, 35th AIAA Aerospace Sciences Meeting, Reno, NV, 1997.
31. S. J. Beresh, S. P. Kearney, C. J. Bourdon, and T. W. Grasser, "Development of a Doppler global velocimeter for a highly-overexpanded supersonic jet," AIAA Paper 2003-0915, 41st AIAA Aerospace Sciences Meeting, Reno, NV, 2003.
32. M. W. Smith and G. B. Northam, "Applications of absorption filter-based Doppler velocimetry to sonic and supersonic jets," *AIAA Journal* **34**, 1996, pp. 434-41.
33. J. Forkey, N. Finkelstein, W. Lempert, and R. Miles, "Demonstration and characterization of filtered Rayleigh scattering for planar velocity measurements," *AIAA Journal* **34**, 1996, pp. 442-48.
34. J. H. Grinstead, N. D. Finkelstein, and W. R. Lempert, "Frequency-locked light scattering: Real-time Doppler velocimetry with closed-loop feedback control", *Appl. Opt.* **37** (9), 1998, pp. 1617-25.
35. J. Crafton, N. M. Messersmith, and J. P. Sullivan, "Filtered Doppler velocimetry: Development of a point system," AIAA Paper 98-0509, 36th AIAA Aerospace Sciences Meeting, Reno, NV, 1998.
36. C. E. Weiman and L. Hollberg, "Using diode lasers for atomic physics," *Rev. Sci. Inst.* **62** (1), 1991, pp. 1-20.
37. Labachelerie, M., Latrasse, C., Kemssu, P., and Cerez, P., "The frequency control of diode lasers", *J. Phys. III France* **2**, 1992, pp. 1557-1589.
38. Stanford Research Systems, Scientific and Engineering Instruments Catalog, 1998-1999.
39. M. Born and E. Wolf, Principles of Optics, 7th (expanded) ed, Cambridge University Press, 1999, pp. 75-115.
40. W. Demtröder, Laser Spectroscopy: Basic Concepts and Instrumentation, 2nd ed, Springer-Verlag, Berlin, 1996.
41. J. D. Jackson, Classical Electrodynamics, 3rd ed., Wiley, New York, 1998.
42. R. B. Miles, W. R. Lempert, and J.N. Forkey, "Laser Rayleigh scattering," *Meas. Sci. Technol.* **12**, 2001, pp. R33-51.
43. J. N. Forkey, "Development and demonstration of filtered Rayleigh scattering – a laser-based flow diagnostic for planar measurement of velocity, temperature and pressure," *PhD. Thesis*, Princeton University MAE Department, 1996.
44. D. R. Bates, "Rayleigh scattering by air," *Planet Space Sci.* **32**, 1984, pp. 785-790.

45. A. Bucholtz, “Rayleigh scattering calculations for the terrestrial atmosphere,” *Appl. Opt.* **34** (15), 1995, pp 2765-2773.
46. A. T. Young, “Rayleigh scattering,” *Phys. Today* **35** (1), 1982, pp. 42-48.
47. A. T. Young, “Rayleigh scattering,” *Appl. Opt.* **20** (4), 1981, pp. 533-535.
48. G. W. Kattawar, A. T. Young, and T. J. Humphreys, “Inelastic scattering in planetary atmosphere. I. The ring effect, without aerosols,” *Astrophys. J.* **243**, 1981, pp. 1049-1057.
49. Hamamatsu Photonics K.K., Photomultiplier Tubes, *Technical Reference*, 1998.
50. D. Bivolaru, P. M. Danehy, J. W. Lee, R. L. Gaffney Jr., L. Richard, and A. D. Cutler, “Single-pulse multi-point multi-component interferometric Rayleigh scattering velocimeter,” AIAA Paper 2006-0836, 44th AIAA Aerospace Sciences Meeting and Exhibit, Reno, NV, 2006, pp. 1-10.
51. Hamamatsu Photonics K.K., *R636-10 PMT (S/N ZJ578) Uniformity Data*, 1999.
52. Melles Griot, “Optical coatings,” The Practical Application of Light Catalog, 1998-present.
53. N. D. Finkelstein, W. R. Lempert, and R. B. Miles, “Narrow linewidth passband filters and UV laser source for rotational Raman imaging,” *SPIA* **3172**, 1997, pp. 656-665.
54. J. N. Forkey, W. R. Lempert, and R. B. Miles, “Corrected and calibrated I_2 absorption model at frequency-doubled Nd:YAG laser wavelengths,” *Appl. Opt.* **36** (27), 1997, pp. 6729-6738.
55. A. R. Jones, “Scattering of electromagnetic radiation in particulate laden fluids,” *Prog. Energy Combust. Sci.* **5**, 1979, pp. 73-96.
56. G. R. Fournier and B. T. N. Evans, “Bridging the gap between the Rayleigh and Thompson limits for spheres and spheroids,” *Appl. Opt.* **32** (30), 1993, pp. 6159-6166.
57. S. Yip and M. Nelkin, “Application of a kinetic model to time-dependent density correlations in fluids,” *Phys. Rev.* **135** (5A), 1964, pp. A1241-A1247.
58. C. D. Boley, Rashmi, R. C. Desai, and G. Tenti, “Kinetic models and Brillouin scattering in a molecular gas,” *Can. J. Phys.* **50**, 1972, pp. 2158-2173.
59. G. Tenti, C. D. Boley, and R. C. Desai, “On the kinetic model description of Rayleigh-Brillouin scattering from molecular gases,” *Can. J. Phys.* **52**, 1974, pp. 285-290.
60. W. Marques Jr. and G. M. Kremer, “Light scattering from extended kinetic models: Monatomic ideal gases,” *Continuum Mech. Thermodyn.* **10**, 1998, pp. 319-329.
61. W. Marques Jr., “Light scattering from extended kinetic models: Polyatomic ideal gases,” *Physica A* **264**, 1999, pp. 40-51.
62. J. N. Forkey, W. R. Lempert, and R. B. Miles, “Accuracy limits for planar measurements of flow field velocity, temperature and pressure using filtered Rayleigh scattering,” *Exp. Fluids* **24**, 1998, pp. 151-162.
63. M. A. Linne, Spectroscopic Measurement: An Introduction to the Fundamentals, Academic Press, Boston, 2002.
64. W. G. Vincenti and C. H. Kruger Jr., Introduction to Physical Gas Dynamics, Krieger, New York, 1982.
65. M. Planck, “On the law of distribution of energy in the normal spectrum,” *Annalen der Physik* **4**, 1901, p. 553.
66. A. A. Radzig, Reference Data on Atoms, Molecules, and Ions, Springer-Verlag, New York, 1985.
67. D. A. Steck, “Rubidium 87 D line data,” rev. 1.6, Los Alamos National Laboratory (avail. online at http://george.ph.utexas.edu/~dsteck/alkalidata/rubidium87numbers.pdf).

68. G. P. Barwood, P. Gill, and W. R. C. Rowley, “Frequency measurements on optically narrowed Rb-stabilized laser diodes at 780 nm and 795 nm,” *Appl. Phys. B* **B53** (3), 1991, pp. 142-147.

69. J. Ye, S. Swartz, P. Jungner, and J. L. Hall, “Hyperfine structure and absolute frequency of the ^{87}Rb $5P_{3/2}$ state,” *Opt. Lett.* **21** (16), 1996, pp. 1280-1282.

70. A. Corney, Atomic and Laser Spectroscopy, Clarendon Press, New York, 1977.

71. E. Arimondo, M. Inguscio, and P. Violino, “Experimental determination of the hyperfine structure in the alkali atoms,” *Rev. Mod. Phys.* **49** (1), 1977, pp. 31-75.

72. U. D. Rapol, A. Krishna, and V. Natarajan, “Precise measurement of hyperfine structure in the $5P_{3/2}$ state of ^{85}Rb,” *Euro. Phys. J. D* **23** (2), 2003, pp. 185-188.

73. S. Bize, Y. Sortais, M. S. Santos, C. Mandache, A. Clairon, and C. Salomon, “High-accuracy measurement of the ^{87}Rb ground-state hyperfine splitting in an atomic fountain,” *Europhys. Lett.* **45** (5), 1999, pp. 558-564.

74. W. F. Buell, “Semiconductor laser experiments with Rb vapor with applications to fundamental and applied physics,” *Ph.D. Dissertation*, The University of Texas at Austin, 1993.

75. A. Gallagher and E. L. Lewis, “Determination of the vapor pressure of rubidium by optical absorption,” *J. Opt. Soc. Am.* **63** (7), 1973, pp. 864-869.

76. A. N. Nesemeyanov, Vapor Pressure of the Chemical Elements, Elsevier Pub. Co., New York, 1963.

77. P. J. Mohr and B. N. Taylor, “CODATA recommended values of the fundamental physical constants: 2002,” *Rev. Mod. Phys.* **77**, 2005, pp. 1-107 (avail. online at http://physics.nist.gov/constants).

78. D. R. Lide ed., CRC Handbook of Chemistry and Physics, 81st ed., CRC Press, Boca Raton, 2000.

79. M. P. Bradley, J. V. Porto, S. Rainville, J. K. Thompson, and D. E. Pritchard, “Penning trap measurements of the masses of ^{133}Cs, ^{87,85}Rb, and ^{23}Na with uncertainties ≤0.2 ppb,” *Phys. Rev. Lett.* **83** (22), 1999, pp. 4510-4513.

80. U. Volz and H. Schmoranzer, “Precision lifetime measurements on alkali atoms and on helium by beam-gas-laser spectroscopy,” *Physica Scripta T* **T65**, 1996, pp. 48-56.

81. A. G. Mitchell and M. W. Zemansky, Resonance Radiation and Excited Atoms, University Press, Cambridge (England), 1961.

82. E. A. Whittaker, P. Pokrowsky, W. Zapka, K. Roche, and G. C. Bjorklund, “Improved laser technique for high sensitivity atomic absorption spectroscopy in flames,” *J. Quant. Spectrosc. Radiat. Transfer* **30**, 1983, pp. 289-296.

83. D. T. Cassidy and J. Reid, “Atmospheric pressure monitoring of trace gases using tunable diode lasers,” *Appl. Opt.* **21**, 1982, pp. 1186-1190.

84. F. Slemr, G. W. Harris, D. R. Hastie, G. I. Mackay, and H. I. Schiff, “Measurement of gas phase hydrogen peroxide in air by tunable diode laser absorption spectroscopy,” *J. Geophys. Res.* **91**, 1986, pp. 5371-5378.

85. P. Pokrowsky, W. Zapka, F. Chu, and G. C. Bjorklund, “High frequency wavelength modulation spectroscopy with diode lasers,” *Opt. Comm.* **44**, 1983, ,pp. 175-179.

86. L. G. Wang, D. A. Tate, H. Riris, and T. F. Gallagher, “High-sensitivity frequency-modulation spectroscopy with GaAlAs diode laser,” *J. Opt. Soc. Am. B* **6**, 1989, pp. 871-876.

87. D. M. Bruce and D. T. Cassidy, “Detection of oxygen using short-extended-cavity GaAs semiconductor diode lasers,” *Appl. Opt.* **29**, 1990, pp.1327-1332.

88. M. Gehrtz, G. C. Bjorklund, and E. A. Whittaker, "Quantum-limited laser frequency-modulation spectroscopy," *J. Opt. Soc. Am. B* **2**, 1985, pp. 1510-1526.
89. G. C. Bjorklund and M. D. Levenson, "Sub-Doppler frequency-modulation spectroscopy of I_2," *Phys. Rev. A* **24**, 1981, pp. 166-169.
90. C. B. Carlisle, D. E. Cooper, and H. Preier, "Quantum noise-limited FM spectroscopy with a lead-salt diode laser," *Appl. Opt.* **28**, 1989, pp. 2567-2576.
91. P. Werle, F. Slemr, M. Gehrtz, and C. Bräuchle, "Quantum-limited FM-spectroscopy with a lead-salt diode laser," *Appl. Phys. B* **49**, 1989, pp. 99-108.
92. E. C. Rea and R. K. Hanson, "Rapid laser-wavelength modulation spectroscopy used as a fast temperature measurement technique in hydrocarbon combustion," *Appl Opt.* **27**, 1988, pp. 4454-4464.
93. A. Y. Chang, M. D. DiRosa, D. F. Davidson, and R. K. Hanson, "Rapid tuning cw laser technique for measurement of gas velocity, temperature, pressure, density, and mass flux using NO," *Appl. Opt.* **30**, 1991, pp. 3011-3022.
94. M. Cardona, Modulation Spectroscopy, Supplement 11 of *Solid State Physics*, F. Seitz, D. Turnbull, and H. Ehrenreich eds., Academic, New York, 1969, pp. 89-115.
95. E. D. Hinkley and P. L. Kelley, "Detection of air pollutants with tunable diode lasers," *Science* **171**, 1971, pp. 635-639.
96. E. I. Moses and C. L. Tang, "High-sensitivity laser wavelength-modulation spectroscopy," *Opt. Lett.* **1**, 1977, pp. 115-117.
97. P. Pokrowsky and W. Herrmann, "Sensitive detection of hydrogen chloride by derivative spectroscopy with a diode laser," in Laser Spectroscopy for Sensitive Detection, J. A. Gelbwachs ed., *Proc. Soc. Photo-Opt. Instrum.* **286**, 1981, pp 33-36.
98. G. C. Bjorklund, "Frequency-modulation spectroscopy: a new method for measuring weak absorptions and dispersions," *Opt. Lett.* **5**, 1980, pp. 15-17.
99. J. L. Hall, L. Hollberg, T. Baer, and H. G. Robinson, "Optical heterodyne saturation spectroscopy," *Appl. Phys. Lett.* **39**, 1981, pp. 680-682.
100. J. A. Silver, "Frequency modulation spectroscopy for trace species detection: theory and comparison among experimental methods," *Applied Optics* **31**, 1992, p. 707-716.
101. J. M. Supplee, E. A. Whittaker, and W. Lenth, "Theoretical description of frequency modulation and wavelength modulation spectroscopy," *Appl. Opt.* **33** (27), 1994, pp. 6294-6302.
102. L. C. Philippe and R. K. Hanson, "Laser diode wavelength-modulation spectroscopy for simultaneous measurement of temperature, pressure, and velocity in shock-heated oxygen flows," *Appl. Opt.* **32** (30), 1993, pp. 6090-6103.
103. J. Reid and D. Labrie, "Second-harmonic detection with tunable diode lasers – Comparison of experiment and theory," *Applied Physics B* **26**, pp. 203-210 (1981).
104. R. A. Serway and J. W. Jewett, Physics for Scientists and Engineers, Brooks/Cole, 2003.
105. Hamamatsu Photonics K.K., Photomultiplier Tubes, Japan, Oct. 1998.
106. Hamamatsu Photonics K.K., Photomultiplier Tubes: Basics and Applications, Toshikazu Hakamata ed., 2nd ed., Apr. 1999 (3rd ed. avail. online at http://sales.hamamatsu.com/assets/applications/ETD/pmt_handbook_complete.pdf).
107. P. Horowitz and W. Hill, The Art of Electronics, 2nd ed., Cambridge University Press, UK, 1999.
108. J. J. Mach, "Diode laser velocimetry using modulated filtered Rayleigh scattering," *MS Thesis*, The University of Texas at Austin, 1998.

109. J. J. Mach and P. L. Varghese, “Velocity measurements using filtered Rayleigh scattering of near-IR diode lasers,” AIAA Paper 98-0510, 36th AIAA Aerospace Sciences Meeting, Reno, NV (1998).
110. Melles Griot Product Catalog, The Practical Application of Light, 2007, pp. 1.27-1.28 (avail. online at http://www.mellesgriot.com).
111. D. C. O’Shea, Elements of Modern Optical Design, Wiley, New York, 1985.
112. D. Malacara and Z. Malacara, Handbook of Lens Design, Marcel Dekker, New York, 1994.
113. K. B. MacAdam, A. Steinbach, and C. Wieman, “A narrow-band tunable diode laser system with grating feedback, and a saturated absorption spectrometer for Cs and Rb,” *Am. J. Phys.* **60** (12), pp. 1098-1111 (1992).
114. L. Ricci, M. Weidemüller, T. Esslinger, A. Hemmerich, C. Zimmermann, V. Vuletic, W. König, and T. W. Hänsch, “A compact grating-stabilized diode laser system for atomic physics,” *Optics Comm.* **117**, pp. 541-549 (1995).
115. T. Kiguchi, A. Uematsu, M. Kitano, and H. Ogura, “Grating External Cavity Diode Lasers with Broad Tunable Range and Narrow Spectral Linewidth for High-Resolution Spectroscopy,” *Jpn. J. Appl. Phys.* **35**, pp. 5890-5895 (1996).
116. C. Wieman, G. Flowers, and S. Gilbert, “Inexpensive laser cooling and trapping experiment for undergraduate laboratories,” *Am. J. Phys.* **63** (4), pp. 317-330 (1995).
117. W. R. Trutna, Jr. and P. Zorabedian, “Research on External-Cavity Lasers,” Hewlett-Packard Journal, pp. 35-38 (1993).
118. K. Gibble and W. Swann (Joint Institute for Laboratory Astrophysics, Univ. of Colorado, Boulder), *Private Communication*.
119. K. C. Harvey and C. J. Myatt, "External-cavity diode laser using grazing-incidence diffraction grating," *Optics Letters* **12**, pp. 910-912 (1991).
120. P. McNicholl and H. J. Metcalf, “Synchronous cavity mode and feedback wavelength scanning dye laser oscillators with gratings,” *Applied Opitcs* **24**, pp. 2757-2761 (1985).
121. G. L. Abbas, S. Yang, V. W. S. Chan, and J. G. Fujimotot, “Injection behavior and modeling of 100 mW broad area diode lasers,” *IEEE J. Quantum Elec.* **24** (4), pp. 609-617 (1988).
122. L. Goldberg and M. K. Chun, “Injection locking characteristics of a 1W broad stripe laser diode,” *Appl. Phys. Lett.* **53** (20), pp. 1900-1902 (1988).
123. I. Shvarchuck, K. Dieckmann, M. Zielonkowski, J. T. M. Walraven, “Broad-area diode-laser system for a rubidium Bose-Einstein condensation experiment,” *Appl. Phys. B* **71**, pp. 475-480 (2000).
124. M. Praeger, V. Vuletic, T. Fischer, T. W. Hänsch, and C. Zimmermann, “A broad emitter diode laser system for lithium spectroscopy,” *Appl. Phys. B* **67**, pp. 163-166 (1998).
125. A. C. Fey-den Boer, H. C. W. Beijerinck, and K. A. H. van Leeuwen, “High-power broad-area diode lasers for laser cooling,” *Appl. Phys. B* **64**, pp. 415-417 (1997).
126. T. Pawletko, M. Houssin, M. Knoop, M. Vedel, and F. Vedel, “High power broad-area diode laser at 794 nm injected by an external cavity laser,” *Optics Comm.* **174**, pp. 223-229 (2000).
127. G. C. Dente and M. L. Tilton, “Modeling broad-area semiconductor optical amplifiers,” *IEEE J. Quan. Elec.* **29** (1), pp. 76-88 (1993).
128. E. Gehrig, B. Beier, K. –J. Boller, R. Wallenstein, “Experimental characterization and numerical modeling of an ALGaAs oscillator broad area double pass amplifier system,” *Appl. Phys. B* **66**, pp. 287-293 (1998).

129. L. Goldberg and J. F. Weller, "Broad-area high-power semiconductor optical amplifier," *Appl. Phys. Lett.* **58** (13), pp. 1357-1359 (1991).
130. L. Goldberg D. Mehuys, M. R. Surette, and D. C. Hall, "High-power, near-diffraction-limited large-area traveling-wave semiconductor amplifiers," *IEEE J. Quan. Elec.* **29** (6), pp. 2028-2043 (1993).
131. M. D. Greenberg, Foundations of Applied Mathematics, Prentice Hall, NJ, 1978.
132. J. C. Maxwell, "On physical lines of force," *Philosophical Magazine* **21**, 1861 (avail. online at http://vacuum-physics.com/Maxwell/maxwell_oplf.pdf).
133. J. C. Maxwell, "A dynamical theory of the electromagnetic field," Philos. Trans. Roy. Soc. 155, 1865, pp. 459-512 (avail. online at http://www.zpenergy.com/downloads/ Maxwell_1864_1.pdf, _2.pdf, _3.pdf, _4.pdf, _5.pdf, _6.pdf).
134. H. A. Lorentz, "Concerning the relation between the velocity of propagation of light and the density and composition of media," 1878, in H. A. Lorentz Collected Papers, Vol. II, P. Zeeman and A. D. Fokker ed., Martinus Nijhoff, The Hague, 1936, pp. 79-80.
135. Hamamatsu Photonics K.K., *Photomultiplier Tubes, R636-10, R758-10, Technical Data*, Apr. 1993.
136. D. E. Cooper and R. E. Warren, "Frequency modulation spectroscopy with lead-salt diode lasers: a comparison of single-tone and two-tone techniques," *Appl. Opt.* **26** (17), 1987, pp. 3726-3732.
137. M. Abramowitz and I. A. Stegun eds., Handbook of Mathematical Functions, Dover, New York, 1972.
138. S. A. Self, "Focusing of spherical Gaussian beams," *Appl. Opt.* **22** (5), pp.658-661 (1983).
139. H. Sun, "Thin lens equation for a real laser beam with weak lens aperture truncation," *Opt. Eng.* **37** (11), pp. 2906-2913 (1998).
140. P. Belland and J. P. Crenn, "Changes in the characteristics of a Gaussian beam weakly diffracted by a circular aperture," *Appl. Opt.* **21** (3), pp. 522-527 (1982).

Vita

Jeremy James Jagodzinski was born in Milwaukee, WI on April 6, 1973, the son of Kathie Carlson-Tripp and James Allen Jagodzinski. He was always loved, nurtured, and encouraged to attend college and upon completing his work at Homestead High School, Mequon, WI in 1991 he entered the Department of Aerospace Engineering at the University of Texas in Austin, TX. He received the degree of Bachlor of Science from the University of Texas in May 1996. After working two years as a measurement while drilling (MWD) engineer for Anadrill-Schlumberger, he returned to the University of Texas in August 1998 to pursue a doctorate in aerospace engineering.

Permanent Address: 5504 Avenue H, Austin, TX 78751

This dissertation was typed by the author.